

A STUDY ON THE STRESS-STRAIN BEHAVIOR OF RAILROAD BALLAST  
MATERIALS BY USE OF PARALLEL GRADATION TECHNIQUE

A THESIS SUBMITTED TO  
THE GRADUATE SCHOOL OF NATURAL AND APPLIED SCIENCES  
OF  
THE MIDDLE EAST TECHNICAL UNIVERSITY

BY

MUSTAFA KAYA

IN PARTIAL FULFILLMENT OF THE REQUIREMENTS FOR THE DEGREE  
OF  
DOCTOR OF PHILOSOPHY  
IN  
THE DEPARTMENT OF CIVIL ENGINEERING

JUNE 2004

Approval of the Graduate School of Natural and Applied Sciences

---

Prof. Dr. Canan ÖZGEN  
Director

I certify that this thesis satisfies all the requirements as a thesis for the degree of Doctor of Philosophy.

---

Prof. Dr. Erdal ÇOKÇA  
Head of Department

This is to certify that we have read this thesis and that in our opinion it is fully adequate, in scope and quality, as a thesis for the degree of Doctor of Philosophy.

---

Prof. Dr. M. Yener ÖZKAN  
Supervisor

Examining Committee Members

Prof. Dr. Orhan EROL (C.E.) \_\_\_\_\_

Prof. Dr. M. Yener ÖZKAN (C.E.) \_\_\_\_\_

Prof. Dr. Erdal ÇOKÇA (C.E.) \_\_\_\_\_

Prof. Dr. Reşat ULUSAY (HACETTEPE U.) \_\_\_\_\_

Assoc. Prof. Dr. Levent TUTLUOĞLU (MINE) \_\_\_\_\_

**I hereby declare that all information in this document has been obtained and presented in accordance with academic rules and ethical conduct. I also declare that, as required by these rules and conduct, I have fully cited and referenced all material and results that are not original to this work.**

Name, Last name : Mustafa KAYA

Signature :

## **ABSTRACT**

### **A STUDY ON THE STRESS-STRAIN BEHAVIOR OF RAILROAD BALLAST MATERIALS BY USE OF PARALLEL GRADATION TECHNIQUE**

KAYA, Mustafa

Ph.D., Department of Civil Engineering

Supervisor: Prof. Dr. M. Yener ÖZKAN

June 2004, 328 pages

The shear strength, elastic moduli and plastic strain characteristics of scaled-down ballast materials are investigated by use of the parallel gradation technique. Uniformly graded ballast materials chosen for the investigation are limestone, basalt and steel-slag. Steel-slag is a byproduct material of Ereğli Iron and Steel Works, which is suitable to meet the durability test requirements as well as the electrical resistivity and the waste contaminants regulatory level. Conventional triaxial testing at a strain rate of 0.4 mm/min is used to obtain these characteristics for the scaled-down materials with a diameter of 100 mm specimen under a confining stress of 35 kPa, 70 kPa and 105 kPa; whereas that of only 35 kPa is used to characterize the accumulated plastic strain.

The angle of internal friction,  $\phi$ , and the apparent cohesion,  $c$ , may be conservatively taken to be  $42^\circ$  and 35 kPa for all materials. The elastic moduli values for all materials may be predicted within an adequate estimate for the engineering purposes by using the power law parameters,  $K$  and  $n$ , determined for L-9.5 ( $D_{50} = 12.7$  mm), the coarsest gradation tested for limestone.  $K$  with a reference pressure,

$p_r = 1$  kPa and  $n$  values for L-9.5, respectively, are 4365 and 0.636 for initial; 8511 and 0.419 for secant; 25704 and 0.430 for unloading-reloading elastic moduli.

The unloading-reloading moduli increased, as the number of cycles increased. An increase in unloading-reloading modulus at  $N = 20$  obtained was roughly 15% for scaled-down limestone; 10% for the basalt; and 5% for the steel-slag.

The plastic strain after first cycle,  $\varepsilon_1$ , and the plastic strain coefficient,  $C$  can be represented as a function of mean particle size for each material type. For the limestone, basalt and steel-slag prototype size,  $D_{50} = 45$  mm,  $\varepsilon_1$  values of 0.59, 0.43 and 0.75 and  $C$  values of 0.54, 1.42 and 0.74 are predicted, respectively.

**Key Words:** Ballast, Coarse-Grained Soil, Elastic Modulus, Parallel Gradation Technique, Plastic Strain, Shear Strength, Slag, Triaxial Test

## ÖZ

### PARALEL TANE ÇAPI DAĞILIMI YÖNTEMİYLE DEMİRYOLU BALAST MALZEMELERİNİN GERİLME-BİRİM DEFORMASYON DAVRANIŞI ÜZERİNE BİR ÇALIŞMA

KAYA, Mustafa

Doktora, İnşaat Mühendisliği Bölümü

Tez Yöneticisi: Prof. Dr. M. Yener ÖZKAN

Haziran 2004, 328 sayfa

Gerçeğinden daha küçük tane çapında balast malzemelerinin kayma dayanımı, elastik modülleri ve plastik birim boy değişimi özellikleri, paralel tane çapı dağılımı tekniğine dayalı olarak incelenmiştir.

Balast malzemeleri üniform tane çapı dağılımlı kireçtaşı, bazalt ve çelik-cürufudur. Çelik-cürufu, dayanıklılık deneyindeki gerek şartları, elektriksel direnç ve çevresel atık değer seviyelerini karşılamaktadır. Yukarıda değinilen mühendislik özelliklerinin incelenmesinde 100 mm çapındaki örneklerin deneyini yapabilen 0.4 mm/dakika hızında konvansiyonel üç eksenli deney ünitesi kullanılmıştır. Örneklerin deneyleri 35 kPa, 70 kPa ve 105 kPa çevre basıncı altında yapılmıştır. Ancak tekrarlı yüke bağlı olarak oluşan plastik özelliklerin belirlenmesinde sadece 35 kPa çevre basıncı kullanılmıştır.

Kullanılan bütün malzemeler için, emniyetli tarafta olarak, içsel sürtünme açısı  $42^\circ$  ve görünürdeki kohezyon 35 kPa alınabilir. Diğer taraftan, kullanılan bütün

malzemeler için elastik modül değerleri, deneyi yapılan en büyük çaplı L-9.5 ( $D_{50} = 12.7$  mm) kireçtaşı için elde edilen K ve n parametreleriyle mühendislik açısından yeterli bir şekilde öngörülebilir. L-9.5 için, 1 kPa referans basınca göre hesaplanan K değerleri ve n değerleri sırasıyla, başlangıç elastik modül için 4365, 0.636; sekant elastik modül için 8511, 0.419; ve boşaltma-tekrar yükleme elastik modül için 25704, 0.430 olarak belirlenmiştir.

Boşaltma-tekrar yükleme elastik modül, devir sayısı arttıkça artış göstermektedir.  $N = 20$  için, boşaltma-tekrar yükleme elastik modül gerçeğinden daha küçük tane çapında kireçtaşı örnekler için , kabaca %15; bazalt için %10; ve çelik-cürufu için %5' dir.

İlk devirden sonraki plastik birim boy değişimi,  $\epsilon_1$ , ve plastik birim boy değişim katsayısı, C, her bir malzeme için ortalama tane çapına bağlı bir fonksiyon olarak gösterilebilir. Prototip tane çapındaki,  $D_{50} = 45$  mm, kireçtaşı, bazalt ve çelik-cürufu  $\epsilon_1$  değerleri sırasıyla, 0.59, 0.43 ve 0.75; ve C değerleri sırasıyla 0.54, 1.42 ve 0.74 olarak öngörülebilir.

Anahtar Kelimeler: Balast, İri taneli Zemin, Elastik Modül, Paralel Tane Çapı Dağılımı Yöntemi, Plastik Birim Boy Değişimi, Kayma Dayanımı, Cüruf, Üç Eksenli Sıkışma Deneyi

To my wife and daughter, Emine and Zeynep Hande,  
My parents, and to my lovely brother, Soner,  
Without whose love and support this would not have been possible.

## ACKNOWLEDGEMENTS

I wish to express my gratitude to certain people who have given support, direction, and encouragement over the course of this research initiating back from Boulder, Colorado that without whose contributions this dissertation would not exist.

First of all, I would like to thank my mother and father for their enduring love and support. I would also like to thank my brothers for their support, in particular to Süleyman who founded my mathematics background on which I built my engineering career.

Special gratitude goes to Dr. Hon-Yim Ko, University of Colorado at Boulder, who has given me the essence of Soil Mechanics. My special gratitude is also due to Dr. Erhan Karaesmen for his support, especially sharing my “hard times”, and assisting me in obtaining admission to the Civil Engineering Department at METU, Ankara.

I would like to express my deep appreciation to my advisor Dr. M. Yener Özkan who has been a source of constant support and encouragement throughout my stay at METU. This research and degree could not have been accomplished without his gentle guidance and unfailing support. I would also like to thank Dr. Erdal Çokça and Dr. Levent Tutluoğlu for serving on various examining committees.

Appreciation is due to Dr. Ülkü Yetiş for allowing me the use of environmental engineering laboratory with Mr. Kemal Demirtaş, whom I am grateful, to perform leachate analysis on the steel-slag, and for her valuable comments on this material. Thanks extended to Mr. Orhan Çevik, Head of Structural Project Division, Mr. Hayrettin Çetiner, Head of Variants and Group Division, and

Mr. Metin Öz, Geological Engineer, of Turkish Railways for providing me the limestone and basalt materials, and for allowing me the use of Turkish Railways Laboratory to perform the ballast characterization tests. Thanks also extended to Mr. Erol Baş, Head of Raw Materials and Steel Production, and Dr. Birol Sönmez, R & D Engineer, of Ereğli Iron and Steel Works for supplying the steel-slag material. Thanks are also due to Dr. Akın Geven, Coordinator of Core Data Bank at Mineral Research and Exploration, for mineralogical analysis of the limestone and basalt materials.

Gratitude is also due to Mr. Ali Bal and Mr. Mehmet Ekinci for their cooperation and for constantly providing me “distilled and de-aired water”. Special thanks are due to my colleagues Ahmet Tüken, Mehmet Özyazıcıoğlu and M. Tolga Yılmaz for their friendship and being there during my “crucial decision”. I am also very grateful to my colleague M. Yavuz Şengör for his friendship and valuable contribution to correcting the draft. Financial support provided by METU under Grant No. BAP-2003-03-03-02 is acknowledged with appreciation.

Finally, I would like to thank my dear wife, Emine, who postponed her medical licensing examination for nothing but only for my research and degree. Also, deep appreciation goes to her for still attempting to be a good mother and wife after returning home from a hard working day. It must only be love, because no one in their straight mind would have done it otherwise.

## TABLE OF CONTENTS

ABSTRACT.....	iv
ÖZ.....	vi
DEDICATION.....	viii
ACKNOWLEDGEMENTS.....	ix
TABLE OF CONTENTS.....	xi
LIST OF TABLES.....	xv
LIST OF FIGURES.....	xix
LIST OF SYMBOLS.....	xxvi
CHAPTER	
1 INTRODUCTION	1
1.1 Problem Statement and Justification.....	1
1.2 Objective and Scope of Work.....	5
2 A REVIEW OF RELEVANT LITERATURE	7
2.1 Introduction.....	7
2.2 Notation.....	7
2.3 Design Considerations in Railway Track Foundation.....	7
2.4 Effects on Railroad Track Performance of Ballast Characteristics.....	9
2.4.1 Resilient Modulus.....	9
2.4.2 Shear Strength in Relation to Plastic Strain.....	12
2.5 Stress States within Ballast.....	14
2.6 Stress Levels in the Ballast Layer.....	16
2.6.1 Vertical Stress.....	16
2.6.2 Horizontal Stress.....	17

2.7	Stress-Strain and Strength Characteristics of Ballast.....	19
2.7.1	Effect of Particle Size on Stress-Strain and Strength Characteristics of Ballast.....	27
2.7.2	Effect of Gradation on Stress-Strain and Strength Characteristics of Ballast.....	41
3	CHARACTERIZATION TESTS OF BALLASTS	44
3.1	Ballast.....	44
3.1.1	Description of Materials.....	44
3.1.1.1	Mineralogical Description of Materials.....	46
3.1.2	Results of Characterization Tests.....	49
4	LABORATORY TESTING PROGRAM	53
4.1	Description of Parallel Gradation Technique.....	53
4.1.1	Description of Scaled-Down Materials.....	54
4.1.2	Results of Characterization Tests.....	54
4.1.2.1	Results of Particle Shape Analysis.....	58
4.2	Density Determination of Samples Tested and Testing Program.....	72
4.3	Triaxial Testing Apparatus.....	75
4.4	Sample Preparation and Test Procedure.....	75
5	TRIAxIAL TEST RESULTS OF SCALED-DOWN MATERIALS BY USE OF PARALLEL GRADATION TECHNIQUE	84
5.1	Introduction.....	84
5.2	Statistical Analysis of Data.....	85
5.2.1	Statistical Analysis of Shear Strength Parameters...	85
5.2.2	Statistical Analysis of Elastic Modulus.....	88
5.3	Peak Shear Strength Trends for Scaled-Down Limestone .....	88
5.4	Peak Shear Strength Trends for Scaled-Down Basalt.....	94
5.5	Peak Shear Strength Trends for Scaled-Down Steel-Slag.....	99

5.6	Comparison of Peak Shear Strength Trends for Scaled-Down Limestone, Basalt and Steel-Slag .....	104
5.7	Effect of Water on Peak Shear Strength of Scaled-Down Materials.....	105
5.8	Effect of Gradation on Peak Shear Strength of Scaled-Down Limestone.....	109
5.9	Elastic Moduli Trends.....	111
5.9.1	Introduction to the Elastic Moduli Studied.....	111
5.9.2	Statistical Analysis of Elastic Moduli.....	114
5.9.3	Elastic Moduli Trends for Scaled-Down Limestone	115
5.9.4	Elastic Moduli Trends for Scaled-Down Basalt.....	138
5.9.5	Elastic Moduli Trends for Scaled-Down Steel-Slag.	158
5.10	Comparison for Elastic Moduli of Scaled-Down Limestone, Basalt and Steel-Slag .....	172
5.11	Effect of Water on Elastic Moduli of Scaled-Down Materials..	177
5.12	Effect of Gradation on Elastic Moduli of Scaled-Down Limestone.....	181
5.13	Effect of Repeated Loading on Elastic Moduli of Scaled-Down Materials.....	184
6	<b>HYPERBOLIC MODELING AND PLASTIC STRAIN BEHAVIOR OF SCALED-MATERIALS</b>	187
6.1	Introduction.....	187
6.2	Hyperbolic Modeling of Scaled-Down Ballast Materials.....	188
6.3	Accumulated Plastic Strain Trends for the Materials.....	205
6.3.1	Accumulated Plastic Strain Trends for Scaled-Down Limestone.....	205
6.3.2	Accumulated Plastic Strain Trends for Scaled-Down Basalt.....	210
6.3.3	Accumulated Plastic Strain Trends for Scaled-Down Steel-Slag.....	215
6.4	Comparison for Accumulated Plastic Strain of Scaled-Down	

	Limestone, Basalt and Steel-Slag.....	220
6.5	Effect of Gradation on Plastic Strain of Scaled-Down Limestone.....	221
7	SUMMARY AND CONCLUSIONS	223
7.1	Summary.....	223
7.2	Conclusions.....	224
7.3	Recommendation.....	228
	REFERENCES	229
	APPENDICES	
	Appendix A: Triaxial Test Results For Scaled-Down Limestone	237
	Appendix B: Triaxial Test Results For Scaled-Down Basalt	282
	Appendix C: Triaxial Test Results For Scaled-Down Steel-Slag	304
	VITA	328

## LIST OF TABLES

TABLES	Page
2.1 Physical characteristics of basaltic ballast (after Indraratna et al., 1998)	26
2.2 Grain size characteristics of basaltic ballast (after Indraratna et al., 1998)	27
2.3 Comparison of axial strain at different shear stress levels (after Janardhanam & Desai, 1983).....	34
2.4 Comparison of axial strain at various shear stress levels (after Kaya et al., 1997).....	38
2.5 Angle of internal friction values for 100 mm and 150 mm diameter quartzite specimens (after Kaya et al., 1997).....	39
3.1 Chemical analysis of ERDEMIR steel-slag (TUBITAK, 2002).....	48
3.2 Qualitative mineralogical analysis of ERDEMIR steel-slag (TUBITAK, 2002).....	48
3.3 Standard characterization test references.....	50
3.4 Results of characterization tests.....	50
3.5 Results of the electrical resistivity of steel-slag ballast (TUBITAK, 2002).....	51
3.6 Resistivities for various materials at 20 °C temperature (Serway, 1996)...	51
3.7 Waste acceptance criteria (Official Gazette, 1996) and test results.....	52
4.1 Standard test references.....	57
4.2 Physical properties of materials tested.....	58
4.3 Summary of the specific gravity and compaction test results.....	59
4.4 Average dimensions of limestone aggregates.....	59
4.5 Average dimensions of basalt aggregates.....	60
4.6 Average dimensions of steel-slag aggregates.....	60
4.7 Particle shape analysis of limestone aggregates.....	63
4.8 Particle shape analysis of basalt aggregates.....	63

4.9	Particle shape analysis of steel-slag aggregates.....	64
4.10	Summary of the triaxial test program.....	74
5.1	Summary of Mohr-Coulomb parameters for scaled-down limestone samples.....	92
5.2	Predicted maximum axial stress with $\sigma_3 = 35$ kPa for crushed limestone samples.....	93
5.3	Summary of Mohr-Coulomb parameters for scaled-down basalt samples..	98
5.4	Predicted maximum axial stress with $\sigma_3 = 35$ kPa for crushed basalt samples.....	98
5.5	Summary of Mohr-Coulomb parameters for scaled-down steel-slag samples.....	103
5.6	Predicted maximum axial stress with $\sigma_3 = 35$ kPa for crushed steel-slag samples.....	103
5.7	Comparison of Mohr-Coulomb parameters for all materials.....	104
5.8	Predicted maximum axial stress with $\sigma_3 = 35$ kPa for all materials.....	105
5.9	Summary of Mohr-Coulomb parameters for various wet samples.....	106
5.10	Predicted maximum axial stress with $\sigma_3 = 35$ kPa for various wet series	109
5.11	Comparison of Mohr-Coulomb parameters for different gradations of limestone.....	110
5.12	Predicted maximum axial stress with $\sigma_3 = 35$ kPa for crushed limestone...	110
5.13	Elastic moduli obtained for series L-2.36, L-4.75 and L-9.5.....	116
5.14	Power law parameters for the initial elastic moduli determined for scaled-down limestone.....	120
5.15	Power law parameters for the secant elastic moduli for scaled-down limestone.....	124
5.16	Power law parameters for the unloading-reloading elastic moduli for scaled-down limestone.....	130
5.17	Comparison of the power law parameters of unloading-reloading moduli for limestone $D_{50} = 30$ mm .....	135
5.18	Comparison of the unloading-reloading elastic moduli for limestone $D_{50} = 30$ mm at $\sigma_3 = 35$ kPa.....	136
5.19	Elastic moduli determined for B-2.36, B-4.75 and B-9.5 series .....	139

5.20	Power law parameters for initial moduli for scaled-down basalt.....	142
5.21	Power law parameters for secant moduli for scaled-down basalt	146
5.22	Power law parameters for unloading-reloading moduli for scaled-down basalt.....	150
5.23	Comparison of the power law parameters of unloading-reloading moduli for basalt $D_{50} = 30$ mm .....	155
5.24	Comparison of unloading-reloading modulus for basalt $D_{50} = 30$ mm at $\sigma_3$ $= 35$ kPa.....	155
5.25	Elastic moduli obtained for series S-4.75, S-6.35 and S-9.5.....	158
5.26	Power law parameters for initial moduli for scaled-down steel-slag.....	161
5.27	Power law parameters for secant moduli for scaled-down steel-slag.....	164
5.28	Power law parameters for unloading-reloading moduli for scaled-down steel-slag.....	167
5.29	Comparison of the predicted initial elastic moduli due to material type at $\sigma_3 = 35$ kPa.....	173
5.30	Comparison of the predicted secant elastic moduli due to material type at $\sigma_3 = 35$ kPa.....	174
5.31	Comparison of the predicted unloading-reloading elastic moduli due to material type at $\sigma_3 = 35$ kPa.....	174
5.32	Summary of the initial moduli values obtained for various wet series.....	178
5.33	Summary of the secant moduli values obtained for various wet series.....	179
5.34	Summary of the unloading-reloading moduli values obtained for various wet series.....	180
5.35	Comparison of initial moduli for different gradations of limestone.....	182
5.36	Comparison of secant moduli for different gradations of limestone.....	182
5.37	Comparison of unloading-reloading moduli for different gradations of limestone.....	184
5.38	Summary of the unloading-reloading moduli at different cycles of load	185
6.1	Summary of parameters used in hyperbolic model for crushed limestone	189
6.2	Summary of parameters used in hyperbolic model for crushed basalt.....	190
6.3	Summary of parameters used in hyperbolic model for crushed steel-slag	190
6.4	Summary of the unloading-reloading modulus parameters for crushed	

limestone.....	196
6.5 Summary of the unloading-reloading modulus parameters for crushed basalt.....	196
6.6 Summary of the unloading-reloading modulus parameters for crushed steel-slag.....	197
6.7 Predicted plastic strain after first cycle at $\sigma_3 = 35$ kPa and $(\sigma_1 - \sigma_3) = 200$ kPa for series of crushed limestone.....	203
6.8 Predicted plastic strain after first cycle at $\sigma_3 = 35$ kPa and $(\sigma_1 - \sigma_3) = 200$ kPa for series of crushed basalt.....	203
6.9 Predicted plastic strain after first cycle at $\sigma_3 = 35$ kPa and $(\sigma_1 - \sigma_3) = 200$ kPa for series of crushed steel-slag.....	204
6.10 Plastic strain slope values for the limestone at $\sigma_3 = 35$ kPa and $(\sigma_1 - \sigma_3) = 200$ kPa.....	207
6.11 Comparison of plastic strains for scaled-down limestone after $N = 20$ ....	209
6.12 Comparison of plastic strains for limestone prototype sizes after $N = 5000$ .....	209
6.13 Plastic strain slope values for the basalt at $\sigma_3 = 35$ kPa and $(\sigma_1 - \sigma_3) = 200$ kPa.....	212
6.14 Comparison of plastic strains for scaled-down basalt after $N = 20$ .....	214
6.15 Comparison of plastic strains for limestone prototype sizes after $N = 5000$ .....	215
6.16 Plastic strain slope values for the steel-salg at $\sigma_3 = 35$ kPa and $(\sigma_1 - \sigma_3) = 200$ kPa.....	218
6.17 Comparison of plastic strains for scaled-down steel-slag after $N = 20$ .....	219
6.18 Accumulated plastic strains predicted for prototype steel-slag after $N = 5000$ .....	219
6.19 Comparison of predicted plastic strain for various series of materials at $N = 5000$ .....	220
6.20 Comparison of plastic strain for different gradations of limestone after $N = 20$ .....	222

## LIST OF FIGURES

FIGURE	Page
1.1 Typical cross-section of a track structure (modified from Peplow et.al, 1996).....	2
1.2 Particle size distribution for ballast used in Turkey (After TS 7043, 1989).....	3
1.3 Example of parallel gradations.....	5
2.1 Effects of ballast layer thickness and stiffness on the deviator stress at the sub-grade surface (after Li & Selig, 1998).....	11
2.2 Stress conditions in ballast (after Tarumi, 1994).....	15
2.3 Stress-strain-volume change behavior for uncompacted ballast samples (1 psi = 6.89 kPa)(after Alva-Hurtado, 1981).....	20
2.4 Stress-strain-volume change behavior for compacted ballast samples (1 psi = 6.89 kPa)(after Alva-Hurtado, 1981).....	21
2.5 Variation of initial Young's modulus with confining pressure (1 psi = 6.89 kPa)(after Alva-Hurtado, 1981).....	23
2.6 Grain size distributions for modeled rockfill materials (1 inch = 25.4 mm) (after Marachi et al., 1972).....	29
2.7 Variation of initial elastic modulus with maximum particle size (after Marachi et al., 1972).....	31
2.8 Particle size distribution curves for granite ballast (after Janardhanam & Desai, 1983).....	33
2.9 Variation of resilient modulus with confining stress (after Janardhanam & Desai, 1983).....	34
2.10 Variation of resilient modulus with mean grain size (after Janardhanam & Desai, 1983).....	36
2.11 Effect of initial void ratio on angle of internal friction (after Selig &	

Roner, 1987).....	37
2.12 Particle size distribution curves for quartzite ballast (after Kaya et al., 1997).....	38
2.13 Variation of unloading-reloading modulus with maximum grain size (after Kaya et al., 1997).....	40
2.14 Ballast grading used in grading research program (after Raymond, 1979).....	42
2.15 Initial elastic modulus for differently graded ballasts ( $\sigma = 35$ kPa) (after Raymond, 1979).....	43
3.1 Particle size distribution for ballast used in Turkey (after TS 7043, 1989).....	45
3.2 Schematic view of production of steel-slag ballast in ERDEMIR.....	47
4.1 Ballast and the scaled-down gradations of crushed limestone samples..	55
4.2 Ballast and the scaled-down gradations of crushed basalt samples.....	56
4.3 Ballast and the scaled-down gradations of crushed steel-salg samples..	56
4.4 Various gradations of crushed limestone samples.....	57
4.5 Chart for estimating sphericity and roundness of aggregates (after Jernigan, 1998 based on Krumbein and Sloss,1963).....	64
4.6 Limestone particles retained on 2.36 mm sieve size.....	65
4.7 Limestone particles retained on 4.75 mm sieve size.....	65
4.8 Limestone particles retained on 9.5 mm sieve size.....	66
4.9 Limestone particles retained on 19.0 mm sieve size.....	66
4.10 Limestone particles retained on 50.0 mm sieve size (prototype).....	67
4.11 Basalt particles retained on 2.36 mm sieve size.....	67
4.12 Basalt particles retained on 4.75 mm sieve size.....	68
4.13 Basalt particles retained on 9.50 mm sieve size.....	68
4.14 Basalt particles retained on 19.0 mm sieve size.....	69
4.15 Basalt particles retained on 37.5 mm sieve size (prototype).....	69
4.16 Steel-Slag particles retained on 4.75 mm sieve size.....	70
4.17 Steel-Slag particles retained on 6.35 mm sieve size.....	70
4.18 Steel-Slag particles retained on 9.50 mm sieve size.....	71
4.19 Steel-Slag particles retained on 12.7 mm sieve size.....	71

4.20	Steel-Slag particles retained on 50.0 mm sieve size (prototype).....	72
4.21	Schematic of 100 mm triaxial apparatus used.....	76
4.22	Special wooden blocks to compact each layer of specimen.....	78
4.23	A typical completed triaxial sample before testing.....	79
4.24	Layout of triaxial cell with the anti-friction guide.....	80
4.25	A typical curve of triaxial loading, unloading and reloading.....	82
4.26	A typical triaxial sample after testing.....	83
5.1	Peak shear strength trend for limestone samples of 2.36 - 4.75 mm.....	89
5.2	Peak shear strength trend for limestone samples of 4.75 - 9.5 mm.....	89
5.3	Peak shear strength trend for limestone samples of 9.5 - 19.0 mm.....	91
5.4	Peak shear strength trend for all scaled-down limestone samples.....	91
5.5	Peak shear strength trend for basalt samples of 2.36 - 4.75 mm.....	95
5.6	Peak shear strength trend for basalt samples of 4.75 - 9.5 mm.....	95
5.7	Peak shear strength trend for basalt samples of 9.5 - 19.0 mm.....	96
5.8	Peak shear strength trend for all scaled-down basalt samples.....	97
5.9	Peak shear strength trend for steel-slag samples of 4.75 - 9.5 mm.....	100
5.10	Peak shear strength trend for steel-slag samples of 6.35 - 12.7 mm.....	100
5.11	Peak shear strength trend for steel-slag samples of 9.5 - 19.0 mm.....	101
5.12	Peak shear strength trend for all scaled-down steel-slag samples.....	102
5.13	Definition of initial elastic modulus with typical stress-strain curve.....	113
5.14	Definition of unloading-reloading modulus with typical stress-strain curve.....	113
5.15	Definition of secant elastic modulus with typical stress-strain curve....	114
5.16	Elastic moduli trends for series L-2.36.....	118
5.17	Elastic moduli trends for series L-4.75.....	118
5.18	Elastic moduli trends for series L-9.5.....	119
5.19	Comparison of trends of initial elastic moduli for all limestone series...	120
5.20	Variation of power law parameters of initial elastic modulus with the mean particle size for the scaled-down limestone samples.....	122
5.21	Prediction of initial Elastic moduli for L-2.36 series.....	123
5.22	Prediction of initial Elastic moduli for L-4.75 series.....	123

5.23	Prediction of initial Elastic moduli for L-9.5 series.....	124
5.24	Comparison of trends of secant elastic moduli for all limestone series..	125
5.25	Variation of power law parameters of secant elastic modulus with the mean particle size for the scaled-down limestone samples.....	127
5.26	Prediction of secant elastic moduli for L-2.36 series.....	128
5.27	Prediction of secant elastic moduli for L-4.75 series.....	128
5.28	Prediction of secant elastic moduli for L-9.5 series.....	129
5.29	Prediction of secant moduli by Vermeer and Schanz for limestone samples.....	129
5.30	Comparison of trends of unloading-reloading elastic moduli for all limestone series.....	130
5.31	Variation of power law parameters of unloading-reloading elastic modulus with the mean particle size for the scaled-down limestone samples.....	132
5.32	Prediction of unloading-reloading elastic moduli for L-2.36 series.....	133
5.33	Prediction of unloading-reloading elastic moduli for L-4.75 series.....	133
5.34	Prediction of unloading-reloading elastic moduli for L-9.5 series.....	134
5.35	Prediction of unloading-reloading moduli by Hertz Contact Theory for limestone samples.....	134
5.36	Prediction of initial elastic modulus for limestone samples with L-9.5 best-fit.....	137
5.37	Prediction of secant elastic modulus for limestone samples with L-9.5 bestt-fit.....	137
5.38	Prediction of unloading-reloading elastic modulus for limestone samples with L-9.5 best-fit.....	138
5.39	Elastic moduli trends for series B-2.36.....	141
5.40	Elastic moduli trends for series B-4.75.....	141
5.41	Elastic moduli trends for series B-9.5.....	142
5.42	Comparison of trends of initial elastic moduli for all basalt series.....	143
5.43	Variation of power law parameters of initial elastic modulus with the mean particle size for the scaled-down basalt samples.....	144

5.44	Prediction of initial Elastic moduli for B-2.36 series.....	145
5.45	Prediction of initial Elastic moduli for B-4.75 series.....	145
5.46	Prediction of initial Elastic moduli for B-9.5 series.....	146
5.47	Comparison of trends of secant elastic moduli for all basalt series.....	147
5.48	Variation of power law parameters of secant elastic modulus with the mean particle size for the scaled-down basalt samples.....	148
5.49	Prediction of secant elastic moduli for B-2.36 series.....	149
5.50	Prediction of secant elastic moduli for B-4.75 series.....	149
5.51	Prediction of secant elastic moduli for B-9.5 series.....	150
5.52	Comparison of trends of unloading-reloading elastic moduli for all basalt series.....	151
5.53	Variation of power law parameters of unloading-reloading elastic modulus with the mean particle size for the scaled-down basalt samples.....	152
5.54	Prediction of unloading-reloading elastic moduli for B-2.36 series.....	153
5.55	Prediction of unloading-reloading elastic moduli for B-4.75 series.....	153
5.56	Prediction of unloading-reloading elastic moduli for B-9.5 series.....	154
5.57	Prediction of initial elastic modulus for basalt samples with B-9.5 best-fit.....	156
5.58	Prediction of secant elastic modulus for basalt samples with B-9.5 best-fit.....	157
5.59	Prediction of unloading-reloading elastic modulus for basalt samples with B-9.5 best-fit.....	157
5.60	Elastic moduli trends for series S-4.75.....	160
5.61	Elastic moduli trends for series S-6.35.....	160
5.62	Elastic moduli trends for series S-9.5.....	161
5.63	Comparison of trends of initial elastic moduli for all steel-slag series...	162
5.64	Variation of power law parameters of initial elastic modulus with the mean particle size for the scaled-down steel-slag samples.....	163
5.65	Prediction of initial elastic moduli for all scaled-down steel-slag samples.....	164
5.66	Comparison of trends of secant elastic moduli for all steel-slag series...	165

5.67	Variation of power law parameters of secant elastic modulus with the mean particle size for the scaled-down steel-slag samples.....	166
5.68	Prediction of secant elastic moduli for all scaled-down steel-slag series	167
5.69	Comparison of trends of unloading-reloading elastic moduli for all steel-slag series.....	168
5.70	Variation of power law parameters of unloading-reloading elastic modulus with the mean particle size for the scaled-down steel-slag samples.....	169
5.71	Prediction of unloading-reloading elastic moduli for all scaled-down steel-slag samples.....	170
5.72	Prediction of initial elastic modulus for steel-slag samples with S-9.5 best-fit.....	171
5.73	Prediction of unloading-reloading elastic modulus for steel-slag samples with S-9.5 best-fit.....	171
5.74	Prediction of secant elastic modulus for steel-slag samples with S-9.5 best-fit.....	172
5.75	Comparison of initial elastic moduli for all materials.....	176
5.76	Comparison of secant elastic moduli for all materials.....	176
5.77	Comparison of unloading-reloading elastic moduli for all materials....	177
5.78	Variation with changing the uniformity coefficient of a) initial elastic moduli b) secant elastic moduli c) unloading-reloading elastic moduli	183
5.79	A typical quasi-cyclic stress-strain response curve.....	186
6.1	Back-prediction of behavior of L-2.36 (Limestone 2.36 - 4.75 mm)....	191
6.2	Back-prediction of behavior of L-4.75 (Limestone 4.75 – 9.5 mm)....	192
6.3	Back-prediction of behavior of L-9.5 (Limestone 9.5 – 19.0 mm).....	192
6.4	Back-prediction of behavior of B-2.36 (Basalt 2.36 - 4.75 mm).....	193
6.5	Back-prediction of behavior of B-4.75 (Basalt 4.75 – 9.5 mm).....	193
6.6	Back-prediction of behavior of B-9.5 (Basalt 9.5 – 19.0 mm).....	194
6.7	Back-prediction of behavior of S-4.75 (Steel-Slag 4.75 – 9.5 mm).....	194
6.8	Back-prediction of behavior of S-6.35 (Steel-Slag 6.35 – 12.7 mm)....	195
6.9	Back-prediction of behavior of S-9.5 (Steel-Slag 9.5 – 19.0 mm).....	195
6.10	Back-prediction of unloading-reloading behavior for L-2.36.....	198

6.11	Back-prediction of unloading-reloading behavior for L-4.75.....	198
6.12	Back-prediction of unloading-reloading behavior for L-9.5.....	199
6.13	Back-prediction of unloading-reloading behavior for B-2.36.....	199
6.14	Back-prediction of unloading-reloading behavior for B-4.75.....	200
6.15	Back-prediction of unloading-reloading behavior for B-9.5.....	200
6.16	Back-prediction of unloading-reloading behavior for S-4.75.....	201
6.17	Back-prediction of unloading-reloading behavior for S-6.35.....	201
6.18	Back-prediction of unloading-reloading behavior for S-9.5.....	202
6.19	Plastic strain accumulation trend for L-2.36.....	205
6.20	Plastic strain accumulation trend for L-4.75.....	206
6.21	Plastic strain accumulation trend for L-9.5.....	206
6.22	Variation of plastic strain slope with mean particle size for limestone..	208
6.23	Plastic strain accumulation trend for B-2.36.....	211
6.24	Plastic strain accumulation trend for B-4.75.....	211
6.25	Plastic strain accumulation trend for B-9.5.....	212
6.26	Variation of plastic strain slope with mean particle size for basalt.....	213
6.27	Plastic strain accumulation trend for S-4.75.....	216
6.28	Plastic strain accumulation trend for S-6.35.....	216
6.29	Plastic strain accumulation trend for S-9.5.....	217
6.30	Variation of plastic strain slope with mean particle size for steel-slag	218

## LIST OF SYMBOLS

### SYMBOL

$c$	Apparent cohesion
$C$	Plastic strain coefficient (slope)
$C_c$	Coefficient of curvature
$C_u$	Coefficient of uniformity
$D$	Particle diameter at any % finer
$D_{10}$	Particle diameter at 10% finer
$D_{30}$	Particle diameter at 30% finer
$D_{50}$	Particle diameter at 50% finer (Mean particle size)
$D_{60}$	Particle diameter at 60% finer
$D_{max}$	Maximum particle size at % finer
$D_r$	Relative density
$d_w$	Driven wheel diameter
$\delta$	Deflection of rail
$\partial\varepsilon_a$	Change in axial strain
$\partial\sigma_1$	Change in axial stress
$\partial\sigma_3$	Change in radial stress
$\Delta\varepsilon_a$	Discrete change in axial strain
$\Delta\sigma_1$	Discrete change in axial stress
$e_o$	Initial void ratio
$E$	Young's modulus (or Elastic modulus)
$E_b$	Resilient modulus for ballast ( $E_{ur}$ )
$E_i$	Initial elastic modulus
$E_{50}$	Secant elastic modulus
$E_s$	Resilient modulus for subgrade
$E_{st}$	Young's modulus of rail

$E_{ur}$	Unloading-reloading elastic modulus (Resilient modulus)
$\epsilon_a$	Axial strain
$\epsilon_1$	Plastic strain after first cycle
$\epsilon_N$	Accumulated plastic strain after a number of load cycle, N
$\epsilon_{ur}$	Recoverable (Resilient ) axial strain
$\phi$	Angle of internal friction at failure
H	Thickness of ballast layer
I	Moment of inertia of rail
K	Material constant (coefficient) of elastic modulus
$K_c$	Cyclic stress ratio
$K_o$	Coefficient of lateral earth pressure at rest
$(K_o)_{max}$	Maximum coefficient of lateral earth pressure ( $K_p$ )
$K_p$	Coefficient of lateral earth pressure at passive state
$\lambda$	Dynamic increasing factor
n	Material constant (power) of elastic modulus
$n_g$	Power for Talbot and Richart's grading equation
N	Number of load cycle
P	Percentage finer than
p	$(\sigma_1 + \sigma_3)/2$
$p_r$	Reference pressure (= 1 kPa)
q	$(\sigma_1 - \sigma_3)/2$
$R_f$	Failure ratio
$\sigma_1$	Major principal (or axial) stress
$\sigma_3$	Minor principal (or radial or confining) stress
$\sigma_{1f}$	Major principal stress at failure
$\sigma_{3f}$	Minor principal stress at failure
$\sigma_c$	Dynamic (cyclic) stress
$\sigma_d$	Deviator stress
$\sigma_h$	Horizontal stress
$\sigma_s$	Static stress
$\sigma_{vo}$	Geostatic pressure plus surcharge pressure

$(\sigma_1 - \sigma_3)$	Deviator stress ( $\sigma_d$ )
$(\sigma_1 - \sigma_3)_{cf}$	Cyclic deviator stress at failure
$(\sigma_1 - \sigma_3)_f$	Deviator stress at failure
$(\sigma_1 - \sigma_3)_{ult}$	Asymptotic stress difference
<b>u</b>	Track modulus
<b>v</b>	Velocity of train

## **CHAPTER I**

### **INTRODUCTION**

#### **1.1. Problem Statement and Justification**

Railroads traditionally have used ballast to support the rail-sleeper (also called 'tie') system and to provide a free draining medium. The ballast is placed on top of the track beds so that it transfers and distributes the load through a sub-ballast layer to the sub-grade. Figure 1.1 shows a schematic view of the cross-section of the track structure (Peplow et al., 1996).

Conventional ballast is composed of crushed and coarse grained hard rock. Several types of crushed rock such as limestone, basalt, slag, etc. with usually uniform gradation are used for ballast. Typical gradation used in Turkey is shown in Figure 1.2 (TS 7043, 1989).

The currently used ballast in Turkish State Railways (TCDD) is limestone on account of its abundance in Turkey; and basalt is considered to be used as ballast in view of the planned high-speed train project; and steel slag, end-product of Ereğli Iron and Steel Works, is proposed to be used to regain to economy as ballast.

The selection of the ballast material used for railroad track support is of major importance in establishing and maintaining the characteristics of the track response and, as a consequence, the riding quality. Also, the material must be laid and compacted on stable, compacted sub-ballast and sub-grade. If these precautions are

not taken, the track system requires a continuous realignment and replacement or addition of ballast (Raymond, 1979). For this purpose, for example, almost 800,000 tons of ballast has been used every year in Turkey for the railways totaling about 500 km (TCDD), 2001).

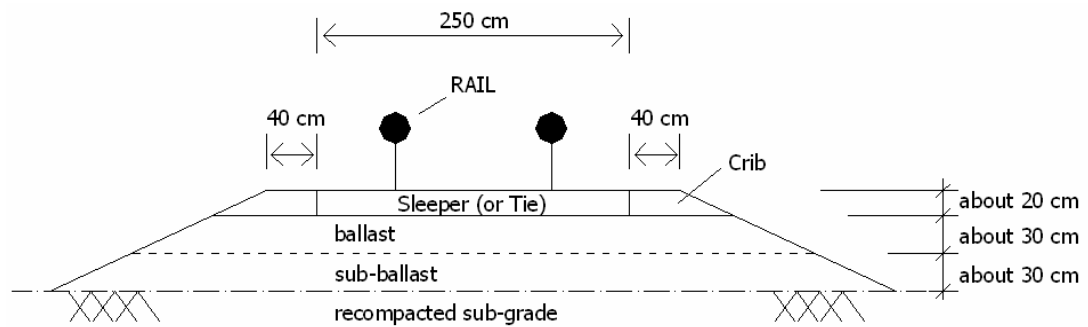


Figure 1.1 Typical Cross-section of a track structure  
(modified from Peplow et al., 1996)

As recommended by different standards and other literature (TS 7043, 1989; Canadian Pacific Rail Specification, 1984; Watters et al., 1987; Boucher & Selig, 1987) and even in a recent report (TUBITAK, 2002) the method of selecting ballast has been based on the physical testing of representative specimens to ensure that materials are of the suitable rock type, with no inherent planes of weakness such as foliation and cleavage (Petrographic Analysis), grain shape and size distribution, adequate wearing resistance (Los Angeles Abrasion), and weathering resistance (Freeze-Thaw, Wetting and Drying, and Absorption) tests. So, the presently used Turkish standard tests (TS 7043, 1989) and the TCDD specification (TCDD, 2001) for quality assessment and their recommended values represent aspects of durability, but they are not directly related to the deformation behavior of the track.

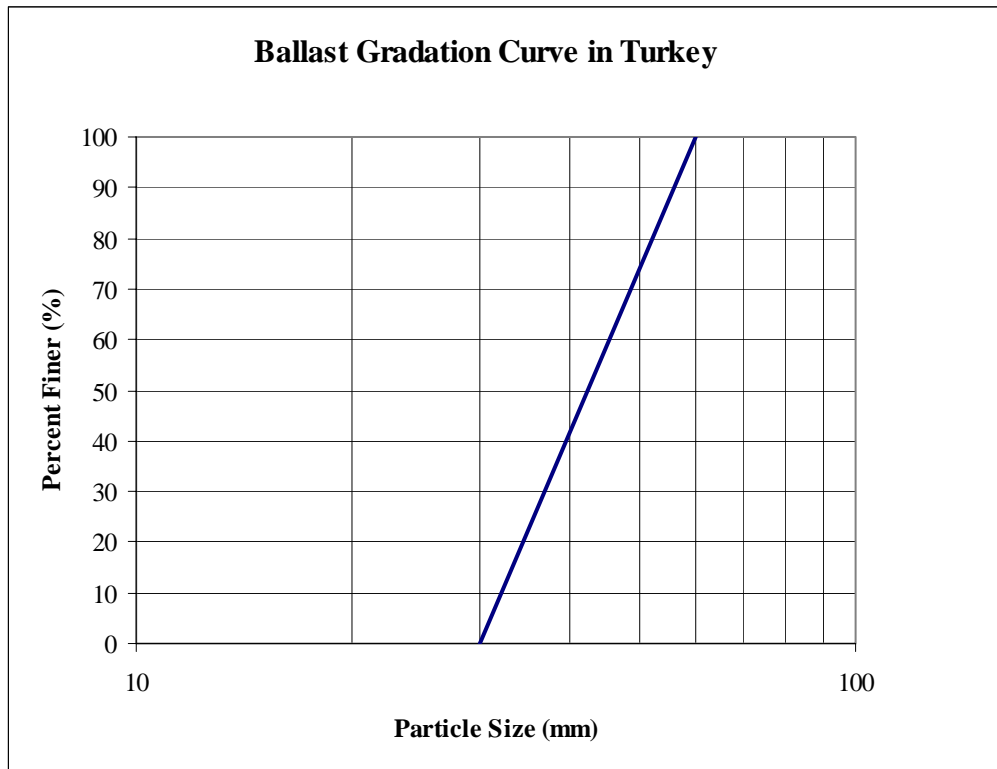


Figure 1.2 Particle size distribution for ballast used in Turkey (after TS 7043, 1989)

From the mechanics of soils point of view, the ballast layer must have enough capacity to withstand both vertical and lateral forces applied repeatedly by wheel load. Moreover, the excessive elastic deformations and plastic deformations in the ballast layer should be prevented, otherwise the former will result in shortening the life of the railway sleepers because of the high fatigue stresses caused by bending, and the latter will result in permanent differential settlements which will distort the track geometry.

To simulate the stress state occurring within the ballast layer, triaxial tests will be used in the laboratory as discussed in section 2.5. In order to reliably measure the shear strength, elasticity and plasticity characteristics from these tests, such tests should be conducted using a specimen diameter at least six times the size of the maximum particle in the specimen to be tested (U.S. Army Corps of Engineers, 1970; Charles & Watts, 1980; Head, 1982; Bowles, 1992). Jernigan (1998) explained

it as follows: “..... For non-cohesive such as sands and gravels, there is little substitute for a well designed laboratory program to determine the shear strength. Since laboratory experiments attempt to predict the behavior of a large volume of soil based on the behavior of a very small volume, it is important that behavior of individual grains do not dominate the behavior of the specimen. Effectively, the volume of soil to be tested must be representative of the soil mass in the field. Consider, for example, an individual particle of gravel in contact with the platen of a triaxial apparatus. Since the solid particle is considerably stiffer than the particulate matrix surrounding it, the influence on the experiment can be large and may, in fact, dominate the results. In contrast, consider that same gravel particle in contact with the base of a concrete footing. In this case, the effect of the behavior of the individual particle is negligible and the gravelly soil will act as a continuum. This problem is often termed the apparatus effect. In order to minimize the apparatus effects on the test specimen, current standards for triaxial tests indicate that they should be conducted using a specimen diameter is at least six times the size of the maximum particle in the soil”.

The specification for railroad ballast in Turkey requires sound rock materials uniformly graded between 30 mm and 60 mm. In order to reliably obtain the peak shear strength and the elastic modulus of this prototype ballast, a test specimen with a minimum diameter of 360 mm and a height of 720 mm would be required as discussed above. This is a volume of 73,287 cm<sup>3</sup>. At a density of 1.5 Mg/m<sup>3</sup>, the specimen alone would have a mass of 110.0 kg. Triaxial cells of this size are very rare and expensive to operate.

Since ballast materials contain particles too large to be tested in standard laboratory apparatuses a soil modeling technique, referred to as the ‘parallel gradation technique’, is proposed. This technique was suggested first by Lowe (1964) for embankment materials (e.g., Fig. 1.3). In this technique, the aim is to preserve the particle shape, particle surface roughness, and particle mineralogy and to create a parallel gradation of soil with a maximum particle size suitable for the available apparatus. With a 100-mm triaxial specimen diameter available in the soil

mechanics laboratory at Middle East Technical University (METU) and by using the 6 to 1 rule, the maximum particle size that could reliably be tested by this equipment would at most be 19 mm.

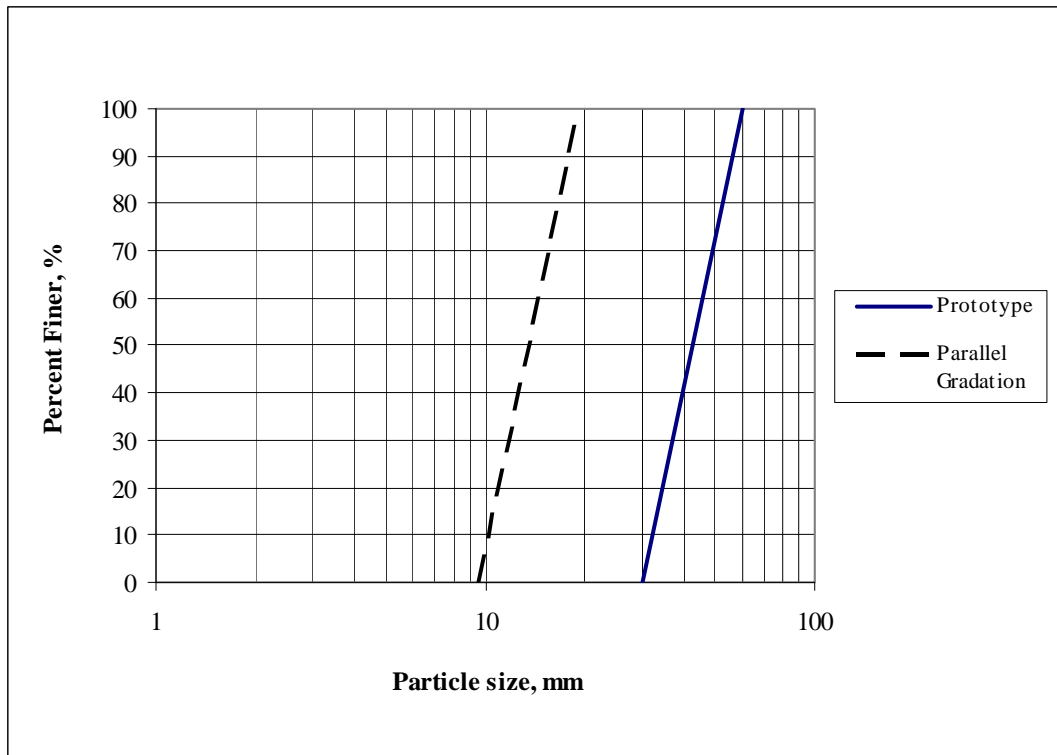


Figure 1.3 Example of parallel gradations

## 1.2. Objective and Scope of Work

The objective of this research is to investigate the stress-strain behavior of several types of ballast materials using conventional triaxial testing through the utilization of parallel gradation technique, and so as to compare the effects of material type, particle size and gradation changes on strength, elastic and plastic behavior of ballast materials.

The present work details the systematic research into the parallel gradation technique. Most of the work discussed herein is experimental. The results are then used in the hyperbolic model by Duncan et al. (1970).

The scope of work follows:

- Chapter II discusses the literature relevant to the prototype ballasts and to the parallel gradation technique.
- Chapter III presents the standard characterization tests conducted on several types of ballast materials, namely limestone, basalt and steel-slag which were obtained from different sources.
- Chapter IV presents the laboratory program of the parallel gradation technique. The materials were prepared in scaled-down particle sizes and various grain size distributions to enable later correlations with the stress-strain behavior of the aggregates. The experimental program was provided, and the equipment and laboratory procedures used were discussed. The materials were subjected to several standard characterization tests.
- Chapter V presents the triaxial test results by use of parallel gradation technique. The results to predict the strength and the elastic characteristics of prototype size (ballast) are also included in this chapter.
- Chapter VI discusses the hyperbolic modeling of the stress-strain behavior of scaled-down materials obtained from experiments. This chapter also presents the results of plastic strain behavior under a number of load applications, which used later in the prediction of plastic characteristics of prototype size (ballast).
- Chapter VII summarizes the experimental and modeling results obtained. Recommendations for further research are also suggested.

## **CHAPTER II**

### **A REVIEW OF RELEVANT LITERATURE**

#### **2.1 Introduction**

Prior to reviewing the previous studies on stress-strain and strength characteristics of ballast, the parameters affecting the performance of railway ballast layer (Fig. 1.1) will be overviewed, and the stress state and the stress levels occurring within ballast layer will be reviewed.

#### **2.2 Notation**

As the ballast material is generally assumed to be under drained conditions, the stresses involved are effective stresses and the applicable shear strength parameters are those expressed in terms of effective stresses. So, for simplicity, the prime sign (') generally used to denote effective stress, and parameters in terms of effective stress will be dropped throughout this document.

#### **2.3 Design Considerations in Railway Track Foundation**

The simplest model for railway track design represents the rail as a beam, with concentrated wheel loads, supported by an elastic foundation (Hay, 1982). The

elastic foundation represents the net effect of the stiffness of the sleepers, ballast and sub-grade. Values of the track modulus are obtained by load tests on representative track. Track modulus ( $u$ ) is defined as the force per unit length of rail per unit deflection in the track system. The equation used to determine the values of track modulus is:

$$u = \frac{1}{4} \left( \left( \frac{P}{\delta} \right)^4 \cdot \frac{1}{E_{st} I} \right)^{1/3} \quad (2.8)$$

where,  $P$  = applied load;  $\delta$  = rail deflection directly under the load;  $E_{st}$  = Young' s modulus of the rail;  $I$  = moment of inertia of the rail.

This simple model, however, is unable to distinguish between the contribution of the sleeper and underlying layers.

More precise analytical models have been developed which represent the rails and sleepers as beams resting on a multiple layer foundation comprised of the ballast layer and sub-grade. These models include computer codes like ILLITRACK (Robnett, Thompson, Knutson & Tayabji, 1975), MULTA (Kennedy & Prause, 1978), GEOTRACK (Chang, Adegoke & Selig, 1980), and KENTRACK (Huang, Kin, Deng & Rose, 1986). Finite element formulations have also been developed based on one-, two-, and three-dimensional idealization for analysis of railroad track support structures (Turcke & Raymond, 1979; Desai & Siriwardane 1982).

Li & Selig (1998a; 1998b) have described a new empirical design method in case there is no computer code available. Part I describes the development for selecting ballast layer thickness for railroad track. The design is based on limiting traffic load-induced deviator stress in the sub-grade. Track variable values for the analysis include rails attached to sleepers with flexible fixings; the mechanical properties and thickness of the ballast and underlying sub-grade layer; and wheel loads. Herein the ballast layer has been taken as the combination of ballast and sub-ballast thicknesses. Design charts are given to cover various ballast layer and sub-

grade conditions. Part II describes the procedures for the practical application of the design method given in Part I.

## **2.4 Effects on Railroad Track Performance of Ballast Characteristics**

The methods mentioned in section 2.3 can be used to implement design of the railroad track structure. For this, it is very obvious that the material parameters are needed.

Two of the problems related to the performance of ballast materials are the excessive elastic deformations caused by loading, unloading and reloading under the wheel loads and the accumulation of plastic deformations resulting from many repetitions of individual wheel loads. The soil properties required for the solution of these problems are given in the following subsections.

### **2.4.1 Resilient Modulus**

The concept of resilient modulus,  $E_{ur}$ , has been used to describe the behavior of the ballast subjected to repeated loading conditions. Resilient modulus is defined as the repeated deviator stress divided by the recoverable portion of the axial strain (Monismith et al., 1969).

Several predictive equations have been developed for the resilient modulus to account for the stress dependency of the materials. These have been verified by laboratory test results on material from a series of loading-unloading-reloading cycles under slow applied loads (Janardhanam & Desai, 1983). The most widely used equation for the resilient modulus,  $E_{ur}$ , analogous to Ohde's (1939) (quoted by Potts et al., 2002) and Janbu's (1963) initial tangent modulus is:

$$E_{ur} = K p_r \left( \frac{\sigma_3}{p_r} \right)^n \quad (2.9)$$

where  $\sigma_3$  is the confining stress;  $p_r$  is the reference pressure expressed in the same pressure units as  $E_{ur}$  and  $\sigma_3$ ;  $K$  and  $n$  are materials constants determined from regression analysis of the laboratory data.

Li & Selig (1998a) found that for a given load condition, one of the most important factors influencing the deviator stress at the surface of the sub-grade is the resilient modulus  $E_b$  ( $= E_{ur}$ ) of the ballast layer (Figure 2.1), in which  $H$ = thickness of the ballast layer;  $E_s$ = elastic modulus of the sub-grade. The difference between Figure 2.1a and 2.1b was a change in value of  $E_{ur}$ . As can be seen, for the smallest ballast layer thickness (i.e., 0.30 m), the deviator stress at the sub-grade surface is highest at the tie (sleeper) end and is the lowest at the sleeper center. For the same ballast thickness, an increase in  $E_{ur}$  from 140 MPa to 550 MPa caused about 35% reduction in the deviator stress at surface of the sub-grade at nearly the sleeper end.

Stewart & Selig (1982) carried out field measurements at the Facility for Accelerated Service Testing (FAST) research track in Pueblo, Colorado to determine the magnitude of resilient stresses, strains and deflections in the ballast, sub-ballast and sub-grade resulting from train loading. GEOTRACK computer code (section 2.3) was used to predict the results measured at FAST for comparison with the experimental data. In order to investigate the sensitivity of the GEOTRACK to the main track variables, a parametric study was done. For all cases, a single wheel load of 146 kN was used. Among the track variables, the resilient modulus ( $E_{ur}$ ) value changing between 689 MPa and 55 MPa had the largest effect on the sleeper vertical deflection beneath the wheel load, equal to the ballast surface deflection at the same location.

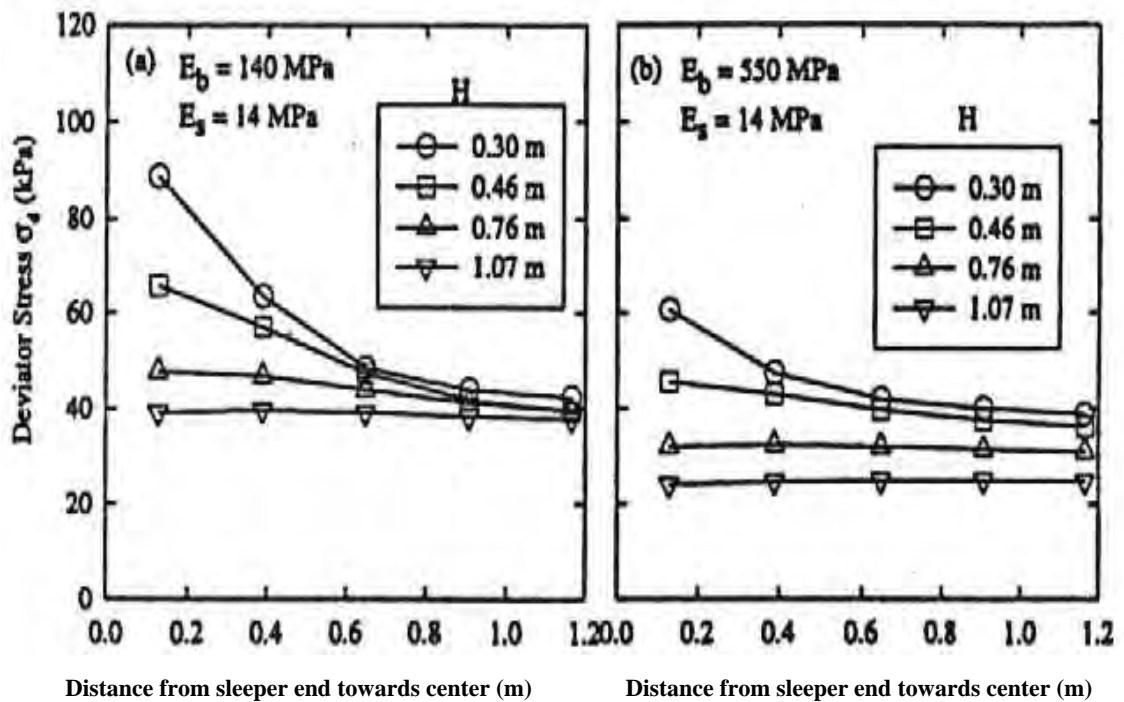


Figure 2.1 Effects of ballast layer thickness and stiffness on the deviator stress at the sub-grade surface (after Li & Selig, 1998)

They have also computed the average ballast vertical strain. The average ballast vertical strain was calculated by dividing the differential displacement between the upper and lower ballast surfaces by the initial layer thickness. By far the greatest effect on ballast vertical strain was caused by the change in  $E_{ur}$  value. A decrease in  $E_{ur}$  from 689 MPa to 55 MPa caused an increase in ballast strain by a factor of about 9.

The track modulus ( $u$ ) (equation (2.8)) was also predicted for each case using the rail deflections calculated by GEOTRACK. Track modulus increased by about 20% by the increase in  $E_{ur}$  value.

## 2.4.2 Plastic Strain in Relation to Shear Strength

Several experimental studies on ballast have been made under repeated triaxial condition (e.g., Raymond & Williams, 1978; Diyaljee & Raymond, 1982; Kempfert & Hu, 1999). One essential result of such studies is that there exists some limit for the ratio  $K_c$  of the cyclic deviator stress at failure  $(\sigma_1 - \sigma_3)_{cf}$  to the static deviator stress at failure  $(\sigma_1 - \sigma_3)_f$ ; i.e.,  $K_c = (\sigma_1 - \sigma_3)_{cf} / (\sigma_1 - \sigma_3)_f$ . If the cyclic stress is smaller than  $K_c(\sigma_1 - \sigma_3)_f$ , the resulting permanent deformation of the soil specimen will gradually converge to a corresponding stable value. In this state the soil specimen behaves as a quasi-elastic material. In contrast to this, the cyclic and plastic deformation increases nearly linearly from cycle to cycle leading to failure within a short time if the limit  $K_c(\sigma_1 - \sigma_3)_f$  is exceeded (Kempfert & Hu, 1999). They quote a value of  $K_c = 0.80$  in their illustrative examples. However, Diyaljee and Raymond (1982) plotted logarithm of plastic strain versus logarithm of number of load repetitions and they have resulted in a slope essentially independent of confining stress or deviator stress levels for  $K_c$  is less than 0.60. Data presented by Alva-Hurtado & Selig (1981) show also  $K_c = 0.60$ .

Many methods have evolved for predicting permanent axial strain caused by repeated loading. One of these methods was proposed by the Office for Research and Experiments, ORE, of the International Union of Railways, the ballast permanent strain can be predicted by the equation (Selig and Waters, 1994):

$$\varepsilon_N = 0.082(100n - 38.2)(\sigma_1 - \sigma_3)^2(1 + 0.2 \log N) \quad (2.10)$$

where,

$\varepsilon_N$  = plastic strain after N loading cycles

n = initial porosity of the sample

$(\sigma_1 - \sigma_3)$  = deviator stress

N = number of load application

Alva-Hurtado and Selig (1981) has given an alternative equation for defining the plastic strain:

$$\varepsilon_N = \varepsilon_1(1 + C \log N) \quad (2.11)$$

where, C is a material constant, may be named plastic strain slope. Typical values are between 0.2 and 0.4.

Equations (2.10) and (2.11) indicated that axial plastic strain at any cycle,  $\varepsilon_N$ , can be predicted as a function of the number of cycles of load applications, N, and the axial plastic strain after the first cycle,  $\varepsilon_1$ , independently of the state of stress and degree of compaction of the specimen. They have also described how to obtain  $\varepsilon_1$  in a conventional triaxial test.  $\varepsilon_1$  remaining after the deviator stress is applied and removed can be represented by

$$\varepsilon_1 = \varepsilon_a - \varepsilon_{ur} \quad (2.12)$$

in which  $\varepsilon_a$  is the axial strain under the applied deviator stress,  $(\sigma_1 - \sigma_3)$ , and  $\varepsilon_{ur}$  is the recoverable or resilient strain upon unloading and it can be calculated through the use of Equation (2.9). The value of  $\varepsilon_a$  might be estimated from the hyperbolic stress-strain relationship (Duncan & Chang, 1970) as a function of  $(\sigma_1 - \sigma_3)$  and confining stress,  $\sigma_3$  as follows:

$$\varepsilon_a = \frac{(\sigma_1 - \sigma_3)/E_i}{1 - \frac{(\sigma_1 - \sigma_3)(1 - \sin \phi)R_f}{2(c \cos \phi + \sigma_3 \sin \phi)}} \quad (2.13)$$

where, c is the apparent cohesion;  $\phi$  is the angle of internal friction;  $R_f$  is the failure ratio as shown by

$$(\sigma_1 - \sigma_3)_f = R_f (\sigma_1 - \sigma_3)_{ult} \quad (2.14)$$

where,  $(\sigma_1 - \sigma_3)_f$  = the compressive strength, or stress difference at failure obtained from conventional triaxial test;  $(\sigma_1 - \sigma_3)_{ult}$  = the asymptotic value of stress difference for the corresponding hyperbola obtained from the test data.  $R_f$  always has a value less than unity and found to be essentially independent of  $\sigma_3$ ; and  $E_i$  is the initial tangent modulus as a function of confining stress (Janbu, 1963)

$$E_i = Kp_r \left( \frac{\sigma_3}{p_r} \right)^n \quad (2.15)$$

where,  $\sigma_3$  is the confining stress;  $p_r$  is the reference pressure expressed in the same pressure units as  $E_i$  and  $\sigma_3$ ;  $K$  is a modulus number, and  $n$  is an exponent determined from regression analysis of the laboratory data. The procedure for evaluating the constants in the hyperbolic stress-strain law for conventional triaxial stress-strain data has been given by Duncan et al. (1980).

## 2.5 Stress States within Ballast

Sleepers (ties) are generally 20 cm wide and spaced every 50 cm. So, the compaction of a new or a maintained ballasted track is usually carried out by means of tamping and surface compaction of the crib (ballast above the level of the bottom of sleepers, Fig. 1.1) and shoulders (sides of railway track). This procedure induces compaction of a limited column of ballast beneath the rails and the crib adjacent to the rails, whereas the surrounded ballast remains relatively uncompacted (Indraratna et al., 1998). Raymond & Davies (1978) claim that for such conditions, to assess the ability to resist vertical forces, triaxial testing is probably more appropriate than other devices such as plane strain testing.

Tarumi (1994) suggested that the stress condition in the ballast during train passage could be classified roughly into triaxial compression just under the sleepers and triaxial extension between the adjacent sleepers. This condition is shown in Fig. 2.2.

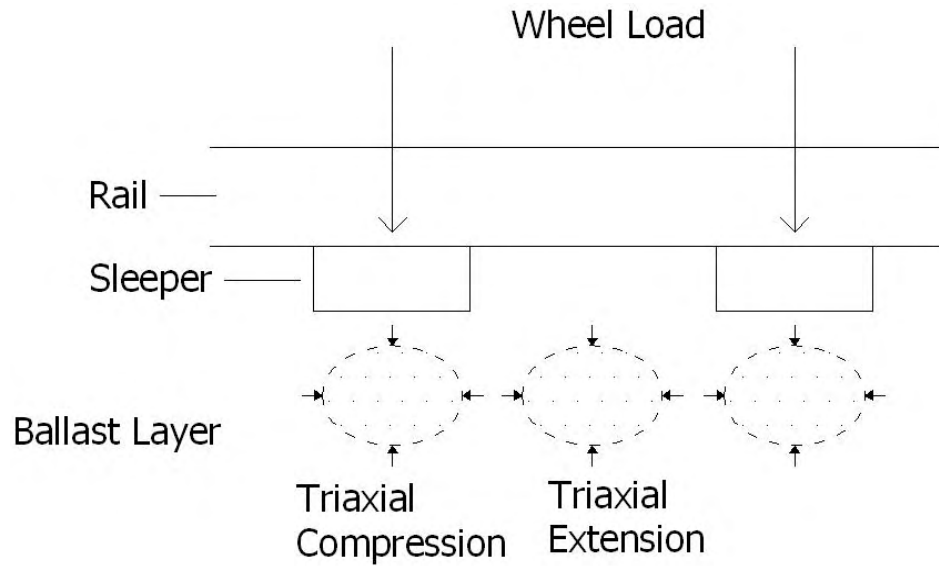


Figure 2.2 Stress conditions in ballast layer (after Tarumi, 1994)

Janardhanam & Desai (1983) have used three-dimensional testing for this purpose. Under train loading, the materials in the track bed were subjected to a series of loading, unloading and reloading cycles. They suggest that as an approximation, the inertia and rate effects on the stress-strain-strength behavior of the material can be ignored. The stress-strain response can then be modeled from a series of loading-unloading-reloading cycles under slow or repeatedly applied loads.

Timmerman and Wu (1969) reported the results of cyclic load tests on coarse-grained soil at frequencies of between 2.5 Hz and 25 Hz. The frequency within this range seemed to affect the rate of strain but not the final strain. It was due to fact that strain increased faster in the 2.5 Hz tests than in the 25 Hz test. The difference in the strain increment per cycle might be attributed to the longer pulse durations at the lower frequencies as long as the stresses applied at the different frequencies are the same.

## **2.6 Stress Levels in the Ballast Layer**

A major concern relating to the performance of ballast is its ability to withstand both axial and lateral forces. In practice, the axial stress and the horizontal stress depend on the train axle load and the restraint provided by the sleepers, the shoulder and crib ballast.

### **2.6.1 Vertical Stress**

The maximum wheel load applied on the rail-sleeper system is 100 kN for locomotives and railway cars available in TCDD traveling at a maximum speed of 120 km/h (TCDD, 1981; 1990).

The American Railway Engineering Association (AREA, 1978) suggested that the pressure at sleeper-ballast interface should not exceed 450 kPa (quoted by Stagliano et al., 1981).

Stagliano et al. (1981) performed an experiment on the Urban Mass Transportation Administration (UMTA) transit track test site at the Transportation Test Center in Pueblo, Colorado. They have measured the vertical stresses at sleeper-ballast interface and in the middle of ballast layer immediately beneath the rail as 175 kPa and 70 kPa, respectively, for a vehicle having a wheel load of approximately 100 kN and traveling with a speed of 85 km/h.

Kempfert & Hu (1999) measured the dependency of the maximum vertical dynamic stress on train speed at two cross sections on the Hannover-Würzburg railway line. They observed a clear increase of the resulting dynamic stress in the ballast layer within the range of the train speed between 150 km/h and 300 km/h. The maximum vertical dynamic stress in the middle of the ballast layer beneath the rail was 70 kPa for a train speed of 150 km/h, whereas it was 100 kPa for a train speed of 300 km/h.

Kempfert & Hu (1999) measured the dynamic loading  $\sigma_c$  in the ballast and the sub-grade layer arising from the railway traffic, and found that with reference to the static stress  $\sigma_s$  in the corresponding zones determined from the wheel set loads, the dynamic increasing factor  $\lambda = \sigma_c / \sigma_s$  is 1.0 up to a train speed of 150 km/h; beyond that point,  $\lambda$  increases linearly with train speed until it reaches a maximum of about 1.7 at 300 km/h; then  $\lambda$  becomes independent of the train speed again. This contradicts by the Association of American Railroads (AAR) (Stagliano et al., 1981), where  $\lambda$  was calculated from

$$\lambda = 1 + 5.2(v/d_w) \quad (2.16)$$

where,  $v$  = velocity in kilometers per hour;  $d_w$  = driven wheel diameter in millimeters. As seen from Equation (2.16)  $\lambda$  increases as velocity increases.

Of interest to the track engineer is the behavior of ballast at low confining pressures since North American design theory results in vertical stresses at the sleeper-ballast interface under static wheel loads that average less than 140 kPa (Raymond & Diyaljee, 1979).

## 2.6.2 Horizontal Stress

As seen from the track configuration (Figure 1.1), the horizontal stress  $\sigma_h$  in the ballast layer changes from zero at sides to some value ( $K_o\sigma_{vo}$ ) beneath sleepers; where  $K_o$  is the coefficient of lateral earth pressure at rest and  $\sigma_{vo}$  is the vertical stress due to the self weight of the ballast and the static surcharge of rail-sleeper segment (i.e.,  $\sigma_{vo}$  is approximately equal to 15 kPa for a 50 cm ballast layer). Typical values of  $K_o$  for ballast preloaded by train wheel might be in the range of 0.6 to 1.2 computed as for granular materials having a stress history load (Holtz & Kovacs, 1981).

Stewart et al. (1985) conducted an experiment to measure the residual stresses in the ballast layer using a laboratory box testing device of 30.5 cm wide, 61 cm long, and 48 cm deep. Experimental results show that relatively large residual stresses, due to reloading-unloading applications of wheel load, can develop in ballast. The ballast material used in these tests was an angular traprock (field term for basaltic rock) with a particle size ranging from 4.8 mm to 51 mm. The loads were applied through a tie segment 23 cm wide by 29 cm long. The ballast depth below the tie segment was about 30.5 cm. The maximum cyclic load was about 18 kN, producing a sleeper contact pressure equivalent to that of a 142 kN wheel load from a train. They measured the residual horizontal stresses at the sides and end panels as 35 kPa and 20 kPa, respectively. The measured residual stresses in the unloaded state were used to calculate values of  $K_o$  based on  $\sigma_{vo}$  and the box test side or end panel measurement. Due to the stress history occurred by repeatedly applied wheel load,  $K_o$  value was found to increase and be greater than 1.0.

Theoretically, the maximum horizontal stress must be limited to stresses at the passive failure condition. The ratio of the major principal stress at failure  $\sigma_{1f}$  to the minor principal stress at failure  $\sigma_{3f}$  at the passive failure condition, for a strictly cohesionless material such as ballast, defined as:

$$\frac{\sigma_{1f}}{\sigma_{3f}} = (K_o)_{\max} = K_p = \frac{1 + \sin\phi}{1 - \sin\phi} \quad (2.17)$$

where,  $K_p$  is the coefficient of lateral earth pressure at passive state; and  $\phi$  is the angle of internal friction. A value of  $K_o = 6$  would be possible for  $\phi = 45.5^\circ$ , which is likely to be for ballast (Stewart et al., 1985). This means that for  $\sigma_{vo} = 15$  kPa, the maximum  $\sigma_h$  in the ballast layer cannot be greater than 90 kPa.

Raymond & Davies (1978) stated that when a maximum static train wheel load of 150 kN could be applied, causing high axial stresses at sleeper/ballast interfaces, the confining stress  $\sigma_3$  would hardly develop over 140 kPa. So, the behavior of ballast is under low confining stresses.

## 2.7 Stress - Strain and Strength Characteristics of Ballast

Alva-Hurtado et al. (1981) performed eleven compression tests with confining stresses (from 35 kPa to 140 kPa) on granite ballast. The maximum particle size of the prototype ballast was 76 mm. The granite ballast was scaled down only to the gradation ranging in size from 5 mm to 30 mm, with a  $d_{50}$  size of 20 mm and a uniformity coefficient  $C_u$  of 2. The specimen size was 203 mm in diameter and 507 mm in height. Both uncompacted and compacted sample states were tested. The average dry unit weight ( $\rho_d$ ) of the six uncompacted specimens was  $1.53 \text{ Mg/m}^3$  with a range from  $1.49 \text{ Mg/m}^3$  to  $1.58 \text{ Mg/m}^3$ . The average  $\rho_d$  of the five compacted specimens was  $1.62 \text{ Mg/m}^3$  with a range from  $1.61 \text{ Mg/m}^3$  to  $1.63 \text{ Mg/m}^3$ .

The stress-strain and volume change relationships for the uncompacted and compacted samples are shown in Figures 2.3 and 2.4 respectively. These stress-strain figures show that the results followed the expected trends for granular material (Holtz & Kovacs, 1981). As  $\sigma_3$  increased, the deviator stress at failure increased. Also, the deviator stress at failure was greater for the compacted samples than for the uncompacted samples. This difference in deviator stress at failure between compacted and uncompacted samples increased with increasing  $\sigma_3$ . As  $\sigma_3$  increased, the axial strain at which the sample failed also increased.

The volumetric strain plots show also that the ballast followed well-established behavior trends for granular material (Holtz & Kovacs, 1981). Volumetric strain was defined as positive when the total specimen volume decreased and negative when the volume increased. As the confining stress was increased, the tendency for sample dilation decreased. The compacted samples tended to dilate at smaller vertical strains than uncompacted samples at corresponding confining pressures. These observations indicate that the behavior of granular materials under low  $\sigma_3$  values is different from that under high  $\sigma_3$  values; e.g., Marachi et al. (1972). The angle of internal friction and the apparent cohesion were calculated for each test. When  $\sigma_3$  values increased, the values of  $\phi$  decreased for both compacted

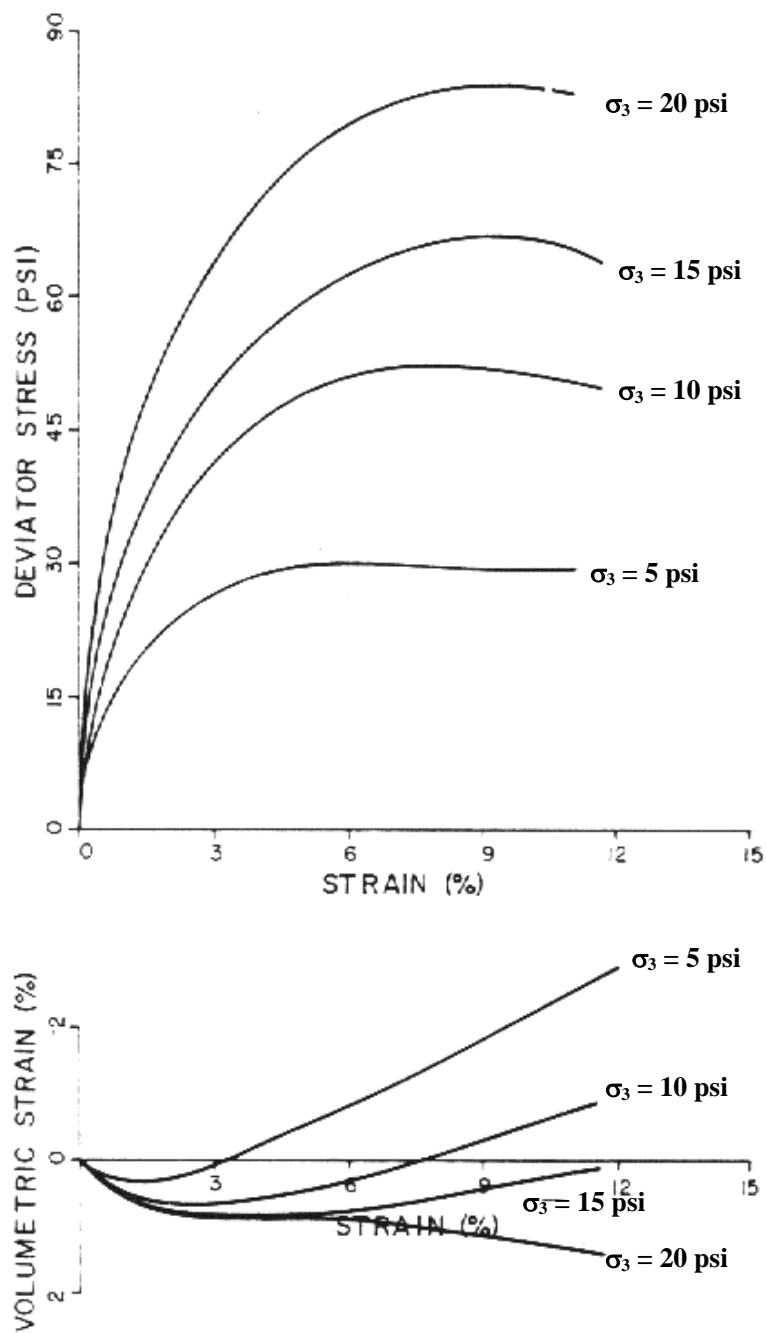


Figure 2.3 Stress-strain-volume change behavior for uncompact ballast samples (1 psi = 6.89 kPa) (after Alva-Hurtado et al., 1981)

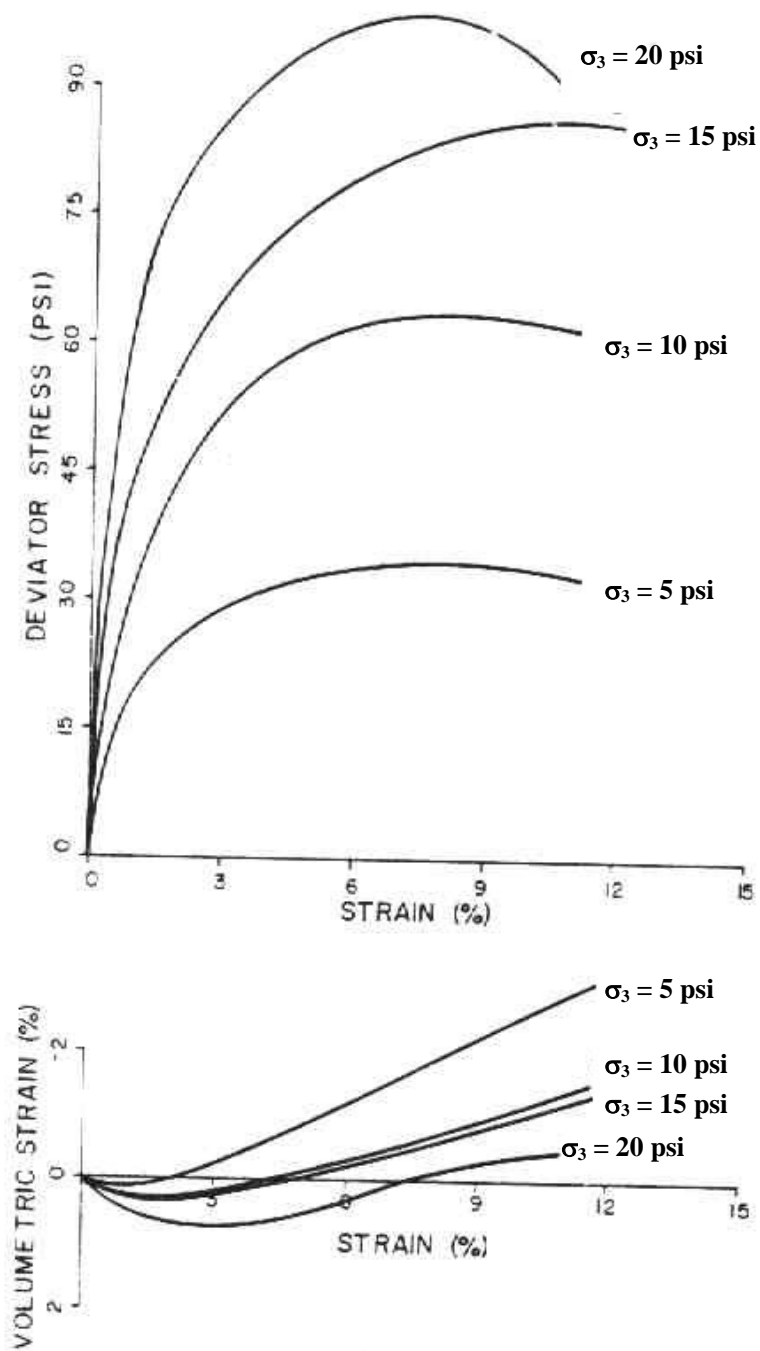


Figure 2.4 Stress-strain-volume change behavior for compacted ballast samples  
(1 psi = 6.89 kPa) (after Alva-Hurtado et al., 1981)

and uncompacted samples. The average  $\phi$  value for the compacted samples was  $44.4^\circ$  degrees and for the uncompacted samples was  $37.8^\circ$ . The apparent cohesion value for the compacted samples was 19 kPa, and the value for the uncompacted samples was 33 kPa.

The hyperbolic transformations (section 2.4.2) were applied to the stress-strain data obtained from the ballast static triaxial tests. The logarithm of the initial tangent modulus computed from the hyperbolic model was plotted in Figure 2.5 as function of the logarithm of  $\sigma_3$  for both compacted and uncompacted samples. It seen that  $E_i$  increases with  $\sigma_3$ , and that the compacted samples have a greater  $E_i$  than the uncompacted samples.

Raymond and Davies (1978) conducted an extensive set of triaxial compression tests at low confining stresses between 8.6 kPa and 310.3 kPa on dolomite ballast. Specimens 225 mm in diameter and 450 mm in height were prepared at  $\rho_d$  varying between  $1.4 \text{ Mg/m}^3$  and  $1.7 \text{ Mg/m}^3$  (corresponding to relative densities  $D_r$  between 0% and 75%). Particle size of specimens ranged between 3.8 mm and 38 mm.

The angle of internal friction  $\phi$  was calculated for each test assuming that the value of cohesion was equal to zero. When the confining stress was increased, the values of  $\phi$  decreased for all samples prepared at any one density. The average  $\phi$  for the densest and loosest state was about  $48^\circ$  and  $38^\circ$ , respectively.  $E_i$  increased significantly with increasing  $\rho_d$  and  $\sigma_3$ . For example,  $\rho_d = 1.5 \text{ Mg/m}^3$ ,  $E_i$  values under  $\sigma_3$  of 50 kPa and 150 kPa were determined as 16 MPa and 25 MPa respectively, whereas the corresponding values for  $\rho_d = 1.6 \text{ Mg/m}^3$  were 23 MPa and 32 MPa.

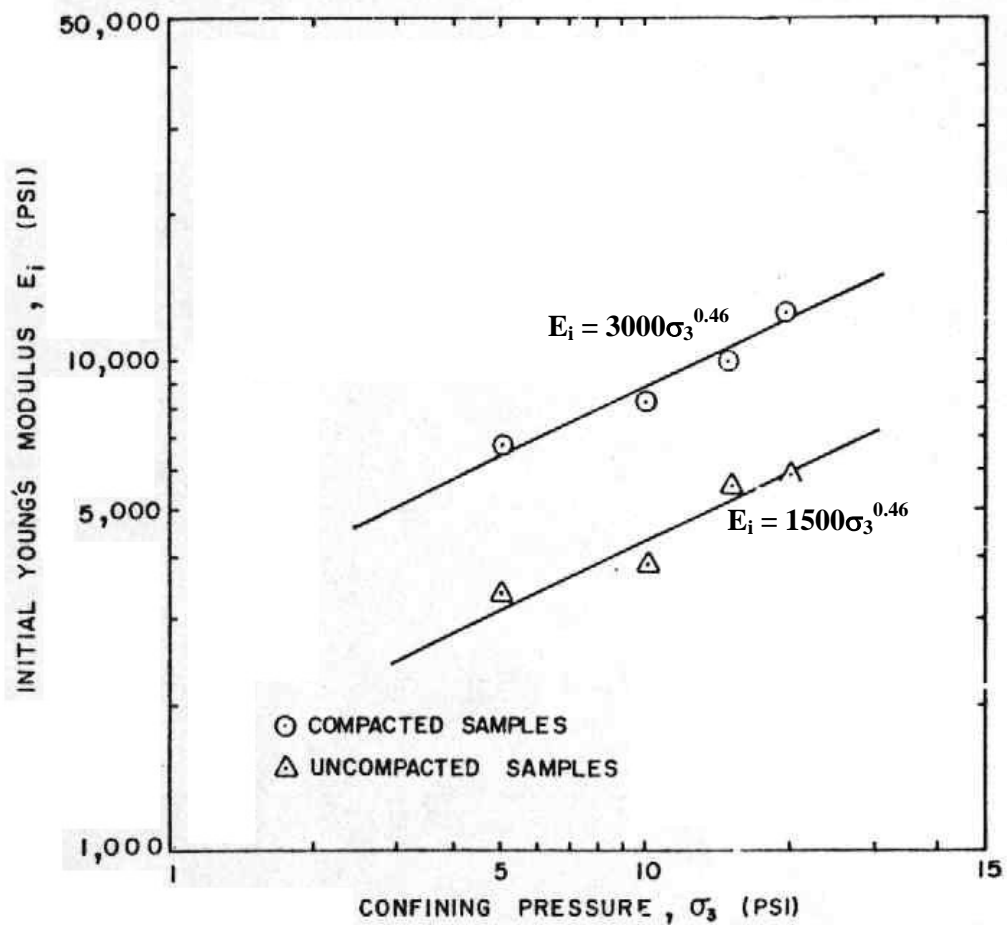


Figure 2.5 Variation of initial Young's modulus with confining pressure  
(1 psi = 6.89 kPa) (after Alva-Hurtado et al., 1981)

Knutson and Thompson (1978) conducted an extensive study to determine the resilient responses of five typical uniformly graded aggregate materials (dolomitic limestone, blast-furnace slag, granitic gneiss, basalt and gravel) that are used for railway ballast were measured in a repeated triaxial cell. Seven stress levels were used. The results were used in regression analysis to develop equations relating the resilient (unloading-reloading) modulus of a specimen to its first stress invariant. Samples 203 mm in diameter with 406 mm in height were used for the No.4 ballast gradation which has a maximum particle size of 51 mm and a minimum particle size of 4.75 mm. To minimize segregation and to ensure gradation control, each specimen

was weighed out by thirds for each of the size fractions. For medium-density specimens, each layer was compacted for 5 second with the vibratory hammer. With a deviator stress of 310 kPa and under a confining stress of 105 kPa, each specimen was conditioned for 5000 load applications. Then they have obtained the following resilient modulus,  $E_{ur}$  (kPa), with respect to confining stress,  $\sigma_3$  (kPa), for dolomitic limestone:

$$E_{ur} = 37982(\sigma_3)^{0.47} \quad (2.18)$$

and for basalt:

$$E_{ur} = 29756(\sigma_3)^{0.65} \quad (2.19)$$

Values for the accumulated plastic strain,  $\epsilon_N$ , were also determined for both the limestone and the basalt specimens. The accumulated plastic strain values for No.4 medium-density limestone and basalt specimens were determined, respectively, to be 2.1% and 2.3%.

Raymond and Diyaljee (1979) conducted cyclic triaxial tests on (apparently) 230 mm diameter samples of eight different materials, including Sudbury slag and St. Isodore Limestone. The same initial grading was given to all ballasts in which the particle size ranged from 38 mm to 2.4 mm. The samples were compacted in eight layers, using a 30-second vibration period of a Kango hammer acting on a 228 mm diameter, 20 mm thick wooden disc to compact each layer in a high density without causing a major breakdown of the ballast particles. Repeated loading was applied using a constant confining pressure of 35 kPa. A deviator stress of 140 kPa was used for 500,000 cycles (Stage I), followed by another 500,000 cycles at 210 kPa (Stage II).

Under Stage I loading, the variation of the resilient modulus  $E_{ur}$  and the logarithm of the number of cycles is characterized by an initially small modulus that increases with the number of cycles before attaining an equilibrium value.  $E_{ur}$  value

for both Sudbury Slag and St. Isodore Limestone was around 400 MPa at the end of Stage I. At the end of Stage II, the value of  $E_{ur}$  was about 300 MPa for both materials. They explained this decrease as due to the “near elastic” behavior of the materials at low stresses and the high apparent cohesion intercept for dense crushed stone.

The deformations at the end of 500, 000 cycles with 140 kPa deviator stress were classified into three distinct groups consisting of small, intermediate and large relative deformations. While the Sudbury Slag has taken place within the small deformation group where  $\epsilon_N$  is around 0.5%, St. Isodore Limestone was grouped into the intermediate deformation group, and  $\epsilon_N = 0.9\%$ .

The stress-strain relationships of the ballasts not subjected to any repeated loading were also determined. The strengths of the Sudbury Slag and St. Isodore Limestone were obtained 233 kPa and 277 kPa, respectively under a confining stress of 35 kPa, and the initial tangent modulus  $E_i$  for Sudbury Slag was 150 MPa, whereas it was 95 MPa for St. Isodore Limestone.

Indraratna et al. (1998) present a series of conventional triaxial compression tests on basaltic ballasts composed of highly angular, crushed rock particles. Table 2.1 summarizes the physical properties of the ballast material used in the study, as evaluated by the standard ballast tests. These tests provide basic guidelines for accepting or rejecting a given material as potential railway ballast.

The peak shear strength and  $E_i$  under  $\sigma_3$  between 1 kPa and 240 kPa were measured for two different gradations of the material. Table 2.2 shows the grain size characteristics of the materials tested. The specimens for all tests were 300 mm in diameter and 600 mm in height. The specimens were compacted by imparting 25 blows with a standard Proctor hammer to each layer of ballast, which had a thickness of between 50 mm and 60 mm. This procedure produced specimens with relative densities ranging from 41 % to 63%. The latex membrane thickness confining the specimens was 4 mm. Membrane corrections were applied to the experimental

results. At high  $\sigma_3$  values ( $\sigma_3 > 120$  kPa) the membrane corrections were less than 2% of the measured principal stresses, whereas at  $\sigma_3 = 1$  kPa the maximum correction was below 8%. In addition, the volume change errors caused by membrane penetration were less than 1.2%, especially when  $\sigma_3$  was relatively small ( $\sigma_3 < 120$  kPa).

Table 2.1 Physical characteristics of basaltic ballast (after Indraratna et al., 1998)

Physical Characteristic Test Result	Test Value	Australian Standard Recommendation
<b>Durability</b>		
Aggregate crushing value	12%	< 25%
Los Angeles abrasion	15%	< 25%
Wet attrition value	8%	< 6%
Point load index	5.4 MPa	–
Crushing strength	130 MPa	–
<b>Shape</b>		
Flakiness	25%	< 30%
Misshapen particle	20%	< 30%

Considerable non-linearity of strength was exhibited by both material gradations as  $\sigma_3$  increased. For sample A the friction angle (obtained by drawing a tangent from the origin to each Mohr circle) ranged from approximately  $77^\circ$  at a  $\sigma_3 = 1$  kPa to about  $45^\circ$  at a  $\sigma_3 = 240$  kPa. For sample B, the corresponding  $\phi$  values ranged from  $79^\circ$  to  $51^\circ$ .

Table 2.2 Grain size characteristics of basaltic ballast (after Indraratna et al., 1998)

Sample	$d_{max}$ (mm)	$d_{10}$ (mm)	$d_{30}$ (mm)	$d_{50}$ (mm)	$d_{60}$ (mm)	$C_u$	$C_c$
A	53	27.1	32.6	38.9	41.3	1.5	0.9
B	53	20.7	26.7	30.3	32.8	1.6	1.0

Indraratna et al. (1998) also examined the variation of  $E_i$  with  $\sigma_3$ . The values  $E_i$  have been determined for an axial strain of 2% to 3%. (Although authors call these 'initial values', they should rather be called as 'secant values', because both were calculated not at the beginning of the test but at 2% to 3% axial strain; in any case, both will be kept as are). Sample A (coarser particles) gave a smaller values of  $E_i$ . For  $\sigma_3 = 1$  kPa and 240 kPa  $E_i$  values for Sample A were 5 MPa and 34 MPa; and 5 MPa and 38 MPa, respectively, for Sample B.

Although the authors state that "Scaled down aggregate cannot be relied upon for the prediction of deformation parameters", no attempt was made to test scaled down material.

### **2.7.1 Effect of Particle Size on Stress-Strain- Strength Characteristics of Ballast**

The effect of particle size not only on the stress-strain and strength characteristics of ballast materials but that of other materials such as dam material will also be reviewed in this sub-section.

Marachi et al. (1972) conducted an experimental program where parallel gradation was used to assess the stress-strain and shear strength of prototype rockfill materials for two different dams and a quarry-blasted material. The three-rockfill

materials were from Pyramid Dam, Oroville Dam, and from the Napa Basalt Company quarry. All the experiments were consolidated-drained conventional triaxial tests. Each series consisted of tests using parallelly graded soil from a particular dam with the maximum permissible particle size  $D_{\max} = 12$  mm for the 71 mm diameter specimen;  $D_{\max} = 51$  mm for the 305 mm diameter specimen; and  $D_{\max} = 152$  mm for the 914 mm diameter specimen,  $D_{\max}$  being one-sixth of the diameter of each specimen. Tests on each specimen used confining stresses  $\sigma_3$  of 210 kPa, 980 kPa, 2900 kPa, and 4485 kPa.

The Pyramid Dam material was composed of argillite particles. Due to the fine-grained, sedimentary nature of this material, the individual particles were strongly anisotropic and very weak. The material was quarry-blasted and very angular. The specific gravity for all particle sizes was 2.62, indicating similar mineral compositions. The maximum particle size for the prototype material was 381 mm. The gradation of the specimens tested is as shown in Figure 2.6a.

The crushed basalt was also quarry-blasted material with a specific gravity of 2.87. It was fine grained, hard and isotropic, with scattered phenocrysts (larger crystals) of olivine and plagioclase. The gradations of the specimens tested are shown in Figure 2.6b.

The material comprising the shell of the Oroville Dam was borrowed from a sedimentary deposit ranging in size from fine sand to cobbles. Most of the particles were amphibolite, with minor percentages of quartz and schist, and diorite was also present. The gravel fractions were rounded to well rounded, the coarse sand was rounded, and the fine sand was sub-rounded to sub-angular. Additionally, the specific gravity also changed, with the gravel materials having a specific gravity of 2.94, while that of the finer portion was 2.86. The maximum particle size of the prototype was 152 mm; so only two additional parallel gradation model soils were prepared (Figure 2.6c).

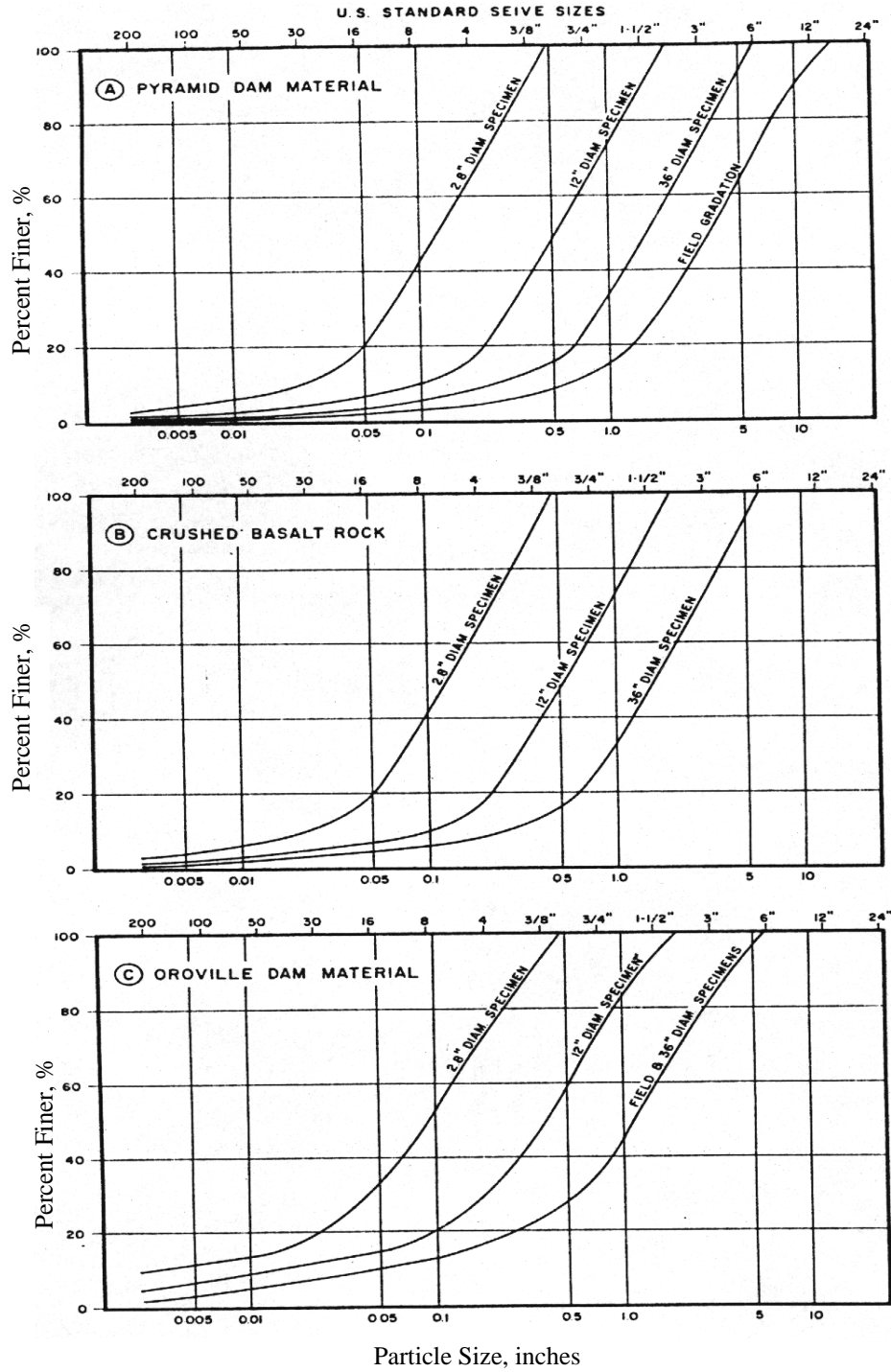


Figure 2.6 Grain size distributions for modeled rockfill materials  
(1 inch = 25.4 mm) (after Marachi et al., 1972)

The method of mixing, placing and compacting was the same for all of the test specimens, and they had essentially uniform density throughout. Initial void ratio ( $e_0$ ) for the specimens was as follows: for the Pyramid Dam material, 0.45; for the crushed basalt, 0.43; and for the Oroville Dam material, 0.42.

Marachi et al. (1972) drew the following conclusions for the three widely different types of materials. The angle of internal friction ( $\phi$ ) for all of the materials and all specimen sizes decreased at a decreasing rate with increasing  $\sigma_3$ ;  $\phi$  was generally about  $50^\circ$  under  $\sigma_3 = 210$  kPa while it was  $37^\circ$  under  $\sigma_3 = 4485$  kPa. The trend of variation of  $\phi$  showed that the  $\phi$  value would not decrease significantly for  $\sigma_3$  values beyond 4485 kPa. The value of  $\phi$  seemed to decrease with increase in the maximum size of the particles or in the size of the test specimen. At any  $\sigma_3$ , the  $\phi$  value for the 914 mm diameter specimens was about  $1^\circ$  and  $1.5^\circ$  lower than that of the 305 mm specimens and  $3^\circ$  to  $4^\circ$  lower than that of the 71 mm diameter specimens. This trend seemed to be unaffected by  $\sigma_3$  or the material type, even though the rock particles of Pyramid Dam, crushed basalt and Oroville Dam were completely different.

The axial strains at failure ( $\epsilon_a$ )<sub>f</sub> showed a steady increase with  $\sigma_3$  for all of the specimens. For both the Pyramid Dam materials and crushed basalt ( $\epsilon_a$ )<sub>f</sub> increased from about 7.5% for tests at  $\sigma_3 = 210$  kPa to about 20% for tests at  $\sigma_3 = 2900$  kPa. However, for  $\sigma_3$  beyond 2900 kPa ( $\epsilon_a$ )<sub>f</sub> did not increase with  $\sigma_3$ . A similar trend was observed for the tests on the Oroville Dam material; however, corresponding values of ( $\epsilon_a$ )<sub>f</sub> were substantially smaller for the Oroville Dam material than for the Pyramid Dam and crushed basalt materials (about 2.5% for  $\sigma_3 = 210$  kPa and about 7% for  $\sigma_3 = 2900$  kPa). For all three-test series it appeared that at any given  $\sigma_3$ , ( $\epsilon_a$ )<sub>f</sub> is lowest for the small specimens and greatest for the large size specimens, with a maximum difference of 4.7% for the crushed basalt at  $\sigma_3 = 4485$  kPa.

The values of the initial tangent modulus ( $E_i$ ) were also presented for all of the materials as a function of  $\sigma_3$ .  $E_i$  increased with  $\sigma_3$  for all samples and all sizes. The difference between the  $E_i$  for the different sizes decreased with increase in  $\sigma_3$ . Of more interest for the present study, the  $E_i$  values at  $\sigma_3 = 210$  kPa are plotted in Figure 2.7 against the maximum size of particles in the specimen for all three samples. As may be seen, although there is some scatter in the data, there seems to be some indication that the  $E_i$  is greater for the small particle size than for the larger particle size.

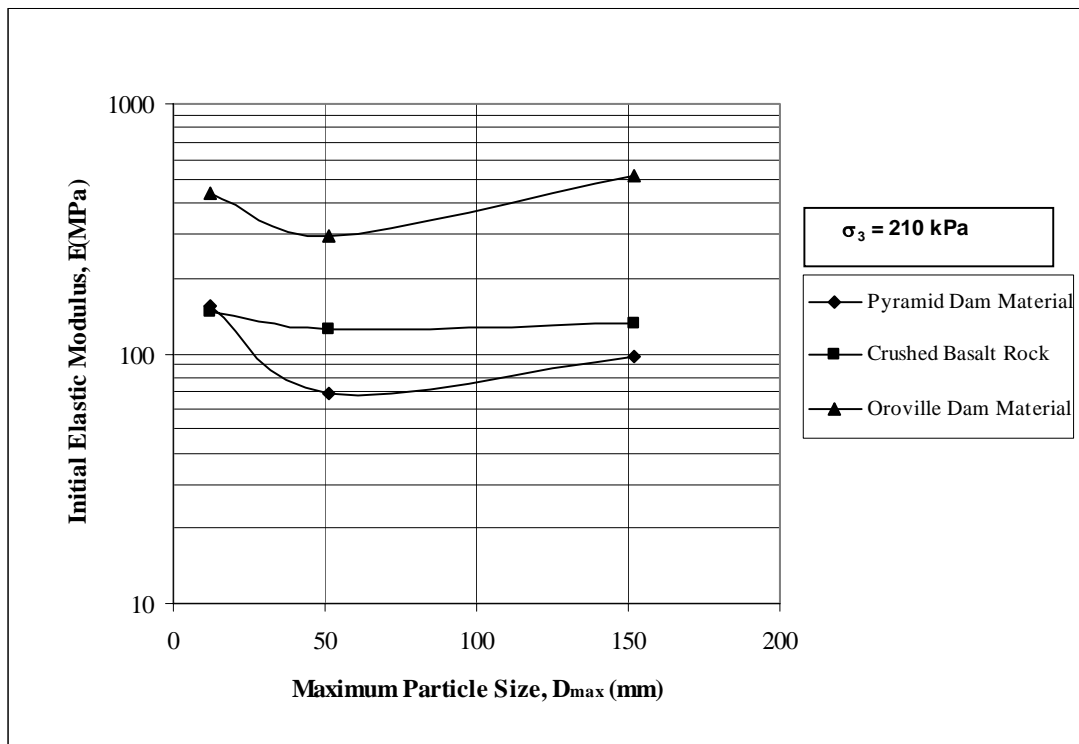


Figure 2.7 Variation of initial elastic modulus with maximum particle size  
(after Marachi et al., 1972)

Goel (1978) has performed tests on uniform gravel of different maximum particle size  $D_{\max}$  varying between 6.7 mm and 25 mm to investigate the effect of particle size using parallel gradation technique on the value of angle of internal friction ( $\phi$ ). The minimum particle size ( $D_{\min}$ ) of the smallest range was 4.75 mm. The quartzite gravelly particles with rounded to sub-rounded particle shape were tested in a 30 cm x 30 cm x 15 cm size direct shear box. Tests were run under a maximum normal load of 200 kPa. The data for the angle of internal friction versus maximum particle size have shown that  $\phi$  value reduced from  $40.5^\circ$  to  $40^\circ$  with the increase of  $D_{\max}$  from 6.7 mm to 25 mm. This indicated that within the tested normal pressure range of 200 kPa, the variation in the value of  $\phi$  with the change of maximum particle size was not significant.

Janardhanam & Desai (1983) tested ballast material composed of granite gneiss with particles ranging from 22 mm to 48 mm (Ballast I in Fig. 2.8), a uniform material with a uniformity coefficient  $C_u$  of about 1.2. With the 100 mm x 100 mm x 100 mm cubical size specimen permitted in the truly triaxial test apparatus, it was difficult to test the field material with the mean particle size  $D_{50}$  of 30 mm. So, the size of the field material (Ballast I) was scaled down using the parallel gradation technique to two smaller sizes, called Ballast II and Ballast III (Figure 2.8). The  $D_{50}$  of Ballast II and Ballast III was 16 mm and 7 mm, respectively. The samples were compacted by vibration to the field density of  $1.45 \text{ Mg/m}^3$ . All samples were then tested under conditions similar to the conventional triaxial compression test, with a confining stress ( $\sigma_3$ ) ranging from 35 kPa to 140 kPa.

They have investigated the effect of particle size on the stress-strain behavior of the ballast material under given  $\sigma_3$  values. Table 2.3 shows values of axial strains at typical levels of deviator stress for  $\sigma_3$  values of 70 kPa, 105 kPa and 140 kPa. It can be seen that, in general, the smaller sized ballast experienced slightly greater axial strains as the deviator stress increased for a given  $\sigma_3$ . On the other hand, the difference in axial strain between Ballast II and Ballast III existing at lower deviator stresses almost disappeared as the deviator stress increased for the lower two  $\sigma_3$

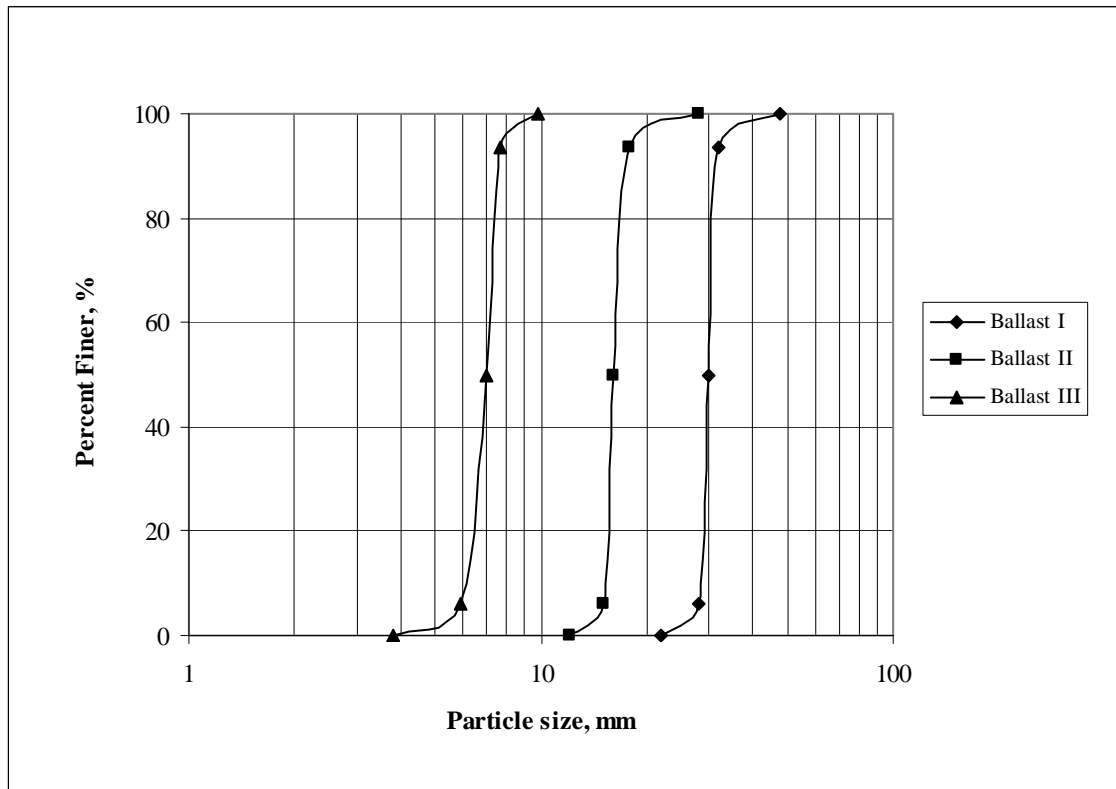


Figure 2.8 Particle size distribution curves for granite ballast  
(after Janardhanam & Desai, 1983)

values; for the highest  $\sigma_3$  value under which the difference in axial strain gradually increased when the deviator stress increased.

They have also determined that there was significant difference in unloading-reloading properties. The unloading modulus was regarded as the resilient modulus  $E_{ur}$ , (section 2.2), and the average of the values of  $E_{ur}$  for various unloading-reloading loops was taken.  $E_{ur}$  values for Ballast II and Ballast III, as determined from various test results with different  $\sigma_3$  (kPa) values, were plotted in Figure 2.9. From this figure, following the procedure given in section 2.4.1, the  $E_{ur}$  (kPa) for Ballast III was found to be:

Table 2.3 Comparison of axial strain at different shear stress levels  
(after Janardhanam & Desai, 1983)

Confining Pressure (kPa)	Deviator Stress (kPa)	Ballast II (D <sub>50</sub> = 16 mm) Axial Strain (%)	Ballast III (D <sub>50</sub> = 7 mm) Axial Strain (%)
70	103	0.32	0.44
	173	0.92	1.52
	242	2.58	2.96
105	103	0.70	1.05
	173	1.93	2.25
	242	3.02	3.10
140	103	0.45	0.50
	173	0.90	1.05
	242	1.88	2.12

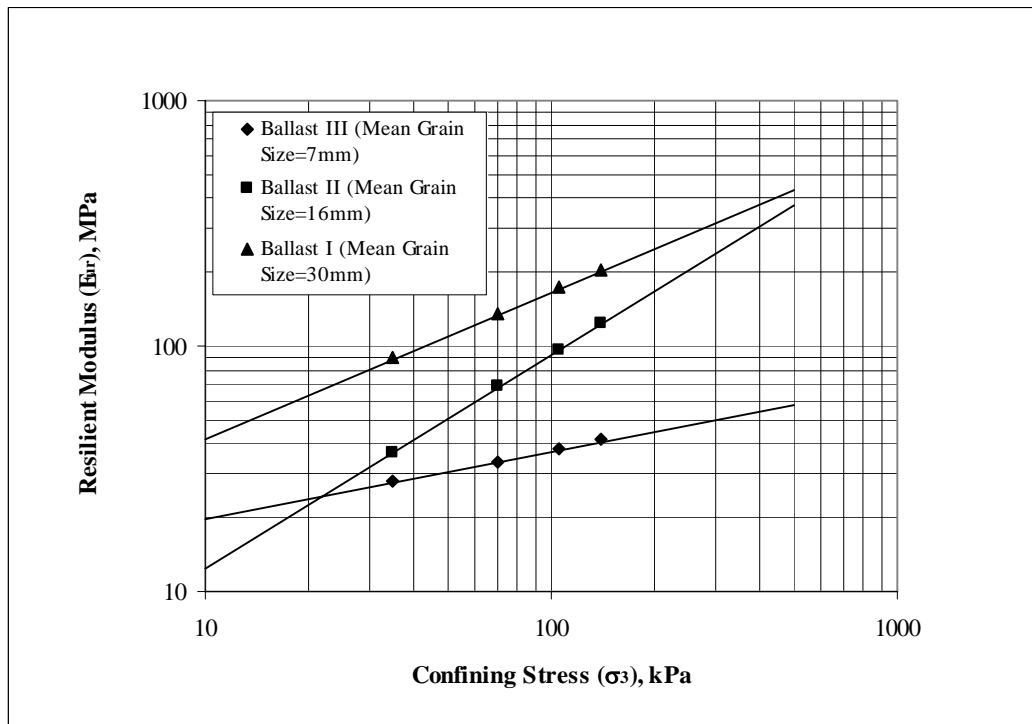


Figure 2.9 Variation of resilient modulus with confining stress  
(after Janardhanam & Desai, 1983)

$$E_{ur} = 10650(\sigma_3)^{0.27} \quad (2.20)$$

Similarly, the  $E_{ur}$  value for Ballast II was found to be

$$E_{ur} = 1671(\sigma_3)^{0.87} \quad (2.21)$$

For the prototype material Ballast I (Figure 2.8), Knutson (1978) (quoted by Janardhanam & Desai, 1983) obtained the value of  $E_{ur}$  shown in Figure 2.9 as:

$$E_{ur} = 10394(\sigma_3)^{0.60} \quad (2.22)$$

From Equations (2.20) to (2.22), Janardhanam & Desai (1983) have shown the variation of  $E_{ur}$  with  $D_{50}$  as in Figure 2.10, from which it is seen that  $E_{ur}$  increases remarkably with increase in  $D_{50}$  for a given  $\sigma_3$ .

Selig & Roner (1987) conducted triaxial tests to determine the effect of particle size on the shear strength of crushed quartzite ballast. Specimens 203 mm in diameter and 508 mm in height at different densities were tested under a confining stress  $\sigma_3 = 35$  kPa. Three gradings parallel to each other were prepared with a uniformity coefficient  $C_u = 1.03$ , and particles ranging between 38 mm and 29 mm (Grading 2); 29 mm and 19 mm (Grading 3); and 19 mm and 13 mm (Grading 4). The Los Angeles abrasion resistance of the ballast material was 20. No significant influence of change in particle size on the shear strength was found for the specimens tested (Figure 2.11).

Kaya et al. (1997) performed three series of tests using conventional triaxial equipment for each of the specimen diameters of 100 mm and 150 mm. The uniformly graded material studied was quartzite. For testing, this material was prepared using the parallel gradation technique as follows: for Series I: 2.36 mm to 4.75 mm; for Series II: 4.75 mm to 12.7 mm; for Series III: 9.52 mm to 19.1 mm (Figure 2.12). As seen, for Series II the gradation curve was somewhat off the

parallel due to sieve size limitations. To obtain as closely as possible the field density of the specimens, a calculated weight of ballast was placed in the specimen preparation mold. The density of the samples compacted by vibration varied between  $1.41 \text{ Mg/m}^3$  and  $1.46 \text{ Mg/m}^3$  with an average of  $1.44 \text{ Mg/m}^3$ . All specimens were then tested under four different confining stresses ( $\sigma_3$ ) ranging between 20 kPa and 160 kPa .

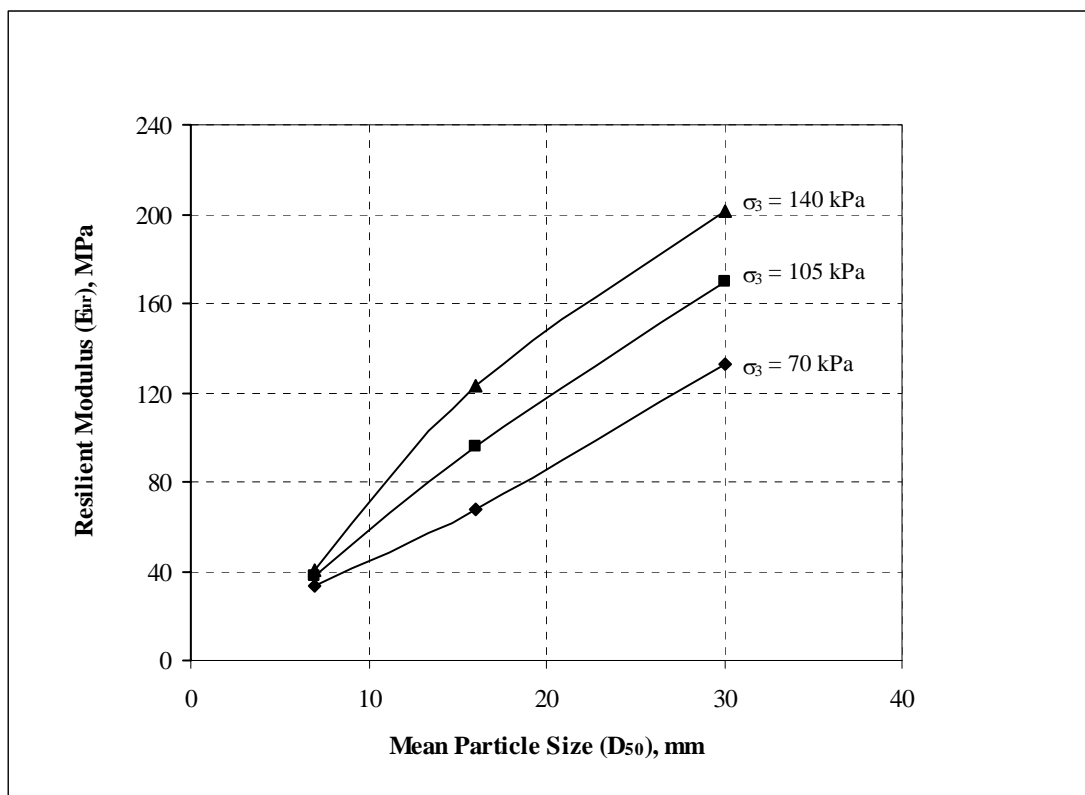


Figure 2.10 Variation of resilient modulus with mean particle size  
(after Janardhanam & Desai, 1983)

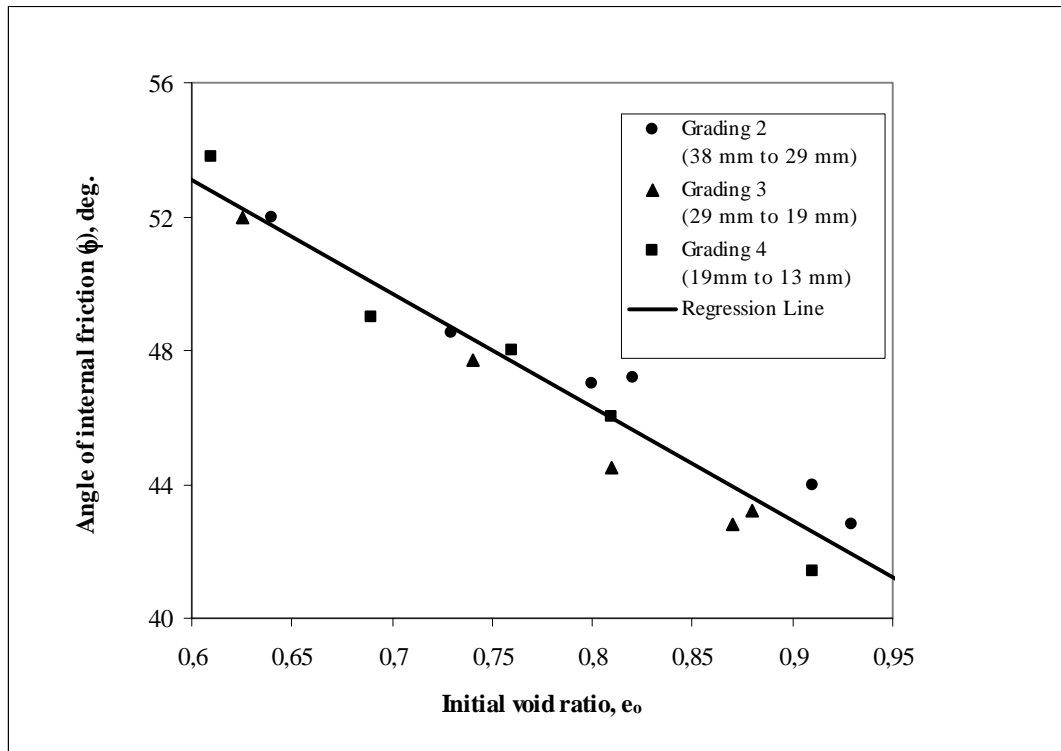


Figure 2.11 Effect of initial void ratio on angle of internal friction  
(after Selig & Roner, 1987)

Table 2.4 shows values of axial strain at typical levels of deviator stress for 100 mm diameter specimens under  $\sigma_3 = 40$  kPa, 80 kPa and 160 kPa. It can be seen that, similar to the observations by Janardhanam & Desai (1983), the smaller sized ballast, in general, experienced slightly greater axial strains with the deviator stress for a given  $\sigma_3$ .

The peak deviator stress  $(\sigma_1 - \sigma_3)_f$  was reached before 10% axial strain  $\epsilon_a$  in tests where  $\sigma_3 \leq 40$  kPa, but  $(\sigma_1 - \sigma_3)$  continued to increase to some extent after  $\epsilon_a = 10\%$  under  $\sigma_3 > 40$  kPa. In determining the angle of internal friction,  $\phi$ , the values of deviator stress at  $\epsilon_a = 10\%$  was taken as  $(\sigma_1 - \sigma_3)_f$  for  $\sigma_3 > 40$  kPa. Table 2.5 summarizes the  $\phi$  values for the three series of tests using 100 mm and 150 mm diameter specimens. As seen,  $\phi$  values obtained for both specimen sizes are close to

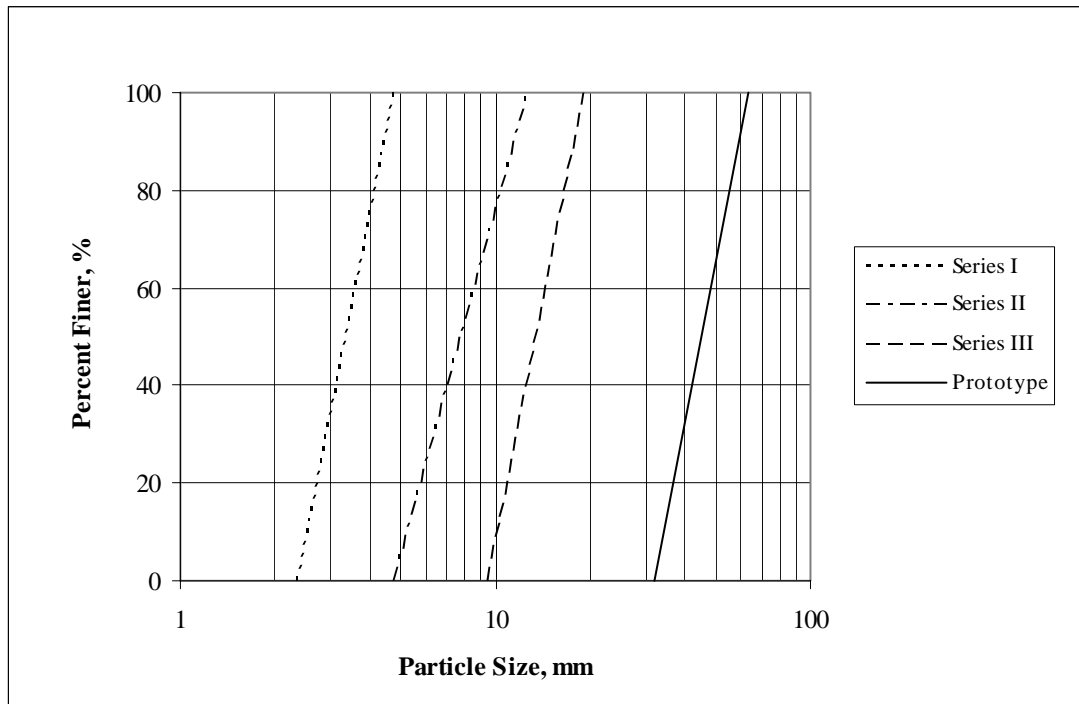


Figure 2.12 Particle size distribution curves for quartzite ballast  
(after Kaya et al., 1997)

Table 2.4 Comparison of axial strain at various stress levels (after Kaya et al., 1997)

Confining Stress (kPa)	Deviator stress (kPa)	Axial Strain (%)		
		(For 100 mm Diameter Specimen Size)		
		Series I (2.26 - 4.75 mm)	Series II (4.75 - 12.7 mm)	Series III (9.5 - 19.0 mm)
40	100	0.40	0.46	0.40
	200	2.95	2.30	2.40
80	100	0.20	0.20	0.18
	200	0.70	0.90	0.90
	400	8.18	7.94	7.70
160	100	0.22	0.22	0.20
	200	0.47	0.46	0.45
	400	2.05	2.05	1.70

Table 2.5 Angle of internal friction values for 100 mm and 150 mm diameter quartzite specimens (after Kaya et al., 1997)

Particle Size, mm	100 mm specimen			150 mm specimen		
	Friction Angle ( $\phi$ ), deg.	Apparent Cohesion (c), kPa	Coefficient of Determination ( $R^2$ )	Friction Angle ( $\phi$ ), deg.	Apparent Cohesion (c), kPa	$R^2$
Series I (2.26 - 4.75)	40.6	17	0.989	40.5	13	0.997
Series II (4.75 - 12.7)	41.0	23	0.991	41.5	13	0.996
Series III (9.5 - 19.0)	42.0	34	0.989	41.0	29	0.972
Combined Data	$\phi = 41.2^\circ$ , $c = 17$ kPa, $R^2 = 0.980$					
$\sigma_3$ is between 20 kPa and 160 kPa.						

each other, and a combined fit for all series of tests using both specimen sizes gave  $\phi = 41.2^\circ$  with an apparent cohesion of 17 kPa; the coefficient of determination  $R^2$  was 0.993, representing a good linear fit of the data. It indicated that the  $\phi$  values were virtually the same as the particle size increased.

The unloading-reloading modulus,  $E_{ur}$ , of the ballast material was also studied as a function of  $\sigma_3$ . The  $E_{ur}$  was taken as the reloading tangent modulus of the unloading-reloading loops.  $E_{ur}$  values showed an increasing trend with increasing mean particle size. To represent it quantitatively, the following  $E_{ur}$  (kPa) values were calculated at 0.5% axial strain for all  $\sigma_3$  (kPa) values. After regression analysis, following the procedure given in section 2.4.1,  $E_{ur}$  for Series I, II, and III was found to be as in Equations (2.23) to (2.25) respectively.

$$E_{ur} = 20,417(\sigma_3)^{0.372} \quad (2.23)$$

$$E_{ur} = 18,621(\sigma_3)^{0.418} \quad (2.24)$$

$$E_{ur} = 35,481(\sigma_3)^{0.300} \quad (2.25)$$

Equations (2.23) to (2.25) are depicted in Figure 2.13 as the variation of  $E_{ur}$  with the maximum grain size  $D_{max}$ , in which it is shown that  $E_{ur}$  increases gradually with increase in  $D_{max}$  for a given  $\sigma_3$ .

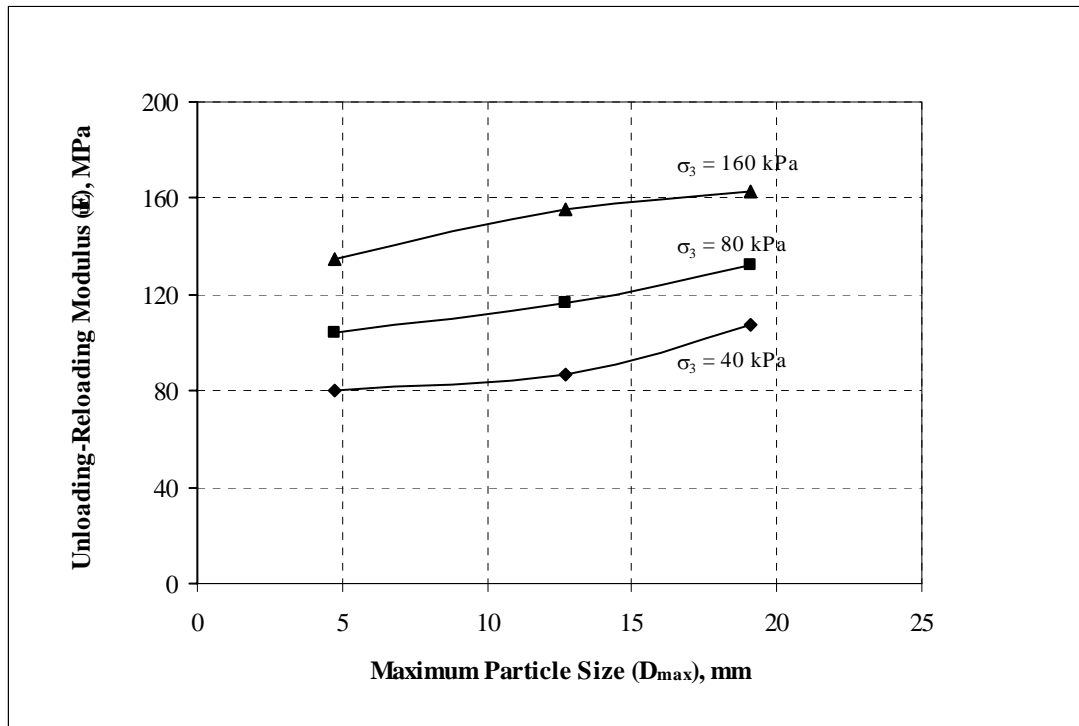


Figure 2.13 Variation of unloading-reloading modulus with maximum particle size (after Kaya et al., 1997)

### 2.7.2 Effect of Gradation on Stress-Strain- Strength Characteristics of Ballast

Raymond (1979) presented the results of triaxial tests on material with different grading curves obtained by Talbot and Richart's (Raymond, 1979) grading Equation (2.26) given in Fig. 2.14. The particles finer than 4.8 mm sieve size were removed. In Talbot and Richart's equation,  $P$  is percentage finer than;  $D$  is particle size in question;  $D_{\max}$  is the maximum particle size; and  $n$  is an exponent to adjust the curve. The confining stress  $\sigma_3$  applied on both loose and dense sample was 35 kPa.

Test results showed that gradation had almost no effect on shear strength. On the other hand, the initial tangent modulus  $E_i$  obtained after fitting the experimental stress-strain relationships to Hyperbolic Equation (2.10) (section 2.4.2) showed an increase in the  $E_i$  of the dense samples using a Talbot and Richart's grading index ( $n$ ) of approximately 0.7, despite there is scatter in the data as shown in Figure 2.15.

Selig and Roner (1987) conducted triaxial tests to determine the effect of gradation on the shear strength using specimens 203 mm in diameter and 508 mm in height under  $\sigma_3 = 35$  kPa. The ballast material used in the tests was crushed quartzite. Its Los Angeles abrasion resistance was 20%. Two ballast gradings at different densities were prepared: particle size between 38 mm to 13 mm with a uniformity coefficient  $C_u = 1.47$  (Grading 1) and that between 38 mm to 29 mm with  $C_u = 1.03$  (Grading 2).

No significant influence of change in gradation on the shear strength of quartzite ballast was found as shown Figure 2.11. For example, for Grading 1, the angle of internal friction  $\phi$  at initial void ratio  $e_o$  of 0.61 was about  $52^\circ$  and at  $e_o = 0.70$   $\phi = 49^\circ$ ; for Grading 2,  $\phi = 52^\circ$  at  $e_o = 0.64$ ; and  $\phi = 48^\circ$  at  $e_o = 0.72$ .

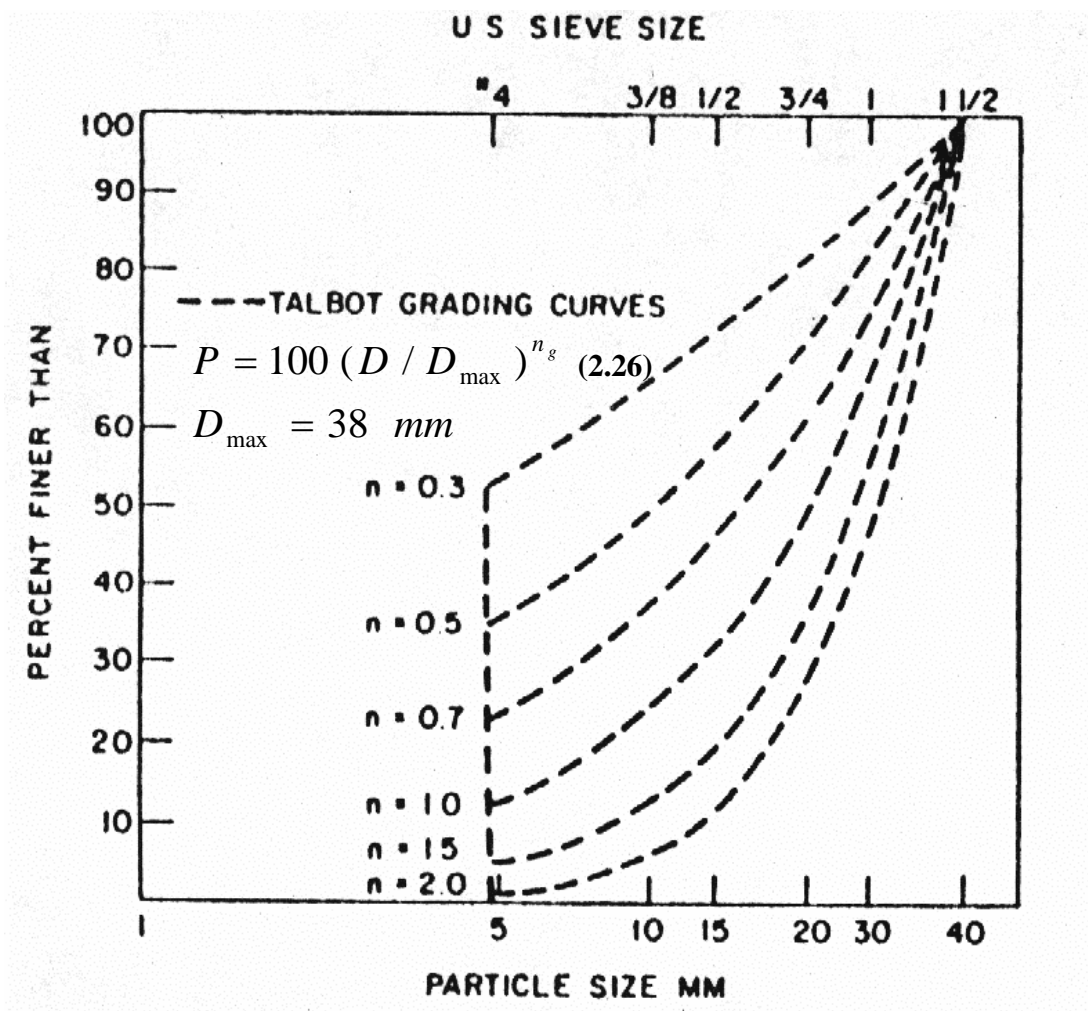


Figure 2.14 Ballast grading used in grading research program (after Raymond, 1979)

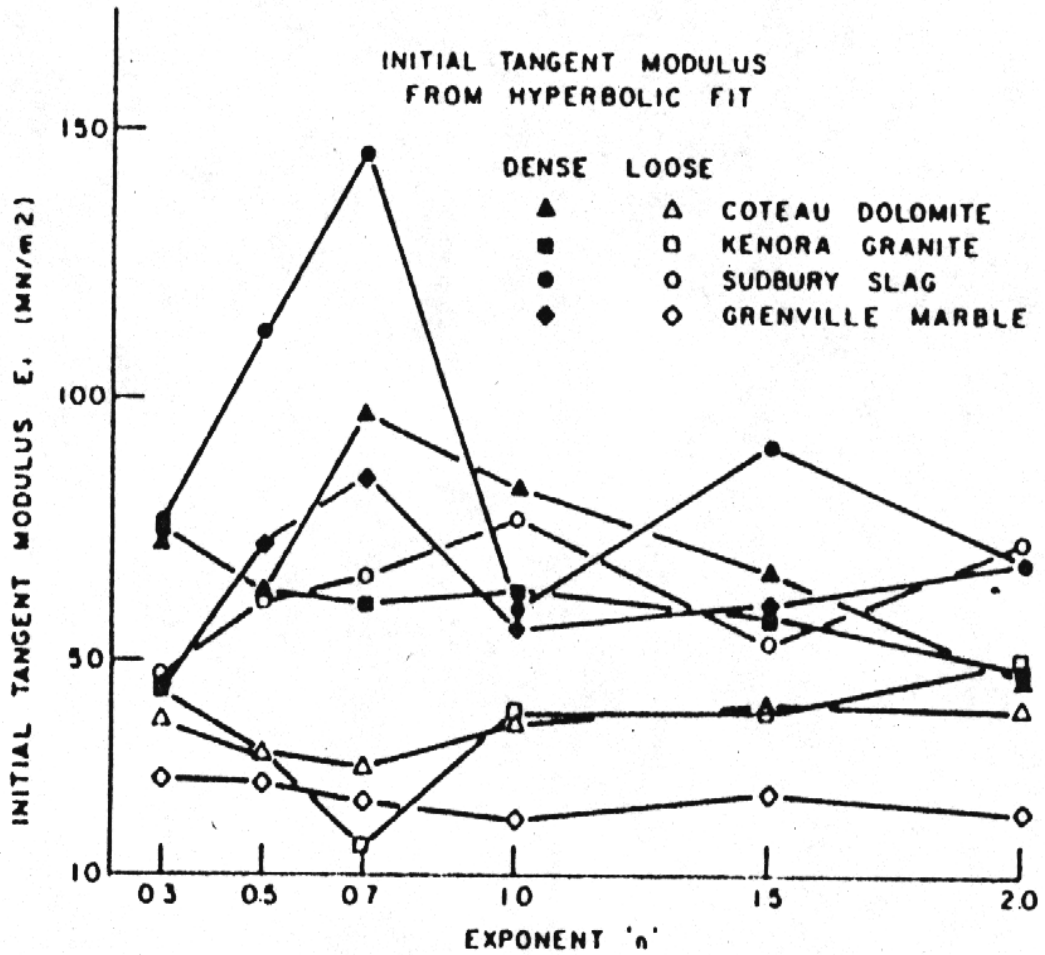


Figure 2.15 Initial elastic modulus for various graded ballasts at  $\sigma_3=35$  kPa (after Raymond, 1979)

## **CHAPTER III**

### **CHARACTERIZATION TESTS OF BALLASTS**

#### **3.1 Ballast**

Several types of materials such as limestone, basalt, and slag are used for ballast. The widespread used ballast in Turkish State Railways (TCDD) is limestone on account of its abundance in Turkey; and basalt is used in a very limited region of Turkey and considered to be increased its use in view of the planned high-speed train project. Steel-slag, byproduct material of Ereğli Iron and Steel Works (ERDEMİR), is proposed to be used to regain to economy as ballast. The standard gradation recommended by TCDD is shown in Figure 3.1. To gain knowledge of strength, elastic and plastic behavior due to material type, crushed rocks from different sources were selected for characterization and for the triaxial testing of scaled-down materials due to parallel gradation technique as will be discussed in the coming chapters.

##### **3.1.1 Description of Materials**

Limestone, basalt and steel-slag ballast materials were chosen so that comparison of their physical characteristics due to material type could be made.

Because limestone is the most commonly used ballast type, preliminary testing for the reproducibility of tests was conducted using a limestone obtained from

a quarry near Kayaş-Ankara, Turkey. The same limestone was used in the main testing program also. The other materials obtained were basalt from a quarry near Çorlu-Tekirdağ, Turkey and steel-slag from Ereğli-Zonguldak, Turkey.

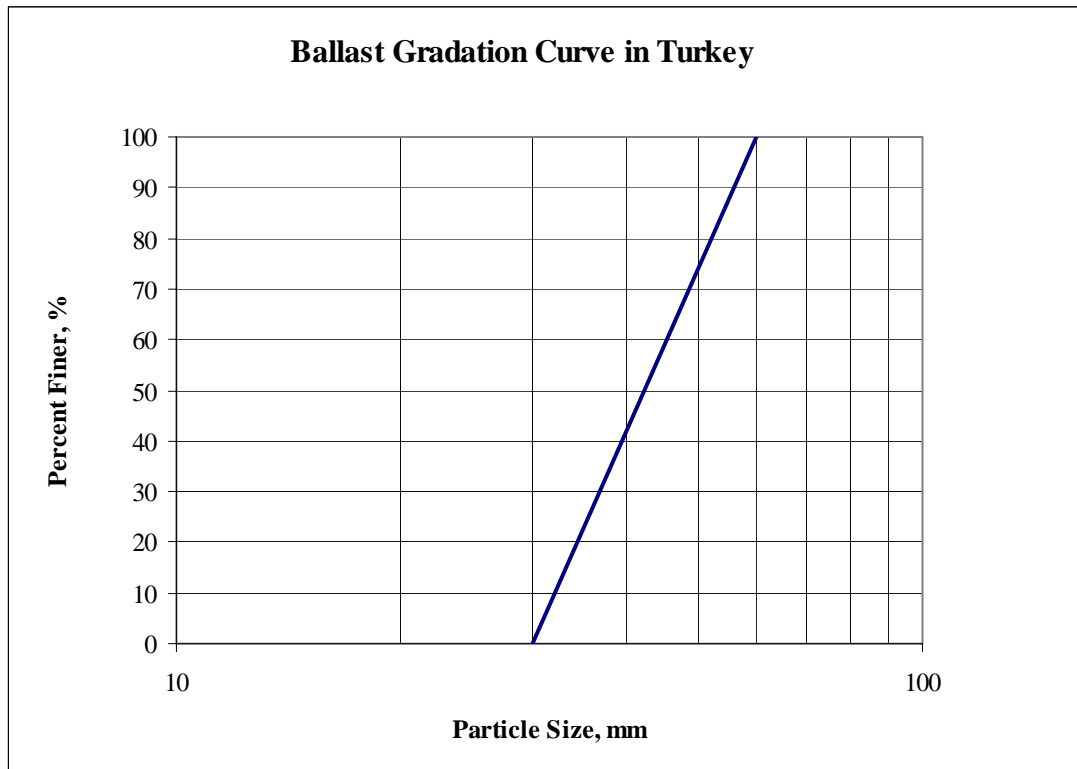


Figure 3.1 Particle size distribution for ballast used in Turkey (after TS 7043, 1989)

Ballast materials like limestone or basalt produced from bedrock are obtained from quarries as stated above. After stripping and opening the quarry, substantial face of rock is exposed. Holes are drilled from the surface. Then dynamite is placed in these holes to break the rock into sizes that can be transported. The rock is then crushed to the ballast sizes in rock crushers and screened. However, steel-slag is byproduct material resulting from the treatment of ore to produce steel. Thus the production of ballast material from steel-slag is a rather complex process. The

following flowchart in Figure 3.2 gives a brief explanation about how steel-slag and ballast from which are produced.

### **3.1.1.1 Mineralogical Description of Materials**

The mineral compositions of the crushed basalt and limestone were determined in The General Directorate of Mineral Research and Exploration's Thin-Section Laboratory, Ankara-Turkey. The freshly broken rock samples were analyzed through the petrographic analysis, with a hand lens or low-powered (stereo) microscope.

The limestone sample contains microfossils, intraclasts composed of cryptocrystalline calcite and pellets within micro-mesocrystalline calcite crystals. Frequently observed joints and pores are filled up with secondary meso-macrocrystalline calcite crystals.

The texture of the crushed basalt is intergranular. The matrix is composed of plagioclase, pyroxene, volcanic glass and olivine as microphenocrystal. Olivine microphenocrystals are recorded as euhedral, subhedral and anhedral. Plagioclases observed in the matrix are subhedral and have polysynthetic twinning. Pyroxenes (Augite) are in the form of subhedral and anhedral. Weak chloritizations derived from pyroxenes are observed. Amount of olivine in the matrix is comparatively lesser than plagioclases and pyroxenes. Disseminated opaque minerals with subhedral form are observed.

The chemical and mineralogical analysis of steel-slag particles randomly collected from ERDEMIR steel-slag site were done by Turkish Scientific and Research Institute (TUBITAK, 2002); results of the analysis are presented in Table 3.1 and 3.2, respectively. The range of constituents in mineralogical composition is due to the process of steel production and the cooling rate of steel-slag.

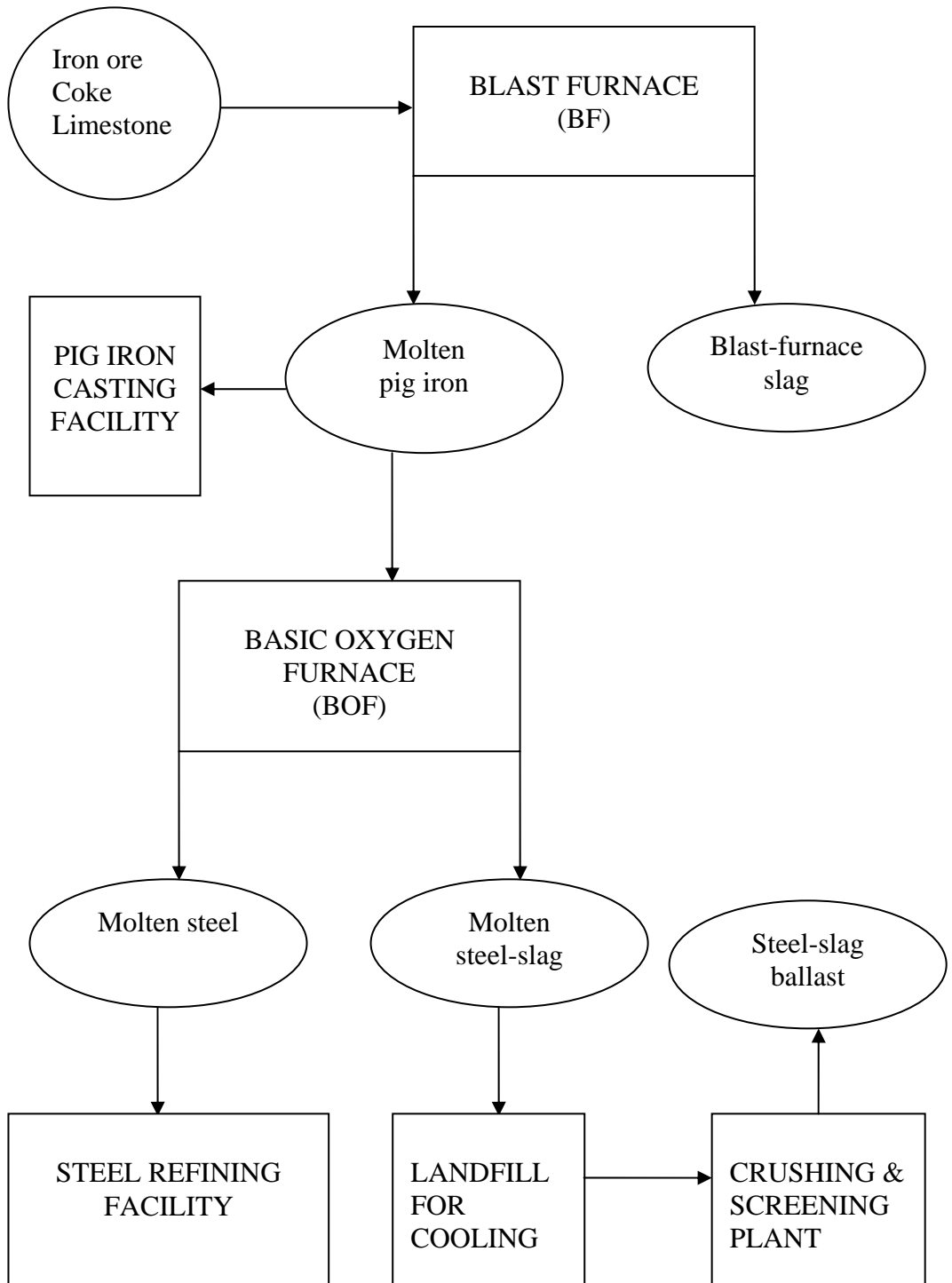


Figure 3.2 Schematic view of production of steel-slag ballast in ERDEMIR

Table 3.1 Chemical analysis of ERDEMİR steel-slag (TUBITAK, 2002)

Element	ERDEMİR Steel-Slag, %
CaO	47 – 55
FeO	17 – 36
SiO <sub>2</sub>	8 – 15
Al <sub>2</sub> O <sub>3</sub>	1.2 – 2.4
MgO	1.3 – 2.7
Total Fe	20 -26
MnO	3.8 – 4.4
Na <sub>2</sub> O	-
K <sub>2</sub> O	-
P <sub>2</sub> O <sub>5</sub>	-
TiO <sub>2</sub>	-
SO <sub>3</sub>	-
S	-

Table 3.2 Qualitative mineralogical analysis of ERDEMİR steel-slag  
(TUBITAK, 2002)

Chemical Formula	Reference
Ca <sub>2</sub> SiO <sub>4</sub>	PDF No : 33-302
CaFeO <sub>2</sub>	PDF No : 21-917
3Ca <sub>2</sub> Fe <sub>2</sub> O <sub>5</sub>	PDF No : 11-675
* PDF No: Powder Diffraction File number (of SHIMADZU XRD-6000 Model X-Ray Powder Diffraction Apparatus)	

### 3.1.2 Characterization Tests

For quality assessment and in order to relate the results of triaxial tests to the material type, standard tests were performed. The standard tests and the corresponding references are included in Table 3.3.

The test results for limestone, basalt and steel-slag are summarized in Table 3.4. In this table, the symbol L-30, for example, means that it is Limestone material having particle sizes of between 30 mm and 60 mm and thus has a minimum particle size of 30 mm. These tests were performed in Variant and Group Laboratory of TCDD. The recommended values are also given in Table 3.4.

Two additional tests are needed for characterization of the steel-slag ballast. Since steel-slag contains iron and aluminum in its chemical composition, electrical resistivity test is performed to determine if steel-slag ballast would provide adequate electrical insulation between the rails for the track signal circuits. Material and Chemical Technology Research Institute (MKTAE) of Marmara Research Center-TUBITAK tested five samples taken from ERDEMİR steel-slag site to characterize the electrical resistivity of these samples using a conductivity apparatus. The resistivity values of ballast materials shall not be less than  $0.002 \Omega \times \text{km}$  according to the standard given by TUBITAK (2002). The results are indicated in Table 3.5. For the sake of comparison, electrical resistivities of some common materials are given in Table 3.6.

The other test is the leachate analysis of the steel-slag ballast because it is considered to be a solid waste material discharged onto railway. Contaminants of waste and their levels are determined to assess the leachate quality. The tests according to Standard methods for the examination of water and wastewater (Clesceri, 1998) were performed in Environmental Engineering Laboratory at METU. The list of contaminants, test results and their regulatory levels are included in Table 3.7.

Table 3.3 Standard characterization test references

Characteristic Test	Test Reference
Los Angeles Abrasion (1000 cycle) (%)	TS 3694
Water Absorption (%)	TS 699
Bulk Specific Gravity	TS 699
Specific Gravity	TS 699
Freeze-Thaw (Na <sub>2</sub> SO <sub>4</sub> Soundness) (%)	TS 3655
Organic Soil Content (%)	TS 3673

Table 3.4 Average results of characterization tests

Material and Gradation	Bulk Specific Gravity	Specific Gravity	Los Angeles Abrasion Loss, %	Water Absorption, %	Freeze-Thaw (Na <sub>2</sub> SO <sub>4</sub> Soundness), %	Organic Soil Content, %
L-30 (30-60 mm)	2.70	2.70	24.25	0.13	0.17	None
B-30 (30-60 mm)	2.93	2.93	9.50	0.07	0.08	None
S-30 (30-60 mm)	3.12	3.24	10.70	0.35	1.65	None
30 - 60 mm*	-*	-*	<30%*	<2%*	<10%*	<0.5%*
L: Limestone; B: Basalt; S: Steel-Slag *: Recommended Values						

Table 3.5 Results of the electrical resistivity of steel-slag ballast (TUBITAK, 2002)

Sample No.	Conductivity, mS/m (=1/ $\Omega \times \text{km}$ )	Resistivity, $\Omega \times \text{km}$
1	$0.9 \pm 0.1$	1.11
2	$37 \pm 9$	0.027
3	$26 \pm 4$	0.038
4	$1 \pm 0.1$	1
5	$10 \pm 0.7$	0.1

Table 3.6 Resistivities for various materials at 20 °C temperature (Serway, 1996)

Material	Resistivity, $\Omega \times \text{km}$
Silver	$1.59 \times 10^{-11}$
Copper	$1.7 \times 10^{-11}$
Gold	$2.44 \times 10^{-11}$
Aluminum	$2.82 \times 10^{-11}$
Iron	$10 \times 10^{-11}$
Lead	$22 \times 10^{-11}$
Carbon	$3.5 \times 10^{-11}$
Silicon	0.640
Glass	$10^7 - 10^{11}$
Hard rubber	$10^{10}$
Quartz (fused)	$75 \times 10^{13}$

Table 3.7 Waste acceptance criteria (Official Gazette, 1996) and test results

Contaminant	Test Results	Regulatory Level
pH	9.23	4 - 13
Total Organic Carbon (TOC)	18.5 mg/l	< 200 mg/l
Arsenic	< 0.002 mg/l	< 0.1 mg/l
Lead	< 0.002 mg/l	< 0.4 mg/l
Cadmium	< 0.002 mg/l	< 0.1 mg/l
Chromium <sup>VI</sup>	< 0.01 mg/l	< 0.1 mg/l
Copper	< 0.001 mg/l	< 2 mg/l
Nickel	< 0.001 mg/l	< 0.4 mg/l
Mercury	< 0.001 mg/l	< 0.02 mg/l
Zinc	0.0176 mg/l	< 2 mg/l
Phenols	< 0.001 mg/l	< 10 mg/l
Fluoride	0.19 mg/l	< 5 mg/l
Ammonium	0.25 mg/l	< 50 mg/l
Chloride	19.2 mg/l	< 0.5 g/l
Cyanide	< 0.001 mg/l	< 0.1 mg/l
Sulphate	< 9.8 mg/l	< 1 g/l
Nitrite	< 0.001 mg/l	< 3 mg/l
Adsorbable Organic Halides (AOX)	< 0.0146 mg/l	< 0.3 mg/l
Solvents	< 0.02 µg Cl/l	< 10 µg Cl/l
Pesticides	< 0.2 µg Cl/l	< 0.5 µg Cl/l
Lipoph. substances	< 0.001 mg/l	< 1 mg/l

## CHAPTER IV

### LABORATORY TESTING PROGRAM

#### 4.1 Description of Parallel Gradation Technique

Since the ballast size discussed in Chapter III is too large to be tested in the available triaxial equipment, the ballast materials are scaled-down using the parallel gradation technique to particle sizes suitable for that equipment so that the effect of particle sizes on strength and deformation characteristics is investigated to enable correlations with that of the ballast. The parallel gradation technique attempts to preserve the particle shape, particle surface roughness and particle mineralogy of the scaled-down particle sizes with that of the prototype soil thus leaving only the particle size as the correlation parameter. In addition, the effect on the stress-strain behavior of material type can be examined.

Experimental investigations were performed with triaxial equipment capable of testing a specimen with 100 mm diameter available in the geotechnical engineering laboratory at METU. With this sample size, the maximum particle size tested in this study was 19.0 mm. Although the ratio of the sample diameter to the maximum particle size being 5.3 is slightly lower than the rule of thumb value of 6, it is virtually within the acceptable limits (Head, 1982; Indraratna et al., 1998). Also, the fact that  $\frac{3}{4}$  inch (19.0 mm) sieve size is the closest sieve size available in the laboratory to enable the ratio as close to 6 as possible.

#### **4.1.1 Description of Scaled-down Materials**

In order to see if use of the parallel gradation technique would lead to reasonable predictions of peak shear strength and deformation characteristics, a series of parallel gradations were prepared. First, the limestone, basalt and steel-slag materials screened-in-place were sieved, washed and dried in oven. Then each size of material was stored in a separate container for recombining into the desired gradation. The railroad ballast prototype is linearly graded from 30 mm to 60 mm in particle size. This gives a maximum particle size to minimum particle size ratio of 2. The ballast and the scaled-down gradations of limestone and basalt materials tested are shown in Figure 4.1 and Figure 4.2, respectively. To preserve as much as possible the homogeneity of the steel-slag ballast as it was scaled-down, the parallel gradations were taken within a narrower range as depicted in Figure 4.3.

To examine the effect of gradations on the stress-strain behavior of ballast, two other gradations were prepared alternatively to the standard gradation. The strength and elastic characteristics of the alternative gradations will be compared to that of the scaled-down aggregate of limestone having gradation limits of 9.5 mm and 19.1 mm only. These gradations are designated as L-6.35 and L-3.15, having particle size ranges from 6.35 mm to 19.0 mm and from 3.15 mm to 19.0 mm, respectively. The various gradations of the samples tested are shown in Figure 4.4.

#### **4.1.2 Characterization Tests**

In order to relate the results of triaxial tests to the physical properties of the materials, standard tests were performed. The tests were done in the geotechnical engineering laboratory of Civil Engineering at METU. The standard tests and references are included in Table 4.1. A detailed discussion of the various test procedures is also included in Filiz (2000). The results of physical properties of the aggregates tested are summarized in Table 4.2. In this table, the symbol L-2.36, for example, means that it is Limestone material and has a minimum particle size of 2.36

mm (retained on No.8 sieve);  $D_{50}$  is the mean particle size, particle size corresponding to 50% of particles passing by weight;  $C_u$  is the coefficient of uniformity;  $C_c$  is the coefficient of curvature; and GP stands for poorly graded gravel. The specific gravity and compaction test results are given in Table 4.3. Unlike limestone and basalt materials, the specific gravity of the steel-slag particles was not constant, indicating that mineralogy changes with size for this material, although the parallel gradations were taken within a narrower range. Nevertheless, the existence of heterogeneous particles might mostly be due to the process of the steel-slag production as explained in section 3.1.1.1.

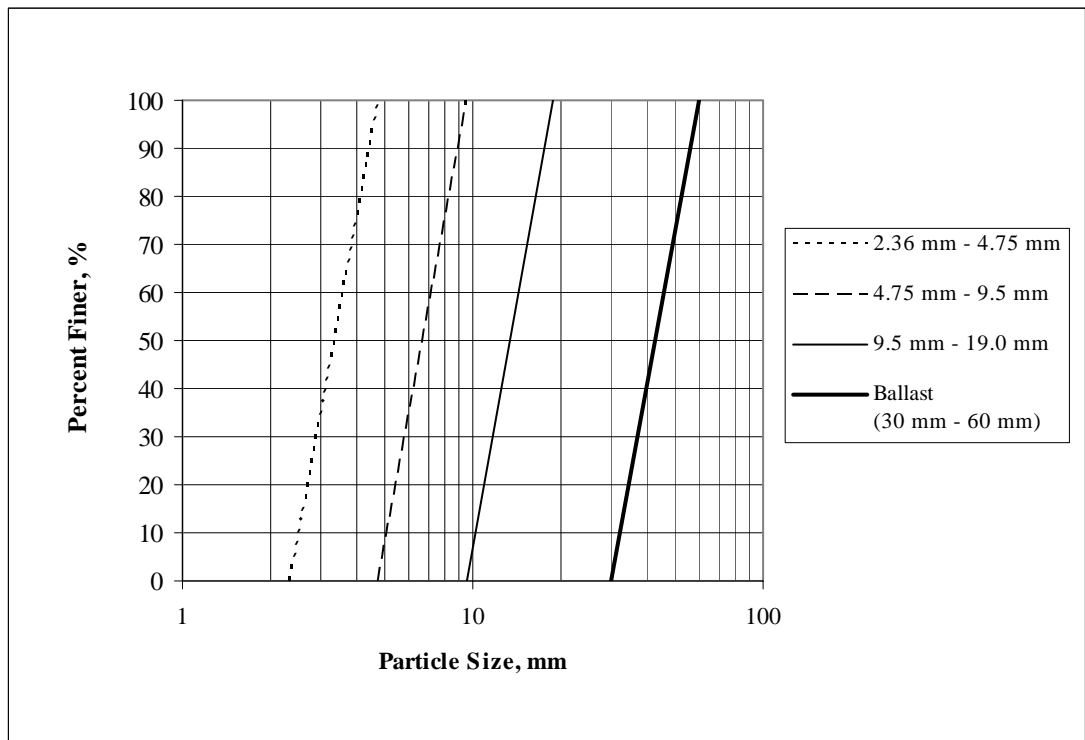


Figure 4.1 Ballast and the scaled-down gradations of crushed Limestone samples

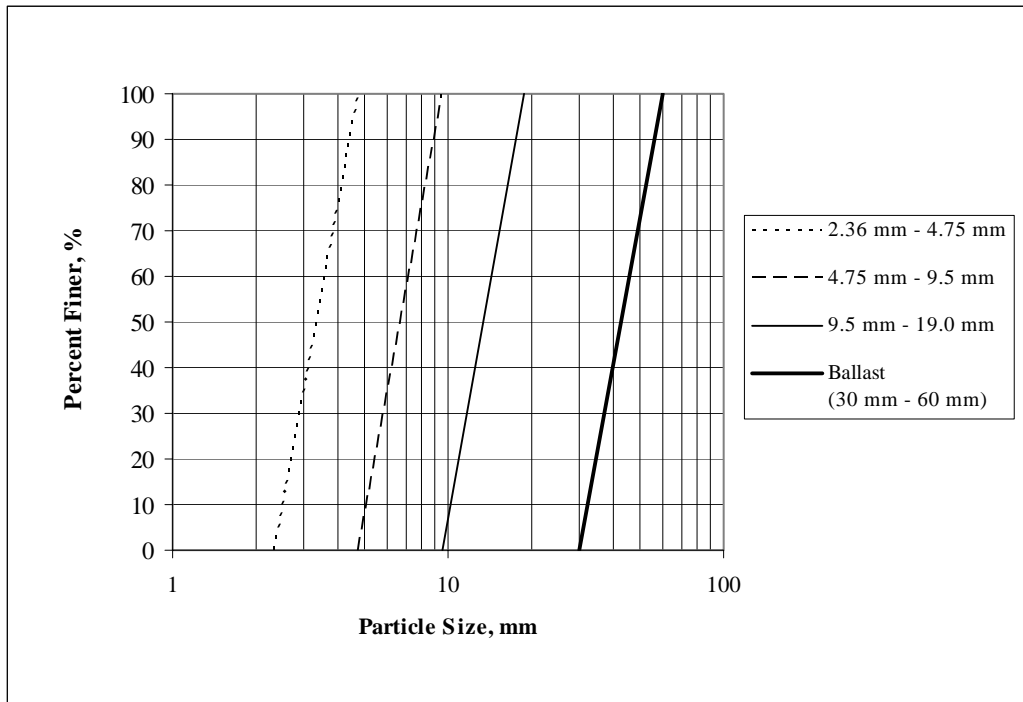


Figure 4.2 Ballast and the scaled-down gradations of crushed Basalt samples

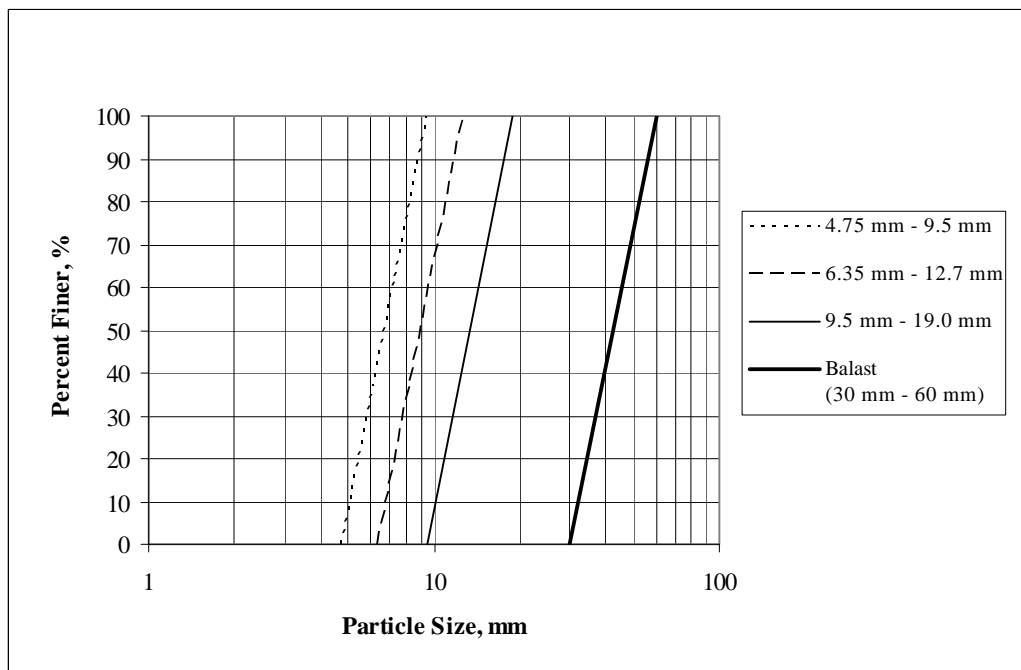


Figure 4.3 Ballast and the scaled-down gradations of crushed Steel-slag samples

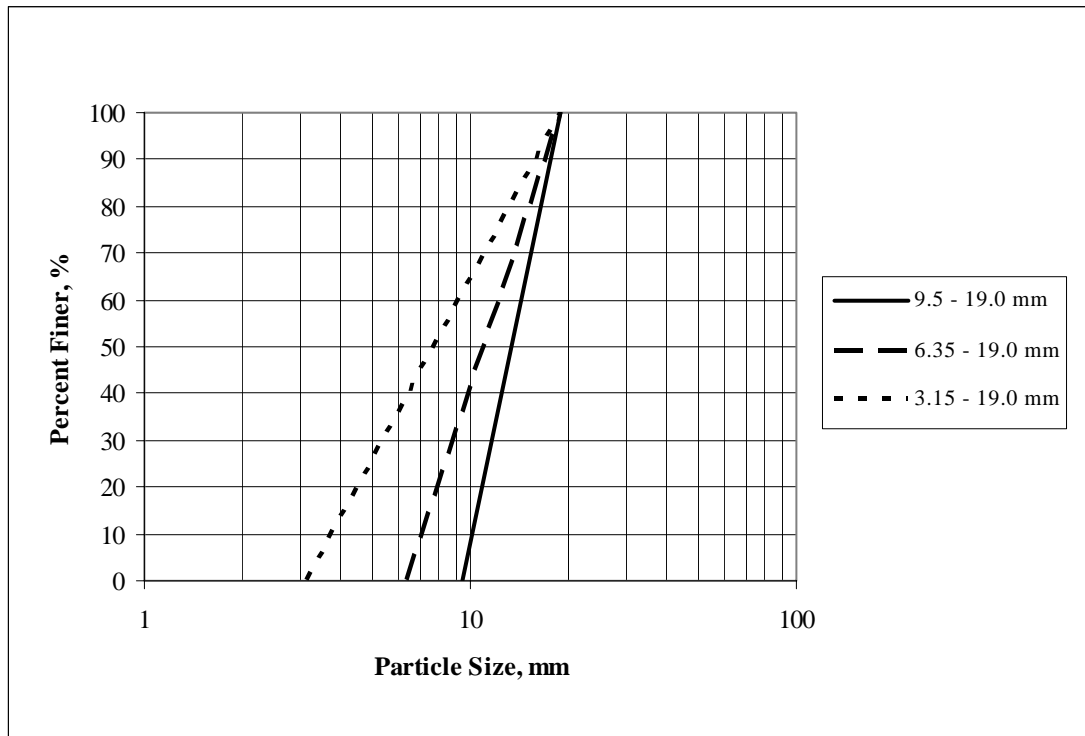


Figure 4.4 Various gradations of crushed limestone samples

Table 4.1 Standard Test References

Test	References
Coefficient of uniformity	TS 1900
Coefficient of curvature	TS 1900
Specific gravity	TS 1900
Minimum density	BS 1377
Maximum density	BS 1377
TS: Turkish Standard; BS: British Standard	

Table 4.2 Physical properties of materials tested

Material	Gradation	Range of Particle Sizes, mm	D <sub>50</sub> , mm	C <sub>u</sub>	C <sub>c</sub>	BS Classification
Limestone	L-2.36	2.36-4.75	3.15	1.40	1.03	GP
	L-4.75	4.75-9.5	6.35	1.40	1.03	GP
	L-9.5	9.5-19.0	12.7	1.40	1.03	GP
	L-6.35	6.35-19.0	11.0	1.75	1.16	GP
	L-3.15	3.15-19.0	8.0	2.38	1.20	GP
Basalt	B-2.36	2.36-4.75	3.15	1.40	1.03	GP
	B-4.75	4.75-9.5	6.35	1.40	1.03	GP
	B-9.5	9.5-19.0	12.7	1.40	1.03	GP
Steel-slag	S-4.75	4.75-9.5	6.35	1.40	1.03	GP
	S-6.35	6.35-12.7	9.5	1.40	1.03	GP
	S-9.5	9.5-19.0	12.7	1.40	1.03	GP

#### 4.1.2.1 Particle Shape Analysis

Particle shape as part of a composition influences the strength and elastic characteristics of soils [Koerner (1970), Lambe and Whitman (1979); Mitchell (1993)]. In order to minimize this effect on the stress-strain behavior of the ballast materials, shape analysis was performed, based on the measurement of each of 20 randomly selected particles from each material type. Table 4.4 through Table 4.6 lists some dimensions including that of ballast of the average length (l), width (w) and thickness (t) for the materials each. Dimension ratios were also calculated in the corresponding tables by simply dividing each dimension to the thickness.

Table 4.3 Summary of the specific gravity and compaction test results

Material	Gradation	Specific Gravity (Gs)	Minimum Density ( $\rho_d$ ) <sub>min</sub> , kN/m <sup>3</sup>	Maximum Density ( $\rho_d$ ) <sub>max</sub> , kN/m <sup>3</sup>
Limestone	L-2.36	2.70	13.28	16.40
	L-4.75	2.70	13.80	16.40
	L-9.5	2.70	13.94	16.50
	L-6.35	2.70	14.22	16.68
	L-3.15	2.70	14.74	17.81
Basalt	B-2.36	2.93	14.36	16.92
	B-4.75	2.93	14.78	16.87
	B-9.5	2.93	14.78	16.77
Steel-slag	S-4.75	3.18	14.62	18.10
	S-6.35	3.12	14.59	17.30
	S-9.5	3.17	15.21	17.82

Table 4.4 Average dimensions of limestone aggregates

Mineralogy and Particle Size, mm	Length (l), mm	Width (w), mm	Thickness (t), mm	Dimension Ratio (l:w:t)
L-50.0	83.1 ± 9.6	60.9 ± 5.6	45.5 ± 6.4	1.9:1.4:1.0
L-19.0	33.9 ± 3.5	24.2 ± 2.8	16.9 ± 3.3	2.1:1.5:1.0
L-9.5	19.5 ± 2.8	12.8 ± 1.9	9.1 ± 1.8	2.2:1.4:1.0
L-4.75	10.5 ± 1.1	6.6 ± 0.7	4.9 ± 0.9	2.2:1.4:1.0

Table 4.5 Average dimensions of basalt aggregates

Mineralogy and Particle Size, mm	Length (l), mm	Width (w), mm	Thickness (t), mm	Dimension Ratio (l:w:t)
B-37.5	78.4 ± 10.7	58.4 ± 2.1	38.1 ± 1.7	2.1:1.5:1.0
B-19.0	38.9 ± 5.4	28.9 ± 3.3	18.2 ± 2.8	2.2:1.6:1.0
B-9.50	20.1 ± 1.9	14.4 ± 2.3	8.1 ± 1.5	2.5:1.8:1.0
B-4.75	9.0 ± 1.7	7.2 ± 0.8	4.3 ± 0.8	2.2:1.7:1.0

Table 4.6 Average dimensions of steel-slag aggregates

Mineralogy and Particle Size, mm	Length (l), mm	Width (w), mm	Thickness (t), mm	Dimension Ratio (l:w:t)
S-50.0	83.4 ± 10.7	64.7 ± 2.9	47.0 ± 5.1	1.8:1.4:1.0
S-19.0	35.8 ± 5.9	25.8 ± 3.4	19.7 ± 4.9	1.9:1.4:1.0
S-9.50	19.9 ± 3.1	14.1 ± 2.5	9.2 ± 1.4	2.2:1.6:1.0
S-4.75	10.2 ± 1.7	6.9 ± 1.0	4.6 ± 0.8	2.3:1.6:1.0

Shape tests consisted of flakiness, elongation, and shape factor, angularity or roundness, and sphericity. A description of shape tests and procedures is given in Selig and Waters (1994):

**“Flakiness:** The British Standard defines a flaky particle as one in which the ratio of width to thickness is greater than 1.7. On the other hand, The U.S. Army Corps of Engineers defines a flaky particle as one with a width-to-thickness ratio of greater than 3. In both cases, the flakiness index is the percent by weight of flaky particles in a sample.

**Elongation:** The British Standard defines an elongated particle as one with a length to width ratio of more than 1.8. On the other hand, The U.S. Army Corps of Engineers defines an elongated particle as one with a length to width ratio of greater than 3. In both cases, the elongation index is the percent by weight of elongated particles in a sample.

**Shape Factor:** A shape factor for ballast was developed by Raymond in conjunction with research for the Canadian railroads. He defines the shape factor as the ratio of summation of the longest dimension of particles to that of the smallest dimension in a representative sample.

**Angularity or Roundness:** Angularity, or its inverse, roundness, is a measure of the sharpness of the edges and corners of an individual particle. Roundness,  $\rho$ , is defined as

$$\rho = \frac{1}{N} \sum_{i=1}^N \left( \frac{r_i}{R} \right) \quad (4.1)$$

where  $r_i$  = individual corner radius,

$R$  = radius of circle inscribed about the particle, and

$N$  = number of corners on particle

A projected image of the particle is used to obtain the measurements. Particles in sample are grouped according to their angularity, with group categories ranging from angular to rounded.

**Sphericity:** Sphericity is a measure of how much the shape of a particle deviates from a sphere. A perfect sphere has sphericity of one. Sphericity,  $S_p$ , is defined as

$$S_p = \frac{\sqrt[3]{\frac{6V}{\pi}}}{l} \quad (4.2)$$

where  $V$  = volume of particle, and

$l$  = diameter of the smallest sphere that circumscribe the particle = length of the particle

If the shape of the particle is approximated by an ellipsoid and the volume of the particle  $V$  is equated to that of ellipsoid (Jernigan, 1998), one gets

$$S_p = \frac{\sqrt[3]{\frac{6V}{\pi}}}{l} \approx \frac{\sqrt[3]{l \cdot w \cdot t}}{l} \quad (4.3)$$

where  $l$ ,  $w$ , and  $t$  were defined previously.”

Visual estimates of particle roundness and sphericity are normally used in lieu of the more laborious method of image measurement. Charts to aid in this estimating are available, for example Figure 4.5 shows a chart of variations in sphericity and roundness. Due to the view of the particles illustrated in Figure 4.5, the values of roundness and sphericity calculated using Equation (4.1) and Equation (4.2), respectively are compared. Figures 4.6 through Figure 4.20 are photographs of the various aggregates, in which all particles are angular due to crushing.

Table 4.7 through Table 4.9 lists the results of shape analysis for various particles; and the corresponding equations were given at the bottom of each table. The lists indicate that the particle shapes are more or less same as the particles scaled-down for each material type. The change in sphericity, for example, is

relatively minor, with the maximum difference in sphericity for crushed limestone and steel- slag being 0.09; for crushed basalt being 0.08. Although the flakiness of various basalt particles is slightly above the limit according to British Standard, it complies with the U.S. Army Corps of Engineers' standard.

Table 4.7 Particle shape analysis of limestone aggregates

Mineralogy and Particle Size, mm	Sphericity ( $S_p$ )*	Flakiness ( $F$ )*	Elongation ( $E$ )*	Shape Factor ( $S_f$ )*
L-50.0	0.74 ± 0.06	1.37 ± 0.31	1.37 ± 0.20	1.82
L-19.0	0.71 ± 0.07	1.49 ± 0.37	1.43 ± 0.27	2.01
L-9.5	0.68 ± 0.09	1.45 ± 0.35	1.56 ± 0.35	2.13
L-4.75	0.66 ± 0.07	1.38 ± 0.30	1.62 ± 0.16	2.15
* $S_p = \frac{\sqrt[3]{l \cdot t \cdot w}}{l_1}$ ; $F = \frac{w}{t}$ ; $E = \frac{l}{w}$ ; $S_f = \frac{\sum l}{\sum t}$				

Table 4.8 Particle shape analysis of basalt aggregates

Mineralogy and Particle Size, mm	Sphericity ( $S_p$ )*	Flakiness ( $F$ )*	Elongation ( $E$ )*	Shape Factor ( $S_f$ )*
B-37.5	0.72 ± 0.07	1.54 ± 0.11	1.35 ± 0.21	2.06
B-19.0	0.71 ± 0.07	1.64 ± 0.39	1.35 ± 0.21	2.13
B-9.5	0.66 ± 0.05	1.81 ± 0.30	1.42 ± 0.19	2.48
B-4.75	0.73 ± 0.08	1.75 ± 0.44	1.28 ± 0.31	2.11
* $S_p = \frac{\sqrt[3]{l \cdot t \cdot w}}{l_1}$ ; $F = \frac{w}{t}$ ; $E = \frac{l}{w}$ ; $S_f = \frac{\sum l}{\sum t}$				

Table 4.9 Particle shape analysis of steel-slag aggregates

Mineralogy and Particle Size, mm	Sphericity ( $S_p$ )*	Flakiness (F)*	Elongation (E)*	Shape Factor ( $S_f$ )*
S-50.0	0.76 ± 0.08	1.39 ± 0.17	1.30 ± 0.21	1.78
S-19.0	0.74 ± 0.09	1.36 ± 0.29	1.40 ± 0.27	1.82
S-9.5	0.69 ± 0.06	1.57 ± 0.39	1.44 ± 0.30	2.16
S-4.75	0.67 ± 0.07	1.58 ± 0.46	1.48 ± 0.19	2.23

\*  $S_p = \frac{\sqrt[3]{l \cdot t \cdot w}}{l_1}$ ;  $F = \frac{w}{t}$ ;  $E = \frac{l}{w}$ ;  $S_f = \frac{\sum l}{\sum t}$

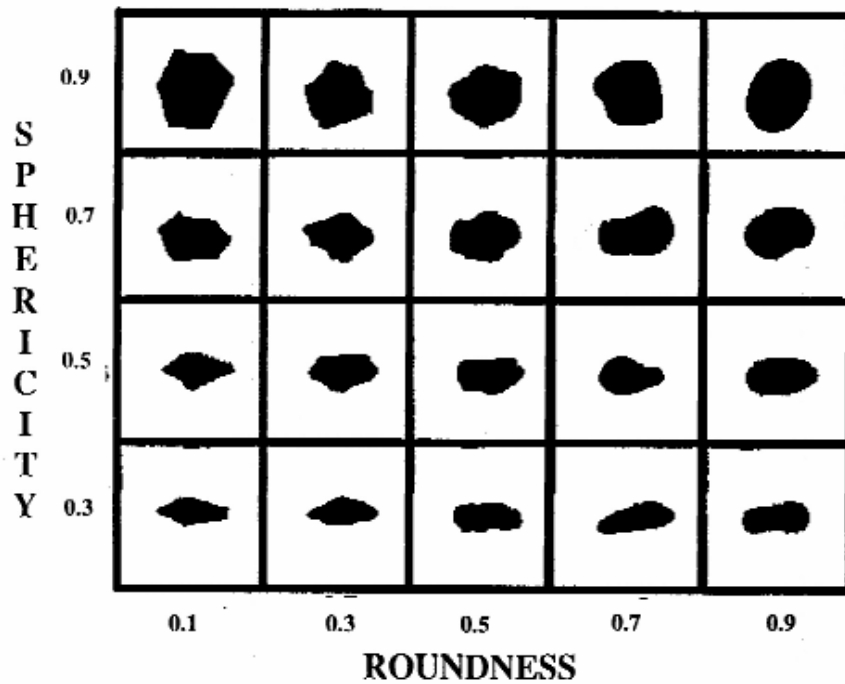


Figure 4.5 Chart for estimating sphericity and roundness of aggregates (after Jernigan, 1998 based on Krumbein and Sloss, 1963)



Figure 4.6 Limestone particles retained on 2.36 mm sieve size



Figure 4.7 Limestone particles retained on 4.75 mm sieve size



Figure 4.8 Limestone particles retained on 9.5 mm sieve size



Figure 4.9 Limestone particles retained on 12.7 mm sieve size



Figure 4.10 Limestone particles retained on 38.0 mm sieve size (prototype)



Figure 4.11 Basalt particles retained on 2.36 mm sieve size



Figure 4.12 Basalt particles retained on 4.75 mm sieve size



Figure 4.13 Basalt particles retained on 9.5 mm sieve size



Figure 4.14 Basalt particles retained on 12.7 mm sieve size



Figure 4.15 Basalt particles retained on 38.0 mm sieve size (prototype)



Figure 4.16 Steel-slag particles retained on 4.75 mm sieve size



Figure 4.17 Steel-slag particles retained on 6.35 mm sieve size



Figure 4.18 Steel-slag particles retained on 9.5 mm sieve size



Figure 4.19 Steel-slag particles retained on 12.7 mm sieve size



Figure 4.20 Steel-slag particles retained on 50.0 mm sieve size (prototype)

#### **4.2 Density Determination of Samples Tested and Testing Program**

Since the purpose of the research was to study the effect of particle size, gradation and material type on the behavior of ballast materials under triaxial stress conditions, different sample gradations as explained in section 4.1.2 were prepared.

Because densities are generally not specified when ballast is placed, no attempt was made to attain specific densities. Instead density compaction was selected. Because the role of composition is most important with regard to embankment construction the comparisons were made at fixed compactive effort (Lambe and Whitman, 1979). For all samples medium density condition was selected, corresponding to the initial field density condition after a typical maintenance cycle (Indraratna et al., 1998). For medium density specimens each layer was compacted for 5 seconds (Knutson and Thompson, 1978).

To determine the medium density of each gradation for each material type, the dry samples were compacted in two layers using a Kango type of vibratory hammer in a CBR mould of 152 mm in diameter, 115 mm in height. The procedure is repeated for the second batch until the difference between the two tests is less than 50 g. The results of the dry density values for each gradation are presented in Table 4.10 before last column.

Since ballast is exposed to climatic conditions, various series was prepared in wet conditions, too, to investigate the effect of water on the stress-strain and strength characteristics of ballast materials. The samples were poured into warm water in a plastic container and allowed to stand overnight. Wet series to be tested are given in Table 4.10.

In order to investigate the repeated loading behavior of ballast materials, unloading-reloading triaxial tests were performed on all dry samples of each material type under a confining stress of 35 kPa only. The series to be tested are again given in Table 4.10.

Each sample had a cylindrical shape, with a standard height to diameter ratio of 2 to minimize the effect of the end restraint on the behavior of the samples (Bishop, 1966). A test series consisted of three tests, typically with confining pressures of 35 kPa, 70 kPa, and 105 kPa. During the early part of the experimental program, additional tests were conducted in order to show consistency of sample preparation and testing procedure described in section 4.4. Table 4.10 lists the materials and gradations used in the experimental series; the confining stress range; the soil condition; the density of the gradations tested and the corresponding void ratios for the samples.

Table 4.10 Summary of the triaxial test program

Material	Gradation	Confining Stress ( $\sigma_3$ ), kPa			Initial Dry Density ( $\rho_d$ ), kN/m <sup>3</sup>	Void Ratio ( $e_0$ )
		Dry Sample for Strength and Modulus	Wet Sample for Strength and Modulus	Dry Sample for Repeated Loading Behavior		
Limestone	L-2.36	35, 70, 105	35, 70, 105	35	15.3	0.73
	L-4.75	35, 70, 105	35, 70, 105	35	15.3	0.73
	L-9.5	35, 70, 105	35, 70, 105	35	15.3	0.73
	L-6.35	35, 70, 105	-	35	15.5	0.71
	L-3.15	35, 70, 105	-	35	16.4	0.61
Basalt	B-2.36	35, 70, 105	-	35	15.9	0.81
	B-4.75	35, 70, 105	-	35	15.9	0.81
	B-9.5	35, 70, 105	35, 70, 105	35	15.9	0.81
Steel-slag	S-4.75	35, 70, 105	-	35	16.9	0.85
	S-6.35	35, 70, 105	-	35	16.3	0.88
	S-9.5	35, 70, 105	35, 70, 105	35	16.9	0.84

### **4.3 Triaxial Testing Apparatus**

The main experimental apparatus used in this investigation was a Wykeham-Farrance 5-Ton loading frame with a triaxial cell capable of testing a specimen with 100 mm in diameter, 200 mm in height. The axial load was supplied by this mechanically controlled, constant displacement loading or unloading frame. By varying gears, a range of displacement rates are possible. All of the tests discussed in this dissertation were conducted at a displacement rate of 0.4 mm/min., which corresponds to a strain rate of 0.2%. This rate was chosen so as to follow the simultaneous readings of axial compression, proving ring dial gauge and the volume change burette conveniently. The confining stress is supplied by means of an Engineering Laboratory Equipment (ELE) pressure supplier, ELE Pressure Test 1700. Figure 4.21 shows a schematic of this experimental setup.

The functions, the application of confining pressure and axial load, axial and volumetric strain measurements of the apparatus will be given in the next subsection with the test procedure.

### **4.4 Sample Preparation and Test Procedure**

As a reminder, all tests performed throughout this dissertation are consolidated-drained triaxial tests. The test procedure was outlined below (adapted from Çağnan, 1990):

1. If sample was in wet state, a 100 ml burette and the attached tubing were filled with de-aired, distilled water and connected to the pore pressure valve  $V_p$  of the cell (Figure 4.21); the pore pressure ducts were flushed up to the top of the cell pedestal by opening the valve  $V_p$ ; then  $V_p$  was closed. Otherwise, if sample was in dry condition, the attached tubing was disconnected and  $V_p$  was kept open during the

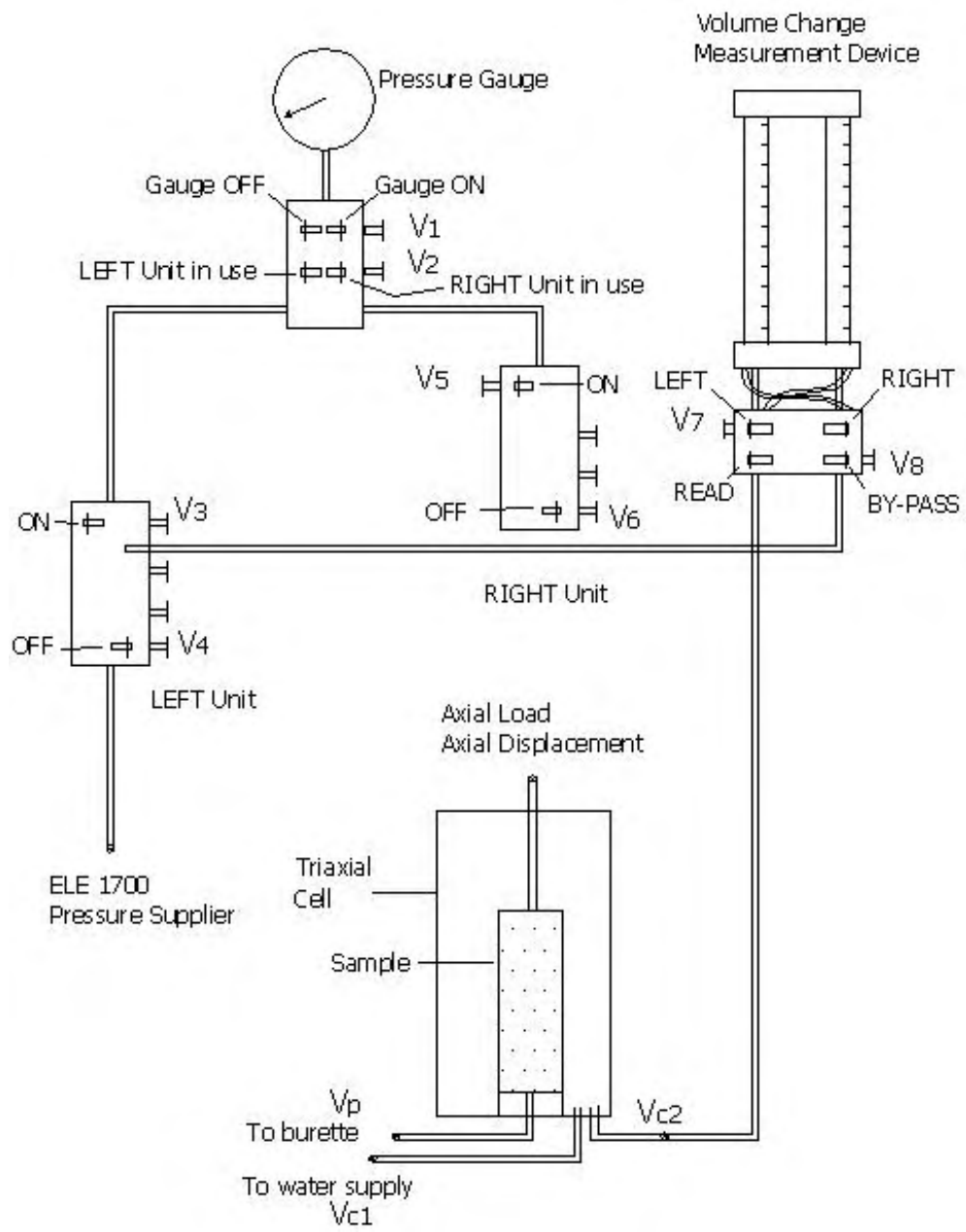


Figure 4.21 Schematic of 100 mm triaxial apparatus used

test. The sides of the pedestal and the top cap were wiped dry and smeared with castor oil for a better seal between the rubber membrane and these components.

2. A 0.3 mm thick rubber membrane was passed through three-part split mould; the ends turned over the mould and held by the rubber O-rings at each end. The mould was placed onto the base plate, and the fastening screws tightened moderately not to damage the membranes. The split ring, carrying three lugs, displaced at 120° with screw welded on each, was then clamped onto the mould. The collar carrying three lugs with holes engaging the screws was then placed on top of the mould, and the gap between the collar and the top of the mould was adjusted by means of the nuts so as not to damage the rubber membranes.

3. To minimize segregation and to insure gradation control each specimen was weighed out by thirds and each third layer was placed in a separate container. The specimen was prepared in the split mold. Each layer was poured into the mold by using a funnel to prevent segregation and the vibration was then applied on specially made three wooden blocks of the same diameter, 97 mm, but different heights of 19.7 mm, 12.7 mm and 6.0 mm respectively, to compact each layer (Figure 4.22). The wooden blocks were used to enable the predetermined density throughout the samples and to minimize the risk of breaking sharp corners and edges during vibration.

4. The collar and the split ring were removed and the top of the specimen smoothed level with the top of the rubber membranes passing over the upper rim of the mould. A perspex was held on top of the specimen and the whole inverted. The base plate was replaced by a filter paper disc and a coarse porous stone, and the whole re-inverted and placed on the cell pedestal. Another filter paper disc and a coarse porous stone were placed on top of the specimen. The top cap was placed on top; the ends of the rubber membranes were turned over the pedestal and the top cap. The clamp of the mould was detached and the three segments of the mould removed. During compaction using the Kango vibrating hammer, the membrane was damaged without exception. So, using a membrane placer, a second intact membrane was placed over the specimen, and it was used during vibratory compaction in subsequent



Figure 4.22 Special wooden blocks to compact each layer of specimen

tests. The rubber membranes were sealed with two rubber O-rings at each end, and the sample dimensions were determined. A typical completed sample is shown in Figure 4.23.

5. The cell ram was adjusted to just touch the top cap. To prevent buckling of the loading system during the axial loading application, the anti-friction guide was passed over the cell ram and was screwed tightly to the loading frame. The proving ring was mounted in position, and the cell was raised until the ram just touch the proving ring (Figure 4.24).

6. The cell was filled with de-aired, distilled water using a separate tube connected to the cell pressure valve  $V_{c1}$  of the cell (Figure 4.21) to speed up the filling; the air vent on top of the cell was closed upon flushing. The volume change measurement device (Figure 4.21) was connected to the valve  $V_{c2}$ . The water level in the burette connected to the valve  $V_p$  was adjusted to the level of the mid-height of

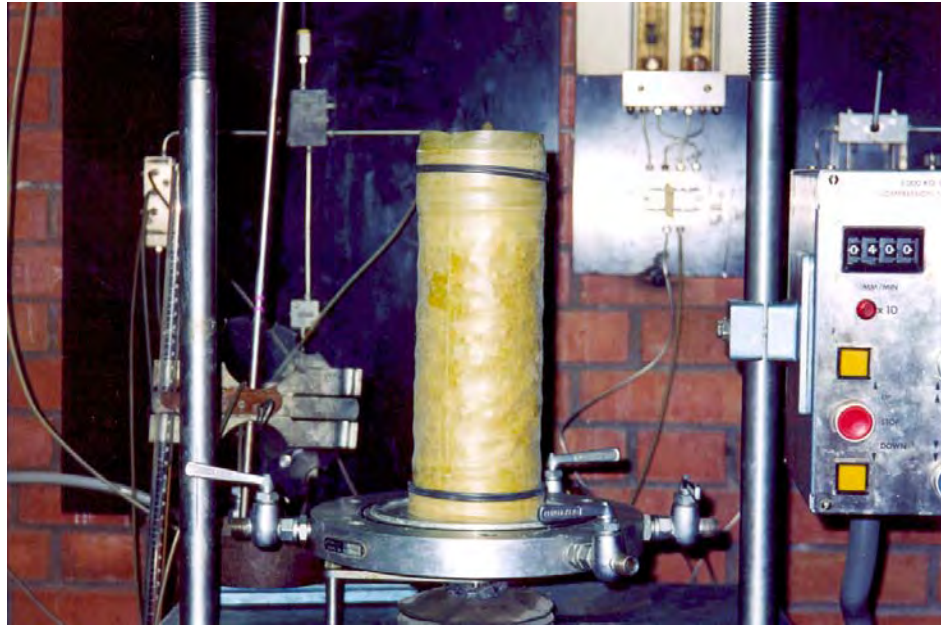


Figure 4.23 A typical completed triaxial sample before testing

the specimen if the sample is wet. This adjustment was done throughout the test by lowering the burette when the specimen compressed, and adding water to the burette when the specimen dilated. If there was a hole in the membrane after the cell pressure was applied, the water level in the burette would rise continuously; when this occurred, the test was stopped, and a new specimen prepared using undamaged membranes. For dry samples, the attached tubing was disconnected and the valve was opened to the atmosphere. If there was a hole in the membrane after the cell pressure was applied this would then be inspected from valve  $V_{c2}$  as stated in Item 1 and 8.

7. The valve  $V_{c2}$  on the cell was shut off. The valve  $V_8$  on the volume change measurement device was set to the “bypass” position. By using ELE pressure supplier, the cell pressure was built up to the desired value. Valves  $V_1$ ,  $V_3$ , and  $V_4$  were opened, valve  $V_2$  was set to “left unit in use” position. Valves  $V_{c2}$  and  $V_p$  on the cell were opened. During this procedure, due to the compression of the specimen, and the penetration of the rubber membrane into the soil pores, air was pressed out of

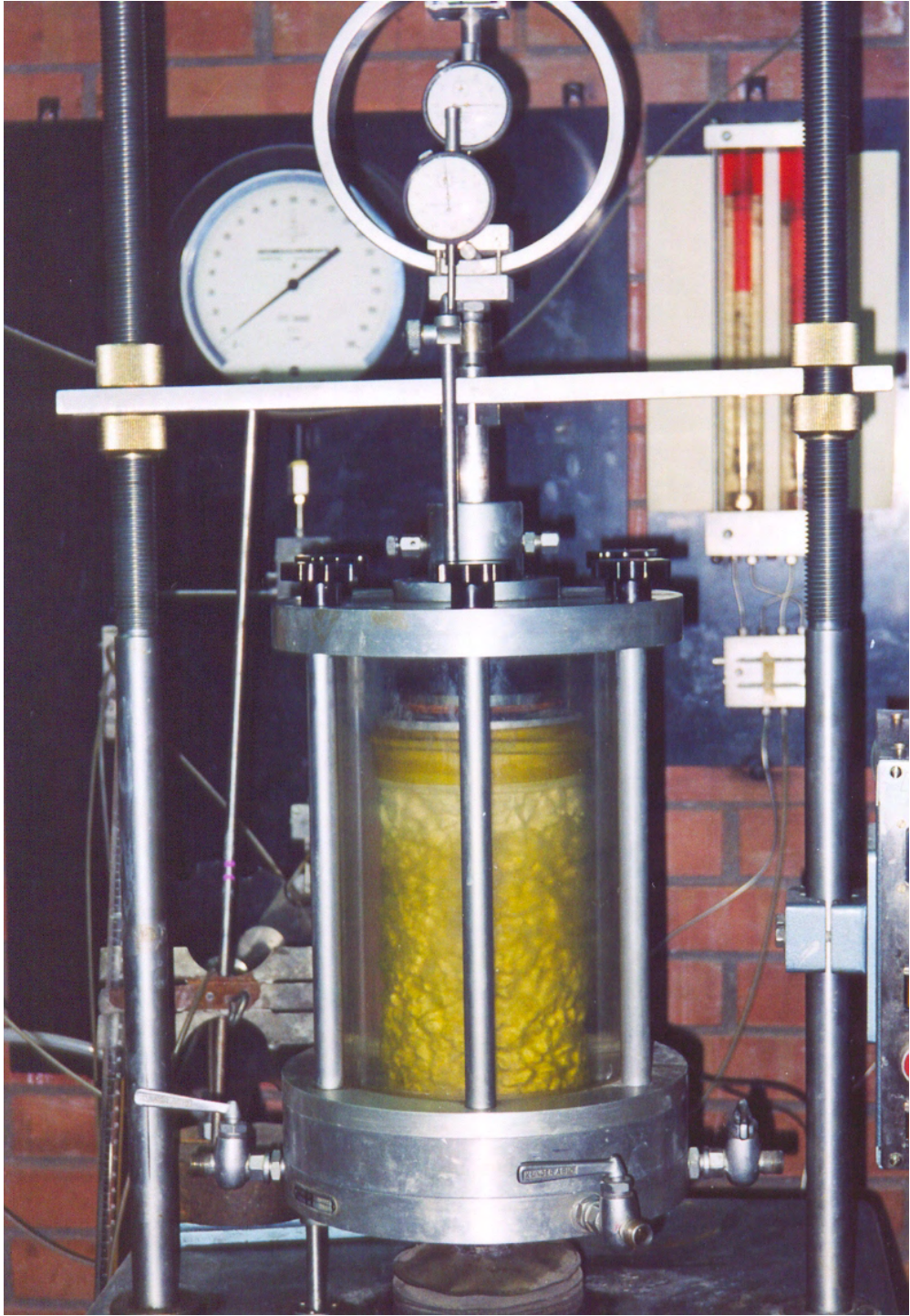


Figure 4.24 Layout of triaxial cell with the anti-friction guide

the specimen pushing the water level in the burette up. This level was restored to the level of the mid-height of the specimen by removing some water from the burette if necessary. The valve  $V_8$  on the volume change measurement device was shifted to the “read” position.

8. The cell was left in this condition for about 8 hours to attain equilibrium in the volume change burette readings, in order to avoid volume change inaccuracies during shearing due to the expansion of the perspex cell body when cell pressure was applied. When the volume change readings became steady, the axial strain and proving ring dials were set to zero. The initial burette readings on the volume change measurement device were taken. The strain rate was set to 0.4 mm/min, and axial loading was started. Axial compression, proving ring dial gauge, and the volume change readings were taken at  $5 \times 10^{-3}$  inch intervals of axial compression up to the readings of  $320 \times 10^{-3}$  inches; thereafter all readings were taken at  $10 \times 10^{-3}$  inch intervals of axial compression. The test was continued at this rate until the proving ring readings became steady or started to drop. During the tests, at  $80 \times 10^{-3}$  inches,  $160 \times 10^{-3}$  inches, and  $320 \times 10^{-3}$  inches readings, the specimen was unloaded to  $5 \times 10^{-3}$  inches reading and then reloaded with the same strain of 0.4 mm/min. A typical unloading-reloading curve is shown in Figure 4.25.

9. At the end of test, the compression machine was stopped, the valve  $V_8$  on the volume change measurement device was shifted to the “bypass” position. The cell pressure was reduced to zero. The valve  $V_{c2}$  on the cell and the valves  $V_1$ ,  $V_3$ , and  $V_4$  were closed. The air vent on top of the cell was opened. The axial load was removed by unloading mechanism. The cell was emptied, discharging the water. The cell was dismantled, and the specimen removed. A typical sample after testing is shown in Figure 4.26.

Each triaxial test, including specimen preparation, took about 14 hours.

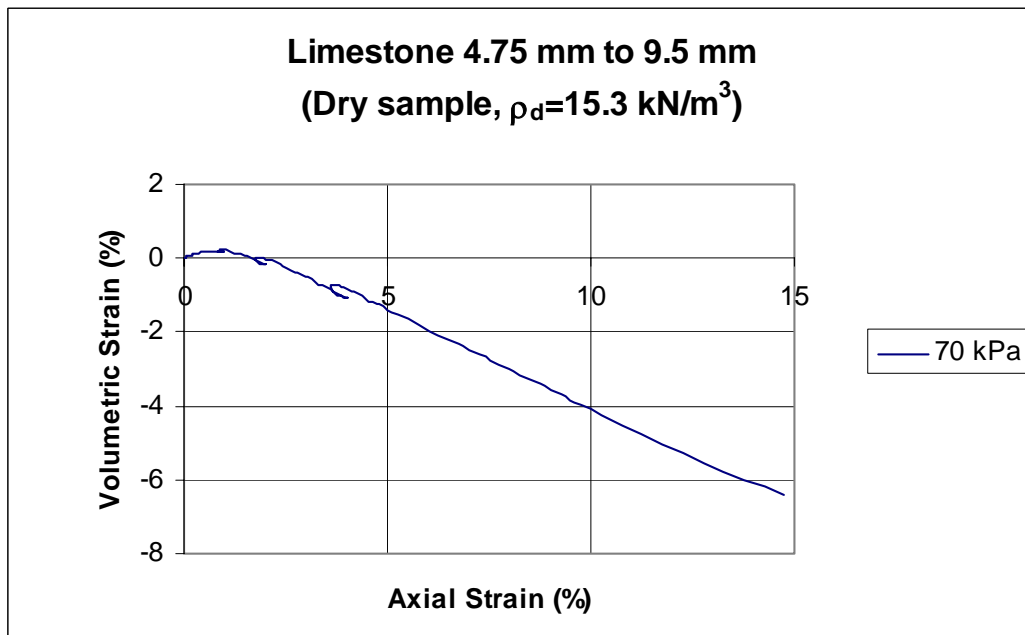
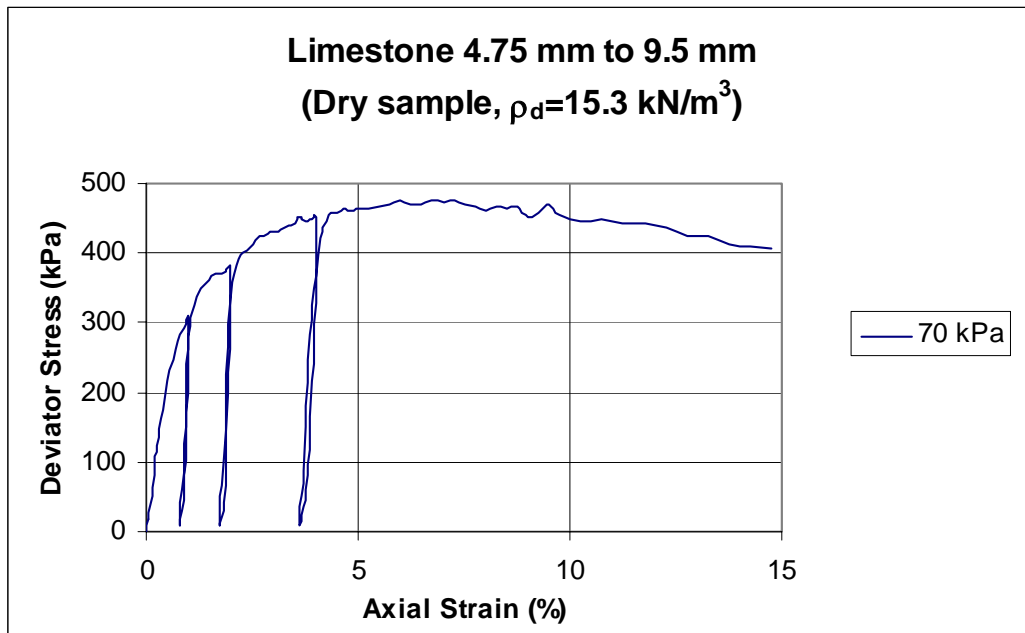


Figure 4.25 A typical curve of triaxial loading, unloading and reloading

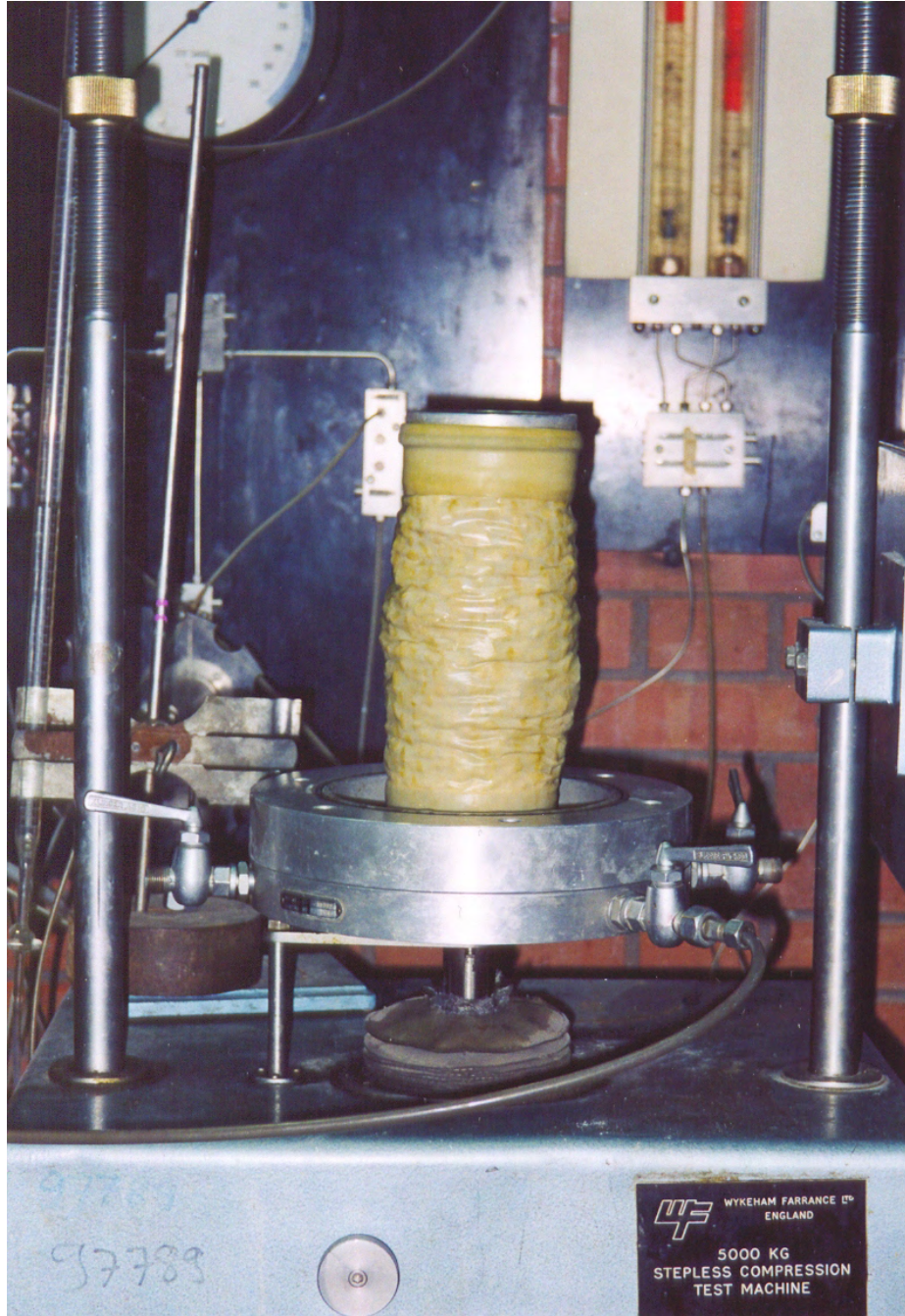


Figure 4.26 A typical triaxial sample after testing

## **CHAPTER V**

### **TRIAXIAL TEST RESULTS OF SCALED-DOWN MATERIALS BY USE OF PARALLEL GRADATION TECHNIQUE**

#### **5.1 Introduction**

As was discussed in testing program, section 4.2 in Chapter IV, the experimental investigations comprising the bulk of this research was based on triaxial testing of the scaled-down crushed ballast materials prepared due to parallel gradation technique at fixed compactive effort. Experimental determination of the peak shear strength and elastic properties are identified at different confining stresses for each gradation. These properties are first determined for the smallest size gradations. After this is accomplished, and the results compared, the next coarsest gradations are similarly tested. This procedure follows for all material type used in this study. The repeated loading behavior is also identified at a specified confining stress for each gradation, and the results are compared with gradations and material type.

All experiment results related to stress-strain and volumetric behavior are shown in the Appendix.

## 5.2 Statistical Analysis of Data

The particular aim in this study is to assess the variation in the Mohr-Coulomb shear strength parameters shown in Equation (5.1) (Craig, 1983) and Janbu elastic modulus parameters represented in Equation (5.2) (Janbu, 1963) for the various test series; where  $p_r$  is a reference pressure. In order to introduce a rational method for determining the apparent cohesion  $c$ , and the angle of internal friction  $\phi$  in Equation (5.1); the coefficient  $K$  corresponding to  $\sigma_3 / p_r = 1$ , and the slope  $n$  of the elastic modulus in Equation (5.2), the following method in the subsections is used.

$$\tau_f = c + \sigma_f \tan \phi \quad (5.1)$$

$$E / p_r = K(\sigma_3 / p_r)^n \quad (5.2)$$

### 5.2.1 Statistical Analysis of Shear Strength Parameters

The shear strength of a soil can also be expressed in terms of the major and minor principal stresses  $\sigma_{1f}$  and  $\sigma_{3f}$  at failure at the point in question (Craig, 1983). At failure the failure envelope represented by Equation (5.1) will be tangential to the Mohr circle representing the state of stress. Then  $\tau_f$  and  $\sigma_f$  can be written using the Mohr circle as follows:

$$\tau_f = \frac{1}{2}(\sigma_{1f} - \sigma_{3f}) \cos \phi \quad (5.3)$$

and

$$\sigma_f = \frac{1}{2}(\sigma_{1f} + \sigma_{3f}) - \frac{1}{2}(\sigma_{1f} - \sigma_{3f}) \sin \phi \quad (5.4)$$

Replacing Equation (5.3) and Equation (5.4) back into Equation (5.1), one can get

$$\frac{1}{2}(\sigma_{1f} - \sigma_{3f}) = \frac{1}{2}(\sigma_{1f} + \sigma_{3f}) \sin \phi + c \cos \phi \quad (5.5)$$

By plotting  $\frac{1}{2}(\sigma_{1f} - \sigma_{3f})$  against  $\frac{1}{2}(\sigma_{1f} + \sigma_{3f})$  any state of stress can also be represented by a stress point rather than a Mohr circle, and a modified failure envelope is obtained. This failure envelope is represented by the equation:

$$q = a + p \cdot \tan \alpha \quad (5.6)$$

where  $a$  and  $\alpha$  are the modified shear strength parameters; and

$$q = \frac{1}{2}(\sigma_{1f} - \sigma_{3f}) \quad (5.7)$$

and

$$p = \frac{1}{2}(\sigma_{1f} + \sigma_{3f}) \quad (5.8)$$

The parameters  $c$  and  $\phi$  are then given by

$$\phi = \sin^{-1}(\tan \alpha) \quad (5.9)$$

$$c = \frac{a}{\cos \phi} \quad (5.10)$$

Since a number of tests exhibited no clear peak strength, the peak strength has been defined for this investigation as being the peak value of  $(\sigma_1 - \sigma_3)$  at an axial strain of 10% or less. Back to the statistical analysis, first, the  $q$  values were plotted against the corresponding  $p$  values, and a best fit of the data was determined by

linear regression analysis. Taking the slope of the equation as being equal to  $\alpha$  and the intercept of the best fit line with the q axis as being equal to a, then  $\alpha$  and a can be obtained from the following equations obtained by analogy from Kurtz (1991):

$$\alpha = \frac{n \sum_{i=1}^n p_i q_i - \sum_{i=1}^n p_i \sum_{i=1}^n q_i}{n \sum_{i=1}^n p_i^2 - (\sum_{i=1}^n p_i)^2} \quad (5.11)$$

and

$$a = \frac{\sum_{i=1}^n q_i - \alpha \sum_{i=1}^n p_i}{n} \quad (5.12)$$

where n is the number of data points;  $p_i$  is the i-th experimental value of p;  $q_i$  is the i-th experimental value of q corresponding to p. Then  $\phi$  and c are found from Equation (5.9) and Equation (5.10) respectively. These coefficients in turn were used to examine the variation of the shear strength parameters with confining stress, particle size and material type.

A benefit of this approach is the ability to assess how well the experimental data matches the linear regression line. One of the measures of the fit to the data is the coefficient of determination  $R^2$ . A value of  $R^2 = 1$  indicates a perfect fit. The value of  $R^2$  is determined by the following equation obtained by analogy from Kurtz (1991):

$$R^2 = \frac{\sum_{i=1}^n (q_i - \bar{q})^2 - \sum_{i=1}^n (q_i - a - \alpha p_i)^2}{\sum_{i=1}^n (q_i - \bar{q})^2} \quad (5.13)$$

where  $\bar{q}$  is the mean value of  $q_i$ .

### 5.2.2 Statistical Analysis of Elastic Modulus

The determination and the analysis of elastic modulus parameters postponed to section 5.9.

### 5.3 Peak Shear Strength Trends for Scaled-down Limestone Materials

In order to provide a baseline for the experiments, a total of 4 separate experiments were conducted using the coarsest scaled-down particle size L-9.5 gradation, limestone particles ranging from 9.5 mm to 19.0 mm, with the 100 mm triaxial specimen. As in the other samples, confining stresses used 35 kPa, 70 kPa and 105 kPa. The results obtained were good, meaning that the preparation and the testing of samples can be reproduced. These results were later included in the main program of L-9.5 as determining its shear strength parameters in the linear regression analysis.

The finest scaled-down particle material for which the peak shear strength determined was the 2.36 mm to 4.75 mm gradation of crushed limestone (L-2.36). For the series using the 100 mm specimen size, three separate tests were conducted. For this experimental series, the angle of internal friction,  $\phi$ , was  $43.3^\circ$ . The apparent cohesion,  $c$ , was 36.5 kPa. The coefficient of determination,  $R^2$ , for series L-2.36 was 0.998. Figure 5.1 shows the data point for this series plotted on a  $p$  versus  $q$  chart for statistical analysis as discussed in section 5.2.1.

The next gradation of scaled-down limestone ballast material to be tested was 4.75 mm to 9.5 mm (L-4.75). For the series using 100 mm sample size, a total of 3 tests were performed. From the statistical analysis of data for this series, the angle of internal friction was  $44.0^\circ$ , with an apparent cohesion of 33.3 kPa. The coefficient of determination was 0.999. Figure 5.2 shows the plot of  $p$  versus  $q$  for series L-4.75.

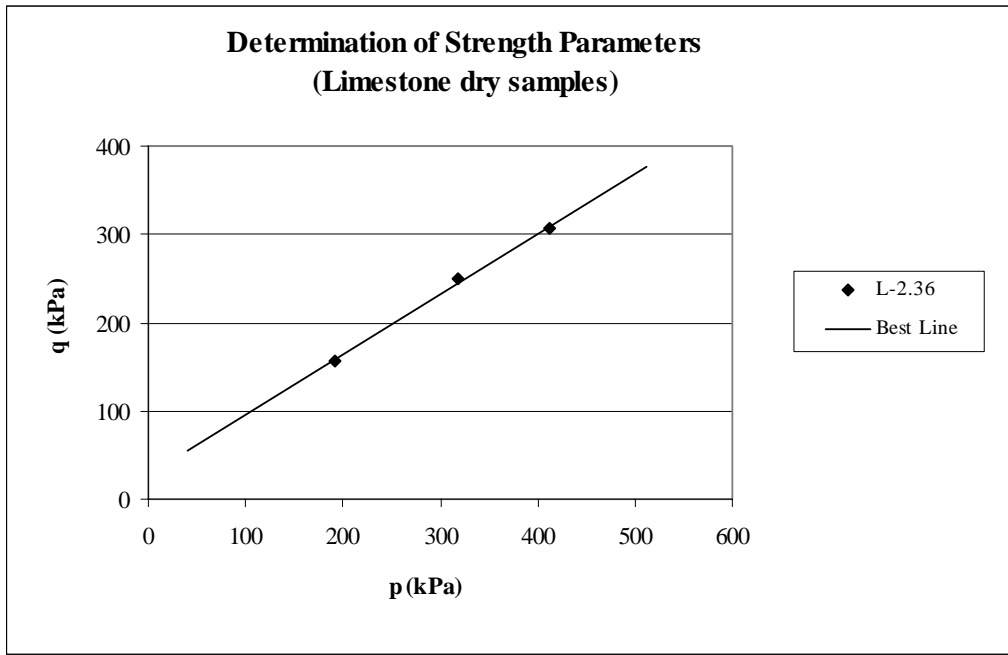


Figure 5.1 Peak shear strength trend for limestone samples of 2.36 mm to 4.75 mm

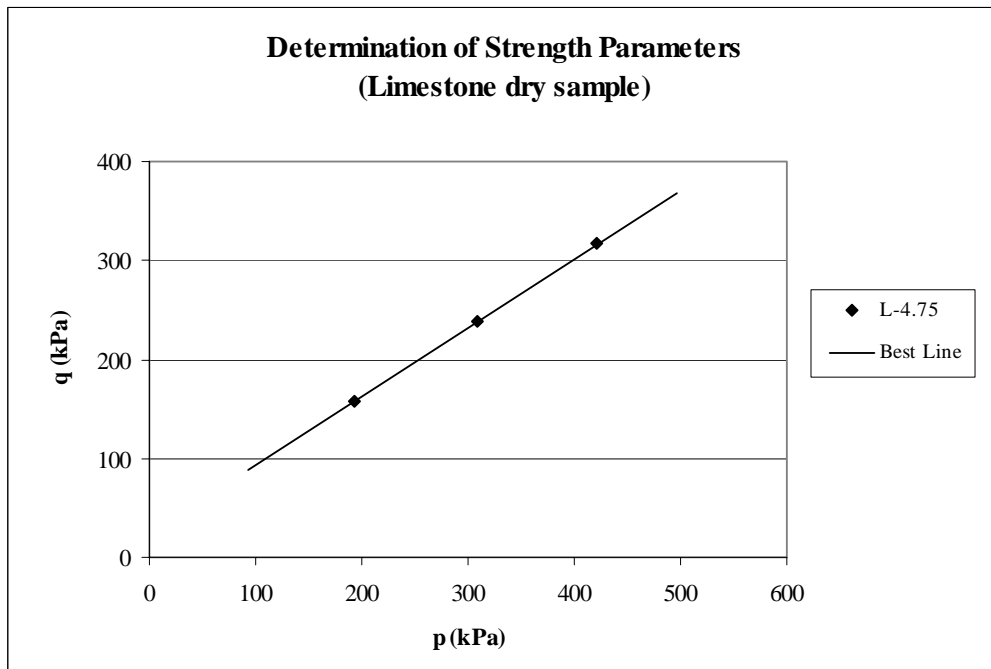


Figure 5.2 Peak shear strength trend for limestone samples of 4.75 mm to 9.5 mm

Comparing L-4.75 to L-2.36, it can be seen that the Mohr-Coulomb parameters are quite close, with a difference in the angle of internal friction less than  $1^\circ$  and a difference in the apparent cohesion of only 3 kPa.

The coarsest gradation of crushed limestone used as mentioned in the beginning of this section was 9.5 mm to 19.0 mm. Test series for L-9.5 consisted of 7 experiments with confining stresses of 35 kPa, 70 kPa and 105 kPa. The determined angle of internal friction was  $45.8^\circ$ , with an apparent cohesion of 32.4 kPa. The coefficient of determination was 0.999, indicating again a good linear fit of data. Figure 5.3 shows the plot of  $p$  versus  $q$  for L-9.5.

Comparing L-9.5 with L-4.75, the difference in the angle of internal friction was  $1.8^\circ$  and that in the apparent cohesion was only 1 kPa. This difference in the angle of internal friction may be due to particle size. In addition, it is worth noting that this difference may also be due to the ratio of the sample diameter (100 mm) to the maximum particle size (19.0 mm) of only 5.3 as discussed in Chapter 4. Since this ratio is below the suggested minimum ratio of 6 it may reasonably be assumed that the result, a higher angle of internal friction, obtained for the larger particle size may be due to the ratio of sample diameter to maximum particle size. This argument is also advocated by Kaya et al. (1997) as represented in Table 2.5.

Nevertheless, combining the data obtained for all of the crushed limestone samples in a  $p$  versus  $q$  chart, the statistical value of the angle of internal friction was  $44.6^\circ$ , with an apparent cohesion of 32.5 kPa. The coefficient of determination was 0.998, indicating a good correlation with the linear trend of the data. Figure 5.4 shows the peak shear strength trend for all scaled-down limestone data combined on a single  $p$  versus  $q$  chart.

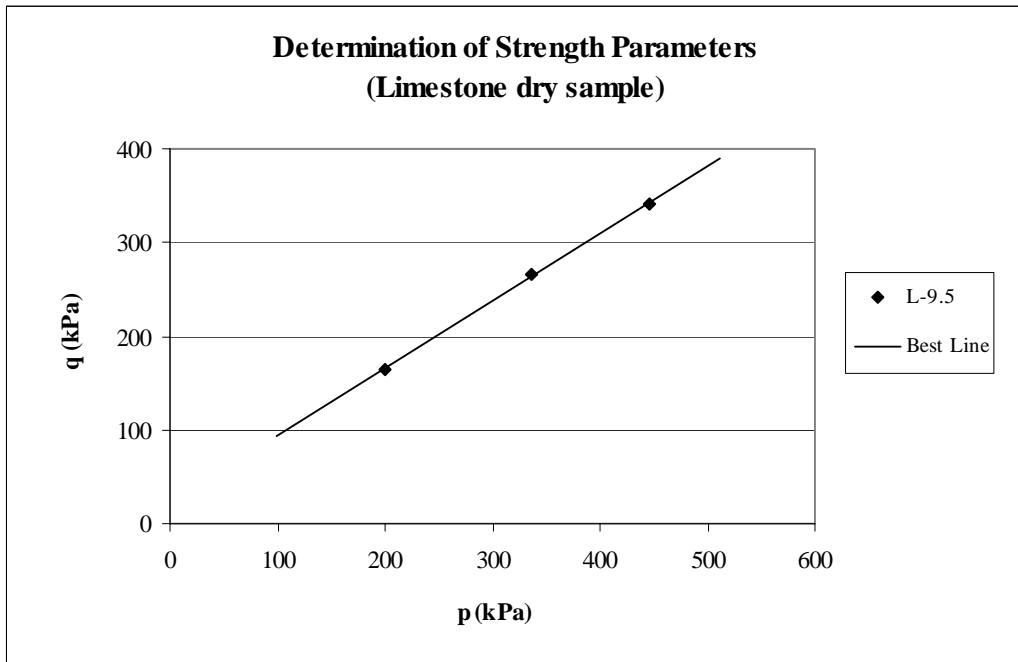


Figure 5.3 Peak shear strength trend for limestone samples of 9.5 mm to 19.0 mm

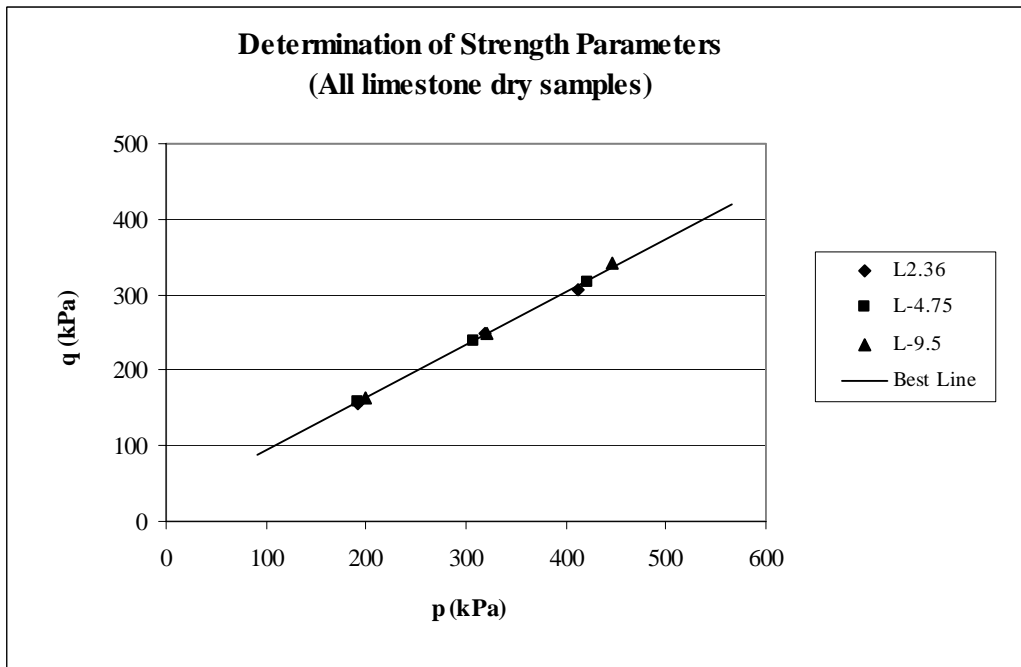


Figure 5.4 Peak shear strength trend for all scaled-down limestone samples

Table 5.1 shows a summary of the Mohr-Coulomb parameters for the three series of scaled-down limestone material as well as the parameters determined for the combined data.

Table 5.1 Summary of Mohr-Coulomb parameters for the scale-down limestone samples

Gradation	Shear Strength Parameters		
	Angle of Internal Friction ( $\phi$ ), degree	Apparent Cohesion (c), kPa	Coefficient of Determination ( $R^2$ )
L-2.36	43.3	36.5	0.998
L-4.75	44.0	33.3	0.999
L-9.5	45.8	32.4	0.999
Combined Data	44.6	32.5	0.998

In Table 5.1, it is interesting to note that there seems to be considerable cohesion for all particle sizes, although they are cohesionless soils. It is a fact that it is not a “true” cohesion, but due to nonlinear behavior of soil with confining stress and the Mohr-Coulomb failure envelope being a linear type of equation, it is nothing but just an intercept and thus called “apparent” cohesion. It is also believed that this apparent cohesion was due to particle interlocking of their highly angular nature (Raymond and Davies, 1978). In addition, this amount of cohesion argues that there might be a membrane effect. Due to the uniform gradations of all materials, there is considerable membrane penetration into the sample. It is probable that some portion of this apparent cohesion is due to the effect of membrane restraint against sample. Nevertheless, using standard membrane thickness, the correction for the strength due to the effect of membrane is insignificant and can be ignored (Bishop and Henkel,

1962). In the calculations, even after adjusting the correction in proportion to the actual thickness of the rubber membrane, a correction to the maximum deviator was calculated as 4.0 kPa according to Bishop and Henkel (1962). Therefore, the corrections were insignificant and the corrections due to membrane effect were ignored. As an alternative to Mohr-Coulomb failure envelope, the shear strength to emphasize the nonlinearity can also be represented in other forms as shown in the Appendix.

By knowing the angle of internal friction angle and the apparent cohesion, it is possible to predict the maximum axial stress ( $\sigma_1$ ) for any given confining stress being within the prescribed range by using the following equation (Craig, 1983):

$$\sigma_1 = \sigma_3 \tan^2\left(45 + \frac{\phi}{2}\right) + 2c \tan\left(45 + \frac{\phi}{2}\right) \quad (5.14)$$

Table 5.2 compares the maximum axial stresses predicted by Equation (5.14) for the various particle sizes at a confining stress of 35 kPa. It can be seen that there was a maximum difference of 5.6 % between L-9.5 and L-4.75. It implies that 5.6% difference in axial stress due to change in particle size may be ignored as the engineering practice is concerned.

Table 5.2 Predicted maximum axial stress with  $\sigma_3 = 35$  kPa  
for crushed limestone samples

Gradation	Predicted Maximum Axial Stress (Equation 5.14), kPa	Difference w.r. to Maximum Axial Stress Predicted For L-9.5, %
L-2.36	357	-4.0
L-4.75	351	-5.6
L-9.5	372	0.0

#### 5.4 Peak Shear Strength Trends for Scaled-down Basalt Materials

The smallest scaled-down particle size of basalt material used in this research ranged from 2.36 mm to 4.75 mm (B-2.36). Since the experimental procedure and the repeatability of the experiments were well established by the experimental work on the scaled-down sizes of limestone ballast material, it was suggested that there was no need to confirm the reproducibility of tests on the basalt materials. The confining stresses, as was the case for the limestone materials, were 35 kPa, 70 kPa, 105 kPa. So, three triaxial tests were conducted on this gradation.

Figure 5.5 shows the data point and the linear best-line for this series plotted on a  $p$  versus  $q$  chart. For this experimental series, the angle of internal friction,  $\phi$ , was  $45.7^\circ$ . The apparent cohesion,  $c$ , was 34.4 kPa. The coefficient of determination,  $R^2$ , for series B-2.36 was 0.998.

The next gradation of scaled-down basalt tested triaxially was 4.75 mm to 9.5 mm (B-4.75). For the series using 100 mm sample size, a total of three tests were performed. From the statistical analysis of data for this series, the angle of internal friction was  $46.5^\circ$ , with an apparent cohesion of 33.7 kPa. The coefficient of determination was 0.999. Figure 5.6 shows the plot of  $p$  versus  $q$  for B-4.75.

By comparing B-4.75 to B-2.36, it can be seen that the Mohr-Coulomb parameters are quite close to each other, with a difference in the angle of internal friction less than  $1^\circ$  and a difference in the apparent cohesion of only about 1 kPa.

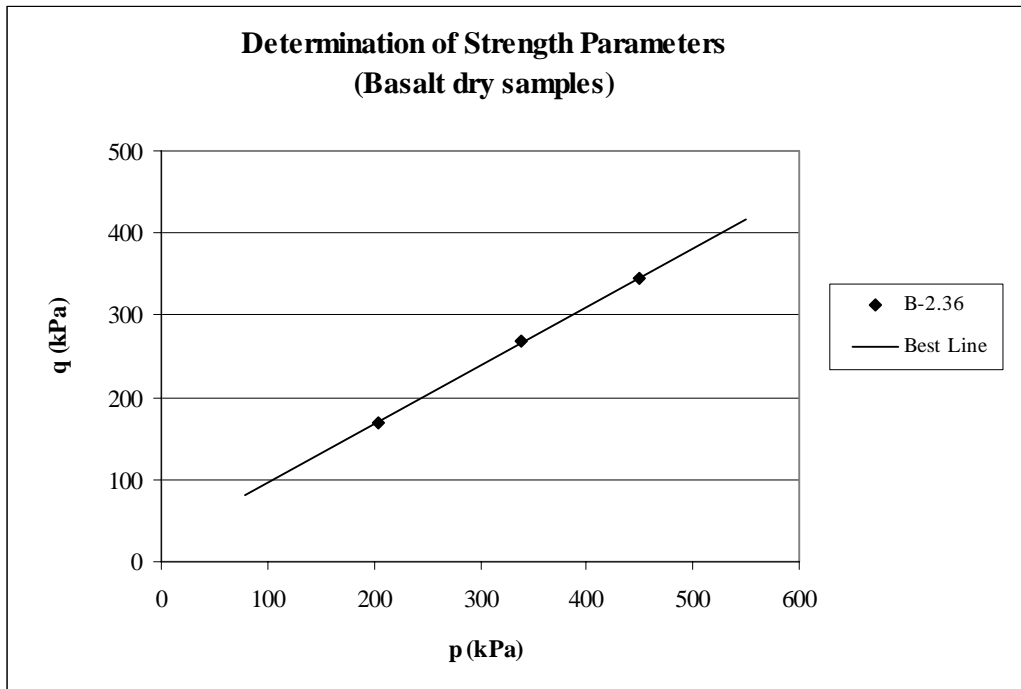


Figure 5.5 Peak shear strength trend for scaled-down basalt of 2.36 mm to 4.75 mm

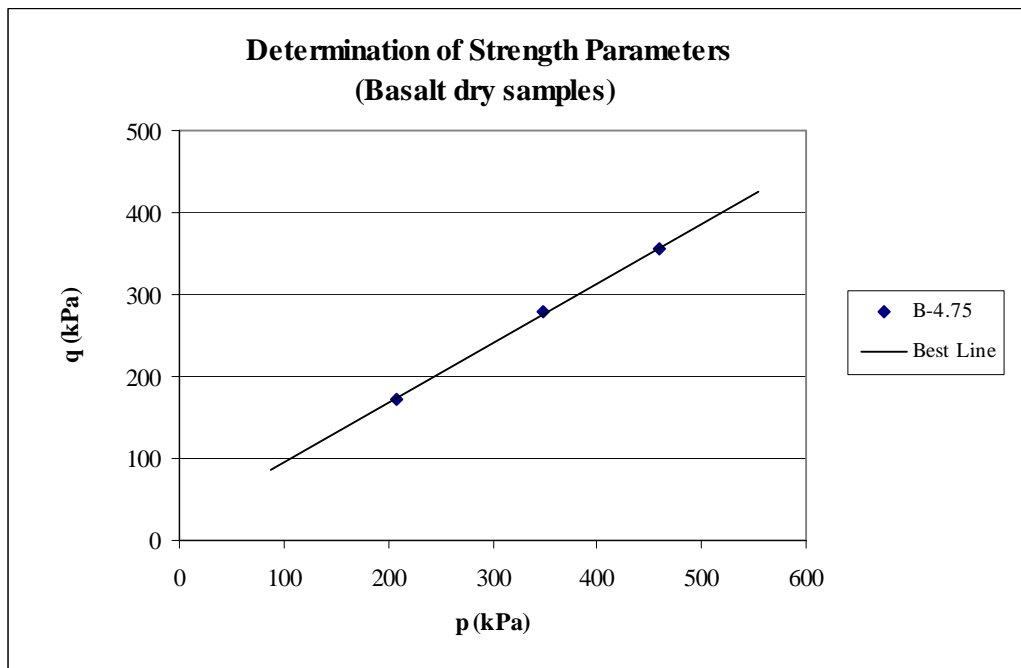


Figure 5.6 Peak shear strength trend for scaled-down basalt of 4.75 mm to 9.5 mm

The coarsest gradation of scaled-down basalt material tested was ranged from 9.5 mm to 19.0 mm particle size (B-9.5). Test series for B-9.5 consisted of 3 experiments with confining stresses of 35 kPa, 70 kPa and 105 kPa. The angle of internal friction established for this series was  $46.5^\circ$ , with an apparent cohesion of 34.2 kPa. The coefficient of determination,  $R^2$ , was 0.999. Figure 5.7 shows the plot of  $p$  versus  $q$  for B-9.5. By comparing B-9.5 with B-4.75, no difference was obtained in the angle of internal friction; and it had a difference in the apparent cohesion of only less than 1 kPa.

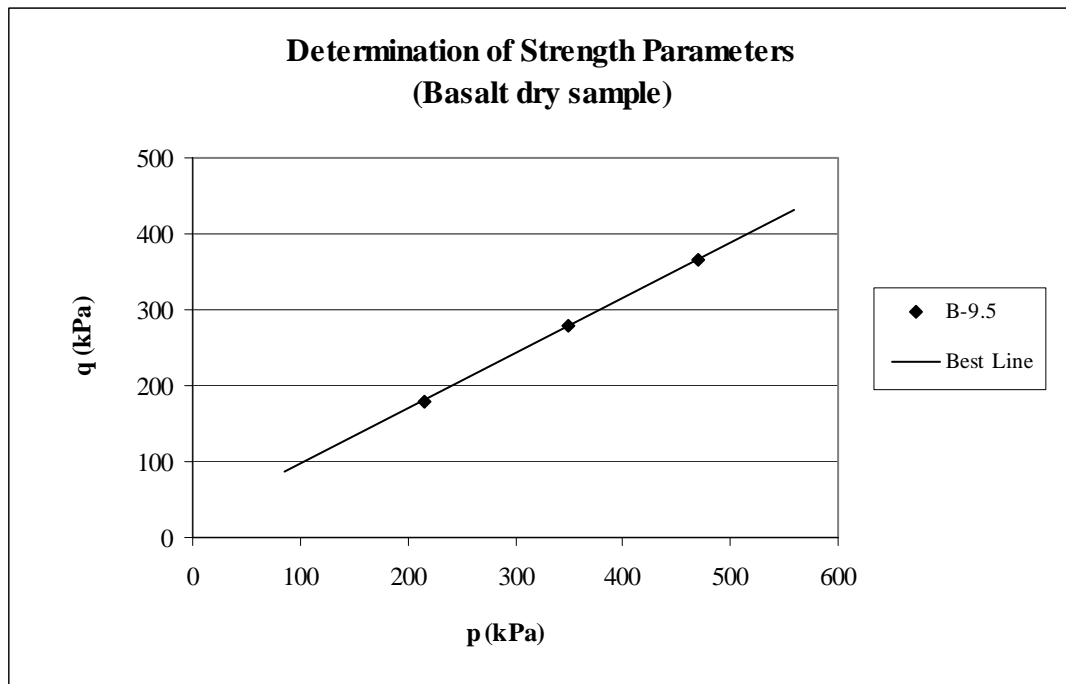


Figure 5.7 Peak shear strength trend for scaled-down basalt of 9.5 mm to 19.0 mm

Combining the data obtained for all of the scaled-down basalt samples, the angle of internal friction,  $\phi$ , after the linear regression analysis was  $46.3^\circ$ , with an

apparent cohesion,  $c$ , of 34.2 kPa. The coefficient of determination,  $R^2$ , was 0.999, indicating that the combined data showed a good linear trend. Figure 5.8 shows all of the peak shear strength data for the scaled-down basalt material combined on a single  $p$  versus  $q$  chart.

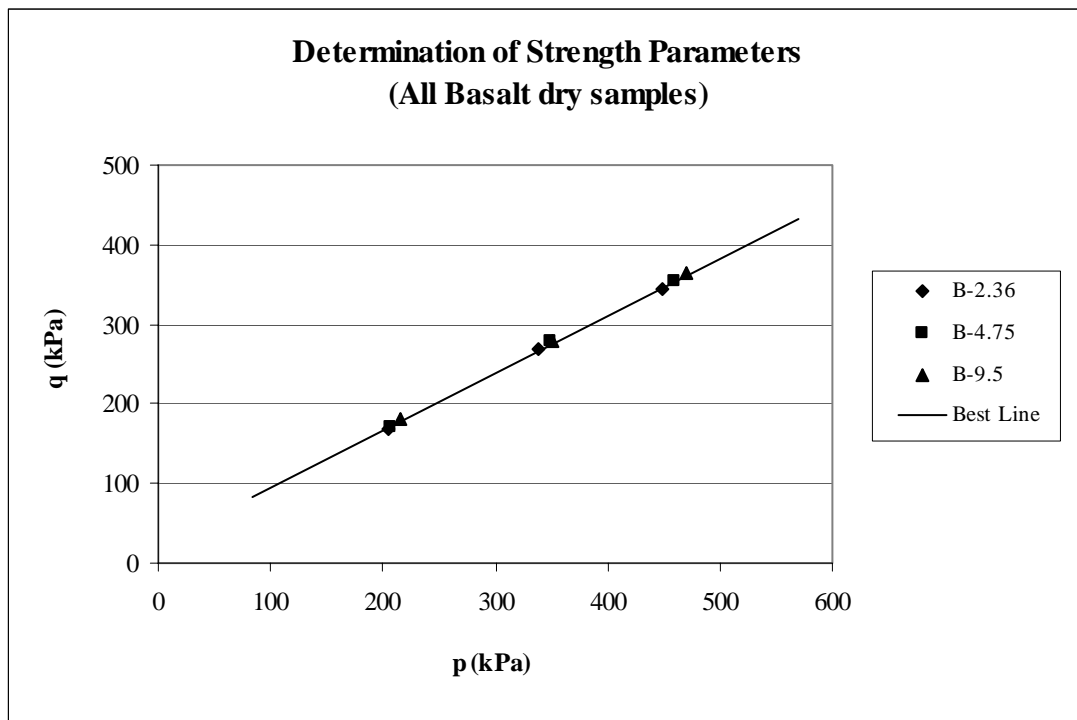


Figure 5.8 Peak shear strength trend for all scaled-down basalt samples

Table 5.3 shows a summary of the Mohr-Coulomb parameters for the three series of scaled-down basalt material as well as the parameters determined for the combined data.

Comparing the maximum axial stresses predicted by Equation (5.14) for the various particle sizes shown in Table 5.4 at a confining stress of 35 kPa, it can be

seen that there was a maximum difference of 5 % between B-9.5 and B-2.36. This 5% difference in axial stress due to change in particle size may be again ignored as the engineering practice is concerned.

Table 5.3 Summary of Mohr-Coulomb parameters  
for the scaled-down basalt samples

Gradation	Shear Strength Parameters		
	Angle of Internal Friction ( $\phi$ ), degree	Apparent Cohesion (c), kPa	Coefficient of Determination ( $R^2$ )
B-2.36	45.7	34.4	0.999
B-4.75	46.5	33.7	0.999
B-9.5	46.5	36.0	0.999
Combined Data	46.3	34.2	0.999

Table 5.4 Predicted maximum axial stress with  $\sigma_3 = 35$  kPa  
for scaled-down ballast samples

Gradation	Predicted Maximum Axial Stress (Equation 5.14), kPa	Difference w.r. to Maximum Axial Stress Predicted For B-9.5, %
B-2.36	380	-5.0
B-4.75	389	-2.8
B-9.5	400	0.0

## 5.5 Peak Shear Strength Trends for Scaled-down Steel-slag Materials

The smallest scaled-down particle size of steel-slag material used in this research ranged from 4.75 mm to 9.5 mm (S-4.75). The confining stresses,  $\sigma_3$ , as was the case for the scaled-down limestone and basalt samples, were 35 kPa, 70 kPa, 105 kPa. So, three triaxial tests were conducted on this gradation.

Figure 5.9 shows the data point for S-4.75 and the linear best fit for this series plotted on a p versus q chart. For this experimental series, the angle of internal friction,  $\phi$ , was  $43.6^\circ$ . The apparent cohesion, c, was 27.0 kPa. The coefficient of determination,  $R^2$ , for series S-4.75 was 0.999.

The next gradation of scaled-down steel-slag tested was varied from 6.35 mm to 12.7 mm particle size (S-6.35). For the series using 100 mm sample size, a total of three tests were performed. From the regression analysis of data for this series, the angle of internal friction obtained was  $43.0^\circ$ , with an apparent cohesion of 40.5 kPa. The coefficient of determination was 0.997. Figure 5.10 shows the plot of p versus q for S-6.35.

By comparing S-6.35 to S-4.75, it can be seen that the angles of internal friction of the Mohr-Coulomb parameters are quite close to each other, with a difference less than  $1^\circ$ ; but, it is interesting to note that, contrary to the limestone and basalt materials, there is a substantial difference in the apparent cohesion of 13.5 kPa. It may be due to the effect of heterogeneity of the steel-slag particles as explained in Chapter IV.

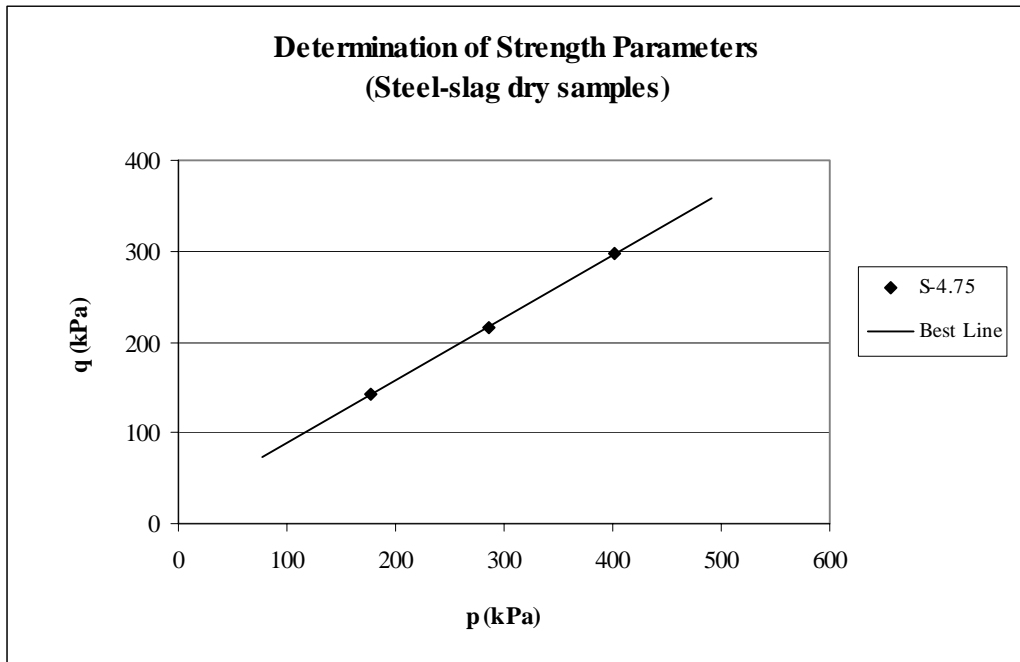


Figure 5.9 Peak shear strength trend for scaled-down steel-slag of 4.75 - 9.5 mm

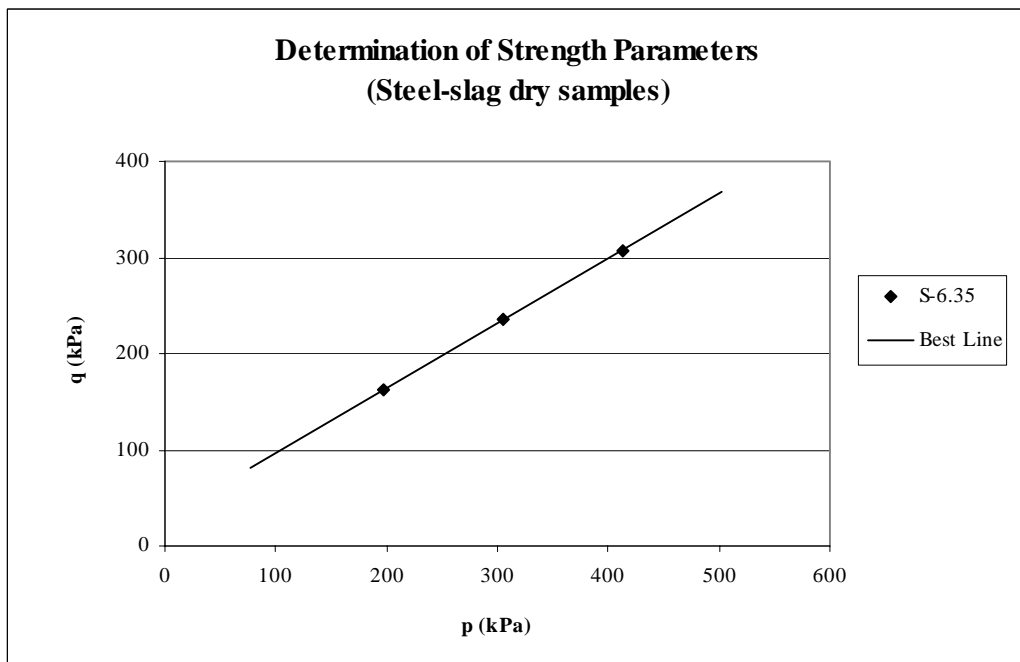


Figure 5.10 Peak shear strength trend for scaled-down steel-slag of 6.35 - 12.7 mm

The coarsest gradation of scaled-down steel-slag material tested was 9.5 mm to 19.0 mm (S-9.5). Test series for S-9.5 consisted of 3 experiments with confining stresses of 35 kPa, 70 kPa and 105 kPa. The angle of internal friction established for this series was  $41.4^\circ$ , with an apparent cohesion of 43.6 kPa. The coefficient of determination was 0.999. Figure 5.11 shows the plot of  $p$  versus  $q$  for S-9.5. By comparing S-9.5 with S-6.35, contrary to the coarsest gradation of limestone and basalt samples, S-9.5 had an angle of internal friction  $1.6^\circ$  less than that of S-6.35; but an apparent cohesion 3.0 kPa greater than that of S-6.35.

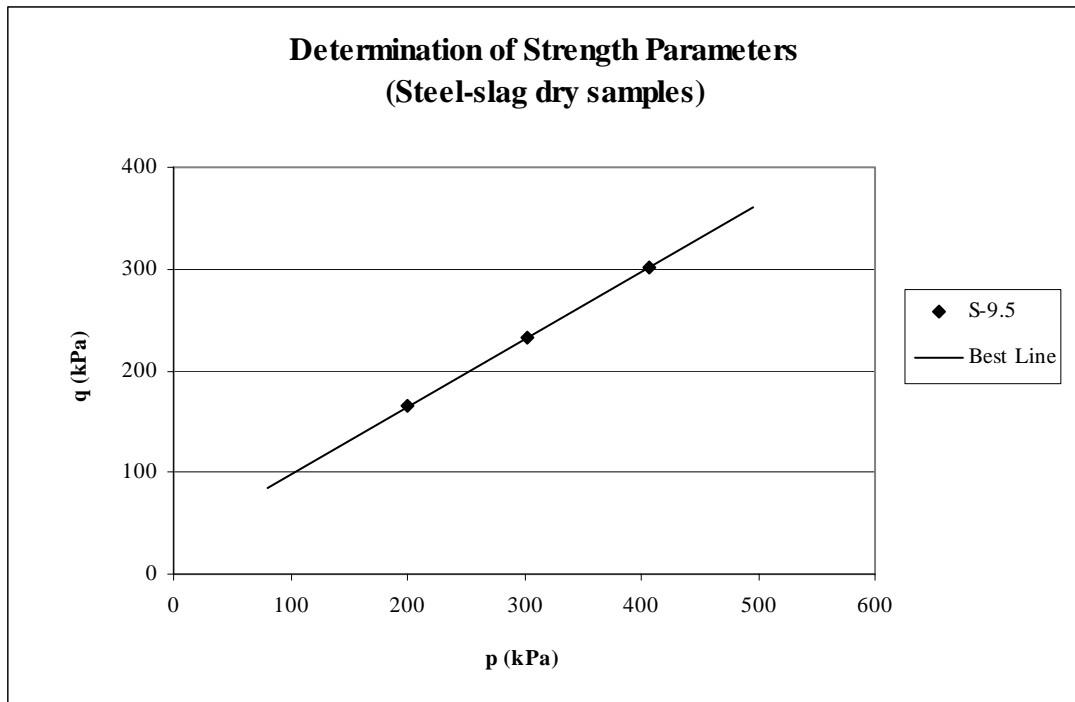


Figure 5.11 Peak shear strength trend for scaled-down steel-slag of 9.5 - 19.0 mm

Combining the results for all of the scaled-down steel-slag samples after the linear regression analysis, the angle of internal friction,  $\phi$ , was  $42.7^\circ$ , with an apparent cohesion of 35.4 kPa. The coefficient of determination was 0.998,

indicating that the combined data showed again a good linear trend. Figure 5.12 shows all of the peak shear strength data for the scaled-down basalt material combined on a single p versus q chart.

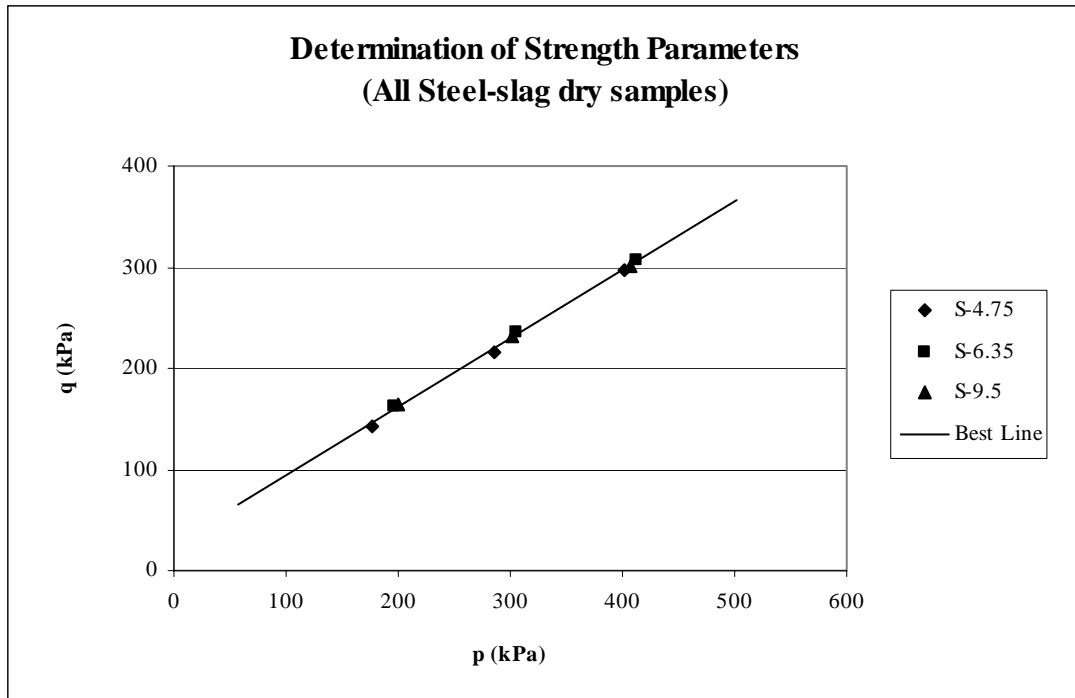


Figure 5.12 Peak shear strength trend for all scaled-down steel-slag samples

Table 5.5 shows a summary of the Mohr-Coulomb parameters for the three series of scaled-down steel-slag material as well as the parameters determined for the combined data.

Comparing the maximum axial stresses predicted by Equation (5.16) for the various particle sizes represented in Table 5.6 at a confining stress of 35 kPa, it can be seen that there was a maximum difference of 14.8 %. This difference in axial

stress due to change in particle size may still be considered within the engineering practice.

Table 5.5 Summary of Mohr-Coulomb parameters  
for the scaled-down steel-slag samples

Gradation	Shear Strength Parameters		
	Angle of Internal Friction ( $\phi$ ), degree	Apparent Cohesion (c), kPa	Coefficient of Determination ( $R^2$ )
S-4.75	43.6	27.0	0.999
S-6.35	43.0	40.5	0.997
S-9.5	41.4	43.6	0.999
Combined Data	42.7	35.4	0.998

Table 5.6 Predicted maximum axial stress with  $\sigma_3 = 35$  kPa  
for crushed steel-slag samples

Gradation	Predicted Maximum Axial Stress (Equation 5.14), kPa	Difference w.r. to Maximum Axial Stress Predicted For S-6.35, %
S-4.75	316	-14.8
S-6.35	371	0.0
S-9.5	365	-1.6

## 5.6 Comparison of Peak Shear Strength of Scaled-down Limestone, Basalt and Steel-slag Materials

Table 5.7 lists the Mohr-Coulomb parameters for the selected series for scaled-down limestone, basalt, and steel-slag, as well as the parameters for the combined data for each material. Examining Table 5.7 shows that the values of the apparent cohesion of Mohr-Coulomb peak shear strength parameters established for all combined series are very close to each other. But the angle of internal friction differs by  $2^\circ$  to  $4^\circ$  due to material type, as such the angle of internal friction established for the combined data for the scaled-down limestone samples is lower by about  $2^\circ$  than that of combined data for the scaled-down basalt series, but is higher by approximately  $2^\circ$  than that of the steel-slag samples.

Table 5.7 Comparison of Mohr-Coulomb parameters for all materials

Gradation	Shear Strength Parameters		
	Angle of Internal Friction ( $\phi$ ), degree	Apparent Cohesion (c), kPa	Coefficient of Determination ( $R^2$ )
L-9.5	45.8	32.4	0.999
B-9.5	46.5	36.0	0.999
S-9.5	41.4	43.6	0.999
Combined Data For Limestone	44.6	32.5	0.998
Combined Data For Basalt	46.3	34.2	0.999
Combined Data For Steel-slag	42.7	35.4	0.998

Table 5.8 examines the predicted maximum axial stress,  $\sigma_1$ , for the corresponding Mohr-Coulomb parameters at a confining stress,  $\sigma_3$ , of 35 kPa. B-9.5 series shows the highest peak shear strength, while steel-slag combined series shows the lowest. However, the maximum difference is only 14%; and it may still be evaluated within the engineering practice.

As a result, it appears that the parallel gradation technique would lead to acceptable predictions of peak shear strength of prototype materials as long as scaled-down material is to be carefully utilized.

Table 5.8 Predicted maximum axial stress with  $\sigma_3 = 35$  kPa for all materials

Gradation	Predicted Maximum Axial Stress (Equation 5.14), kPa	Difference w.r.t. Maximum Axial Stress Predicted For B-9.5, %
L-9.5	372	-7.0
B-9.5	400	0.0
S-9.5	365	-8.8
Combined Data for Limestone	355	-11.3
Combined Data for Basalt	388	-3.0
Combined Data for Steel-slag	344	-14.0

### 5.7 Effect of Water on Peak Shear Strength of Materials

The Mohr-Coulomb parameters for wet samples of the different materials are examined in this section. The stress- strain behavior of wet samples is similar to that of dry samples as expected for each material type. The results are given in

Appendix. The confining stress applied in the triaxial tests for wet samples, as was the case for the dry samples, was 35 kPa, 70 kPa, and 105 kPa. Triaxial tests were performed on all scaled-down limestone gradations, whereas only on one gradation the test was conducted for basalt and slag materials, B-9.5 and S-9.5 respectively.

Table 5.9 shows the Mohr-Coulomb parameters determined for various series using linear regression analysis described in section 5.2.2, and the parameters determined for the combined data for the scaled-down limestone samples, in which the coefficient of determination,  $R^2$ , was at least 0.996. For comparison, the corresponding Mohr-Coulomb parameters for dry samples were also given in Table 5.9.

Table 5.9 Summary of Mohr-Coulomb parameters for various wet samples

Gradation	Shear Strength Parameters					
	Wet Samples			Dry Samples		
	$\phi$ , degree	c, kPa	$R^2$	$\phi$ , degree	c, kPa	$R^2$
L-2.36	41.5	38.3	0.998	43.3	36.5	0.998
L-4.75	43.0	31.4	0.996	44.0	33.3	0.999
L-9.5	44.4	32.0	0.999	45.8	32.4	0.999
Combined Data For Limestone	43.3	32.6	0.996	44.6	32.5	0.998
B-9.5	48.1	28.6	0.999	46.5	36.0	0.999
S-9.5	41.5	45.1	0.999	41.4	43.6	0.999

Comparing limestone series L-4.75 to L-2.36, both had three tests using 100 mm specimen size, it can be seen that the Mohr-Coulomb parameters are quite close

to each other, with a difference in the angle of internal friction,  $\phi$ , of  $1.5^\circ$ , and a difference in the apparent cohesion,  $c$ , of 7 kPa.

Series L-9.5 had three experimental data points. Comparing L-9.5 to L-4.75, the Mohr-Coulomb parameters are again very close to each other, with a difference in the angle of internal friction of only less than  $1^\circ$ , and a difference in the apparent cohesion of about 1 kPa.

Combining the data obtained for all of the limestone wet series in a  $p$  versus  $q$  chart, the statistical value of the angle of internal friction,  $\phi$ , was  $43.3^\circ$ , with an apparent cohesion,  $c$ , of 32 kPa. The coefficient of determination,  $R^2$ , was 0.996, indicating again a good correlation with linear trend of the data. Comparing this with that of the combined data for limestone dry series, there is a difference in the angle of internal friction of less than  $1^\circ$ ; while no difference was observed in the apparent cohesion between them.

Comparing B-9.5 wet series to that of dry series, although the Mohr-Coulomb parameters are, in general, close to each other, the angle of internal friction of wet samples was about  $2^\circ$  higher than that of dry samples; but the apparent cohesion of wet series experienced 7 kPa lower than that of dry series.

For S-9.5 wet series comparing to the wet series almost no difference was observed in the Mohr-Coulomb parameters determined. The angle of internal friction angle of wet samples was found to be  $41.5^\circ$ , with an apparent cohesion of 45.1 kPa, whereas that of dry samples was  $41.4^\circ$ , with an apparent cohesion of 43.6 kPa.

Consequently, it appears that there is not a significant effect of water on the Mohr-Coulomb parameters determined for all materials used in this study for the engineering purposes. This study supports the statement by Sowers (1979): “The angle of internal friction of most bulky grains is not changed appreciably by water”.

Sowers (1979), and Lambe and Whitman (1979) have emphasized the significance in wet cohesionless soils of the changes in effective stress rather than small differences in the angle of internal friction angle. Because capillary stresses cause an increase of effective stresses within partly saturated soils. Such soils can exhibit a large apparent cohesion even though they possess little or no true cohesion. This apparent cohesion is fully explained by effective stress increment due to capillary water. However, since the capillary stresses are inversely proportional to particle size in diameter (Mitchell, 1993), and the particle sizes tested in this study are coarse-grained soils, the apparent cohesion obtained due to the capillary stresses ought to be negligible. So, the reason of obtaining an apparent cohesion value for wet samples can be explained by the reasons as explained in Section 5.3 for dry samples. Comparison of the apparent cohesion values of wet and dry samples in Table 5.9 supports this argument, and differences in the apparent cohesion seem to be negligible.

Table 5.10 examines the predicted maximum axial stresses,  $\sigma_1$  (Equation 5.14) for the above parameters at a confining stress of 35 kPa for various wet series. For ease of comparison, the corresponding values for dry samples were also included in this table. Dry series B-9.5 shows the highest peak shear strength, while wet series L-9.5 shows the lowest, where the difference is about 12.5%.

Consequently, from Table 5.9 and Table 5.10, it appears that use of dry samples only may lead to acceptable predictions of peak shear strength of the materials tested.

Table 5.10 Predicted maximum axial stress with  $\sigma_3 = 35$  kPa  
for various wet series

Gradation	Predicted Maximum Axial Stress (Equation 5.14), kPa		Difference w.r. to Maximum Axial Stress Predicted For B-9.5, %	
	Wet Samples	Dry Samples	Wet Samples	Dry Samples
L-9.5	350	372	-12.5	-7.0
B-9.5	388	400	-3.0	0.0
S-9.5	372	365	-7.0	-8.8

### 5.8 Effect of Gradation on Peak Shear Strength of Materials

The effect of gradations prepared only for the scaled-down limestone on Mohr-Coulomb parameters is examined in this section.

Table 5.11 lists the Mohr-Coulomb parameters for the alternative gradations of limestone materials. The test series using these gradations were labeled L-6.35, meaning limestone material having minimum particle size of 6.35 mm, particle size ranged from 6.35 mm to 19.0 mm; and L-3.15, meaning limestone material having minimum particle size of 3.15 mm, ranging from 3.15 mm to 19.0 mm as shown in Figure 4.4. The uniformity coefficients of these gradations together with L-9.5, particle size of 9.5 mm to 19.0 mm, are given in the table below. The confining stresses used 35 kPa, 70 kPa, and 105 kPa with 100 mm specimens. So, three tests were run in each series. The related stress-strain and volumetric strain curves are presented in Appendix.

Table 5.11 after linear regression analysis shows that the Mohr-Coulomb peak shear strength parameters established for L-6.35 and L-3.15 are quite close to that of L-9.5.

Table 5.11 Comparison of Mohr-Coulomb parameters  
for different gradations of limestone

Gradation	Uniformity Coefficient ( $C_u$ )	Shear Strength Parameters		
		Angle of Internal Friction ( $\phi$ ), degree	Apparent Cohesion (c), kPa	Coefficient of Determination ( $R^2$ )
L-9.5 (Table 5.1)	1.40	45.8	32.4	0.999
L-6.35	1.75	45.0	33.8	0.999
L-3.15	2.38	44.4	47.4	0.999

Table 5.12 examines the maximum axial stresses,  $\sigma_1$ , predicted by Equation (5.14) for the above parameters at a confining stress of 35 kPa for L-6.35 and L-3.15 series. Series L-3.15 shows higher peak shear strength than series L-9.5. Although there seems to be an increase in the maximum axial stress, the difference is about 12.0%.

Table 5.12 Predicted maximum axial stress with  $\sigma_3 = 35$  kPa for crushed limestone

Gradation	Uniformity Coefficient ( $C_u$ )	Predicted Maximum Axial Stress (Equation 5.14), kPa	Difference w.r.t. Maximum Axial Stress Predicted For L-3.15, %
L-9.5 (Table 5.2)	1.40	372	-12.0
L-6.35	1.75	367	-13.2
L-3.15	2.38	423	0.0

Consequently, it appears that use of alternative gradations as far as they were prepared in the prescribed uniformity coefficients does not have a significant effect on the peak shear strength of limestone materials.

## 5.9 Elastic Moduli Trends

### 5.9.1 Introduction of the Elastic Moduli Studied

The basic definition of the elastic modulus,  $E$ , for a specimen tested in conventional triaxial test (CTC) using generalized Hooke's law (Wood, 1990) is:

$$E = \frac{\partial \sigma_a}{\partial \varepsilon_a} - 2\nu \frac{\partial \sigma_3}{\partial \varepsilon_a} \quad (5.15)$$

where  $\partial \sigma_a$  is the change in axial stress on the specimen;  $\partial \sigma_3$  is the change in confining stress;  $\nu$  is Poisson's ratio, and  $\partial \varepsilon_a$  is the change in axial strain. Since, for the CTC tests, the confining stress is kept constant, Equation (5.15) becomes simply:

$$E = \frac{\partial \sigma_a}{\partial \varepsilon_a} \quad (5.16)$$

Because we are working with data taken at discrete time intervals, Equation (5.16) then becomes:

$$E = \frac{\Delta \sigma_a}{\Delta \varepsilon_a} \quad (5.17)$$

Soils are not linear elastic materials but behave in an elasto-plastic way over a wide range of loading and unloading. So, there is more than one way to define an "elastic modulus".

The elastic moduli of interest in relation to railway ballast are: (i) the initial elastic modulus ( $E_i$ ) defined as the initial slope of the stress-strain curve (Lambe & Whitman, 1979); and (ii) the unloading-reloading or resilient modulus ( $E_{ur}$ ) defined as the ratio of deviator stress at the end of an unloading-reloading cycle in conventional triaxial compression test to the corresponding axial strain (Janardhanam & Desai, 1983); (iii) although it is not needed in the design of railway ballast, just for the sake of comparison, the secant modulus ( $E_{50}$ ) is also determined. It is defined as the ratio of half the maximum deviator stress divided by the axial strain associated with that.

The initial elastic modulus,  $E_i$ , for this study was calculated, in general, using the difference between the second and third data point after the axial load has been applied. This was to avoid the “seating” problem of the equipment. Figure 5.13 shows  $E_i$  in relation to a typical sample stress-strain curve.

The resilient or unloading-reloading modulus,  $E_{ur}$ , was calculated from the trend of the reloading portion of an unloading-reloading curve. This modulus was typically used as the best estimate of the elastic behavior of soils under repeated loading cycles. The unloading-reloading modulus was examined approximately at an axial strain of 1%. The axial stress associated with this axial strain level is well above the working stress level for railway ballast. Figure 5.14 illustrates  $E_{ur}$  in relation to a typical sample stress-strain curve.

The use of the secant modulus is supported by Vermeer and Schanz (1996) as the best approximation of a soil stress-strain path. It is particularly useful in the design of foundations, because of its ability to linearly approximate the strain associated with the original loading of a soil. Figure 5.15 shows  $E_{50}$  in relation to a typical sample stress-strain curve.

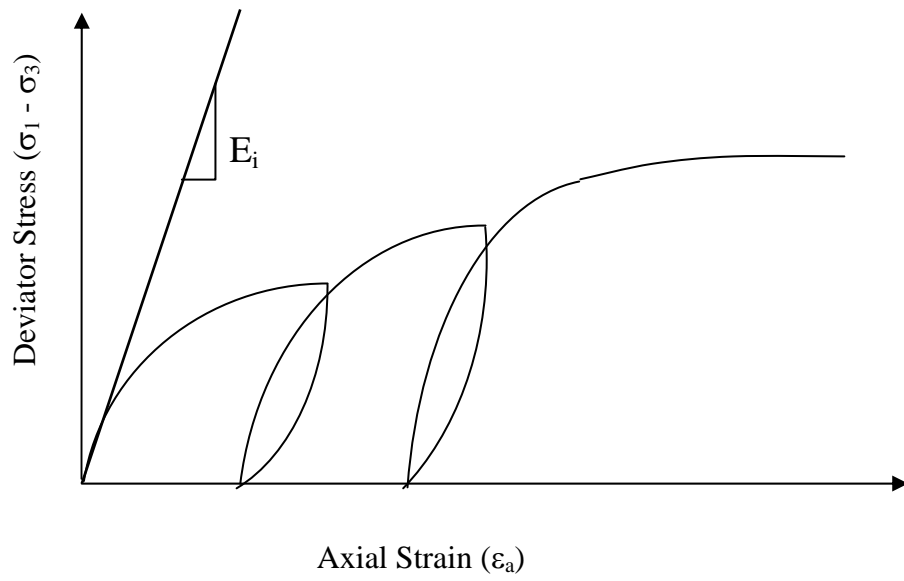


Figure 5.13 Definition of initial elastic modulus with typical stress-strain curve

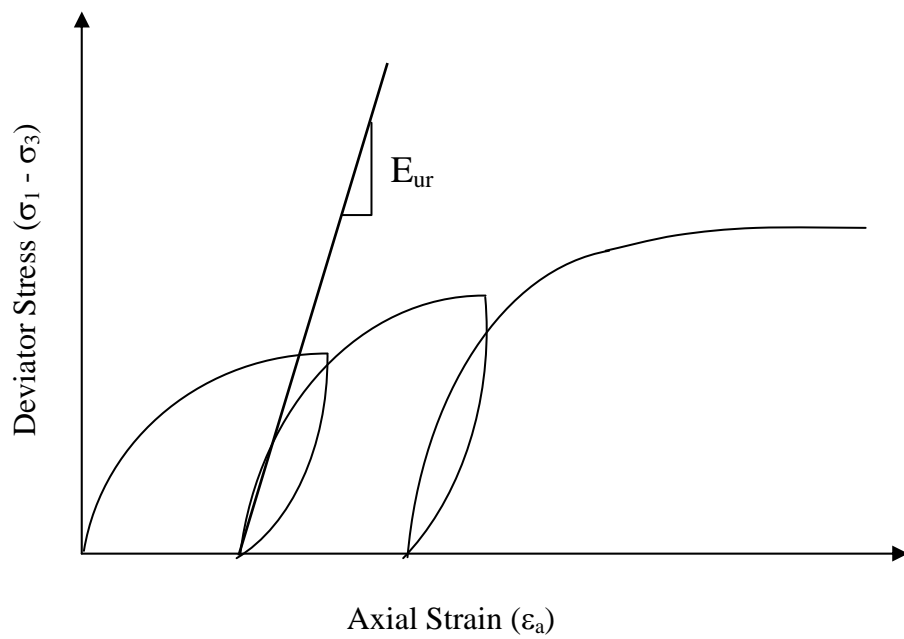


Figure 5.14 Definition of unloading-reloading elastic modulus with typical stress-strain curve

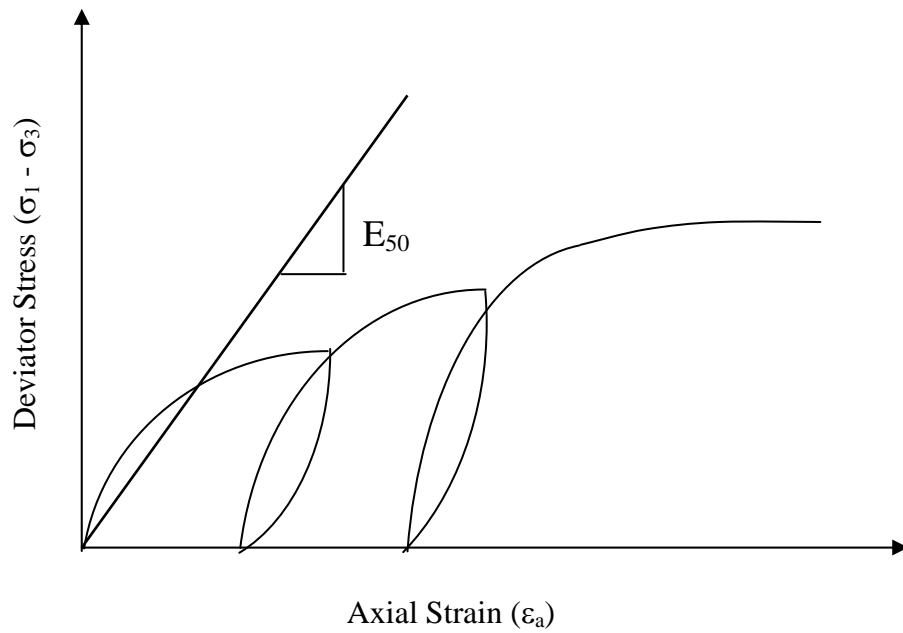


Figure 5.15 Definition of secant elastic modulus with typical stress-strain curve

### 5.9.2 Statistical Analysis of Elastic Moduli

The trend of each elastic modulus can be modeled by the below expression suggested by Ohde (1939) and Janbu (1963) for the initial elastic modulus; the unloading-reloading elastic modulus by Duncan and Chang, 1980; and the secant elastic modulus by Vermeer, 1996:

$$E / p_r = K(\sigma_3 / p_r)^n \quad (5.18)$$

where  $p_r$  is a reference pressure (typically 1 kPa). In order to introduce a rational method for determining the coefficient,  $K$ , corresponding to  $\sigma_3 / p_r = 1$ ; and the slope of the elastic modulus equation,  $n$ , the following method is used.

Equation (5.18) can be rewritten to be linear using a logarithmic base scale  $\log_{10}$ :

$$\log_{10}(E/p_r) = \log_{10} K + n \log_{10}(\sigma_3/p_r) \quad (5.19)$$

For the data from experiments conducted at the prescribed confining stresses, a linear regression analysis similar to that for determining the shear strength parameters in section 5.2.2 was run to obtain the elastic modulus intercept  $\log_{10}K$  and the slope  $n$ . Basically,  $E/p_r$  values were plotted against the corresponding  $\sigma_3/p_r$  values, and a best fit of the data was determined by linear regression. Then the slope of the equation is taken as being equal to  $n$  and the intercept of the best fit line with the  $E$  axis as being equal to  $\log_{10}K$ . These coefficients in turn were used to examine the variation of the elastic modulus with confining stress, particle size, and material type.

### **5.9.3 Elastic Moduli Trends for Scaled-down Limestone Materials**

Experimental series L-2.36 (scaled-down limestone ballast, minimum particle size of 2.36 mm) using 100 mm triaxial specimen size as well as L-4.75 and L-9.5 had the following values of elastic moduli, shown in Table 5.13.

Using the analysis technique suggested in 5.9.2, and setting  $p_r = 1$  kPa, it is possible to fit the data from Table 5.13 to a best-fit power equation of the form of Equation 5.19. The parameters of the best fit will be the power coefficient,  $n$ , and the intercept of  $\log_{10}K$ .

Table 5.13 Elastic moduli determined for series L-2.36, L-4.75 and L-9.5

Gradation	Confining Stress ( $\sigma_3$ ), kPa	Initial Modulus ( $E_i$ ), kPa	Secant Modulus ( $E_{50}$ ), kPa	Unloading-reloading Modulus ( $E_{ur}$ ), kPa
L-2.36	35	$3.14 \times 10^4$	$2.75 \times 10^4$	$9.09 \times 10^4$
	70	$5.23 \times 10^4$	$3.42 \times 10^4$	$1.42 \times 10^5$
	105	$6.10 \times 10^4$	$5.04 \times 10^4$	$1.62 \times 10^5$
L-4.75	35	$4.19 \times 10^4$	$2.85 \times 10^4$	$1.15 \times 10^5$
	70	$7.20 \times 10^4$	$4.40 \times 10^4$	$1.36 \times 10^5$
	105	$8.11 \times 10^4$	$5.79 \times 10^4$	$1.63 \times 10^5$
L-9.5	35	$4.19 \times 10^4$	$3.76 \times 10^4$	$1.15 \times 10^5$
	70	$6.68 \times 10^4$	$5.20 \times 10^4$	$1.69 \times 10^5$
	105	$8.38 \times 10^4$	$5.91 \times 10^4$	$1.81 \times 10^5$

For series L-2.36, the best fit power law equations are:

$$E_i = 3580(\sigma_3)^{0.617} \quad ; \quad R^2 = 0.977 \quad (5.20a)$$

$$E_{50} = 4076(\sigma_3)^{0.526} \quad ; \quad R^2 = 0.907 \quad (5.20b)$$

$$E_{ur} = 13574(\sigma_3)^{0.540} \quad ; \quad R^2 = 0.978 \quad (5.20c)$$

It is interesting to note, at least for the series L-2.36, that the value of  $n = 0.617$  for the initial elastic modulus is within the range of that values given by Lambe and Whitman (1979), in which  $n$  is between 0.4 and 1.0; and  $n = 0.526$  found for the secant elastic modulus is close to that proposed by Vermeer and Schanz

(1996), in which  $n = 0.5$ . On the other hand, for the unloading-reloading elastic modulus, the value of  $n = 0.540$  obtained is somewhat skewed from that predicted by Hertz contact theory (Timoshenko, 1956; Sture, 1996), in which  $n = 0.333$ . The Hertz contact theory states that the modulus is independent of particle size.

For series L-4.75, the best fit power law equations are:

$$E_i = 4756(\sigma_3)^{0.621} \quad ; \quad R^2 = 0.959 \quad (5.21a)$$

$$E_{50} = 2891(\sigma_3)^{0.643} \quad ; \quad R^2 = 0.999 \quad (5.21b)$$

$$E_{ur} = 38291(\sigma_3)^{0.307} \quad ; \quad R^2 = 0.999 \quad (5.21c)$$

and for series L-9.5, the best fit power law equations are:

$$E_i = 4401(\sigma_3)^{0.636} \quad ; \quad R^2 = 0.998 \quad (5.22a)$$

$$E_{50} = 8566(\sigma_3)^{0.419} \quad ; \quad R^2 = 0.991 \quad (5.22b)$$

$$E_{ur} = 25556(\sigma_3)^{0.430} \quad ; \quad R^2 = 0.944 \quad (5.22c)$$

It is clear for the data calculated from all experimental series that all three elastic moduli follow the general power law suggested in Equation (5.18). The coefficient of determination,  $R^2$  for all moduli values computed over 0.9 advocates this, in other words, they indicate a good power law fit to the data. From Figure 5.16 to Figure 5.18 shows the trend of the elastic moduli of Equation 5.20 through 5.22 for series L-2.36, L-4.75 and L-9.5, respectively and clearly illustrate also that the

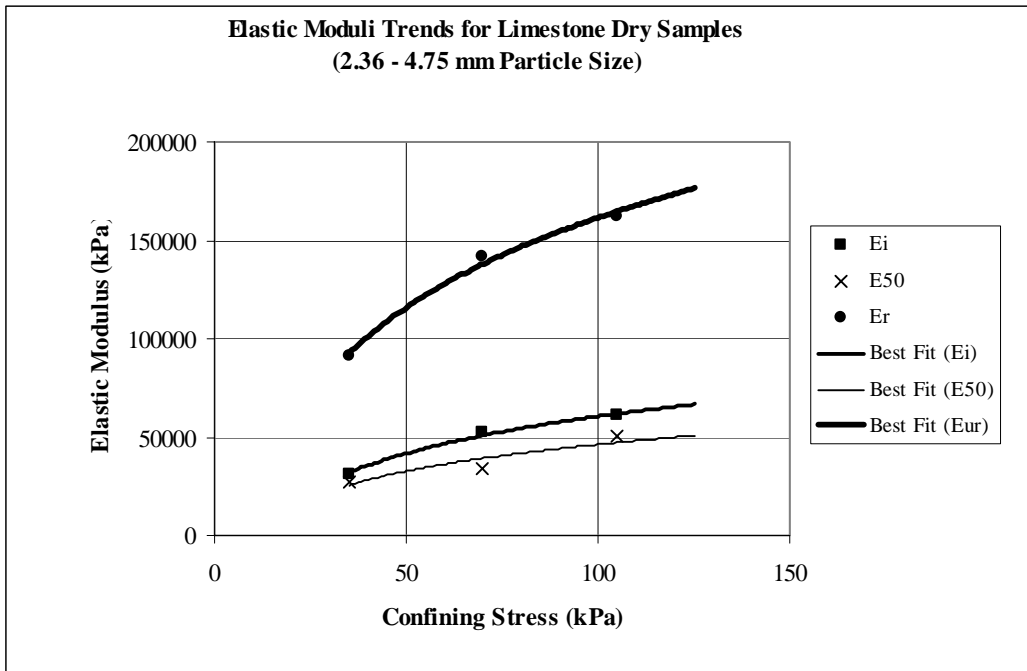


Figure 5.16 Elastic moduli trends for series L-2.36

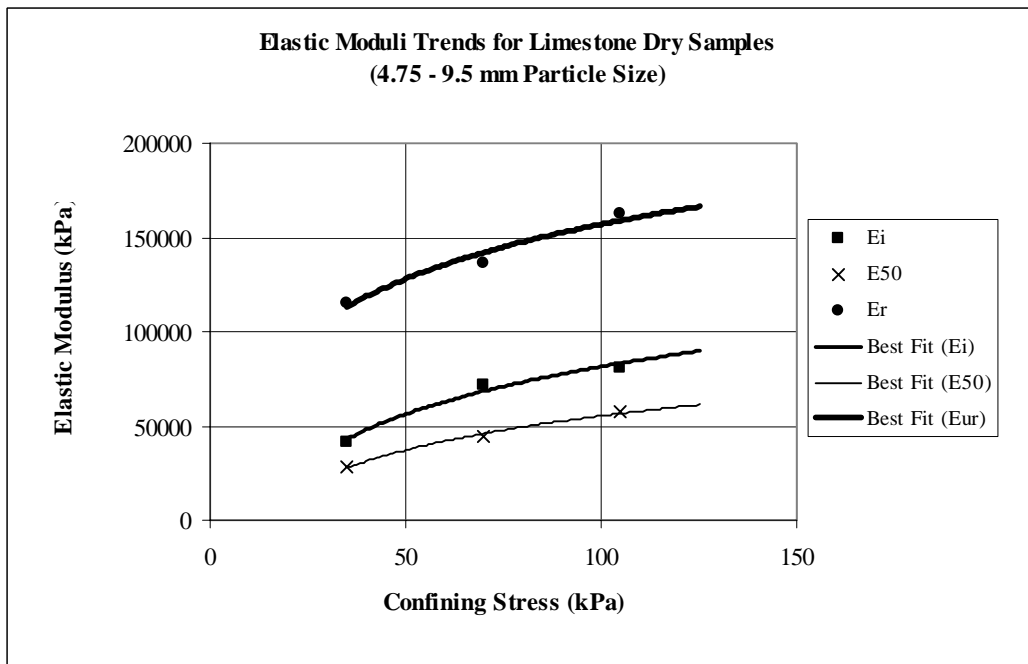


Figure 5.17 Elastic moduli trends for series L-4.75

power law equation accurately predicts the trend of the three elastic moduli for all of the experimental series.

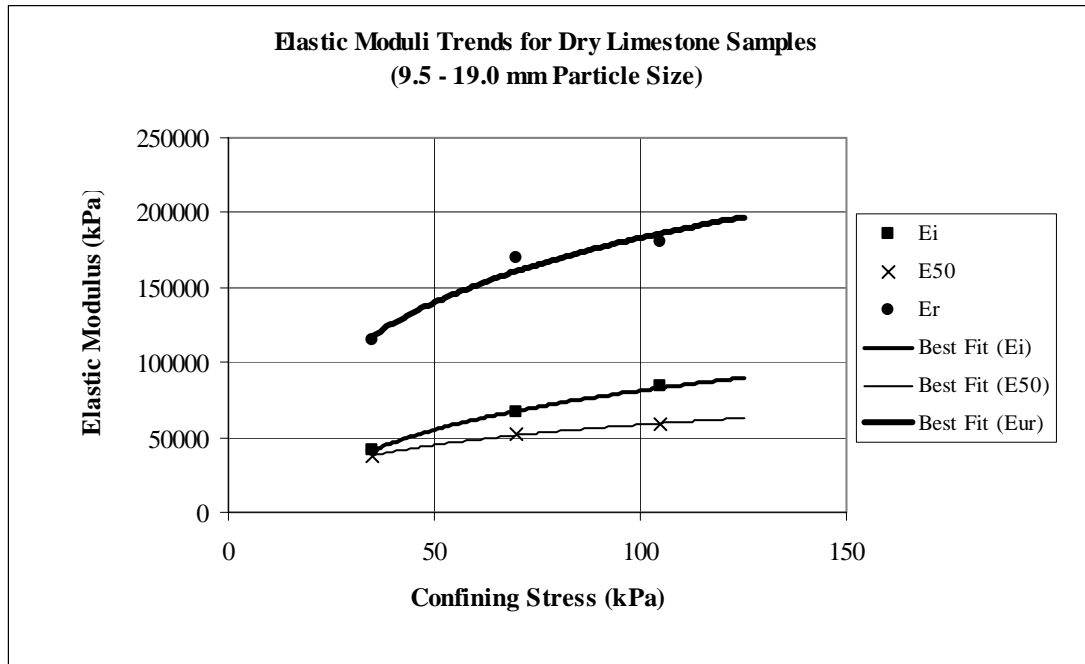


Figure 5.18 Elastic moduli trends for series L-9.5

Table 5.14 lists the calculated values for  $n$  and  $\log_{10}K$  for the initial moduli for all of the experimental series using scaled-down limestone samples. Figure 5.19 shows the best fit power law curves for each series listed in Table 5.14. There is a general trend of increasing initial modulus with increasing mean particle size, although the difference in the modulus values between the coarser particle sizes is undistinguishable.

Table 5.14 Power law parameters for the initial elastic moduli  
for scaled-down limestone

Gradation	Power Law Slope, n	Power Law Intercept, $\log_{10}K$	Coefficient of Determination, $R^2$
L-2.36	0.617	3.55	0.977
L-4.75	0.621	3.68	0.959
L-9.5	0.636	3.64	0.998

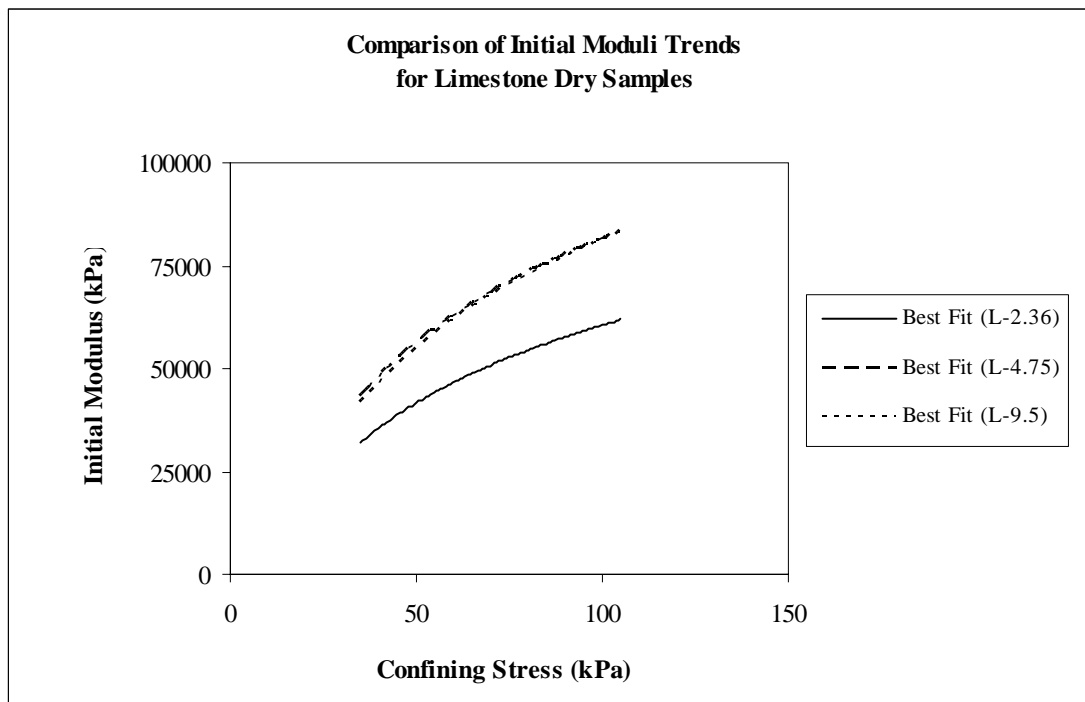


Figure 5.19 Comparison of trends of initial elastic moduli for all limestone series

The purpose of preparing parallel gradations was to predict the properties of the prototype material. Then the question is that how the initial elastic moduli varies with the change in mean particle size, and whether a trend with respect to mean particle size can be obtained. Figure 5.20 shows the variation of the power law parameters  $n$  and  $\log_{10}K$  of the initial elastic moduli with the mean particle size of the scaled-down limestone samples. The tendency of power law parameters of the initial elastic modulus is approximated with a power law fit to the data. The corresponding equations for  $n$  and  $\log_{10}K$  of the initial modulus in Figure 5.20 are given in Equation (5.23a) and Equation (5.23b). The power law slope,  $n$ , increases as the mean particle size increases; and the power law intercept,  $\log_{10}K$ , increases with increasing mean particle size. As it can be seen that the coefficient of determination of 0.879 for  $n$  indicates a good fit to the change in particle size; whereas that of 0.50 for  $\log_{10}K$  implies that the statistical fit is not very good. Nevertheless, Figure 5.21 through Figure 5.23, respectively for L-2.36, L-4.75, and L-9.5 illustrate that the power law with the parameters given in Equation (5.23) for the initial modulus,  $E_i$ , predicts the values within a  $\pm 20\%$  confidence envelope. Consequently, the parallel gradation technique for these series provides an adequate prediction of the initial elastic modulus.

$$n = 0.6006(D_{50})^{0.021} \quad ; \quad R^2 = 0.879 \quad (5.23a)$$

$$\log_{10} K = 3.5065(D_{50})^{0.0179} \quad ; \quad R^2 = 0.501 \quad (5.23b)$$

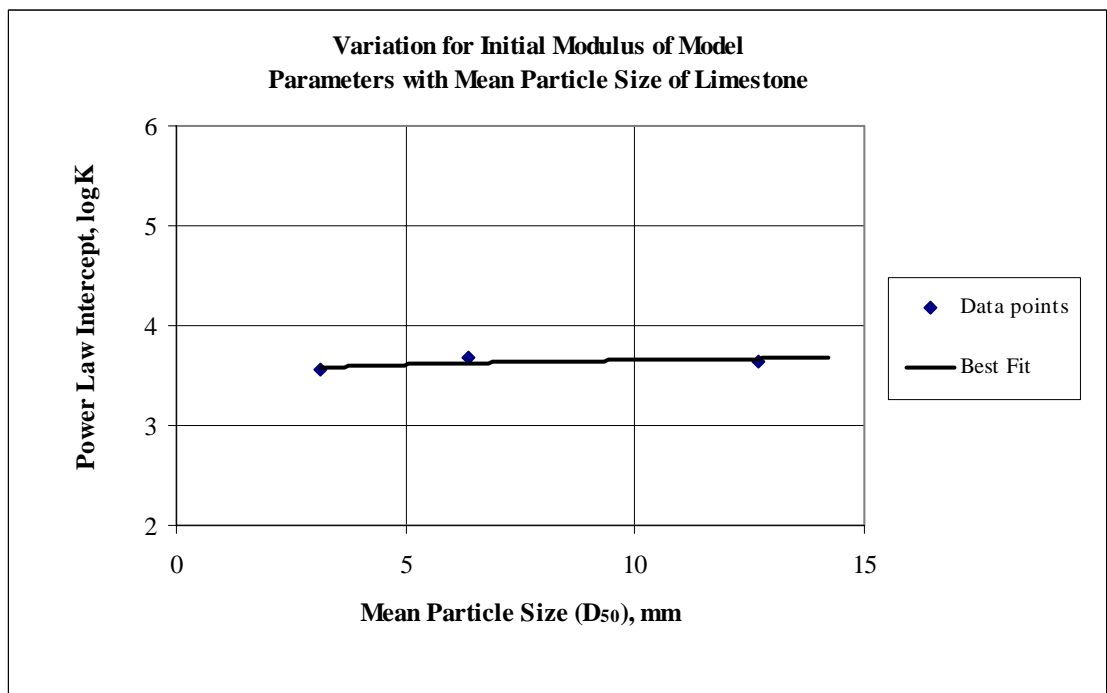
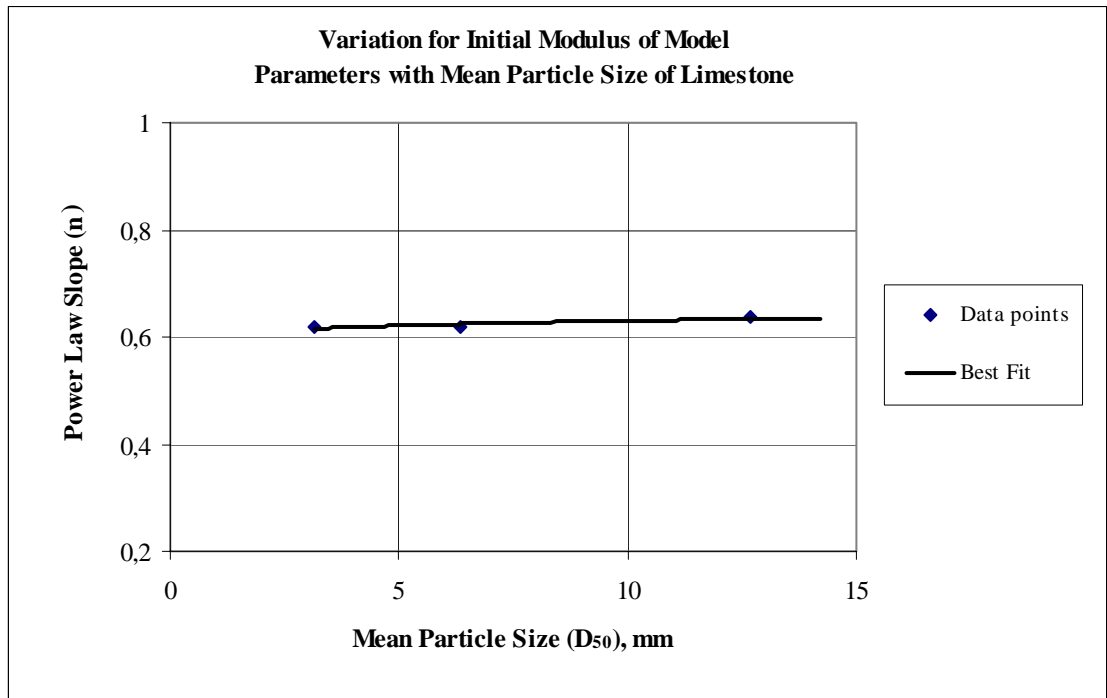


Figure 5.20 Variation of power law parameters of initial elastic moduli with the mean particle size for the scaled-down limestone samples

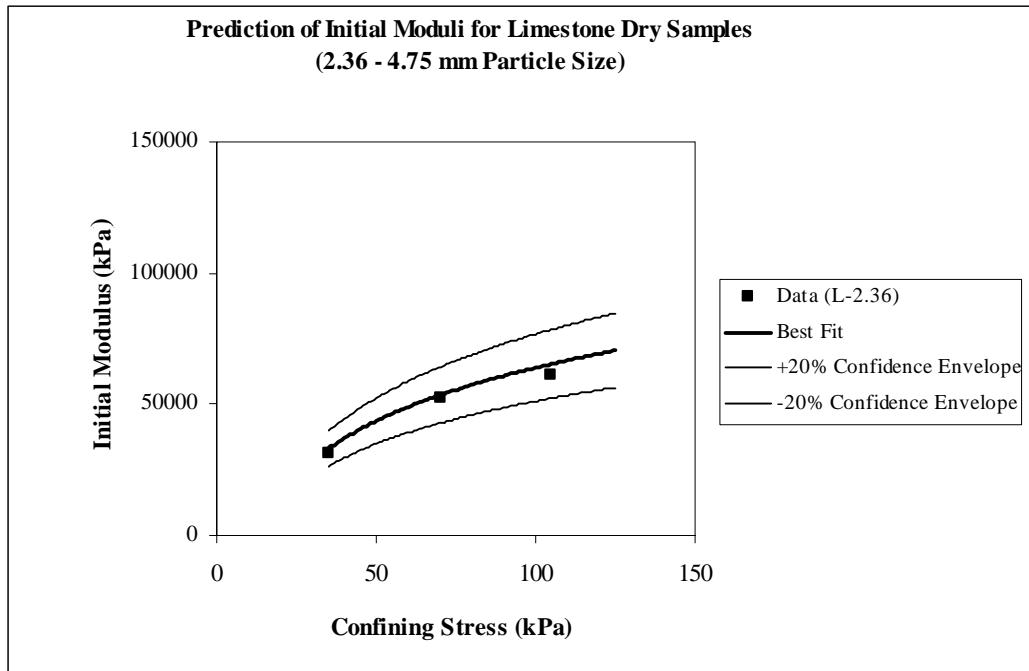


Figure 5.21 Prediction of Initial Elastic moduli for L-2.36 series

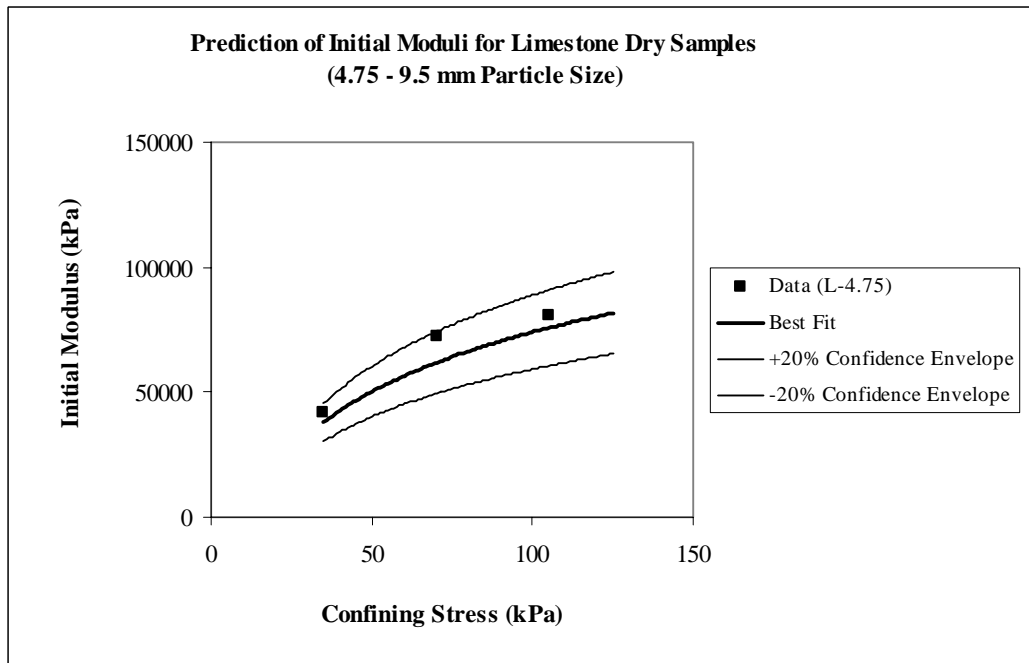


Figure 5.22 Prediction of Initial Elastic moduli for L-4.75 series

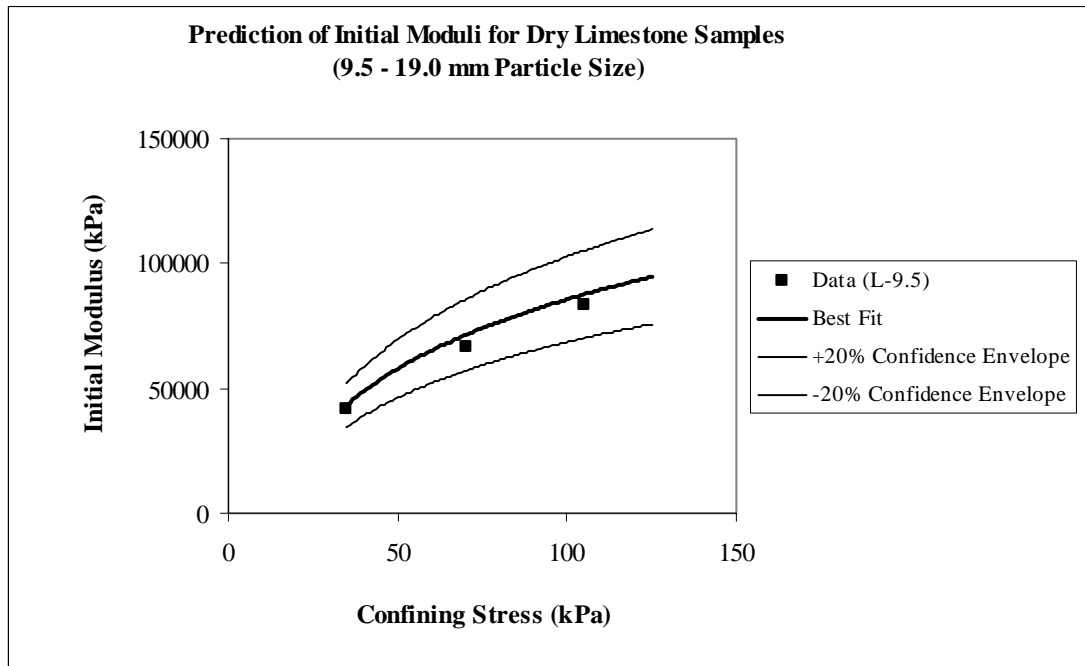


Figure 5.23 Prediction of Initial Elastic moduli for L-9.5 series

Table 5.15 lists the determined values for  $n$  and  $\log_{10}K$  of the power law parameters for the secant moduli for all of the experimental series using scaled-down limestone samples. Figure 5.24 illustrates the best fit power law curves for each series listed in Table 5.15. The secant elastic moduli for scaled-down limestone show an increasing trend with increasing mean particle size.

Table 5.15 Power law parameters for the secant elastic moduli for scaled-down limestone

Gradation	Power Law Slope, $n$	Power Law Intercept, $\log_{10}K$	Coefficient of Determination, $R^2$
L-2.36	0.526	3.61	0.907
L-4.75	0.643	3.46	0.999
L-9.5	0.419	3.93	0.991

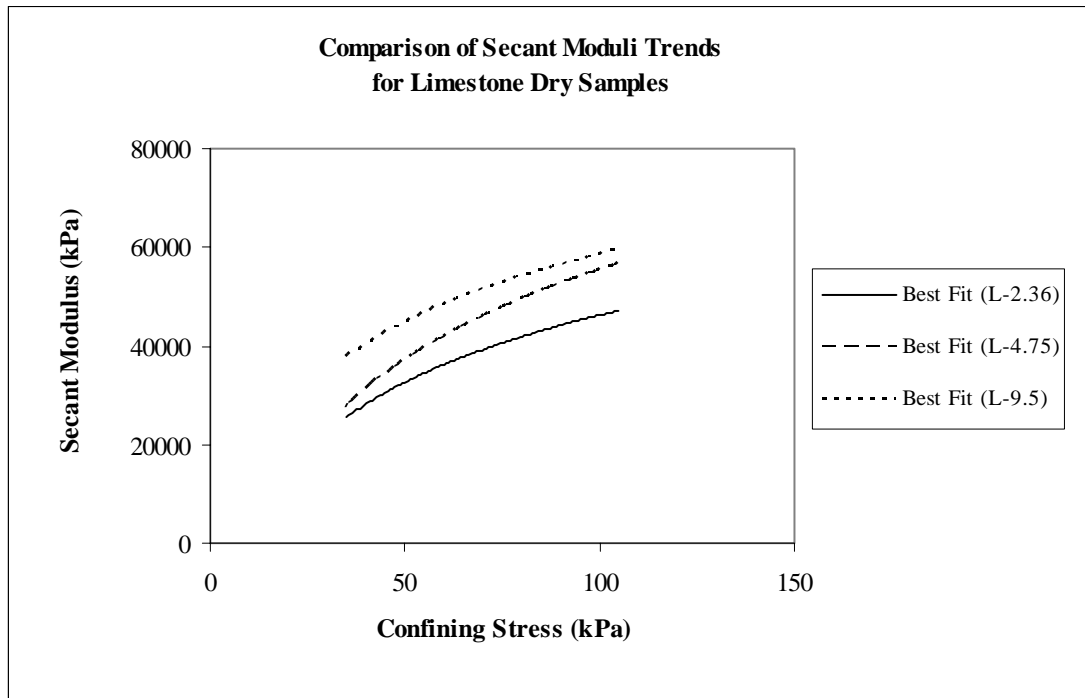


Figure 5.24 Comparison of trends of secant elastic moduli for all limestone series

As with the initial elastic moduli, the question again is that how the secant elastic moduli may vary with the change in mean particle size. Figure 5.25 shows the variation of the power law parameters  $n$  and  $\log_{10}K$  of the secant elastic moduli with the mean particle size for crushed limestone. The tendency of power law parameters for the secant elastic modulus is again approximated with a power law fit to the data. The corresponding equations for  $n$  and  $\log_{10}K$  of the secant elastic moduli in Figure 5.25 are given in Equation (5.24a) and Equation (5.24b). The power law slope,  $n$ , decreases as the mean particle size increases; whereas the power law intercept,  $\log_{10}K$ , increases with increasing mean particle size. As it can be seen, the data is so scattered that the statistical fit is poor. However, Figure 5.26 through Figure 5.27, respectively for L-2.36, L-4.75, and L-9.5 illustrate that the power law with the parameters given in Equation (5.24) for the secant elastic modulus,  $E_{50}$ , predicts the value within a  $\pm 20\%$  confidence envelope. Consequently, the parallel gradation

technique for these series provides again an adequate prediction of the secant elastic modulus.

$$n = 0.7045(D_{50})^{-0.1633} \quad ; \quad R^2 = 0.283 \quad (5.24a)$$

$$\log_{10} K = 3.2719(D_{50})^{0.0611} \quad ; \quad R^2 = 0.429 \quad (5.24b)$$

It is interesting to note that the values of power law slope,  $n$ , of the secant moduli are scattered, but almost equal as an average value to that predicted by Vermeer and Schanz, in which  $n = 0.5$ . Figure 5.29 illustrates the use of  $n = 0.5$  and the value of  $\log_{10}K = 3.61$  deduced for the data L-2.36 given in Table 5.14. While the use of Vermeer and Schanz,  $n = 0.5$  and  $\log_{10}K = 3.61$  underestimates the secant moduli for scaled-down limestone including the prototype materials  $D_{50} = 30$  mm and  $D_{50} = 45$  mm for which the secant moduli were computed from Equation (5.24), the values are within  $\pm 100\%$  confidence envelope. Therefore, Vermeer and Schanz' prediction might be an adequate predictor of the secant moduli as long as it is used with a rationally determined value for  $\log_{10}K$ .

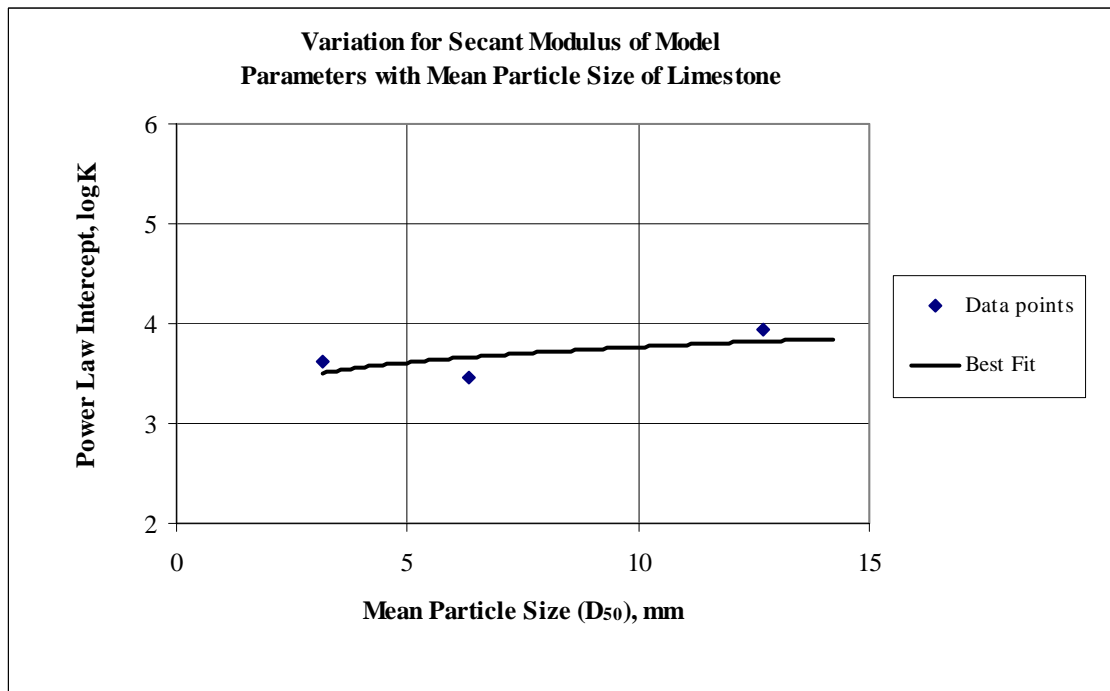
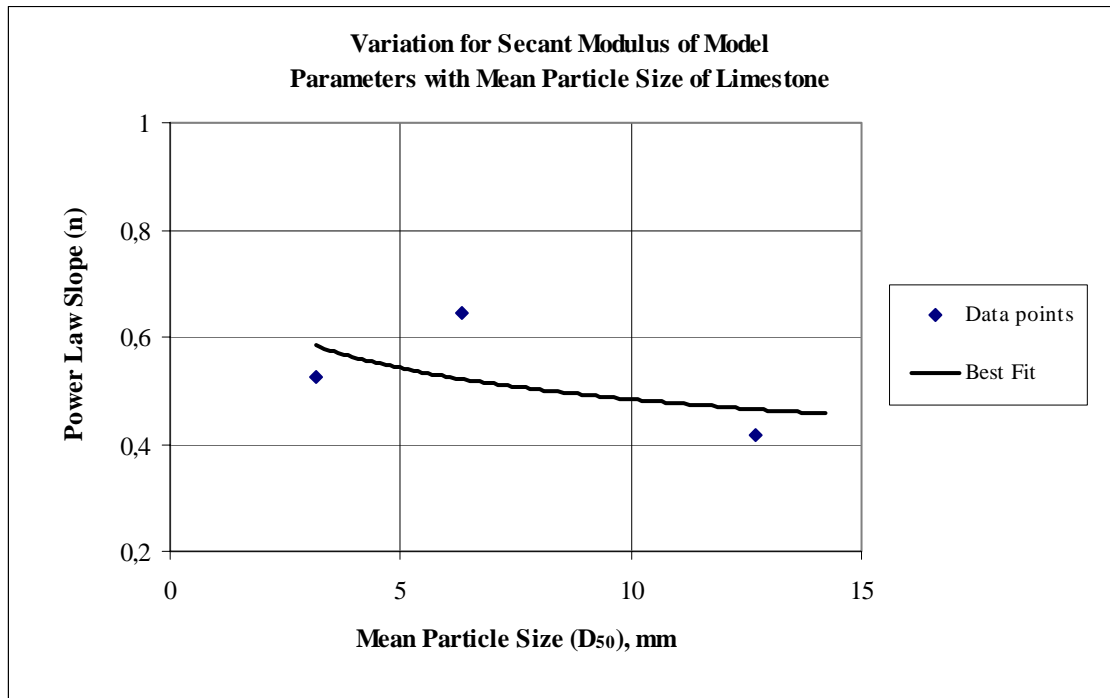


Figure 5.25 Variation of power law parameters of secant elastic moduli with the mean particle size for the scaled-down limestone samples

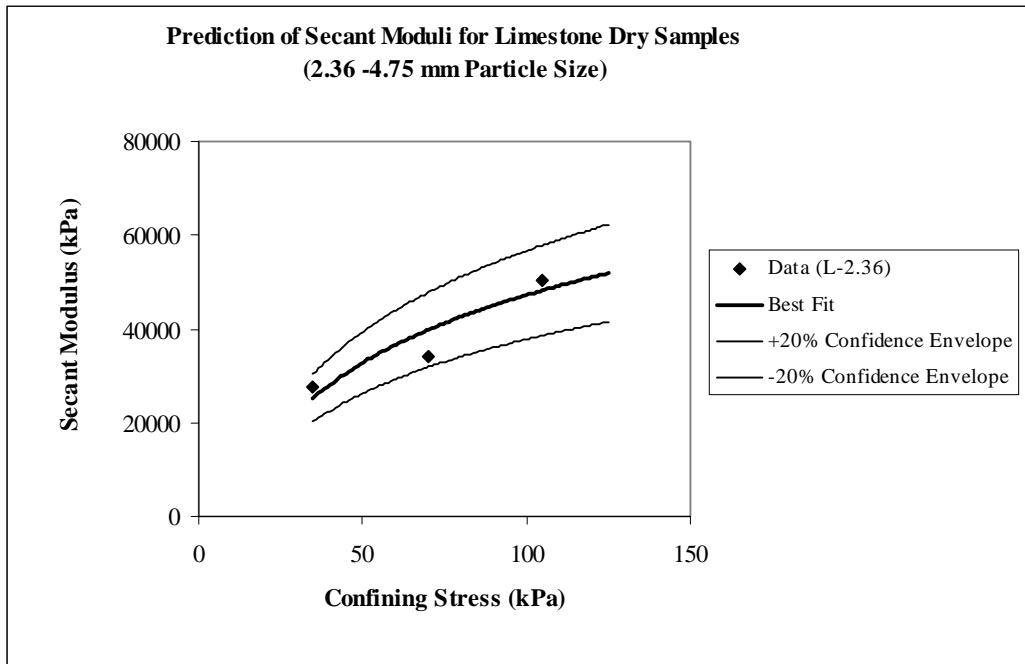


Figure 5.26 Prediction of secant elastic moduli for L-2.36 series

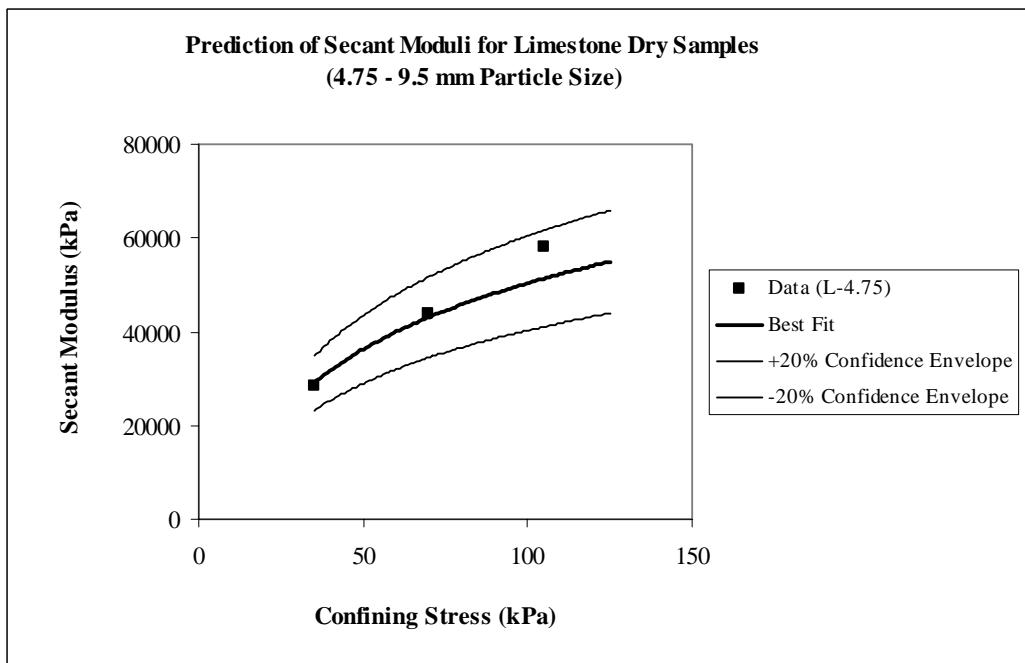


Figure 5.27 Prediction of secant elastic moduli for L-4.75 series

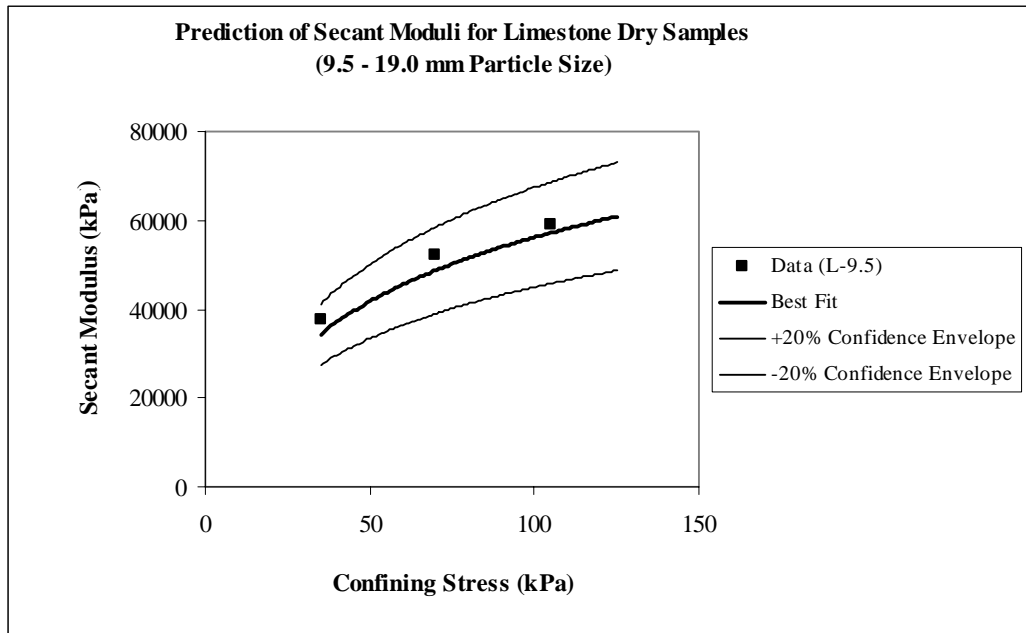


Figure 5.28 Prediction of secant elastic moduli for L-9.5 series

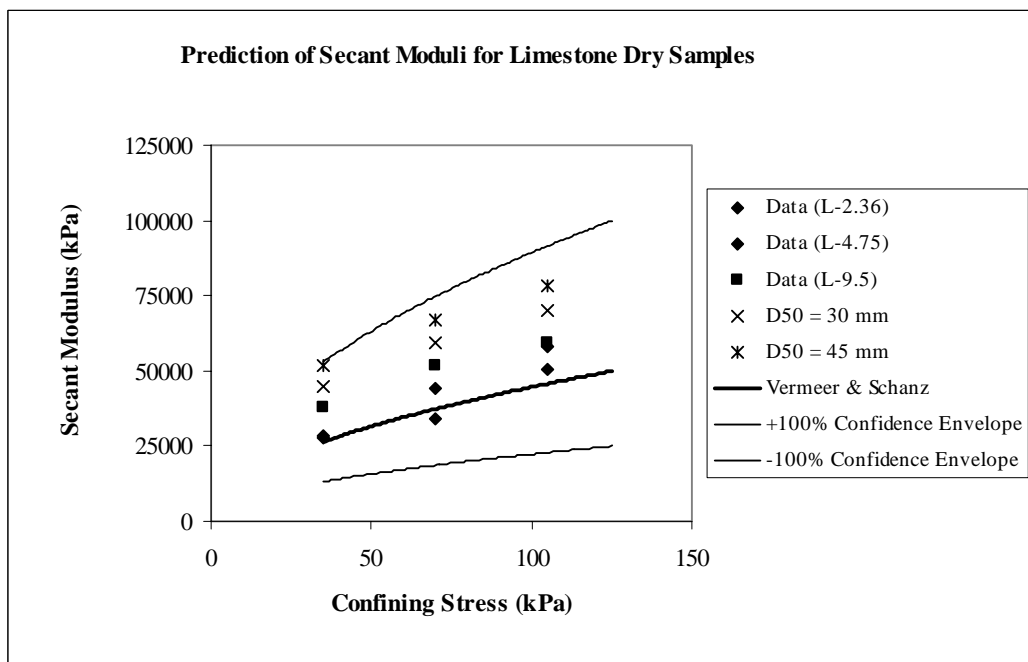


Figure 5.29 Prediction of secant moduli by Vermeer and Schanz for limestone samples

Table 5.16 lists the power law parameters for the unloading-reloading elastic moduli for all of the scaled-down limestone samples. Figure 5.30 illustrates the best fit power law curves for each series listed in Table 5.16. The unloading-reloading elastic moduli for limestone show that a general trend of increasing stiffness is observed with increasing mean particle size.

Table 5.16 Power law parameters for the unloading-reloading elastic moduli for scaled-down limestone limestone

Gradation	Power Law Slope, n	Power Law Intercept, $\log_{10}K$	Coefficient of Determination, $R^2$
L-2.36	0.540	4.13	0.978
L-4.75	0.307	4.58	0.973
L-9.5	0.430	4.41	0.944

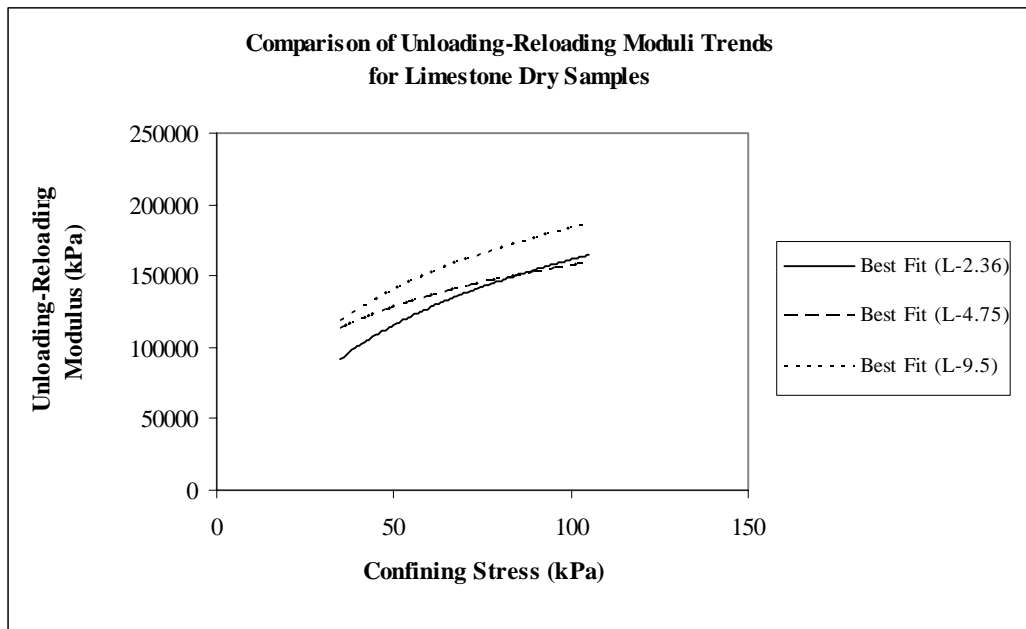


Figure 5.30 Comparison of unloading-reloading moduli trends for limestone series

Figure 5.31 shows the variation of the power law parameters of the unloading-reloading elastic moduli with the mean particle size for limestone. As with initial and secant elastic moduli, Equation (5.25a) and Equation (5.25b) are derived using a power law fit to the data given in Table 5.15. The power law slope,  $n$ , decreases as the mean particle size increases; whereas the power law intercept,  $\log_{10}K$ , increases with increasing mean particle size. The low values of coefficient of determination,  $R^2$ , indicate that the statistical fit is poor for the unloading-reloading moduli of the limestone material. However, Figure 5.32 through Figure 5.34, respectively for L-2.36, L-4.75, and L-9.5 show that the power law with the parameters given in Equation (5.25) for the unloading-reloading elastic modulus,  $E_{ur}$ , predicts the values within a  $\pm 20\%$  confidence envelope. Consequently, the parallel gradation technique for these series provides again an adequate prediction of the unloading-reloading elastic modulus.

$$n = 0.5624(D_{50})^{-0.1655} \quad ; \quad R^2 = 0.164 \quad (5.25a)$$

$$\log_{10} K = 4.012(D_{50})^{0.0464} \quad ; \quad R^2 = 0.383 \quad (5.25b)$$

It is interesting to note that the values of power law slope,  $n$ , obtained for all experimental series are generally higher than that predicted by Hertz Contact Theory, in which  $n = 0.333$ . Figure 5.35, including the unloading-reloading modulus values for the mean particle sizes of  $D_{50} = 30$  mm and  $D_{50} = 45$  mm predicted by Equation (5.25), illustrates the use of  $n = 0.333$  and the value of  $\log_{10}K = 4.58$  deduced for the data L-4.75 given in Table 5.14. The use of Hertz contact theory,  $n = 0.333$  and  $\log_{10}K = 4.58$  estimates the unloading-reloading moduli for scaled-down limestone within  $\pm 50\%$  confidence envelope. Therefore, Hertz Contact Theory can be an adequate predictor of the unloading-reloading moduli as long as coupled with a rationally determined value for  $\log_{10}K$ .

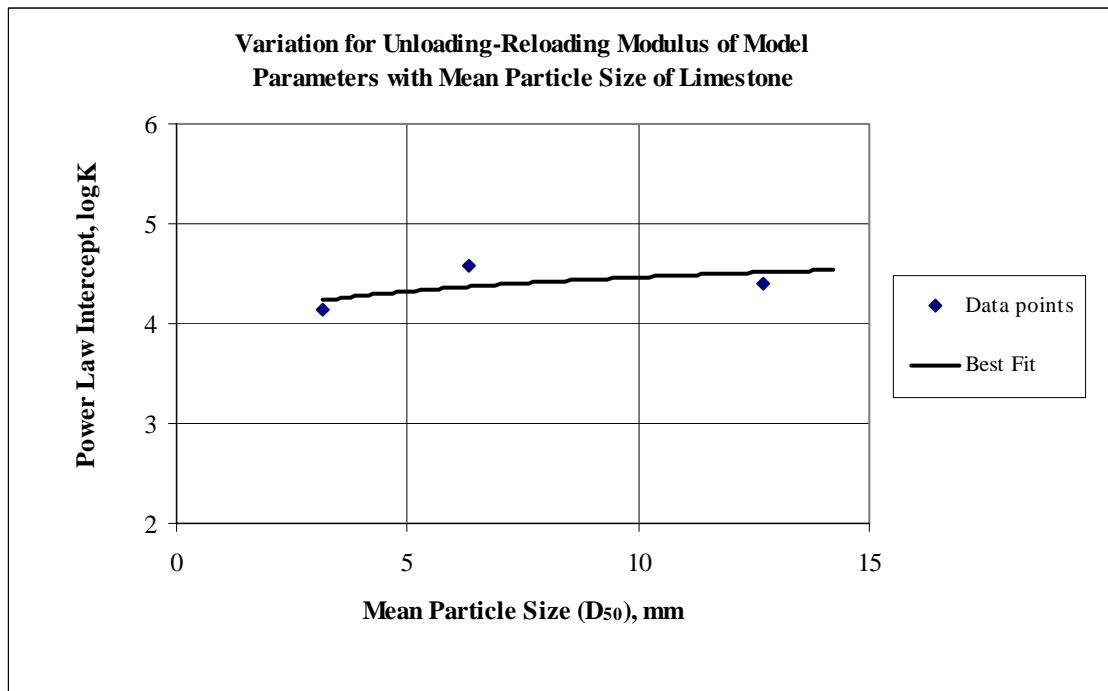
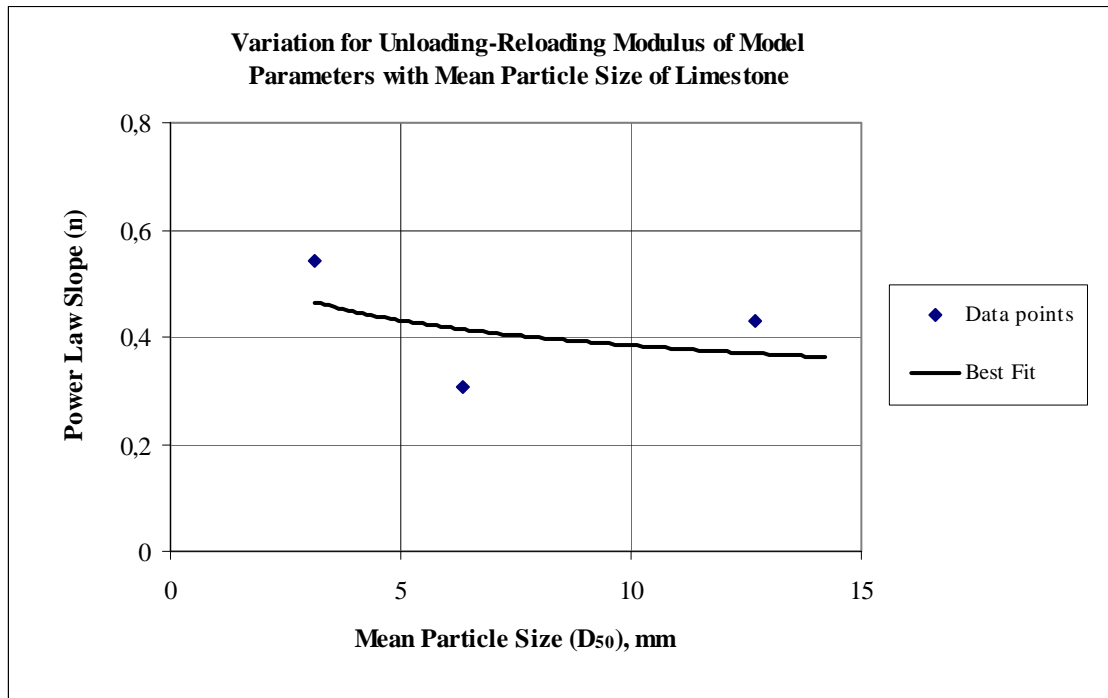


Figure 5.31 Variation of power law parameters of unloading-reloading elastic moduli with the mean particle size for scaled-down limestone samples

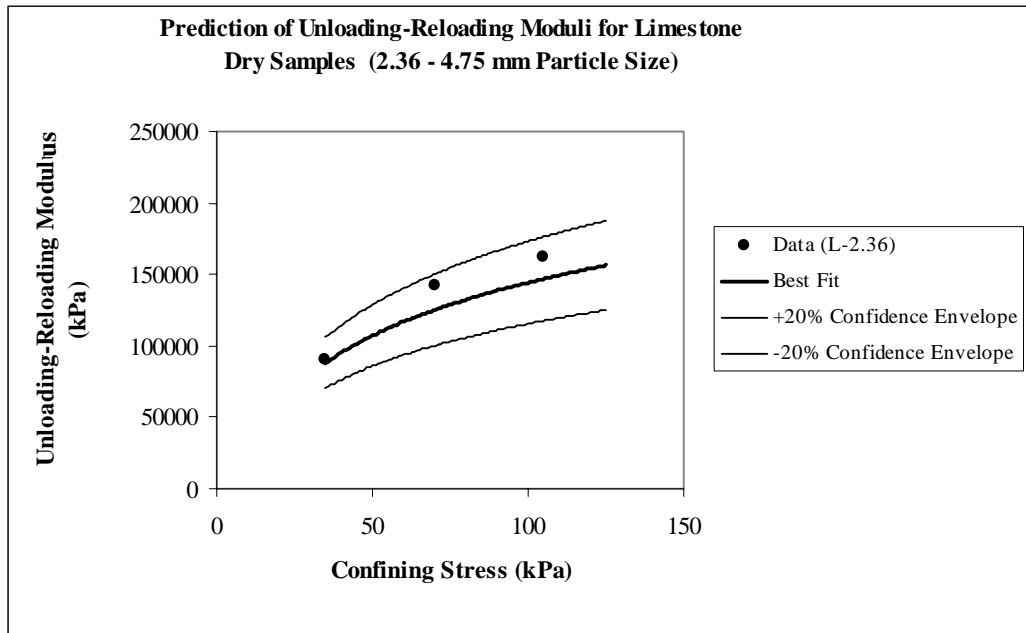


Figure 5.32 Prediction of unloading-reloading elastic moduli for L-2.36 series

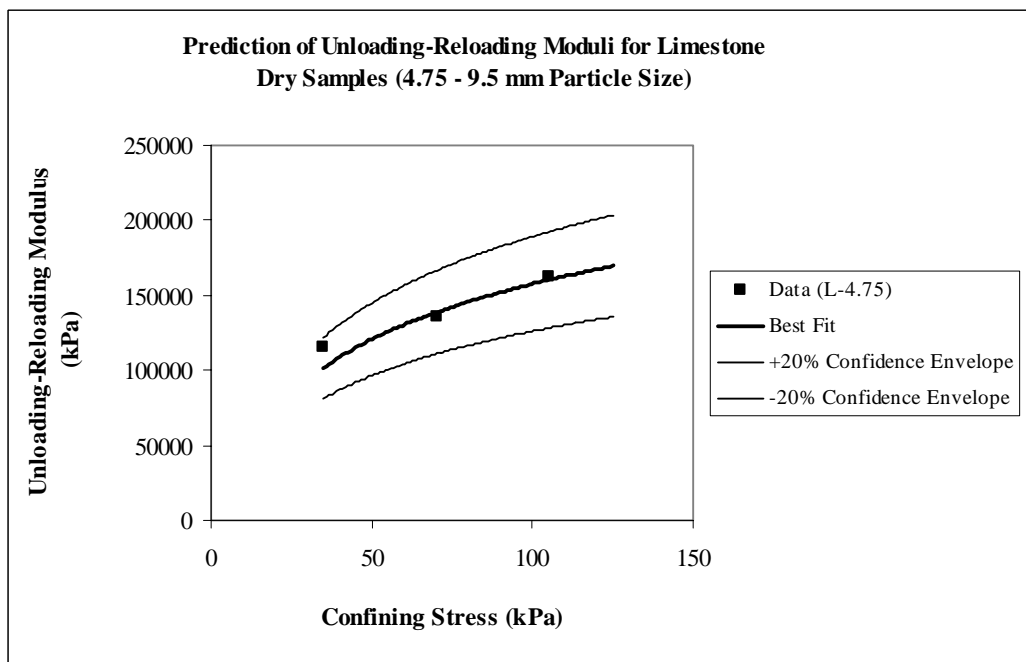


Figure 5.33 Prediction of unloading-reloading elastic moduli for L-4.75 series

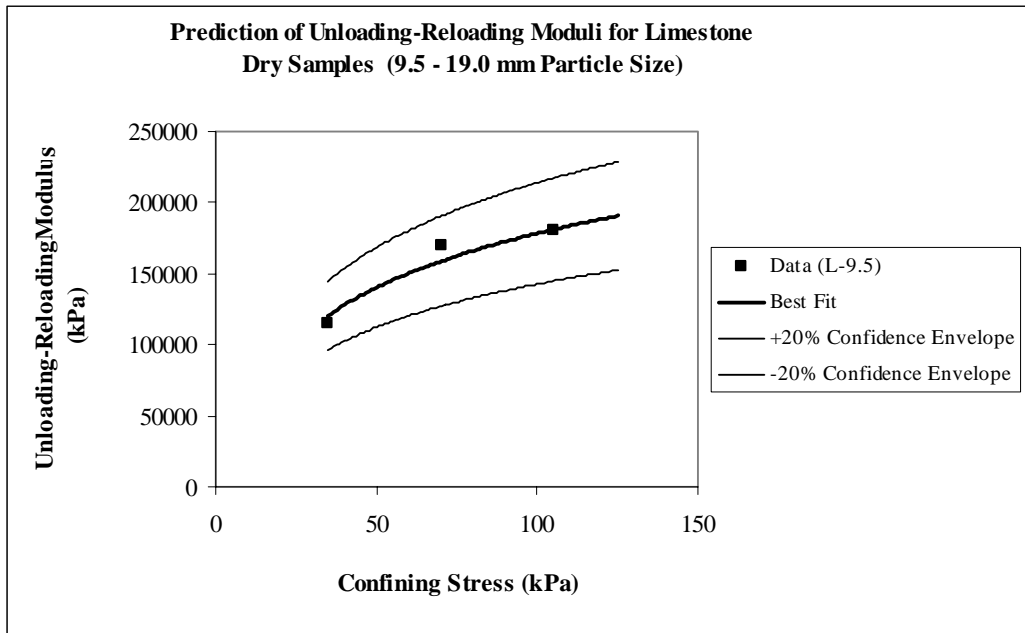


Figure 5.34 Prediction of unloading-reloading elastic moduli for L-9.5 series

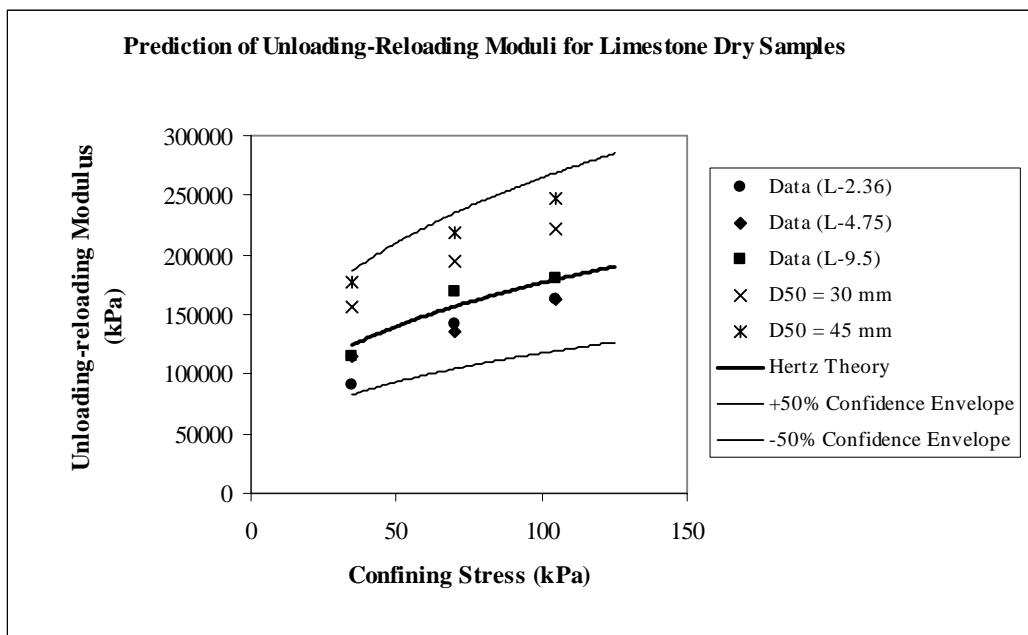


Figure 5.35 Prediction of unloading-reloading moduli by Hertz Contact Theory for limestone samples

It is worth noting that for the prototype mean size  $D_{50} = 30$  mm of crushed limestone, Table 5.17 compares the power law parameters for the unloading-reloading modulus predicted by Equation (5.24) with that predicted by Equation (2.17), which has been derived after an extensive experimental study by Knutson and Thompson (1978) for a confining stress ranging from 35 kPa to 140 kPa. Table 5.18 gives the values of unloading-reloading (resilient) modulus obtained from these equations at a confining stress of 35 kPa. It can be seen that the modulus predicted from Equation (5.24) is 23% less than that of predicted by Knutson and Thompson and is conservative (within about -20% confidence envelope); in the latter a repeated loading had been conducted at a cycle rate of approximately 1 Hz. Therefore, the difference can be due to both the rate and the number of load cycles applied (Lambe and Whitman, 1979). Consequently, the parallel gradation technique to predict the unloading-reloading modulus (resilient) of prototype size provides an adequate estimate for engineering purposes.

Table 5.17 Comparison of the power law parameters of unloading-reloading moduli for limestone  $D_{50} = 30$  mm

Source	Confining Stress Range (kPa)	Power Law Parameters	
		n	Log <sub>10</sub> K
Equation (2.17) (Knutson and Thompson, 1978)	35 to 140	0.470	4.58
Equation (5.25)	35 to 105	0.320	4.70
Hertz Contact Theory	-	0.333	-

Table 5.18 Comparison of unloading-reloading elastic modulus  
for limestone  $D_{50} = 30$  mm at  $\sigma_3 = 35$  kPa

Source	Unloading-Reloading Modulus ( $E_{ur}$ ), kPa	Difference w.r.t. Result of Equation (2.17), %
Equation (2.17) (Knutson and Thompson, 1978)	$2.02 \times 10^5$	0.0
Equation (5.18)	$1.56 \times 10^5$	-23.0
Hertz Contact Theory (with $\log_{10}K = 4.58$ )	$1.24 \times 10^5$	-38.4

In summary, the power law slope,  $n$ , tends to increase for the initial elastic modulus, whereas for the secant and unloading-reloading modulus it has a tendency to decrease as the mean particle size increases. The power law intercept,  $\log_{10}K$ , tends to increase for all three elastic moduli with increasing the mean particle size. When the trend of power law parameters as a function of the mean particle size is preserved, the parallel gradation technique as a predictor of the initial elastic moduli provides an adequate estimate within  $\pm 20\%$  confidence envelope. For the secant as well as the unloading-reloading elastic moduli also show increasing stiffness with increasing mean particle size, and the parallel gradation technique provides an adequate estimate within  $\pm 20\%$  confidence envelope as the corresponding trends of power law parameters with the change in mean particle are preserved.

It is also worth noting that the elastic moduli values may be predicted within an adequate estimate for engineering purposes by using the power law parameters determined for L-9.5 ( $D_{50} = 12.7$  mm), the coarsest gradation tested for limestone. Figure 5.36 to Figure 5.38 show the experimental data, predicted data for prototype sizes, and the best-fit to the data for L-9.5 with the associated confidence envelopes for the initial elastic modulus, secant elastic modulus, and the unloading-reloading

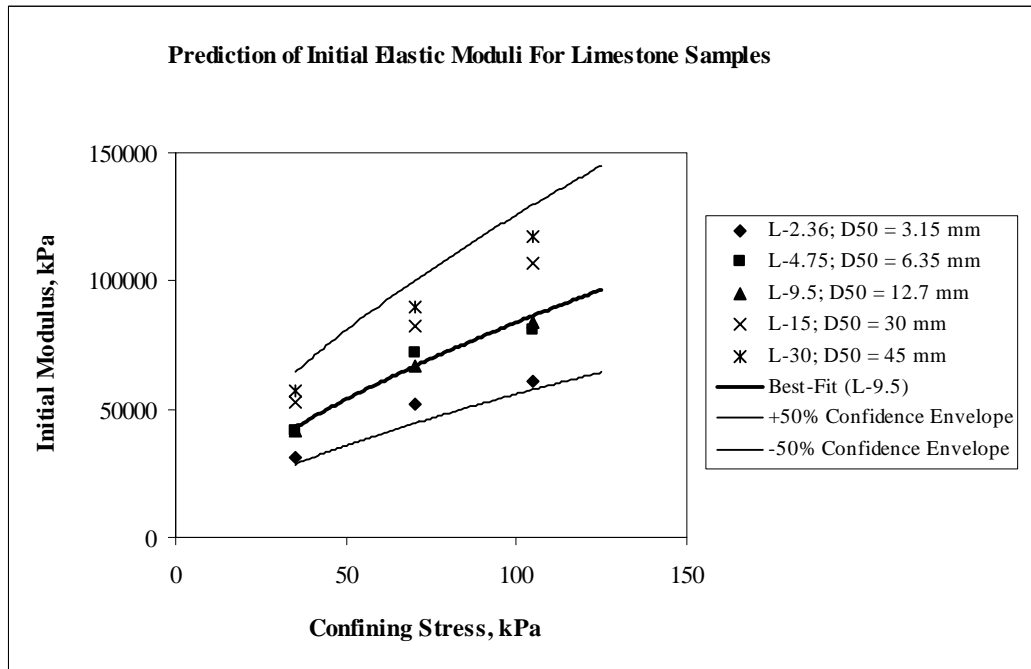


Figure 5.36 Prediction of initial modulus for limestone samples with L-9.5 best-fit

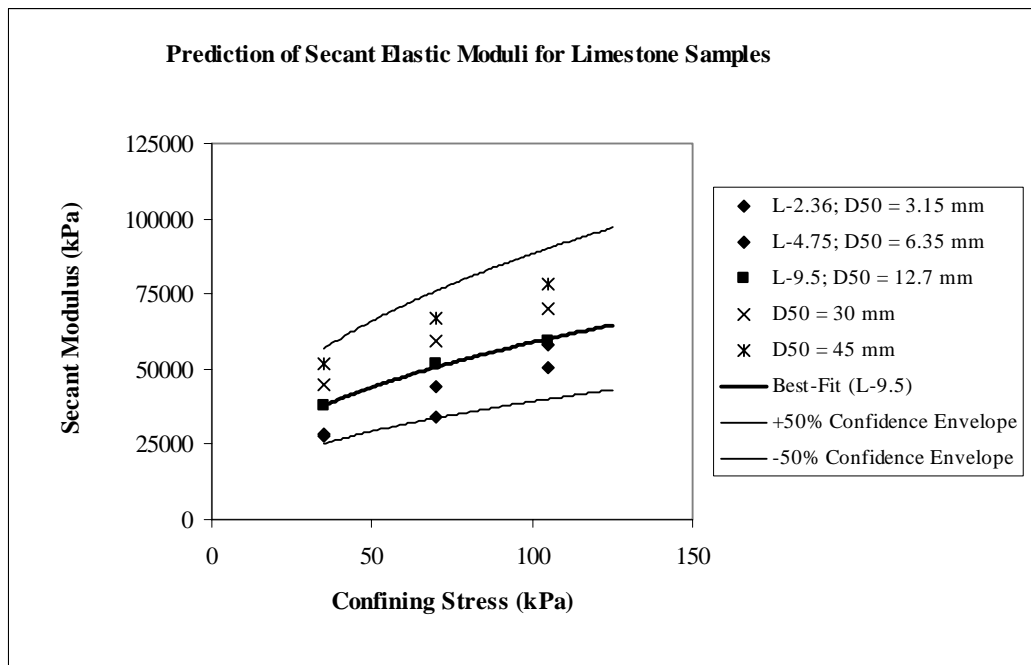


Figure 5.37 Prediction of secant modulus for limestone samples with L-9.5 best-fit

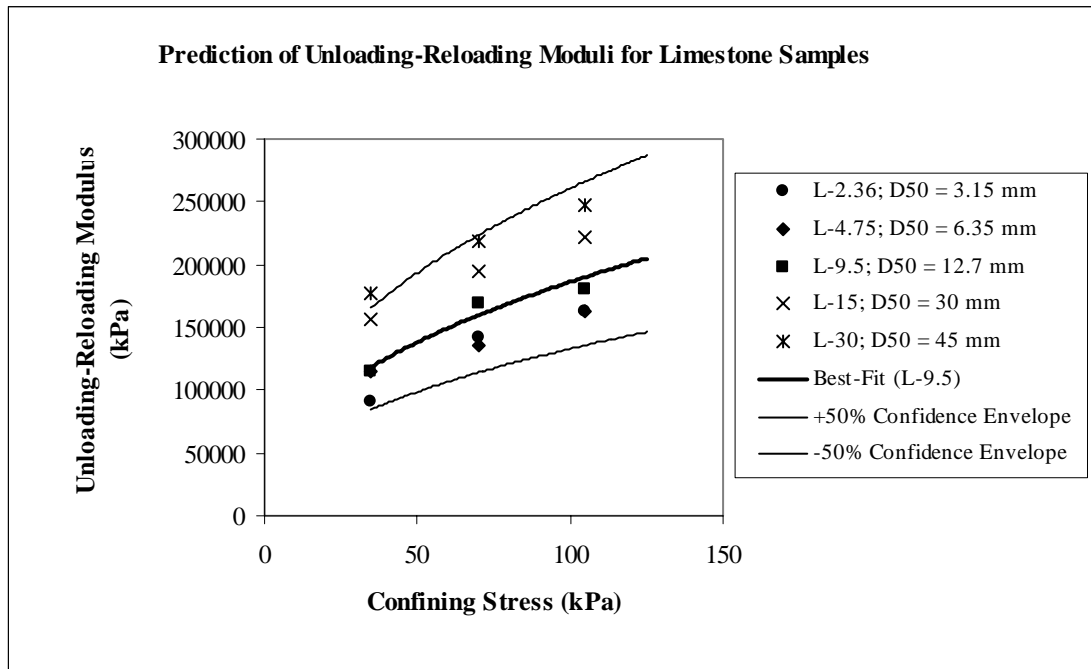


Figure 5.38 Prediction of unloading-reloading elastic modulus for limestone samples with L-9.5 best-fit

elastic modulus, respectively. All elastic modulus values including that of predicted for prototype sizes were obtained within  $\pm 50\%$  confidence envelope.

The suggestion by Vermeer and Schanz ( $n = 0.5$ ) can be an adequate predictor of the secant moduli as long as coupled with a rationally determined value for  $\log_{10}K$ .

Hertz Contact Theory ( $n = 0.333$ ) can be an adequate predictor of the unloading-reloading moduli if a rationally determined value for  $\log_{10}K$  can be used.

#### 5.9.4 Elastic Moduli Trends for Scaled-down Basalt Materials

The elastic moduli computed from three experimental series, as with limestone experimental series, will be discussed in this section. The series are B-

2.36, B-4.75, and B-9.5. Table 5.19 shows the calculated values of the initial elastic moduli,  $E_i$ , the secant elastic moduli,  $E_{50}$ , and the unloading-reloading moduli,  $E_{ur}$ , for all three series.

Table 5.19 Elastic moduli determined for B-2.36, B-4.75 and B-9.5 series

Gradation	Confining Stress ( $\sigma_3$ ), kPa	Initial Modulus ( $E_i$ ), kPa	Secant Modulus ( $E_{50}$ ), kPa	Unloading-Reloading Modulus ( $E_{ur}$ ), kPa
B-2.36	35	$4.58 \times 10^4$	$2.71 \times 10^4$	$1.04 \times 10^5$
	70	$5.76 \times 10^4$	$4.24 \times 10^4$	$1.20 \times 10^5$
	105	$7.32 \times 10^4$	$4.57 \times 10^4$	$1.39 \times 10^5$
B-4.75	35	$4.72 \times 10^4$	$2.44 \times 10^4$	$1.06 \times 10^5$
	70	$5.49 \times 10^4$	$3.71 \times 10^4$	$1.28 \times 10^5$
	105	$7.33 \times 10^4$	$4.25 \times 10^4$	$1.45 \times 10^5$
B-9.5	35	$5.76 \times 10^4$	$5.11 \times 10^4$	$1.10 \times 10^5$
	70	$7.59 \times 10^4$	$5.92 \times 10^4$	$1.62 \times 10^5$
	105	$9.42 \times 10^4$	$6.81 \times 10^4$	$1.64 \times 10^5$

Using the analysis technique suggested in 5.9.2, and setting  $p_r = 1$  kPa, the data from Table 5.19 can be represented by a best-fit power equation of the form of Equation 5.19.

For series B-2.36, the best fit power law equations are:

$$E_i = 10247(\sigma_3)^{0.417} \quad ; \quad R^2 = 0.973 \quad (5.26a)$$

$$E_{50} = 4796(\sigma_3)^{0.495} \quad ; \quad R^2 = 0.943 \quad (5.26b)$$

$$E_{ur} = 41191(\sigma_3)^{0.257} \quad ; \quad R^2 = 0.971 \quad (5.26c)$$

for series B-4.75, the best fit power law equations are:

$$E_i = 11790(\sigma_3)^{0.381} \quad ; \quad R^2 = 0.898 \quad (5.27a)$$

$$E_{50} = 3939(\sigma_3)^{0.517} \quad ; \quad R^2 = 0.982 \quad (5.27b)$$

$$E_{ur} = 39138(\sigma_3)^{0.286} \quad ; \quad R^2 = 0.998 \quad (5.27c)$$

and for series B-9.5, the best fit power law equations are:

$$E_i = 11833(\sigma_3)^{0.443} \quad ; \quad R^2 = 0.994 \quad (5.28a)$$

$$E_{50} = 20441(\sigma_3)^{0.256} \quad ; \quad R^2 = 0.982 \quad (5.28b)$$

$$E_{ur} = 29000(\sigma_3)^{0.384} \quad ; \quad R^2 = 0.883 \quad (5.28c)$$

From Figure 5.39 to 5.41 shows the data and the trend of the elastic moduli of Equation 5.26 through 5.28 for series B-2.36, B-4.75 and B-9.5, respectively and clearly illustrate also that the power law equation accurately predicts the trend of the three elastic moduli for all of the experimental series.

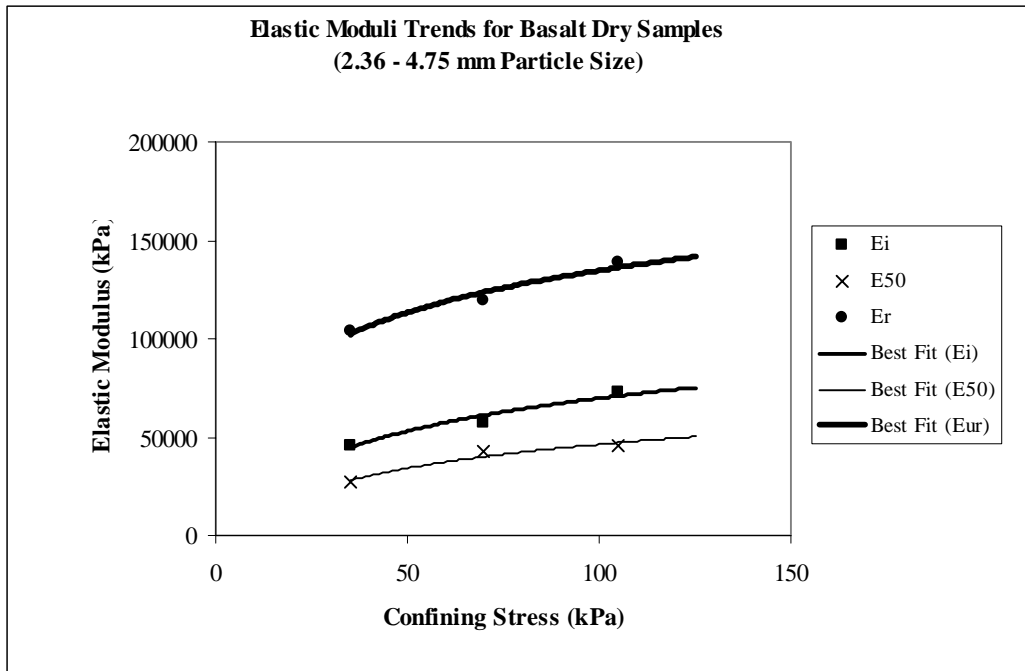


Figure 5.39 Elastic moduli trends for series B-2.36

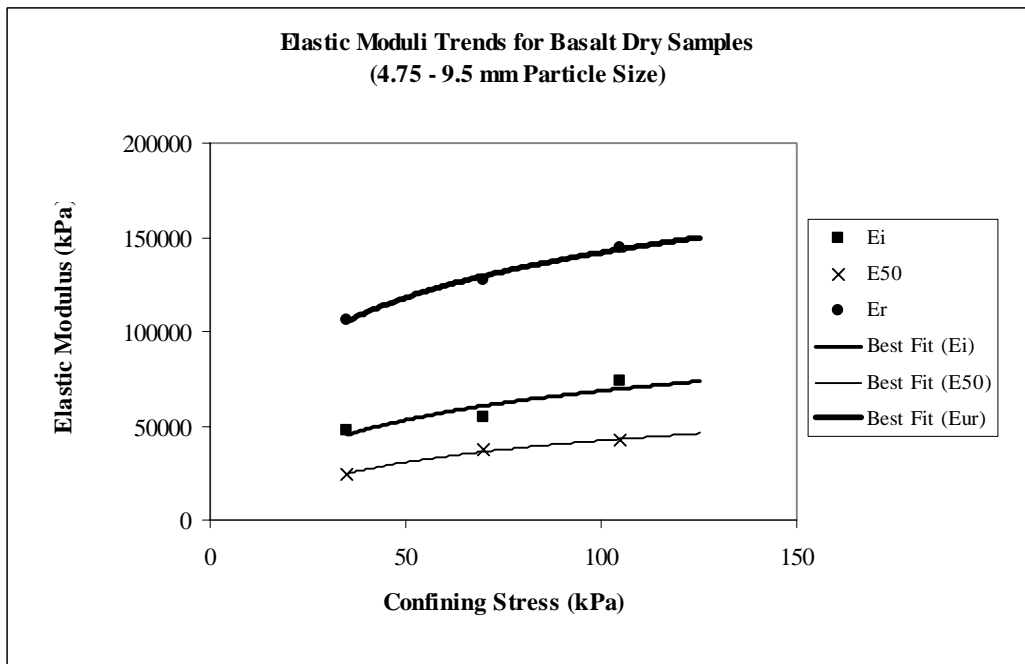


Figure 5.40 Elastic moduli trends for series B-4.75

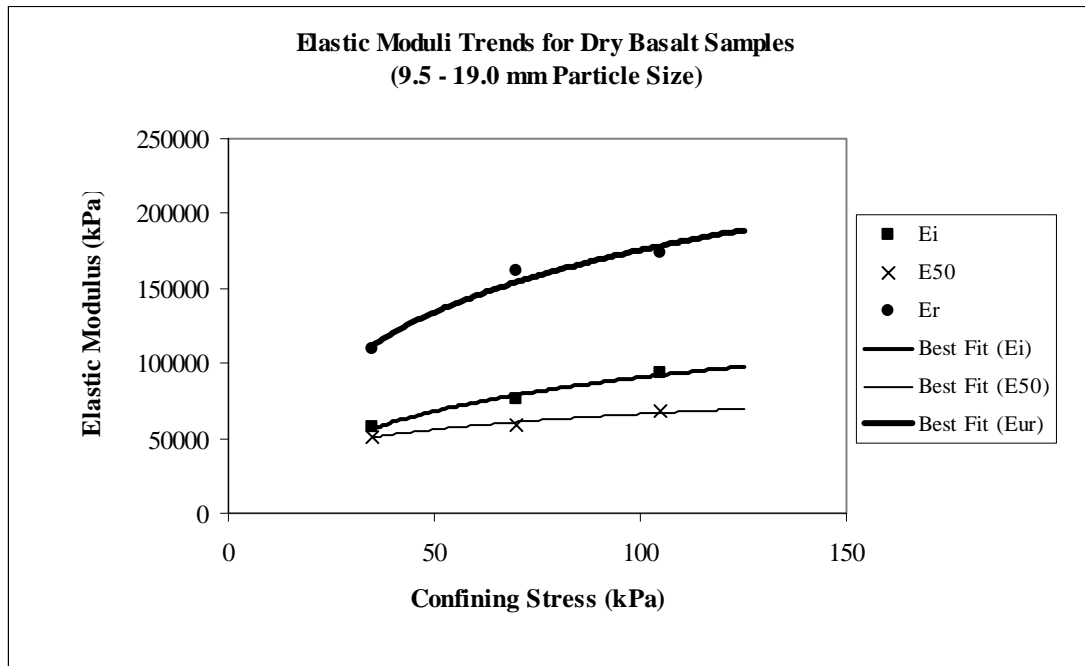


Figure 5.41 Elastic moduli trends for series B-9.5

Table 5.20 lists the calculated values for  $n$  and  $\log_{10}K$  for the initial moduli for all of the experimental series using scaled-down basalt samples. Figure 5.42 shows the best fit power law curves for each series listed in Table 5.20. There is a general trend of increasing initial modulus with increasing mean particle size, although the modulus values for the finer particle sizes seem to duplicate each other.

Table 5.20 Power law parameters for the initial elastic moduli for scaled-down basalt

Gradation	Power Law Slope, $n$	Power Law Intercept, $\log_{10}K$	Coefficient of Determination, $R^2$
B-2.36	0.417	4.01	0.973
B-4.75	0.381	4.07	0.898
B-9.5	0.443	4.07	0.994

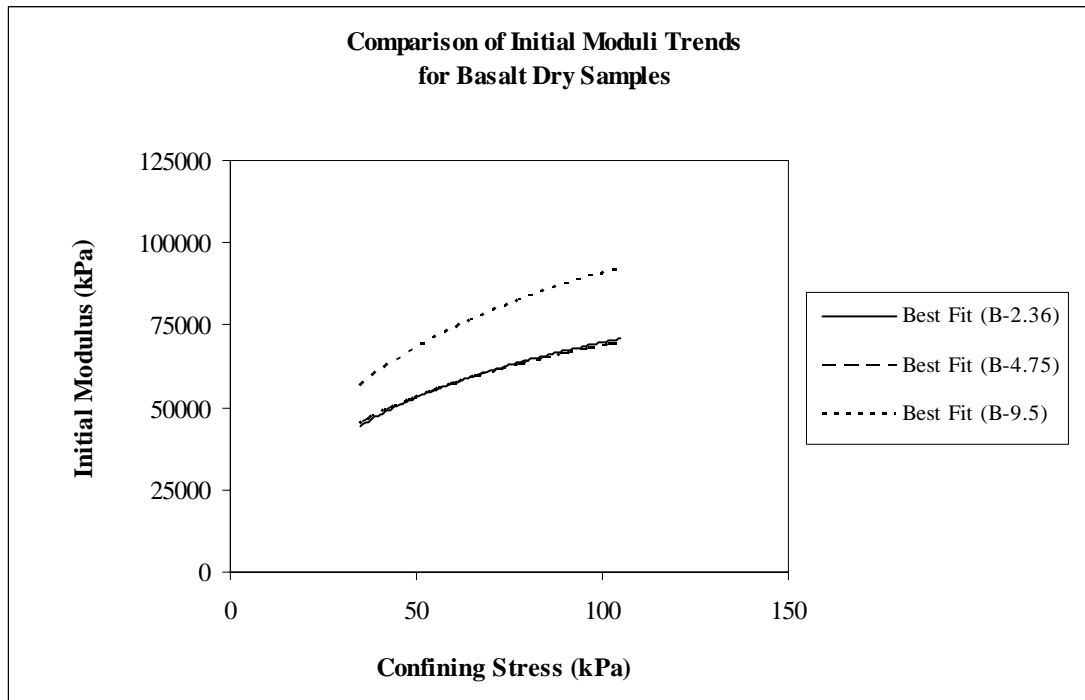


Figure 5.42 Comparison of trends of initial elastic moduli for all basalt series

The question again is that how the initial elastic moduli may vary with the change in mean particle size for basalt. Figure 5.43 shows the variation of the power law parameters  $n$  and  $\log_{10}K$  of the initial elastic moduli with the mean particle size of the scaled-down basalt samples. The tendency of power law parameters for the initial elastic modulus is fitted with a power line for  $n$  and with a linear line for  $\log_{10}K$  to the data. The corresponding equations for  $n$  and  $\log_{10}K$  of the initial modulus in Figure 5.43 are given in Equation (5.29a) and Equation (5.29b). The power law slope,  $n$ , increases as the mean particle size increases; and the power law intercept,  $\log_{10}K$ , increases with increasing mean particle size.

$$n = 0.381(D_{50})^{0.0434} \quad ; \quad R^2 = 0.163 \quad (5.29a)$$

$$\log_{10} K = 0.0057(D_{50}) + 4.0099 \quad ; \quad R^2 = 0.595 \quad (5.29b)$$

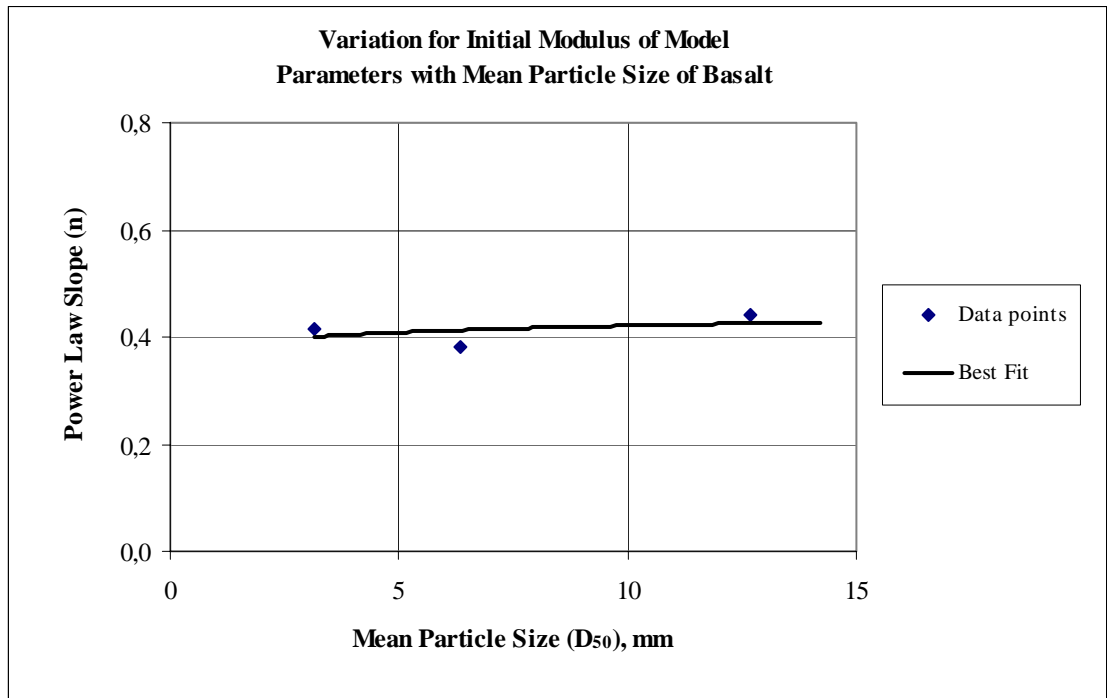


Figure 5.43 Variation of power law parameters of initial elastic moduli with the mean particle size for the scaled-down basalt samples

Figure 5.44 through Figure 5.46, respectively for B-2.36, B-4.75, and B-9.5 illustrate that the power law with the parameters given in Equation (5.29) for the initial modulus,  $E_i$ , predicts the values within a  $\pm 20\%$  confidence envelope. Consequently, the parallel gradation technique for these series provides an adequate prediction of the initial elastic modulus.

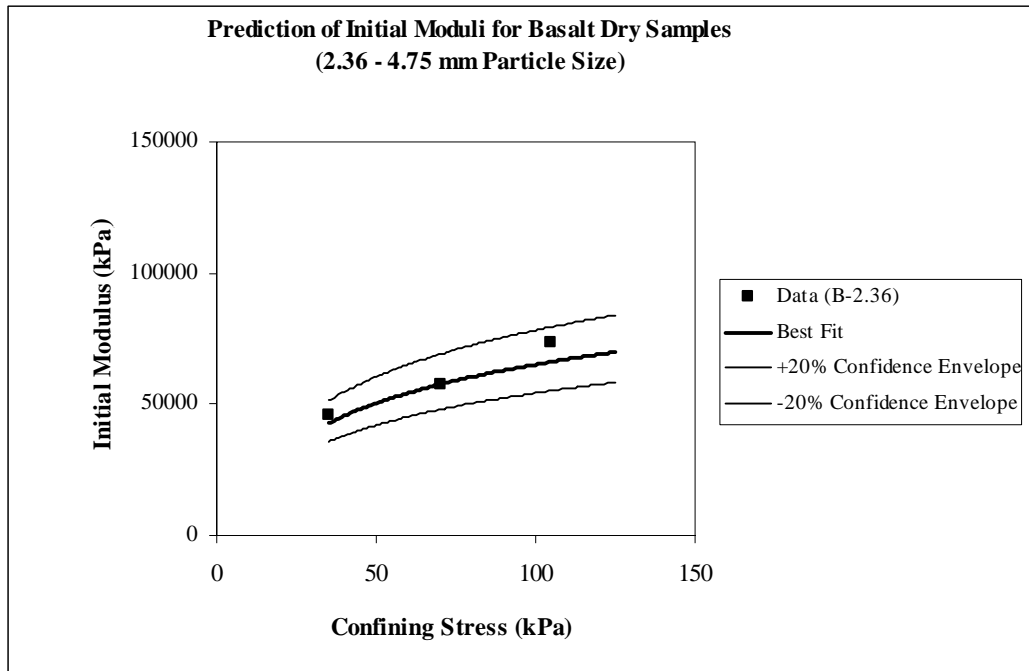


Figure 5.44 Prediction of Initial Elastic moduli for B-2.36 series

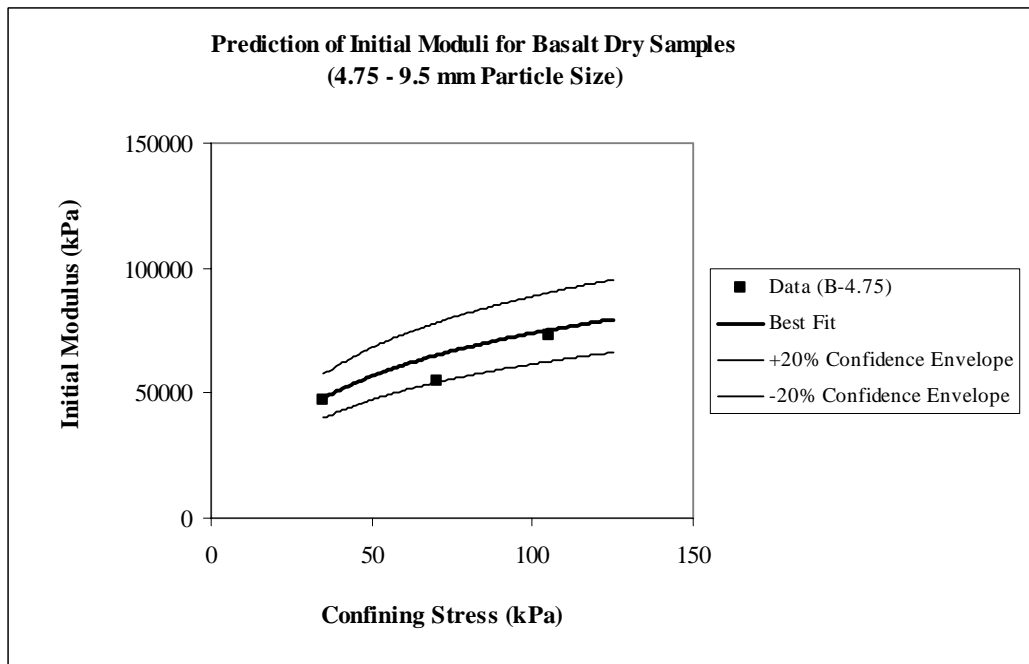


Figure 5.45 Prediction of Initial Elastic moduli for B-4.75 series

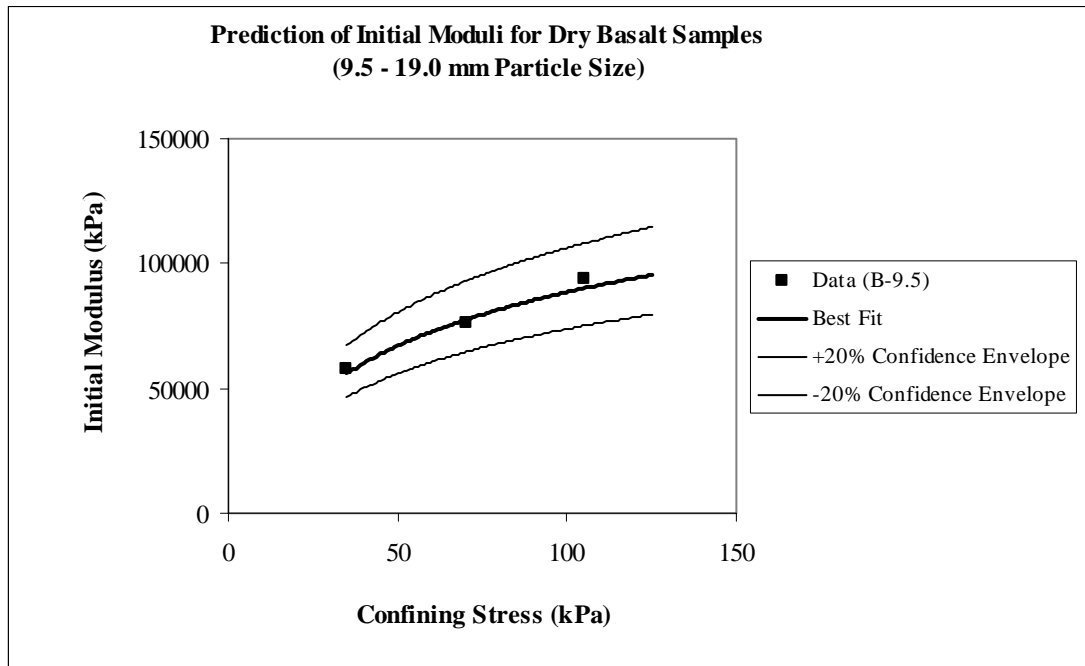


Figure 5.46 Prediction of initial elastic moduli for B-9.5 series

Table 5.21 lists the calculated values for  $n$  and  $\log_{10}K$  of the power law parameters of the secant moduli for all of the experimental series using scaled-down basalt samples. Figure 5.47 illustrates the best fit power law curves for each series listed in Table 5.21. The secant elastic moduli for scaled-down basalt show a trend of increasing stiffness with increasing mean particle size.

Table 5.21 Power law parameters for the secant elastic moduli for scaled-down basalt

Gradation	Power Law Slope, $n$	Power Law Intercept, $\log_{10}K$	Coefficient of Determination, $R^2$
B-2.36	0.495	3.68	0.943
B-4.75	0.517	3.60	0.982
B-9.5	0.256	4.31	0.982

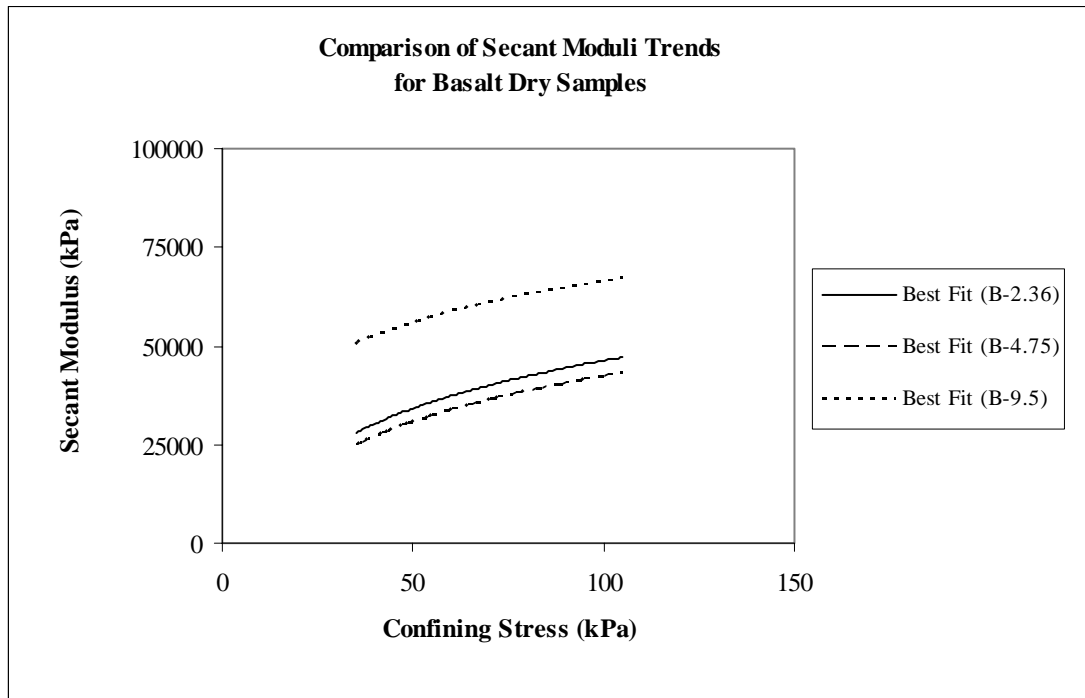


Figure 5.47 Comparison of trends of secant elastic moduli for all basalt series

As with the initial elastic moduli, the question is that how the secant elastic moduli may vary with the change in mean particle size for basalt. Figure 5.48 shows the variation of the power law parameters  $n$  and  $\log_{10}K$  of the secant elastic moduli with the mean particle size of crushed basalt. The corresponding equations for  $n$  and  $\log_{10}K$  of the secant moduli in Figure 5.48 are given in Equation (5.30a) and Equation (5.30b). The power law slope decreases as the mean particle size increases; whereas the power law intercept increases with increasing mean particle size.

$$n = 0.9647(D_{50})^{-0.473} \quad ; \quad R^2 = 0.697 \quad (5.30a)$$

$$\log_{10} K = 0.4505 \ln(D_{50}) + 3.0307 \quad ; \quad R^2 = 0.647 \quad (5.30b)$$

Figure 5.49 through Figure 5.51, respectively, for B-2.36, B-4.75, and B-9.5 illustrate that the power law with the parameters given in Equation (5.30) for the secant elastic modulus,  $E_{50}$ , predicts the value within a  $\pm 25\%$  confidence envelope. Consequently, the parallel gradation technique for these series provides again an adequate prediction of the secant elastic modulus.

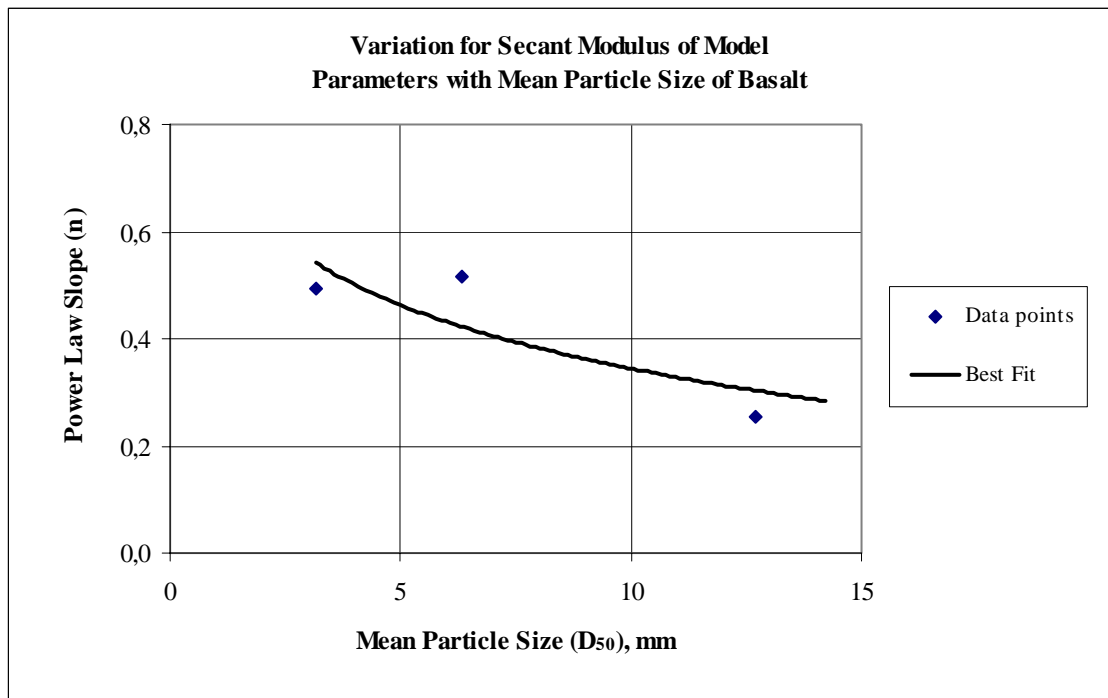


Figure 5.48 Variation of power law parameters of secant elastic moduli with the mean particle size for the scaled-down basalt samples

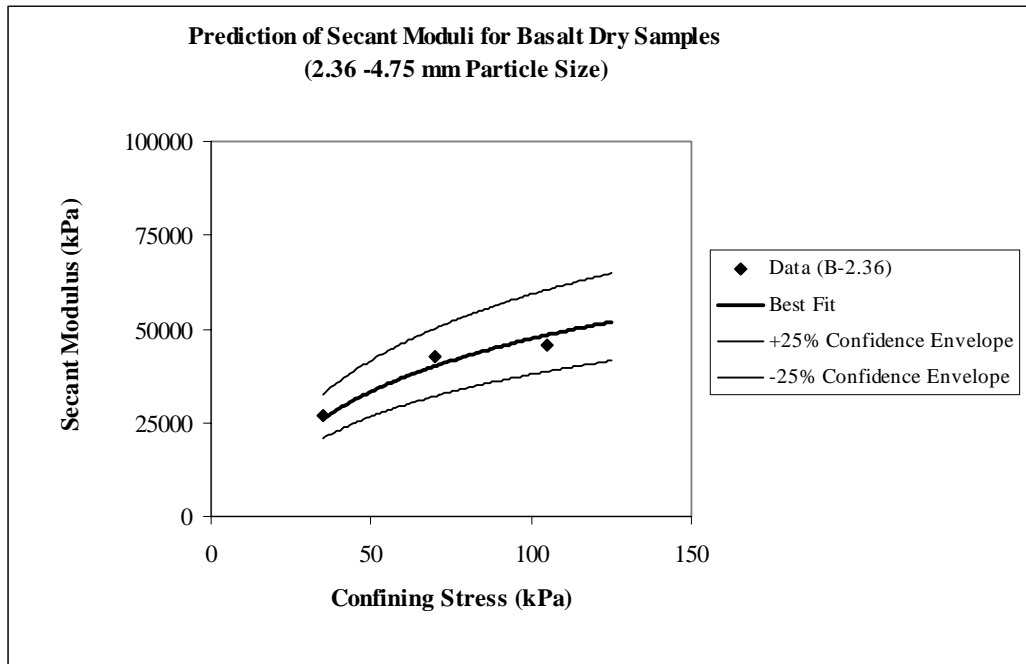


Figure 5.49 Prediction of secant elastic moduli for B-2.36 series

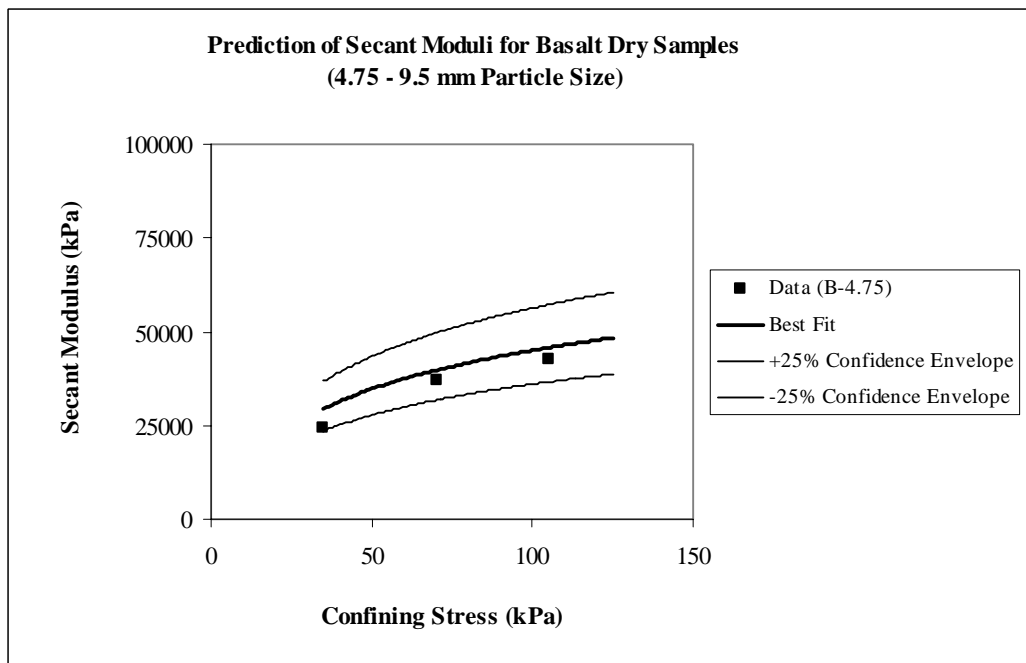


Figure 5.50 Prediction of secant elastic moduli for B-4.75 series

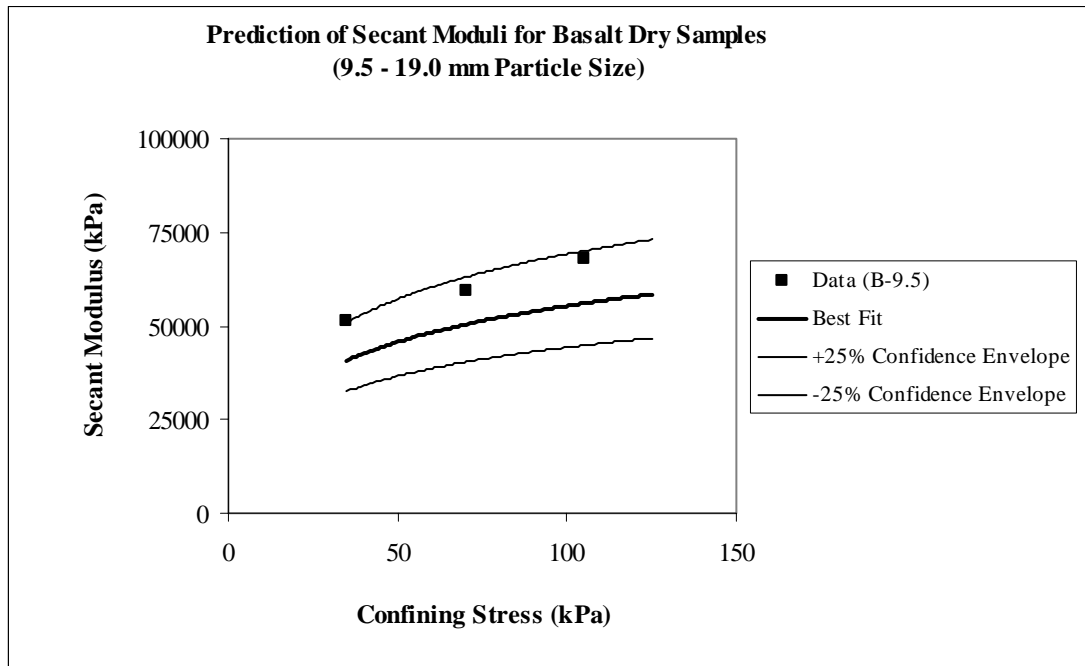


Figure 5.51 Prediction of secant elastic moduli for B-9.5 series

Table 5.22 lists the power law parameters for the unloading-reloading elastic moduli for all of the experimental series using scaled-down basalt samples. Figure 5.52 illustrates the best fit power law curves for each series listed in Table 5.22. The unloading-reloading elastic moduli for basalt show that a trend of increasing stiffness is observed with increasing mean particle size.

Table 5.22 Power law parameters for the unloading-reloading elastic moduli for scaled-down basalt

Gradation	Power Law Slope, n	Power Law Intercept, $\log_{10}K$	Coefficient of Determination, $R^2$
B-2.36	0.257	4.61	0.971
B-4.75	0.286	4.59	0.998
B-9.5	0.384	4.46	0.883

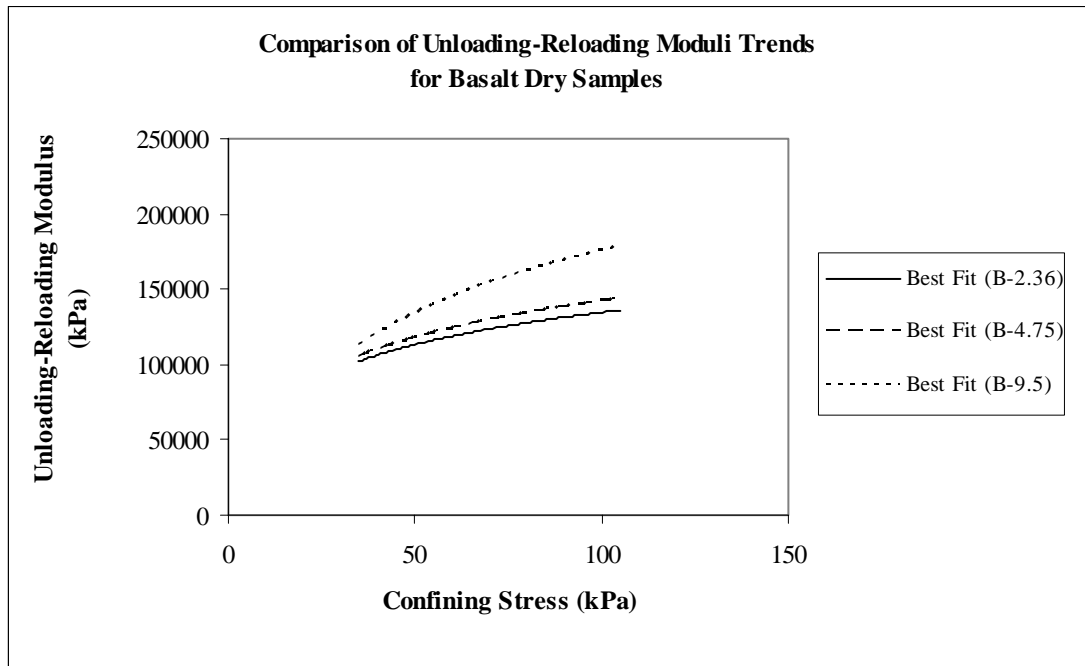


Figure 5.52 Comparison of trends of unloading-reloading elastic moduli for all basalt series

Figure 5.53 shows the variation of the power law parameters of the unloading-reloading elastic moduli with the mean particle size for crushed basalt. Equation (5.31a) and Equation (5.31b) are derived using a power law fit to the data given in Table 5.15. The power law slope,  $n$ , increases as the mean particle size increases; whereas the power law intercept,  $\log_{10}K$ , unlike that of limestone, decreases with increasing mean particle size.

$$n = 0.1794(D_{50})^{0.2869} \quad ; \quad R^2 = 0.930 \quad (5.31a)$$

$$\log_{10} K = 4.763(D_{50})^{-0.0241} \quad ; \quad R^2 = 0.853 \quad (5.31b)$$

Figure 5.54 through Figure 5.56, respectively for B-2.36, B-4.75, and B-9.5 show that the power law with the parameters given in Equation (5.31) for the unloading-reloading elastic modulus,  $E_{ur}$ , predicts the values within a  $\pm 20\%$  confidence envelope. Consequently, the parallel gradation technique for these series provides again an adequate prediction of the unloading-reloading elastic modulus.

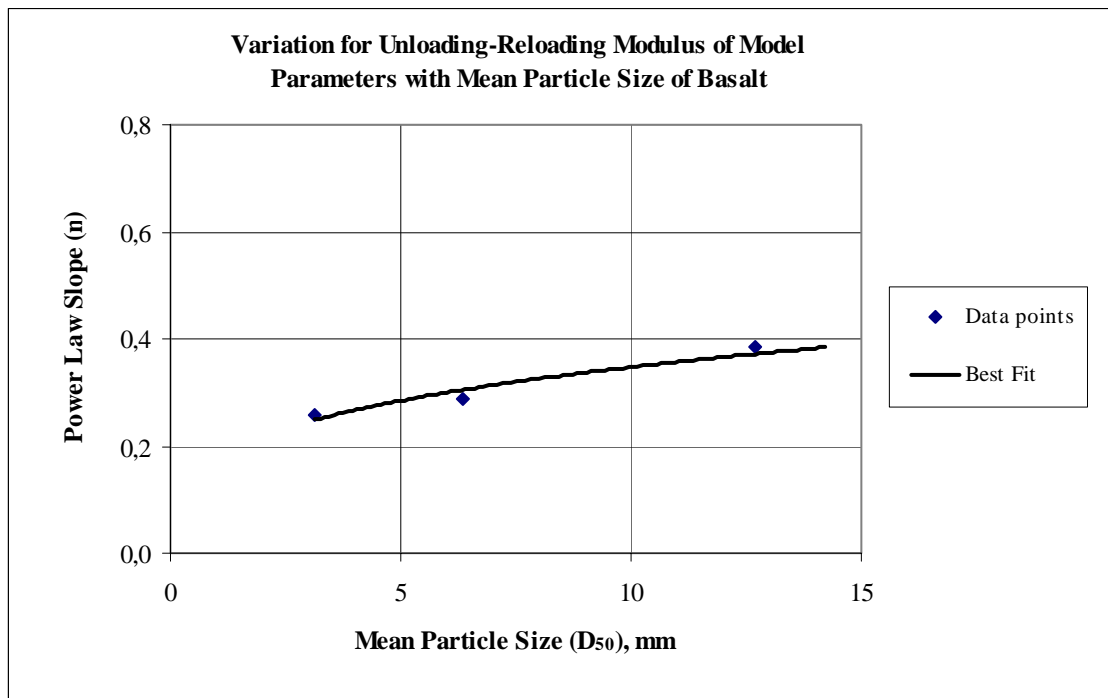


Figure 5.53 Variation of power law parameters of unloading-reloading elastic moduli with the mean particle size of scaled-down basalt samples

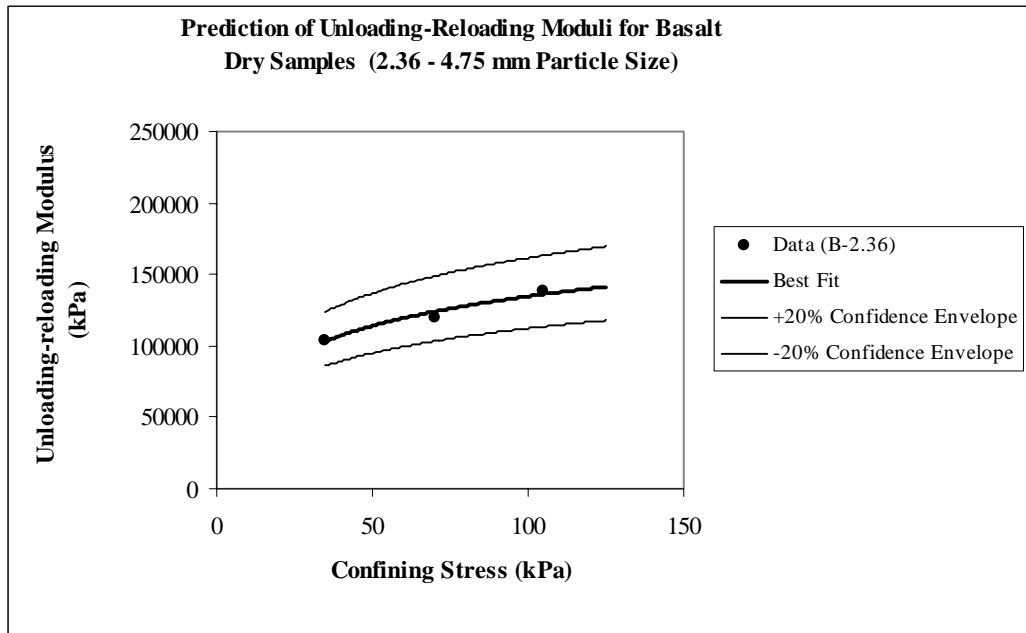


Figure 5.54 Prediction of unloading-reloading elastic moduli for B-2.36 series

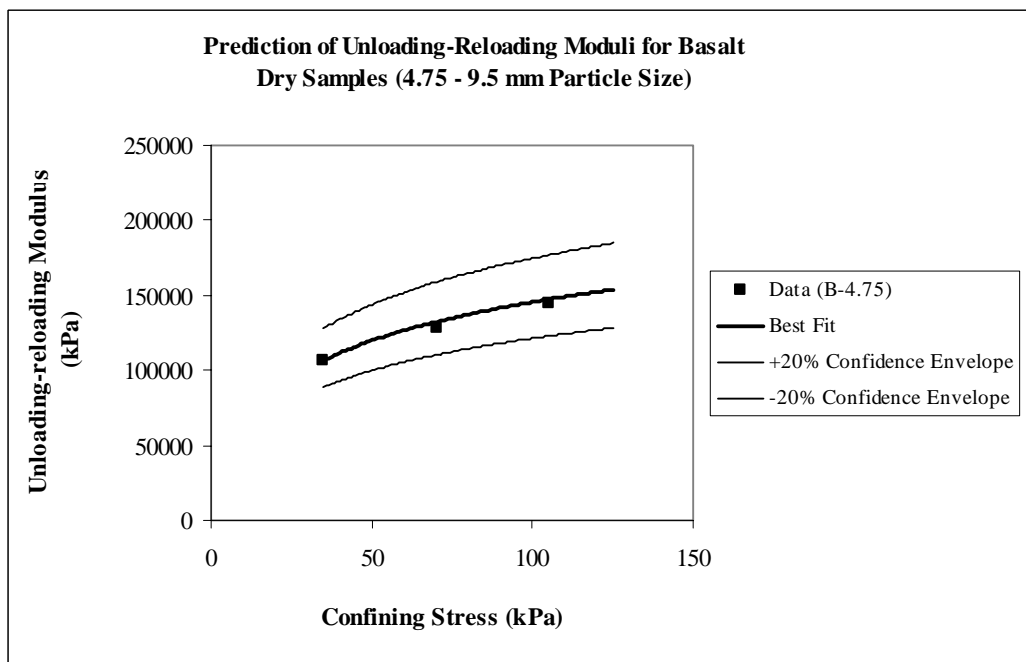


Figure 5.55 Prediction of unloading-reloading elastic moduli for B-4.75 series

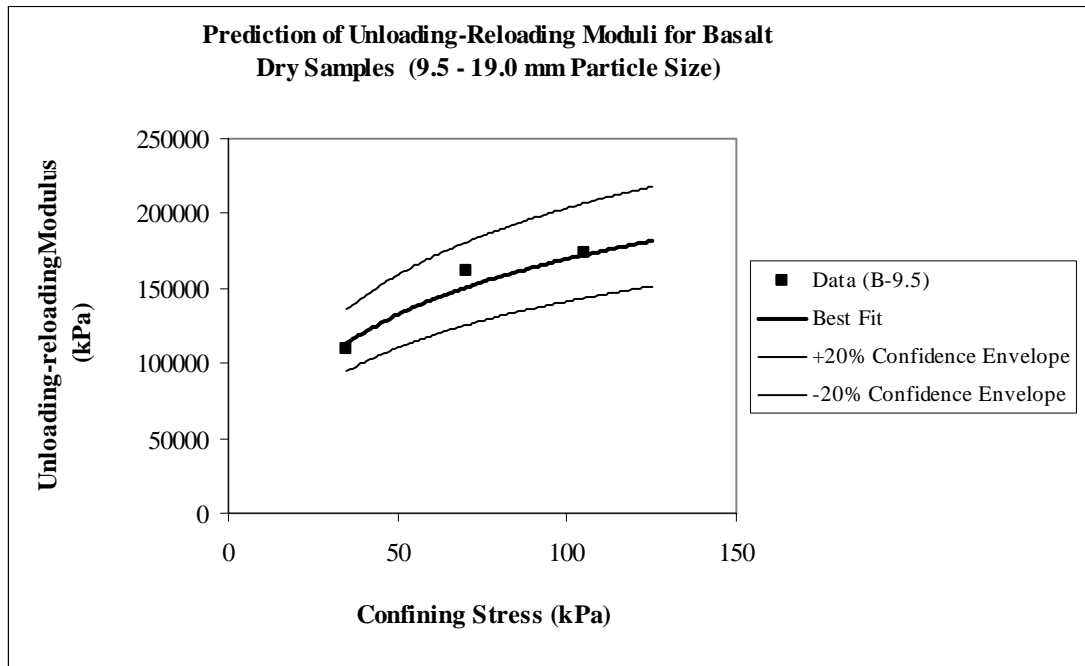


Figure 5.56 Prediction of unloading-reloading elastic moduli for B-9.5 series

For the prototype mean size  $D_{50} = 30$  mm of crushed basalt, Table 5.23 compares the power law parameters for the unloading-reloading modulus predicted by Equation (5.31) with that predicted by Equation (2.17) by Knutson and Thompson (1978). Table 5.24 gives the values of unloading-reloading (resilient) modulus obtained from these equations at a confining stress of 35 kPa. It can be seen that the modulus predicted from Equation (5.31) is 56% less than that of predicted by Knutson and Thompson and as can be seen it is conservative (within about -50% confidence envelope). As stated for the prototype limestone sample, the difference can be due to both the rate and the number of load cycles applied. Consequently, the parallel gradation technique to predict the prototype size provides an adequate estimate for engineering purposes.

Table 5.23 Comparison of the power law parameters of unloading-reloading moduli for basalt prototype mean size  $D_{50} = 30$  mm

Source	Confining Stress Range (kPa)	Power Law Parameters	
		n	Log <sub>10</sub> K
Equation (2.17) (Knutson and Thompson, 1978)	35 to 140	0.650	4.47
Equation (5.31)	35 to 105	0.617	4.18

Table 5.24 Comparison of unloading-reloading modulus for basalt  $D_{50}=30$  mm at  $\sigma_3 = 35$  kPa

Source	Unloading-Reloading Modulus ( $E_{ur}$ ), kPa	Difference w.r.t. Result of Equation (2.17), %
Equation (2.17) (Knutson and Thompson, 1978)	$3.00 \times 10^5$	0.0
Equation (5.18)	$1.33 \times 10^5$	-56.0

In summary, the power law slope,  $n$ , tends to increase for the initial and the unloading-reloading elastic modulus, whereas for the secant elastic modulus it tends to decrease as the mean particle size increases. The power law intercept,  $\log_{10}K$ , tends to increase for the initial and secant elastic moduli, contrary to that of unloading-reloading for which it tends to decrease as the mean particle size increases. When the trend of power law parameters as a function of the mean particle size is preserved, the parallel gradation technique as a predictor of the initial elastic moduli provides an adequate estimate within  $\pm 20\%$  confidence envelope. For the secant as well as the unloading-reloading elastic moduli also show increasing

stiffness with increasing mean particle size, and the parallel gradation technique provides an adequate estimate within  $\pm 25\%$  confidence envelope for the secant moduli and within  $\pm 20\%$  confidence envelope for the unloading-reloading moduli.

It is also worth noting that the elastic moduli values may be predicted within an adequate estimate for the engineering purposes by using the power law parameters determined for B-9.5 ( $D_{50} = 12.7$  mm), the coarsest gradation tested for basalt. Figure 5.57 to Figure 5.59 show the experimental data, predicted data for prototype sizes, and the best-fit to the data for B-9.5 with the associated confidence envelopes for the initial elastic modulus, secant elastic modulus, and the unloading-reloading elastic modulus respectively. The initial and the unloading-reloading elastic modulus values with the predicted data for prototype sizes were within  $\pm 50\%$  confidence envelope, whereas the best-fit to B-9.5 data predicted the secant elastic moduli with the predicted data for prototype sizes within  $\pm 100\%$  confidence envelope.

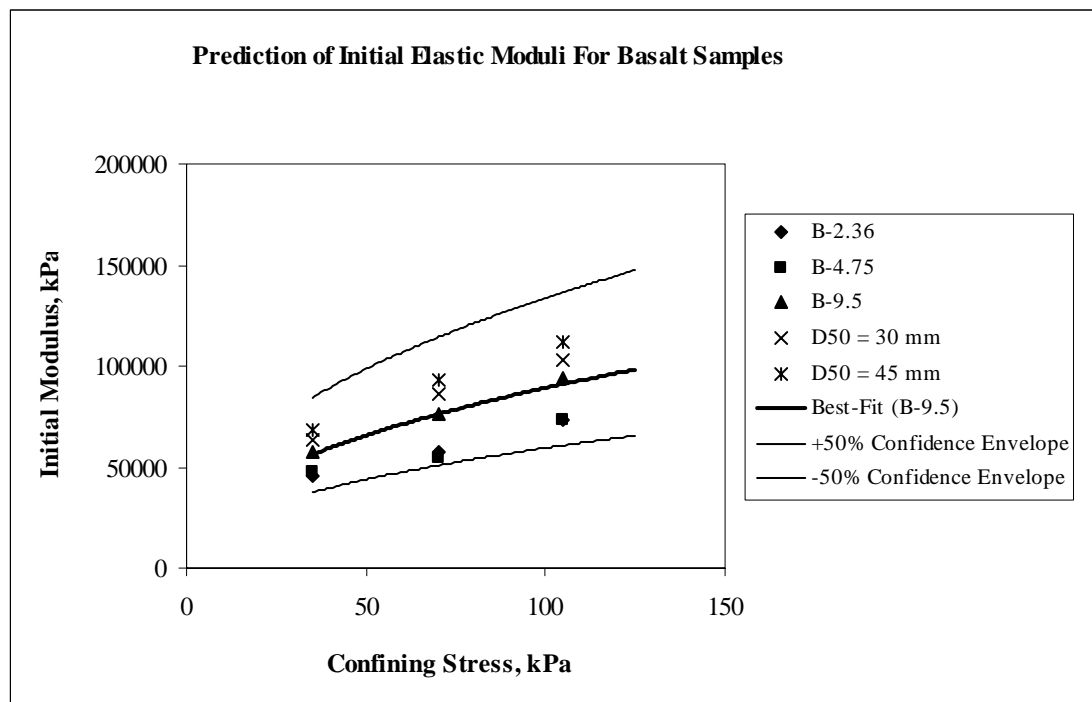


Figure 5.57 Prediction of initial elastic modulus for basalt samples with B-9.5 best-fit

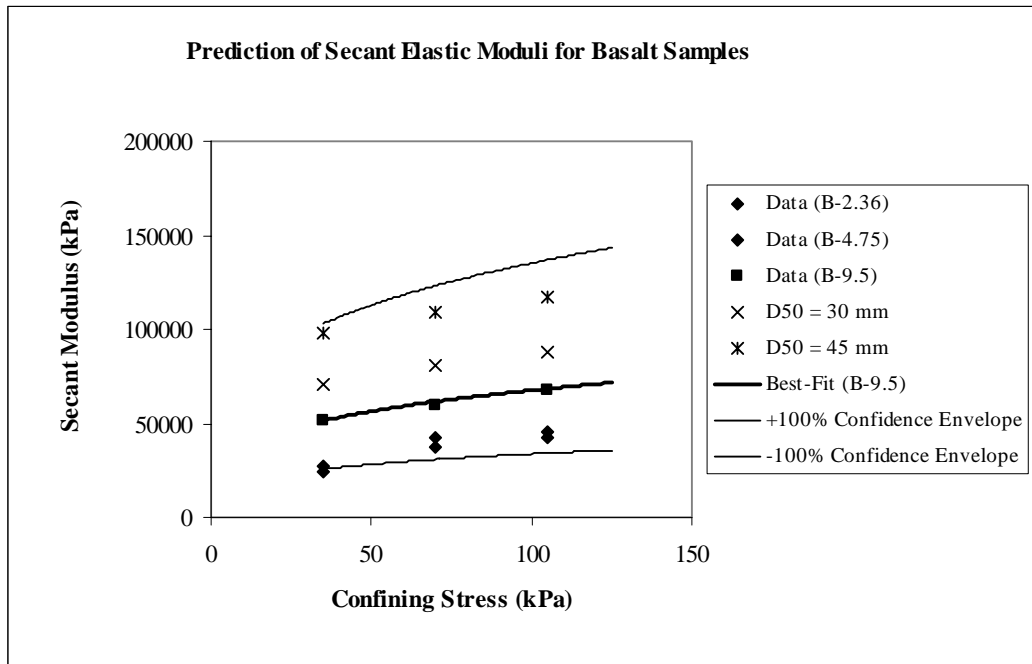


Figure 5.58 Prediction of secant elastic modulus for basalt samples with B-9.5 best-fit

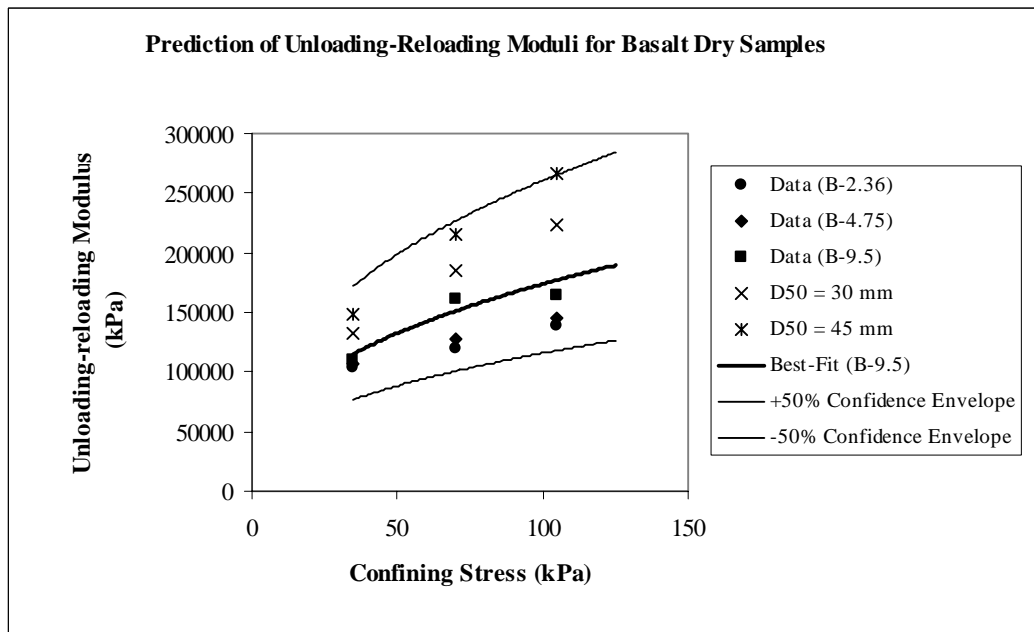


Figure 5.59 Prediction of unloading-reloading elastic modulus for basalt samples with B-9.5 best-fit

### 5.9.5 Elastic Moduli Trends for Scaled-Down Steel-Slag Materials

The elastic moduli obtained from three experimental series for scaled-down steel-slag materials were discussed in this section. The series are S-4.75, S-6.35, and S-9.5. Table 5.25 shows the calculated values of the initial moduli  $E_i$ , the secant moduli  $E_{50}$ , and the unloading-reloading moduli  $E_{ur}$  for all three series.

Table 5.25 Elastic moduli determined for S-4.75, S-6.35, and S-9.5 series

Gradation	Confining Stress ( $\sigma_3$ ), kPa	Initial Modulus ( $E_i$ ), kPa	Secant Modulus ( $E_{50}$ ), kPa	Unloading-Reloading Modulus ( $E_{ur}$ ), kPa
S-4.75	35	$4.19 \times 10^4$	$2.03 \times 10^4$	$9.80 \times 10^4$
	70	$7.20 \times 10^4$	$3.10 \times 10^4$	$1.34 \times 10^5$
	105	$9.16 \times 10^4$	$4.87 \times 10^4$	$1.65 \times 10^5$
S-6.35	35	$4.71 \times 10^4$	$3.73 \times 10^4$	$1.12 \times 10^5$
	70	$6.54 \times 10^4$	$5.93 \times 10^4$	$1.38 \times 10^5$
	105	$8.37 \times 10^4$	$7.56 \times 10^4$	$1.62 \times 10^5$
S-9.5	35	$4.72 \times 10^4$	$3.13 \times 10^4$	$1.13 \times 10^5$
	70	$6.55 \times 10^4$	$4.24 \times 10^4$	$1.36 \times 10^5$
	105	$9.95 \times 10^4$	$7.15 \times 10^4$	$1.73 \times 10^5$

The data from Table 5.24 can be represented by a best-fit power equation of the form of Equation 5.19 using the analysis technique suggested in 5.9.2.

For series S-4.75, the best fit power law equations are:

$$E_i = 3267(\sigma_3)^{0.721} \quad ; \quad R^2 = 0.999 \quad (5.32a)$$

$$E_{50} = 1254(\sigma_3)^{0.775} \quad ; \quad R^2 = 0.972 \quad (5.32b)$$

$$E_{ur} = 18076(\sigma_3)^{0.474} \quad ; \quad R^2 = 0.995 \quad (5.32c)$$

for series S-6.35, the best fit power law equations are:

$$E_i = 7437(\sigma_3)^{0.517} \quad ; \quad R^2 = 0.966 \quad (5.33a)$$

$$E_{50} = 3757(\sigma_3)^{0.647} \quad ; \quad R^2 = 0.999 \quad (5.33b)$$

$$E_{ur} = 34467(\sigma_3)^{0.331} \quad ; \quad R^2 = 0.995 \quad (5.33c)$$

and for series S-9.5, the best fit power law equations are:

$$E_i = 4405(\sigma_3)^{0.657} \quad ; \quad R^2 = 0.951 \quad (5.34a)$$

$$E_{50} = 2317(\sigma_3)^{0.718} \quad ; \quad R^2 = 0.911 \quad (5.34b)$$

$$E_{ur} = 28840(\sigma_3)^{0.378} \quad ; \quad R^2 = 0.953 \quad (5.34c)$$

Figure 5.60 through Figure 5.62 show the data and the trend of the elastic moduli of Equation 5.31 to 5.34 for series S-4.75, S-6.35, and S-9.5, respectively. It is again clear that the power law equation accurately predicts the trend of the three elastic moduli for all of the experimental series.

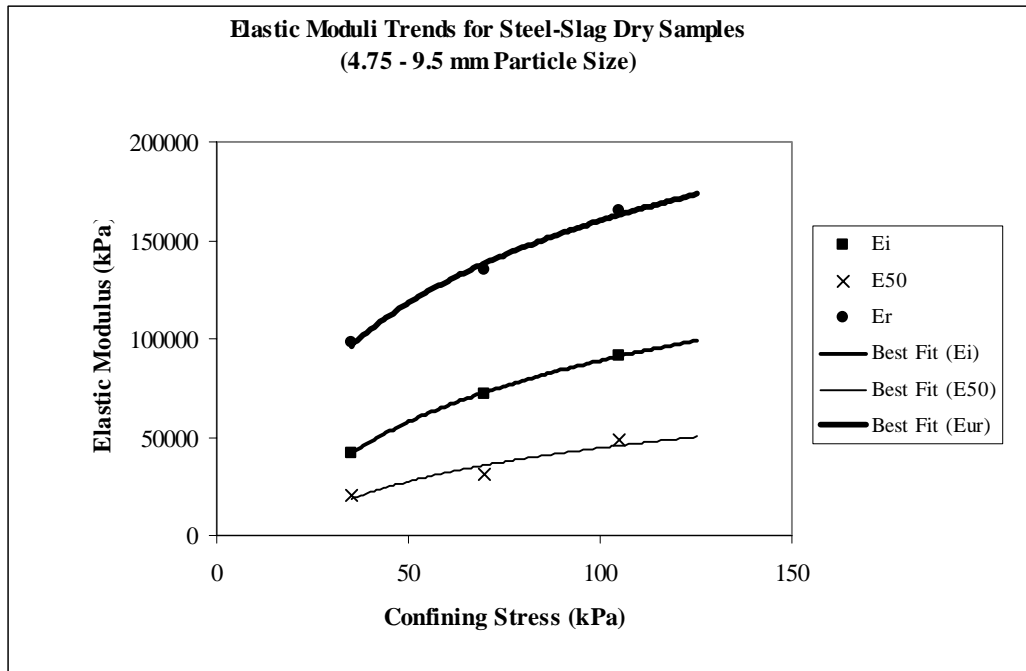


Figure 5.60 Elastic moduli trends for series S-4.75

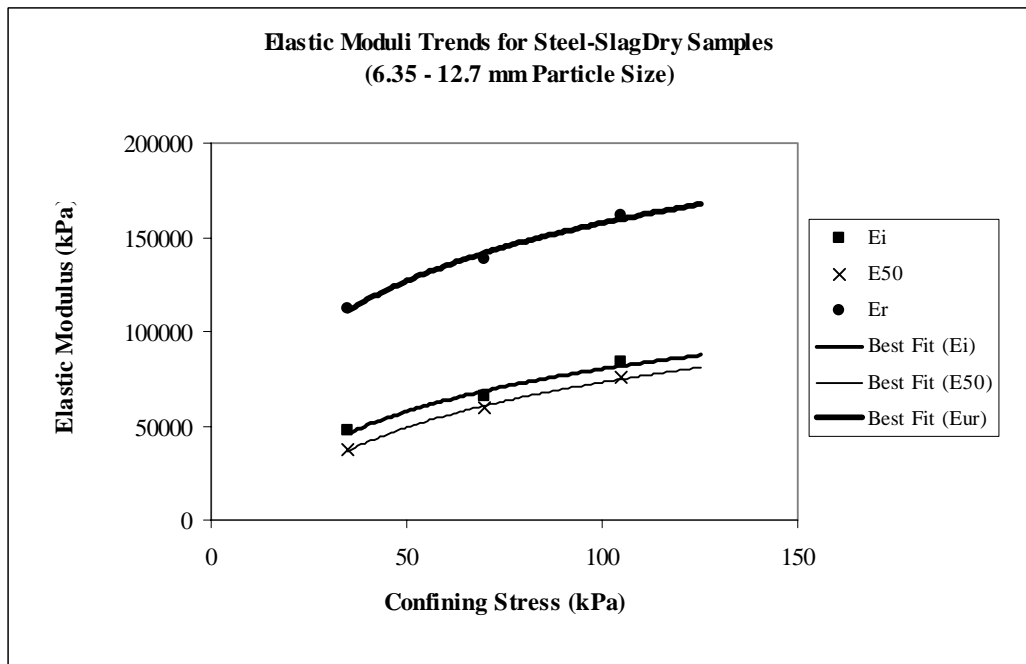


Figure 5.61 Elastic moduli trends for series S-6.35

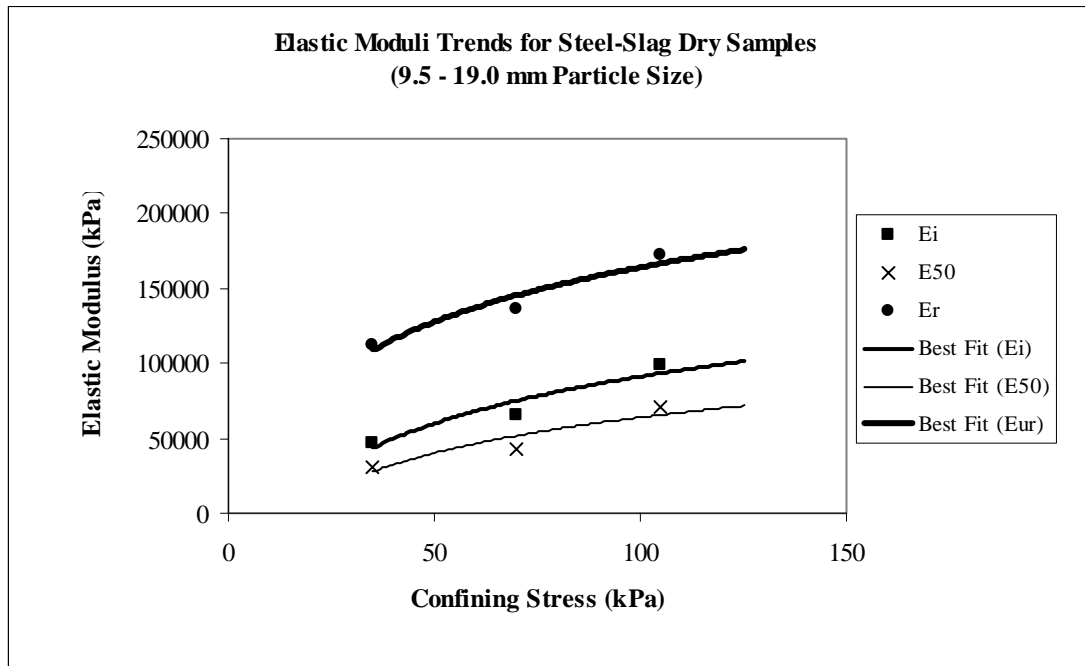


Figure 5.62 Elastic moduli trends for series S-9.5

Continuing with evaluation for the variation in the elastic moduli, Table 5.26 lists the calculated values for  $n$  and  $\log_{10}K$  for the initial moduli for all of the experimental series using scaled-down steel-slag. Figure 5.63 shows the best fit power law curves for each series listed in Table 5.26.

Table 5.26 Power law parameters for the initial elastic moduli for scaled-down steel-slag

Gradation	Power Law Slope, $n$	Power Law Intercept, $\log_{10}K$	Coefficient of Determination, $R^2$
S-4.75	0.721	3.51	0.999
S-6.35	0.517	3.87	0.966
S-9.5	0.657	3.65	0.951

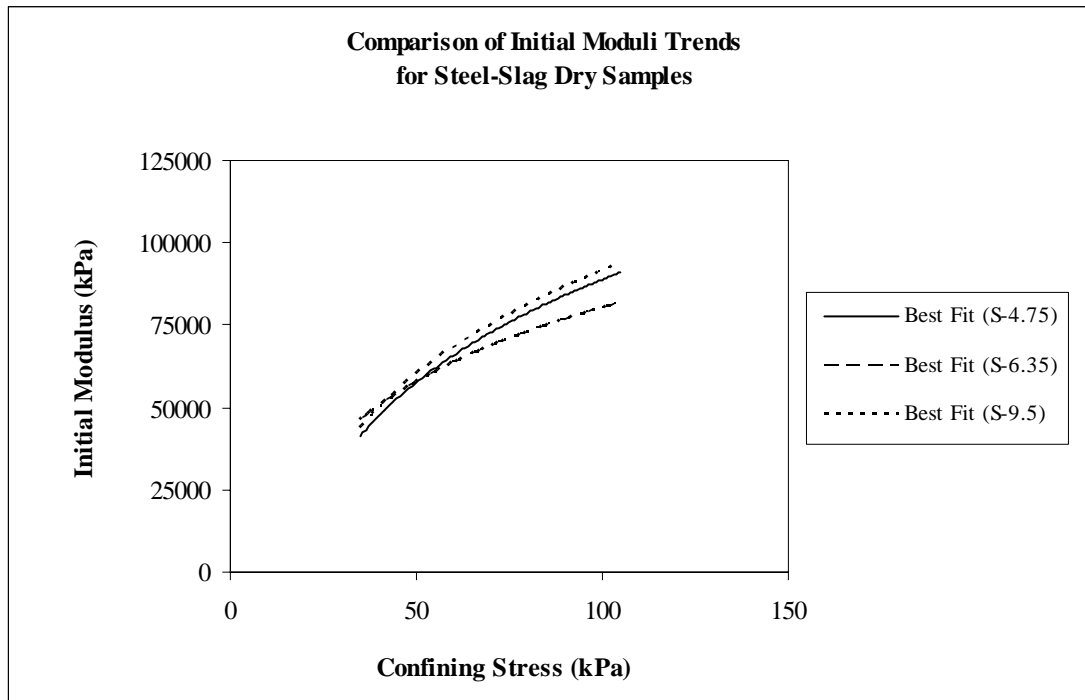


Figure 5.63 Comparison of trends of initial elastic moduli for all steel-slag series

Figure 5.64 shows the variation of the power law parameters  $n$  and  $\log_{10}K$  of the initial elastic moduli with the mean particle size for the scaled-down steel-slag. The figure clearly shows that the power law parameters describing the initial moduli of scaled-down steel-slag are very scattered. The tendency of power law parameters for the initial elastic modulus is fitted with an average value to the data. The corresponding values for the power law slope,  $n$ , and the power law intercept,  $\log_{10}K$ ,  $n$  and  $\log_{10}K$  of the initial modulus are given in Equation (5.35a) and Equation (5.35b).

$$n = 0.632 \pm 0.104 \quad (5.35a)$$

$$\log_{10} K = 3.677 \pm 0.181 \quad (5.35b)$$

Figure 5.65 shows that the power law with the parameters given in Equation (5.35) predicts the initial elastic modulus,  $E_i$ , values within a very narrow range of  $\pm 10\%$  confidence envelope for all scaled-down steel-slag samples.

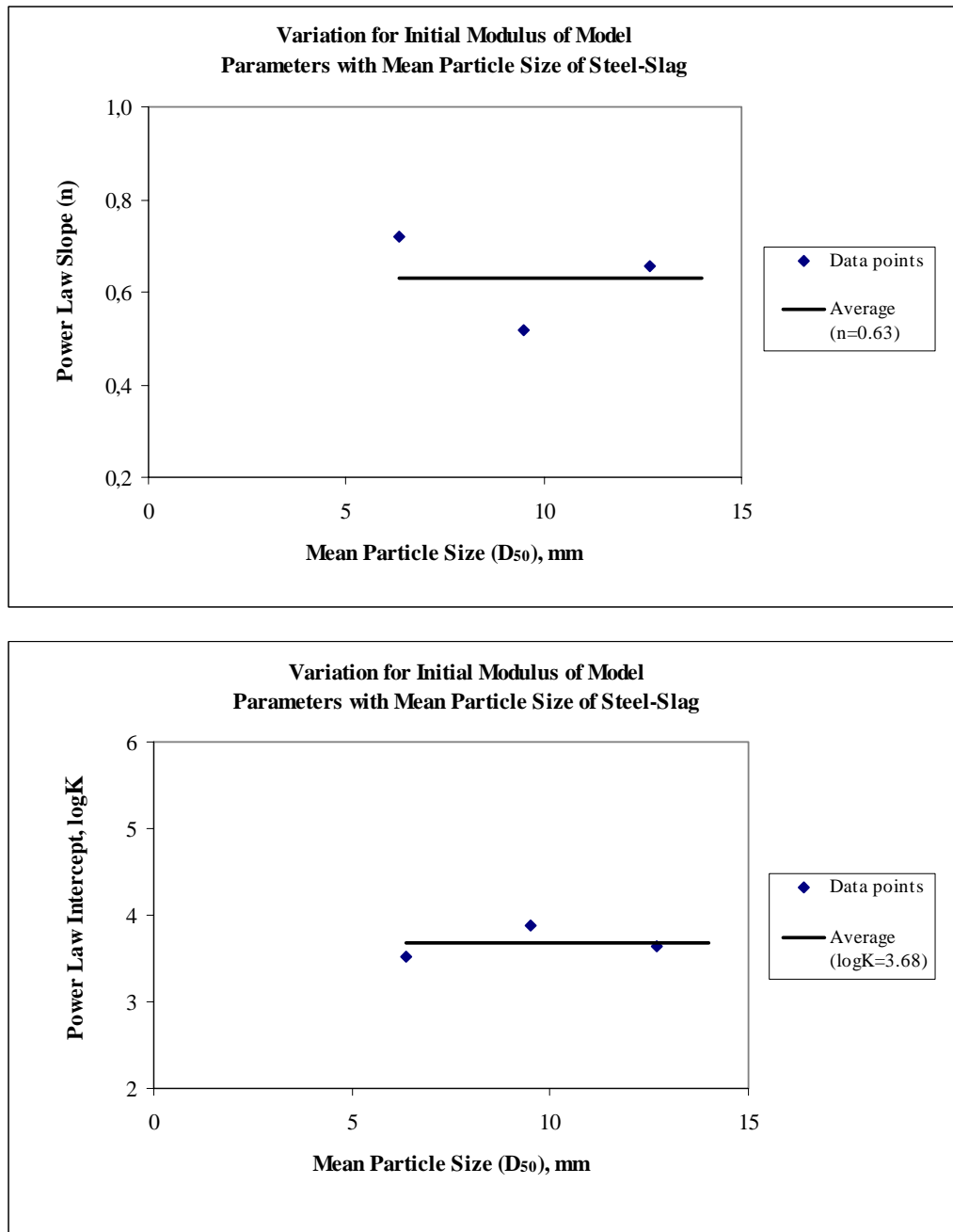


Figure 5.64 Variation of power law parameters of initial elastic moduli with the mean particle size for the scaled-down steel-slag samples

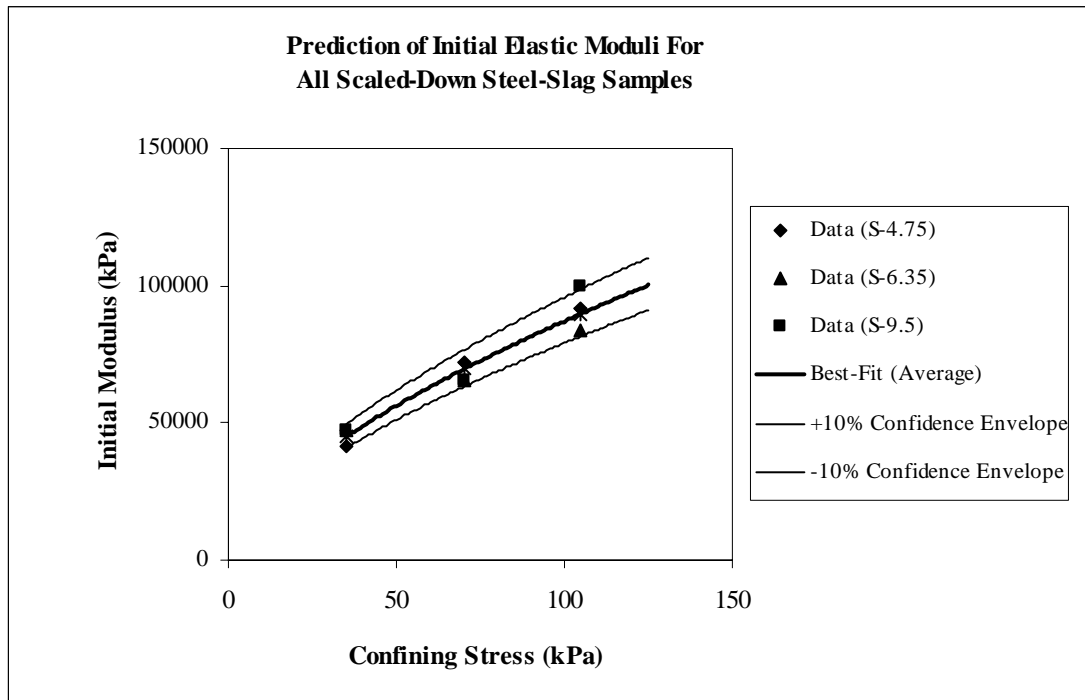


Figure 5.65 Prediction of initial elastic moduli for all scaled-down steel-slag samples

Table 5.27 lists the values for  $n$  and  $\log_{10}K$  of the power law parameters determined for all of the experimental series using scaled-down steel-slag samples. Figure 5.66 illustrates the best fit power law curves for each series listed in Table 5.27.

Table 5.27 Power law parameters for the secant elastic moduli for scaled-down steel-slag

Gradation	Power Law Slope, $n$	Power Law Intercept, $\log_{10}K$	Coefficient of Determination, $R^2$
S-4.75	0.775	3.10	0.972
S-6.35	0.647	3.57	0.999
S-9.5	0.718	3.36	0.911

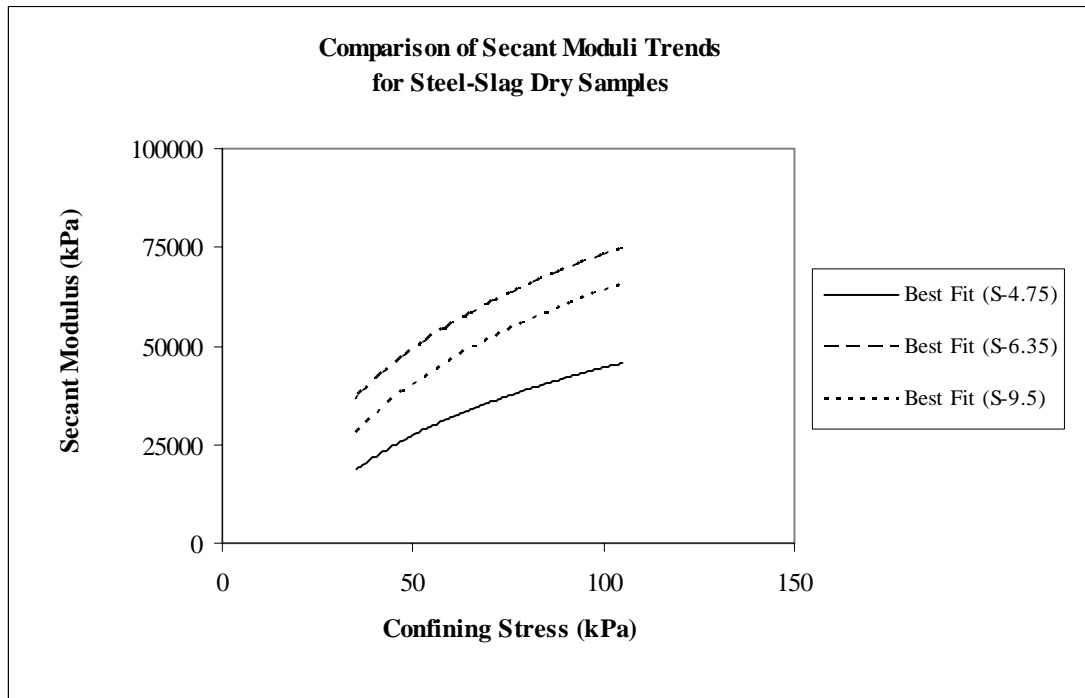


Figure 5.66 Comparison of trends of secant elastic moduli for all steel-slag series

For the variation of the secant elastic moduli with the change in mean particle size for scaled-down steel-slag samples, Figure 5.67 shows the variation of the power law parameters  $n$  and  $\log_{10}K$  of the secant elastic moduli with the mean particle size of steel-slag. The figure shows that the power law parameters describing the secant moduli as the initial moduli for scaled-down steel-slag are very scattered. The tendency of power law parameters for the initial elastic modulus is again fitted with an average value to the data. The corresponding values for the power law slope,  $n$ , and the power law intercept,  $\log_{10}K$ ,  $n$  and  $\log_{10}K$  of the initial modulus are given in Equation (5.36a) and Equation (5.36b).

$$n = 0.713 \pm 0.064 \quad (5.36a)$$

$$\log_{10} K = 3.343 \pm 0.235 \quad (5.36b)$$

Figure 5.68 illustrates that the power law with the parameters given in Equation (5.36) predicts the secant elastic modulus,  $E_{50}$ , values within a  $\pm 50\%$  confidence envelope for all scaled-down steel-slag samples.

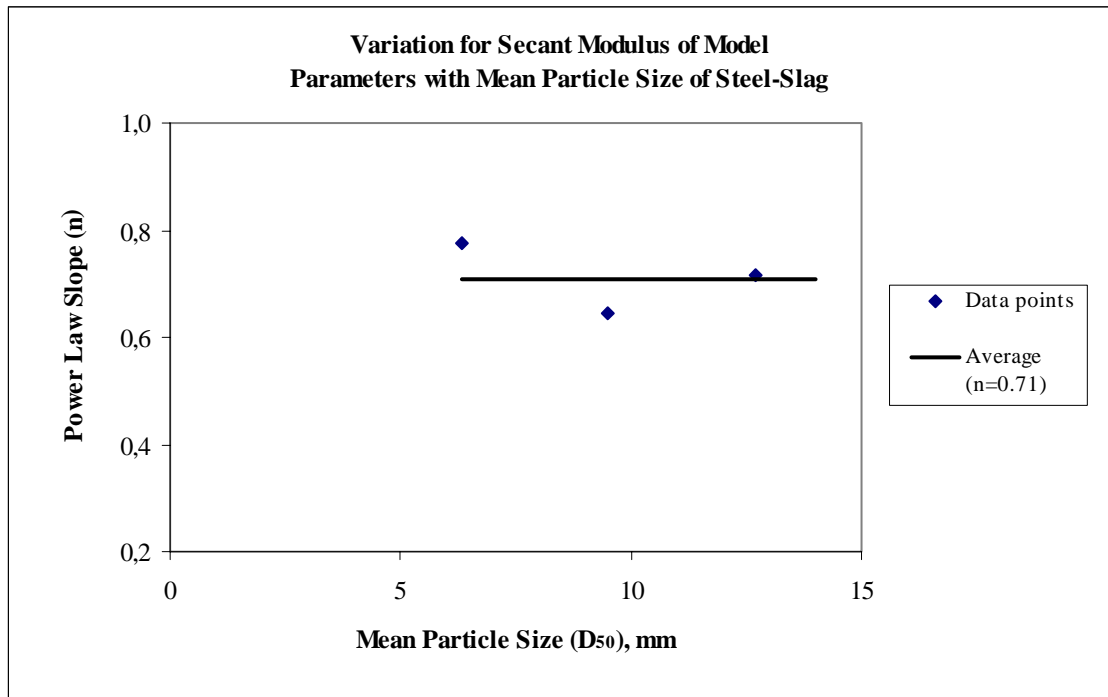


Figure 5.67 Variation of power law parameters of secant elastic moduli with the mean particle size for the scaled-down steel-slag samples

Table 5.28 lists the power law parameters for the unloading-reloading elastic moduli for scaled-down steel-slag samples. Figure 5.69 illustrates the best fit power law curves for each series listed in the table.

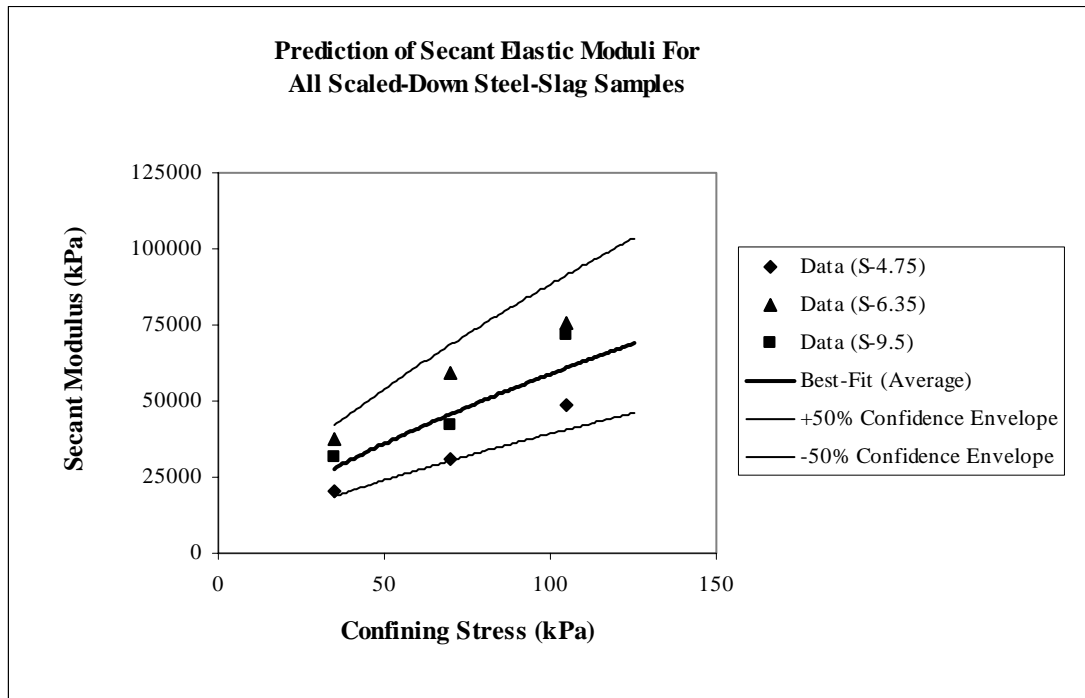


Figure 5.68 Prediction of secant elastic moduli for all scaled-down steel-slag samples

Table 5.28 Power law parameters for the unloading-reloading elastic moduli for scaled-down steel-slag

Gradation	Power Law Slope, n	Power Law Intercept, $\log_{10}K$	Coefficient of Determination, $R^2$
S-4.75	0.474	4.26	0.995
S-6.35	0.331	4.54	0.995
S-9.5	0.378	4.46	0.953

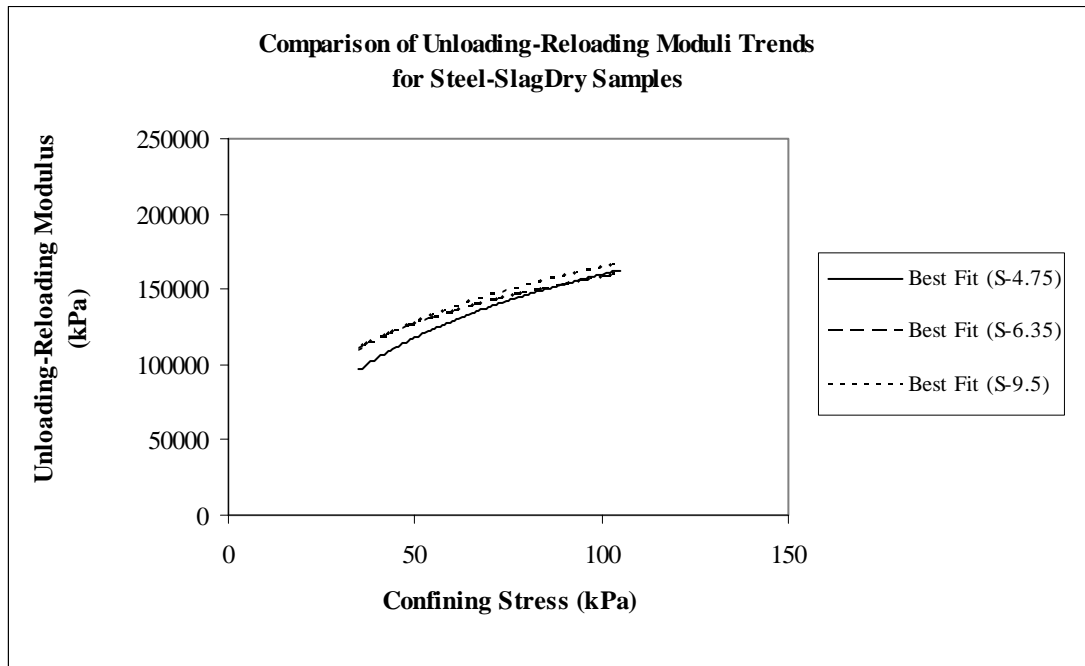


Figure 5.69 Comparison of trends of unloading-reloading elastic moduli for all steel-slag series

Figure 5.70 shows the variation of the power law parameters of the unloading-reloading elastic moduli with the mean particle size for steel-slag. As with initial and secant moduli the data for the unloading-reloading elastic moduli are also scattered with the mean particle size. Equation (5.37a) and Equation (5.37b) are average values to the data given in Table 5.27 for the power law slope,  $n$ , and the power law intercept,  $\log_{10}K$ , respectively.

$$n = 0.394 \pm 0.073 \quad (5.37a)$$

$$\log_{10} K = 4.420 \pm 0.144 \quad (5.37b)$$

Figure 5.71 shows that the power law with the parameters given in Equation (5.37) predicts the unloading-reloading elastic modulus,  $E_{ur}$ , values within a  $\pm 10\%$  confidence envelope for all scaled-down steel-slag samples.

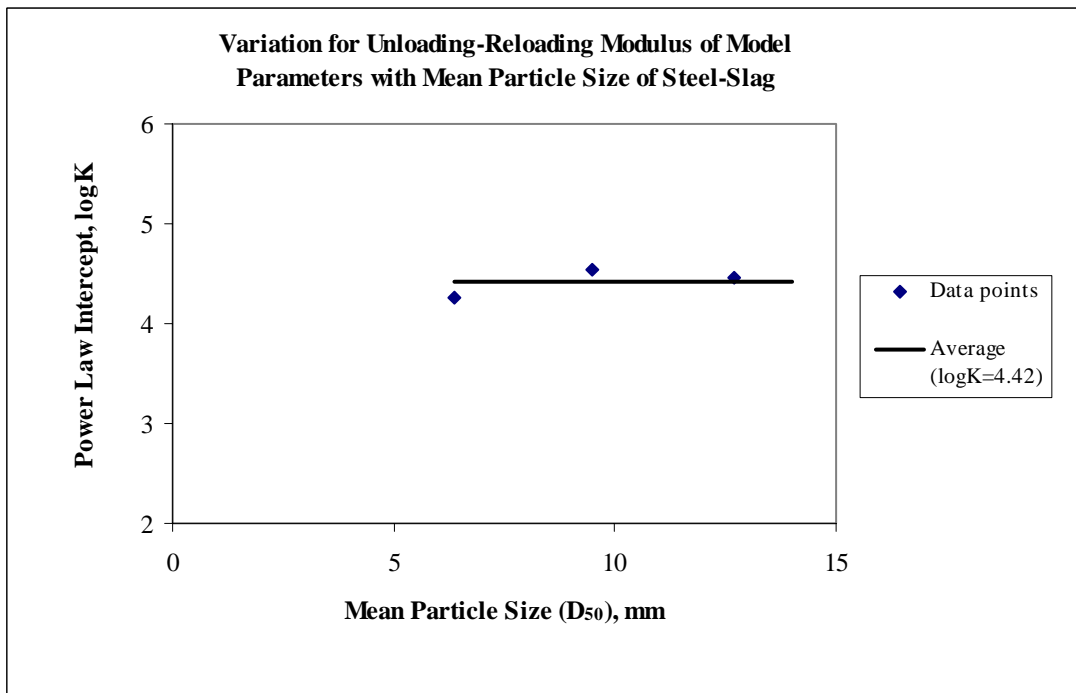
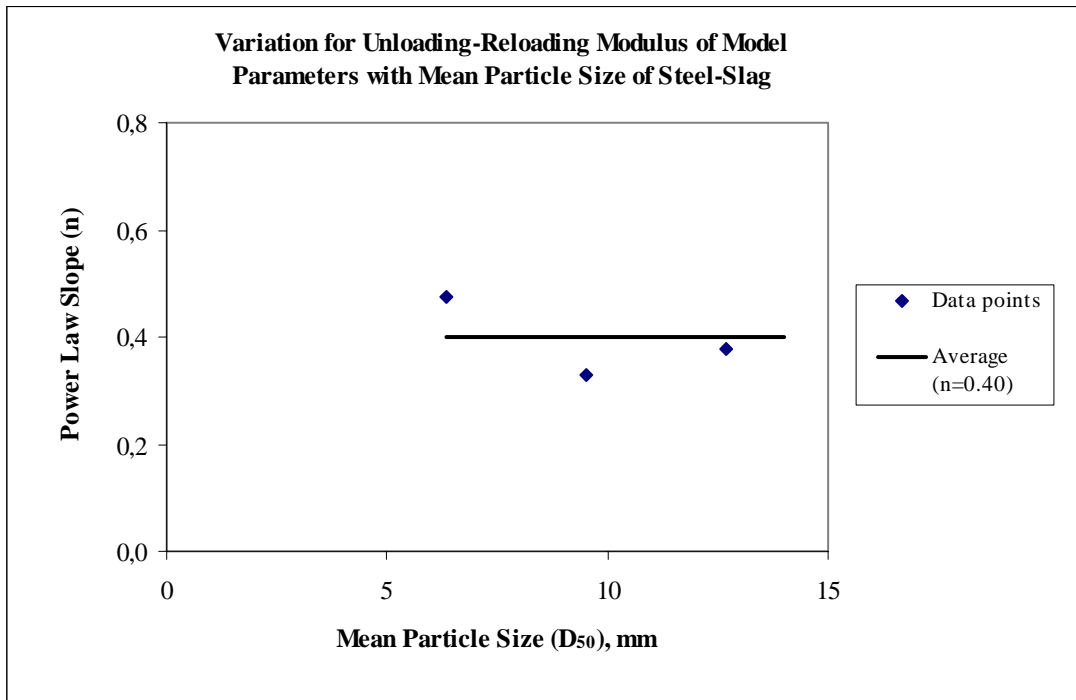


Figure 5.70 Variation of power law parameters of unloading-reloading elastic moduli with the mean particle size of scaled-down steel-slag samples

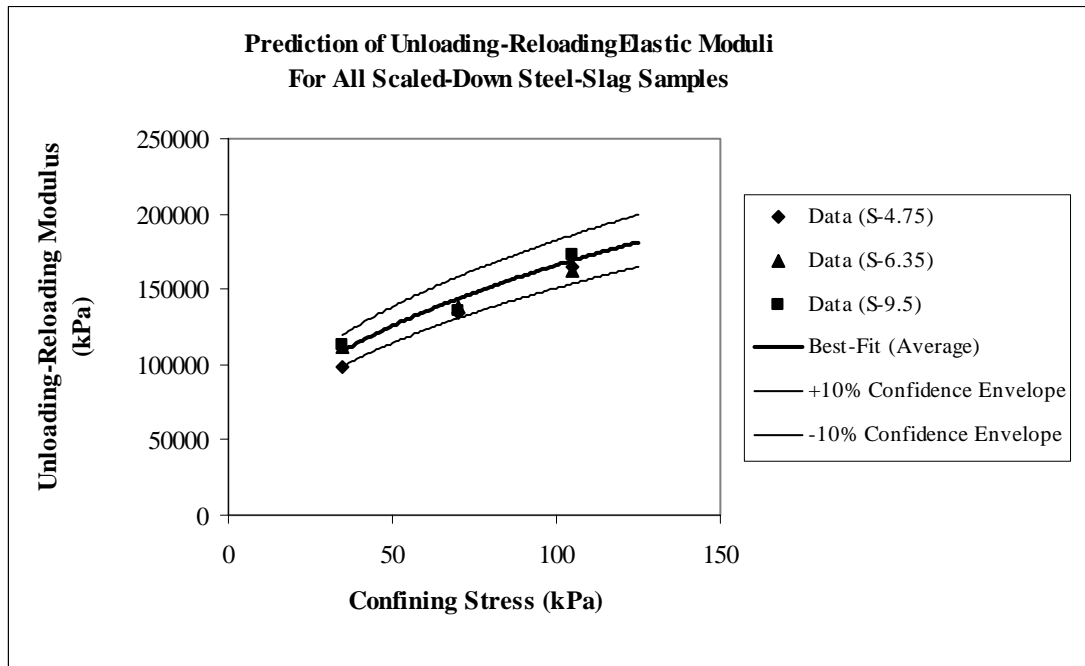


Figure 5.71 Prediction of unloading-reloading elastic moduli for all scaled-down steel-slag samples

In summary, the elastic moduli values for all scaled-down steel-slag are very scattered with the mean particle size. The trends are fitted to the data as average. When the trend of power law parameters is preserved, the parallel gradation technique as a predictor of the initial and unloading-reloading elastic moduli provides an adequate estimate within a  $\pm 10\%$  confidence envelope, but the best-fit for secant elastic moduli provides an estimate within a  $\pm 50\%$  confidence envelope. It may be concluded that the values of the elastic moduli for steel-slag samples using the parallel gradation technique are adequately estimated for engineering purposes.

The initial and unloading-reloading elastic moduli for all series may be predicted from the power law parameters determined for series S-9.5, coarsest gradation tested for steel-slag material. Figure 5.72 and Figure 5.73 show all data and the trends of best-fit for the initial and unloading-reloading elastic moduli, respectively. The confidence envelope was obtained as  $\pm 20\%$  for both the initial and unloading-reloading elastic moduli. On the other hand, the power law parameters of

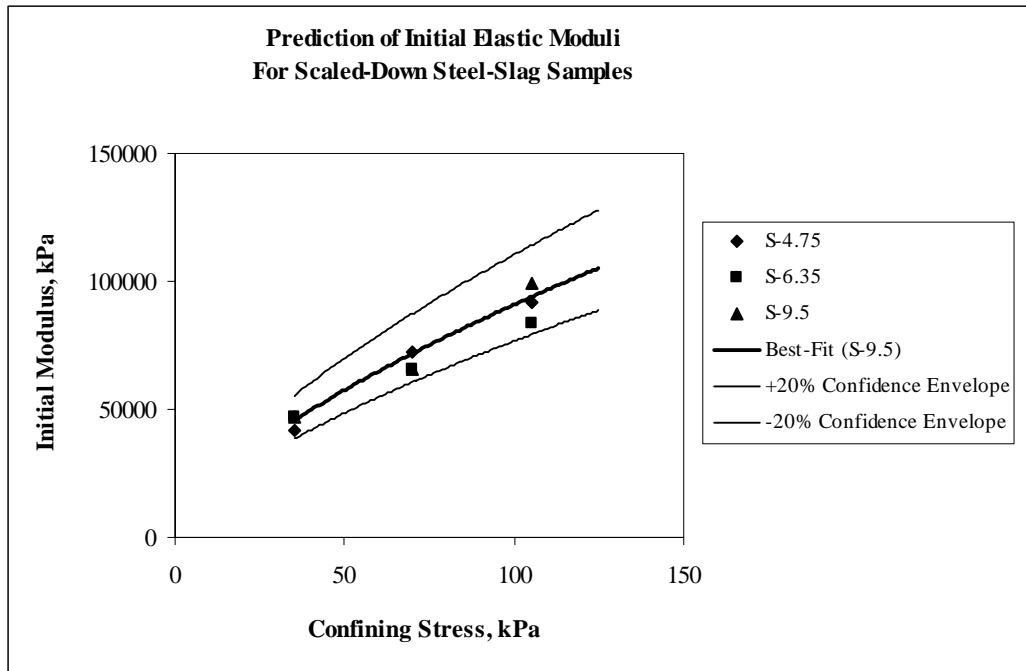


Figure 5.72 Prediction of initial moduli for steel-slag samples with S-9.5 best-fit

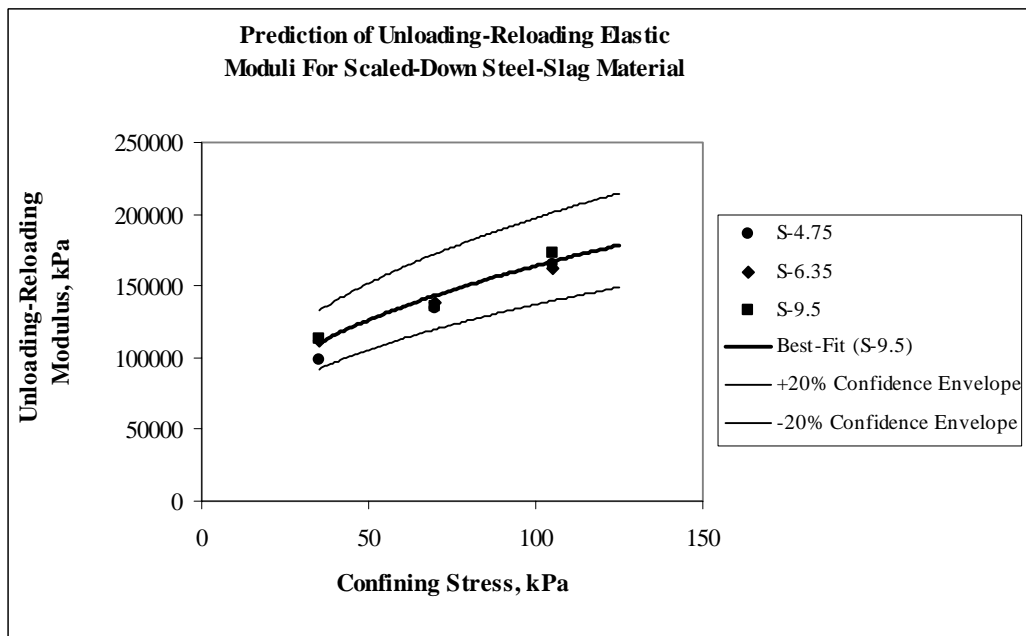


Figure 5.73 Prediction of unloading-reloading moduli for steel-slag samples with S-9.5 best-fit

secant moduli evaluated for series S-9.5 underestimated the secant elastic moduli data obtained for all series; confidence envelope was  $\pm 60\%$  as shown in Figure 5.74

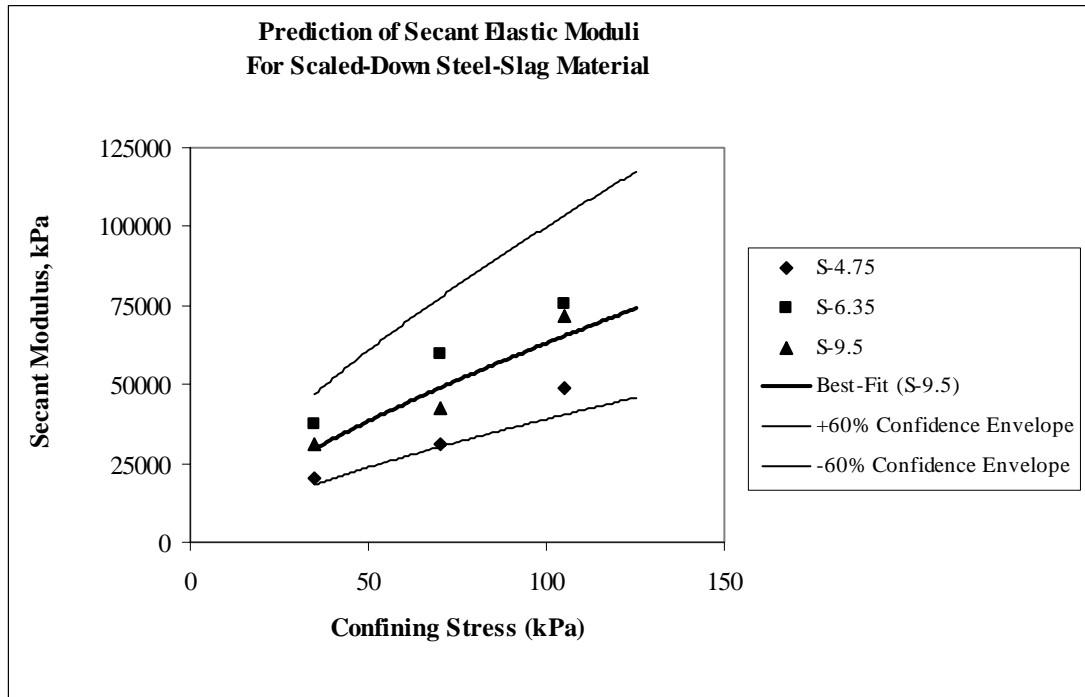


Figure 5.74 Prediction of secant elastic moduli for steel-slag samples with S-9.5 best-fit

### 5.10 Comparison of Elastic Moduli of Scaled-Down Limestone, Basalt and Steel-Slag Materials

Table 5.29 lists the initial elastic modulus values predicted for selected series of scaled-down limestone, basalt, and steel-slag, as well as the moduli values for the prototype size  $D_{50} = 45$  mm at a confining stress of 35 kPa. Examining Table 5.29 shows that the initial elastic modulus values for all basalt series are higher, except  $D_{50} = 6.35$  mm for limestone, than those of limestone and steel-slag. However, no

substantial difference is found in the values of initial elastic modulus between limestone and steel-slag series.

Table 5.29 Comparison of the predicted initial elastic moduli due to material type at  $\sigma_3 = 35$  kPa

Gradation	Predicted Initial Elastic Modulus ( $E_i$ ), kPa		
	Limestone	Basalt	Steel-Slag
4.75 mm to 9.5 mm ( $D_{50} = 6.35$ mm)	$3.88 \times 10^4$	$4.89 \times 10^4$	$4.53 \times 10^4$
9.5 mm to 19.0 mm ( $D_{50} = 12.7$ mm)	$4.45 \times 10^4$	$5.49 \times 10^4$	$4.53 \times 10^4$
30.0 mm to 60.0 mm ( $D_{50} = 45$ mm)	$5.73 \times 10^4$	$6.83 \times 10^4$	$4.53 \times 10^4$

Table 5.30 lists the secant elastic modulus values predicted for selected series of scaled-down limestone, basalt, and steel-slag, as well as the moduli values for the prototype size  $D_{50} = 45$  mm at a confining stress of 35 kPa. Table 5.30 shows that the secant elastic modulus values for basalt series are higher than those of limestone and steel-slag, and the secant elastic modulus values for limestone series are higher than those of steel-slag.

Table 5.31 lists the unloading-reloading values predicted for again selected series of scaled-down limestone, basalt, and steel-slag, as well as the moduli values for the prototype size  $D_{50} = 45$  mm at a confining stress of 35 kPa. Table 5.31 shows that the unloading-reloading elastic moduli for crushed limestone are higher than those of basalt and steel-slag, but the difference is not so great and may be concluded that material type has almost no effect on the unloading-reloading moduli.

Table 5.30 Comparison of the predicted secant elastic moduli due to material type at  $\sigma_3 = 35$  kPa

Gradation	Predicted Secant Elastic Modulus ( $E_{50}$ ), kPa		
	Limestone	Basalt	Steel-Slag
4.75 mm to 9.5 mm ( $D_{50} = 6.35$ mm)	$2.93 \times 10^4$	$3.05 \times 10^4$	$2.78 \times 10^4$
9.5 mm to 19.0 mm ( $D_{50} = 12.7$ mm)	$3.47 \times 10^4$	$4.20 \times 10^4$	$2.78 \times 10^4$
30.0 mm to 60.0 mm ( $D_{50} = 45$ mm)	$5.16 \times 10^4$	$9.81 \times 10^4$	$2.78 \times 10^4$

Table 5.31 Comparison of the predicted unloading-reloading elastic modulus due to material type at  $\sigma_3 = 35$  kPa

Gradation	Predicted Unloading-Reloading Elastic Modulus ( $E_{ur}$ ), kPa		
	Limestone	Basalt	Steel-Slag
4.75 mm to 9.5 mm ( $D_{50} = 6.35$ mm)	$1.02 \times 10^5$	$1.06 \times 10^5$	$1.09 \times 10^5$
9.5 mm to 19.0 mm ( $D_{50} = 12.7$ mm)	$1.21 \times 10^5$	$1.13 \times 10^5$	$1.09 \times 10^5$
30.0 mm to 60.0 mm ( $D_{50} = 45$ mm)	$1.77 \times 10^5$	$1.48 \times 10^5$	$1.09 \times 10^5$

As a result, elastic moduli for limestone and basalt materials increase as the particle size increases, whereas elastic moduli for steel-slag material are very scattered, and are evaluated as constant with changing the mean particle size. Also, it appears that material type has an effect on secant moduli, while it has almost no effect on the initial and the unloading-reloading moduli.

As an overall evaluation, the comparison for elastic moduli determined for all materials can be viewed in the same figure. Figure 5.75 to Figure 5.77 shows the initial elastic modulus, secant elastic modulus and the unloading-reloading elastic modulus for all materials with the predicted data for prototype size, respectively. It is worth noting that the elastic moduli values for all materials may be predicted within an adequate estimate for the engineering purposes by using the power law parameters determined for L-9.5 ( $D_{50} = 12.7$  mm), the coarsest gradation tested for limestone. The data for initial and the unloading-reloading elastic modulus values with the predicted data for prototype size were within  $\pm 50\%$  confidence envelope, whereas the best-fit to the data for L-9.5 predicted the secant elastic moduli for all materials with the predicted data for prototype sizes within  $\pm 100\%$  confidence envelope. Consequently, the parallel gradation technique would lead to acceptable predictions of elastic moduli for prototype materials if scaled-down materials may carefully be utilized.

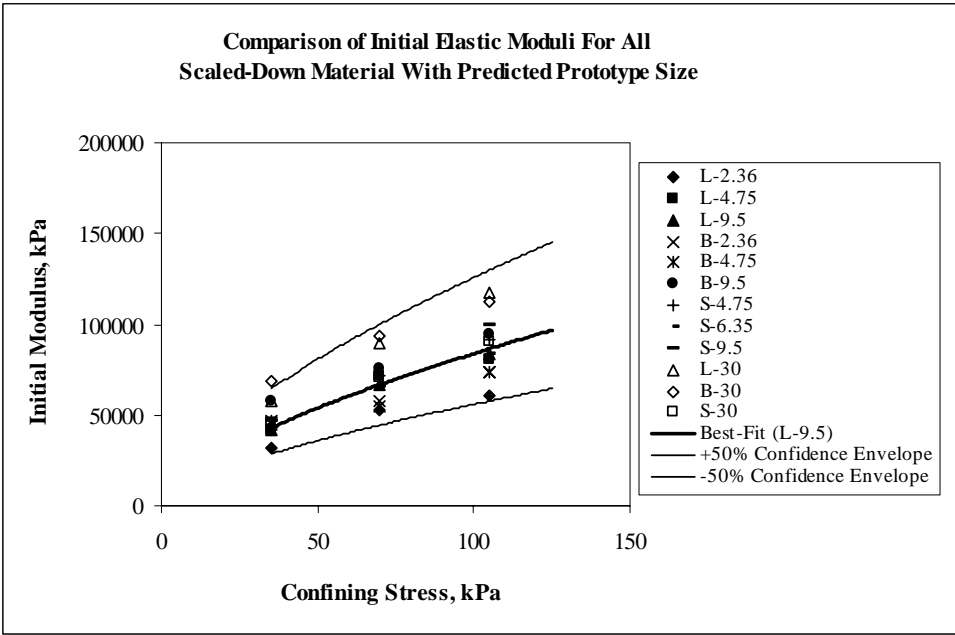


Figure 5.75 Comparison of initial elastic moduli for all materials with the best fit to L-9.5 values

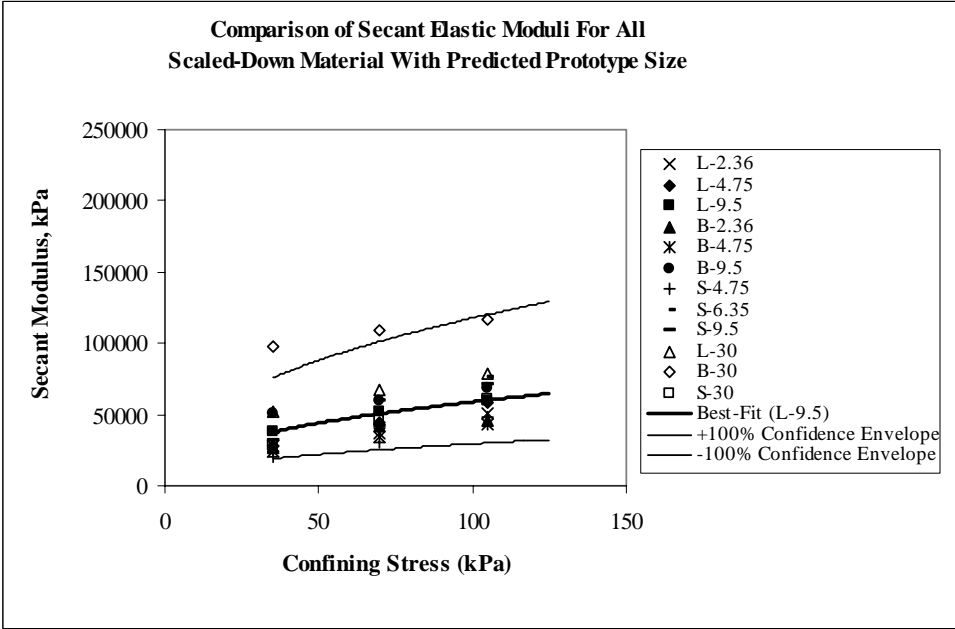


Figure 5.76 Comparison of secant elastic moduli for all materials with the best fit to L-9.5 values

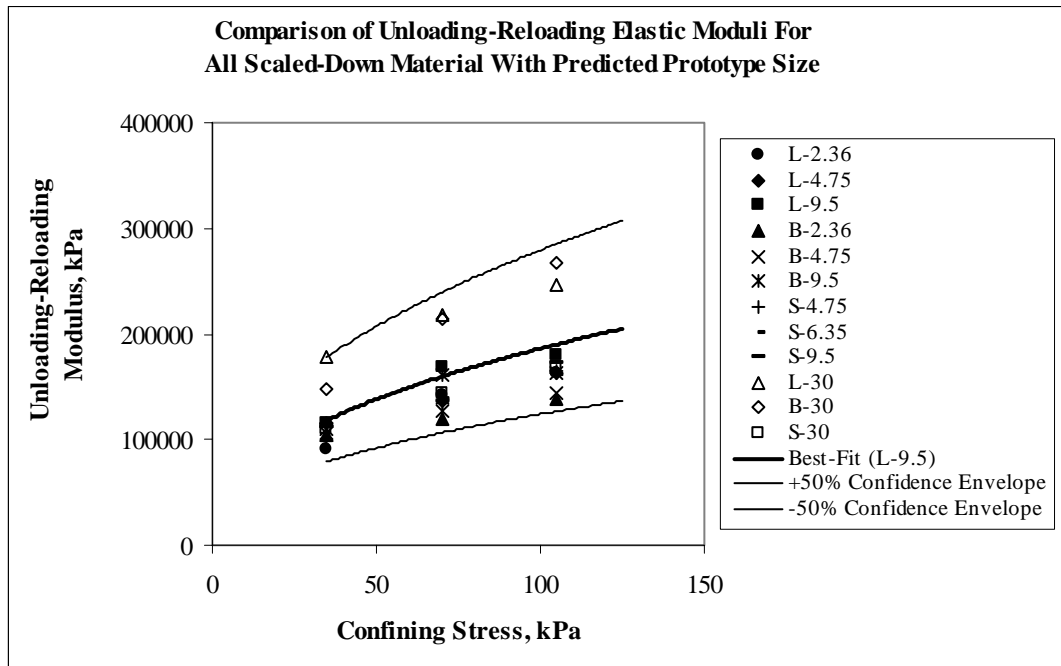


Figure 5.77 Comparison of unloading-reloading elastic moduli for all materials with the best fit to L-9.5 values

### 5.11 Effect of Water on Elastic Moduli of Materials

The elastic moduli for wet samples of the different materials are examined in this section. As stated in section 5.7, the stress-strain behavior of wet samples is similar to that of dry samples for each material type. The results are given in Appendix. The confining stresses applied in the triaxial tests for wet samples using 100 mm specimen diameter, as was the case for the dry samples, were 35 kPa, 70 kPa, and 105 kPa. Triaxial tests were performed on all scaled-down limestone gradations, namely L-2.36, L-4.75, and L-9.5, whereas only on one gradation the test was conducted for basalt and slag materials, B-9.5 and S-9.5, respectively.

Table 5.32 shows the initial elastic moduli,  $E_i$ , values obtained for various wet series. For comparison, the corresponding initial elastic moduli values for dry series were also given in the same table.

Table 5.32 Summary of the initial elastic moduli values determined for various wet series

Gradation	Confining Stress ( $\sigma_3$ ), kPa	Initial Moduli ( $E_i$ ), kPa	
		Wet Sample	Dry Sample
L-2.36	35	$3.32 \times 10^4$	$3.14 \times 10^4$
	70	$5.34 \times 10^4$	$5.23 \times 10^4$
	105	$6.02 \times 10^4$	$6.10 \times 10^4$
L-4.75	35	$4.45 \times 10^4$	$4.19 \times 10^4$
	70	$8.12 \times 10^4$	$7.20 \times 10^4$
	105	$8.91 \times 10^4$	$8.11 \times 10^4$
L-9.5	35	$5.76 \times 10^4$	$4.19 \times 10^4$
	70	$7.86 \times 10^4$	$6.68 \times 10^4$
	105	$10.21 \times 10^4$	$8.38 \times 10^4$
B-9.5	35	$7.34 \times 10^4$	$5.76 \times 10^4$
	70	$8.38 \times 10^4$	$7.59 \times 10^4$
	105	$1.07 \times 10^4$	$9.42 \times 10^4$
S-9.5	35	$5.24 \times 10^4$	$4.72 \times 10^4$
	70	$8.12 \times 10^4$	$6.55 \times 10^4$
	105	$11.13 \times 10^4$	$9.95 \times 10^4$

Table 5.33 shows the secant elastic moduli,  $E_{50}$ , values determined for various wet series. For comparison, the corresponding secant elastic moduli values for dry series were also given in Table 5.33.

Table 5.33 Summary of the secant elastic moduli values determined for various wet series

Gradation	Confining Stress ( $\sigma_3$ ), kPa	Secant Moduli ( $E_{50}$ ), kPa	
		Wet Sample	Dry Sample
L-2.36	35	$2.84 \times 10^4$	$2.75 \times 10^4$
	70	$4.35 \times 10^4$	$3.42 \times 10^4$
	105	$4.63 \times 10^4$	$5.04 \times 10^4$
L-4.75	35	$2.88 \times 10^4$	$2.85 \times 10^4$
	70	$4.91 \times 10^4$	$4.40 \times 10^4$
	105	$6.19 \times 10^4$	$5.79 \times 10^4$
L-9.5	35	$4.66 \times 10^4$	$3.76 \times 10^4$
	70	$6.06 \times 10^4$	$5.20 \times 10^4$
	105	$6.53 \times 10^4$	$5.91 \times 10^4$
B-9.5	35	$4.53 \times 10^4$	$5.11 \times 10^4$
	70	$7.31 \times 10^4$	$5.92 \times 10^4$
	105	$6.71 \times 10^4$	$6.81 \times 10^4$
S-9.5	35	$5.01 \times 10^4$	$3.13 \times 10^4$
	70	$5.44 \times 10^4$	$4.24 \times 10^4$
	105	$6.62 \times 10^4$	$7.15 \times 10^4$

Table 5.34 shows the unloading-reloading elastic moduli,  $E_{ur}$ , obtained for various wet series. Again for comparison, the corresponding unloading-reloading values for dry series were also given in the same table.

Table 5.34 Summary of the unloading-reloading elastic moduli values determined for various wet series

Gradation	Confining Stress ( $\sigma_3$ ), kPa	Unloading-Reloading Moduli ( $E_{ur}$ ), kPa	
		Wet Sample	Dry Sample
L-2.36	35	$1.17 \times 10^5$	$9.09 \times 10^4$
	70	$1.46 \times 10^5$	$1.42 \times 10^5$
	105	$1.82 \times 10^5$	$1.62 \times 10^5$
L-4.75	35	$9.49 \times 10^4$	$1.15 \times 10^5$
	70	$1.50 \times 10^5$	$1.36 \times 10^5$
	105	$1.68 \times 10^5$	$1.63 \times 10^5$
L-9.5	35	$1.16 \times 10^5$	$1.15 \times 10^5$
	70	$1.51 \times 10^5$	$1.69 \times 10^5$
	105	$1.94 \times 10^5$	$1.81 \times 10^5$
B-9.5	35	$1.11 \times 10^5$	$1.10 \times 10^5$
	70	$1.54 \times 10^5$	$1.62 \times 10^5$
	105	$1.53 \times 10^5$	$1.64 \times 10^5$
S-9.5	35	$1.25 \times 10^5$	$1.13 \times 10^5$
	70	$1.34 \times 10^5$	$1.36 \times 10^5$
	105	$1.65 \times 10^5$	$1.73 \times 10^5$

Comparing all limestone, basalt, and steel-slag wet series to that of related dry series indicate that the values of initial or secant or unloading-reloading elastic moduli are close to but generally higher than those calculated for the dry series. In other words, the values for elastic moduli of dry series are, in general, 25% less than the values for wet series, and are conservative. The higher elastic moduli values for wet samples can be explained again by the capillary stresses as Anderson et al.

(1993) suggested: “as suction increases the compressibility of the soil decreases and the stiffness increases, even for the coarse-grained soil”.

Consequently, it appears that the presence of water slightly increases the elastic moduli for all materials used in this study.

## **5.12 Effect of Gradation on Elastic Moduli of Materials**

The effect on elastic moduli of gradations prepared only for the scaled-down limestone was examined in this section. The test series using the alternative gradations were labeled L-6.35, meaning limestone material having minimum particle size of 6.35 mm, particle size ranged from 6.35 mm to 19.0 mm; and L-3.15, meaning limestone material having minimum particle size of 3.15 mm, particle size ranged from 3.15 mm to 19.0 mm as shown in Figure 4.4. The confining stresses used 35 kPa, 70 kPa, and 105 kPa with 100 mm specimens. So, three tests were run in each series. The related stress-strain and volumetric strain curves are presented in the Appendix.

Table 5.35 lists the initial elastic moduli values determined for the alternative gradations for limestone materials, L-3.15, L-6.35 and L-9.5 having a minimum particle size of 9.5 mm, particle size ranged from 9.5 mm to 19.0 mm.

Table 5.35 shows that the initial elastic moduli values determined did not differ significantly by changing the uniformity coefficient of scaled-down limestone as also illustrated in Figure 5.78a.

Table 5.36 lists the secant elastic moduli values obtained for different gradations of limestone materials, L-3.15, L-6.35 and L-9.5.

Table 5.35 Comparison of initial elastic moduli for different gradations of limestone

Confining Stress ( $\sigma_3$ ), kPa	Initial Elastic Moduli ( $E_i$ ), kPa		
	L-3.15 ( $C_u = 2.38$ )	L-6.35 ( $C_u = 1.75$ )	L-9.5 ( $C_u = 1.40$ )
35	$4.71 \times 10^4$	$4.45 \times 10^4$	$4.19 \times 10^4$
70	$6.02 \times 10^4$	$6.54 \times 10^4$	$6.68 \times 10^4$
105	$7.07 \times 10^4$	$9.16 \times 10^4$	$8.38 \times 10^4$

Table 5.36 Comparison of secant elastic moduli for different gradations of limestone

Confining Stress ( $\sigma_3$ ), kPa	Secant Elastic Moduli ( $E_{50}$ ), kPa		
	L-3.15 ( $C_u = 2.38$ )	L-6.35 ( $C_u = 1.75$ )	L-9.5 ( $C_u = 1.40$ )
35	$2.74 \times 10^4$	$3.39 \times 10^4$	$3.76 \times 10^4$
70	$3.45 \times 10^4$	$3.42 \times 10^4$	$5.20 \times 10^4$
105	$4.28 \times 10^4$	$4.97 \times 10^4$	$5.91 \times 10^4$

Table 5.36 indicates that the secant elastic moduli values obtained for alternative gradations, L-3.15 or L-6.35, were less than those for L-9.5 as also shown in Figure 5.78b. The difference, for example, can be reached to 34% between L-9.5 and L-3.15 or L-9.5 and L-6.35 at a confining stress of 70 kPa.

Table 5.37 lists the unloading-reloading elastic moduli values determined for the gradations of limestone, L-3.15, L-6.35 and L-9.5.

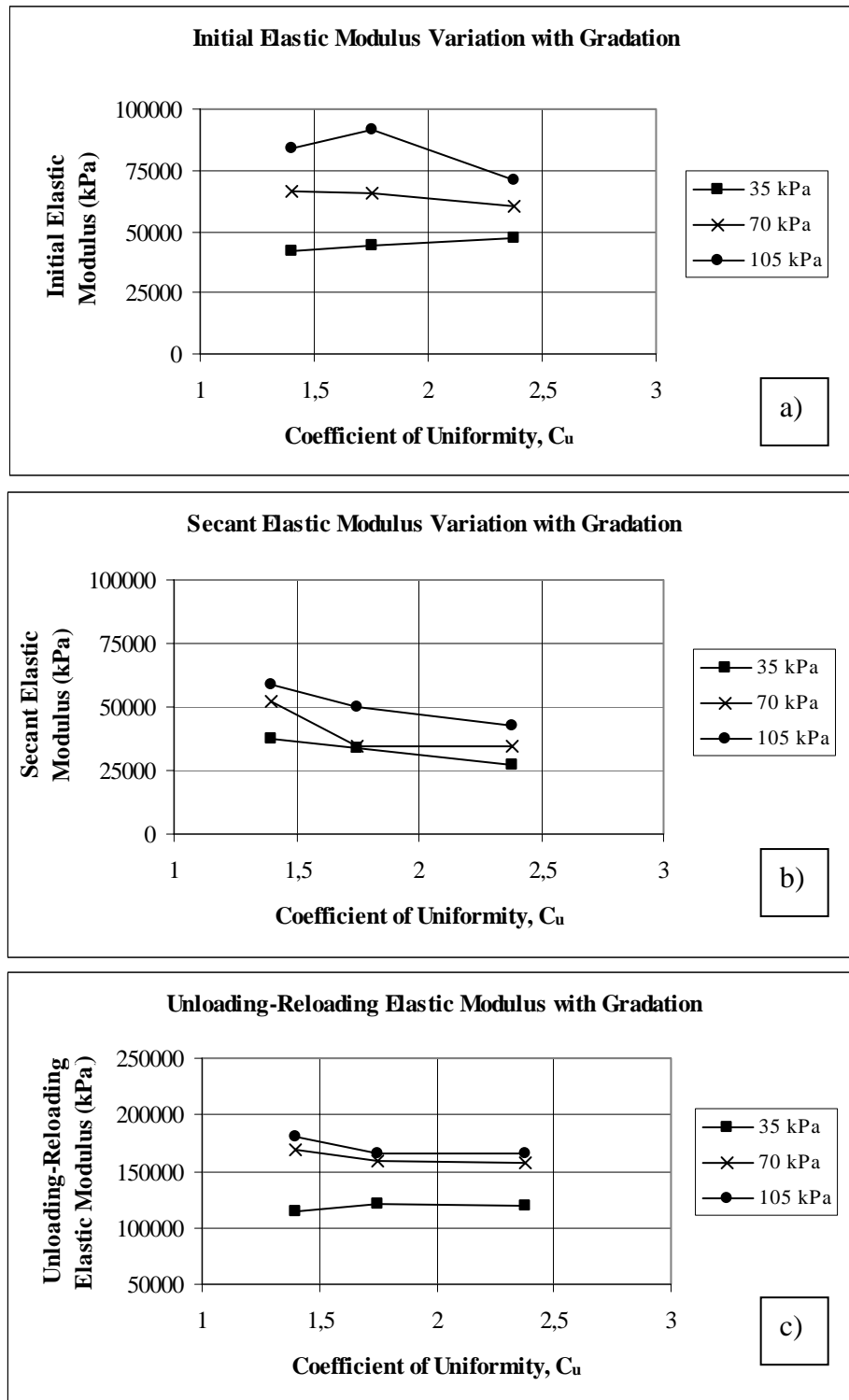


Figure 5.78 Variation with uniformity coefficient of a) initial elastic moduli b) secant elastic moduli c) unloading-reloading elastic moduli for limestone

Table 5.37 Comparison of unloading-reloading elastic moduli for different gradations of limestone

Confining Stress ( $\sigma_3$ ), kPa	Unloading-Reloading Elastic Moduli ( $E_{ur}$ ), kPa		
	L-3.15 ( $C_u = 2.38$ )	L-6.35 ( $C_u = 1.75$ )	L-9.5 ( $C_u = 1.40$ )
35	$1.20 \times 10^5$	$1.21 \times 10^5$	$1.15 \times 10^5$
70	$1.57 \times 10^5$	$1.58 \times 10^5$	$1.69 \times 10^5$
105	$1.65 \times 10^5$	$1.66 \times 10^5$	$1.81 \times 10^5$

Table 5.37 shows that the unloading-reloading elastic moduli values did not change significantly as the uniformity coefficient of scaled-down limestone changes as also illustrated in Figure 5.76c. The values for L-9.5, original gradation, were even greater by an amount of 10% than those of L-6.35 or L-3.15 at a confining stress of 105 kPa.

As a result, it appears that the use of different gradations as far as they were prepared in the prescribed uniformity coefficients does not seem to contribute to the elastic moduli of limestone.

### 5.13 Effect of Repeated Loading on Elastic Moduli of Materials

Only with a confining stress of 35 kPa dry quasi-cyclic experiments were run using all scaled-down samples. All of the experiments were conducted using the conventional triaxial equipment with the 100 mm specimen size as used for the static testing of materials. After the specimen was brought approximately to 1% axial strain and the associated deviator stress, ( $\sigma_1 - \sigma_3$ ) approximately equals to 200 kPa, was marked, 20 cycles were then applied for each test at that level. Thereafter the

sample was typically loaded monotonically to 15% axial strain. The same strain rate of 0.4 mm/min as for the static testing of materials was used in each stage of testing. During the test, data was collected beginning with the first cycle at every fifth cycle with  $5 \times 10^{-3}$  inch interval readings of axial compression. All tests results are presented in Appendix. A typical result is shown in Figure 5.79.

Table 5.38 compares the data determined for the unloading-reloading moduli at 1<sup>st</sup> cycle,  $E_{ur1}$ , and the moduli values at 20<sup>th</sup> cycle,  $E_{ur20}$ , at a confining stress of 35 kPa .

Table 5.38 Summary of the unloading-reloading elastic moduli at different cycles of load application

Gradation	Unloading-reloading Modulus, $E_{ur}$ (kPa)	
	1 <sup>st</sup> cycle	20 <sup>th</sup> cycle
L-2.36	$1.15 \times 10^5$	$1.25 \times 10^5$
L-4.75	$1.05 \times 10^5$	$1.26 \times 10^5$
L-9.50	$1.24 \times 10^5$	$1.42 \times 10^5$
B-2.36	$0.99 \times 10^5$	$1.08 \times 10^5$
B-4.75	$1.10 \times 10^5$	$1.23 \times 10^5$
B-9.50	$1.15 \times 10^5$	$1.31 \times 10^5$
S-4.75	$1.09 \times 10^5$	$1.15 \times 10^5$
S-6.35	$1.08 \times 10^5$	$1.15 \times 10^5$
S-9.50	$1.20 \times 10^5$	$1.26 \times 10^5$

Table 5.38 shows that the unloading-reloading moduli increased, in general, as the number of cycles increased. An increase in unloading-reloading modulus obtained was roughly 15% for scaled-down limestone; 10% for the basalt; and 5% for the scaled-down steel-slag.

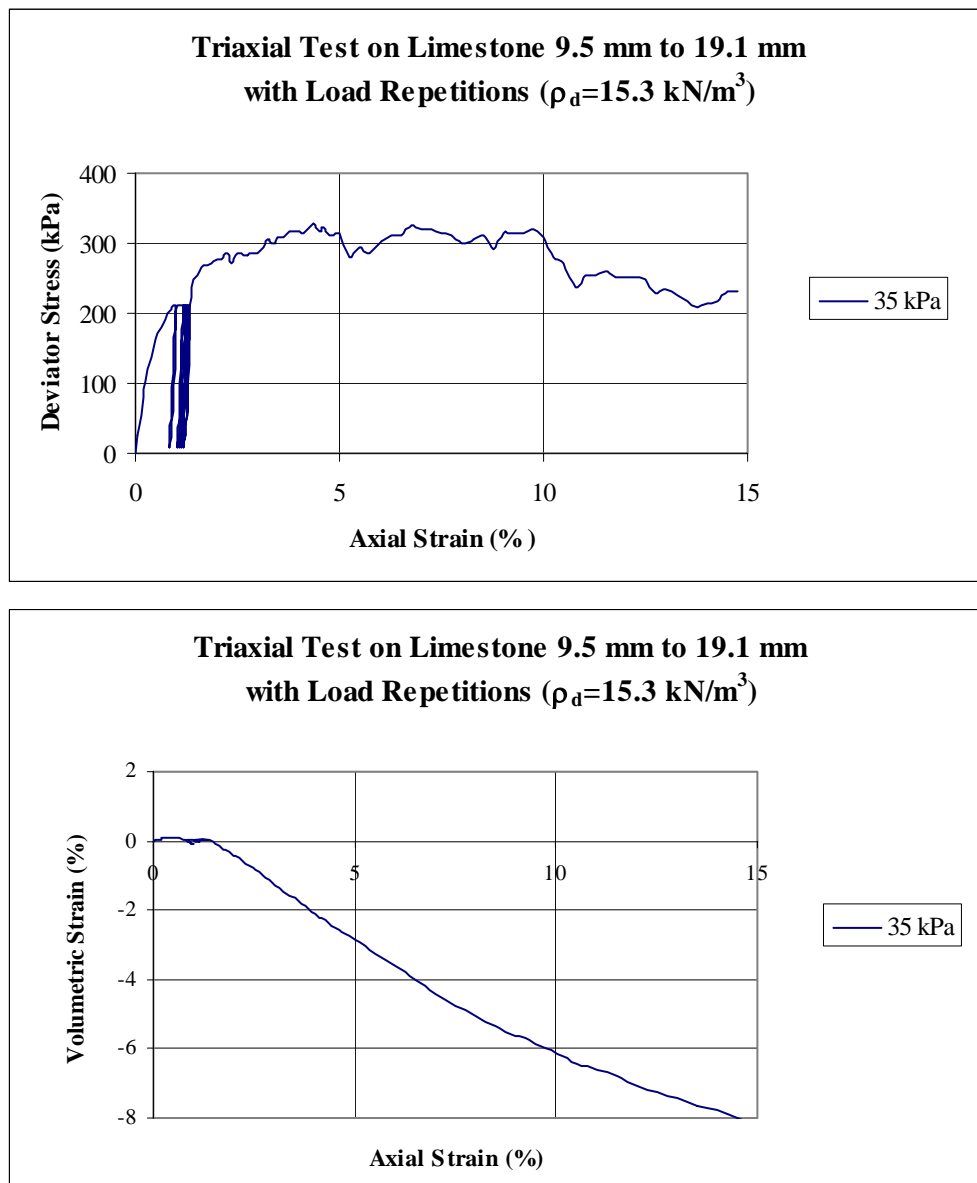


Figure 5.79 A typical quasi-cyclic stress-strain response curve

## CHAPTER VI

### HYPERBOLIC MODELING AND PLASTIC STRAIN BEHAVIOR OF SCALED-DOWN MATERIALS

#### 6.1 Introduction

This chapter presents the modeling of stress-strain behavior with unloading-reloading using the hyperbolic model of scaled-down materials analyzed in Chapter V. This is a versatile model which is identified in Equation (2.13) by Duncan and Chang (1970). As a reminder the equations in Chapter II required in this chapter are given below:

$$\varepsilon_N = \varepsilon_1 (1 + C \log N) \quad (2.11)$$

where,  $\varepsilon_N$  is the accumulated axial plastic strain at any cycle;  $\varepsilon_1$  is the axial plastic strain after the first cycle;  $C$  is a material constant, named as plastic strain slope; and  $N$  is the number of load applications.

$$\varepsilon_1 = \varepsilon_a - \varepsilon_r \quad (2.12)$$

in which  $\varepsilon_a$  is the axial strain under the applied deviator stress,  $(\sigma_1 - \sigma_3)$ , and  $\varepsilon_r$  is the recoverable or resilient strain upon unloading.

$$\varepsilon_a = \frac{(\sigma_1 - \sigma_3) / E_i}{1 - \frac{(\sigma_1 - \sigma_3)(1 - \sin \phi) R_f}{2(c \cos \phi + \sigma_3 \sin \phi)}} \quad (2.13)$$

where,  $c$  is the apparent cohesion;  $\phi$  is the angle of internal friction;  $R_f$  is the failure ratio as shown by

$$(\sigma_1 - \sigma_3)_f = R_f (\sigma_1 - \sigma_3)_{ult} \quad (2.14)$$

where,  $(\sigma_1 - \sigma_3)_f$  = the maximum stress difference or the stress difference at failure obtained from conventional triaxial test;  $(\sigma_1 - \sigma_3)_{ult}$  = the asymptotic value of stress difference for the corresponding hyperbola obtained from the test data.  $R_f$  always has a value less than unity.

The aim is to estimate the axial strain,  $\epsilon_a$ , associated with the axial stress within the working stress range and the recoverable strain,  $\epsilon_r$ , upon unloading, and thus the plastic strain after the first cycle,  $\epsilon_1$ , can be calculated using Equation (2.12). This chapter also presents, as was introduced in section 5.13 of the previous chapter, the accumulated plastic strain results of the repeated load tests conducted on the scaled-down materials. The entire test program is included in Table 4.10. The tests were performed only at a confining stress of 35 kPa for each of scaled-down samples. All experiment results related to the quasi-cyclic stress-strain response curves are shown in Appendix. The results after analysis are used in the calibration of the parameter the plastic strain slope,  $C$ , in Equation 2.11. Then the plastic strain slopes are correlated for the scaled-down gradations to later enable the prediction of the plastic strain,  $\epsilon_N$ , of both the scaled-down and the prototype ballast materials. At the end, the predicted results of the prototype materials used in this study are compared to the experimental results of those found in the literature.

## 6.2 Hyperbolic Modeling of Scaled-Down Ballast Materials

The parameters required in the hyperbolic model, except the failure ratio,  $R_f$ , given in Equation 2.14 have been determined for all scaled-down materials used in this study in the foregoing chapter. The failure ratio is calibrated with respect to 90%

of the maximum deviator stress for each test to back-predict the stress-strain behavior obtained from experiments.

The value of failure ratio,  $R_f$ , was found to be 0.81, 0.87 and 0.84 for series of L-2.36, L-4.75 and L-9.5 respectively, with an average value of  $0.84 \pm 0.03$ ; 0.83, 0.85 and 0.93 for series of B-2.36, B-4.75 and B-9.5, respectively, with an average value of  $0.87 \pm 0.05$ ; and 0.90, 0.72 and 0.91 for series of S-4.75, S-6.35 and L-9.5, respectively, with an average value of  $0.83 \pm 0.11$ . For the prototype gradations, the average values were taken as the failure ratio.

From Table 6.1 to Table 6.3 provide a summary of the scaled-down material parameters with the predicted values for the prototype sizes obtained in the previous chapter, and the failure ratio of hyperbolic model to predict the stress-strain behavior for the series of crushed limestone, basalt and steel-slag respectively.

Table 6.1 Summary of the parameters used in hyperbolic model for the limestone

Gradation	Hyperbolic Model Parameters				
	$\phi$ , deg.	c, kPa	K	n	$R_f$
L-2.36 ( $D_{50} = 3.15$ mm)	44.6	32.5	3796	0.615	0.81
L-4.75 ( $D_{50} = 6.35$ mm)	44.6	32.5	4212	0.624	0.87
L-9.5 ( $D_{50} = 12.7$ mm)	44.6	32.5	4674	0.634	0.84
L-15 $D_{50} = 30$ mm	44.6	32.5	5329	0.645	0.83
L-30 $D_{50} = 45$ mm	44.6	32.5	5673	0.651	0.83

Table 6.2 Summary of the parameters used in hyperbolic model for the basalt

Gradation	Hyperbolic Model Parameters				
	$\phi$ , deg.	c, kPa	K	n	$R_f$
B-2.36 ( $D_{50} = 3.15$ mm)	46.3	34.2	10480	0.400	0.83
B-4.75 ( $D_{50} = 6.35$ mm)	46.3	34.2	11264	0.413	0.85
B-9.5 ( $D_{50} = 12.7$ mm)	46.3	34.2	12106	0.425	0.93
B-15 ( $D_{50} = 30$ mm)	46.3	34.2	13246	0.442	0.87
B-30 ( $D_{50} = 45$ mm)	46.3	34.2	13826	0.450	0.87

Table 6.3 Summary of the parameters used in hyperbolic model for the steel-slag

Gradation	Hyperbolic Model Parameters				
	$\phi$ , deg.	c, kPa	K	n	$R_f$
S-4.75 ( $D_{50} = 6.35$ mm)	42.7	35.4	4786	0.632	0.90
S-6.35 ( $D_{50} = 9.5$ mm)	42.7	35.4	4786	0.632	0.72
S-9.5 ( $D_{50} = 12.7$ mm)	42.7	35.4	4786	0.632	0.91
S-15 ( $D_{50} = 30$ mm)	42.7	35.4	4786	0.632	0.83
S-30 ( $D_{50} = 45$ mm)	42.7	35.4	4786	0.632	0.83

Presented are comparisons between the experimental and back-predicted stress-strain curves using Equation (2.11) for each series of scaled-down limestone in Figures from 6.1 through 6.3; for those of basalt in Figures from 6.4 through 6.6; and for each series of scaled-down steel-slag in Figures from 6.7 through 6.9. The unloading-reloading part of the stress-strain curves was excluded from the figures to avoid contamination. As can be seen, the experimental and back-predicted curves are in very close agreement. It is important, however, to note that the hyperbolic model is not valid beyond the peak of the stress-strain diagram. This is because the hyperbola cannot capture the post-peak strain softening behavior.

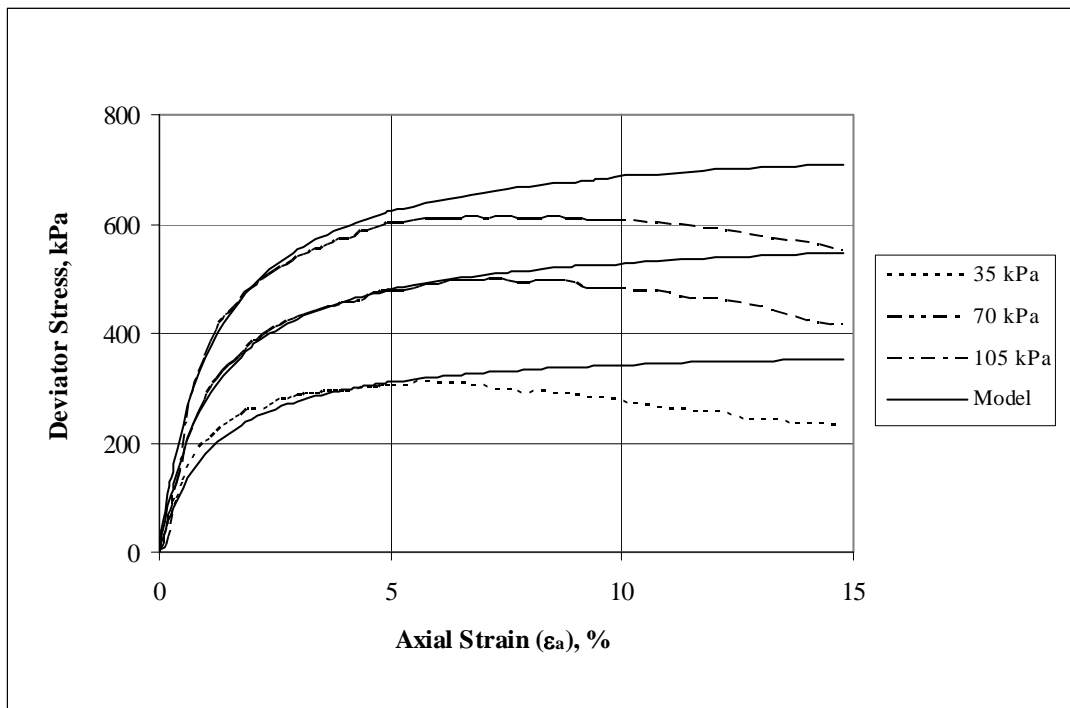


Figure 6.1 Back-prediction of the behavior of L-2.36 (Limestone 2.36 - 4.75 mm)

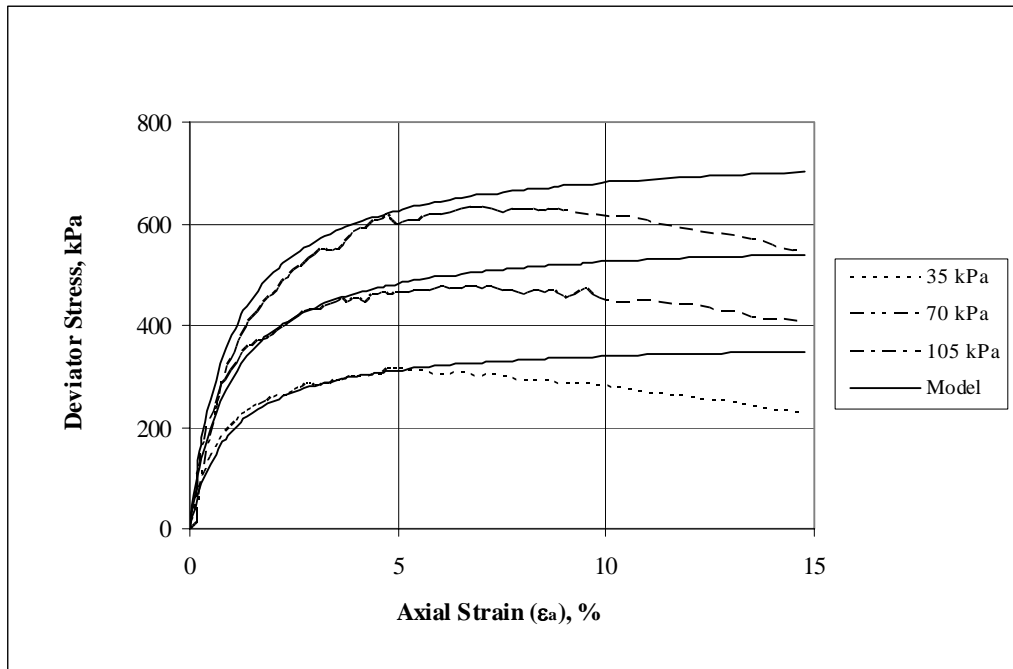


Figure 6.2 Back-prediction of the behavior of L-4.75 (Limestone 4.75 - 9.5 mm)

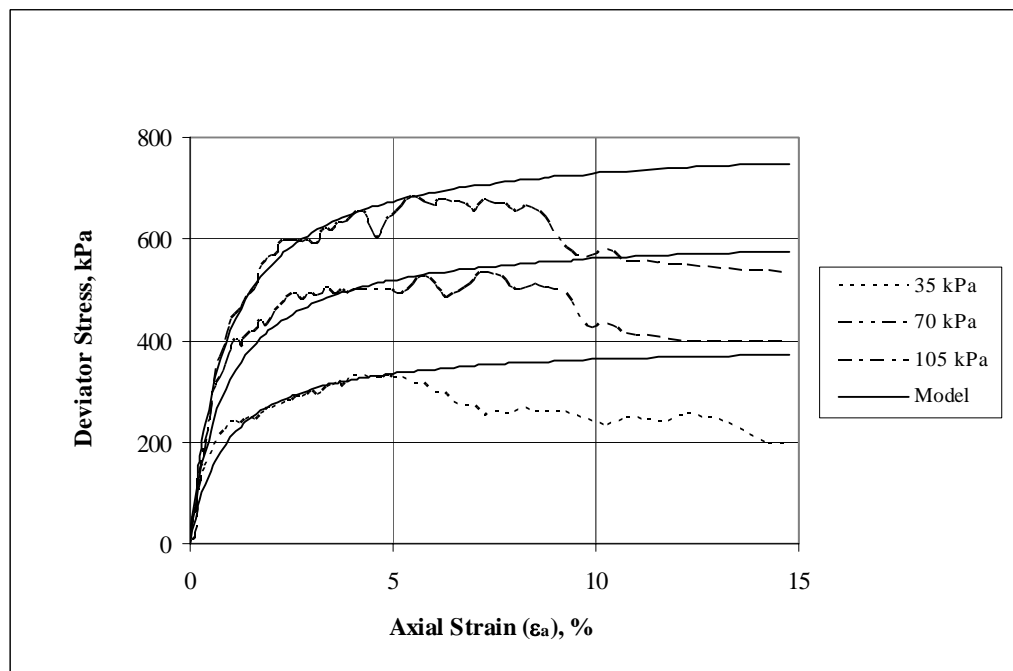


Figure 6.3 Back-prediction of the behavior of L-9.5 (Limestone 9.5 - 19.0 mm)

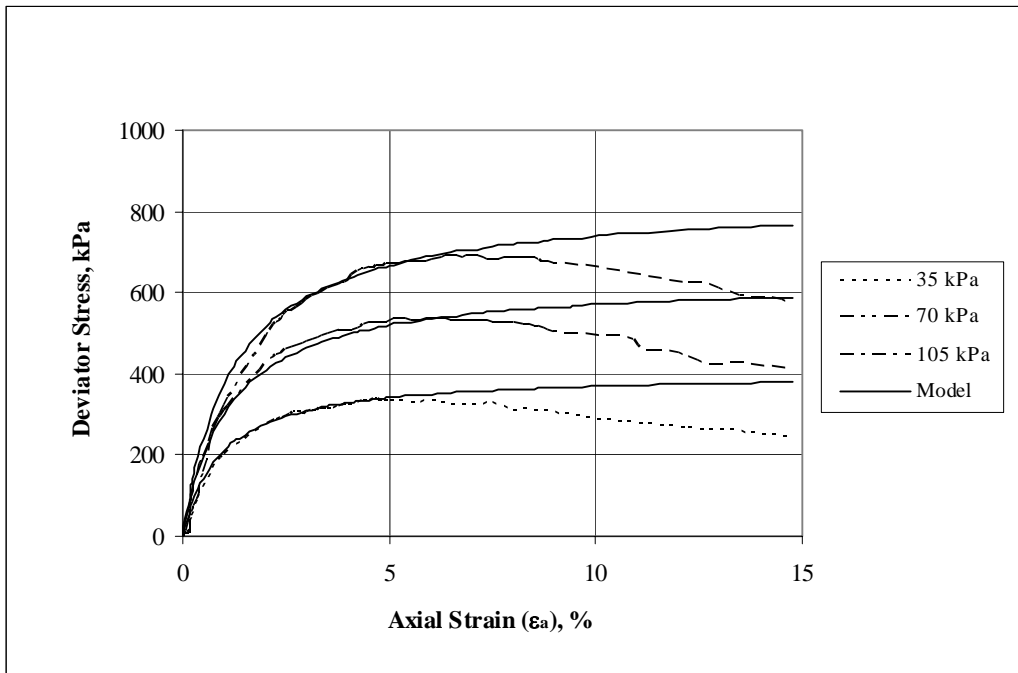


Figure 6.4 Back-prediction of the behavior of B-2.36 (Basalt 2.36 - 4.75 mm)

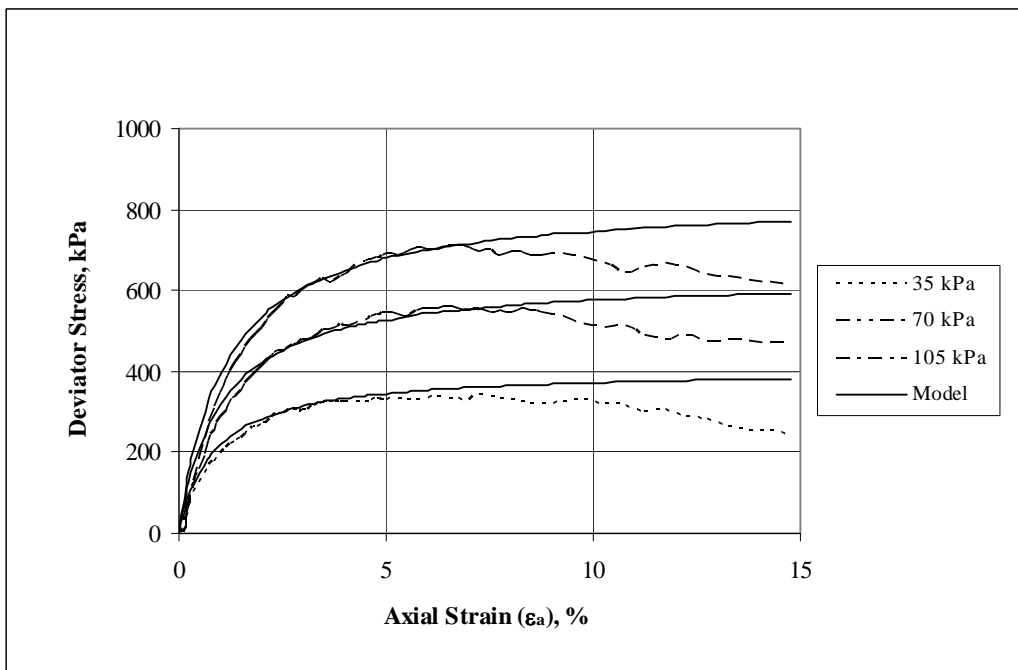


Figure 6.5 Back-prediction of the behavior of B-4.75 (Basalt 4.75 - 9.5 mm)

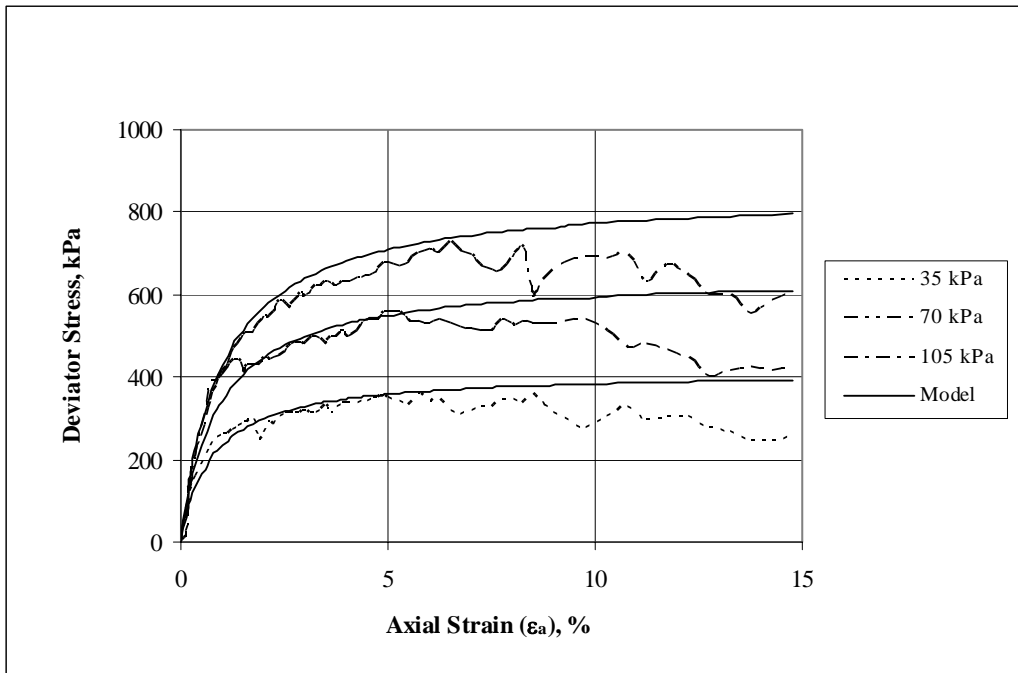


Figure 6.6 Back-prediction of the behavior of B-9.5 (Basalt 9.5 - 19.0 mm)

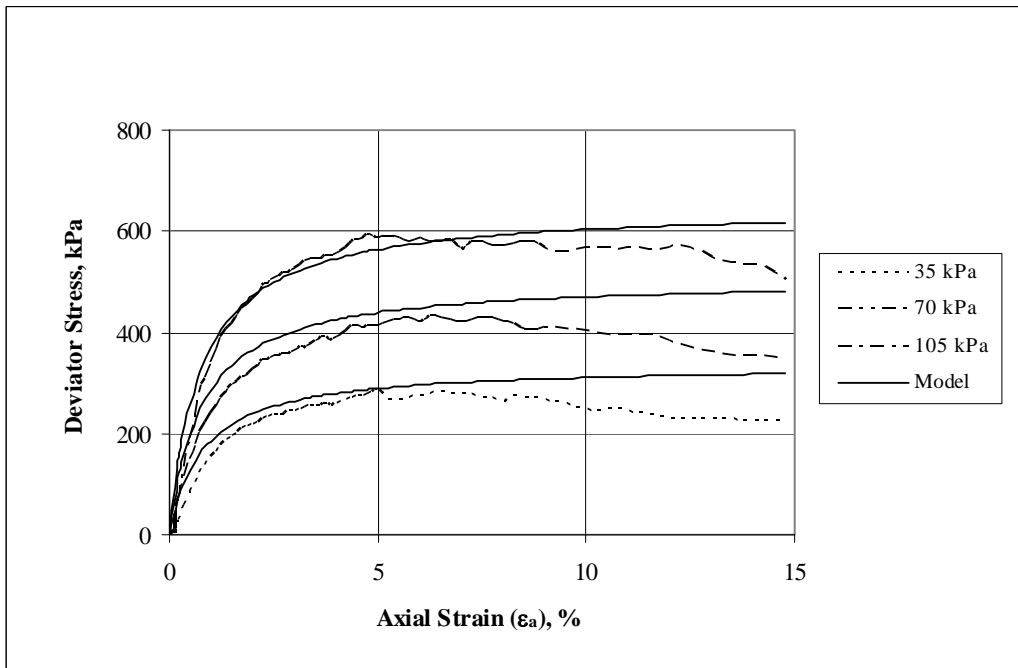


Figure 6.7 Back-prediction of the behavior of S-4.75 (Steel-Slag 4.75 - 9.5 mm)

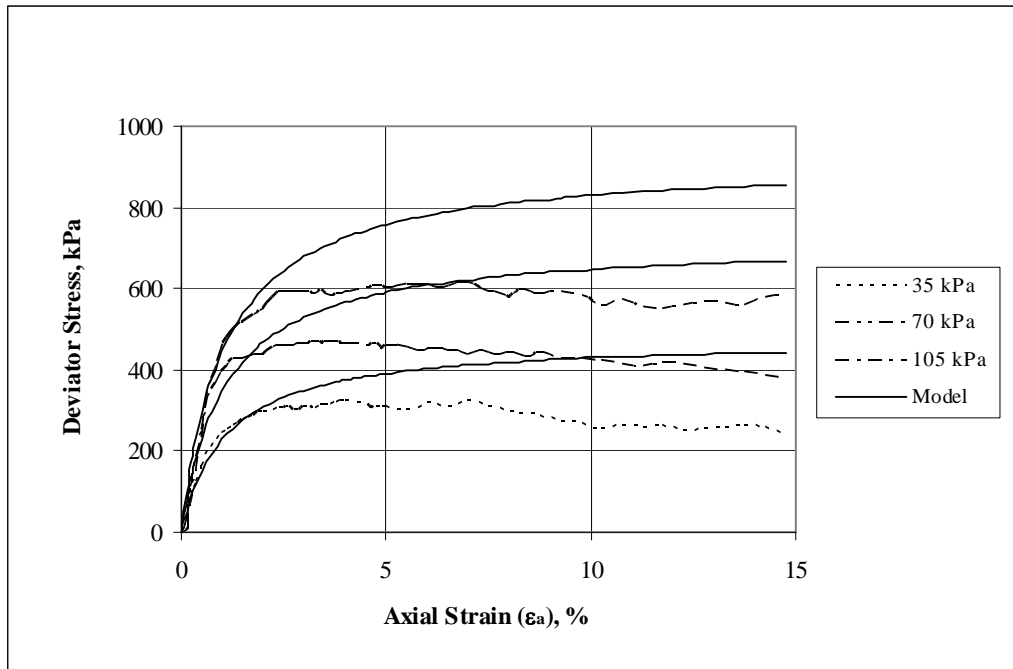


Figure 6.8 Back-prediction of the behavior of S-6.35 (Steel-Slag 6.35 - 12.7 mm)

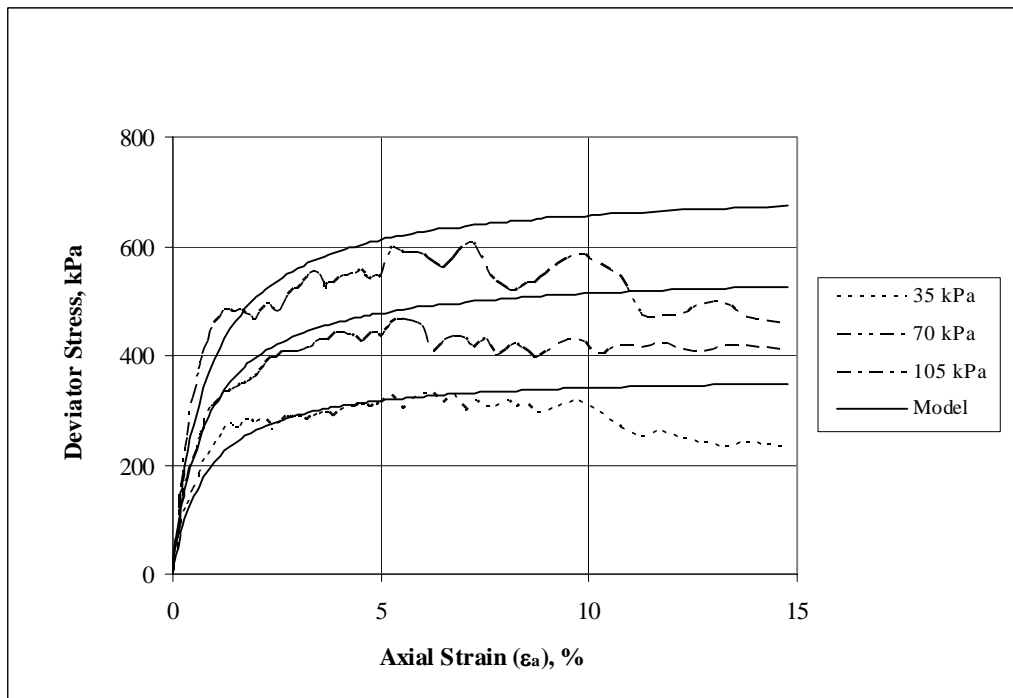


Figure 6.9 Back-prediction of the behavior of S-9.5 (Steel-Slag 9.5 - 19.0 mm)

The unloading–reloading elastic modulus parameters obtained in the previous chapter are rearranged and listed in Table 6.4 to predict the unloading-reloading part of the stress-strain behavior for the series of crushed limestone; Table 6.5 for those of crushed basalt; and Table 6.6 for the series of crushed steel-slag.

Table 6.4 Summary of the unloading-reloading moduli parameters for the limestone

Gradation	Unloading-Reloading Parameters	
	K	n
L-2.36 ( $D_{50} = 3.15$ mm)	17038	0.465
L-4.75 ( $D_{50} = 6.35$ mm)	23513	0.414
L-9.5 ( $D_{50} = 12.7$ mm)	32674	0.369
L-15 ( $D_{50} = 30$ mm)	49877	0.321
L-30 ( $D_{50} = 45$ mm)	61249	0.300

Table 6.5 Summary of the unloading-reloading moduli parameters for the basalt

Gradation	Unloading-Reloading Parameters	
	K	n
B-2.36 ( $D_{50} = 3.15$ mm)	42963	0.252
B-4.75 ( $D_{50} = 6.35$ mm)	35934	0.295
B-9.5 ( $D_{50} = 12.7$ mm)	30200	0.382
B-15 ( $D_{50} = 30$ mm)	24446	0.617
B-30 ( $D_{50} = 45$ mm)	22157	0.821

Table 6.6 Summary of the unloading-reloading moduli parameters for the steel-slag

Gradation	Unloading-Reloading Parameters	
	K	n
S-4.75 ( $D_{50} = 6.35$ mm)	26303	0.400
S-6.35 ( $D_{50} = 9.5$ mm)	26303	0.400
S-9.5 ( $D_{50} = 12.7$ mm)	26303	0.400
S-15 ( $D_{50} = 30$ mm)	26303	0.400
S-30 ( $D_{50} = 45$ mm)	26303	0.400

Figures from 6.10 to 6.12 present the comparisons between the experimental and the back-predicted unloading-reloading curves for the scaled-down limestone L-2.36, L-4.75 and L-9.5, respectively, approximately at an axial strain of 1% and under a confining stress of 35 kPa. For the scaled-down basalt of B-2.36, B-4.75 and B-9.5 the comparisons of the experimental and the back-predicted unloading-reloading curves are illustrated, respectively, in Figures 6.13, 6.14 and 6.15, and Figures from 6.13 to 6.15 show the comparisons for the scaled-down steel-slag of S-4.75, S-6.35 and S-9.5, respectively. It may be noted that unloading-reloading curves are slightly hysteretic, otherwise are almost linear. So, the experimental and back-predicted curves are in close agreement.

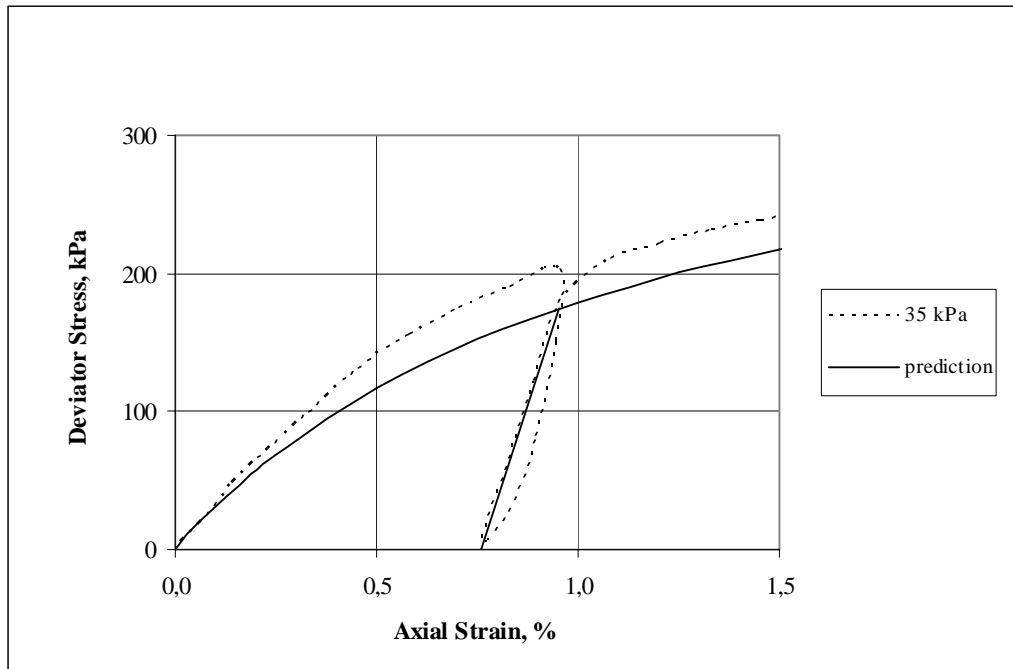


Figure 6.10 Back-prediction of the unloading-reloading behavior for L-2.36

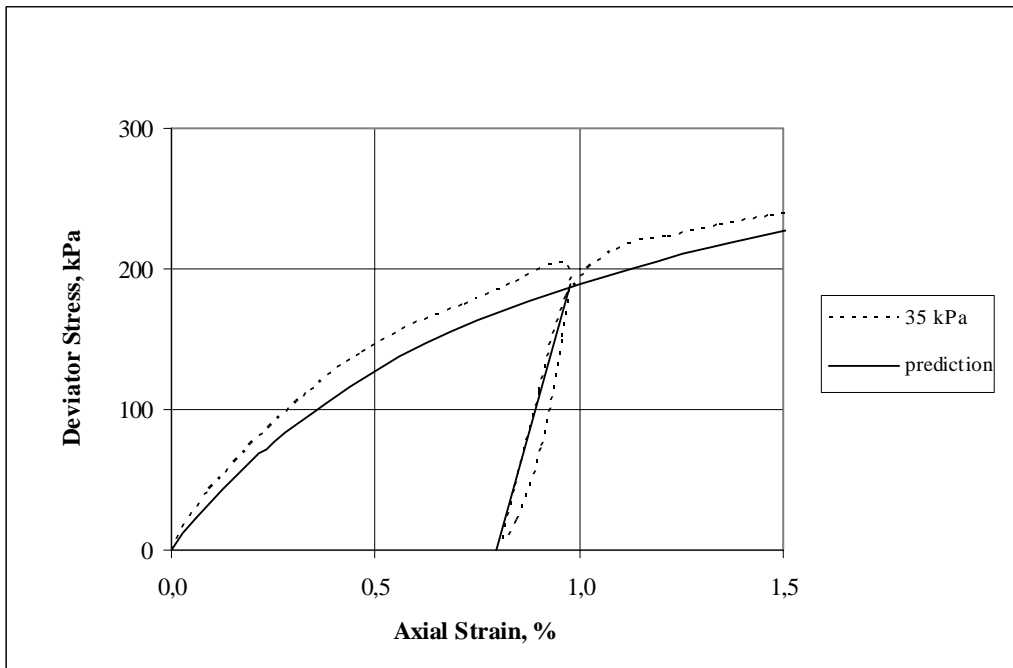


Figure 6.11 Back-prediction of the unloading-reloading behavior for L-4.75

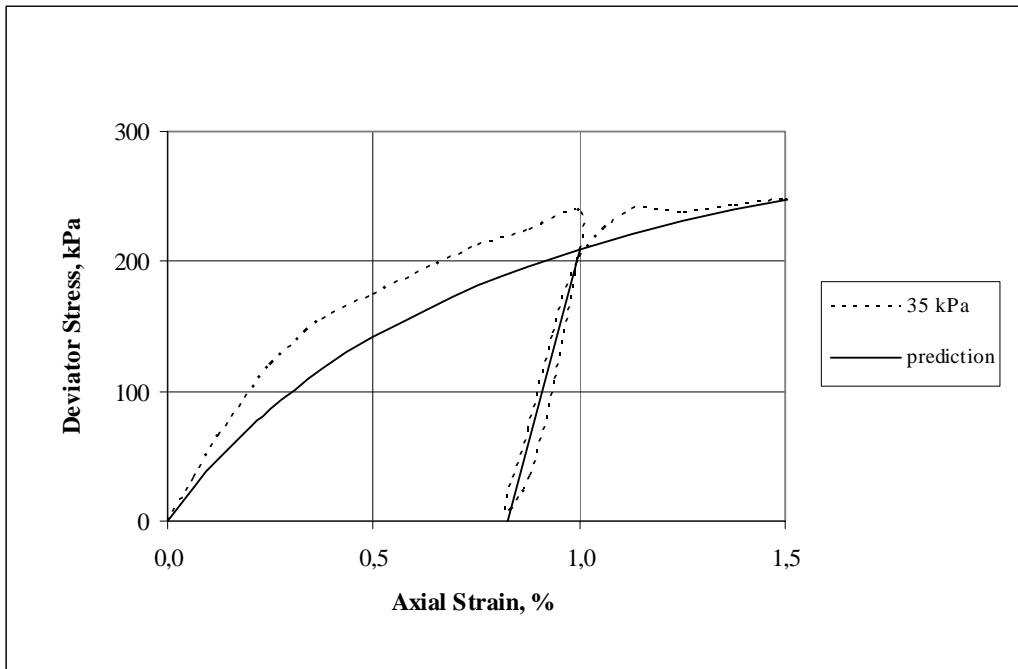


Figure 6.12 Back-prediction of the unloading-reloading behavior for L-9.5

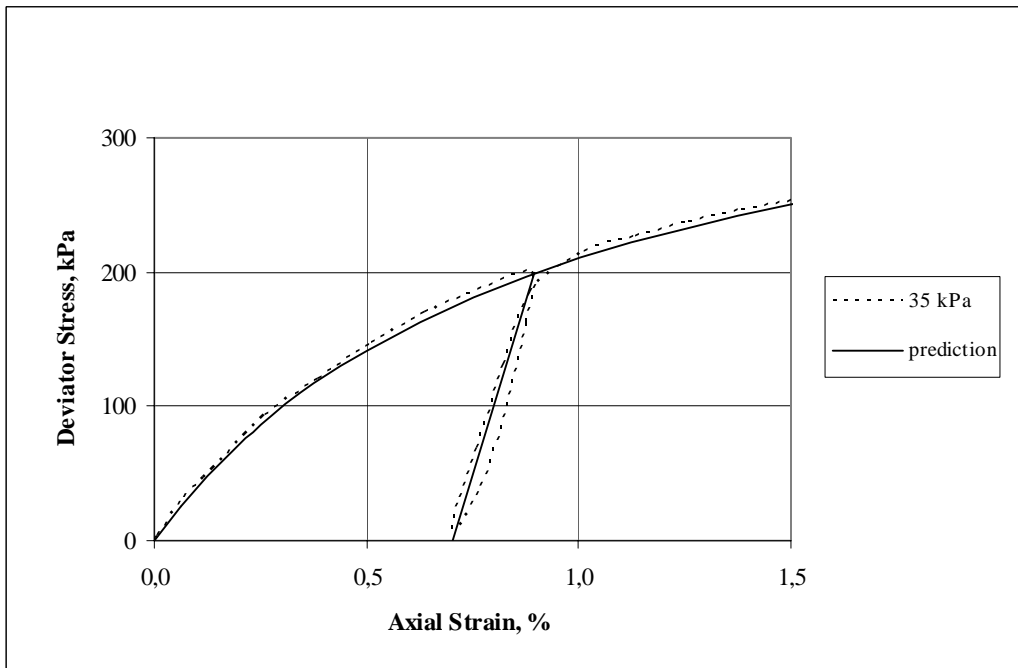


Figure 6.13 Back-prediction of the unloading-reloading behavior for B-2.36

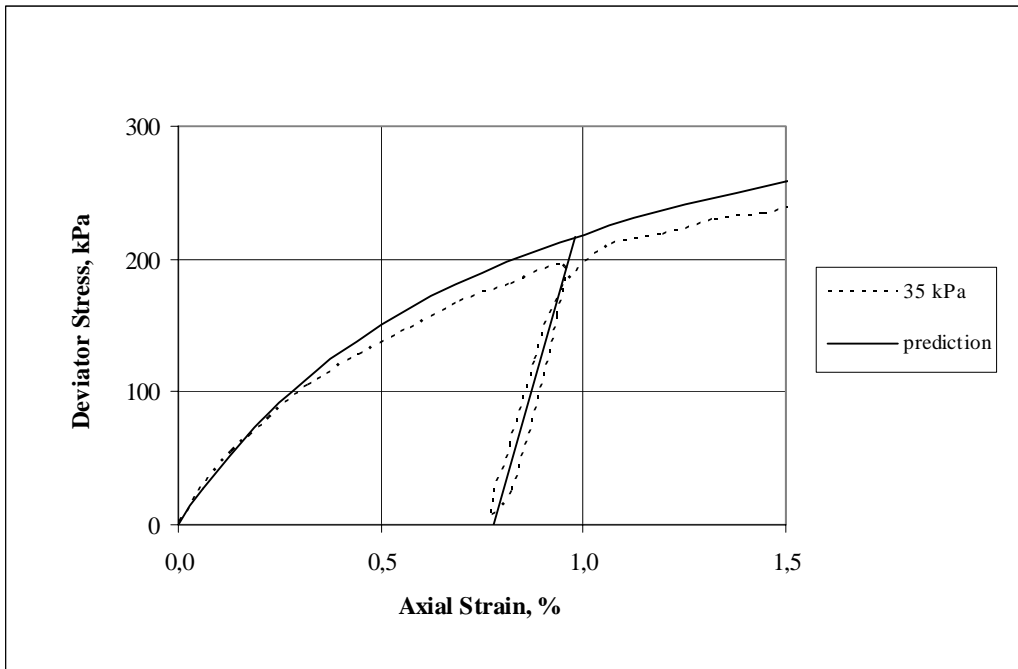


Figure 6.14 Back-prediction of the unloading-reloading behavior for B-4.75

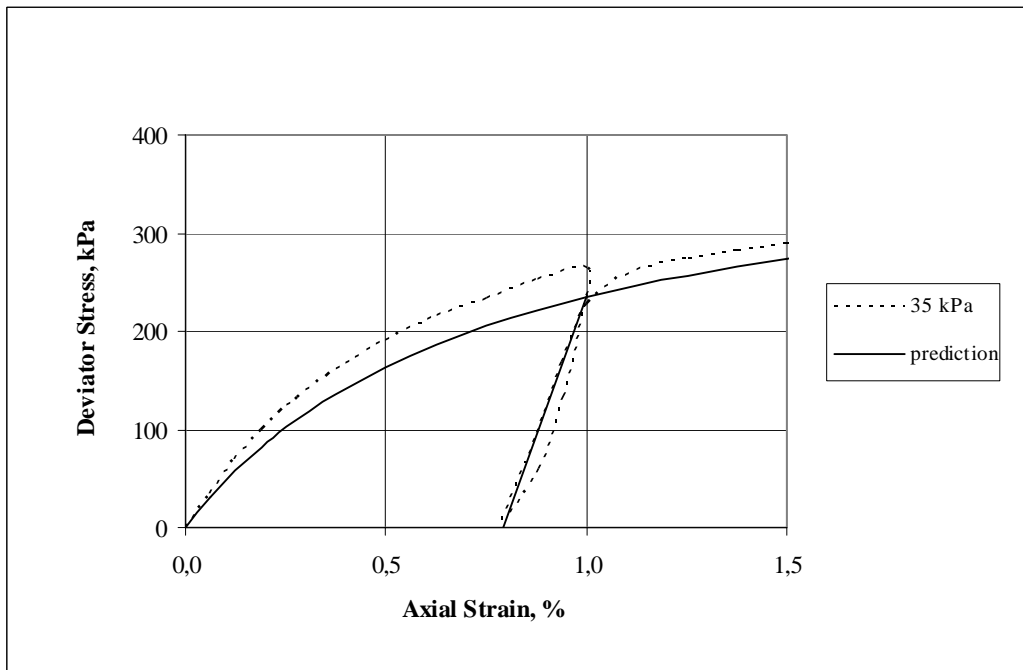


Figure 6.15 Back-prediction of the unloading-reloading behavior for B-9.5

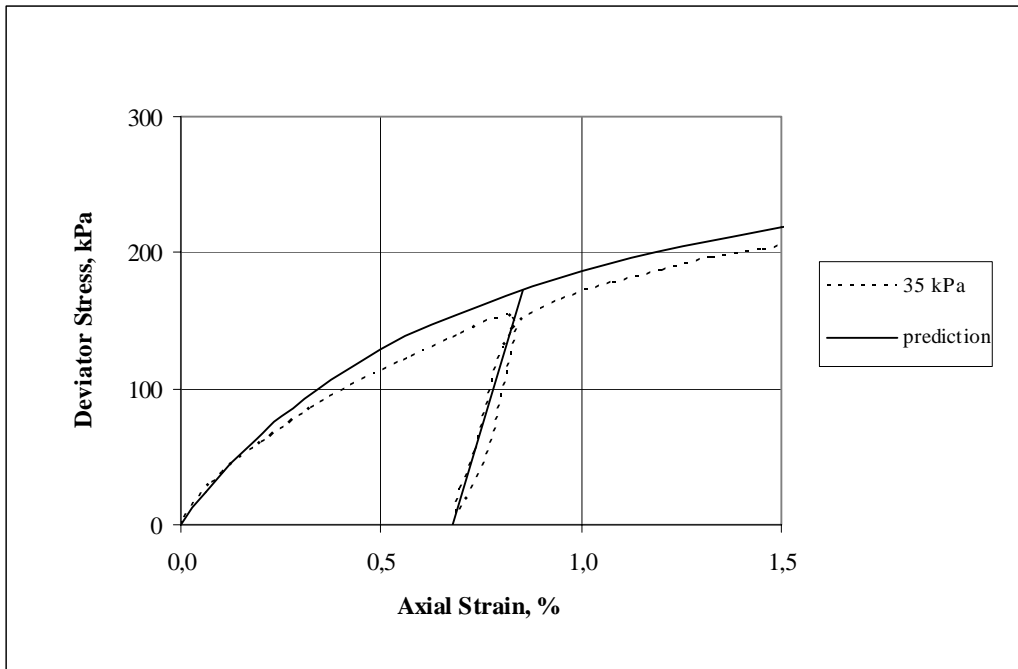


Figure 6.16 Back-prediction of the unloading-reloading behavior for S-4.75

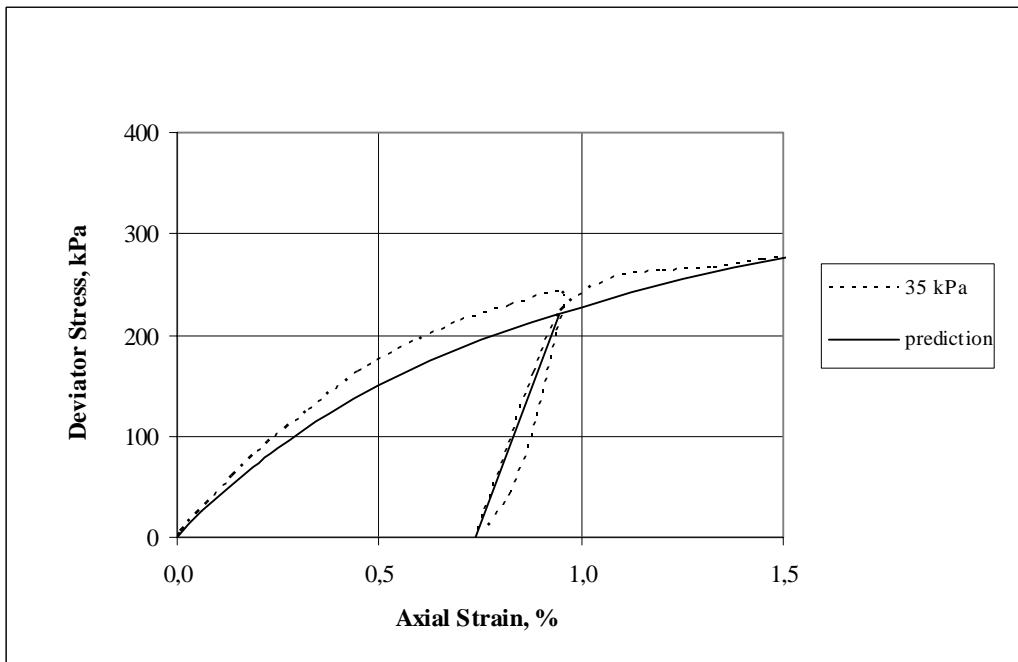


Figure 6.17 Back-prediction of the unloading-reloading behavior for S-6.35

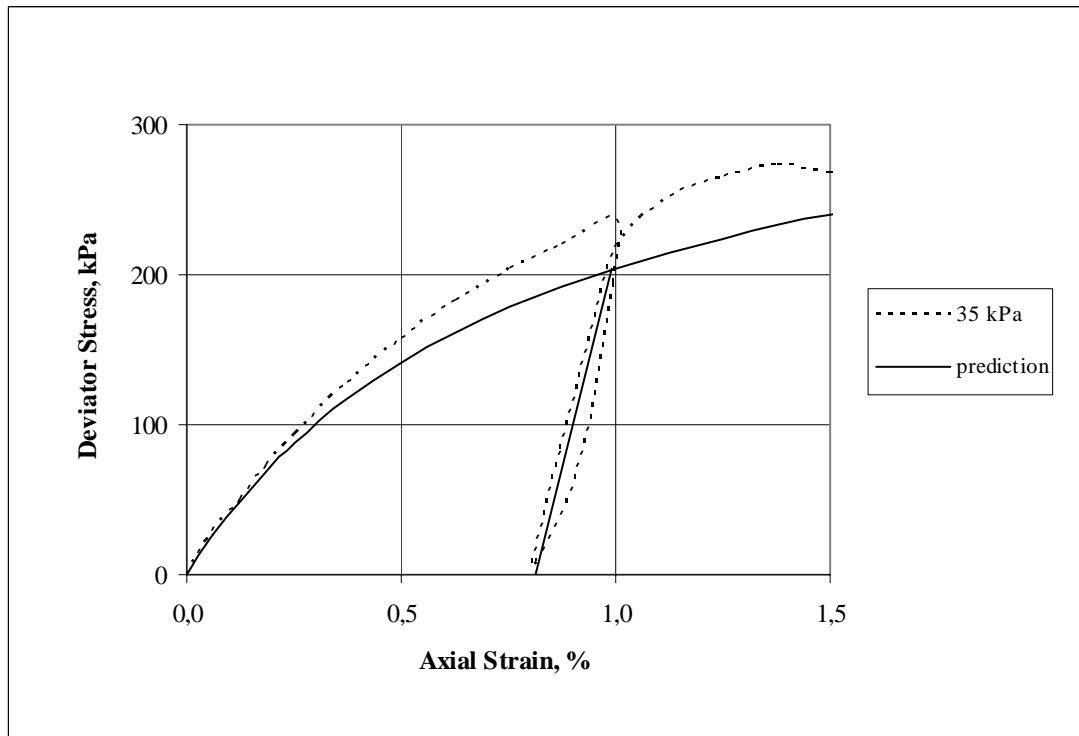


Figure 6.18 Back-prediction of unloading-reloading behavior for S-9.5

Now, the plastic strain after first cycle,  $\epsilon_1$ , within the range of working stress can be calculated. From Table 6.7 to Table 6.9 list the predicted axial strain,  $\epsilon_a$ , recoverable (or resilient) strain,  $\epsilon_r$ , and plastic strain after first cycle,  $\epsilon_1$ , using Equations (2.11) to (2.14) for the series of crushed limestone, basalt, and steel-slag, respectively, at a deviator stress  $(\sigma_1 - \sigma_3) \approx 200$  kPa which is approximately associated with 1% axial strain under a confining stress,  $\sigma_3 = 35$  kPa.

Table 6.7 Predicted plastic strain after first cycle at  $\sigma_3 = 35$  kPa and  
 $(\sigma_1 - \sigma_3) \approx 200$  kPa for series of crushed limestone

Gradation	Axial Strain ( $\epsilon_a$ ), %	Recoverable Strain ( $\epsilon_r$ ), %	Plastic Strain after First Cycle ( $\epsilon_1$ ), %
L-2.36 ( $D_{50} = 3.15$ mm)	1.18	0.22	0.96
L-4.75 ( $D_{50} = 6.35$ mm)	1.03	0.20	0.84
L-9.5 ( $D_{50} = 12.7$ mm)	0.90	0.16	0.74
L-15 ( $D_{50} = 30$ mm)	0.76	0.13	0.63
L-30 ( $D_{50} = 45$ mm)	0.70	0.11	0.59

Table 6.8 Predicted plastic strain after first cycle at  $\sigma_3 = 35$  kPa and  
 $(\sigma_1 - \sigma_3) = 200$  kPa for series of crushed basalt

Gradation	Axial Strain ( $\epsilon_a$ ), %	Recoverable Strain ( $\epsilon_r$ ), %	Plastic Strain after First Cycle ( $\epsilon_1$ ), %
B-2.36 ( $D_{50} = 3.15$ mm)	0.89	0.19	0.69
B-4.75 ( $D_{50} = 6.35$ mm)	0.79	0.19	0.60
B-9.5 ( $D_{50} = 12.7$ mm)	0.70	0.18	0.53
B-15 ( $D_{50} = 30$ mm)	0.61	0.15	0.46
B-30 ( $D_{50} = 45$ mm)	0.56	0.13	0.43

Table 6.9 Predicted plastic strain after first cycle at  $\sigma_3 = 35$  kPa and  
 $(\sigma_1 - \sigma_3) \approx 200$  kPa for series of crushed steel-slag

Gradation	Axial Strain ( $\epsilon_a$ ), %	Recoverable Strain ( $\epsilon_r$ ), %	Plastic Strain after First Cycle ( $\epsilon_1$ ), %
S-4.75 ( $D_{50} = 6.35$ mm)	0.94	0.18	0.75
S-6.35 ( $D_{50} = 9.5$ mm)	0.94	0.18	0.75
S-9.5 ( $D_{50} = 12.7$ mm)	0.94	0.18	0.75
S-15 ( $D_{50} = 30$ mm)	0.94	0.18	0.75
S-30 ( $D_{50} = 45$ mm)	0.94	0.18	0.75

Examining Table 6.7 to Table 6.9 indicates that the plastic strains after first cycle,  $\epsilon_1$ , decreased as the mean particle size increased. This was similar to the results obtained by Janardhanam and Desai (1983) for gneiss materials using slow cyclic stress-controlled tests and Kaya et al. (1997) for quartzite ballast material using a conventional triaxial test. Using the analysis technique suggested in 5.2.1, it is possible to obtain a best-fit for the plastic strains after first cycle,  $\epsilon_1$ , given in Table 6.7 to Table 6.9 for crushed limestone, basalt and steel-slag, respectively. The following equation was obtained to predict the plastic strain after first cycle for crushed limestone;

$$\epsilon_1 = -0.0079(D_{50}) + 0.9033 \quad (6.1)$$

and for crushed basalt;

$$\epsilon_1 = -0.0056(D_{50}) + 0.6494 \quad (6.2)$$

and for crushed steel-slag;

$$\varepsilon_1 = 0.75 \quad (6.3)$$

### 6.3 Accumulated Plastic Strain Trends of Materials

#### 6.3.1 Accumulated Plastic Strain Trends of Scaled-down Limestone

The results of the plastic strain accumulated with the number of load application for all scaled-down limestone, L-2.36, L-4.75 and L-9.5 are illustrated, respectively in Figure 6.19 to Figure 6.21. In these figures, the accumulated plastic strain, after the plastic strain due to the first cycle of load application was deducted, was drawn against the number of load applications.

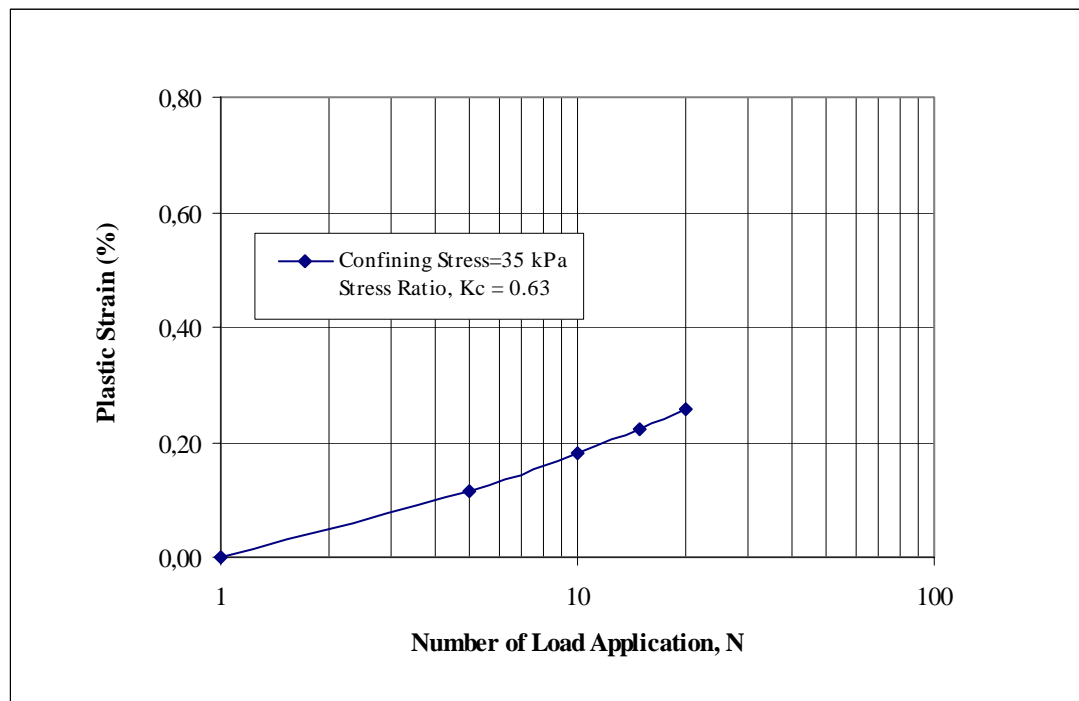


Figure 6.19 Accumulated plastic strain trend for L-2.36

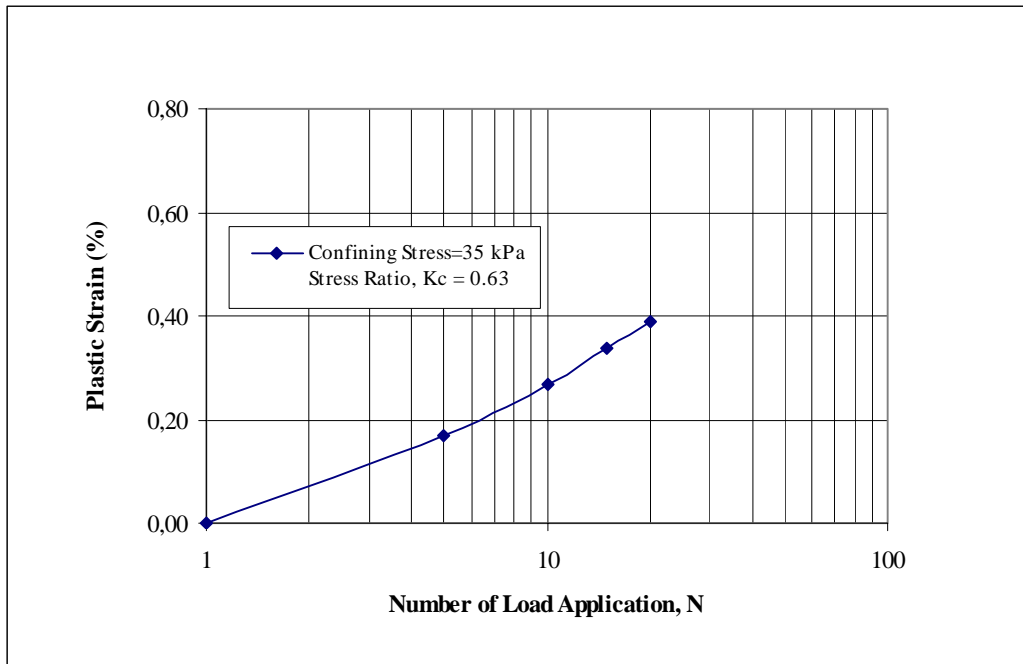


Figure 6.20 Accumulated plastic strain trend for L-4.75

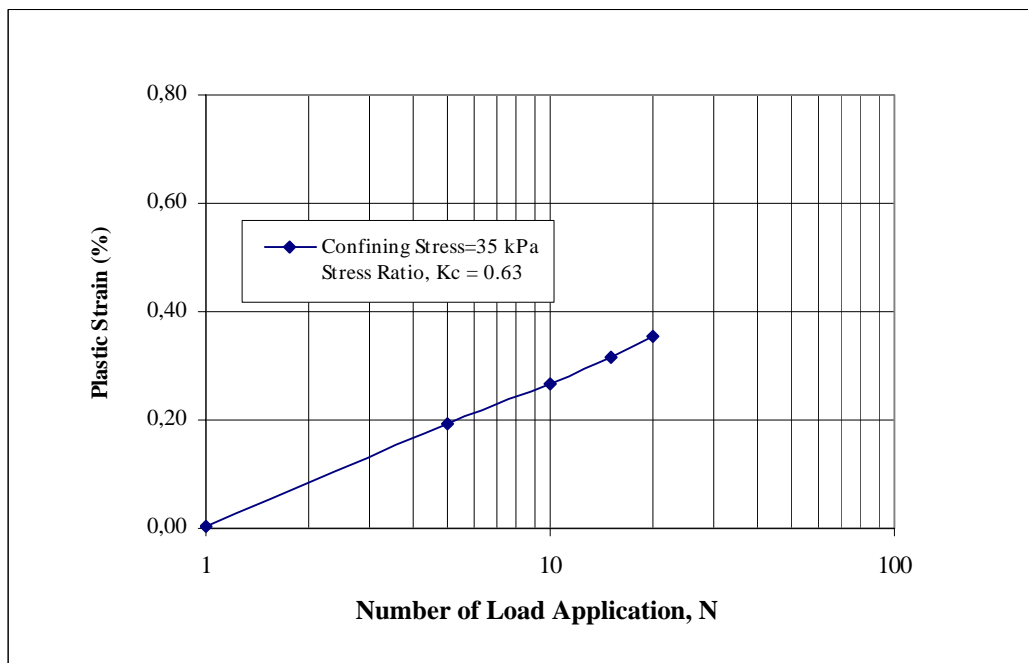


Figure 6.21 Accumulated plastic strain trend for L-9.5

Using the regression analysis technique suggested in 5.2.1, it is possible to fit the data for L-2.36, L-4.75 and L-9.5 to linear best-lines. The parameter of the best-fit is the slope. It is corrected with the corresponding plastic strain after first cycle,  $\epsilon_1$ , values of 0.96; 0.84; 0.74 given in Table 6.7 at a deviator stress  $(\sigma_1 - \sigma_3) \approx 200$  kPa for each scaled-down limestone to get the plastic strain slope, C, in Equation 2.11. The applied deviator stress corresponds to a stress ratio,  $K_c$ , of 0.63, which is the ratio of applied deviator stress to deviator stress at failure. Table 6.10 lists the plastic strain slope, C, values for all of the scaled-down limestone. The coefficient of determination,  $R^2$ , above 0.9 indicates a good correlation of linear fit to the data for each of scaled-down limestone.

Table 6.10 Plastic strain slope values for the scaled-down limestone at  $\sigma_3 = 35$  kPa and  $(\sigma_1 - \sigma_3) \approx 200$  kPa

Gradation	Plastic Strain Slope (C)	Coefficient of Determination, $R^2$
L-2.36	0.20	0.987
L-4.75	0.34	0.984
L-9.5	0.37	0.999

The question is that how the plastic strain varies with the change in mean particle size of limestone, and whether a trend with respect to mean particle size can be obtained. Figure 6.22 shows the variation of the plastic strain slope, C, with the mean particle size of the scaled-down limestone samples. The tendency of the plastic strain slope is fitted with a linear best-line to the data. The corresponding equation for C of the accumulated plastic strain depicted in Figure 6.22 is given in Equation (6.4). The coefficient of determination,  $R^2$ , is found as 0.879 for C.

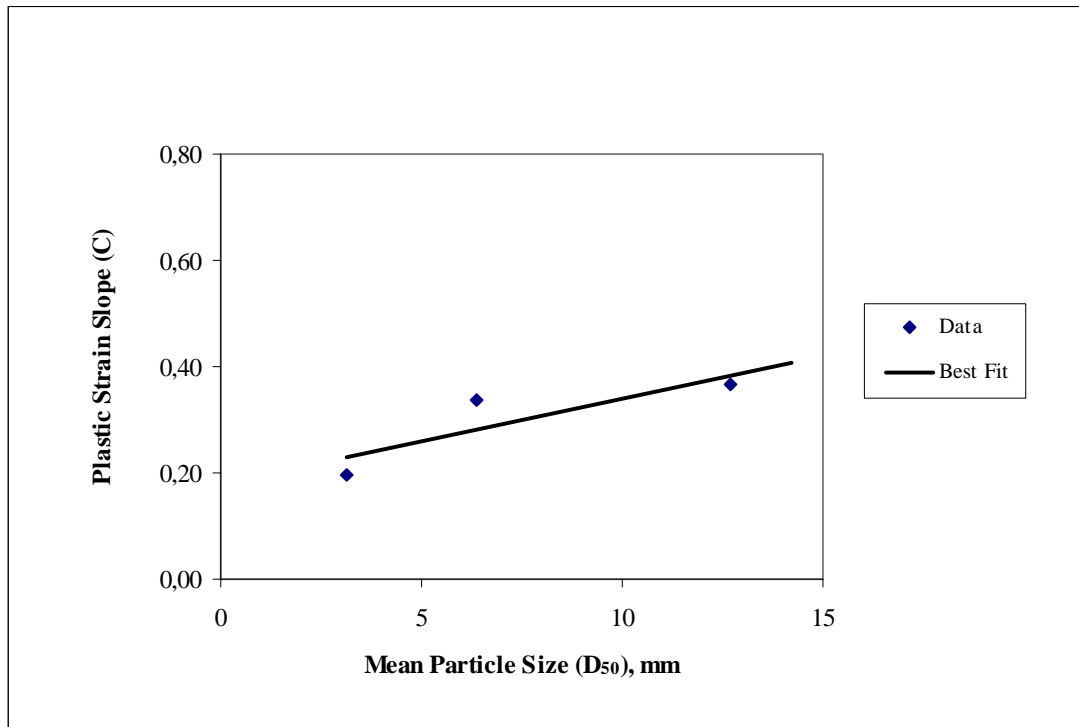


Figure 6.22 Variation of plastic strain slope with mean particle size for the limestone

$$C = 0.0159(D_{50}) + 0.1809 \quad ; \quad R^2 = 0.729 \quad (6.4)$$

Table 6.11 compares the predicted plastic strain values using Equation (2.11) to that of experimental values accumulated after 20 cycles of load for all scaled-down limestone.

Examining Table 6.11 shows that the maximum difference in accumulated plastic strain after 20 cycles of load between the predicted and the experimental values is 3.6%. So, the representation of the values of the plastic strain for limestone is reasonable for engineering estimation purposes.

Table 6.11 Comparison of accumulated plastic strains for scaled-down limestone after  $N = 20$

Gradation	Accumulated Plastic Strain ( $\epsilon_N$ ), %		Difference Between Predicted and Experimental, %
	Predicted	Experimental	
L-2.36	1.14	1.10	3.6
L-4.75	1.16	1.16	0.0
L-9.5	1.20	1.19	0.9

Table 6.12 compares the accumulated plastic strain predicted again by Equation (2.11) to that obtained experimentally by Knutson and Thompson (1978) after 5000 cycles of load at a stress ratio,  $K_c$ , of 0.6 for the mean size  $D_{50} = 30$  mm of crushed limestone. Table 6.12 also includes the predicted plastic strain values for the prototype size  $D_{50} = 45$  mm and the values of plastic strain slope for  $D_{50} = 30$  mm and  $D_{50} = 45$  mm.

Table 6.12 Comparison of accumulated plastic strains for limestone prototype sizes after  $N = 5000$

Mean Particle Size ( $D_{50}$ ), mm	Predicted Plastic Strain Slope (C)	Accumulated Plastic Strain ( $\epsilon_N$ ), %		Difference Between Predicted and Experimental, %
		Predicted	Experimental (Knutson and Thompson, 1978)	
30	0.66	2.28	2.10	8.6
45	0.90	2.36	-	-

It can be seen from Table 6.12 that the plastic strain determined using Equation (2.11) well predicts the accumulated plastic strain obtained by Knutson and Thompson (1978) at the end of 5000 cycles of load for the mean particle size of 30 mm for crushed limestone. This is supported by Timmerman and Wu (1969) qualitatively stating “The frequency between 2.5 Hz and 25 Hz seems to affect the rate of strain but not the final strain”. For the prototype limestone  $D_{50} = 45$  mm, the plastic strain accumulated at the end of 5000 cycles of load application using Equation (2.11) is predicted as 2.36%, which seems to be reasonable. Consequently, the parallel gradation technique to predict the accumulated plastic strain of prototype size provides adequate estimate for engineering purposes.

### **6.3.2 Plastic Strain Trends of Scaled-down Basalt**

The results of the plastic strain accumulated with the number of load application for all scaled-down basalt, namely B-2.36, B-4.75 and B-9.5 are illustrated, respectively in Figure 6.23 through Figure 6.25.

Using the statistical analysis suggested in 5.2.1, linear best-fit to the data for each of B-2.36, B-4.75 and B-9.5 is possible to obtain. The slope of the linear best-fit is corrected with the corresponding first cycle of plastic strain,  $\epsilon_1$  values of 0.69; 0.60; 0.53 given in Table 6.8 at a deviator stress  $(\sigma_1 - \sigma_3) \approx 200$  kPa for each scaled-down basalt to get the plastic strain slope,  $C$ , in Equation 2.11. The applied deviator stress corresponds to a stress ratio,  $K_c$ , of 0.57. Table 6.13 lists the plastic strain slope,  $C$ , for all of the scaled-down basalt. All coefficient of determination,  $R^2$ , values are calculated as above 0.9.

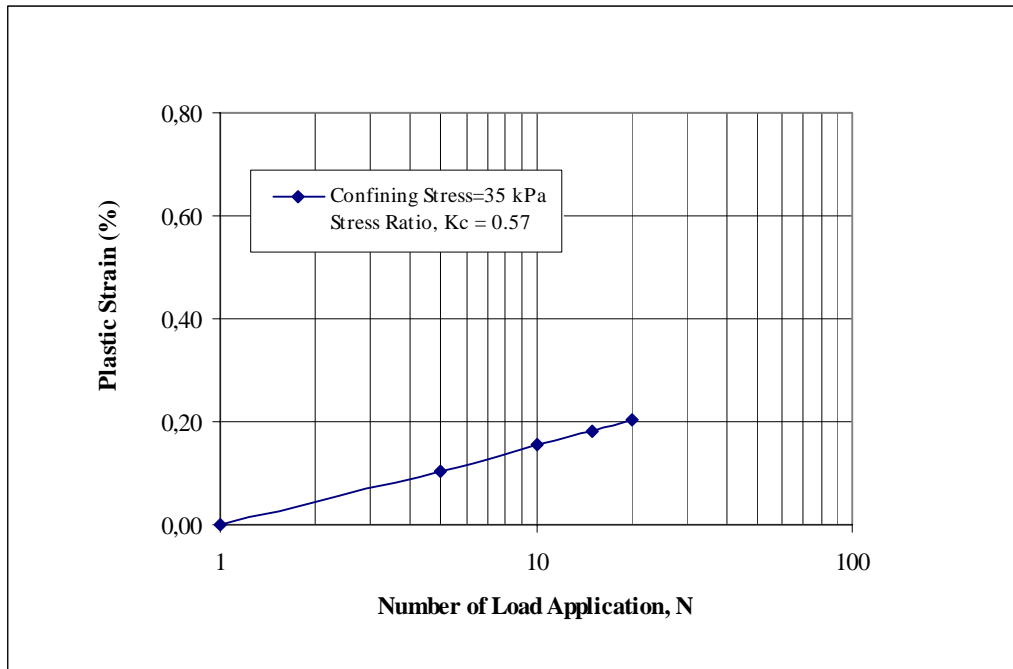


Figure 6.23 Accumulated plastic strain trend for B-2.36

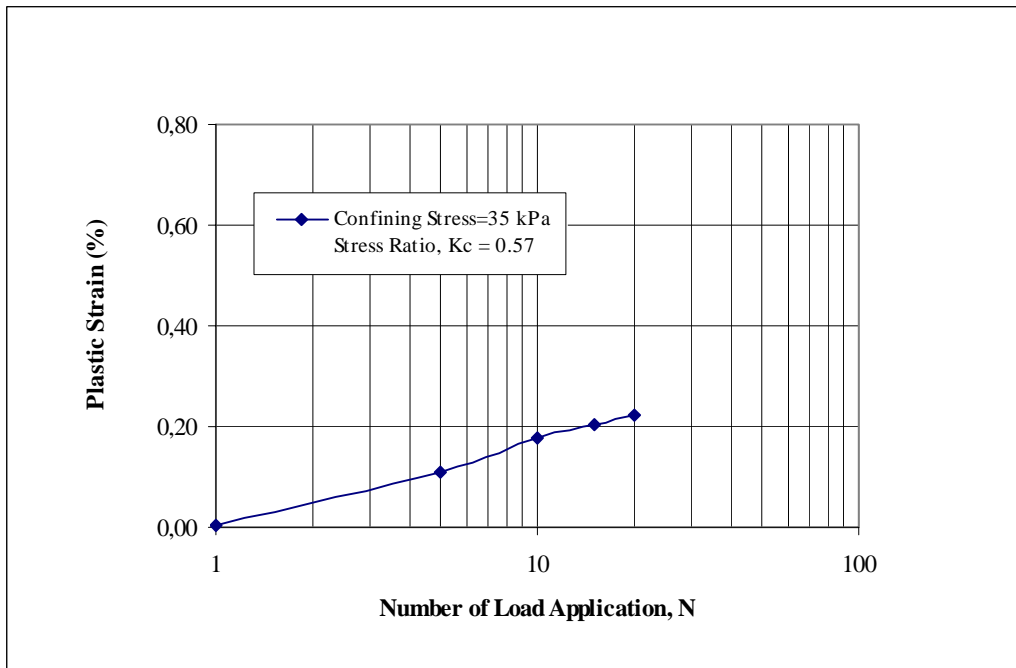


Figure 6.24 Accumulated plastic strain trend for B-4.75

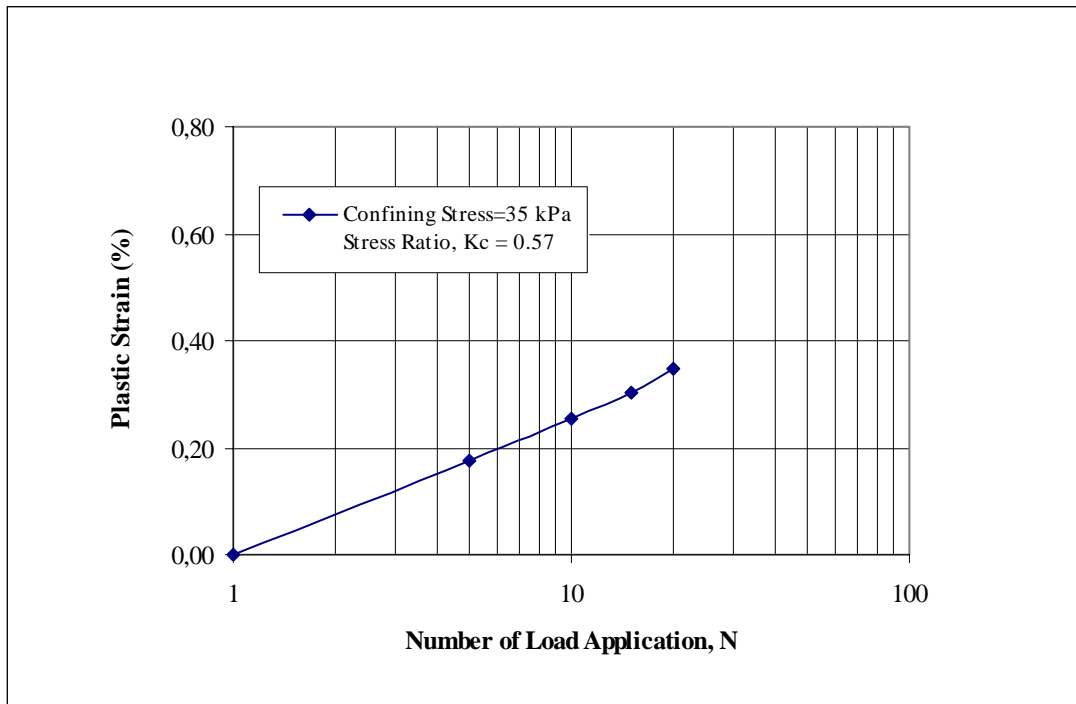


Figure 6.25 Accumulated plastic strain trend for B-9.5

Table 6.13 Plastic strain slope values for the scaled-down basalt at  $\sigma_3 = 35 \text{ kPa}$  and  $(\sigma_1 - \sigma_3) \approx 200 \text{ kPa}$

Gradation	Plastic Strain Slope (C)	Coefficient of Determination, $R^2$
B-2.36	0.23	0.999
B-4.75	0.28	0.996
B-9.5	0.49	0.998

Figure 6.26 shows the variation of the plastic strain slope,  $C$ , with the mean particle size of the scaled-down basalt samples. The tendency of the plastic strain slope values is fitted with a linear best-line to the data. The corresponding equation for the plastic strain slope shown in Figure 6.26 is given in Equation (6.5). The coefficient of determination,  $R^2$ , is 0.977.

$$C = 0.0287(D_{50}) + 0.1186 \quad ; \quad R^2 = 0.977 \quad (6.5)$$

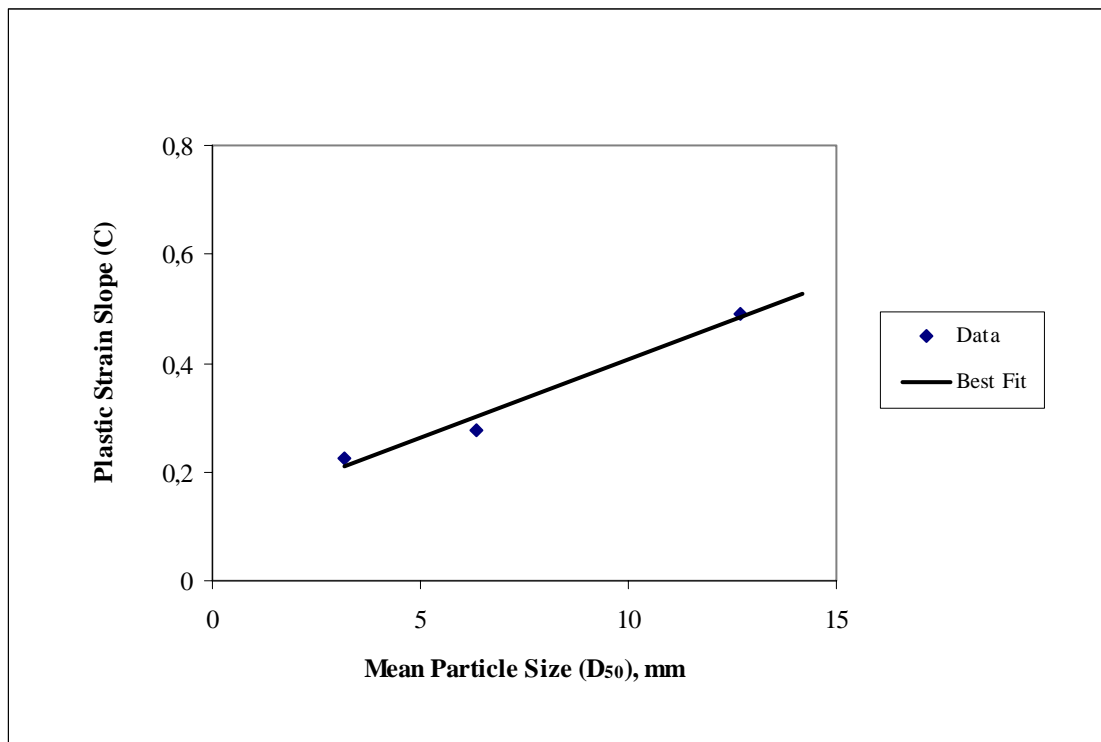


Figure 6.26 Variation of plastic strain slope with mean particle size for the basalt

Table 6.14 compares the predicted plastic strain values using Equation (2.11) to that of experimental values accumulated after 20 cycles of load for all scaled-down basalt.

Table 6.14 Comparison of accumulated plastic strains for the scaled-down basalt after N=20

Gradation	Accumulated Plastic Strain ( $\epsilon_N$ ), %		Difference Between Predicted and Experimental, %
	Predicted	Experimental	
B-2.36	0.81	0.92	-12.0
B-4.75	0.86	0.95	-9.5
B-9.5	0.95	1.14	-16.7

Examining Table 6.14 shows that the predicted plastic strain accumulated after 20 cycles of load differs by 16.7% from the experimental values for scaled-down basalt. So, the representation of the values of the plastic strain for crushed basalt is reasonable for engineering estimation purposes.

Table 6.15 compares the accumulated plastic strain predicted by Equation (2.11) to that obtained experimentally by Knutson and Thompson (1978) after 5000 cycles of load at a stress ratio,  $K_c$ , of 0.55 for the mean size  $D_{50} = 30$  mm of crushed basalt. The predicted plastic strain values for the prototype size  $D_{50} = 45$  mm, and the values of plastic strain slope for  $D_{50} = 30$  mm and  $D_{50} = 45$  mm are also included in Table 6.15.

Table 6.15 shows that Equation (2.11) well predicts the accumulated plastic strain only 2.6% less than that obtained experimentally by Knutson and Thompson

(1978) at the end of 5000 cycles of load for the mean particle size of 30 mm for crushed basalt.

For the prototype basalt  $D_{50} = 45$  mm, the plastic strain accumulated at the end of 5000 cycles of load application using Equation (2.11) is predicted as 2.48%, which seems to be reasonable. Consequently, the parallel gradation technique to predict the accumulated plastic strain of prototype sizes of the basalt provides a good estimate for engineering purposes.

Table 6.15 Comparison of accumulated plastic strains for basalt prototype sizes after  $N = 5000$

Mean Particle Size ( $D_{50}$ ), mm	Plastic Strain Slope (C)	Accumulated Plastic Strain ( $\epsilon_N$ ), %		Difference Between Predicted and Experimental, %
		Predicted	Experimental (Knutson and Thompson, 1978)	
30	0.99	2.24	2.30	-2.6
45	1.42	2.48	-	-

### 6.3.3 Plastic Strain Trends of Scaled-down Steel-Slag

In this section, the results of the plastic strain accumulated with the number of load application for all scaled-down basalt, namely S-4.75, S-6.35 and S-9.5 are shown, respectively in Figure 6.27 through Figure 6.29.

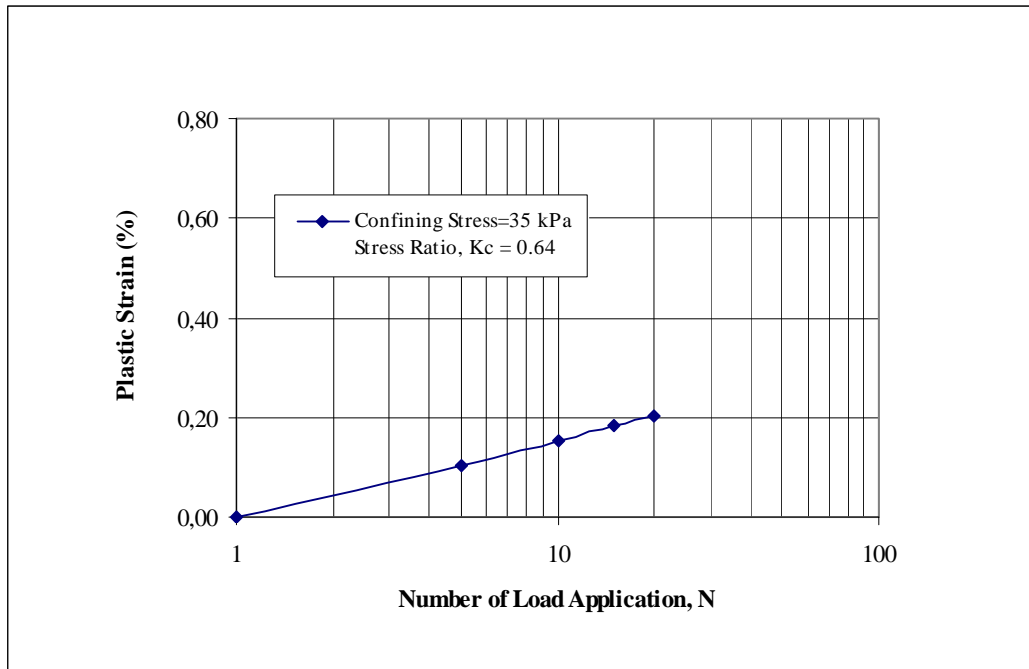


Figure 6.27 Accumulated plastic strain trend for S-4.75

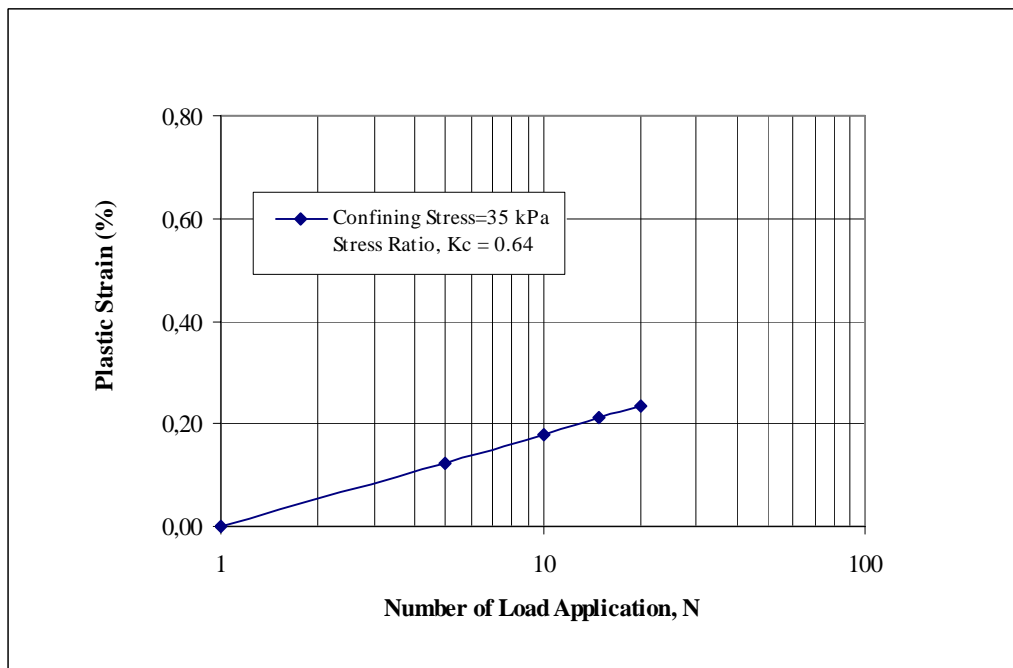


Figure 6.28 Accumulated plastic strain trend for S-6.35

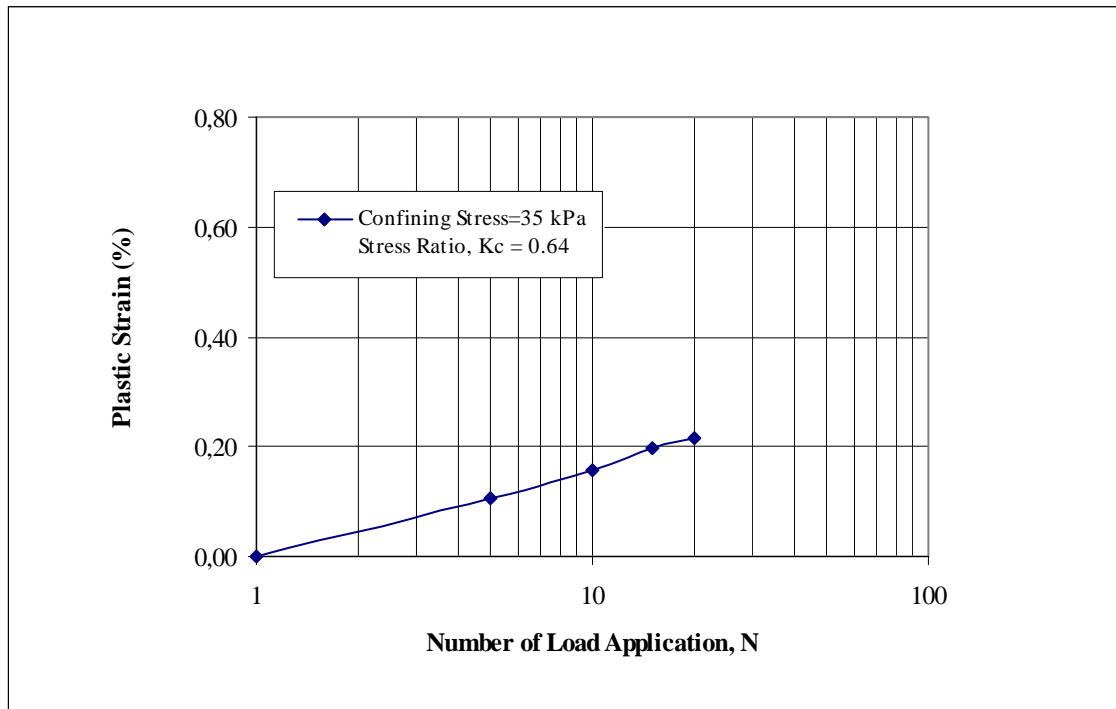


Figure 6.29 Accumulated plastic strain trend for S-9.5

Again, using the statistical analysis technique suggested in 5.2.1, it is possible to fit the data for S-4.75, S-6.35 and S-9.5 to linear best-lines. The associated first cycle of plastic strain,  $\varepsilon_1$  values of 0.75; 0.75; 0.75 given in Table 6.9 for scaled-down steel-slag at a deviator stress  $(\sigma_1 - \sigma_3) \approx 200$  kPa and  $\sigma_3 = 35$  kPa are used to get the plastic strain slope, C, in Equation 2.11. Stress ratio,  $K_c = 0.70$ . Table 6.16 lists the plastic strain slope values for all of the scaled-down steel-slag.

Figure 6.30 shows the variation of the plastic strain slope, C, with the mean particle size of the scaled-down steel-slag. The tendency of the plastic strain slope is fitted with a linear best-line to the data. The corresponding equation for the plastic strain slope shown in Figure 6.30 is given in Equation (6.6). The coefficient of determination is 0.977, indicating a good enough linear fit to the data.

$$C = 0.0294(D_{50}) + 0.0272 \quad ; \quad R^2 = 0.977 \quad (6.6)$$

Table 6.16 Plastic strain slope values for the steel-slag at  $\sigma_3 = 35$  kPa and  $(\sigma_1 - \sigma_3) \approx 200$  kPa

Gradation	Plastic Strain Slope (C)	Coefficient of Determination, $R^2$
S-4.75	0.20	0.999
S-6.35	0.32	0.983
S-9.5	0.39	0.982

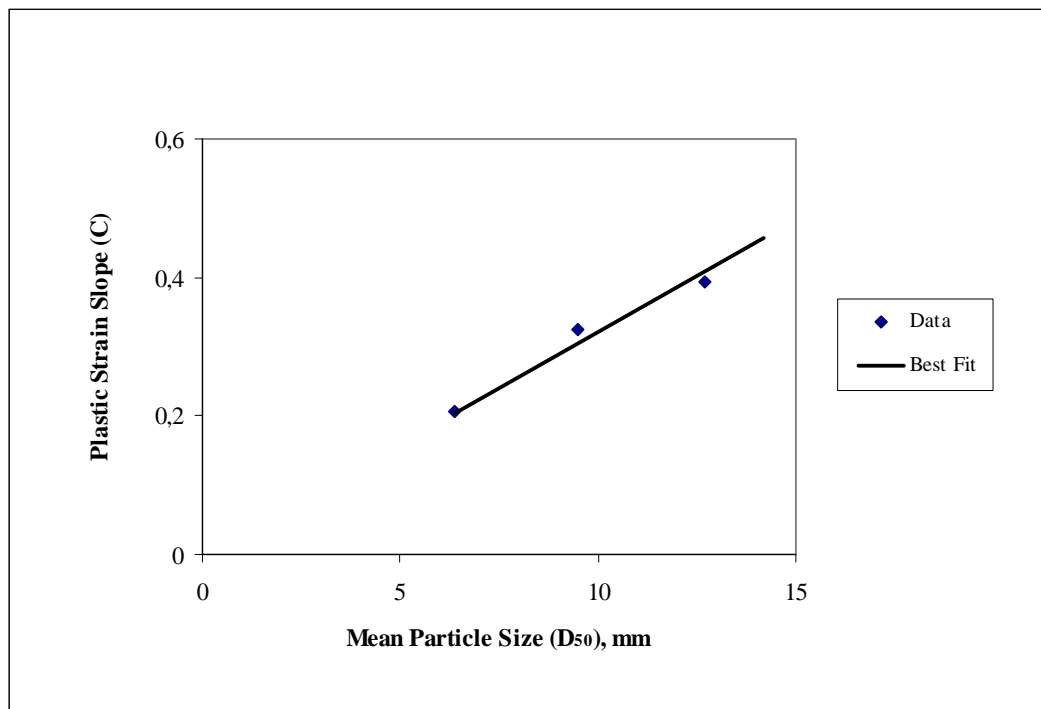


Figure 6.30 Variation of plastic strain slope with mean particle size for the steel-slag

Table 6.17 compares the predicted plastic strain values using Equation (2.11) to that of experimental values accumulated after 20 cycles of load application for all scaled-down steel-slag.

Table 6.17 Comparison of accumulated plastic strains for scaled-down steel-slag after N=20

Gradation	Plastic Strain ( $\epsilon_N$ ), %		Difference Between Predicted and Experimental, %
	Predicted	Experimental	
S-4.75	0.96	0.95	0.0
S-6.35	1.05	0.99	7.0
S-9.5	1.14	1.16	-1.7

Table 6.18 includes the predicted values for both plastic strain slope and the accumulated plastic strain after 5000 cycles of load application for crushed steel-slag of  $D_{50} = 30$  mm and  $D_{50} = 45$  mm by Equation (2.11).

Table 6.18 Accumulated plastic strains for steel-slag prototype sizes after N = 5000

Mean Particle Size ( $D_{50}$ ), mm	Plastic Strain Slope (C)	Predicted Plastic Strain ( $\epsilon_N$ ), %
30	0.91	3.27
45	1.35	4.50

## 6.4 Comparison of Accumulated Plastic Strain of Limestone, Basalt and Steel-Slag

Table 6.19 lists the accumulated plastic strain predicted for selected series of scaled-down limestone, basalt, and steel-slag, as well as the plastic strain slope values,  $C$ , for the prototype size  $D_{50} = 45$  mm at a deviator stress of 200 kPa under a confining stress of 35 kPa after a predicted number of load application,  $N = 5000$ .

Table 6.19 Comparison of predicted plastic strain for various series of materials at  $N = 5000$

Characteristics	Limestone		Basalt		Steel-Slag	
	L-9.5, $D_{50} =$ 6.35 mm	L-30, $D_{50} =$ 45 mm	B-9.5, $D_{50} =$ 6.35 mm	B-30, $D_{50} =$ 45 mm	S-9.5 $D_{50} =$ 6.35 mm	S-30, $D_{50} =$ 45 mm
Stress Ratio ( $K_c$ )	0.63	0.63	0.57	0.57	0.70	0.70
Plastic Strain After First Cycle, ( $\epsilon_1$ ), %	0.74	0.59	0.53	0.43	0.75	0.75
Plastic Strain Slope ( $C$ )	0.38	0.90	0.49	1.42	0.40	1.35
Predicted Plastic Strain ( $\epsilon_N$ ), %	1.79	2.55	1.50	2.69	1.86	4.50

Examining Table 6.19 indicates that the predicted rate of plastic strain (slope),  $C$ , for all materials increases as increasing the mean particle size. Also, the predicted accumulated plastic strain,  $\epsilon_N$ , for all materials increases as the mean particle size increases. This is similar to the findings in a stress-controlled test conducted with a cycle rate of 1 Hz by Raymond and Diyaljee (1978) who conclude that “In a comparison of uniformly graded ballast alone the result showed that smaller size ballast deform less than larger size ballast provided that stress levels do not exceed a critical level”.

Table 6.19 shows also that the crushed steel-slag samples experienced accumulated plastic strains more than did the limestone or basalt samples. It is worth to note, however, that the accumulated plastic strain the steel-slag specimens attained was comparable to that for the crushed limestone or basalt samples, even though the stress ratio,  $K_c$ , was 0.7 which was higher than that of the limestone or basalt, and was greater than that of the rule of thumb  $K_c$  value of 0.6. The accumulated plastic strains for the limestone and basalt samples were almost identical.

### **6.5 Effect of Gradation on Plastic Strain for Scaled-Down Limestone**

Table 6.20 compares the plastic strain values accumulated after the first cycle for the alternative gradations of limestone material, L-3.15 and L-6.35, at the end of a number of load application,  $N = 20$ . For comparison, the plastic strain value for L-9.5 was also provided in the table.

Table 6.20 shows that the plastic strain accumulated after first cycle is in the range of 0.30% to 0.40% for the range of uniformity coefficient,  $C_u$ , of 1.40 to 2.38 for limestone samples at a number of load application,  $N = 20$ .

Table 6.20 Comparison of accumulated plastic strain after first cycle for different gradations of limestone after  $N = 20$

Gradation	Uniformity Coefficient ( $C_u$ )	Plastic Strain, %
L-9.50	1.40	0.35
L-6.35	1.75	0.29
L-3.15	2.38	0.38

## CHAPTER VII

### SUMMARY AND CONCLUSIONS

#### 7.1 Summary

The main purpose for this investigation was to understand whether it was possible to use parallel gradation technique to estimate the engineering properties of ballast materials consisting of coarse-gravel size aggregates. In this technique, the aim is to preserve the particle shape, particle surface roughness, and particle mineralogy and to create a parallel gradation of soil with a maximum particle size not more than one over six that of the specimen diameter of the available triaxial apparatus. The strength, elastic moduli and plastic strain characteristics of scaled-down ballast materials were determined; thus the variables considered included particle size, material type, and gradation. The Mohr-Coulomb parameters identifying the strength, the elastic modulus, and plastic strain results were analyzed with respect to particle size, and comparisons were made between the results according to material type.

Ballast materials chosen for the investigation of parallel gradation technique were limestone, basalt and steel-slag. Both basalt and limestone ballast materials are manufactured from rocks by crushing and grading so that all of the materials was between 30 mm and 60 mm. Scaled-down limestone and basalt from the same source were used as the modeling material, with gradations of 2.36 mm to 4.75 mm, 4.75 mm to 9.5 mm, and 9.5 mm to 19.1 mm. Steel slag is a byproduct material of Ereğli Iron and Steel Works, which is suitable to meet the durability test requirements as

well as the electrical resistivity and the solid waste contaminants regulatory level. The scaled-down steel-slag was manufactured from the same source as the modeling material, with gradations of 4.75 mm to 9.5 mm, 6.35 mm to 12.7 mm, and 9.5 mm to 19.1 mm.

Conventional triaxial testing was used to obtain the peak shear strength and the elastic moduli characteristics of scaled-down specimens of 100 mm in diameter with a confining stress of 35 kPa, 70 kPa and 105 kPa; whereas that of only 35 kPa was used to characterize the accumulated plastic strain.

## 7.2 Conclusions

At the end of the study, the following conclusions were reached:

1. There seems to be a high correlation between the peak shear strength or the elastic moduli obtained by parallel gradation technique and the mean particle size,  $D_{50}$ , under the confining stresses of 35 kPa, 70 kPa and 105 kPa, and for the prototype mean particle sizes of  $D_{50} = 30$  mm and  $D_{50} = 45$  mm thus the technique may lead to reasonable predictions of the peak shear strength or the elastic moduli.
2. It is possible to prepare a scaled-down material using parallel gradation technique with a different mineralogy and still produce acceptable results of peak shear strength or elastic moduli characteristic as long as the crushed materials have a similar durability property.
3. For uniformly graded crushed material used in this study, the angle of internal friction,  $\phi$ , and the apparent cohesion,  $c$ , may be conservatively taken to be  $42^\circ$  and 35 kPa, respectively for the confining stress ranging from 35 kPa to 105 kPa.

4. It appears that there is virtually no effect of water on the peak shear strength or on the elastic modulus determined for all crushed materials for the engineering purposes.
5. It appears that changing the grain size distribution does not affect significantly the peak shear strength or the elastic moduli for the limestone material tested.
6. For all materials, the initial elastic modulus,  $E_i$ , the secant elastic modulus,  $E_{50}$ , and the unloading-reloading elastic modulus,  $E_{ur}$ , may all be represented by the equation:

$$\frac{E}{p_r} = K \left( \frac{\sigma_3}{p_r} \right)^n$$

where  $p_r$ , a reference confining stress, equals to 1 kPa, and  $K$  and  $n$  are material constants.

7. The power law parameters in the above equation,  $K$  and  $n$ , are functions of mean particle size,  $D_{50}$ , for the limestone and basalt materials. When the trend of power law parameters is preserved the above equation may reasonably predict the initial elastic modulus and unloading-reloading elastic modulus within  $\pm 20\%$ , and the secant elastic modulus within  $\pm 25\%$  for the limestone and basalt materials. For the scaled-down steel-slag,  $K$  and  $n$  are very scattered and thus taken as an average of parameters determined; the best-fit for the initial and unloading-reloading elastic moduli provides an estimate within a  $\pm 10\%$  confidence envelope, but the best-fit for secant elastic moduli provides an estimate within a  $\pm 50\%$  confidence envelope.
8. The elastic moduli values for all materials may be predicted within an adequate estimate for the engineering purposes by using the power law

parameters determined for L-9.5 ( $D_{50} = 12.7$  mm), the coarsest gradation tested for limestone.  $K$  with a reference pressure,  $p_r = 1$  kPa and  $n$  values for L-9.5, respectively, are 4365 and 0.636 for initial elastic moduli; 8511 and 0.419 for secant elastic moduli; 25704 and 0.430 for unloading-reloading elastic moduli. All data for the initial and unloading-reloading elastic moduli with the predicted data for prototype sizes are within  $\pm 50\%$  confidence envelope, whereas the best-fit to the data for L-9.5 predicts the secant elastic moduli for all materials with the predicted data for prototype sizes within  $\pm 100\%$  confidence envelope.

9. The unloading-reloading moduli increased, in general, as the number of cycles increased. An increase in unloading-reloading modulus obtained was roughly 15% for scaled-down limestone; 10% for the basalt; and 5% for the steel-slag.
10. It is observed that material type has almost no effect on either initial or unloading-reloading moduli, whereas it has an effect on the secant elastic moduli. The initial and secant elastic modulus values for the crushed basalt are greater than those of limestone or steel-slag; on the other hand, no substantial difference is found in the values of initial elastic modulus between the limestone and steel-slag series, whereas the secant elastic modulus values for limestone series are higher than those of steel-slag samples. The material type has almost no effect on the unloading-reloading elastic moduli.
11. For all materials, the accumulated plastic strain may be represented by the equation:

$$\varepsilon_N = \varepsilon_1 (1 + C \log N)$$

where,  $\varepsilon_N$  is accumulated plastic strain after a number of load applications,  $N$ ;  $\varepsilon_1$  is the axial plastic strain after the first cycle; and  $C$  is a material constant, which may be named as plastic strain slope. The plastic strain,  $\varepsilon_1$ , remaining

after the deviator stress is applied and removed can be represented by:

$$\varepsilon_1 = \varepsilon_a - \varepsilon_r$$

in which  $\varepsilon_a$  is the axial strain under the applied deviator stress,  $(\sigma_1 - \sigma_3)$ , and  $\varepsilon_r$  is the recoverable or resilient strain upon unloading. The value of  $\varepsilon_a$  might be estimated from the hyperbolic stress-strain relationship:

$$\varepsilon_a = \frac{(\sigma_1 - \sigma_3) / E_i}{1 - \frac{(\sigma_1 - \sigma_3)(1 - \sin \phi) R_f}{2(c \cos \phi + \sigma_3 \sin \phi)}}$$

where,  $c$  is the apparent cohesion;  $\phi$  is the angle of internal friction;  $R_f$  is the failure ratio as:

$$(\sigma_1 - \sigma_3)_f = R_f (\sigma_1 - \sigma_3)_{ult}$$

where,  $(\sigma_1 - \sigma_3)_f$  is the peak shear strength; and  $(\sigma_1 - \sigma_3)_{ult}$  is the asymptotic value of stress difference for the corresponding hyperbola obtained from the test data. Value of  $R_f$  may be assumed to be  $0.84 \pm 0.03$  for crushed limestone;  $0.87 \pm 0.05$  for crushed basalt; and  $0.83 \pm 0.11$  for crushed steel-slag samples.

12. The plastic strain after first cycle,  $\varepsilon_1$ , and the plastic strain slope,  $C$ , can be represented as a function of mean particle size for each material type. Unlike  $\varepsilon_1$ ,  $C$  increases as the mean particle size increases. The predicted  $\varepsilon_1$  values are 0.59, 0.43 and 0.75 for the limestone, basalt and steel-slag prototype size,  $D_{50} = 45$  mm, respectively.  $C$  values are predicted as 0.54, 1.42 and 0.74 for the limestone, basalt and steel-slag prototype size,  $D_{50} = 45$  mm, respectively. By use of parallel gradation technique, reasonable estimates of accumulated plastic strains for the prototype may also be predicted. The crushed steel-slag samples experience accumulated plastic strains more than do the limestone or basalt samples. It is worth to note, however, that the accumulated plastic

strain the steel-slag specimens attained is comparable to that for the crushed limestone or basalt samples, even though the stress ratio,  $K_c$ , was 0.7 which was higher than that of the limestone or basalt, and was greater than that of the rule of thumb  $K_c$  value of 0.6. The accumulated plastic strains for the limestone and basalt samples are identical.

13. It is observed that the accumulated plastic strain for all materials increases as the mean particle size increases.
14. For the range of uniformity coefficient,  $C_u$ , of 1.40 to 2.38 for limestone samples, plastic strain accumulated after first cycle is in the range of 0.30% to 0.40% at a number of load application,  $N = 20$ .

### **7.3 Recommendations**

The experimental work presented in this study investigated the question of the parallel gradation technique. It provided indications that the technique may predict the peak shear strength, the elastic moduli, and the plastic strain characteristics of the ballast materials. The number of tests performed within the confining stress range used can be increased with using fully automated triaxial apparatus to have a better reliability of the prediction by use of the parallel gradation technique. The work presented in this study is conducted under conventional triaxial test which is a strain-controlled test in nature. However, ballast materials are subjected to stress states with a much higher frequency and many number of load cycles. Therefore, an additional systematic research may be needed to establish testing and analysis procedures for the parallel gradation technique using a stress-controlled test, then comparison can be made to the results of strain-controlled test obtained in this dissertation.

## REFERENCES

- Alva-Hurdato, J. E., and Selig, E. T. (1981). Permanent strain behavior of railroad ballast, Proceedings of the 10<sup>th</sup> International Conference on Soil Mechanics and Foundation Engineering, Vol.4, pp. 543-546.
- Alva-Hurdato, J. E., McMahon, D. R. and Stewart, H. E. (1981). Apparatus and techniques for static triaxial testing of ballast, Laboratory Shear Strength of Soil, ASTM, STP 740, pp. 94-113.
- Anderson, W. F., Pyrah I. C., McKinlay, A., Salmon, T. H., and Goodwin, A. K. (1993). The deformation behaviour of partially saturated granular fill at low stress levels. Engineered fills. Thomas Telford, London.
- Bishop, A. W. and Henkel, D. J (1962). The Measurement of Soil Properties in the Triaxial test. 2<sup>nd</sup> edition, pp. 167-170. Edward Arnold, London.
- Bishop, A. W. (1966). The strength of soils as engineering materials, Milestones in Soils Mechanics 1975, The Institution of Civil Engineers, pp. 131-171.
- Boucher, D. L. and Selig, E. T. (1987). Application of petrographic analysis to ballast performance evaluation, Transportation Research Record 1131, pp. 15-25.
- Canadian Pacific Rail. (1984). CP Rail Specification for ballast. Transportation Research Record 1131, pp. 59-63.

Charles, J. A. and Watts, K.S. (1980). The influence of confining pressure on the shear strength of compacted rockfill, *Geotechnique* 30, No 4, pp. 353-367.

Clesceri, L. S., Greenberg, A. E. and Eaton, A. D. (1998). Standard methods for the examination of waste and wastewater, 20<sup>th</sup> edition, American Public Health Association, American Water Works, Water Environment Federation.

Craig, R. F. (1983). *Soil Mechanics*. 3<sup>rd</sup> edition, pp. 107-110. Van Nostrand Reinhold (UK) Co. Ltd, England.

Çağnan, Ş. (1990). Measurement of shear strength of coarse gravels by the wedge shear test, Master Thesis, METU, Ankara.

Duncan, J. M. and Chang, C. Y. (1970). Nonlinear analysis of stress and strain in soils, *Journal of the Soil Mechanics and Foundation Division*, Vol. 96, SM5, pp. 1629-1653.

Duncan, J. M., Byrne, P., Wong, K. S. and Mabry P. (1980). Strength, stress-strain and bulk modulus parameters for finite element analysis of stresses and movements in soil masses, Report N. UCB/GT/80-01, College of Engineering, Office of Research Services, University of California, Berkeley, California.

Filiz, T. E. (2000). Effect on shear strength of the clearance between the two halves of the prismatic wedge shear test mould. Master Thesis. METU, Ankara.

Goel, M. C. (1990). Evaluation of shear strength of coarse grained soils. *Indian Geotechnical Journal*, No3, pp141-151.

Head, K.H. (1982). *Manual of Soil Laboratory Testing*, V.2, pp.617, Engineering Laboratory Equipment Limited.

Indraratna, B., Ionescu, D., and Christie, H.D. (1998). Shear behavior of railway ballast based on large-scale triaxial tests, *ASCE Journal of Geotechnical and Geoenvironmental Engineering*, Vol. 124, No.5, pp. 439-449

Janardhanam, R. and Desai, C.S. (1983). Three-Dimensional testing and modeling of ballast, *Journal of the Geotechnical Engineering*, vol. 109, No.6, pp. 783-796.

Janbu, N. (1968). Soil compressibility as determined by oedometer and triaxial tests, *European Conference on Soil Mechanics and Foundation Engineering*, Wiesbaden, Germany, Vol. 1, pp. 19-25.

Jernigan, R. L. (1998). The physical modeling of soils containing oversized particles. Ph.D. Thesis. University of Colorado at Boulder, Boulder, Department of Civil, Environmental and Architectural Engineering, pp. 2.

Kaya, M., Jernigan, R., Runesson, K., and Sture, S. (1997a; 1997b) Reproducibility and conventional triaxial tests on ballast material. Technical Report, Department of Civil Environmental and Architectural Engineering, University of Colorado at Boulder, Boulder, Colorado, USA.

Koerner, R. M. (1970). Effect of particle characteristics on soil strength, *Journal of the Soil Mechanics and Foundations Division*, vol. 96, No. SM4, pp.1221-1234.

Knutson, R. M. and Thompson, M. R. (1978). Resilient response of railway ballast, *Transportation Research Record* 694, pp. 31-39.

Knutson, R. M. and Thompson, M. R. (1978). Permanent-Deformation behavior of railway ballast, *Transportation Research Record* 694, pp. 47-53.

Kurtz, M. (1991). *Handbook of Applied Mathematics for Engineers and Scientists*, McGraw-Hill, pp.10.38.

Lambe, T. W. and Whitman, R. V. (1979). Soil Mechanics, SI Version, John Wiley and Sons, pp. 145-148, 155-159.

Leslie, D.D. (1963). Large Scale Triaxial Tests on Gravelly Soils, Proceedings, 2nd Pan American Conference on Soil Mechanics and Foundation Engineering, Vol.1, pp. 181-202.

Li, D. and Selig, E. T. (1997a). Method for railroad track foundation design. I: Development, Journal of Geotechnical and Geoenvironmental Engineering, Vol. 124, No. 4, pp.316-322.

Li, D. and Selig, E. T. (1997b). Method for railroad track foundation design. I: Application, Journal of Geotechnical and Geoenvironmental Engineering, Vol. 124, No. 4, pp.322-329.

Lowe, J. (1964). Shear Strength of Coarse Embankment Dam Materials, Proceedings, 8th Congress on Large Dams, pp. 745-761

Marachi, N.D., Chan, C.K., and Seed, H.B. (1972). Evaluation of Properties of Rockfill Materials, Proceedings of ASCE Journal of the Soil Mechanics and Foundations Division, Vol. 98, No. SM1, pp 95-114.

Mitchell, J. K. (1993). Fundamentals of Soil Behavior. 2<sup>nd</sup> edition, pp. 164, 342, 363-382, John Wiley and Sons.

Monismith, C. L., Seed, H. B., Mitry, F. G. and Chan, C. K. (1969). Prediction of pavement deflections from laboratory tests, Proceedings of International Conference on Structural Design of Asphalt Pavements, University of Michigan, Ann Arbor, Michigan, USA.

Peplow, A. T., Oscarsson, J., and Dahlberg, T. (1996). Review of Research on Ballast as Track Substructure, Report F189, Chalmers University of Technology, Gothenburg, Sweden.

Potts, D., Axelsson, K., Grande, L., Schweiger, H., and Long, M. (2002). Guidelines for the use of advanced numerical analysis, pp. 36-37. Thomas Telford Ltd., London.

Raymond, G. P. (1978). Design for railroad ballast and subgrade support, Journal of the Geotechnical Engineering Division, Vol. 104, No. GT1, pp. 45-60.

Raymond, G. P. (1979). Railroad ballast prescription: State-of-the-art, Journal of the Geotechnical Engineering Division, ASCE, vol. 105, No. GT2, pp. 305-322.

Raymond, G. P. (1985). Research on railroad ballast specification and evaluation, Transportation Research Record 1006, pp. 1-8.

Raymond, G. P. and Davies, J. R. (1978). Triaxial tests on dolomite railroad ballast, Journal of the Geotechnical Engineering Division, ASCE, vol. 104, No. GT6, pp. 737-751.

Selig, E. T. and Rorer, C. J. (1987). Effects of particle characteristics on behavior of granular material, Transportation Research Record 1131, pp. 1-6.

Selig, E. T. and Waters, J. M. (1994). Track Geotechnology and Substructure Management, Thomas Telford, pp. 7.34.

Serway, R. A. (1996). Physics for scientists and engineers with modern physics, 4<sup>th</sup> edition, pp.777, Saunders College Publishing.

Sitharam, T. G. and Nimbkar M. S. (2000). Micromechanical modeling of granular materials: Effect of particle size and gradation, *Geotechnical and Geological Engineering* 18: 91-117.

Sowers, G. F. (1979). *Introductory soil mechanics and foundations: Geotechnical engineering*, 4<sup>th</sup> edition, pp.201-203, Macmillan Publishing Co., Inc.

Sture, S. (1996). CVEN-7718: Engineering Properties of Soils' class notes, University of Colorado at Boulder.

Timmerman, D. H. and Wu, T. H. (1969). Behavior of dry sands under cycling loading, *Journal of the Soil Mechanics and Foundation Division, ASCE*, vol. 95, No. SM4, pp. 1097-1112.

Timoshenko, S. (1956). *Theory of Elasticity*. McGraw-Hill, New York.

Vermeer, P. A. and Schanz, T. (1996). Evaluation of soil stiffness parameters, ASCE Workshop on Computational Geotechnics, 1998, University of Colorado, Boulder, pp. 5.

Watters, B. R., Klassen, M. J. and Clifton, A.W. (1987). Evaluation of ballast materials using petrographic criteria, *Transportation Research Record* 1131, pp. 45-58.

Wood, D. M. (1994). *Soil Behavior and Critical State Soil Mechanics*, Cambridge University Press, pp. 256.

\_\_\_\_\_ (1981). *Locomotives and railway cars*, Turkish State Railways, Ankara.

\_\_\_\_\_ (1990). *TCDD yük ve yolcu vagonları*, Türkiye Cumhuriyeti Devlet Demiryolları, Ankara.

\_\_\_\_\_ (2001). Balast şartnamesi, Türkiye Cumhuriyeti Devlet Demiryolları, Ankara.

\_\_\_\_\_ (1989). TS 7043, Balast – Demiryollarında kullanılan, Türk Standartları Enstitüsü, Birinci Baskı, Ankara.

\_\_\_\_\_ (1990). Soils for civil engineering purposes; part 4, compaction related tests. BS 1377 British Standard Institutions.

\_\_\_\_\_ (1987). TS 699, Tabii yapı taşları – Muayene ve deney metotları, Türk Standartları Enstitüsü, Birinci Baskı, Ankara.

\_\_\_\_\_ (1981). TS 3694, Beton agregalarında aşınmaya dayanıklılık (Aşınma oranı) tayini metodu, Türk Standartları Enstitüsü, Birinci Baskı, Ankara.

\_\_\_\_\_ (1981). TS 3655, Beton agregalarında dona dayanıklılık tayini, Türk Standartları Enstitüsü, Birinci Baskı, Ankara.

\_\_\_\_\_ (1973). TS 3673, Beton agregalarında organic kökenli madde tayini Balast – Demiryollarında kullanılan (Ballast), Türk Standartları Enstitüsü, Birinci Baskı, Ankara.

\_\_\_\_\_ (1970). EM 1110-2-1906, Engineering and design laboratory soils testing, pp. X-11, Department of the Army, U.S. Army Corps of Engineers, Washington, D.C.

\_\_\_\_\_ (1996). Ek 11-A, Atıkların düzenli depo tesislerine depolanabilme kriterleri, Resmi Gazete, Sayı : 22858, sayfa : 57.

\_\_\_\_\_ (2002). MKTAE.5.02.040, elikhane cürufunun farklı uygulama alanlarında deęerlendirilmesi, Türkiye Bilimsel ve Teknik Arařtırma Kurumu (TUBITAK), Marmara Arařtırma Merkezi (MAM).

APPENDIX A - LIMESTONE

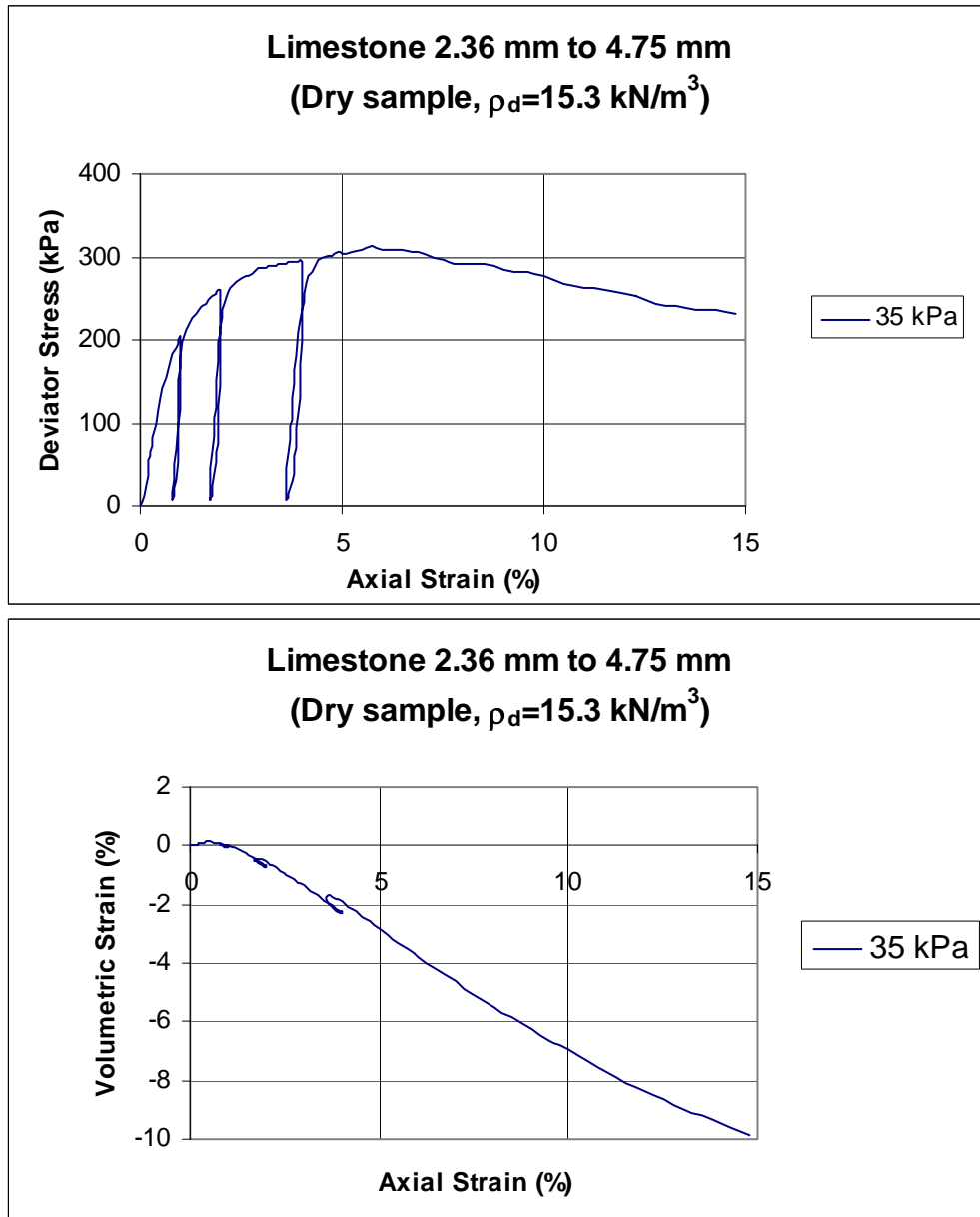


Figure A1

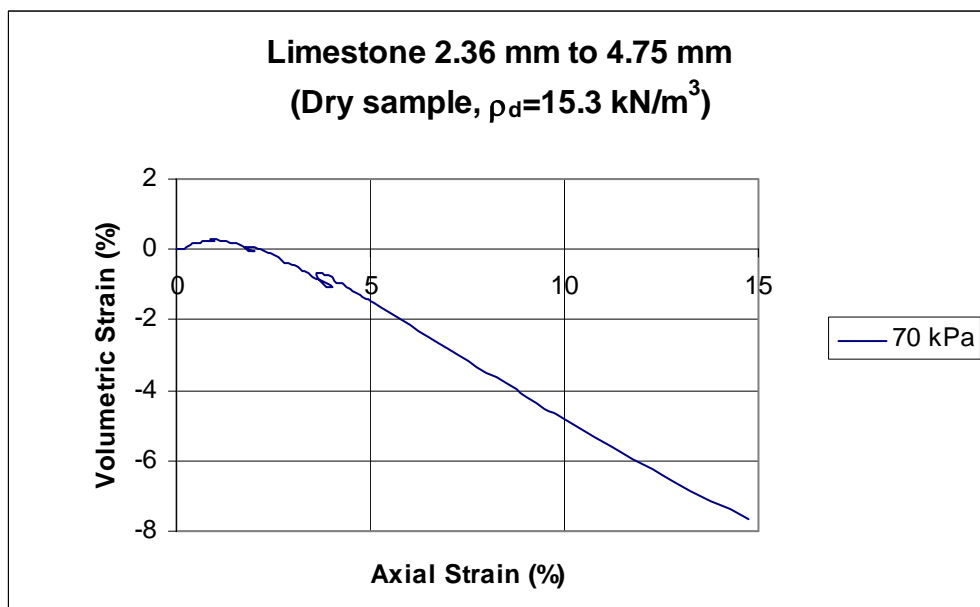
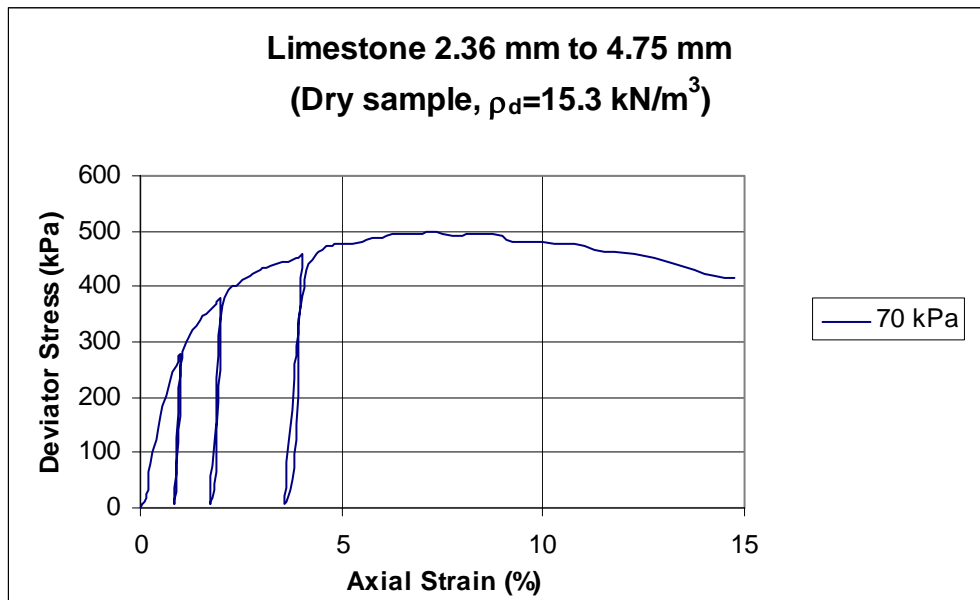


Figure A2

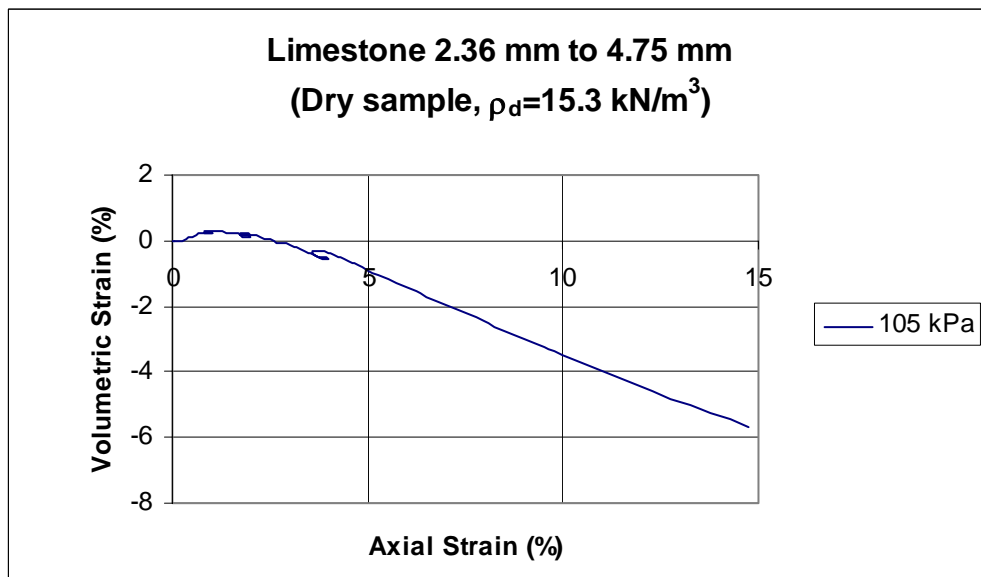
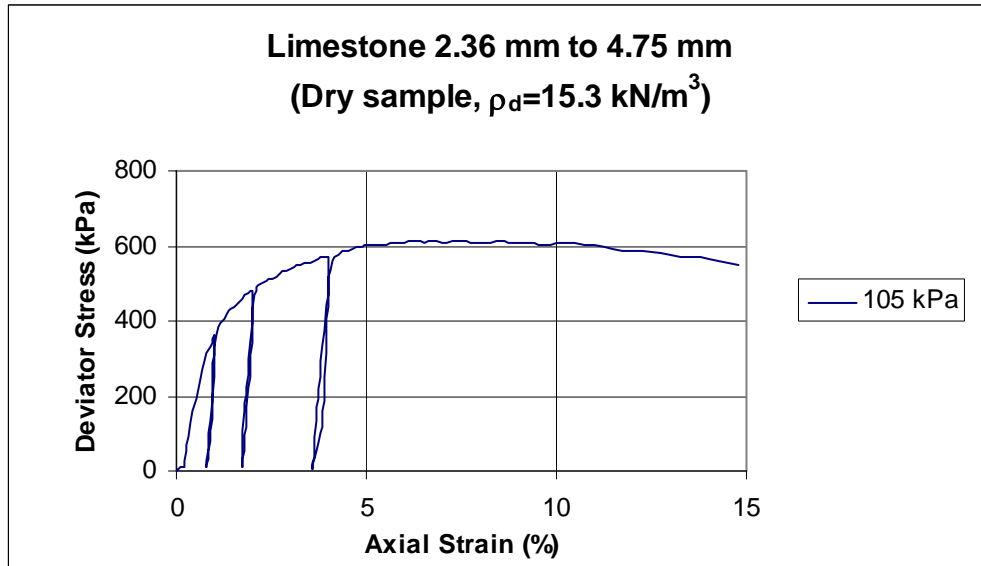


Figure A3

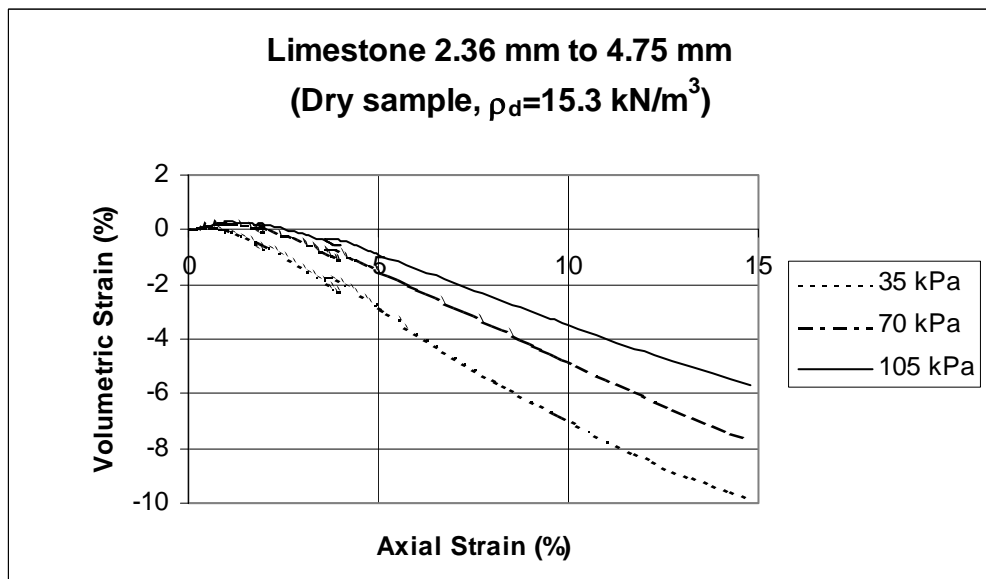
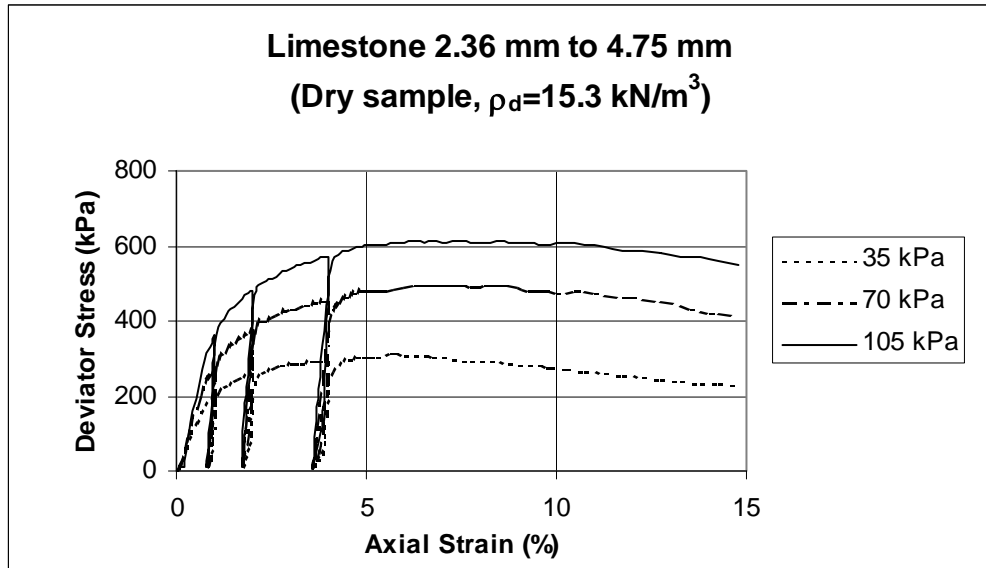


Figure A4

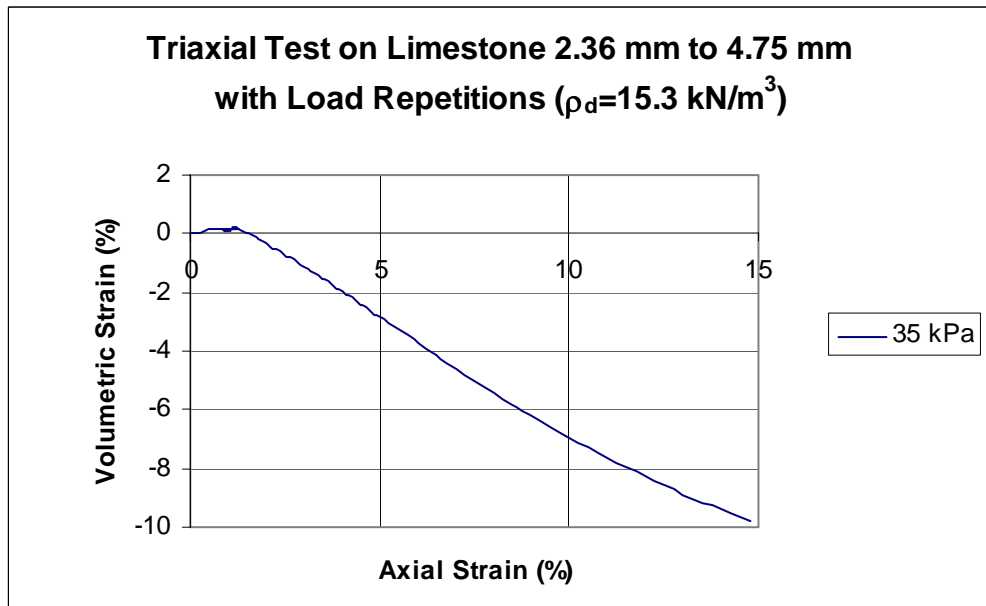
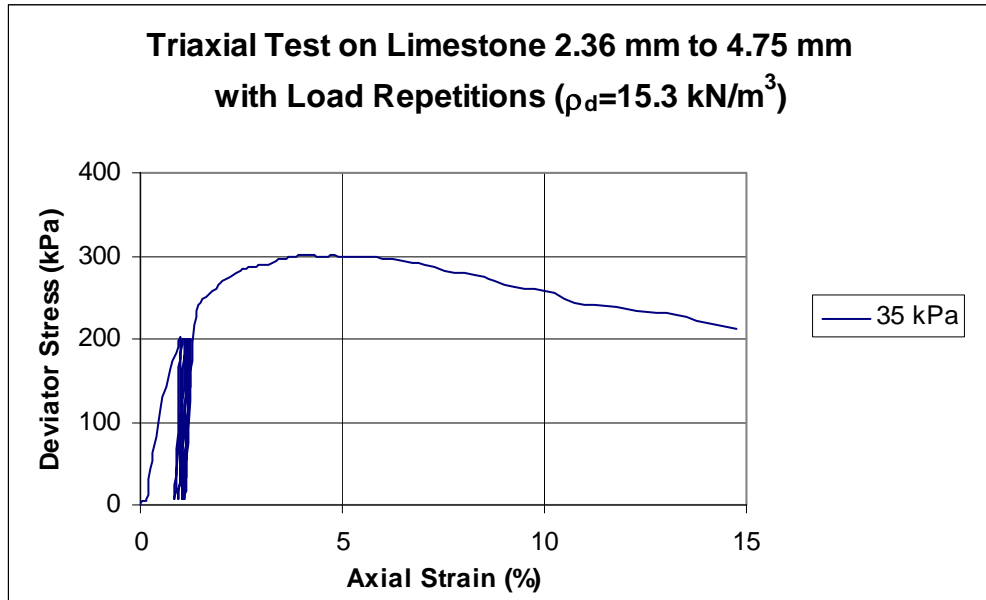


Figure A5

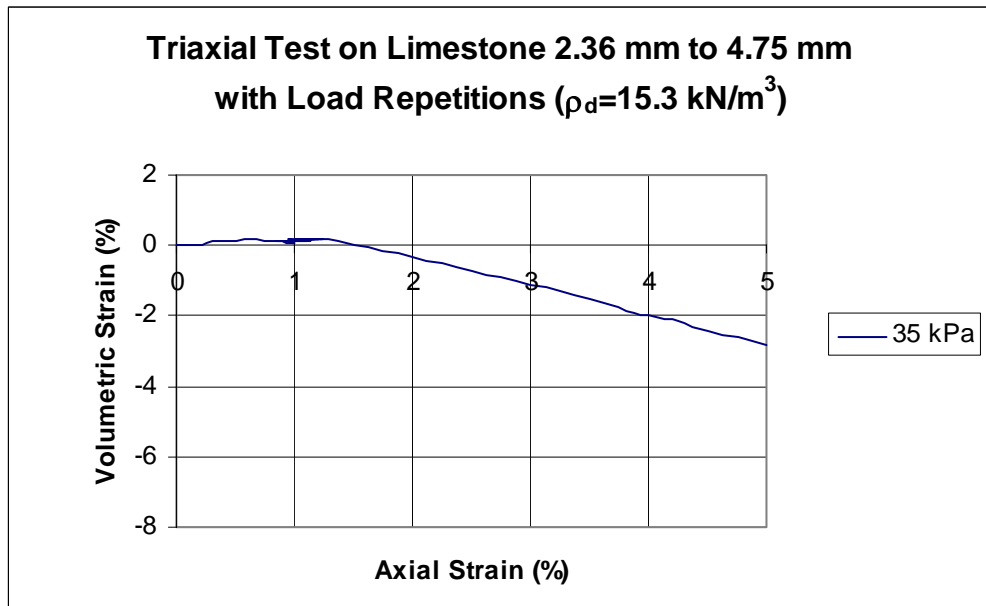
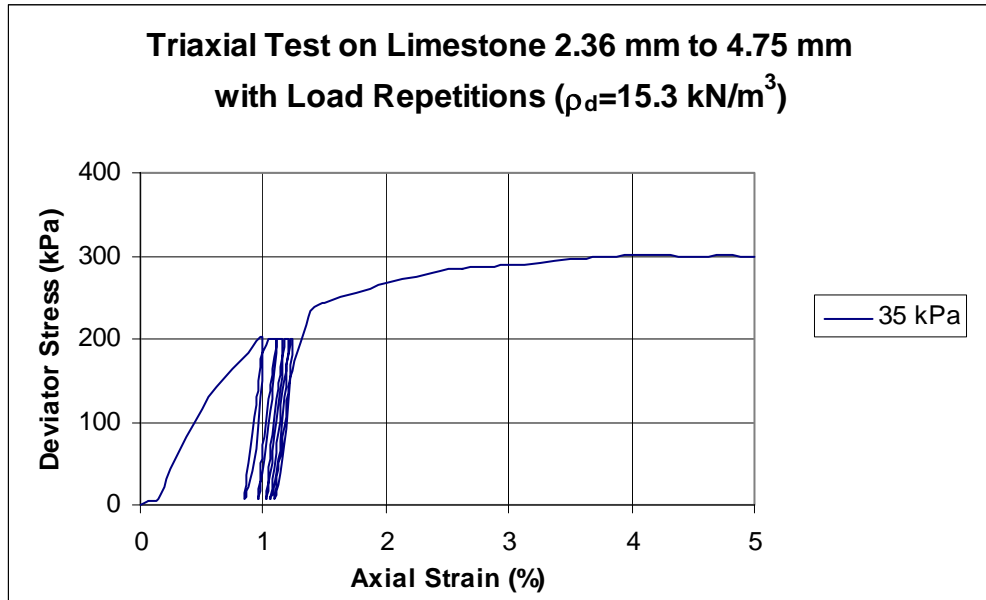


Figure A6

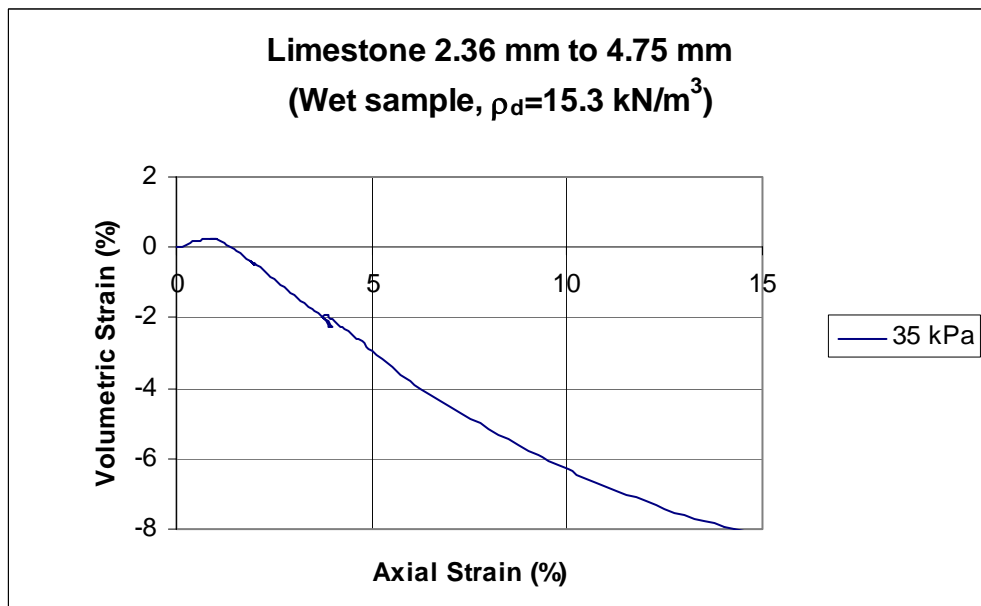
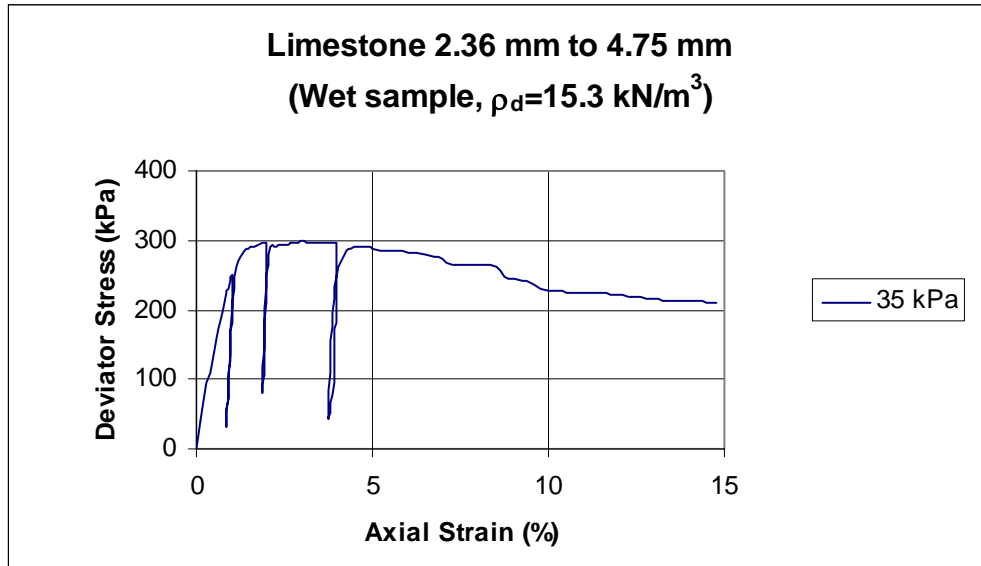


Figure A7

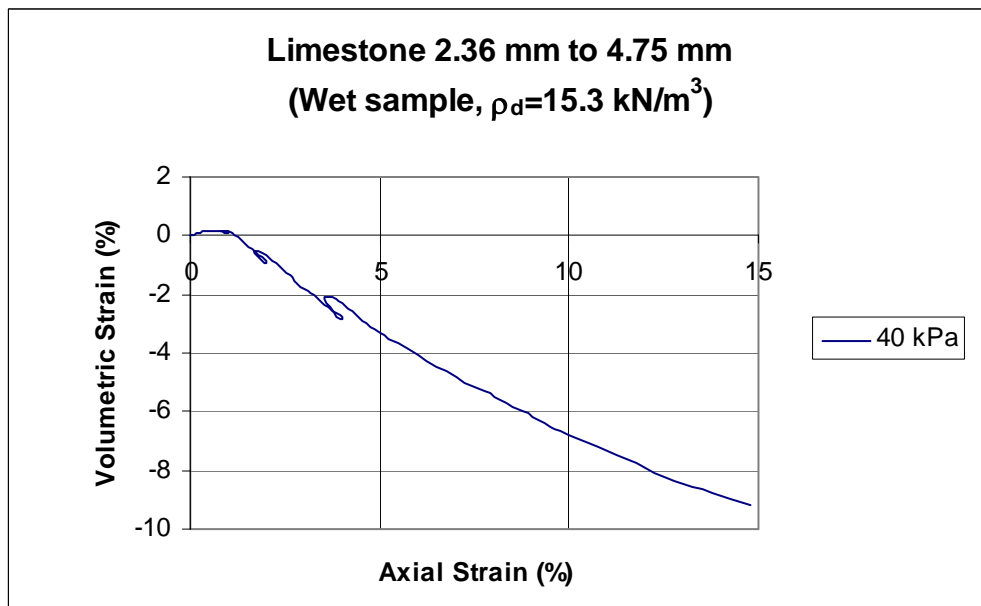
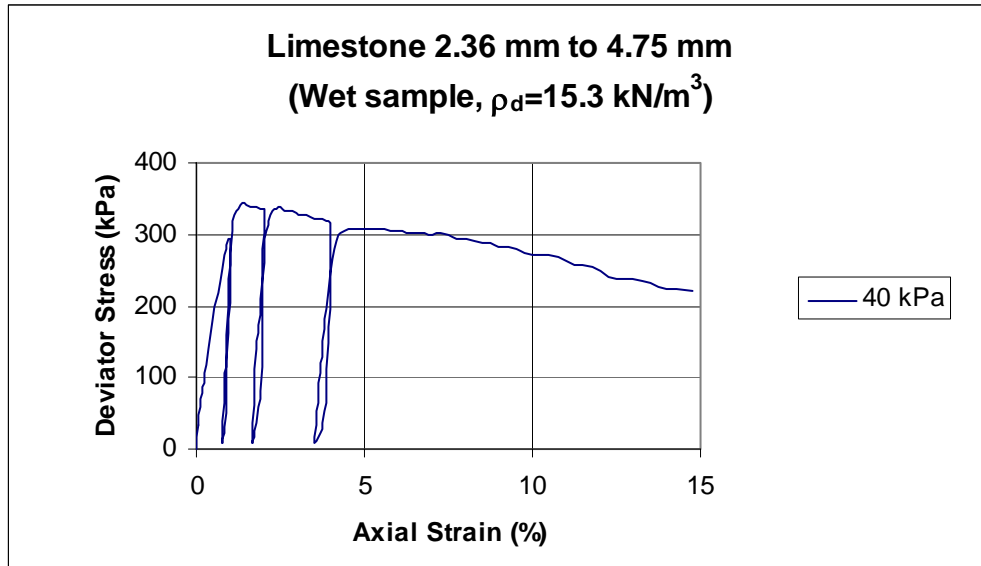


Figure A8

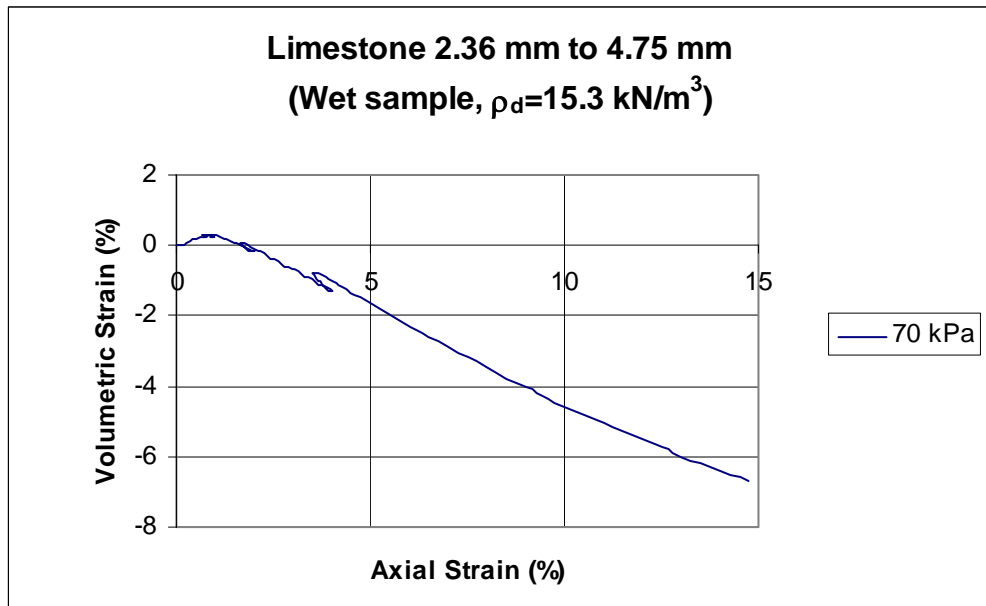
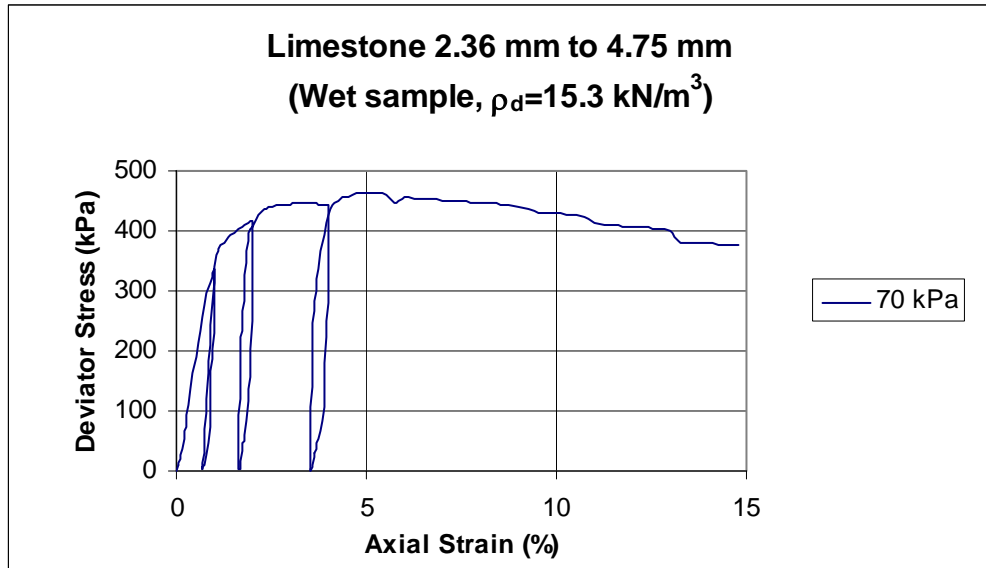


Figure A9

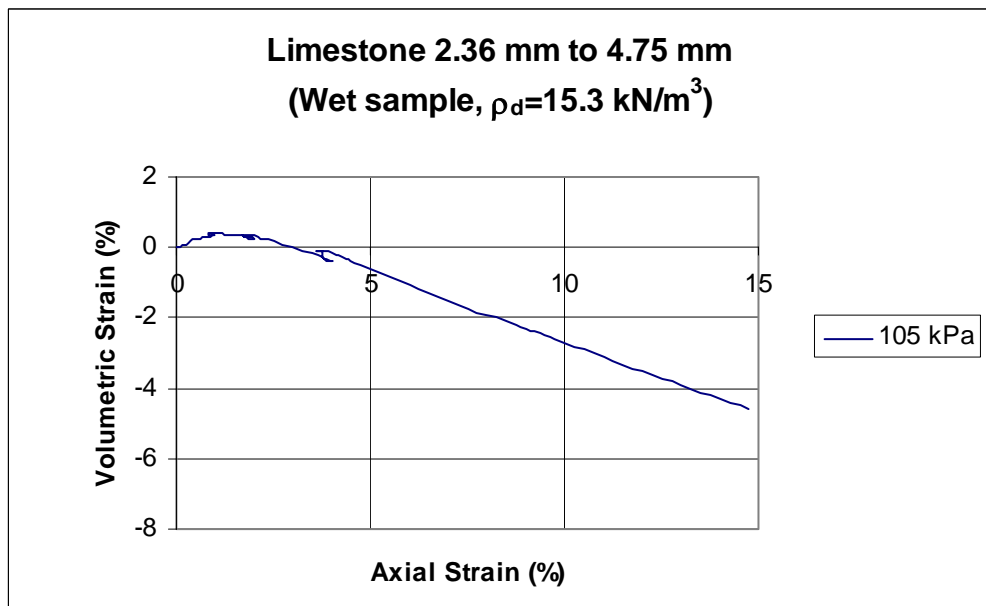
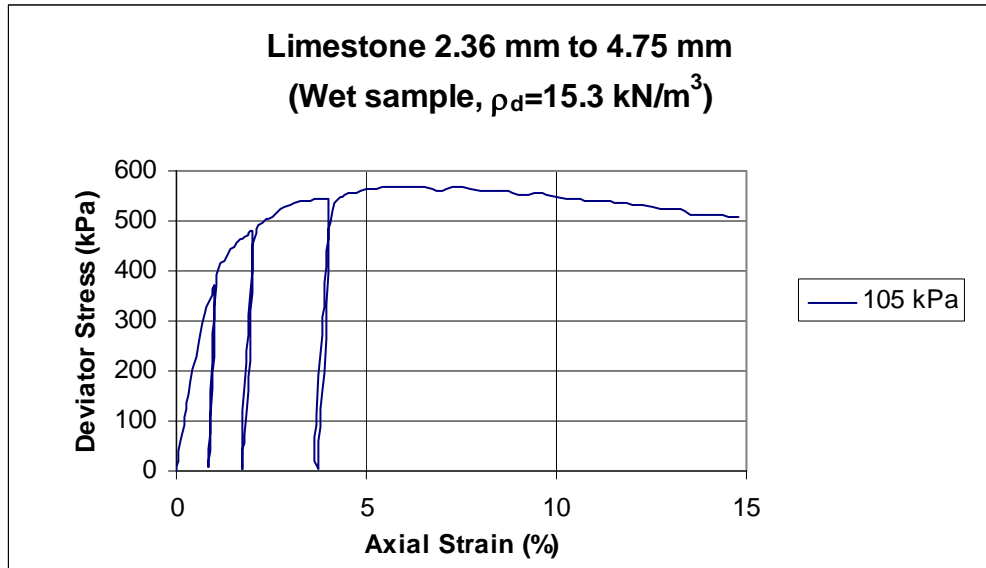


Figure A10

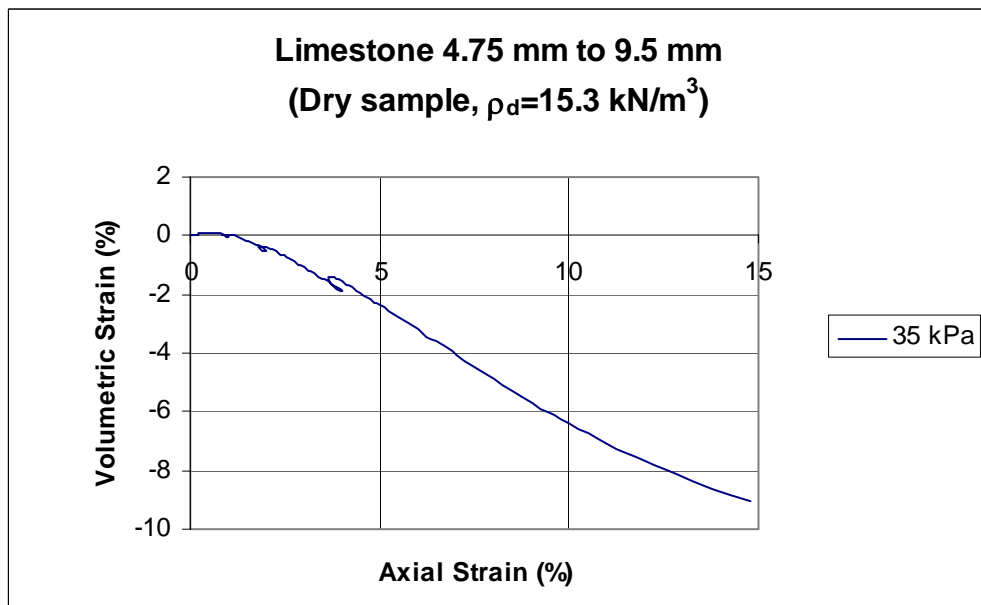
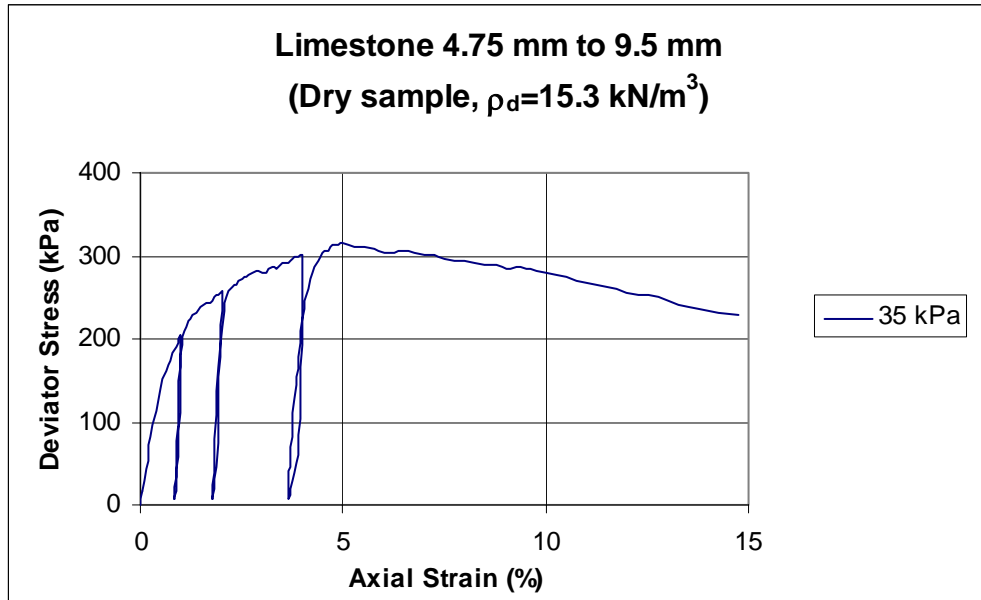


Figure A11

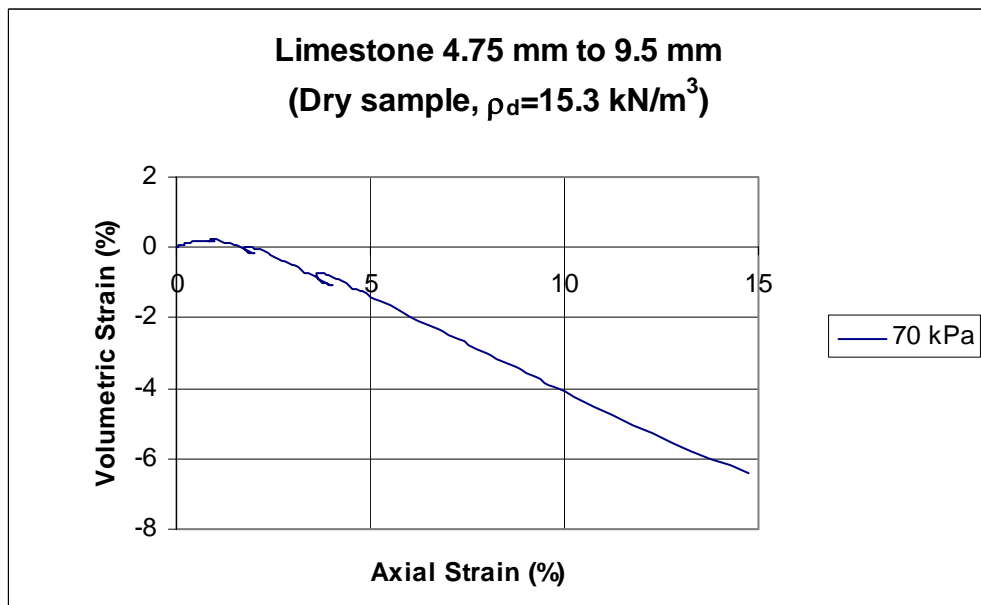
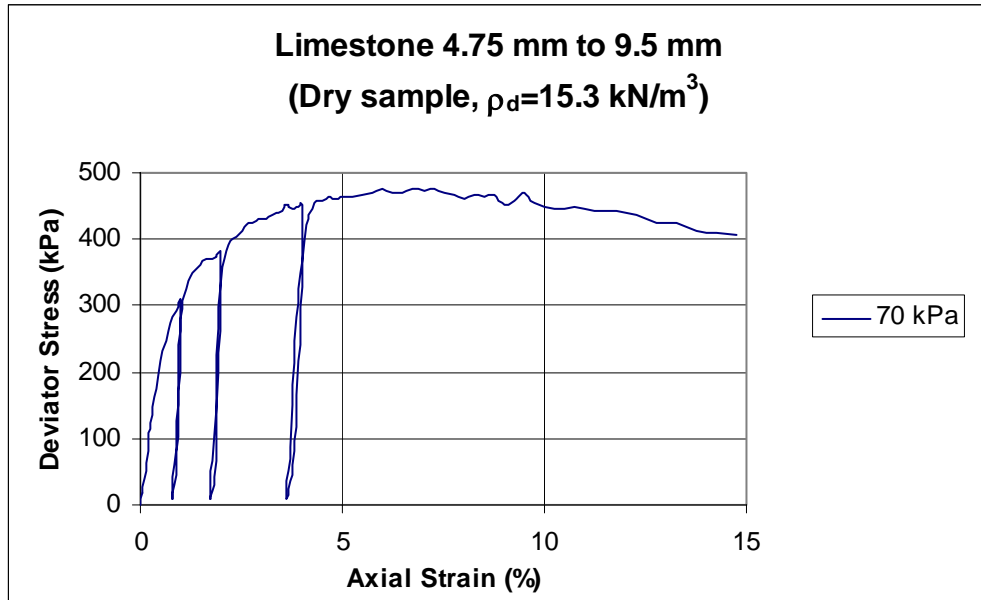


Figure A12

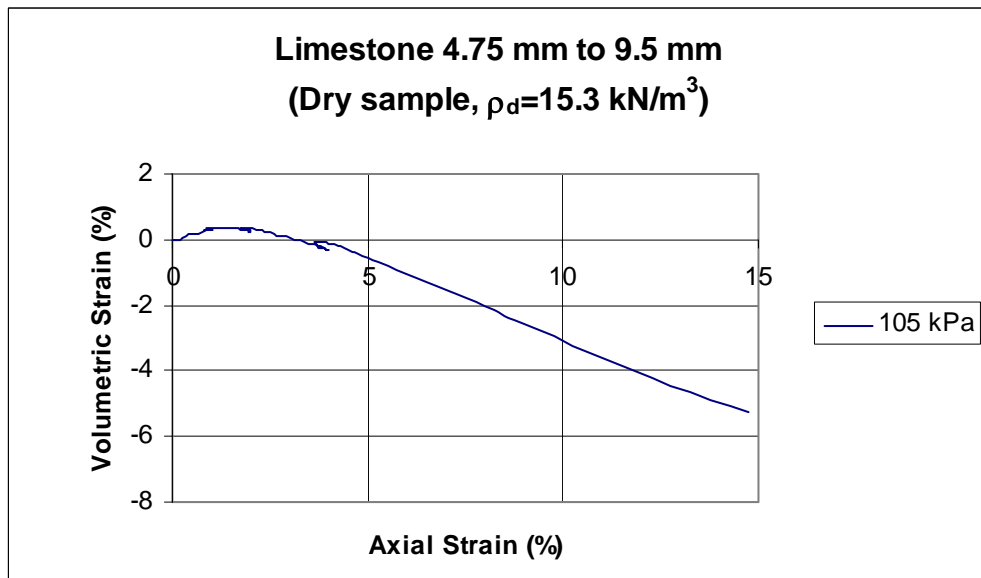
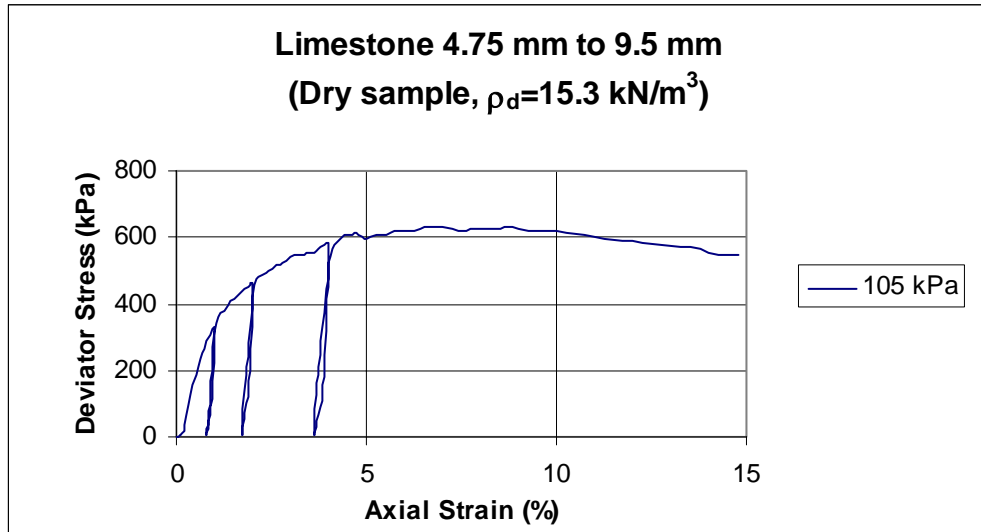


Figure A13

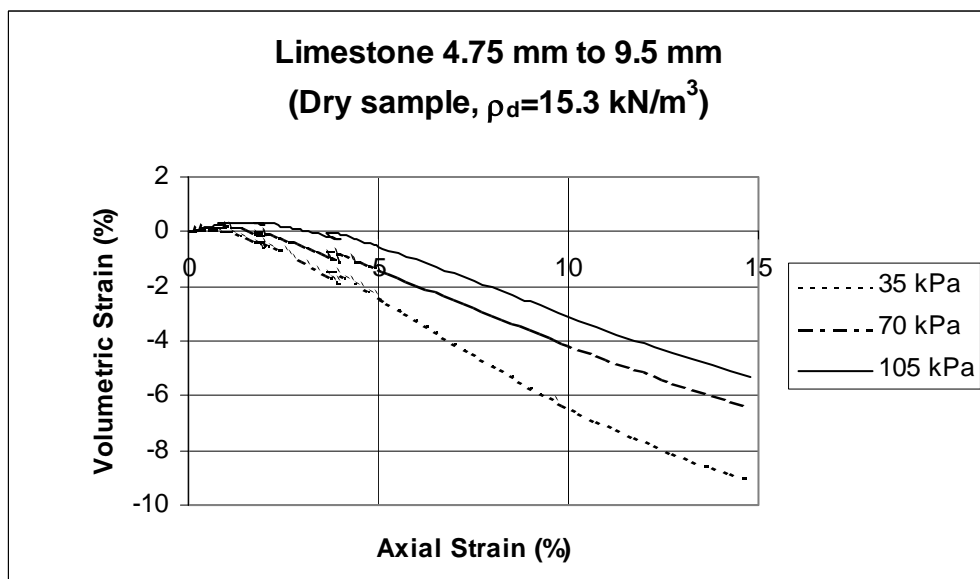
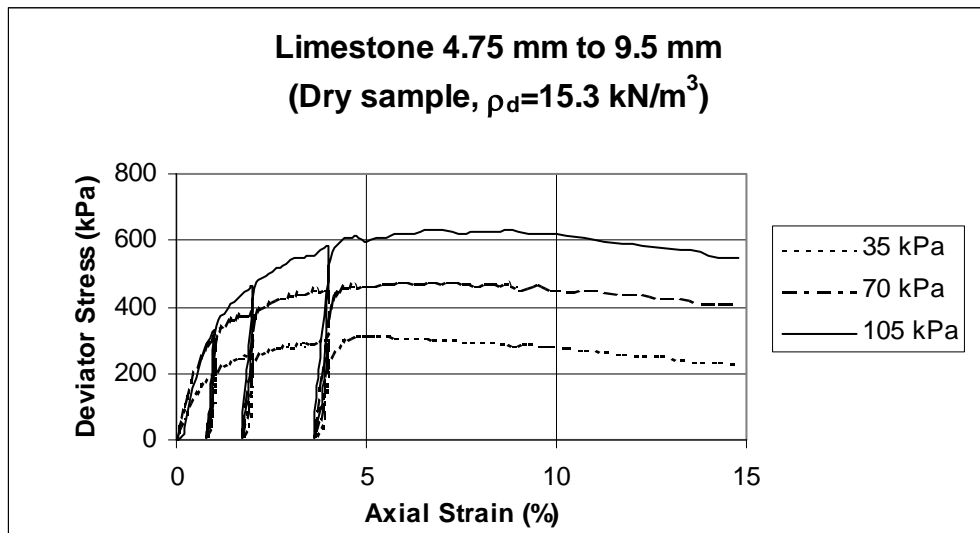


Figure A14

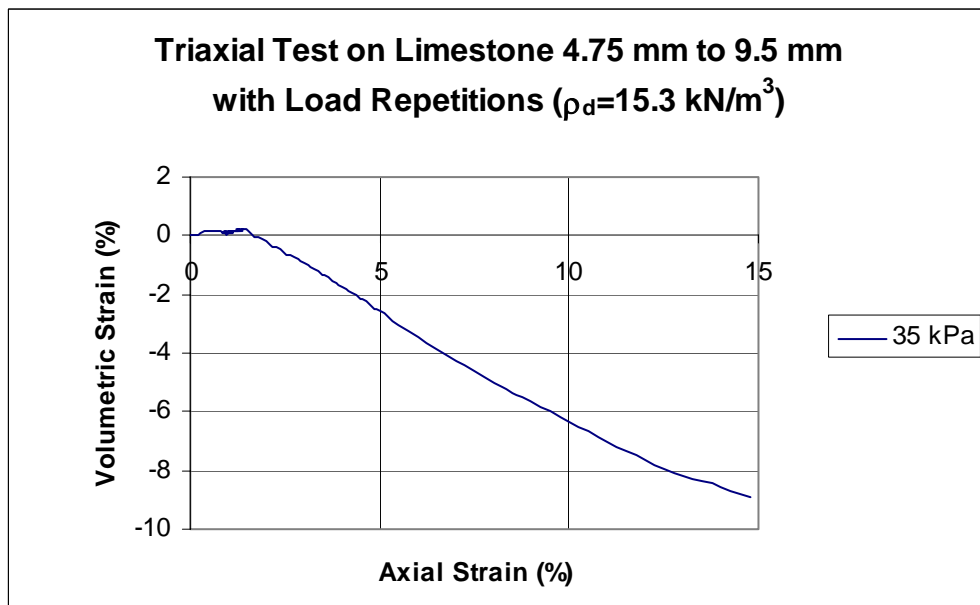
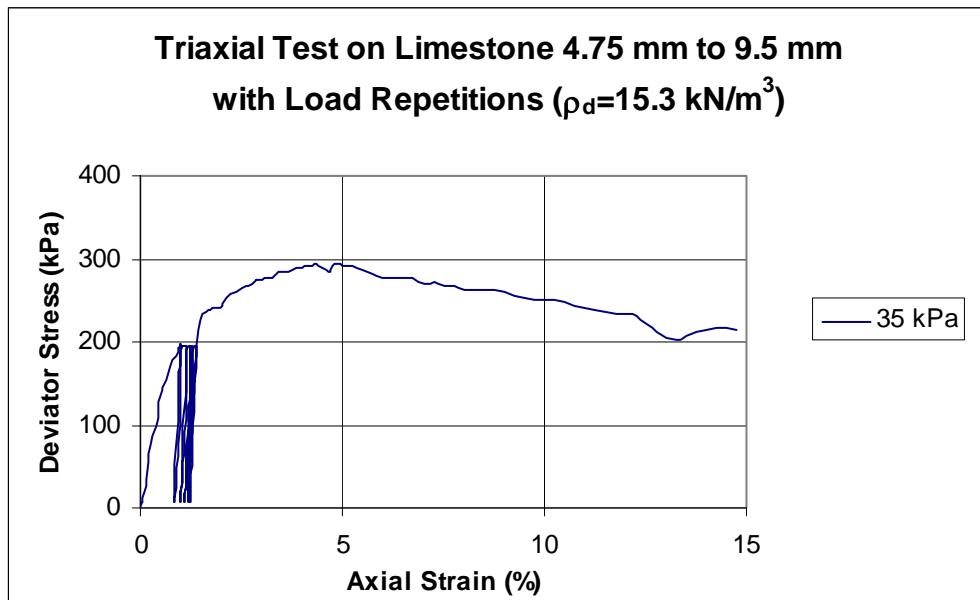


Figure A15

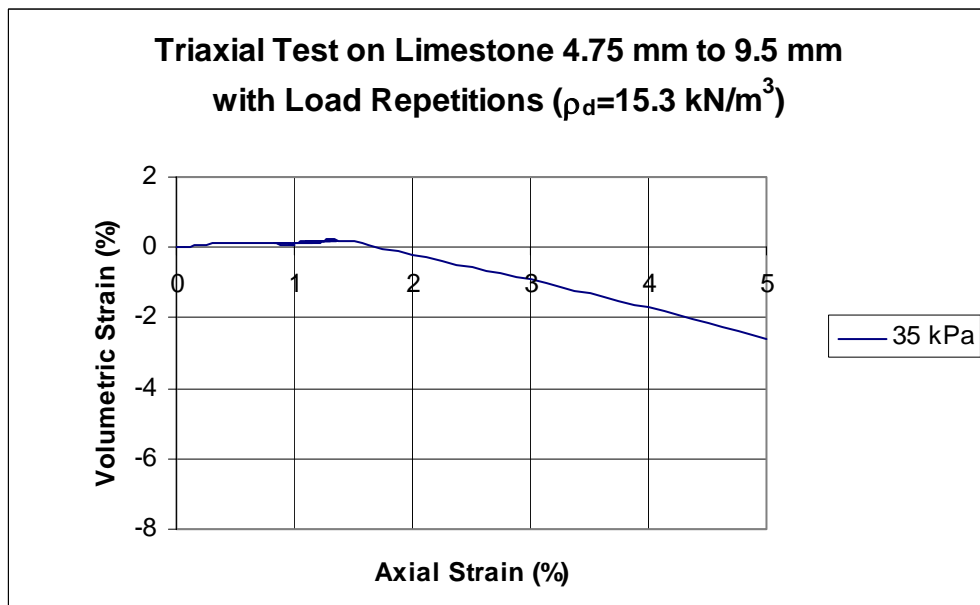
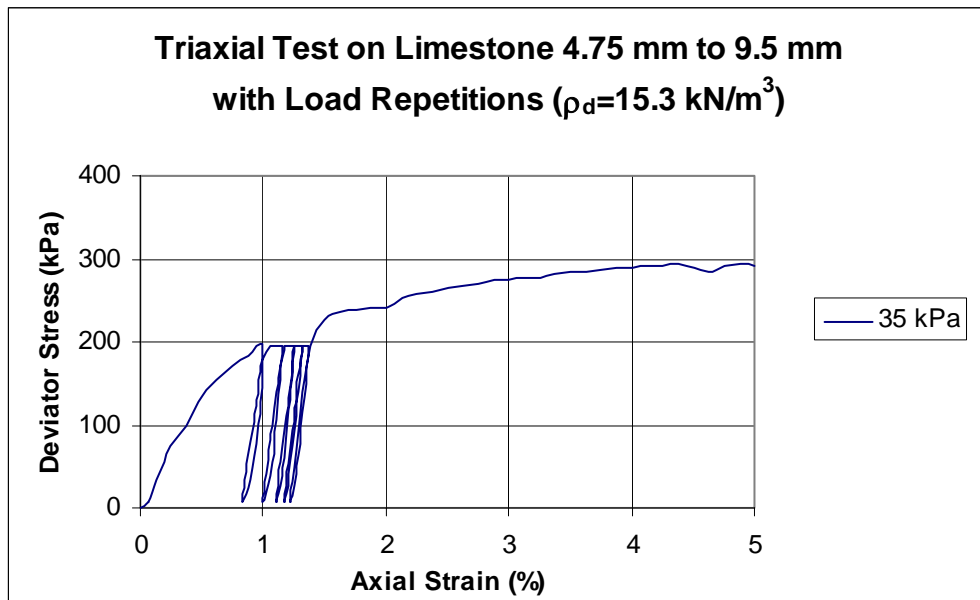


Figure A16

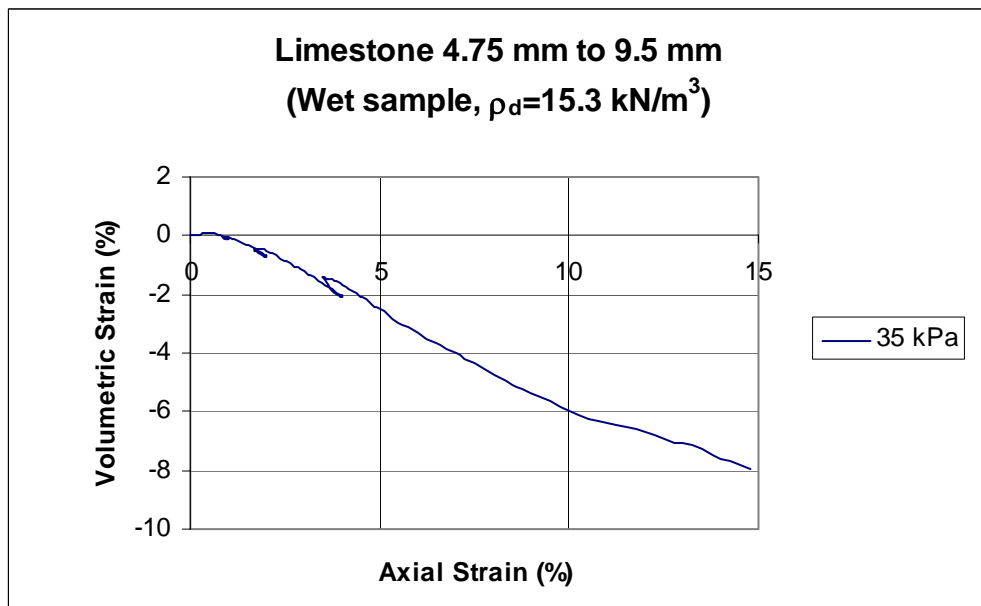
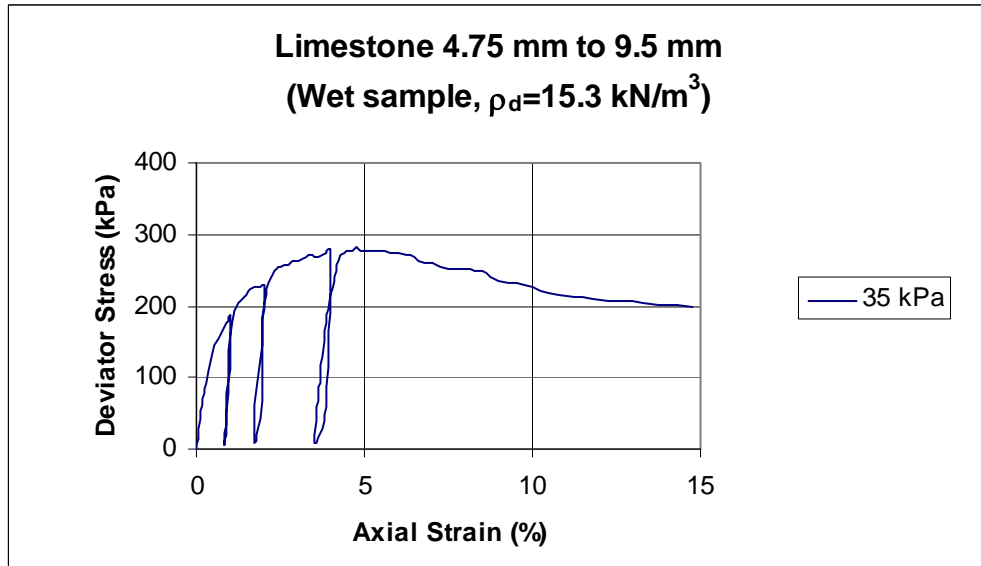


Figure A17

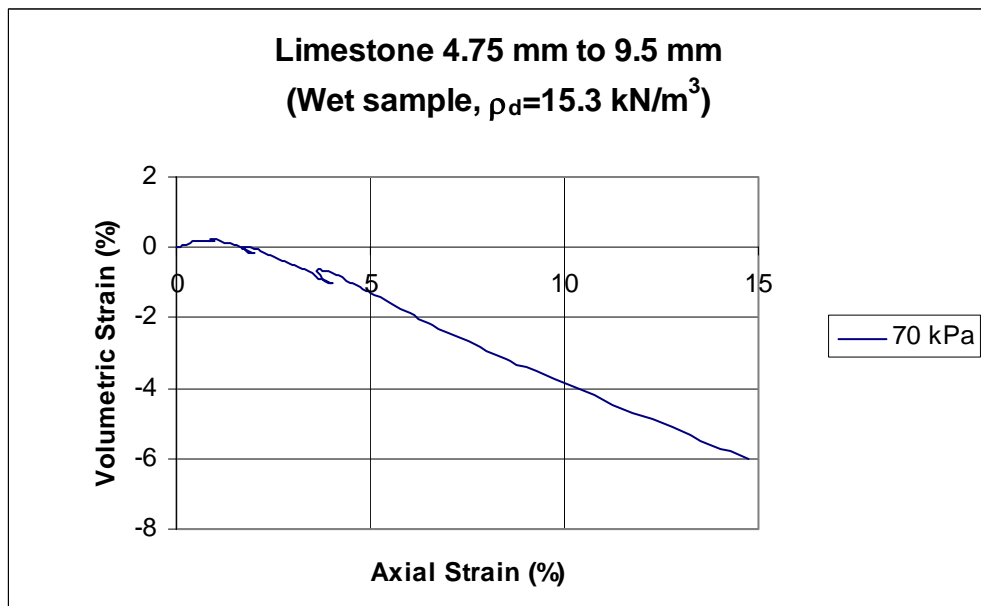
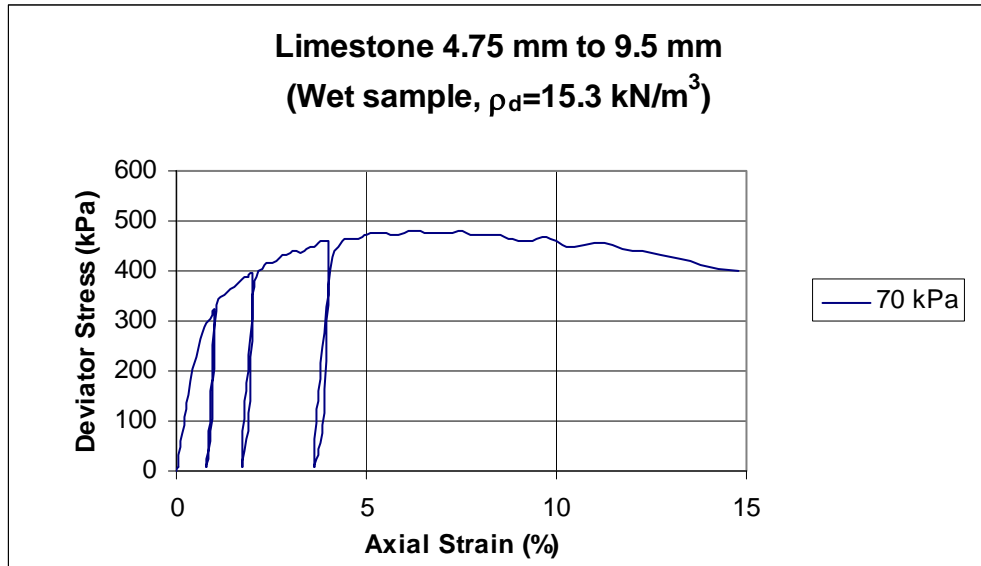


Figure A18

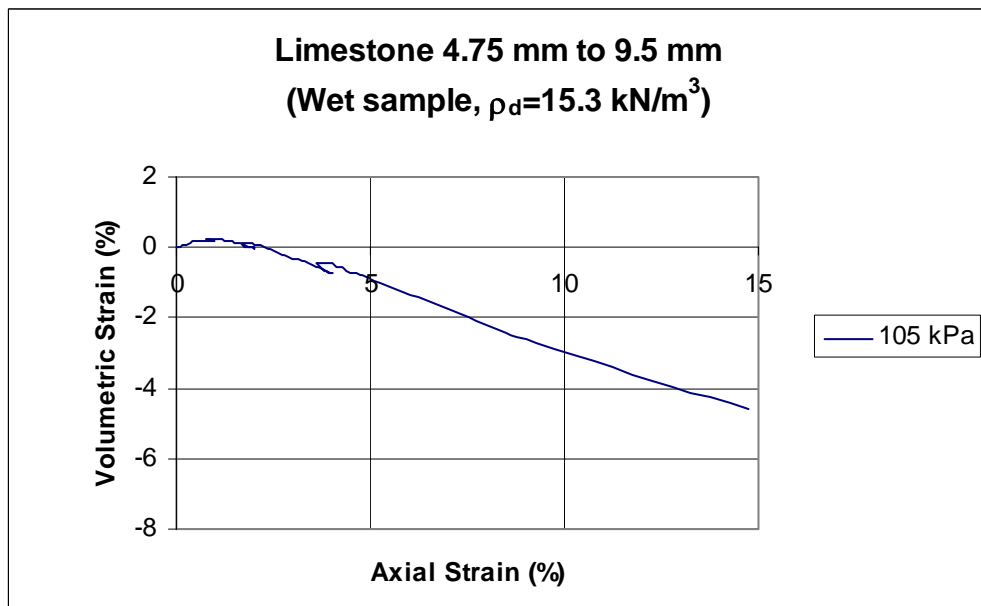
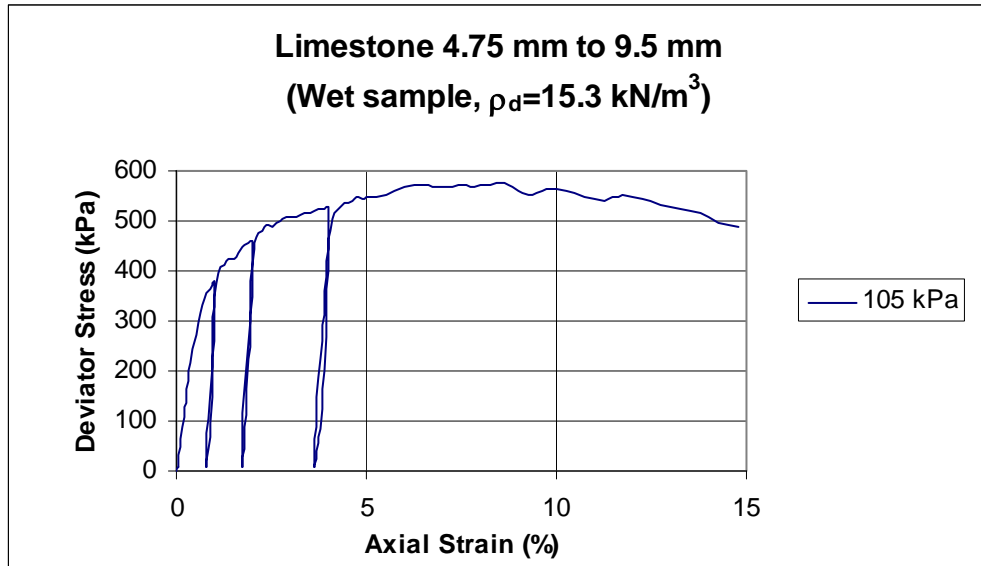


Figure A19

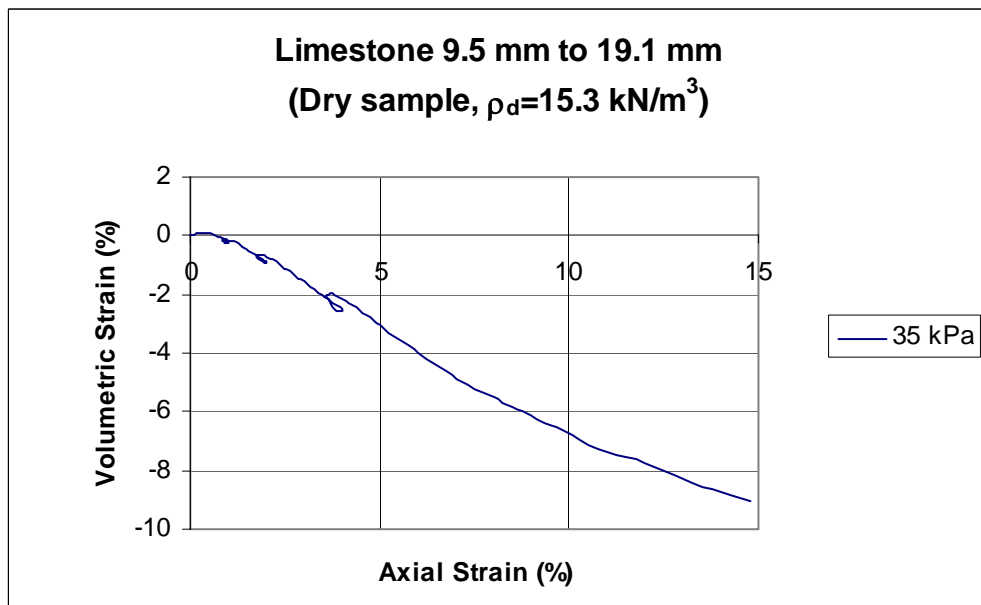
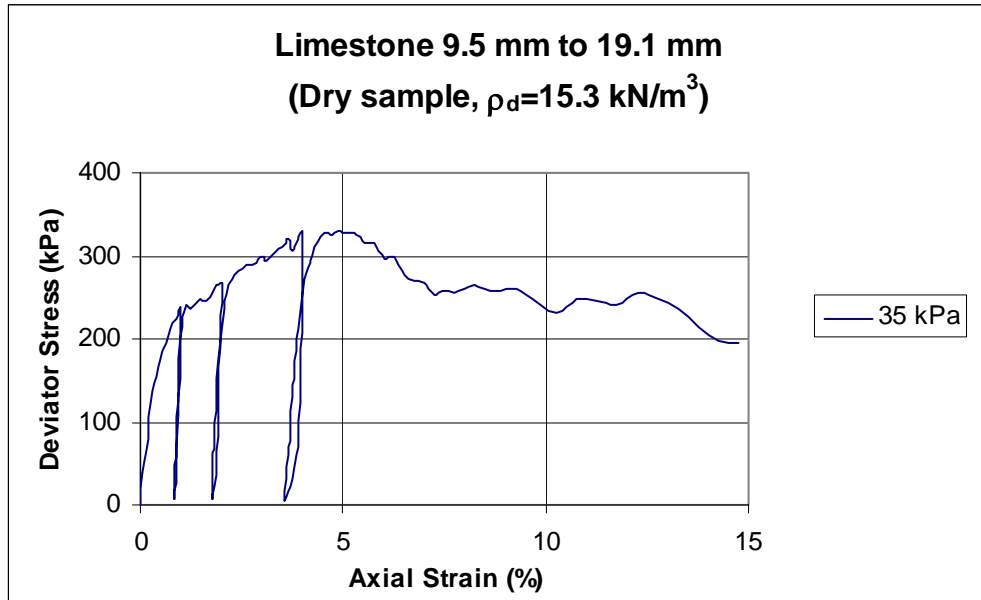


Figure A20

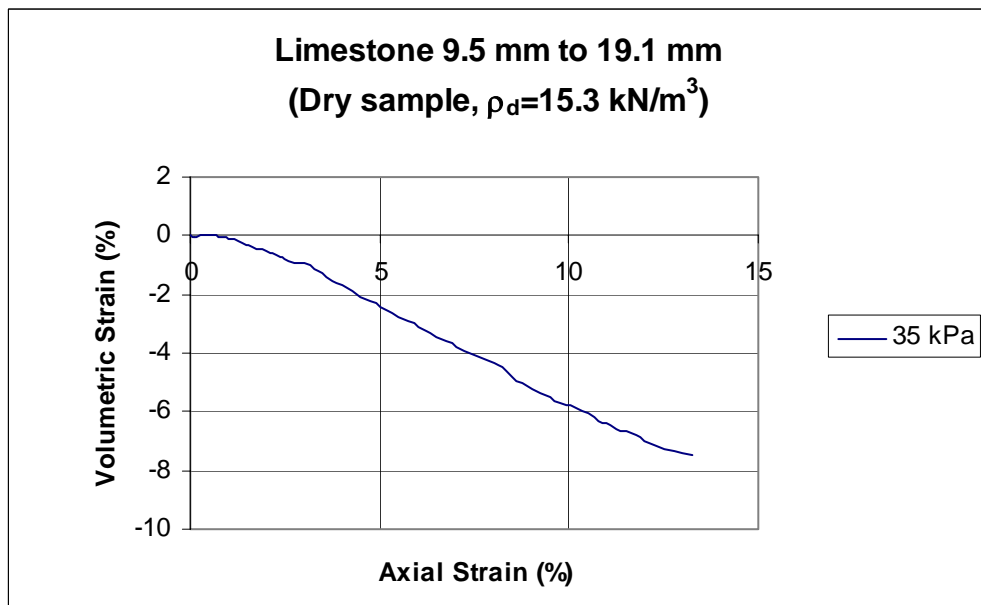
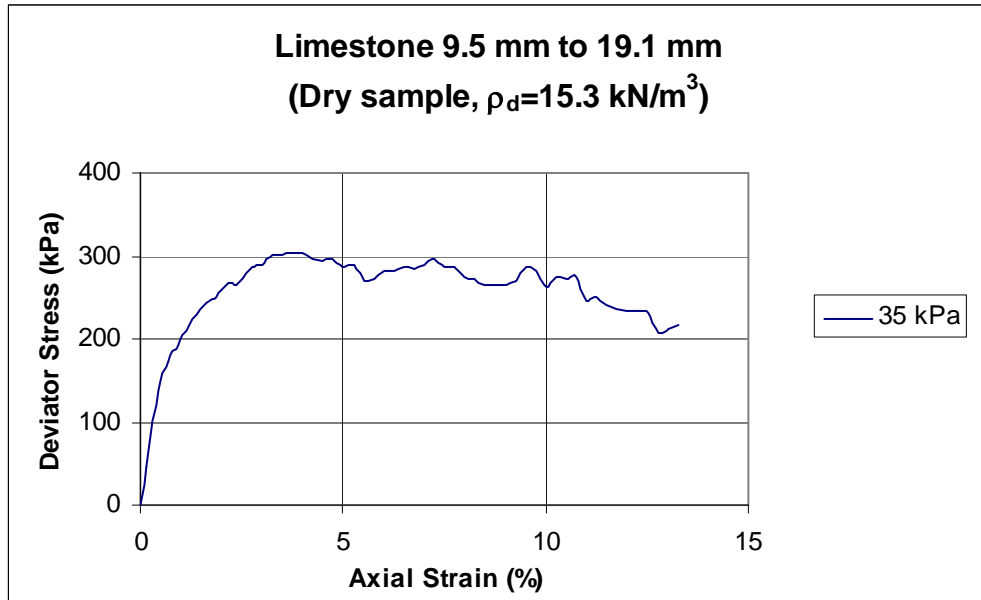


Figure A21

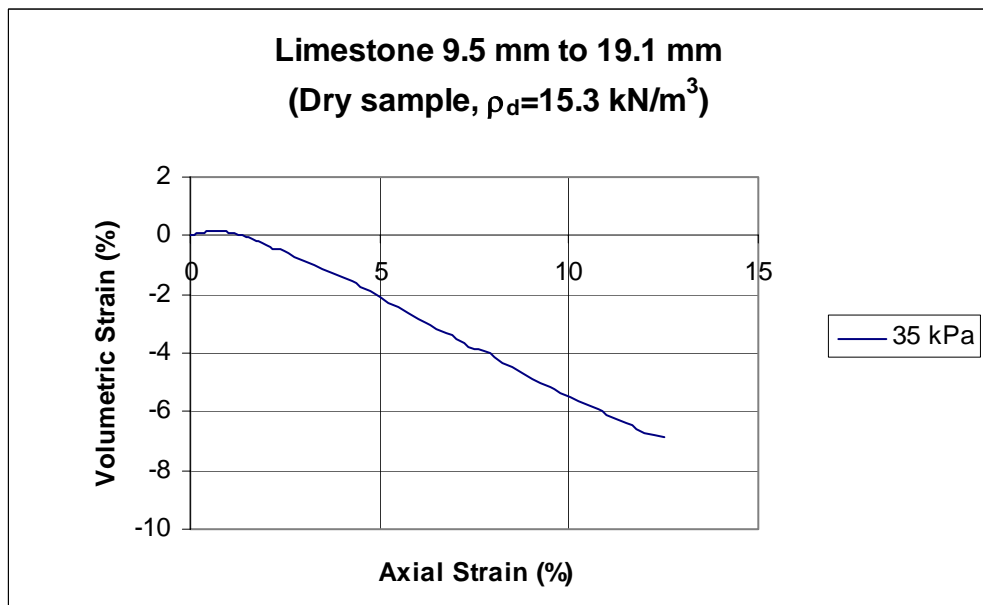
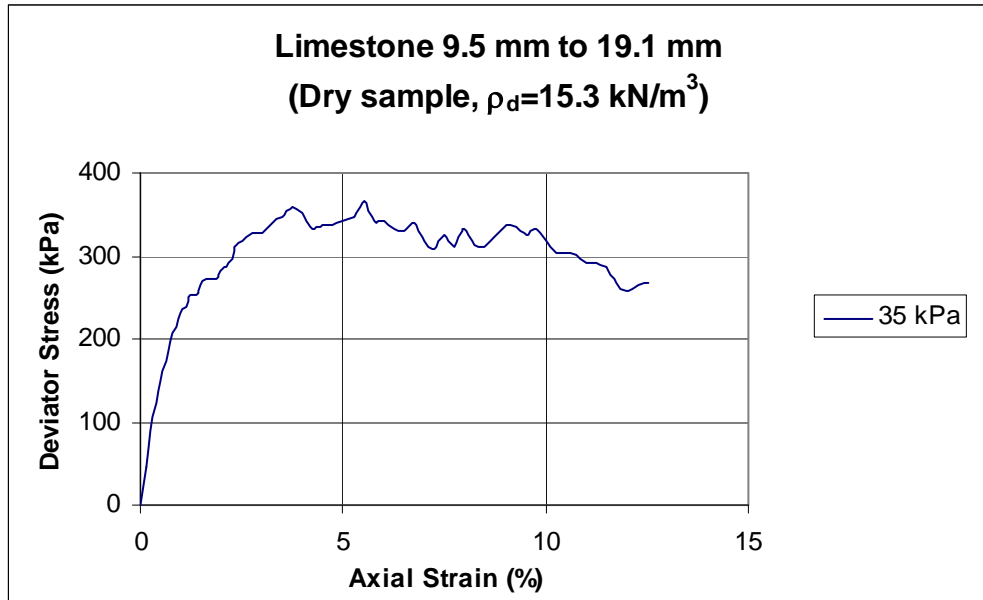


Figure A22

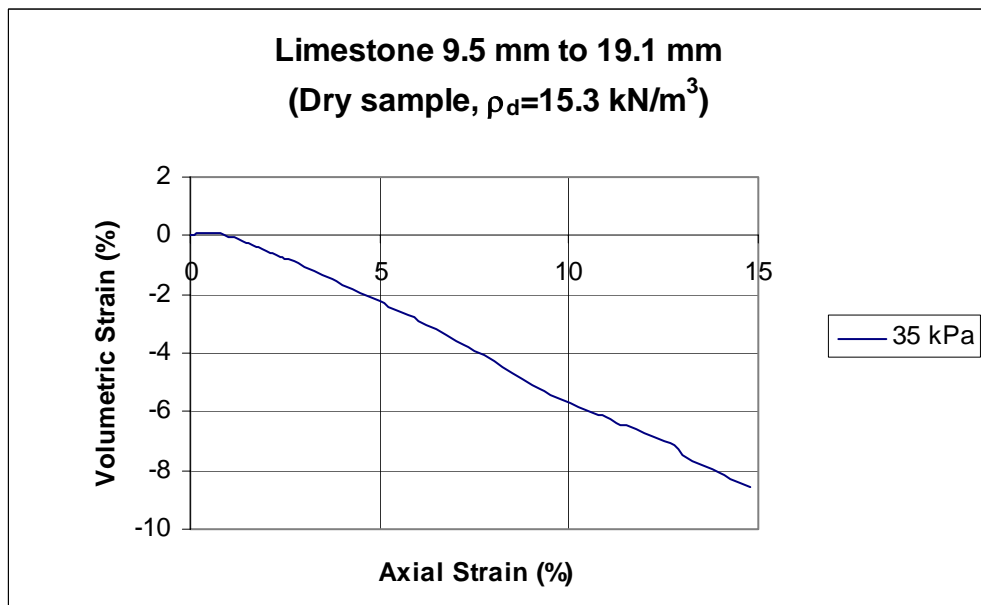
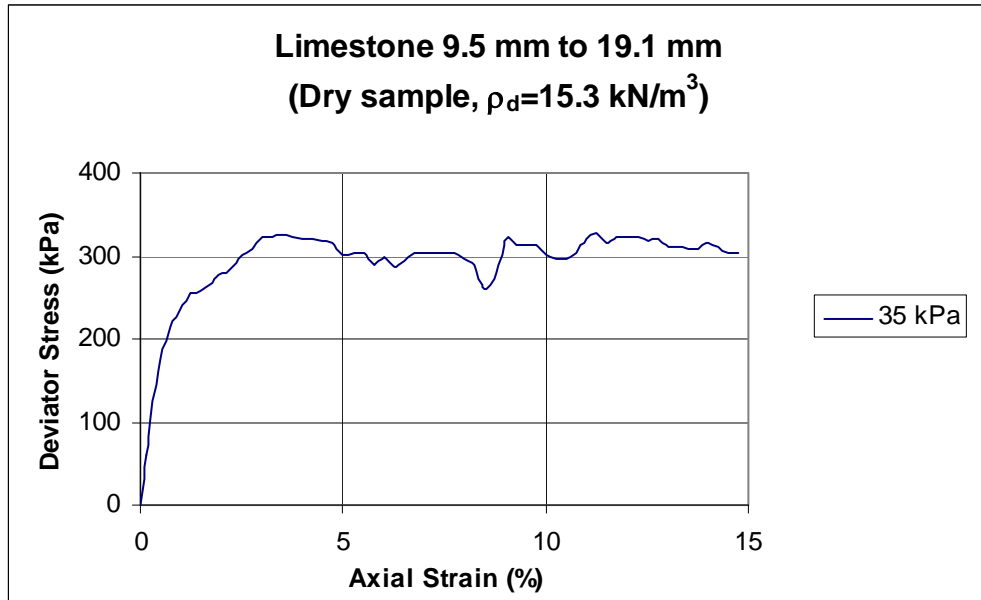


Figure A23

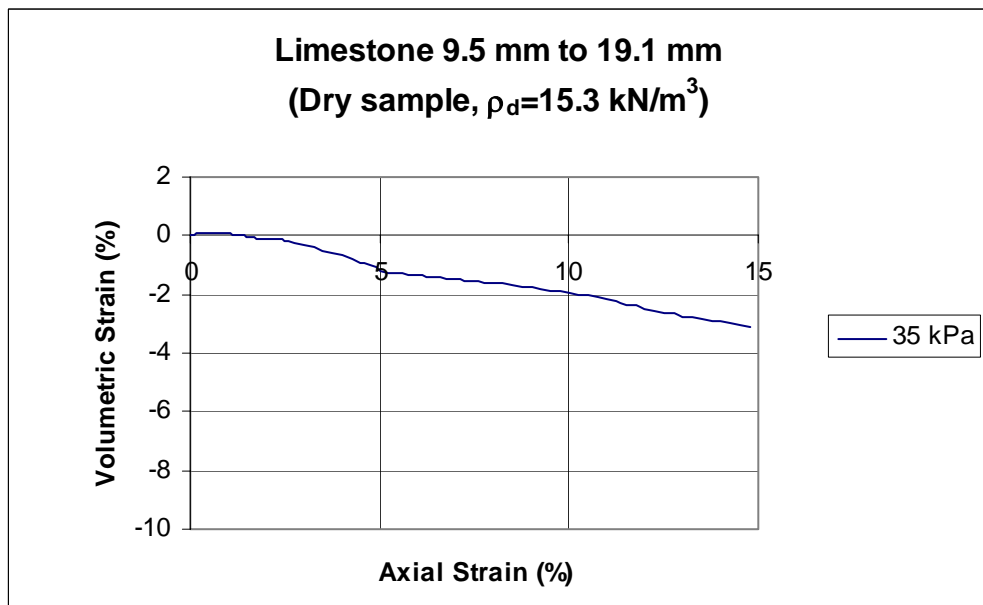
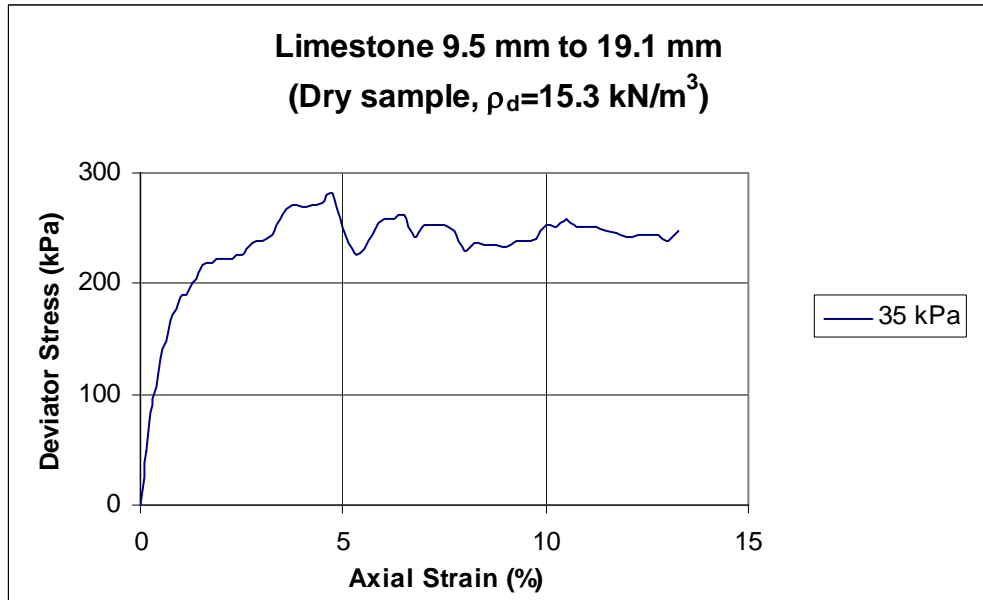


Figure A24

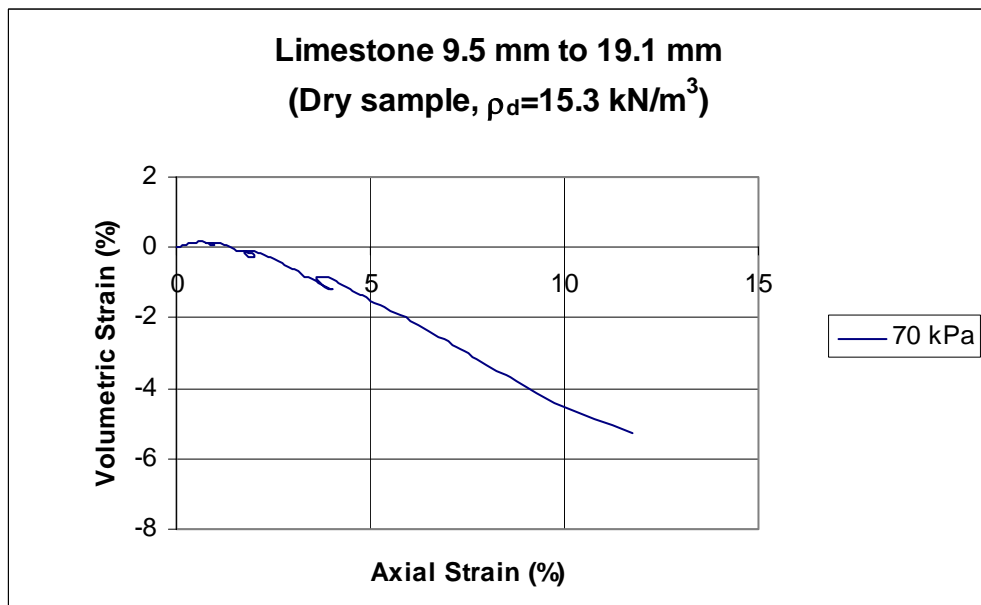
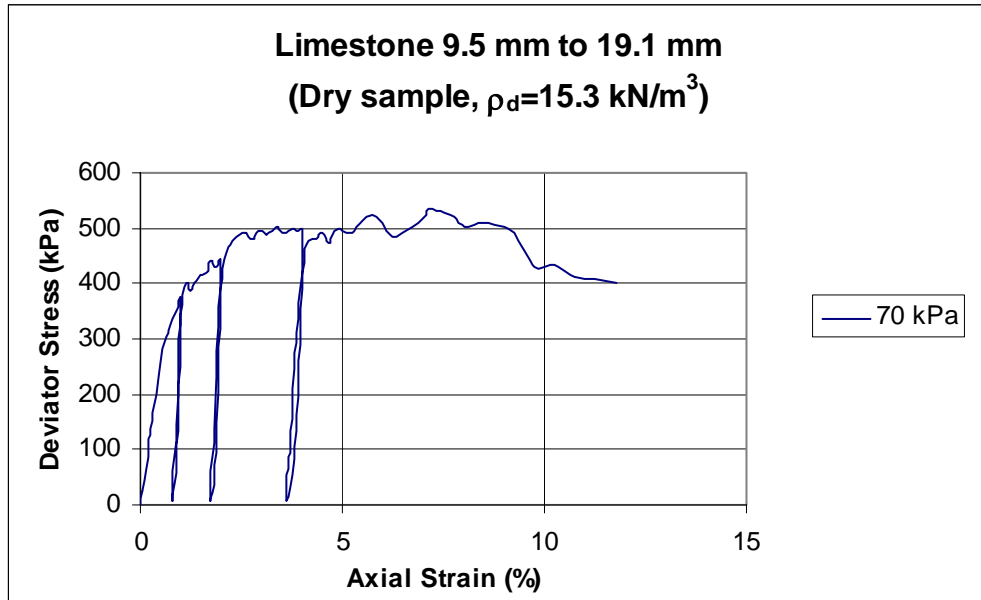


Figure A25

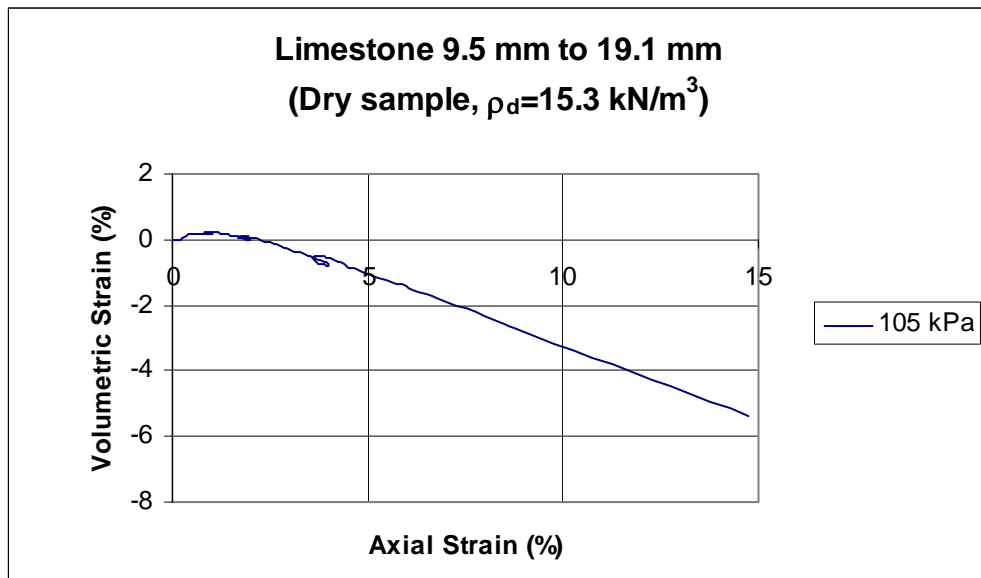
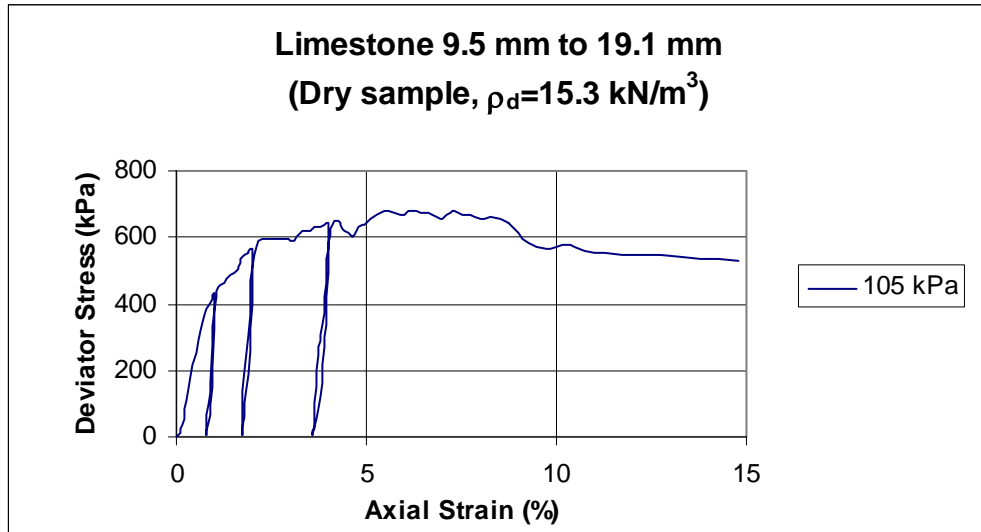


Figure A26

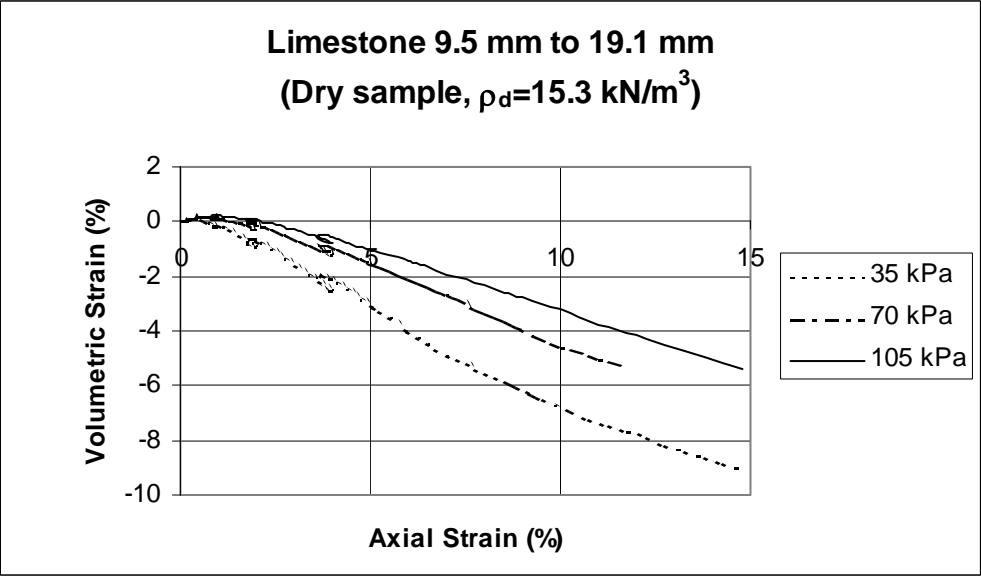
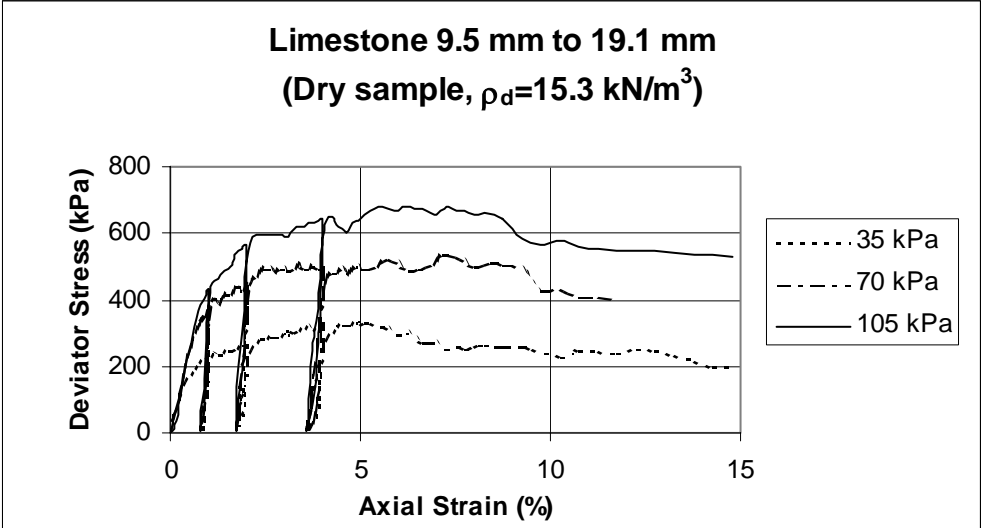


Figure A27

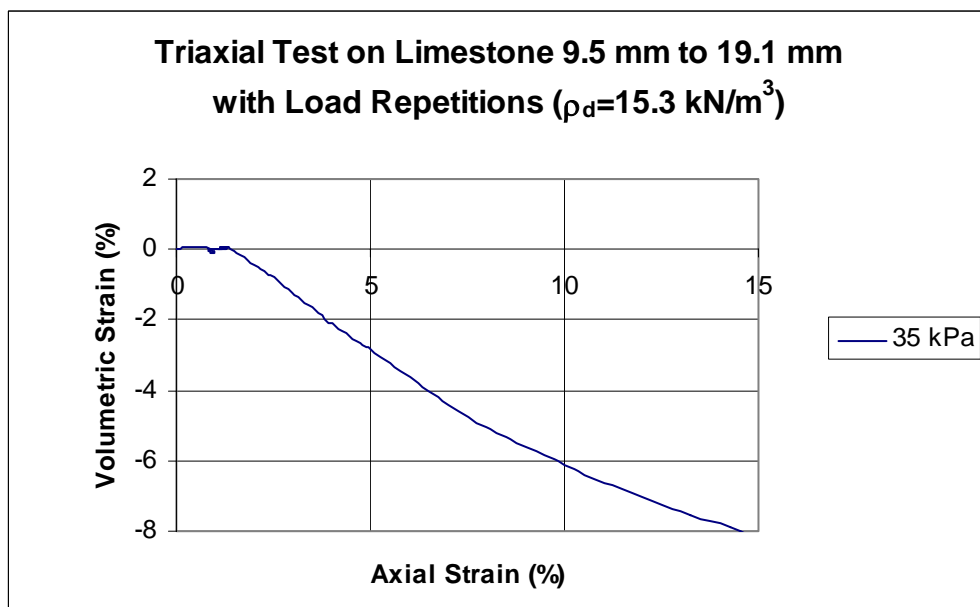
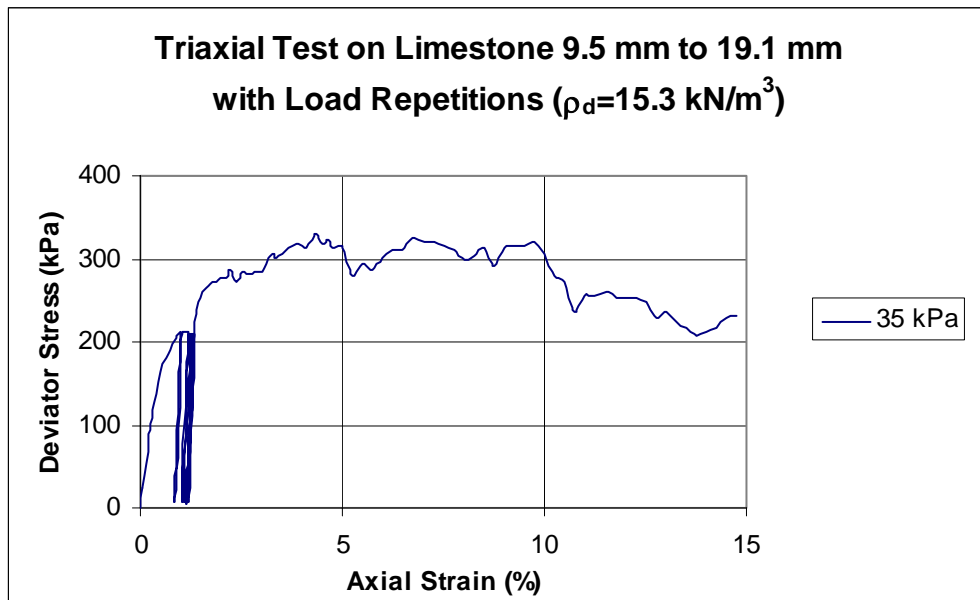


Figure A28

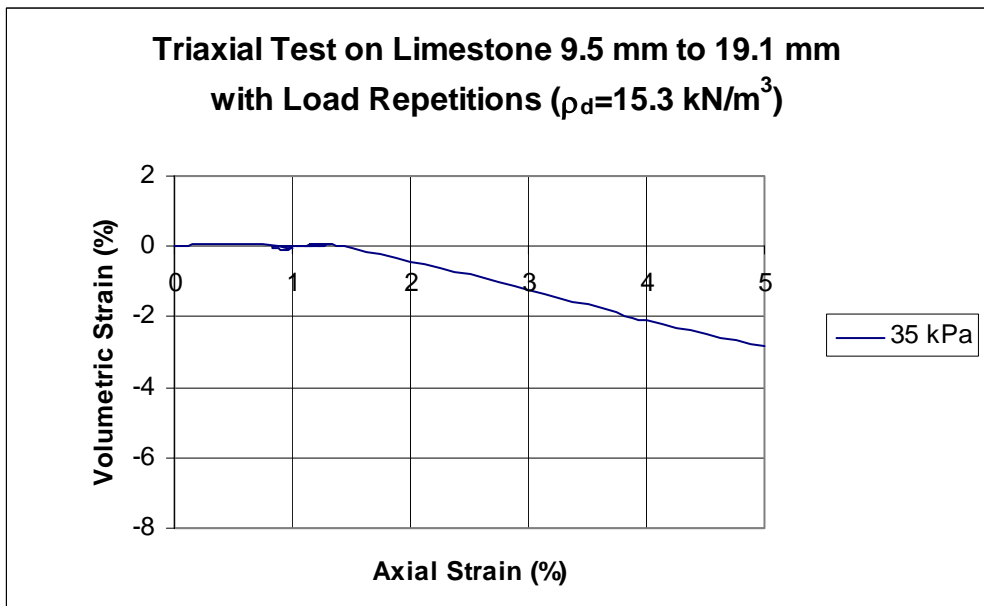
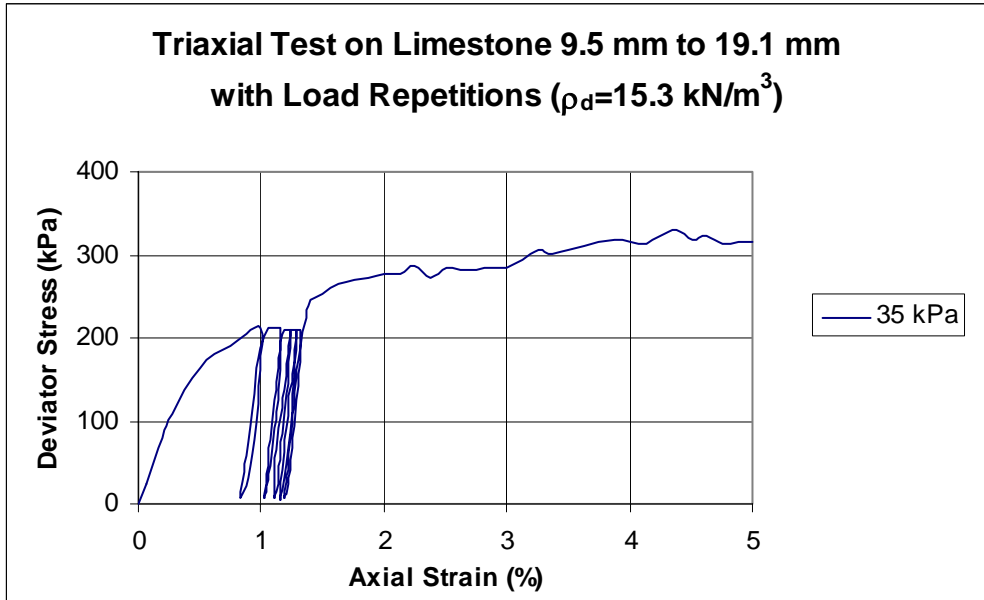


Figure A29

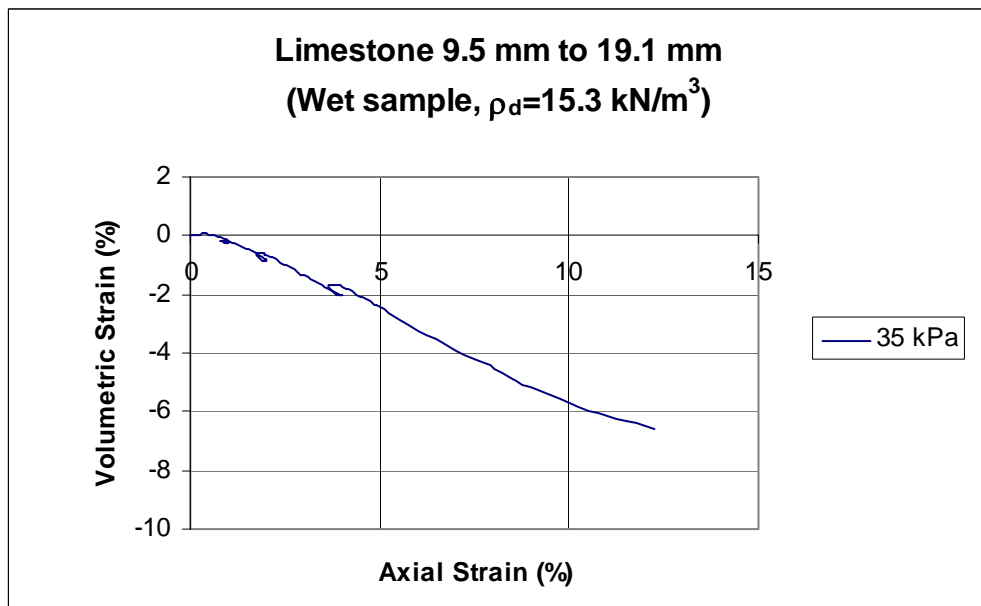
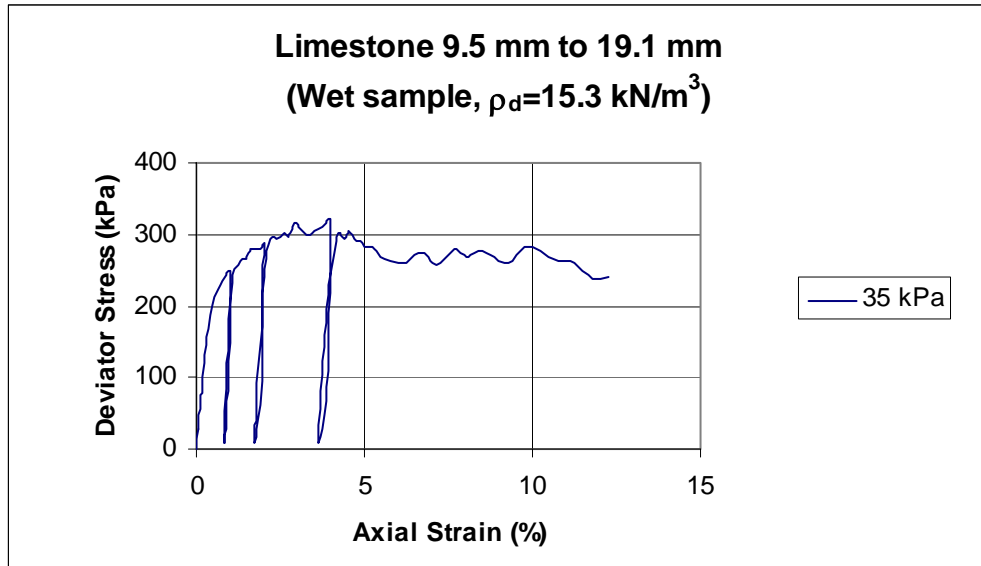


Figure A30

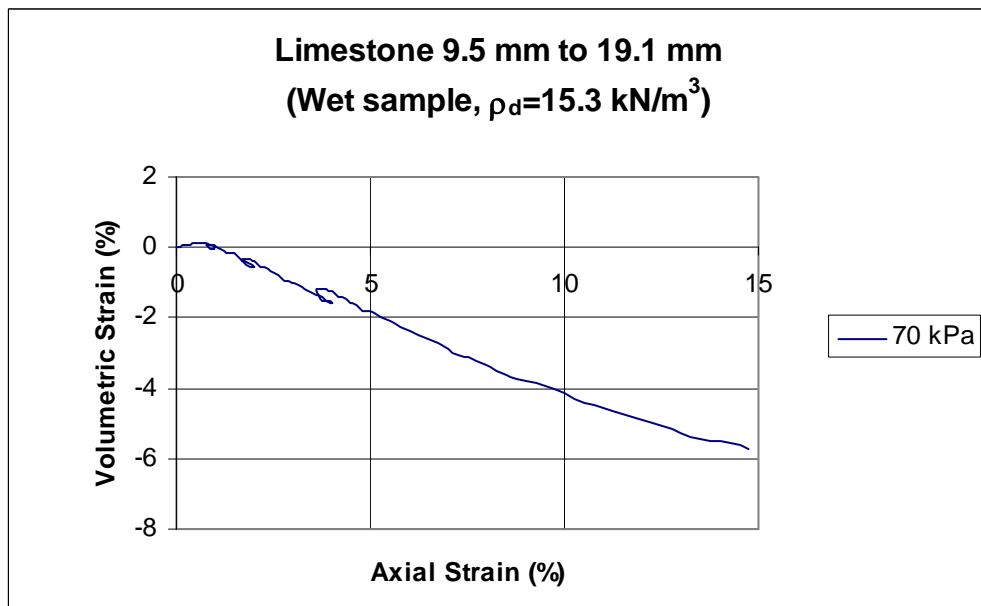
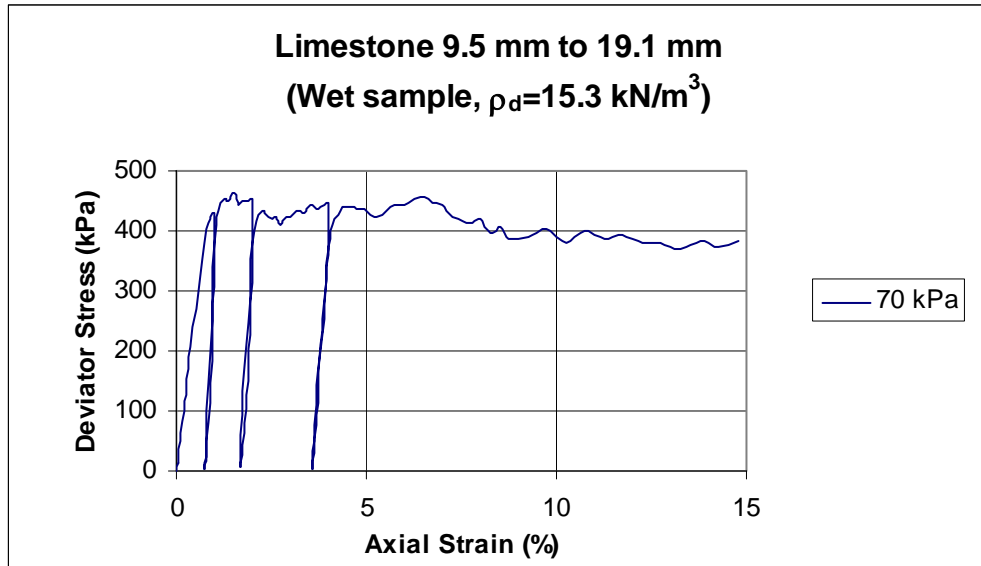


Figure A31

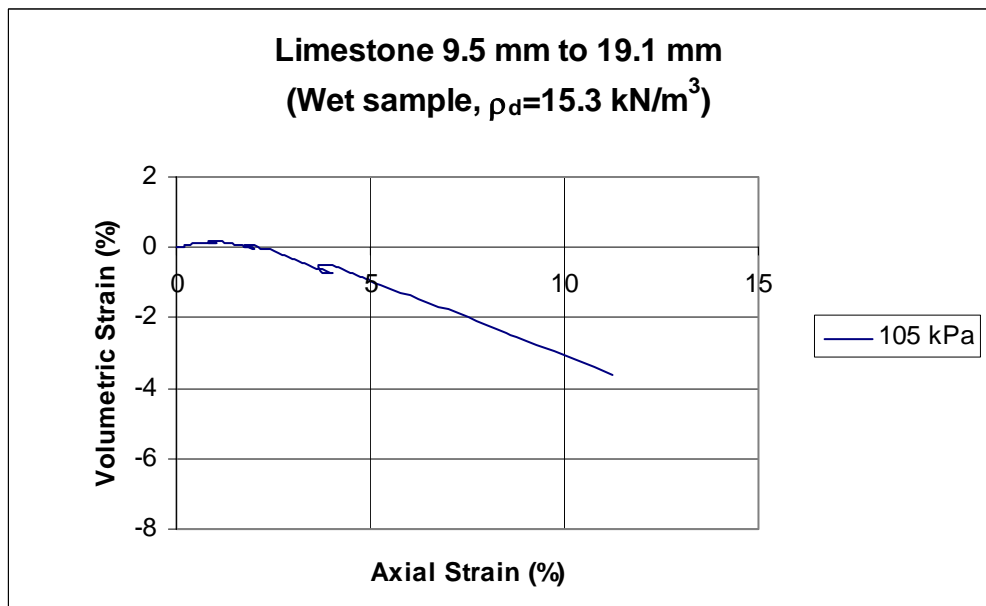
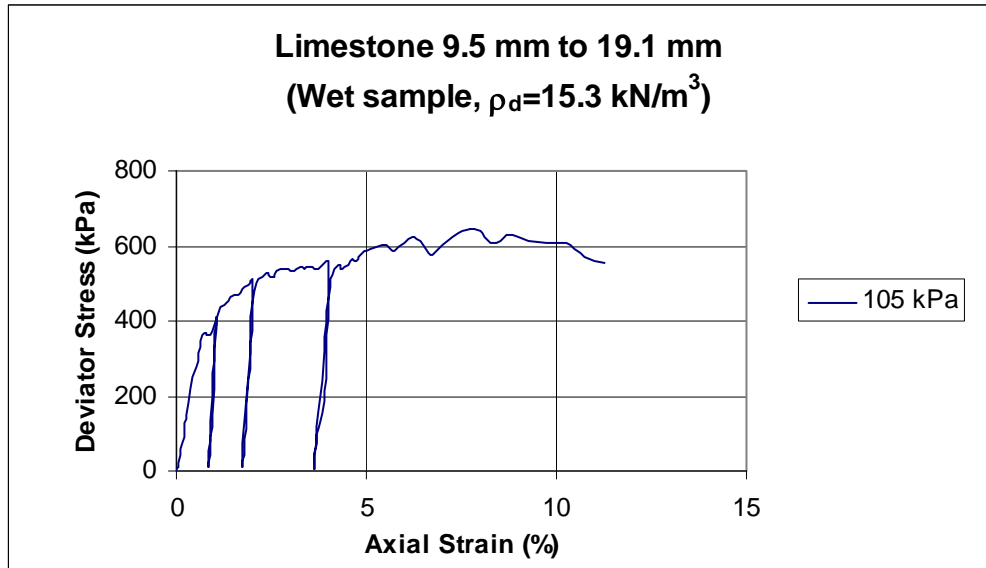


Figure A32

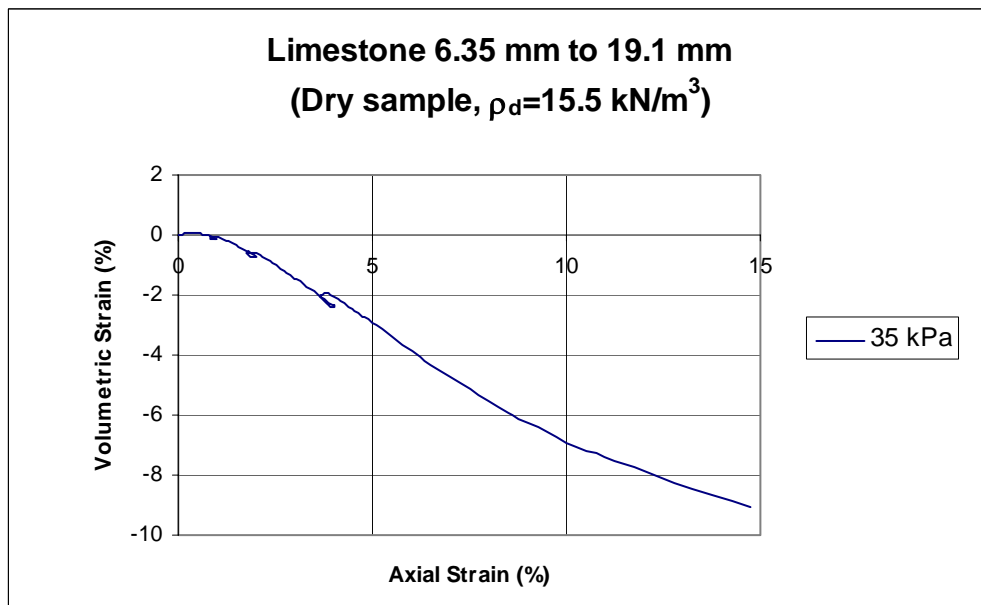
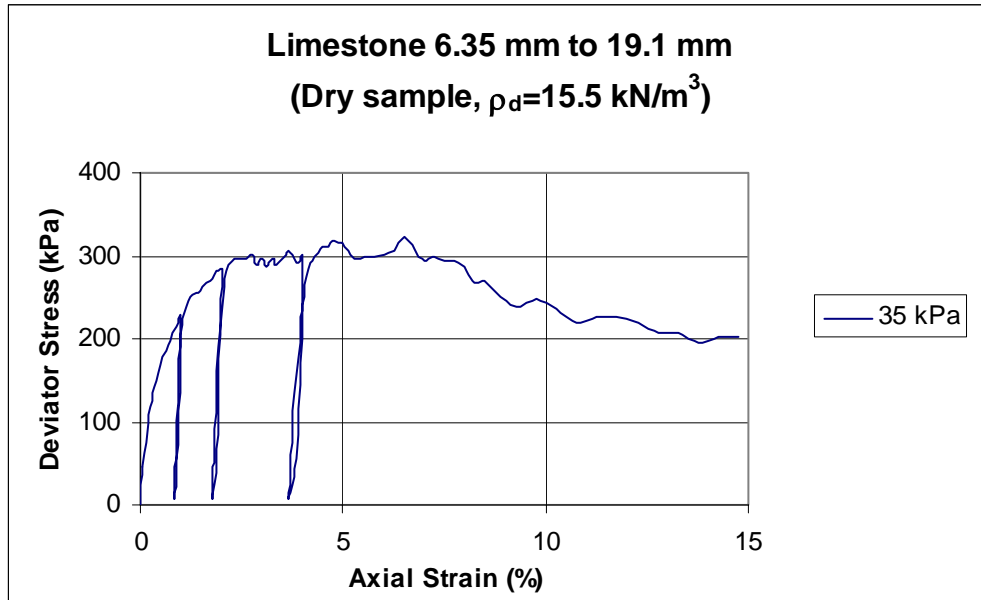


Figure A33

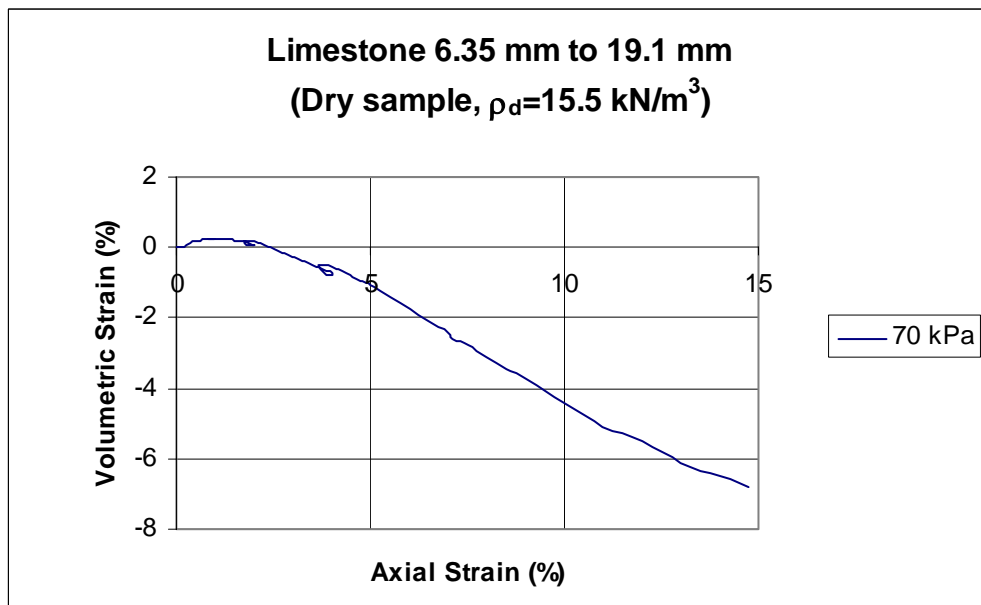
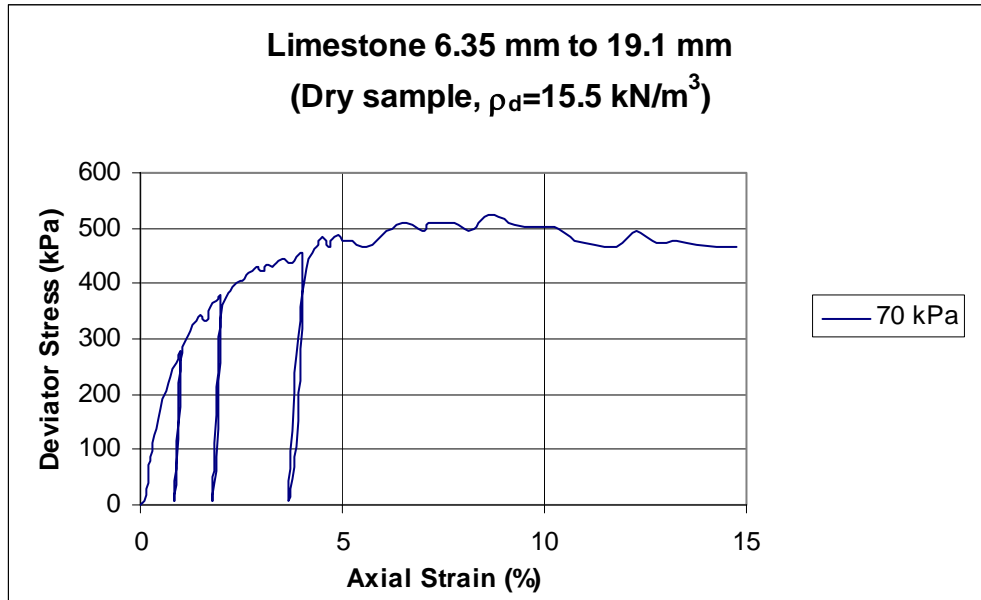


Figure A34

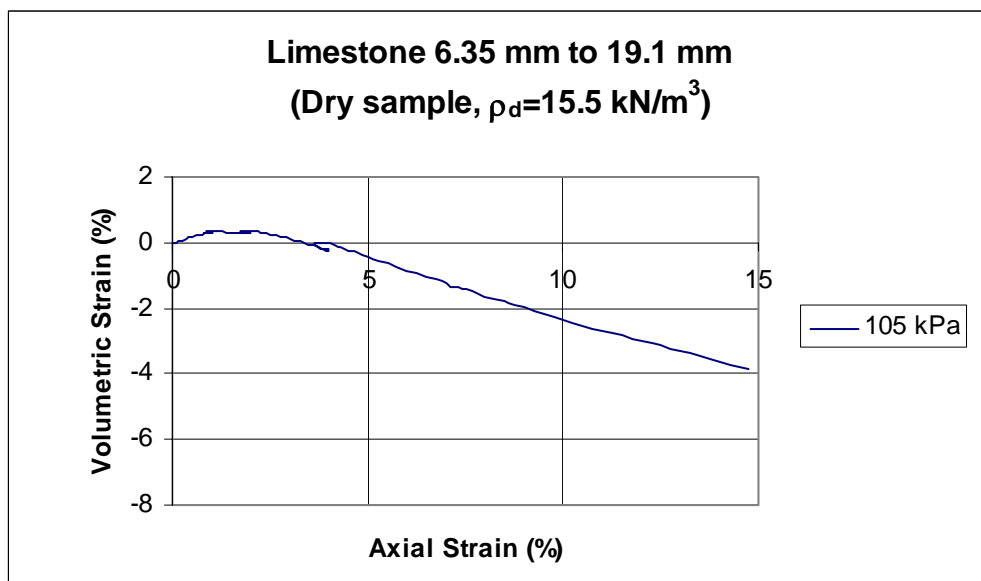
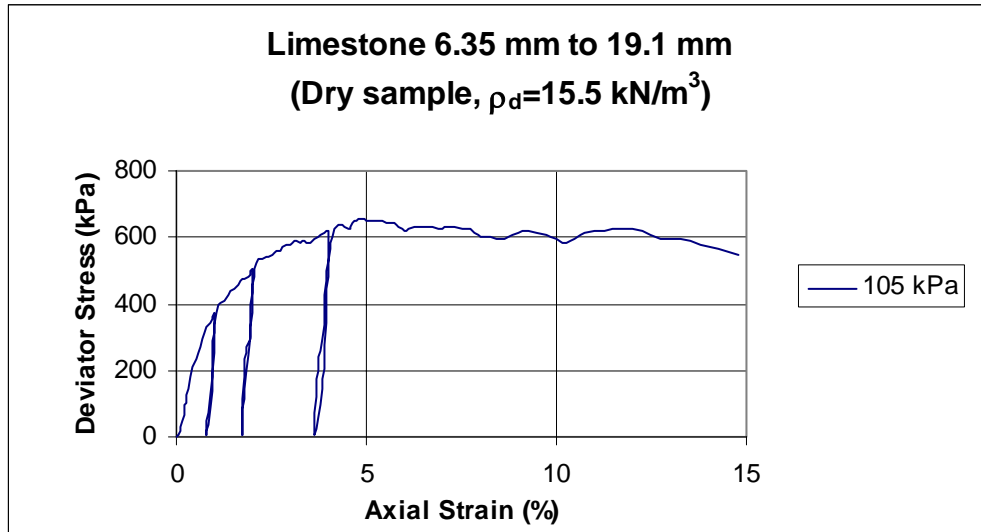


Figure A35

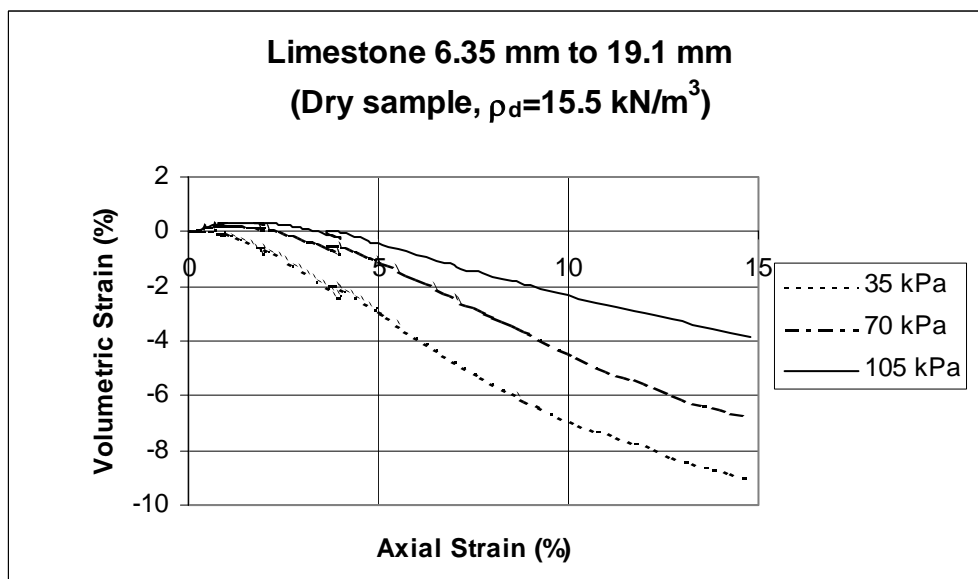
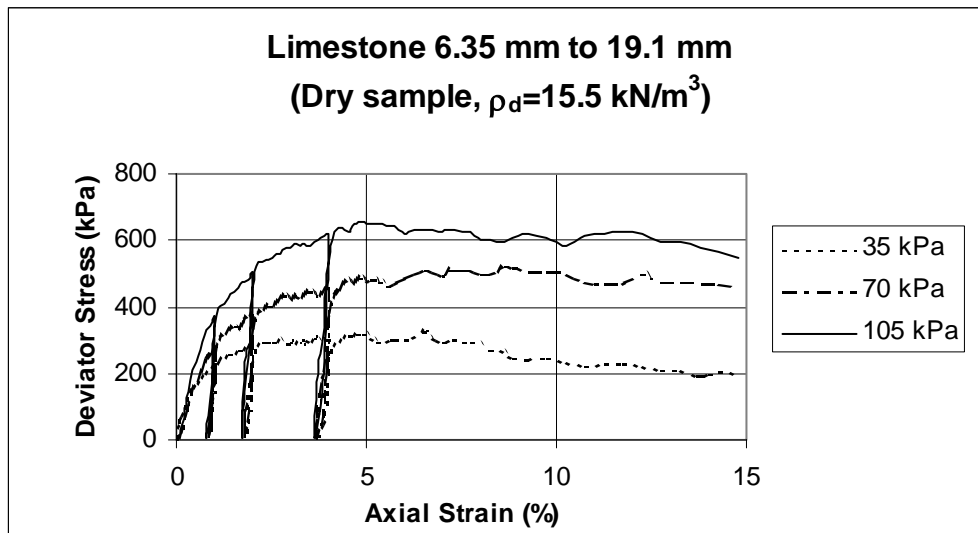


Figure A36

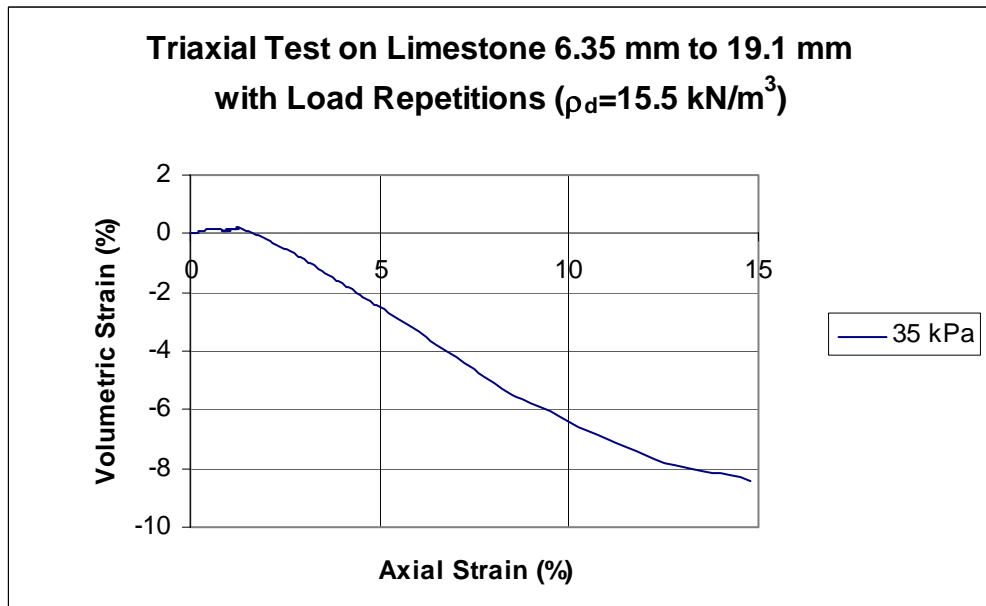
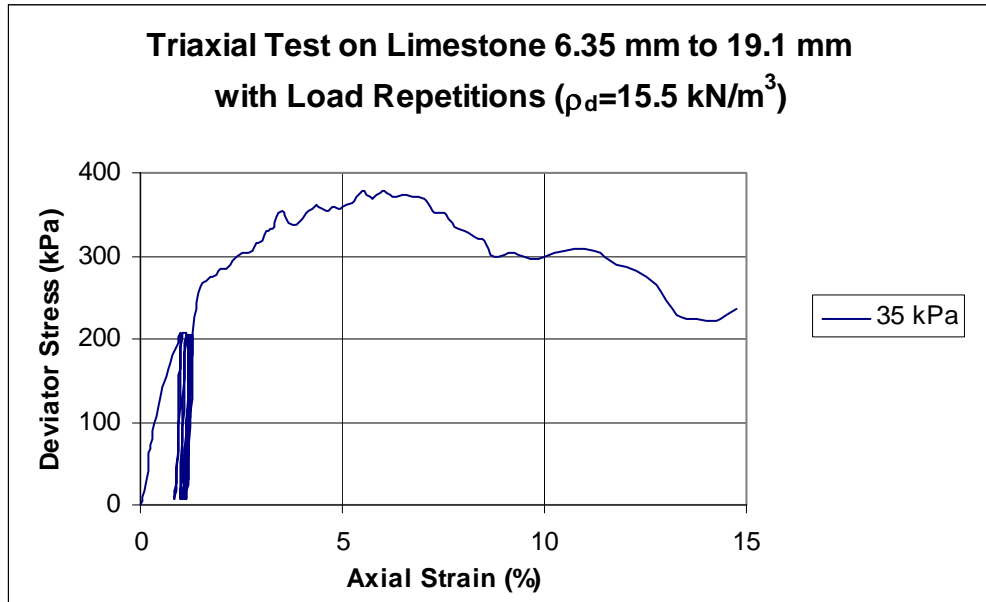


Figure A37

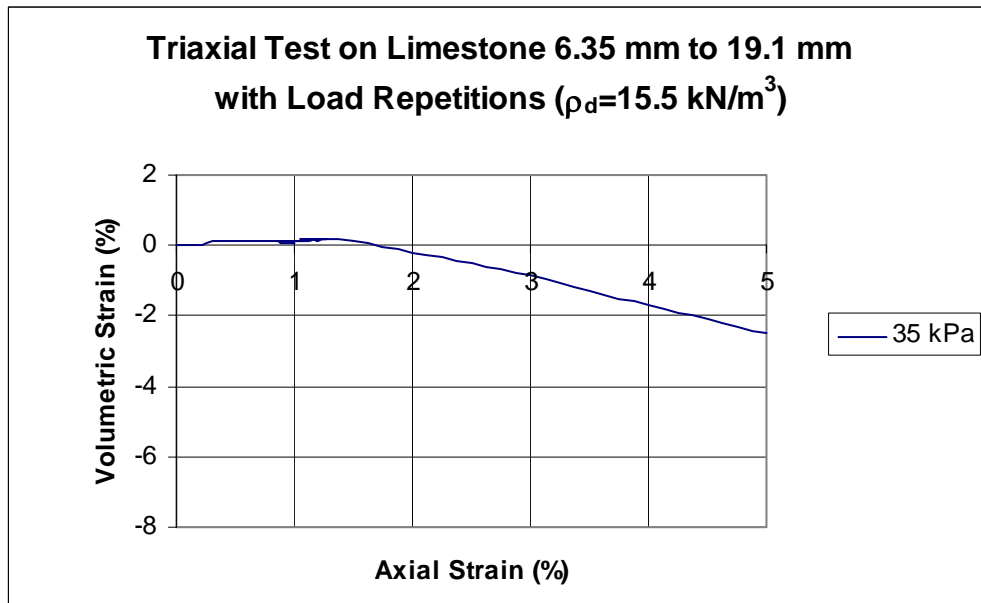
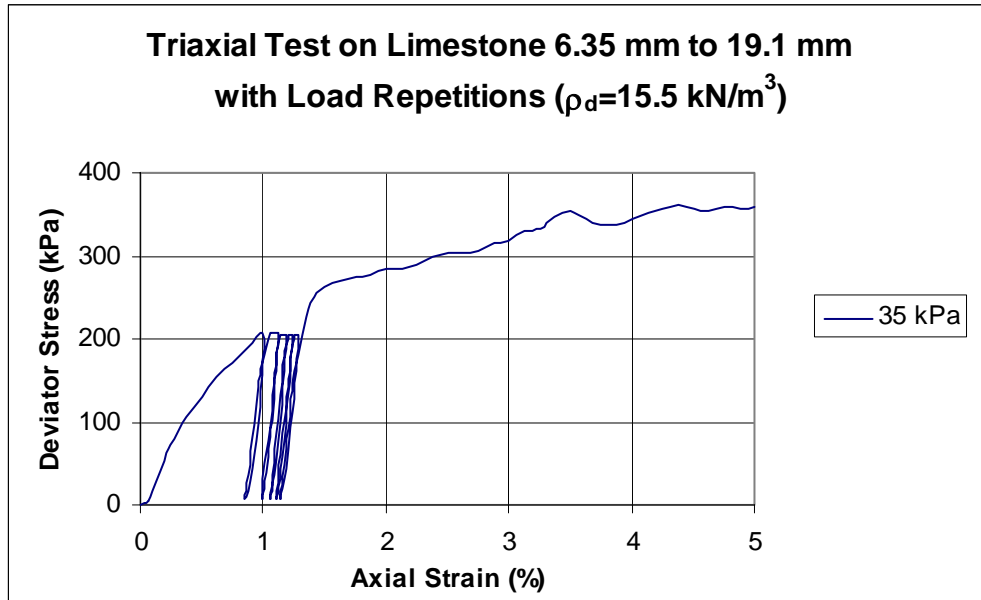


Figure A38

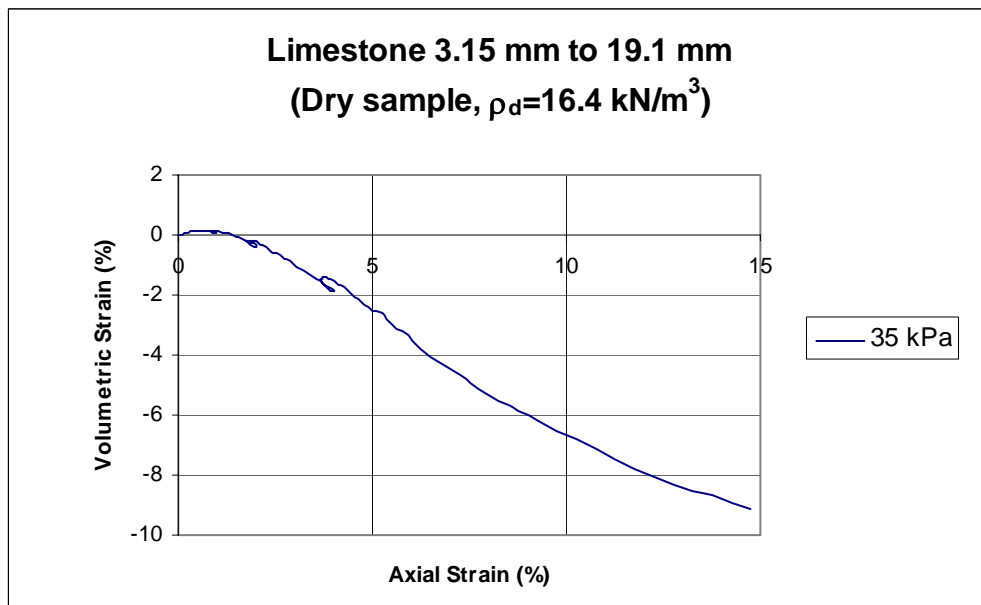
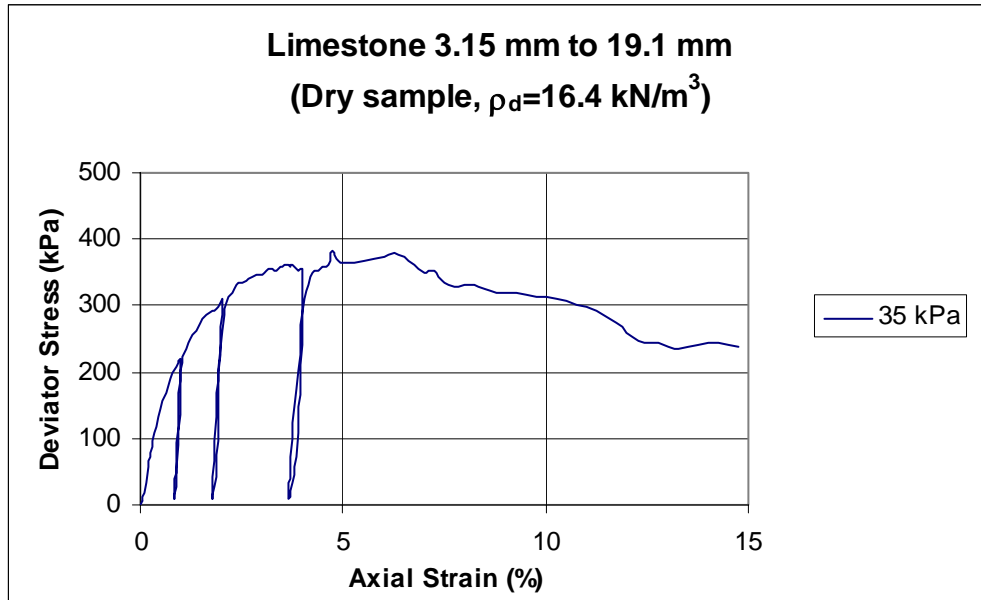


Figure A39

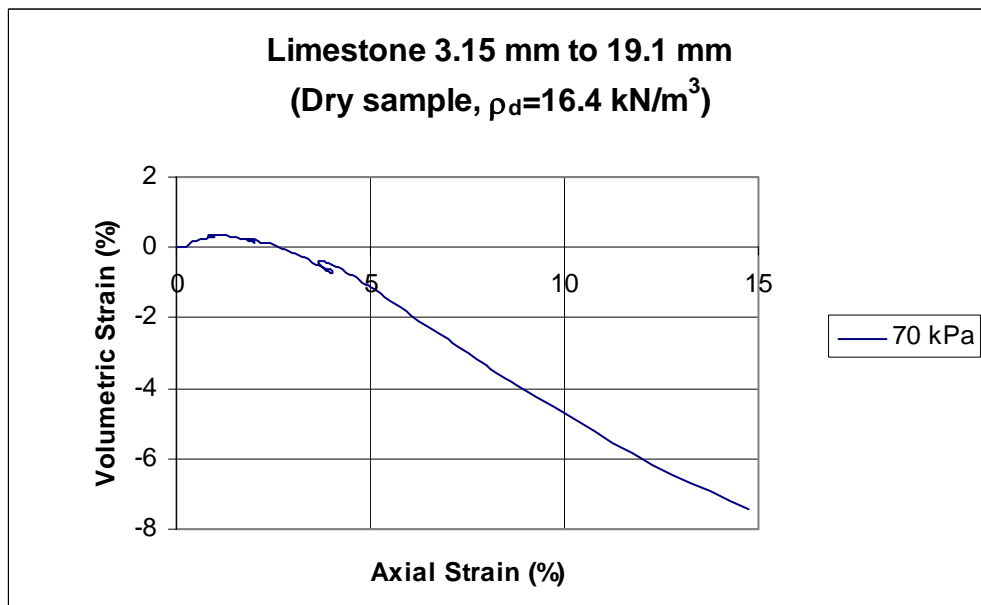
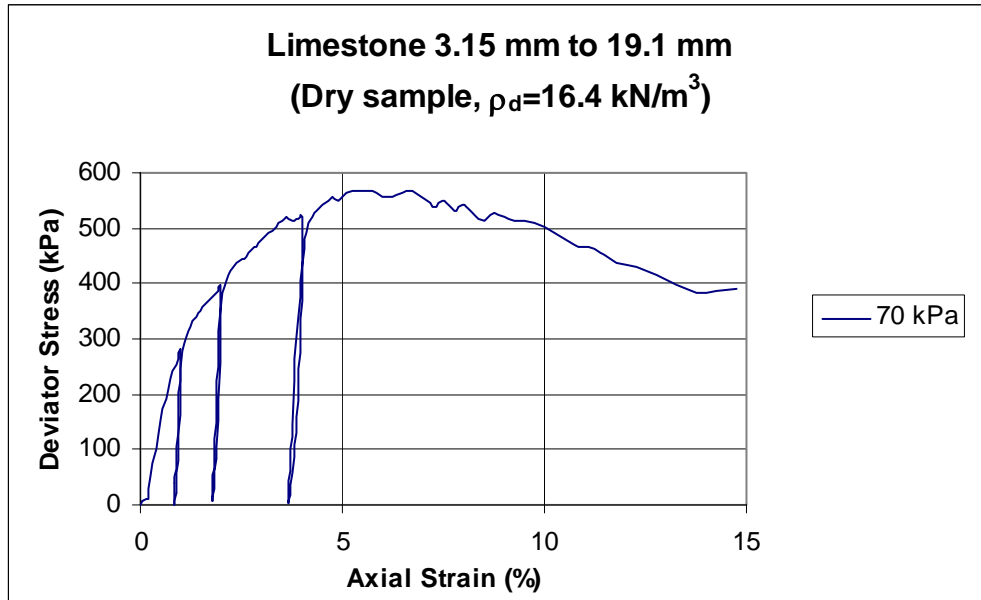


Figure A40

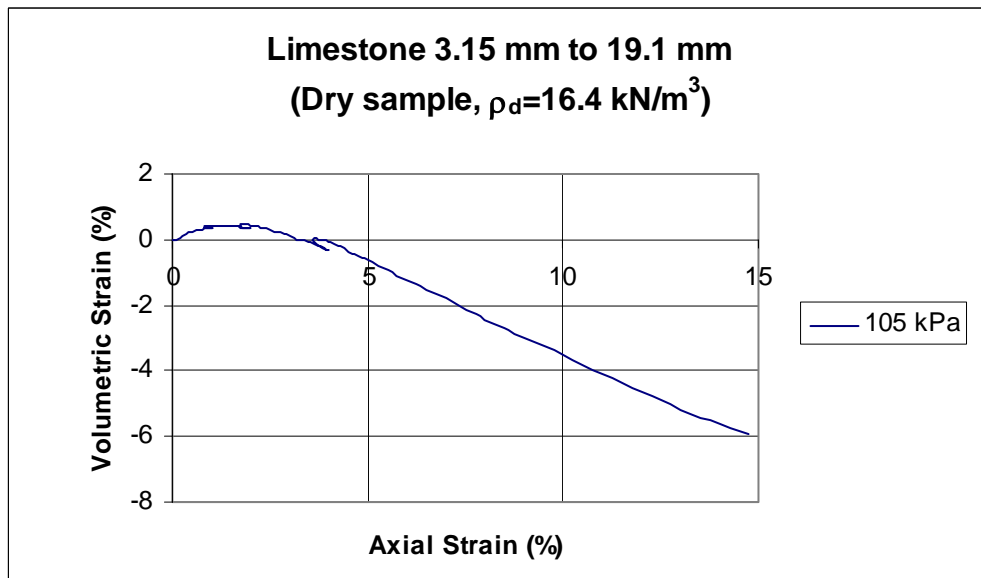
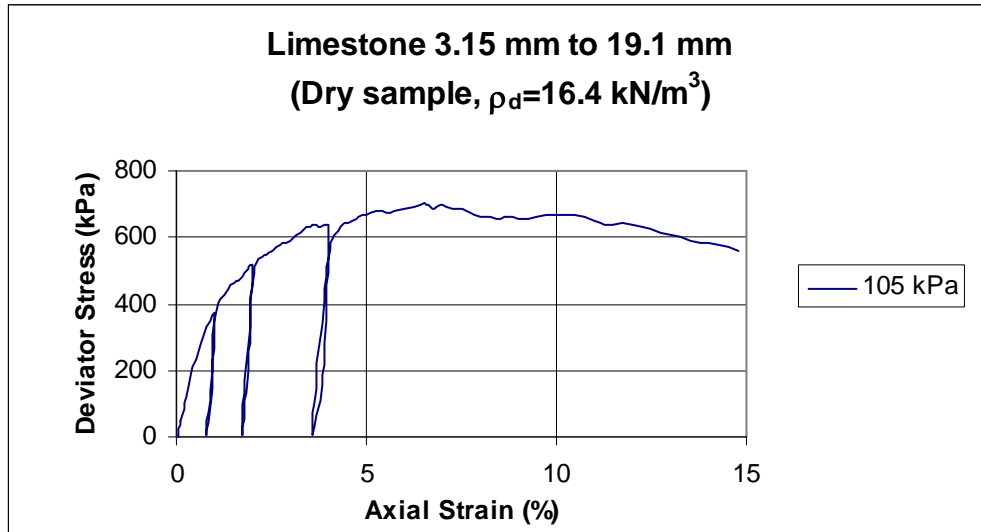


Figure A41

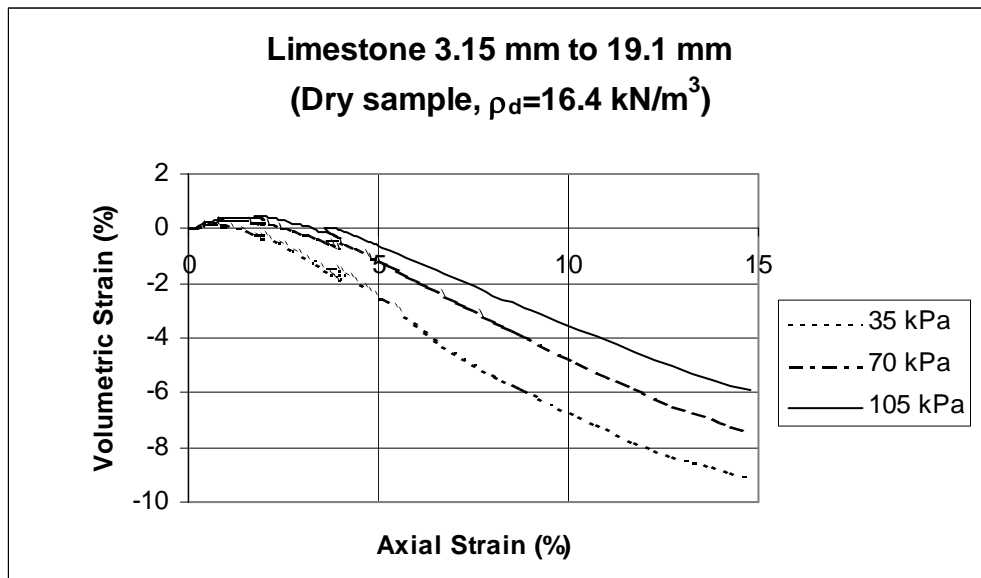
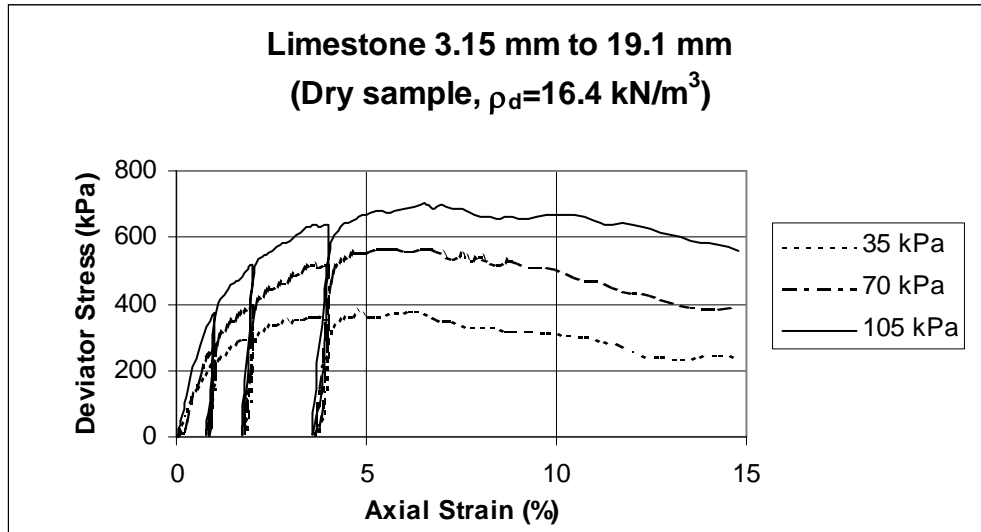


Figure A42

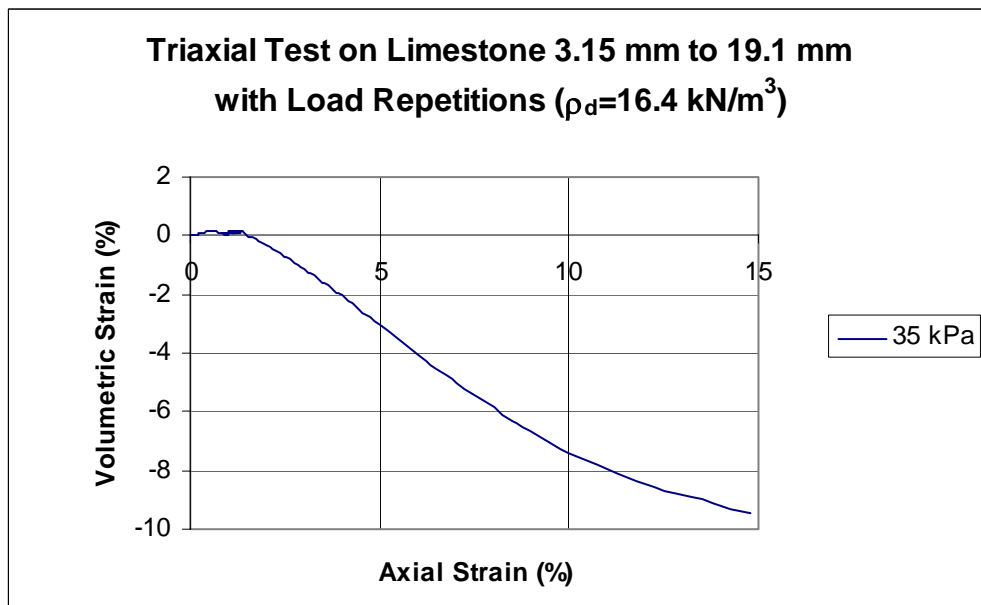
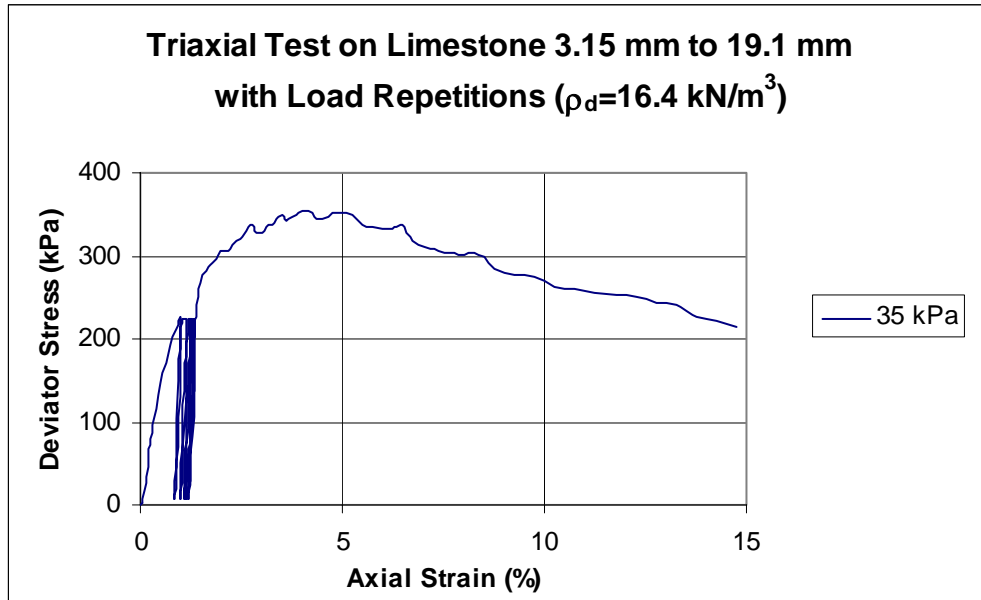


Figure A43

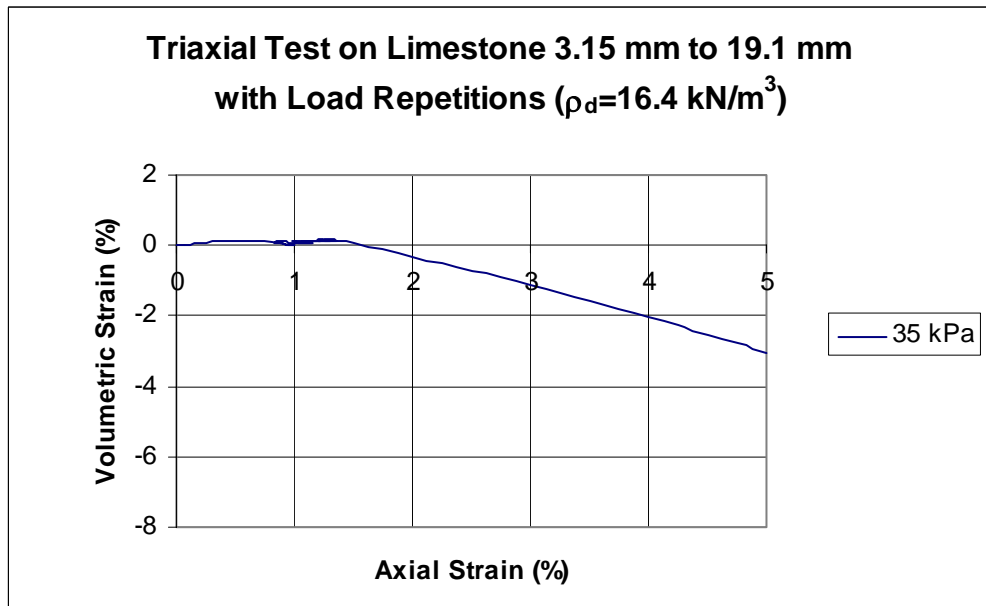
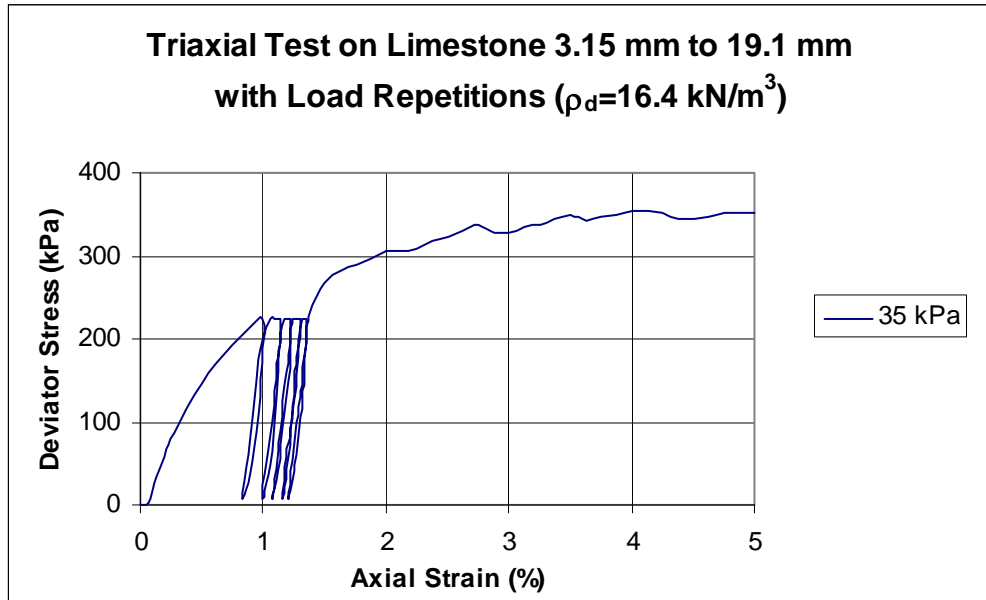


Figure A44

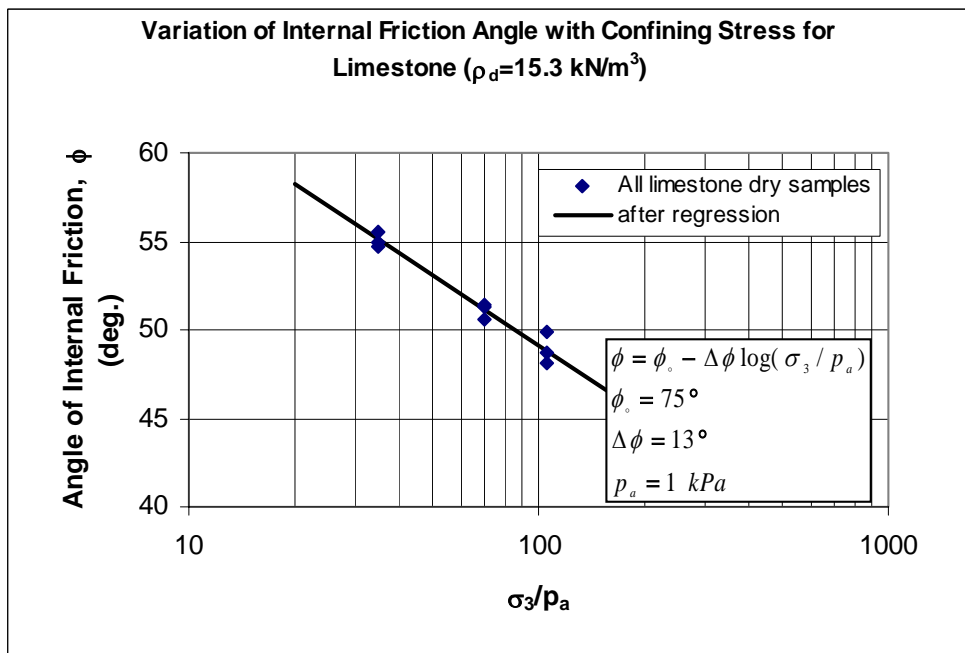
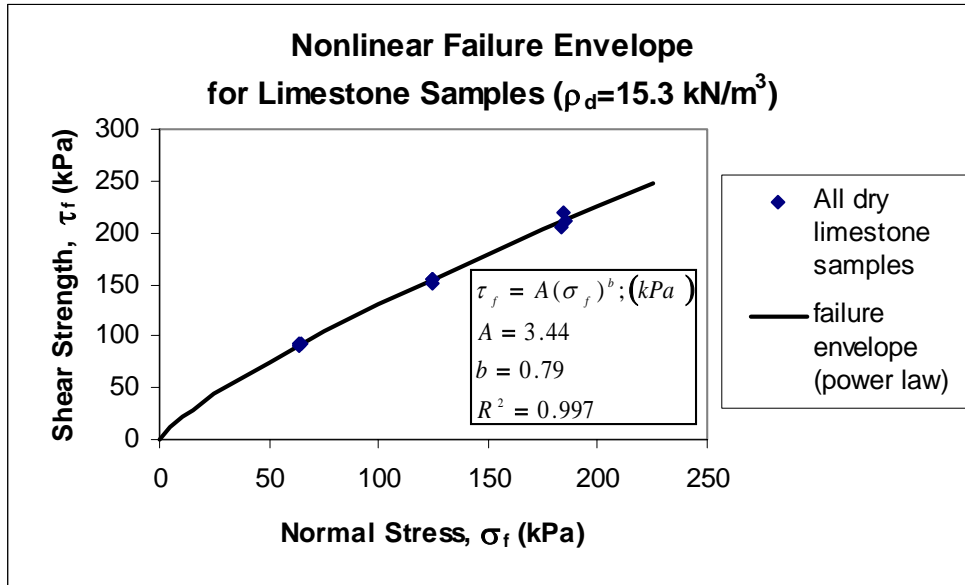


Figure A45

APPENDIX B - BASALT

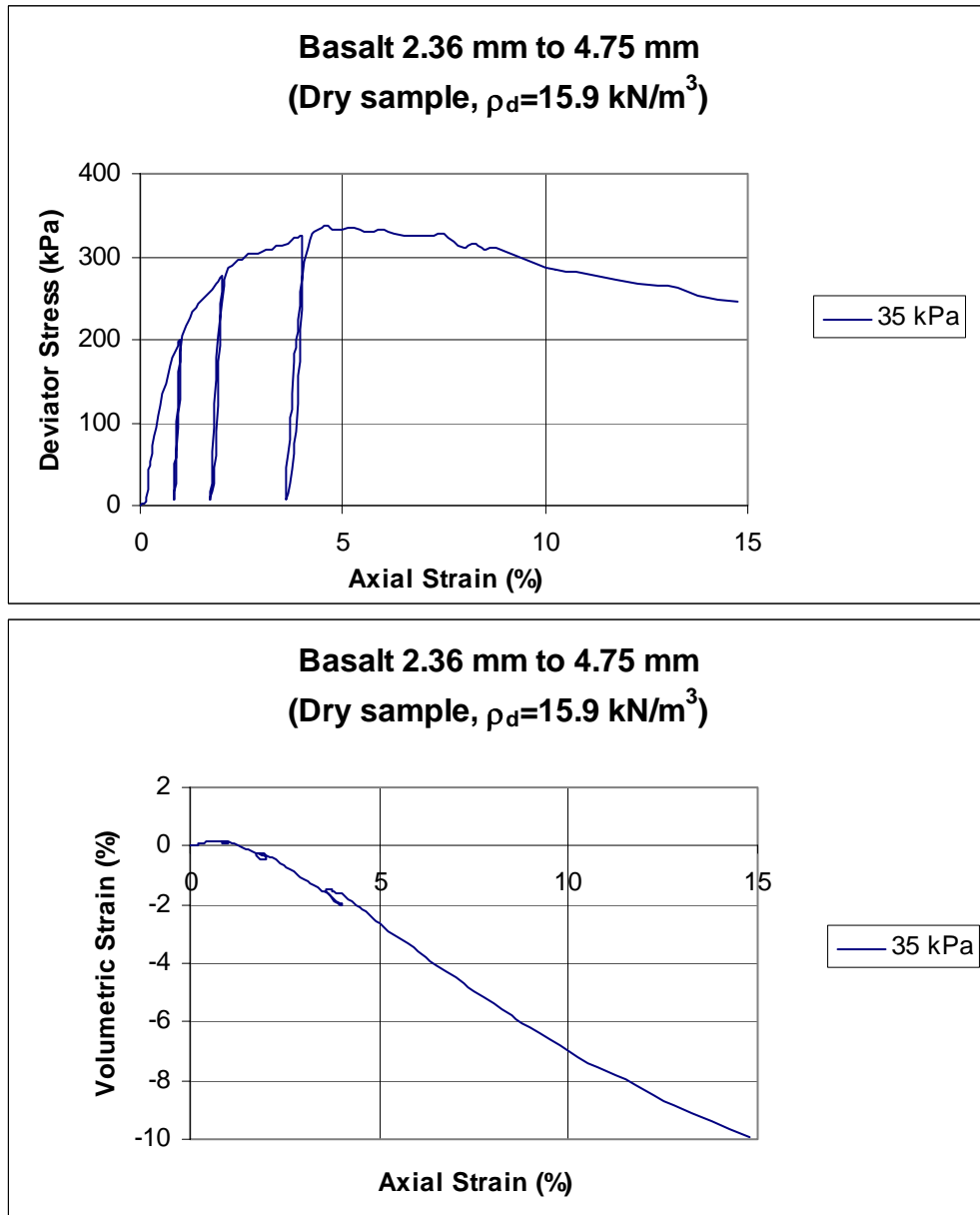


Figure B1

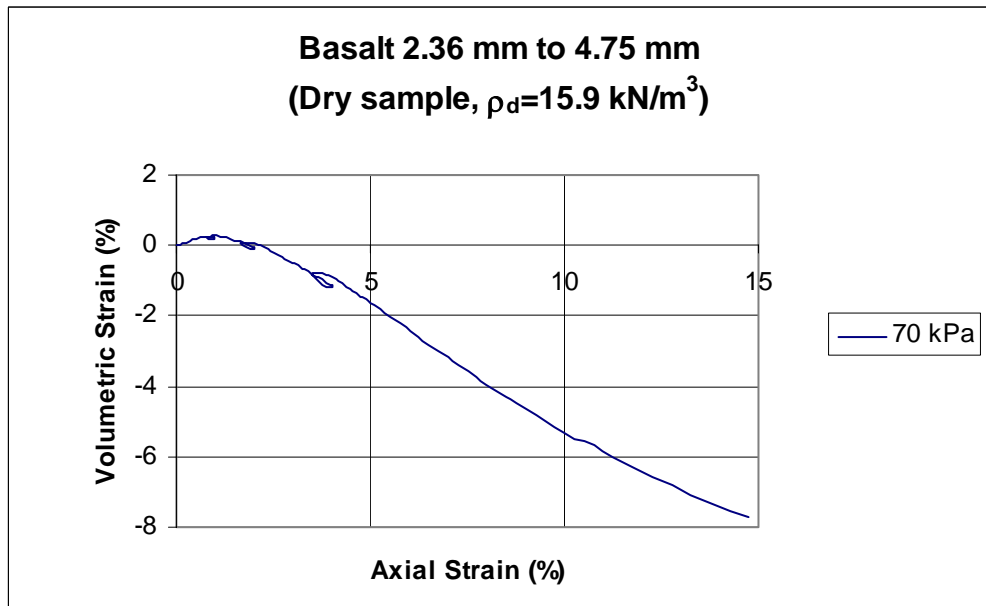
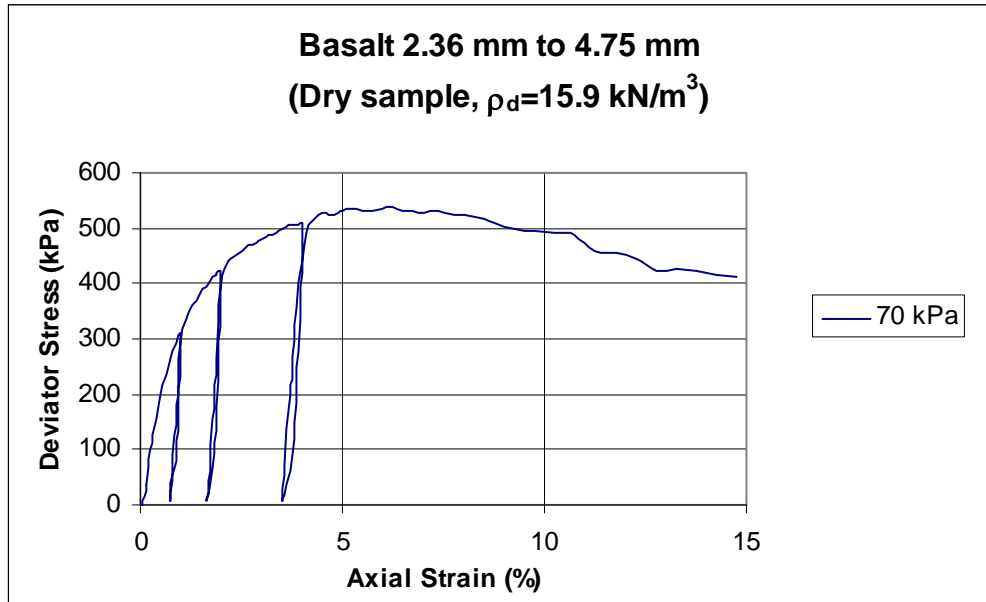


Figure B2

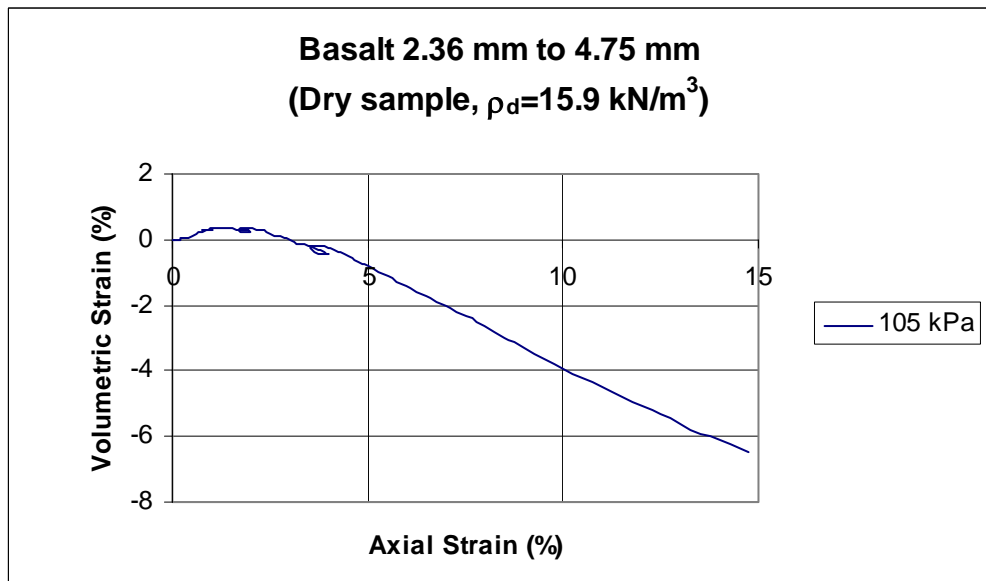
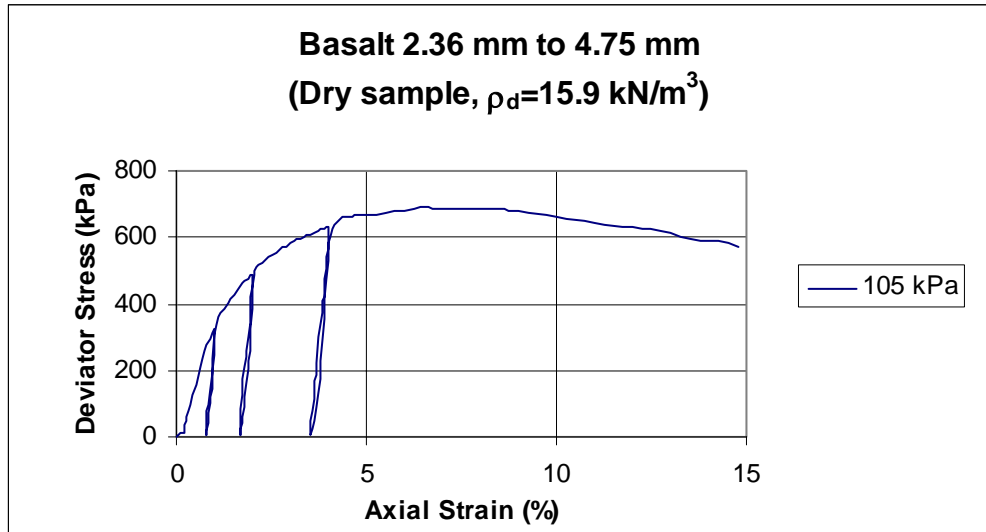


Figure B3

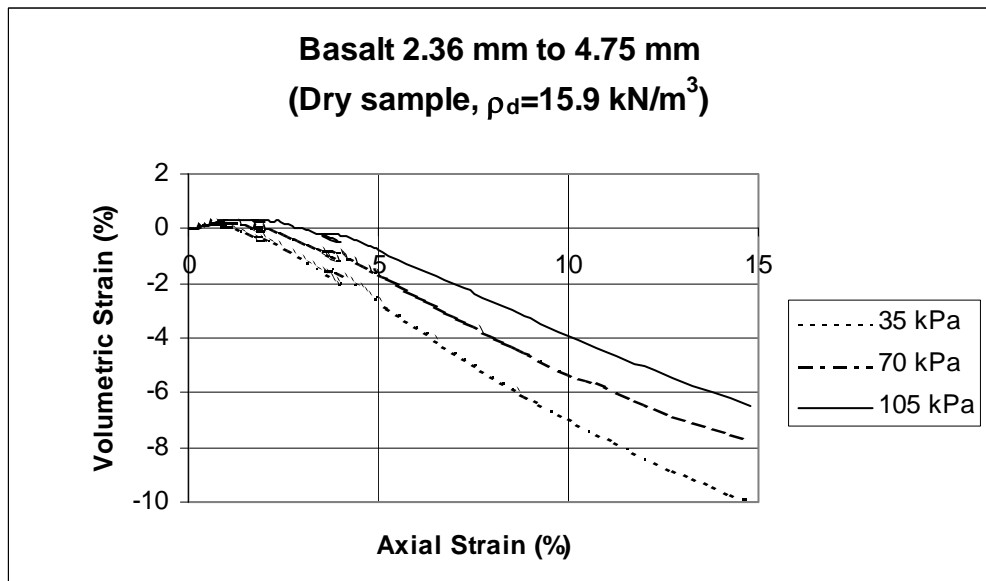
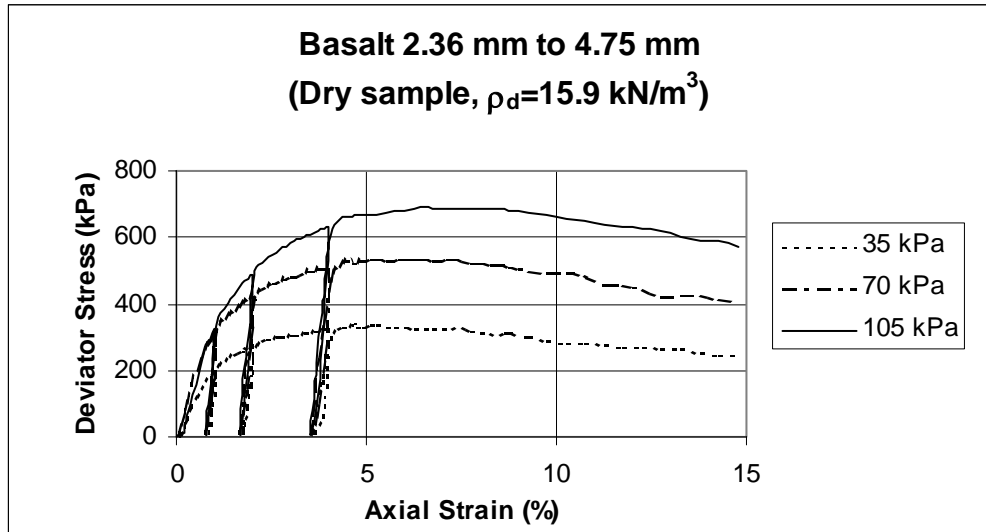


Figure B4

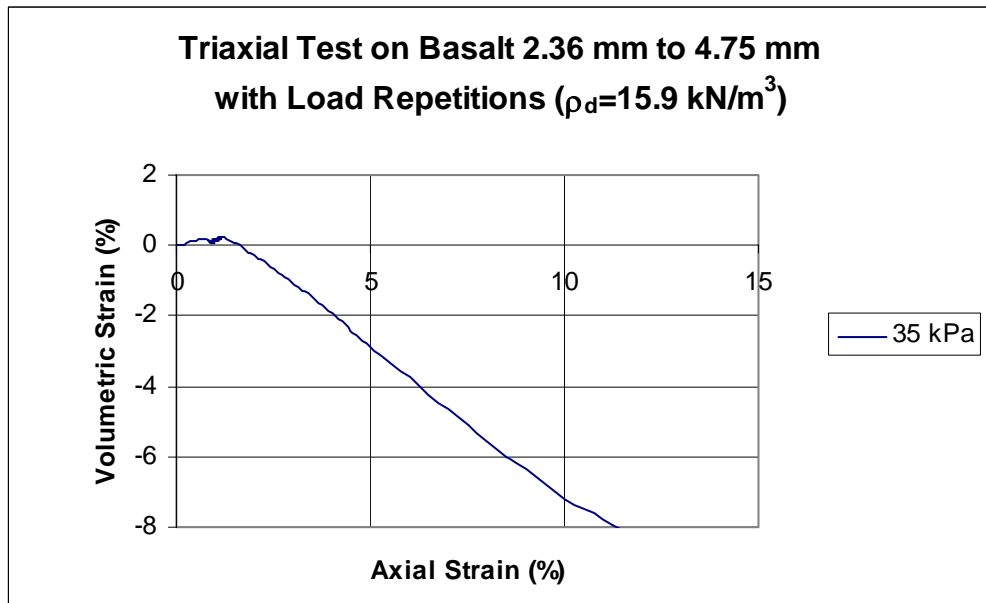
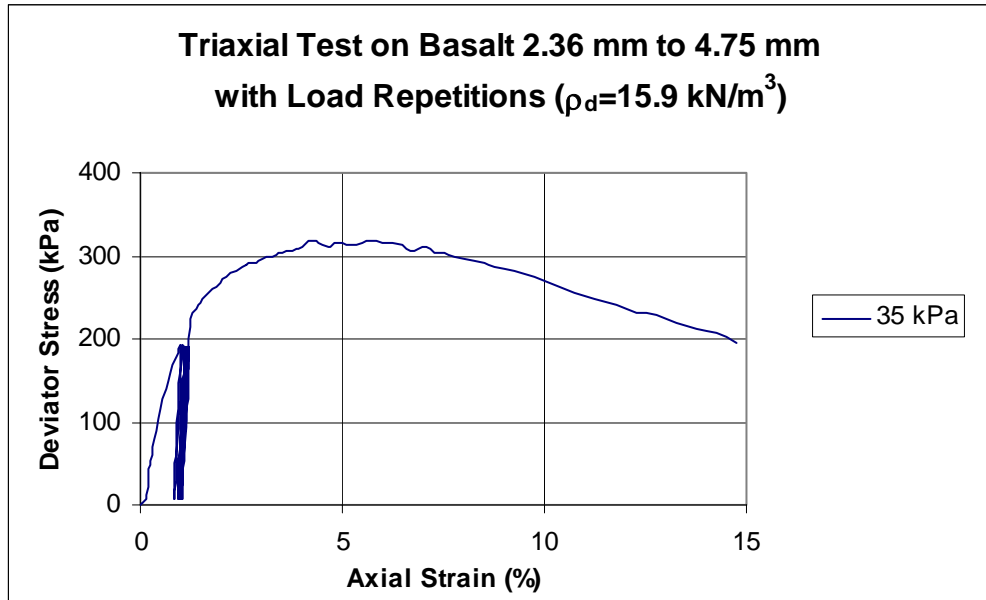


Figure B5

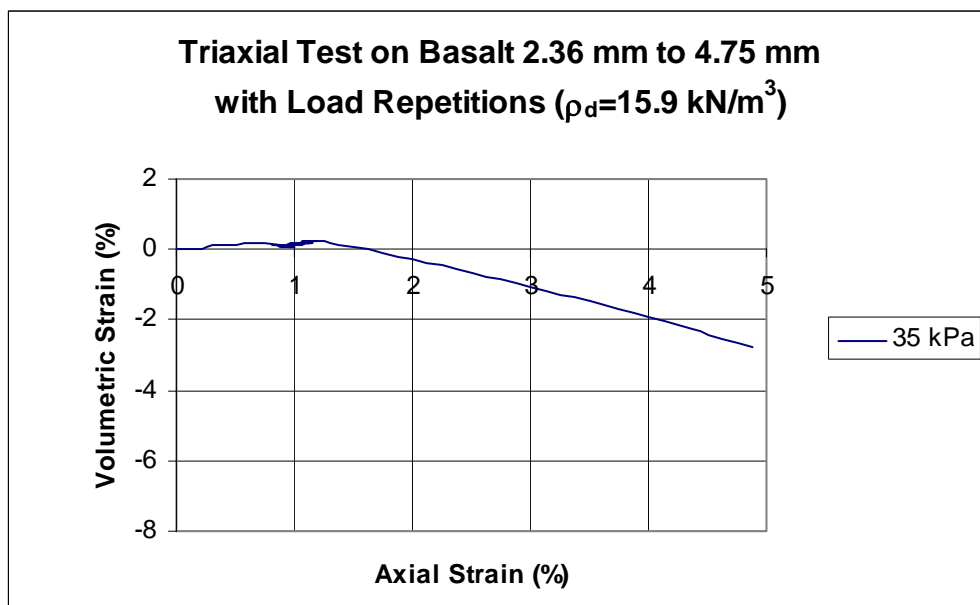
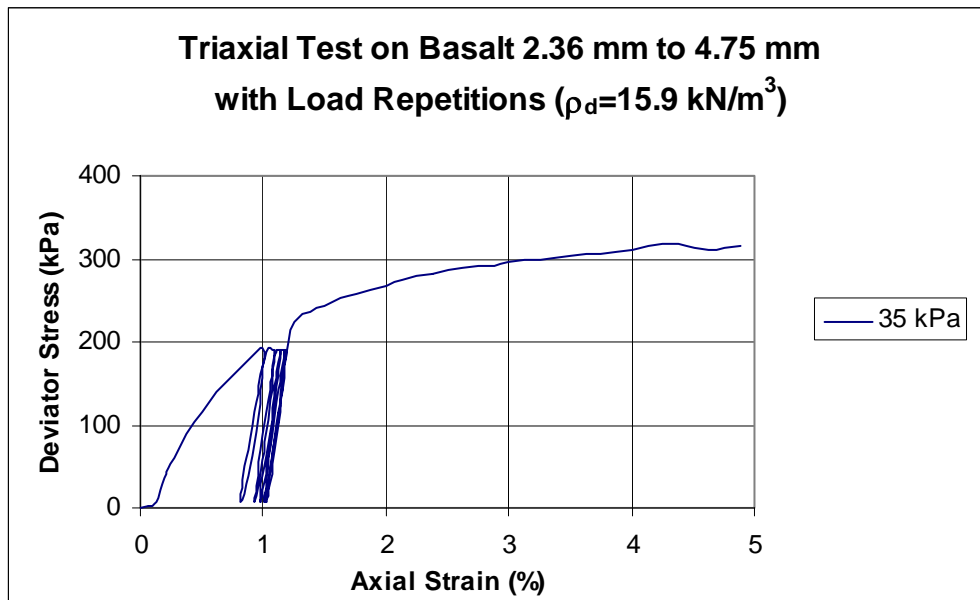


Figure B6

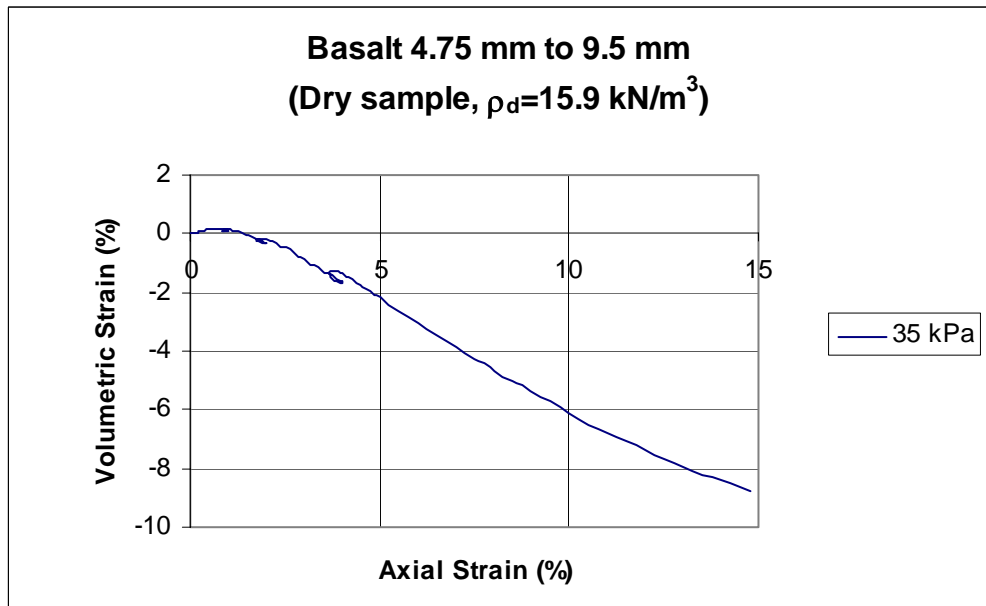
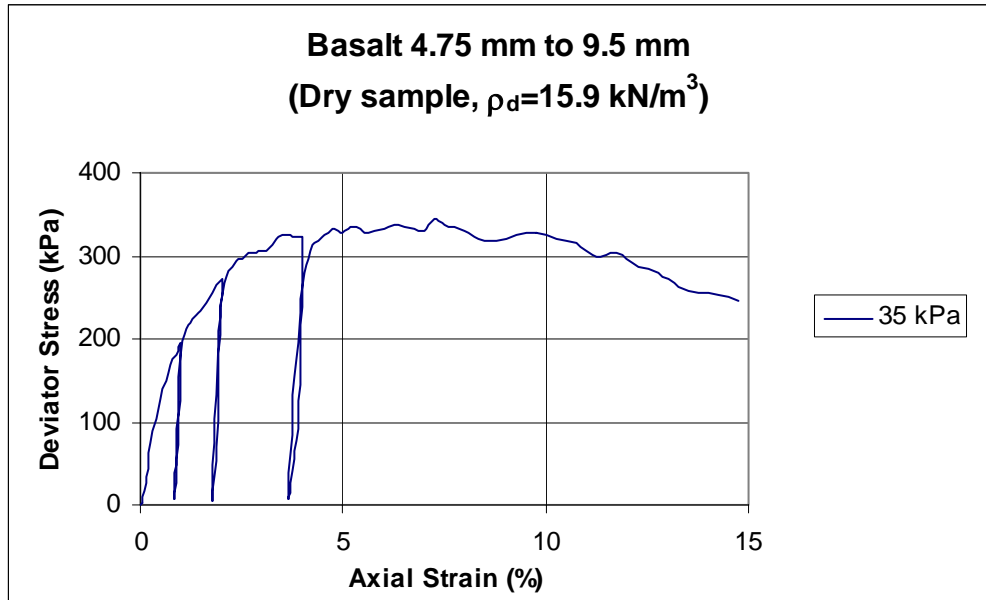


Figure B7

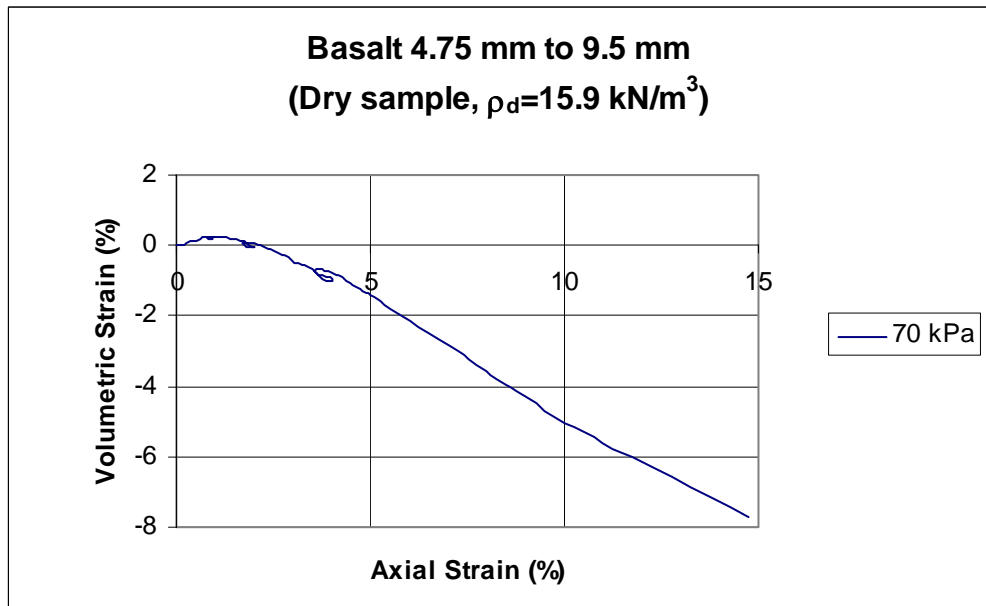
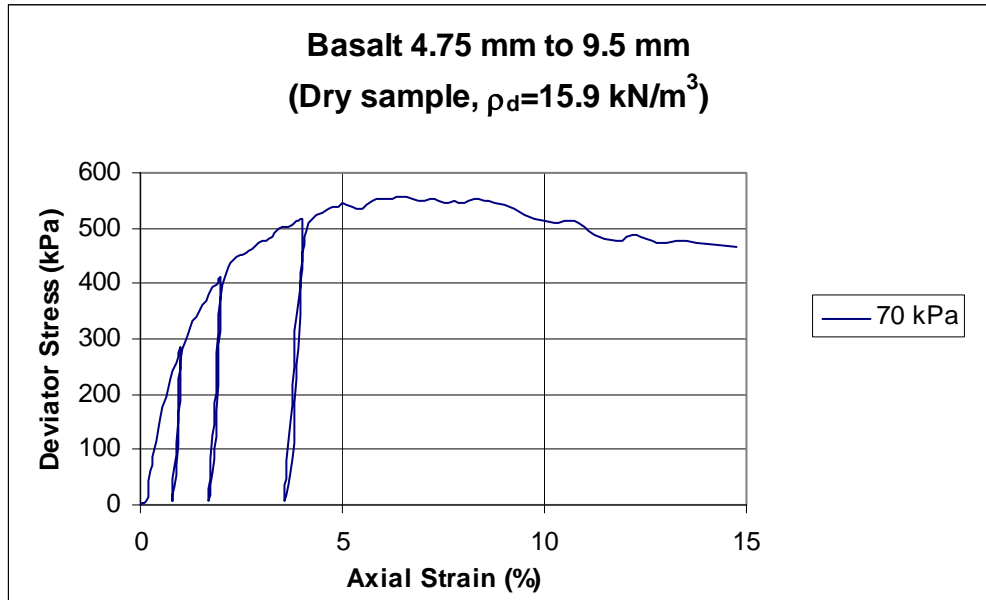


Figure B8

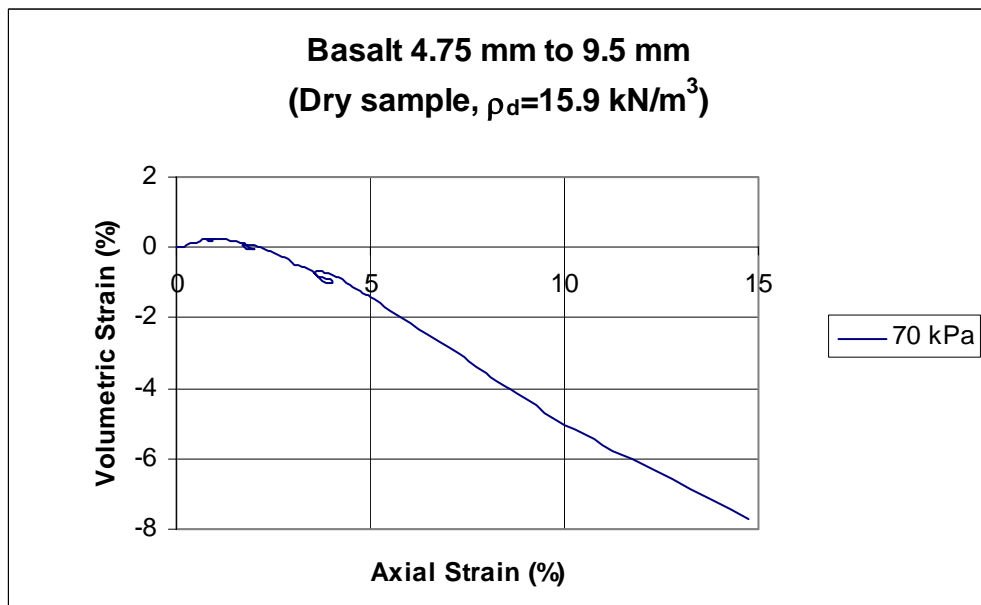
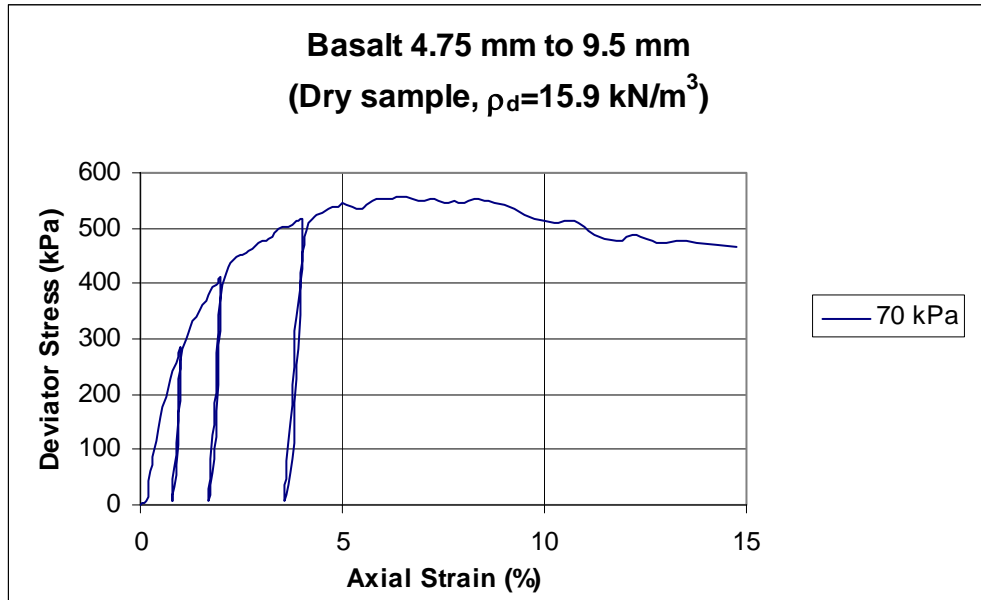


Figure B9

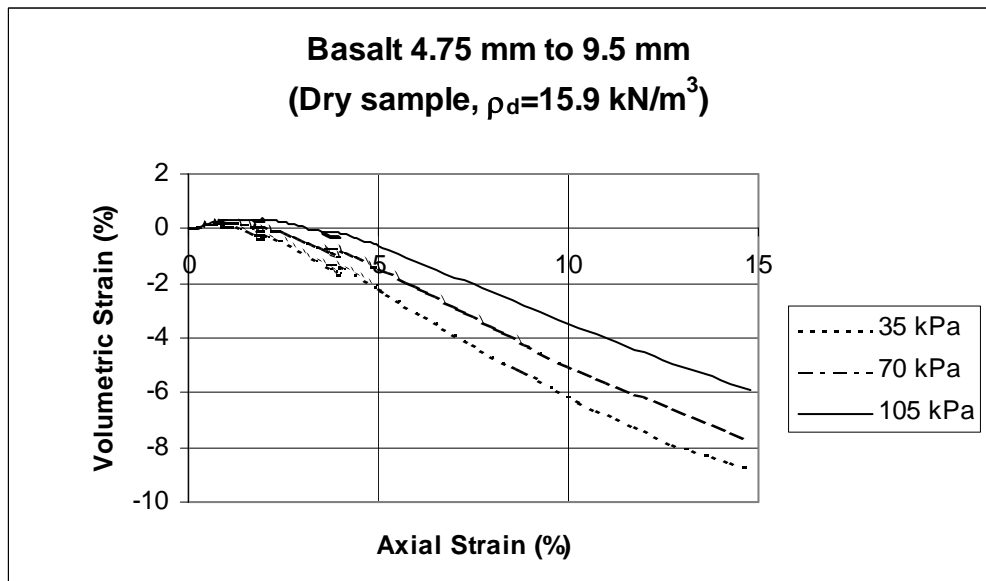
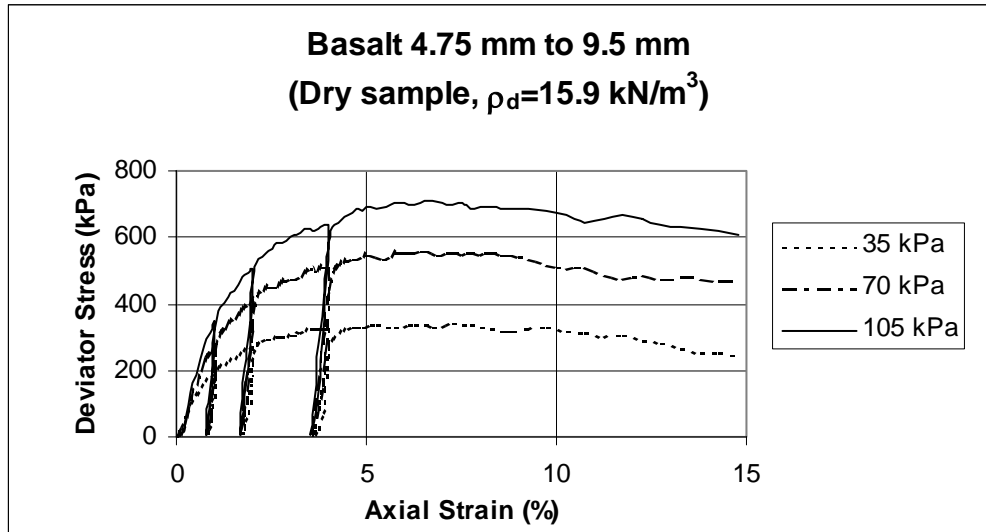


Figure B10

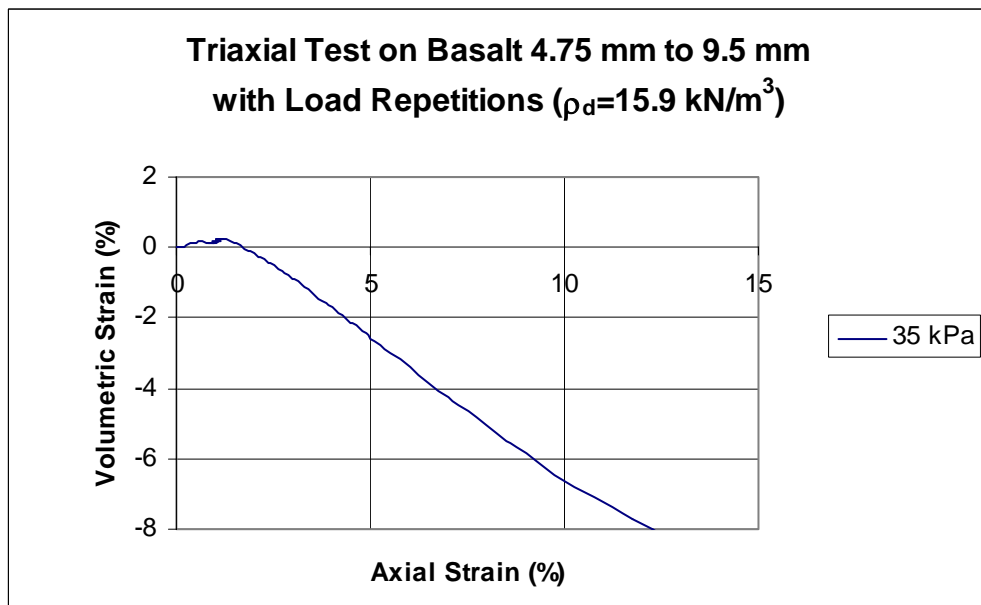
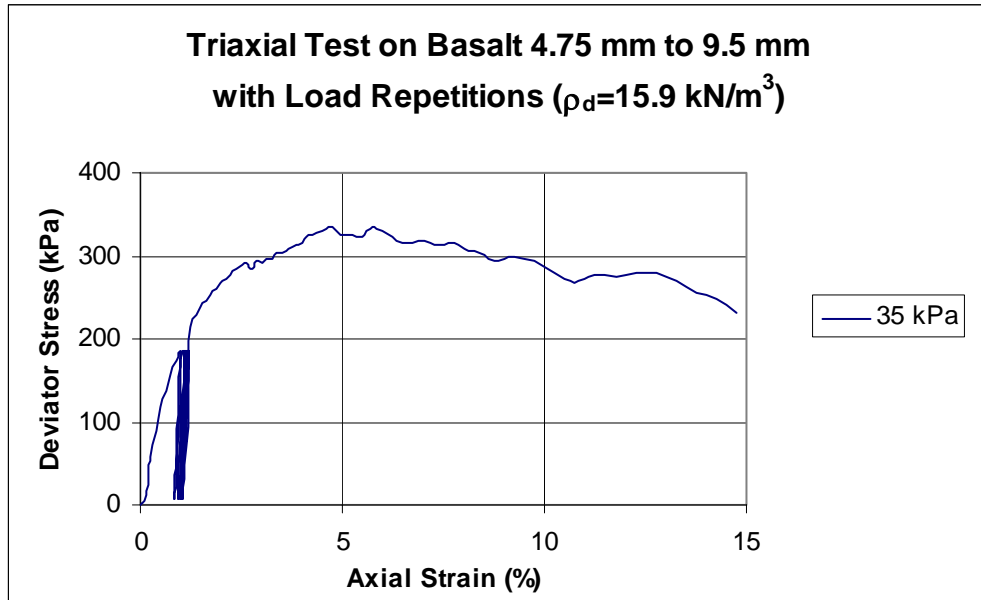


Figure B11

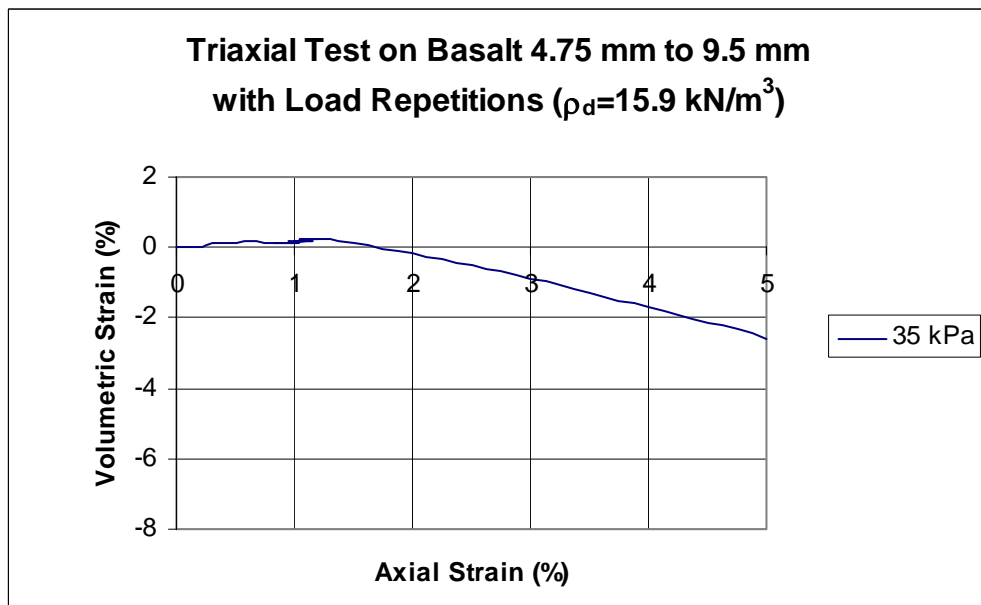
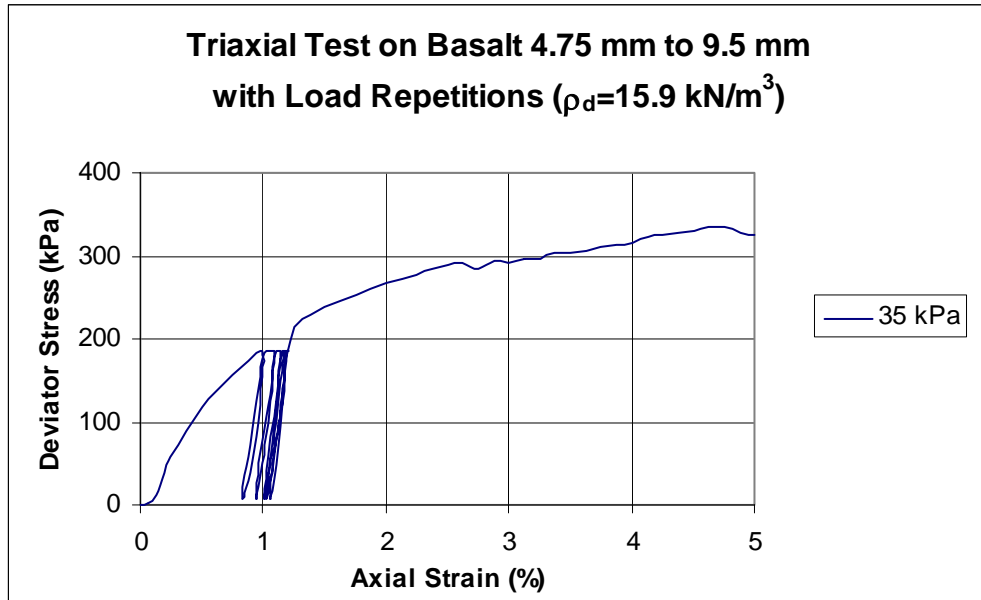


Figure B12

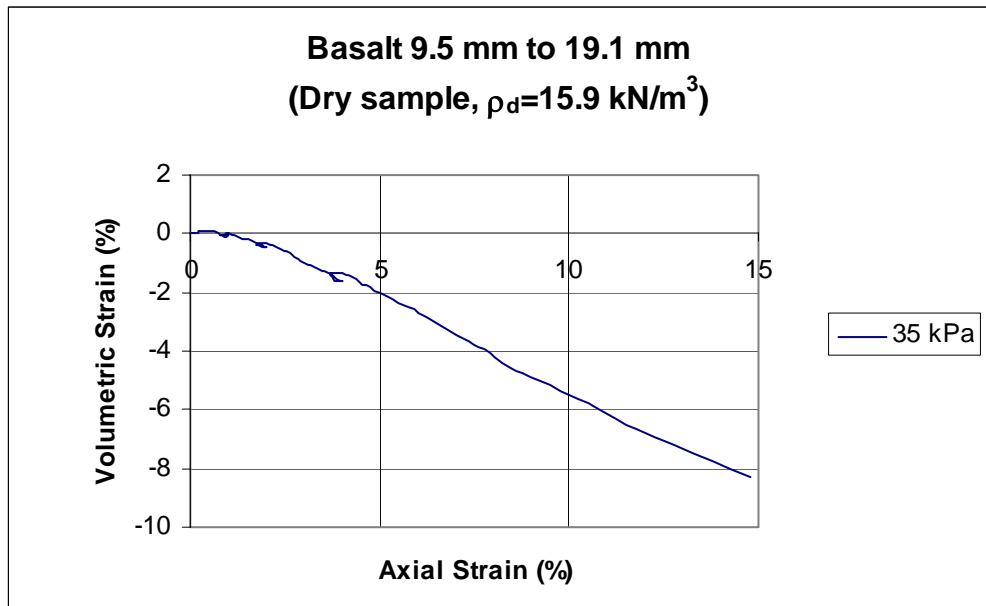
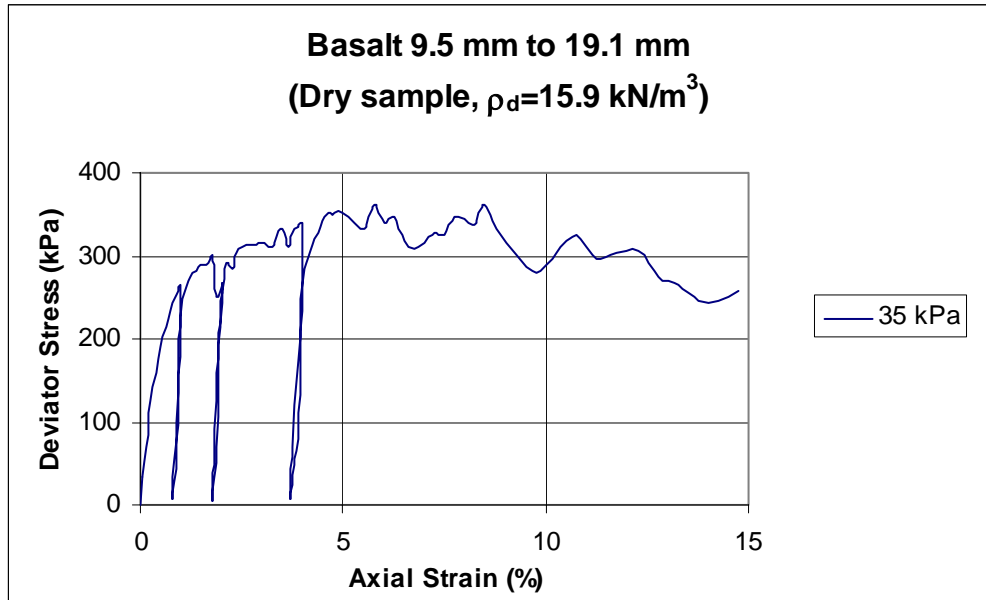


Figure B13

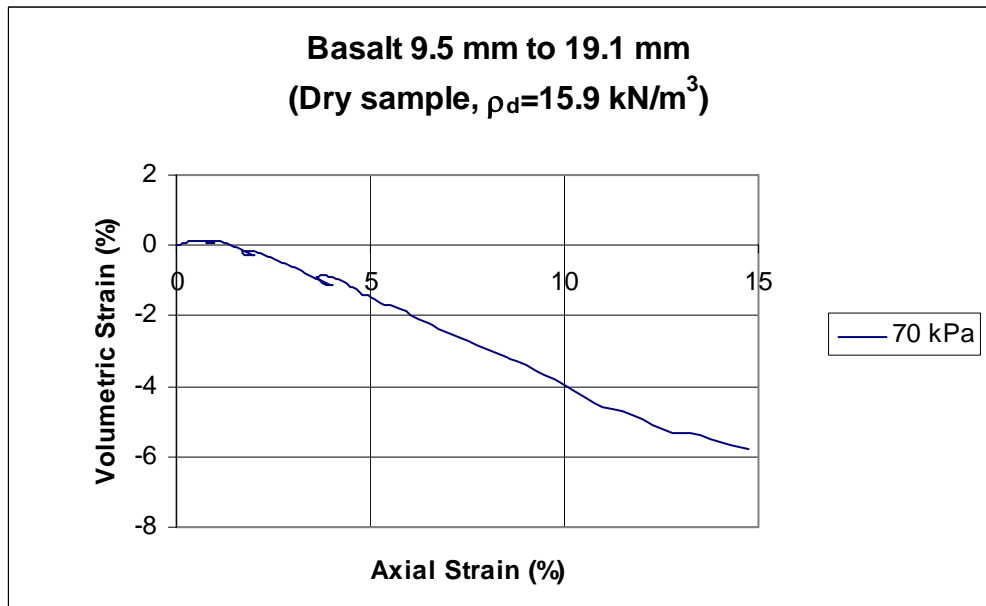
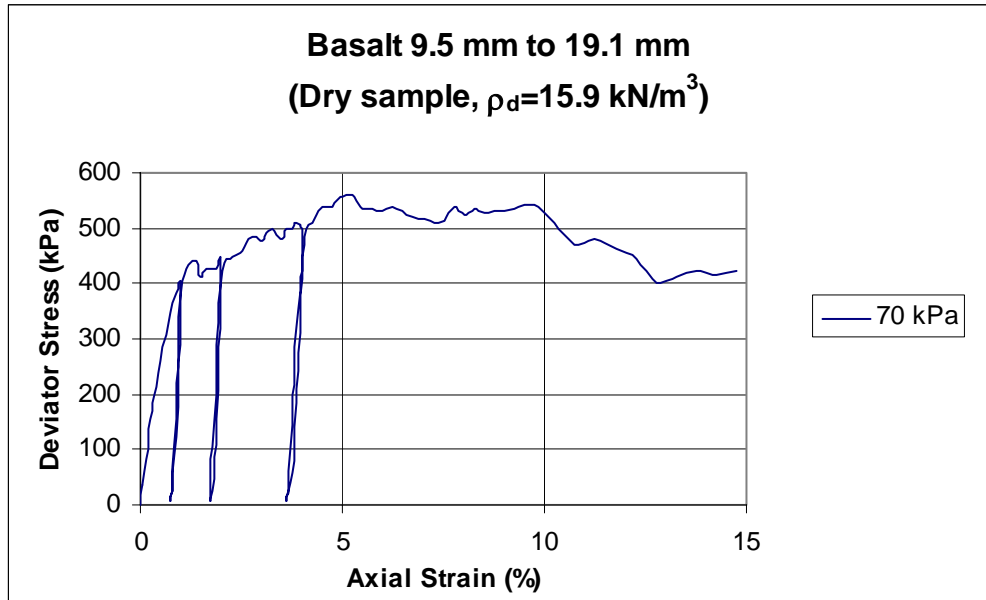


Figure B14

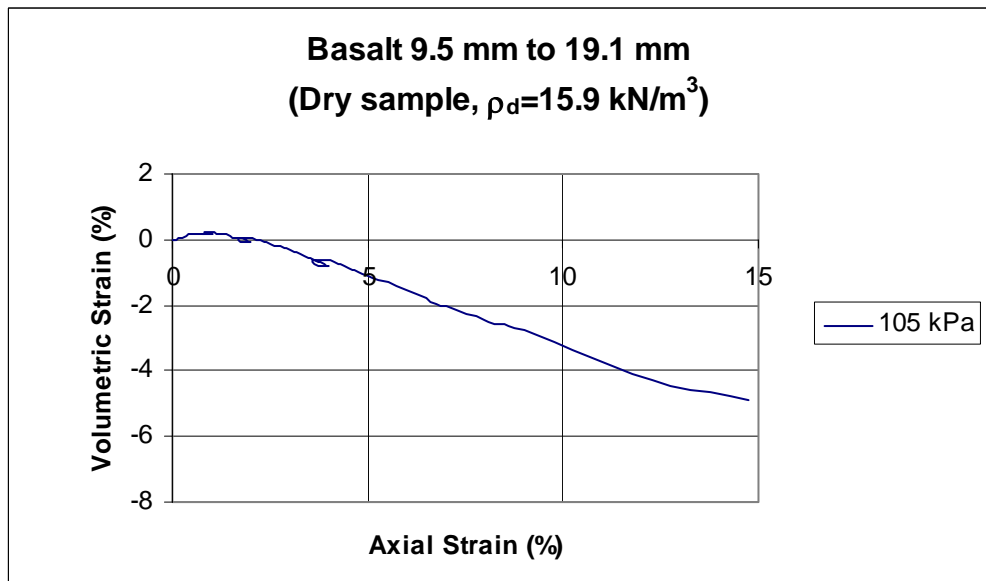
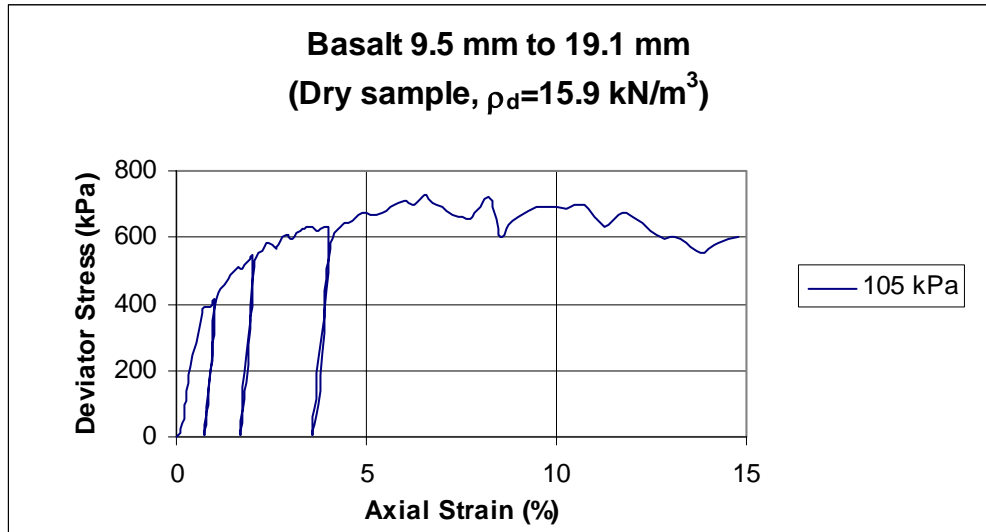


Figure B15

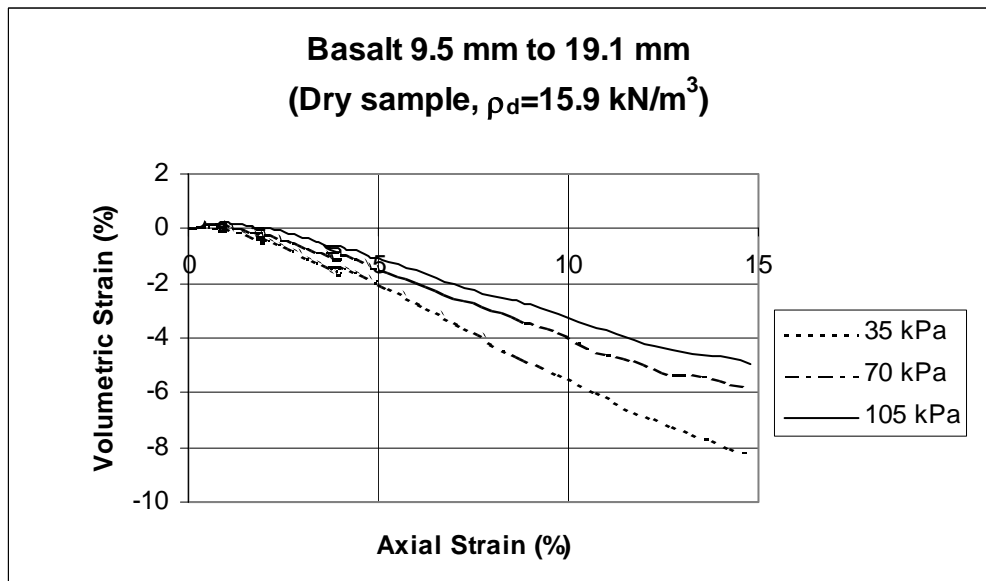
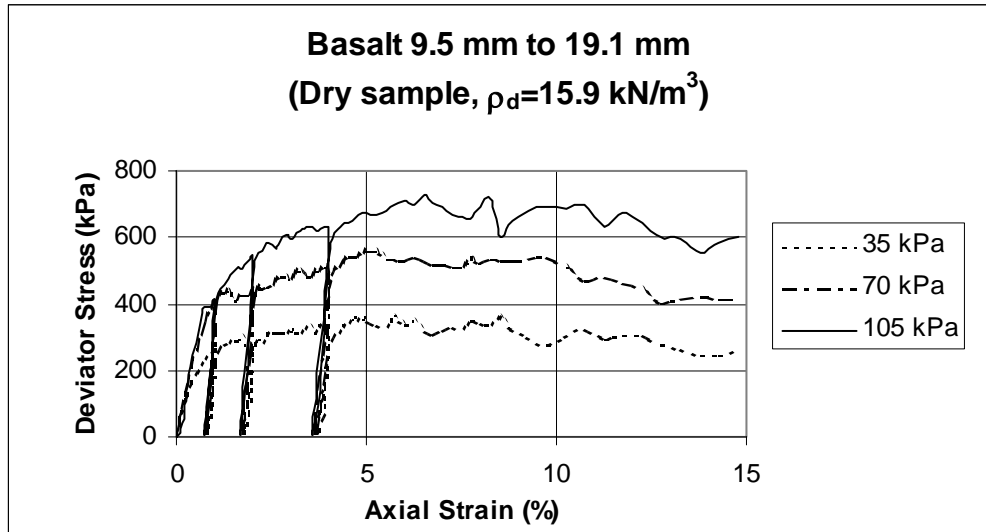


Figure B16

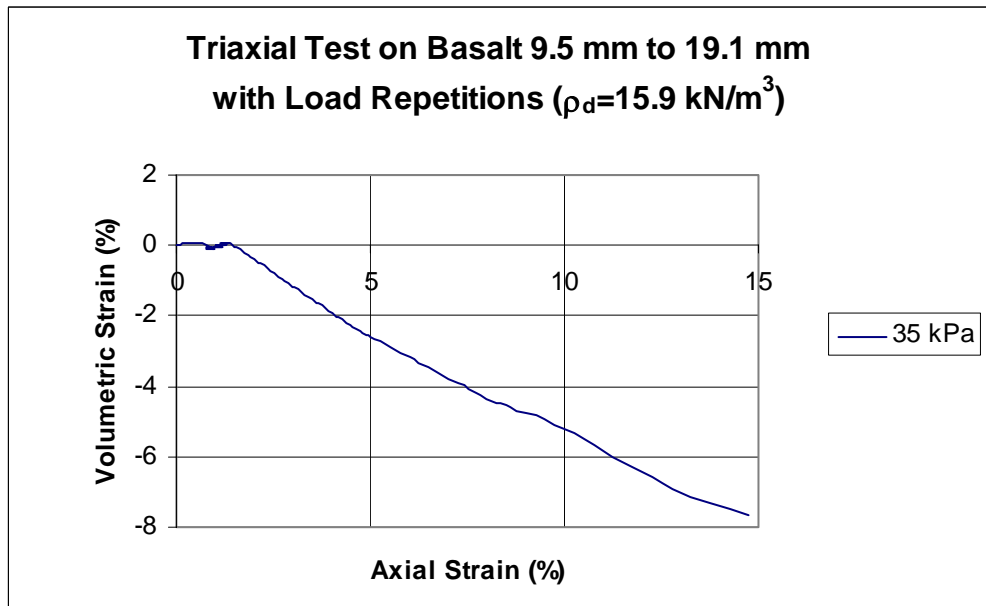
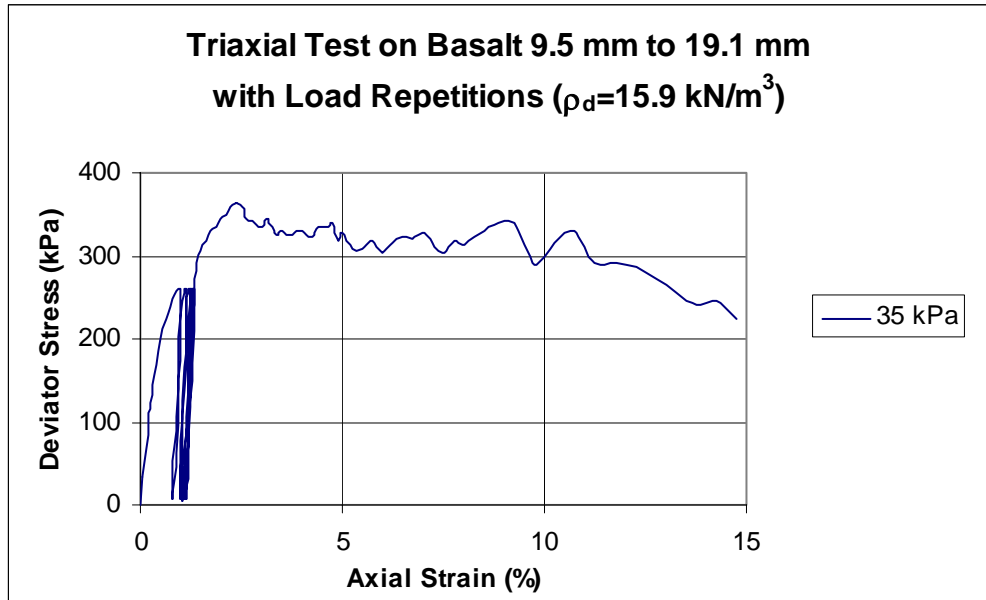


Figure B17

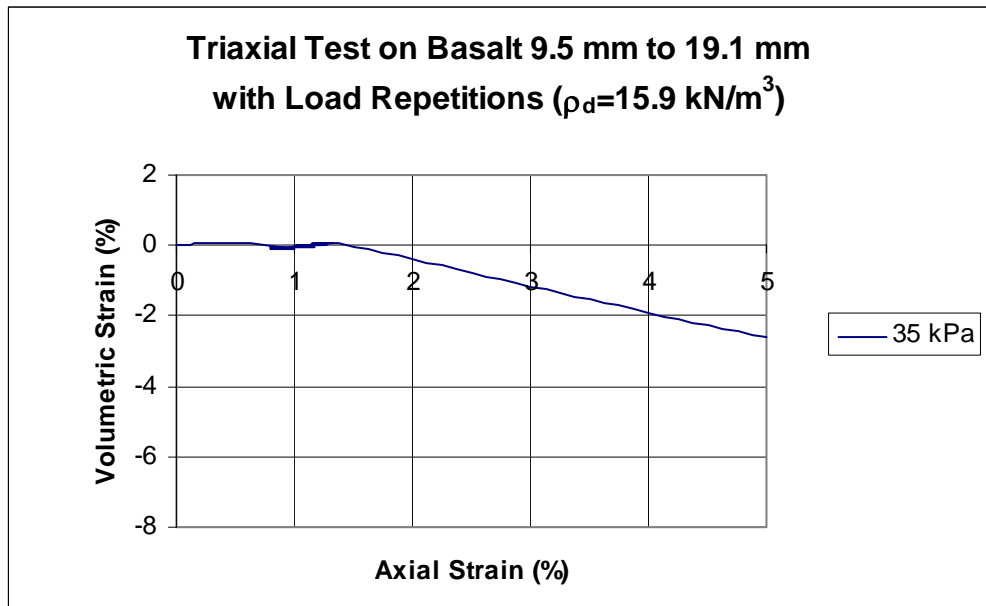
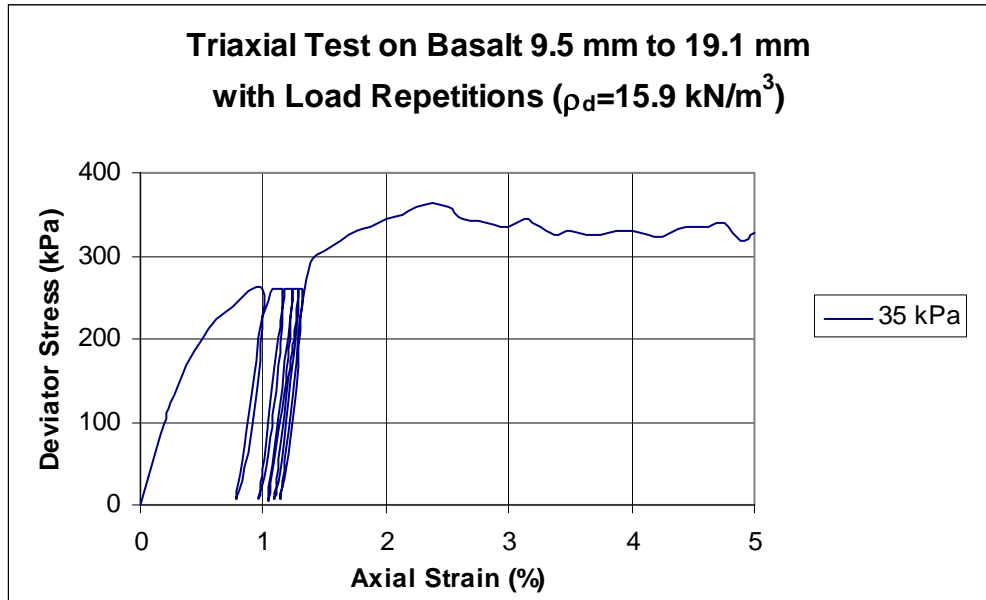


Figure B18

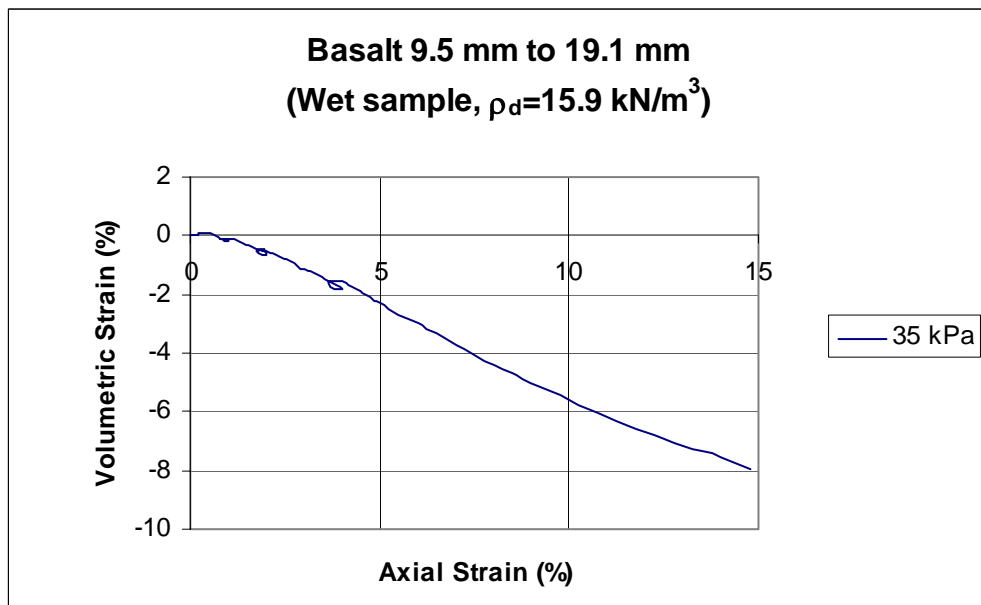
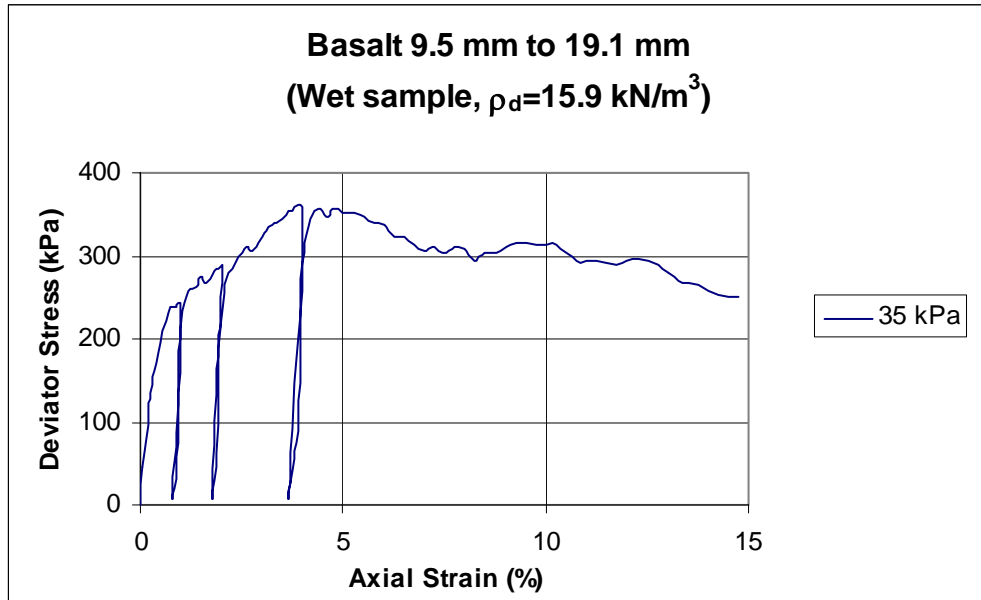


Figure B19

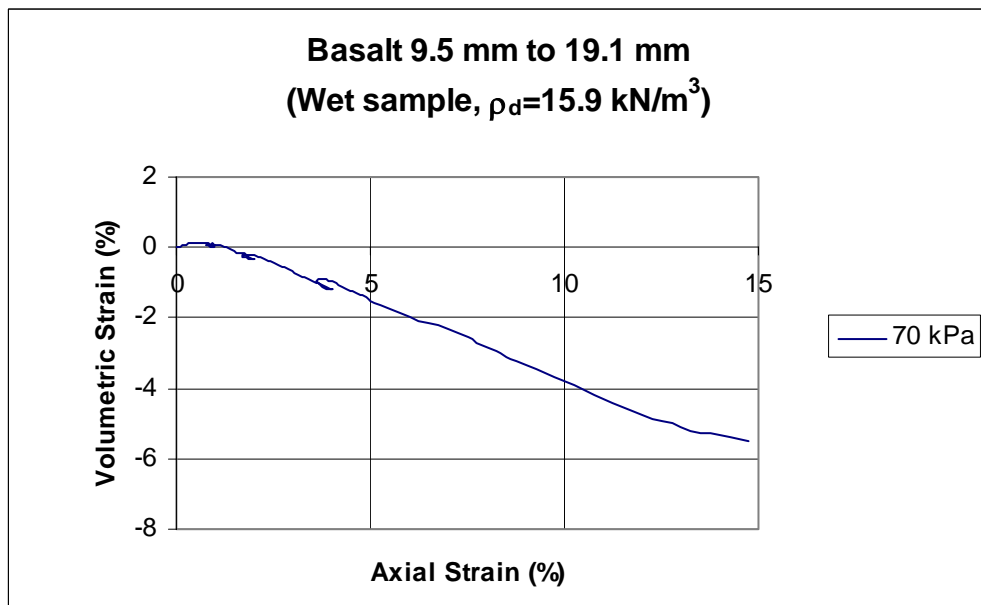
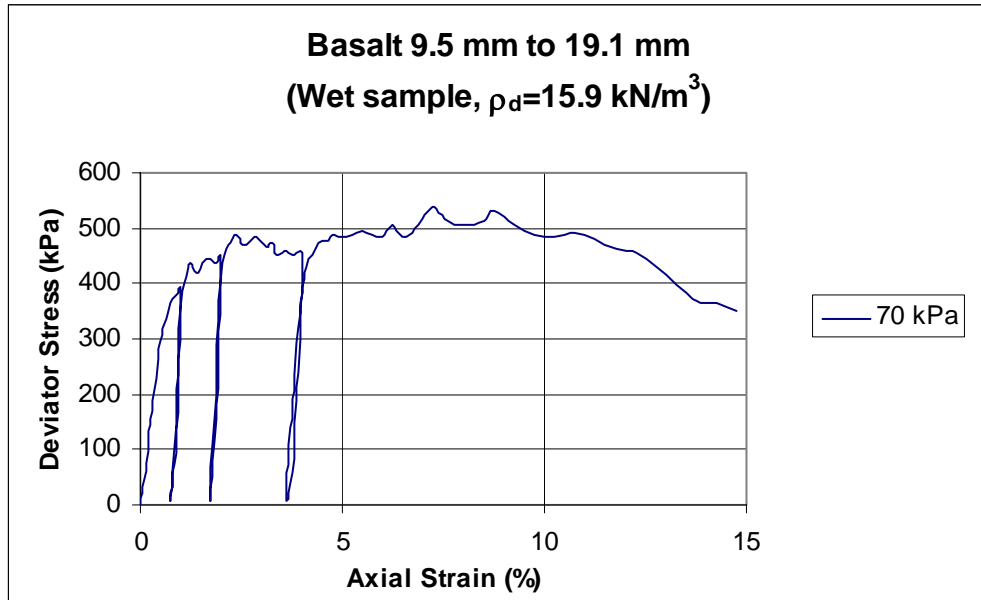


Figure B20

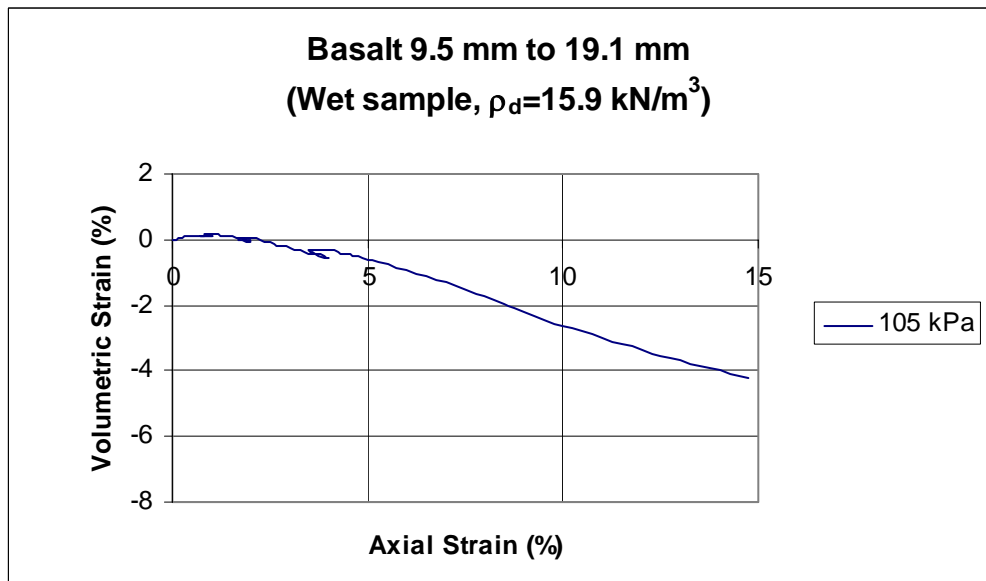
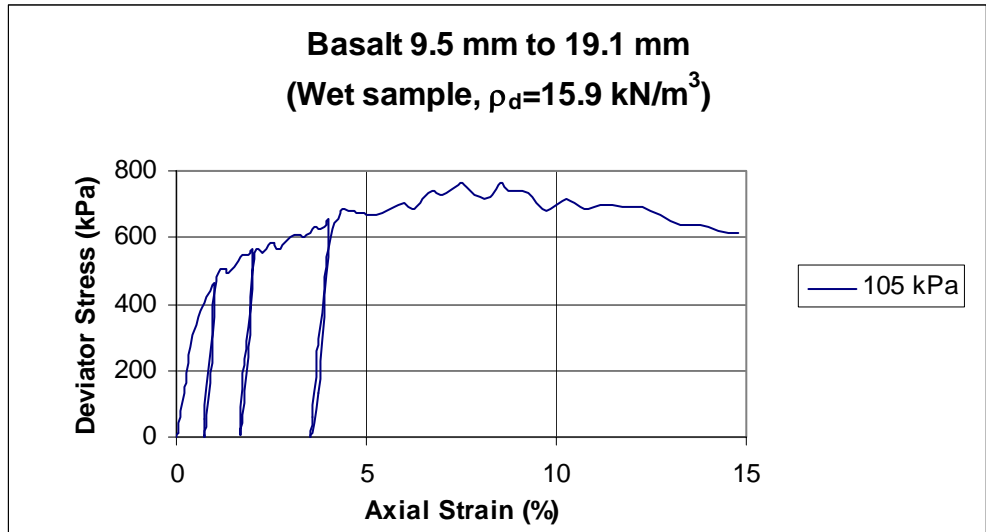


Figure B21

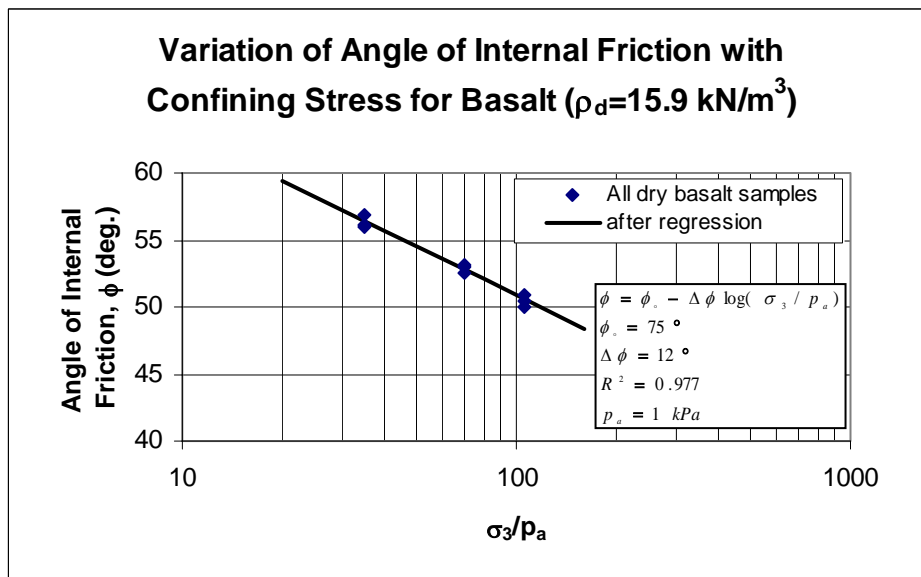
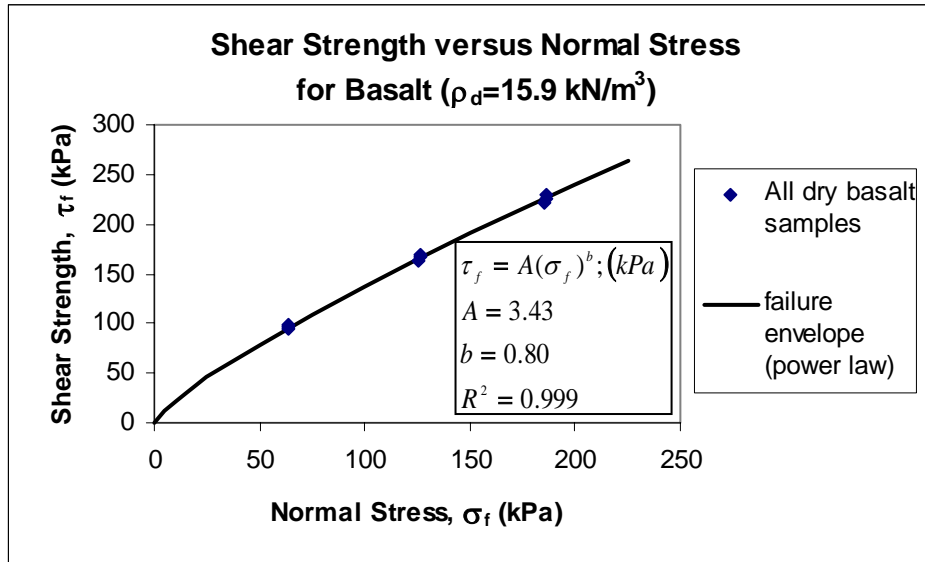


Figure B22

APPENDIX C – STEEL-SLAG

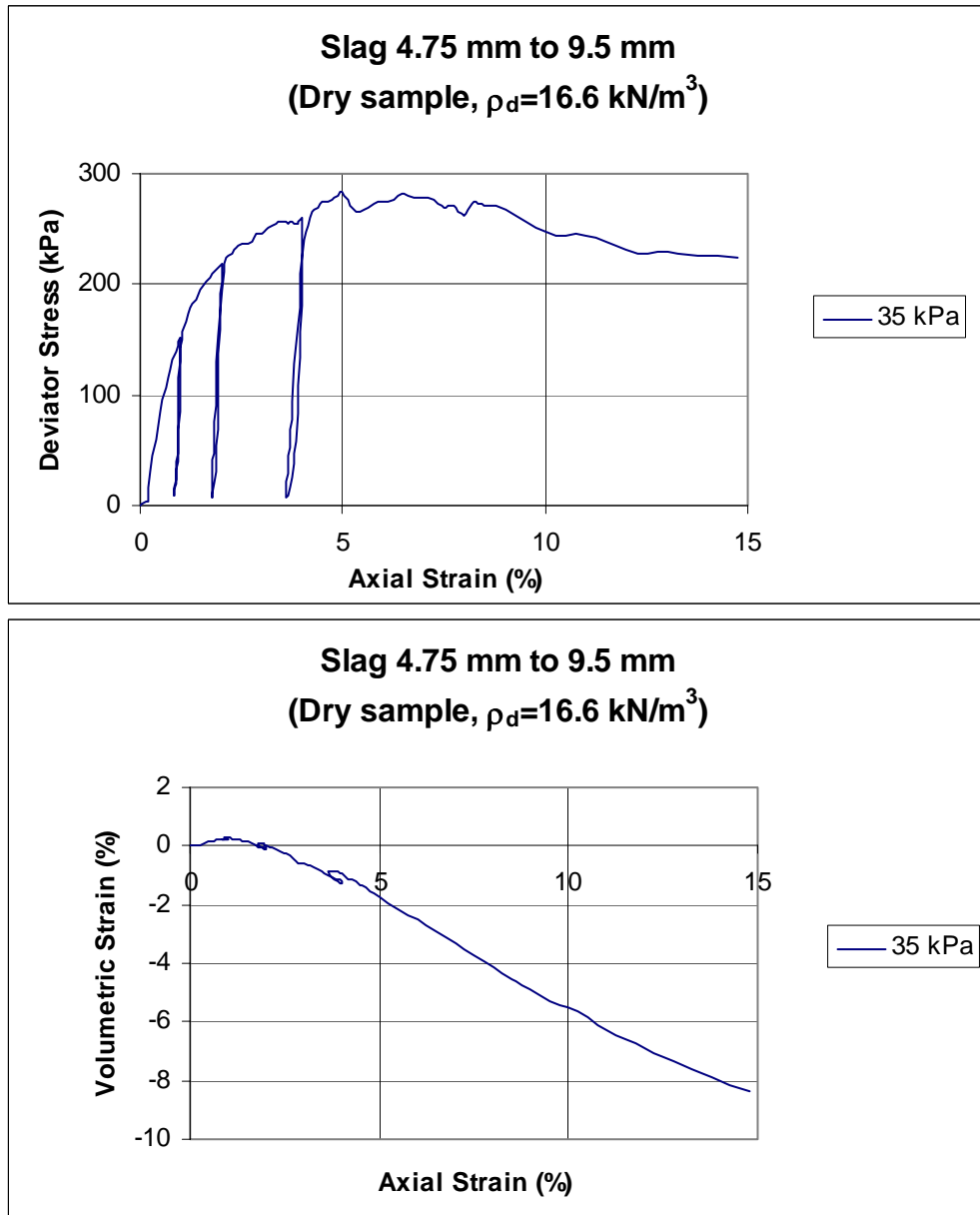


Figure C1

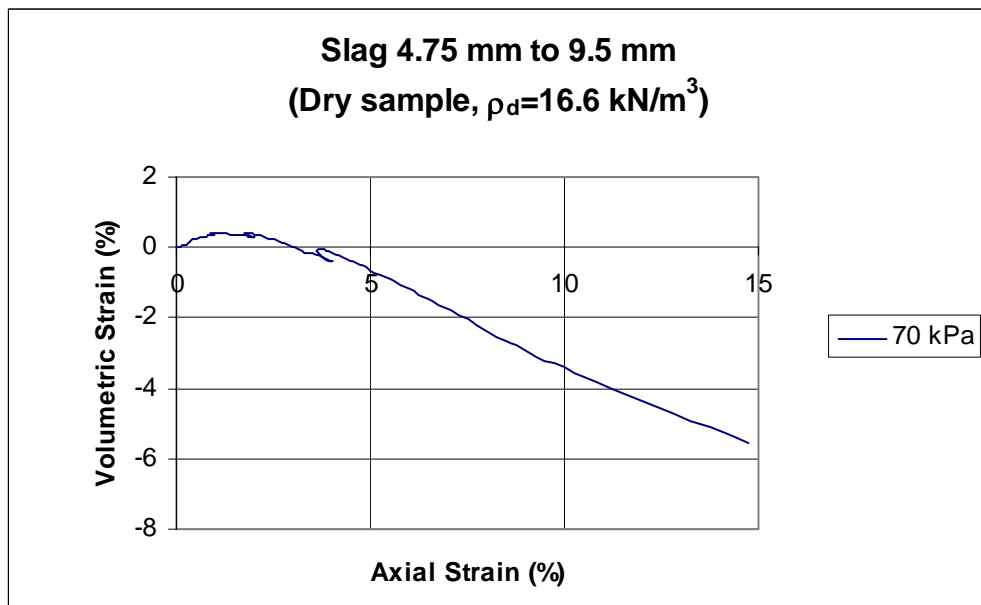
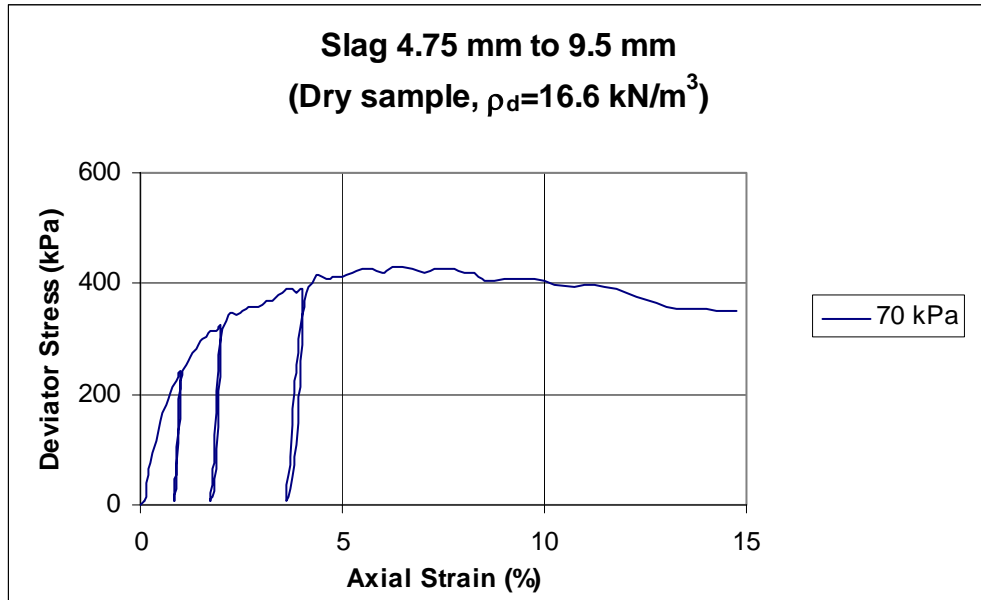


Figure C2

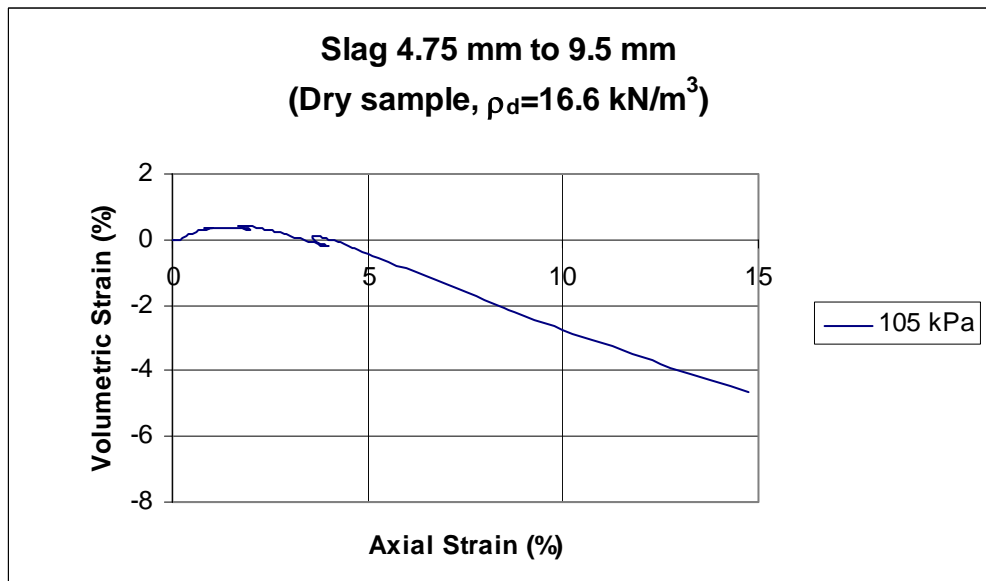
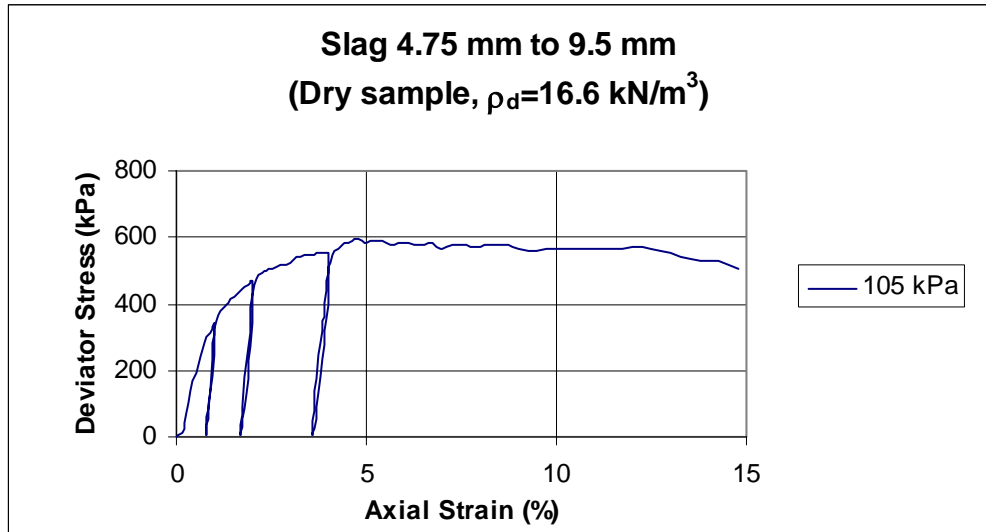


Figure C3

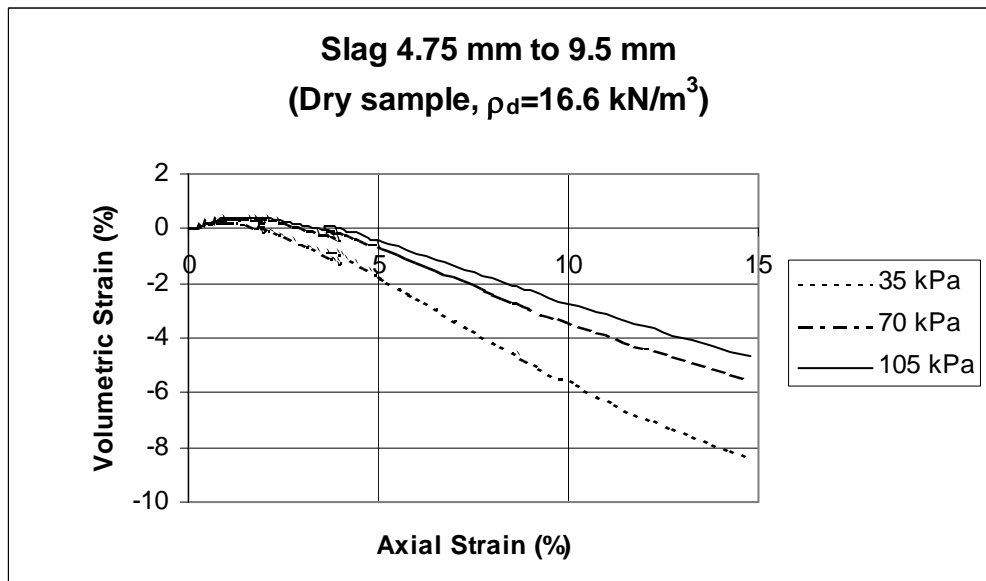
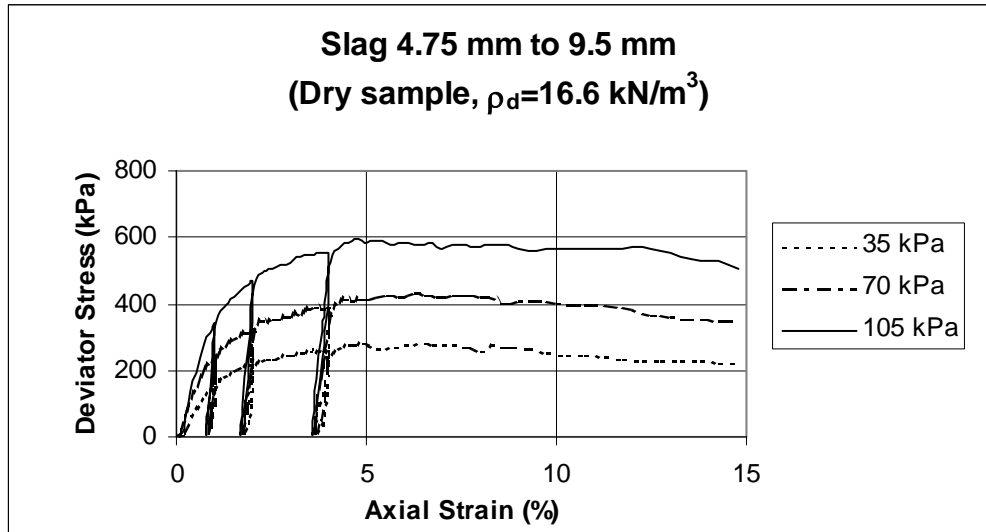


Figure C4

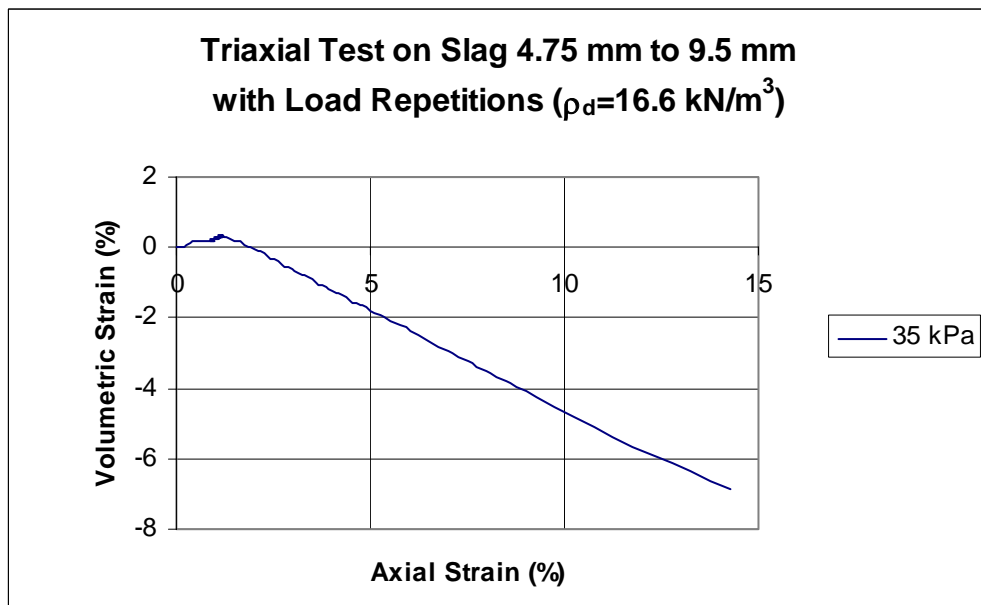
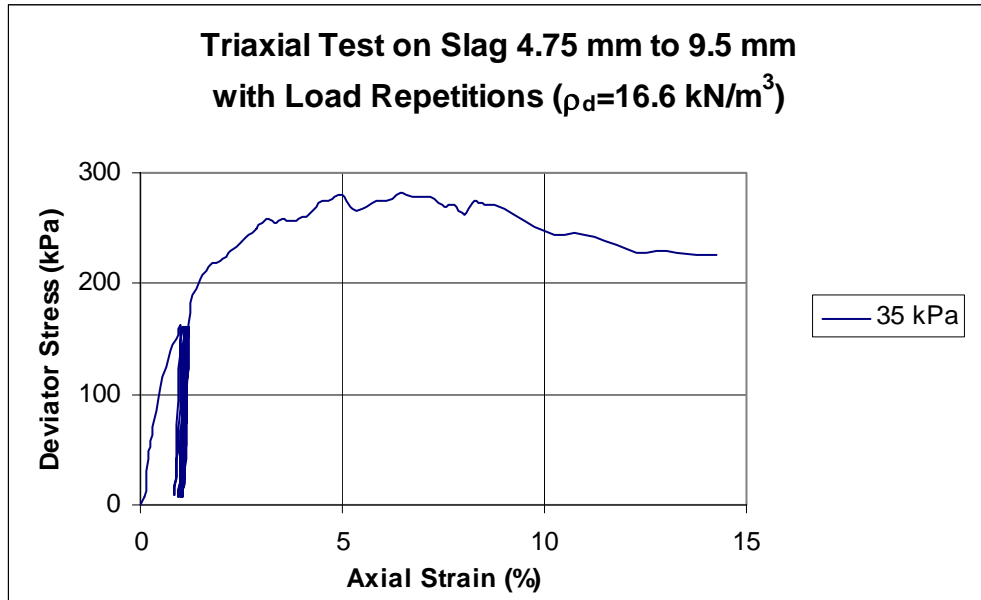


Figure C5

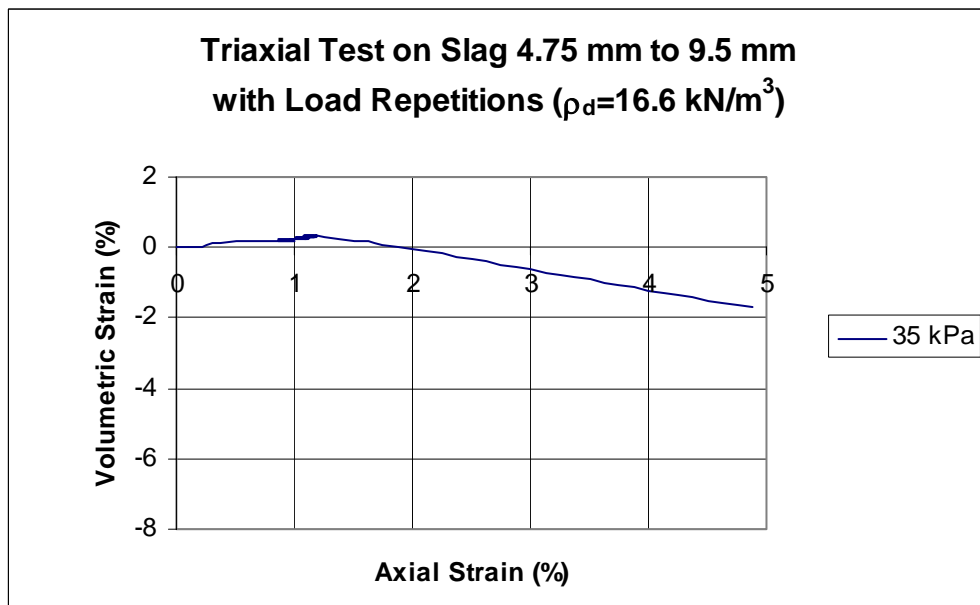
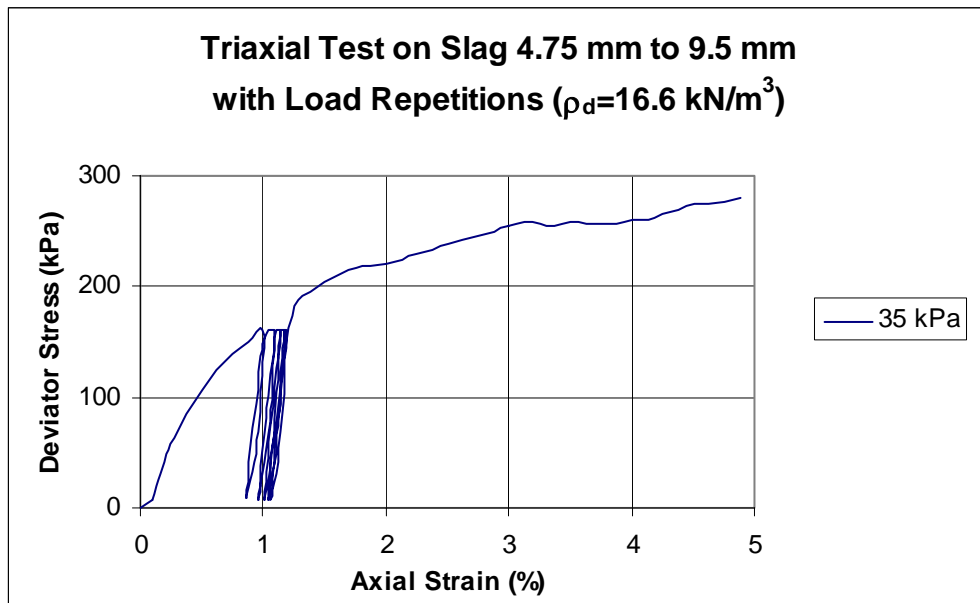


Figure C6

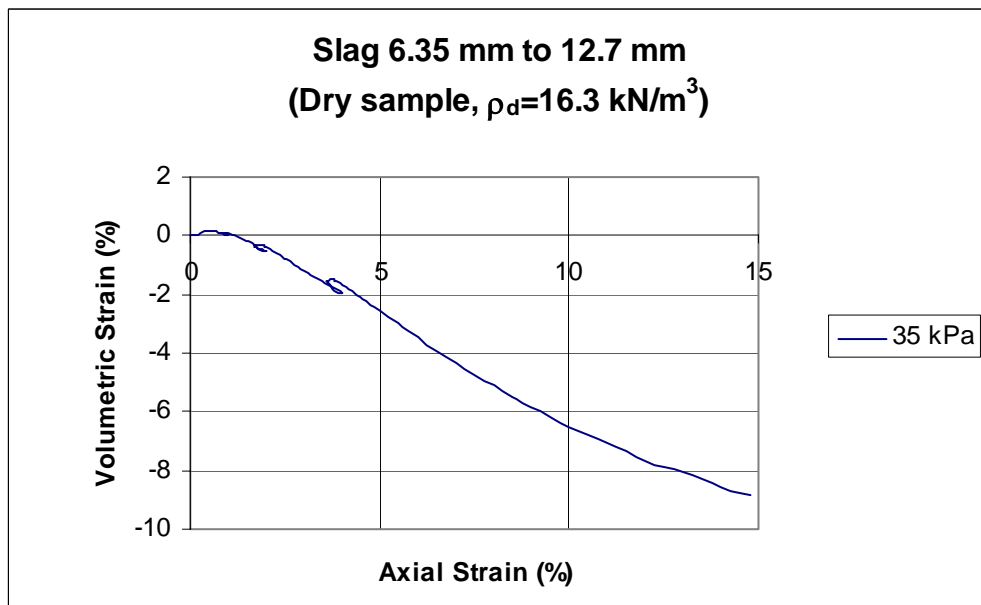
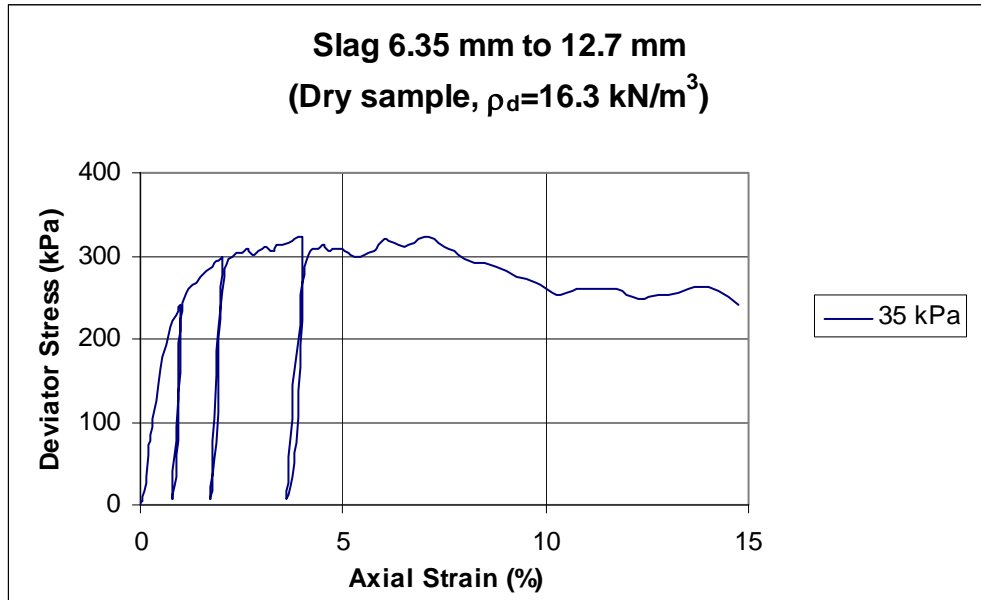


Figure C7

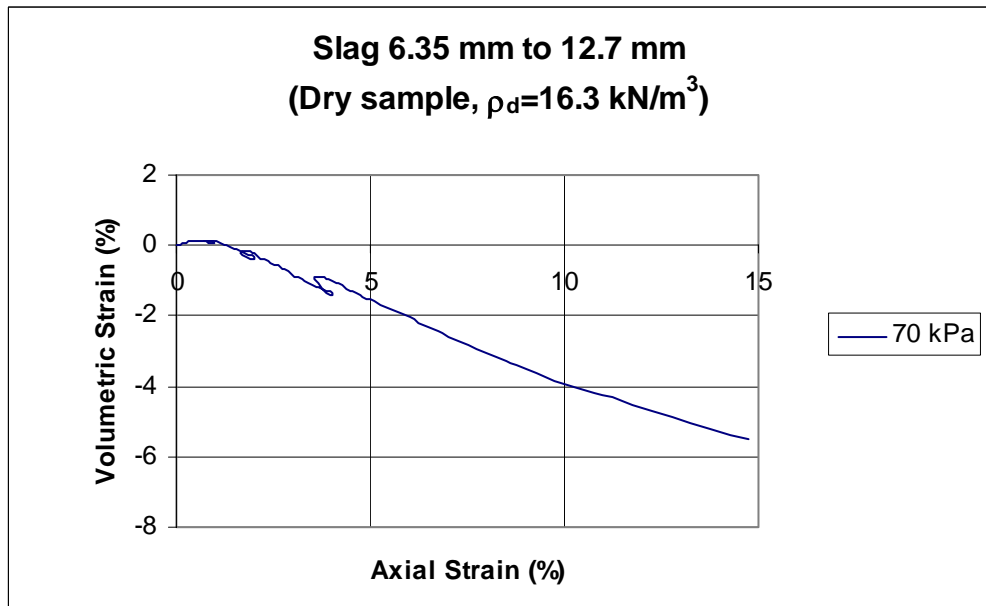
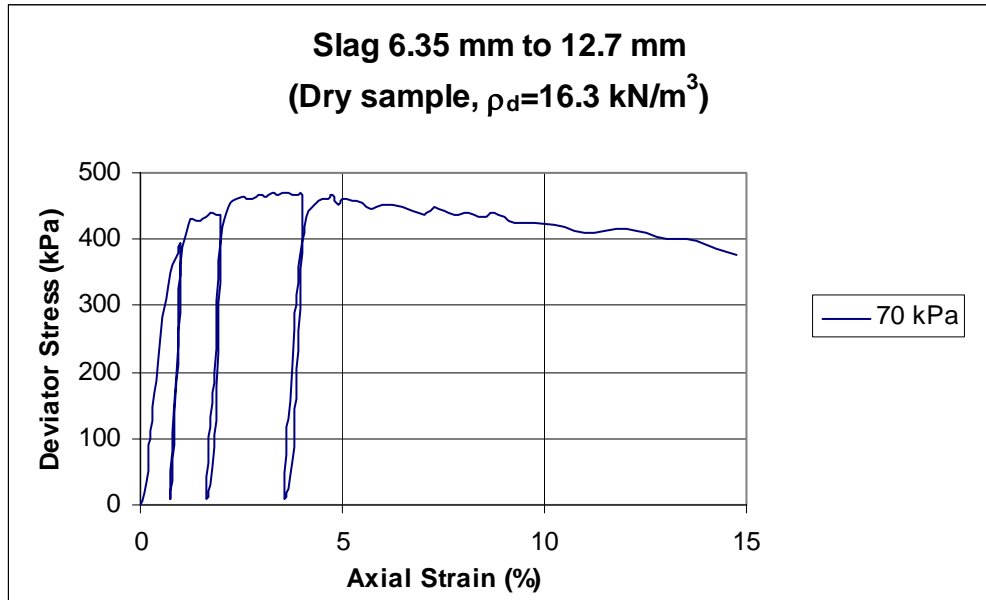


Figure C8

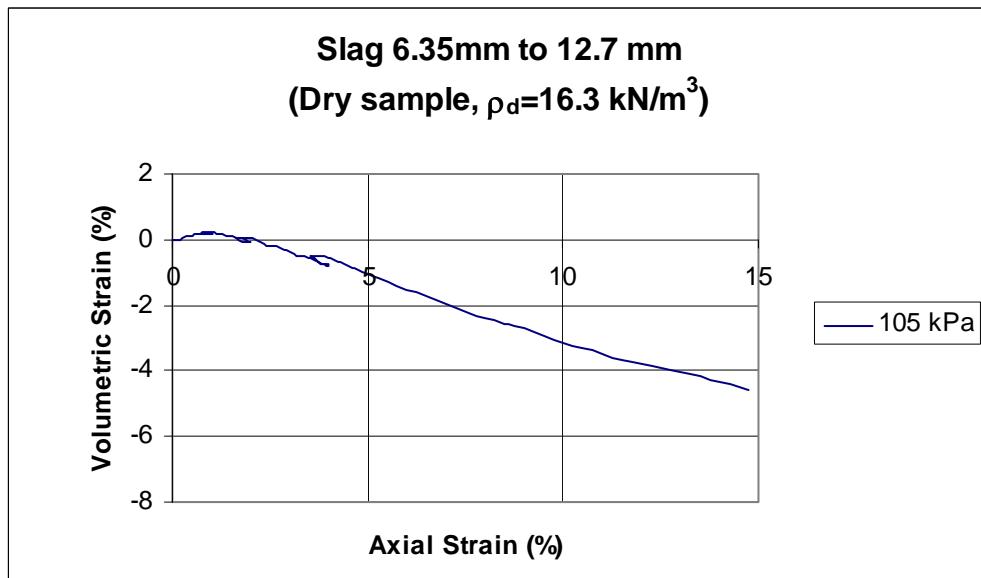
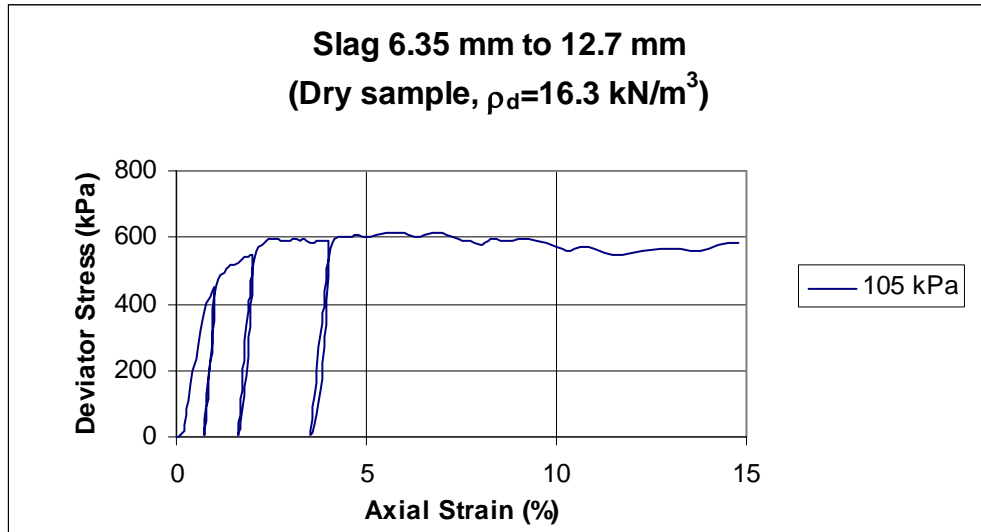


Figure C9

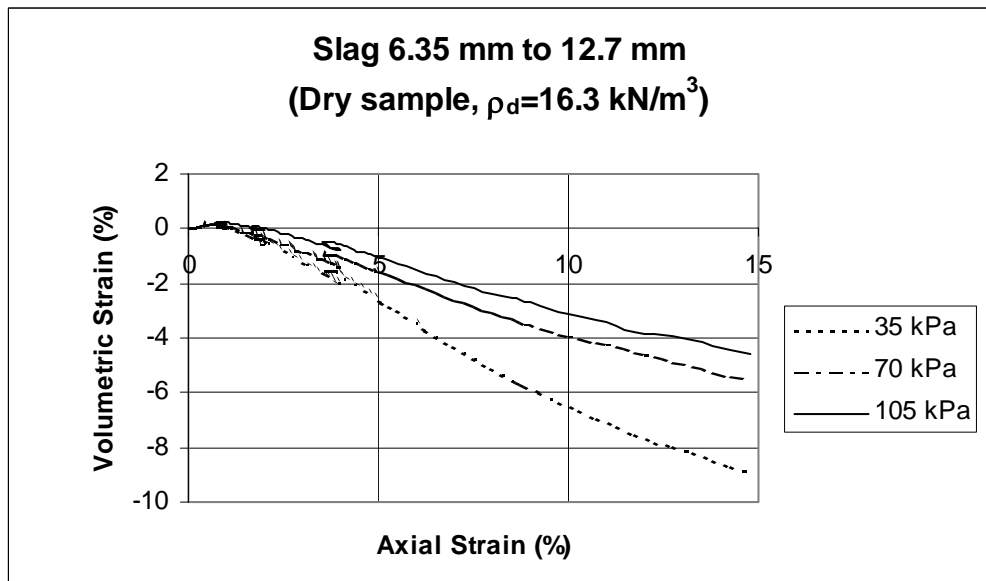
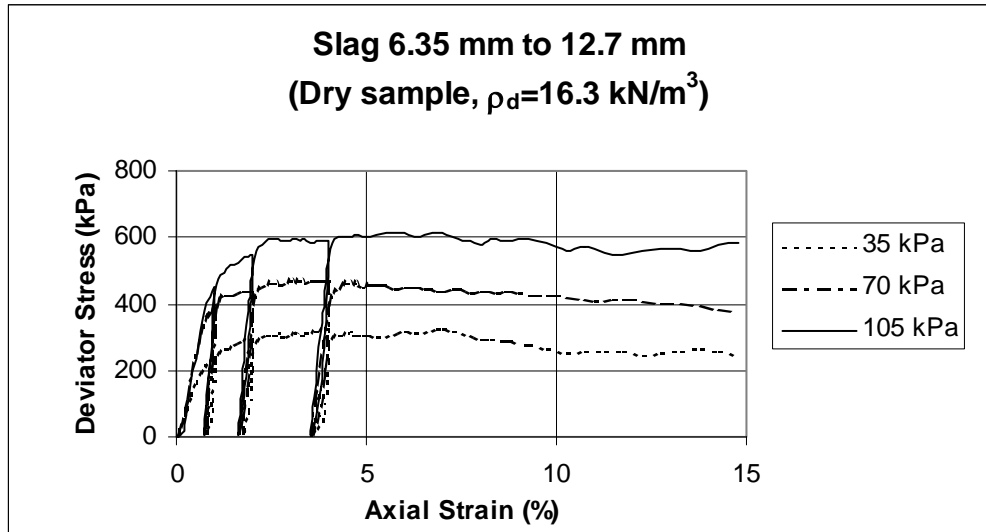


Figure C10

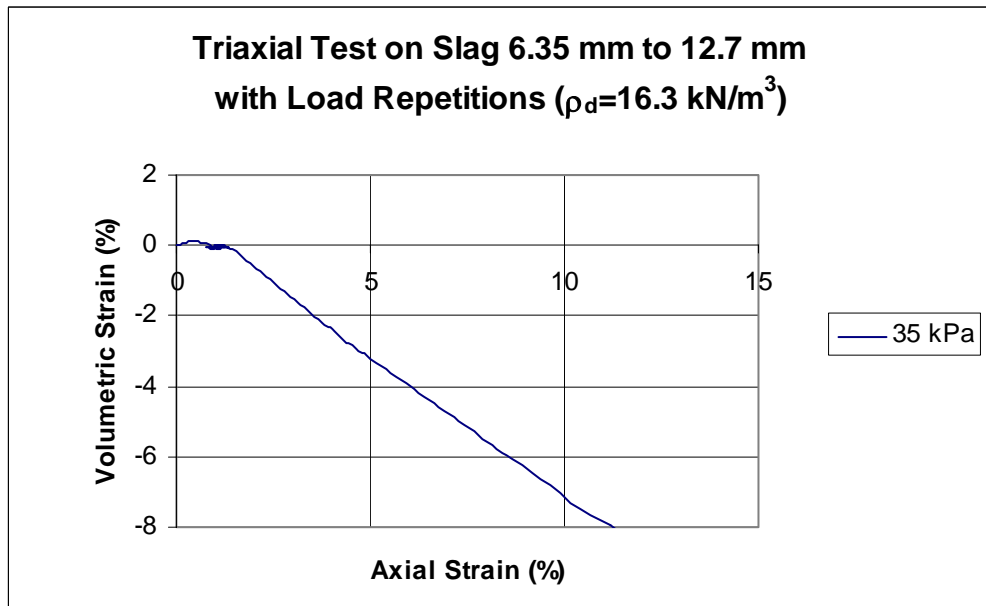
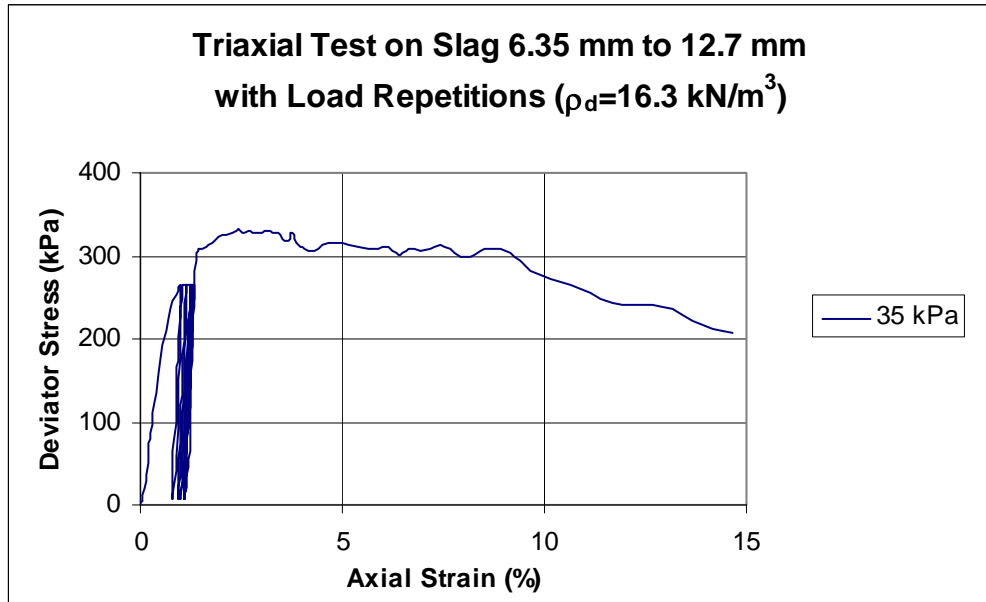


Figure C11

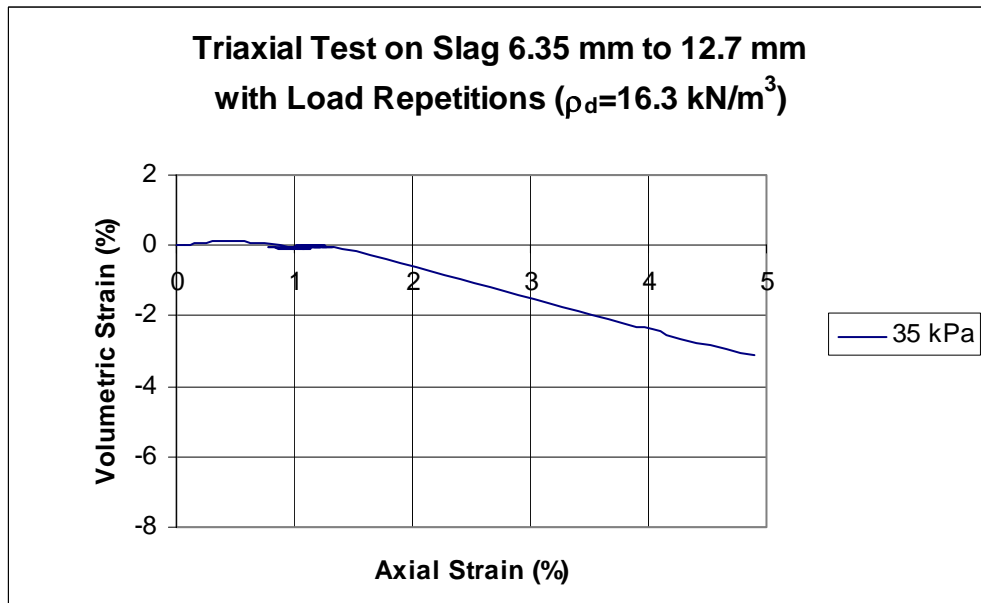
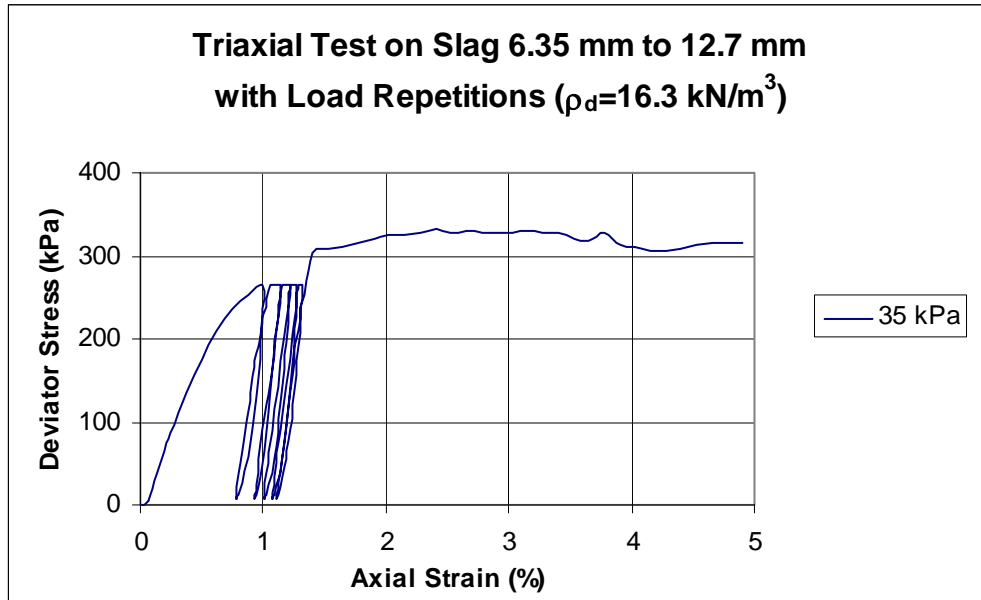


Figure C12

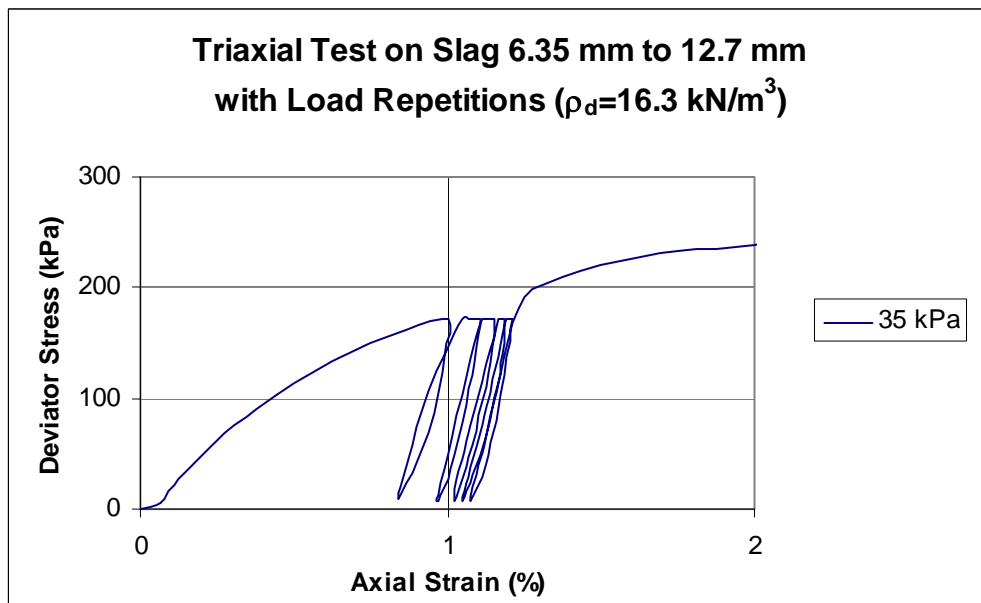
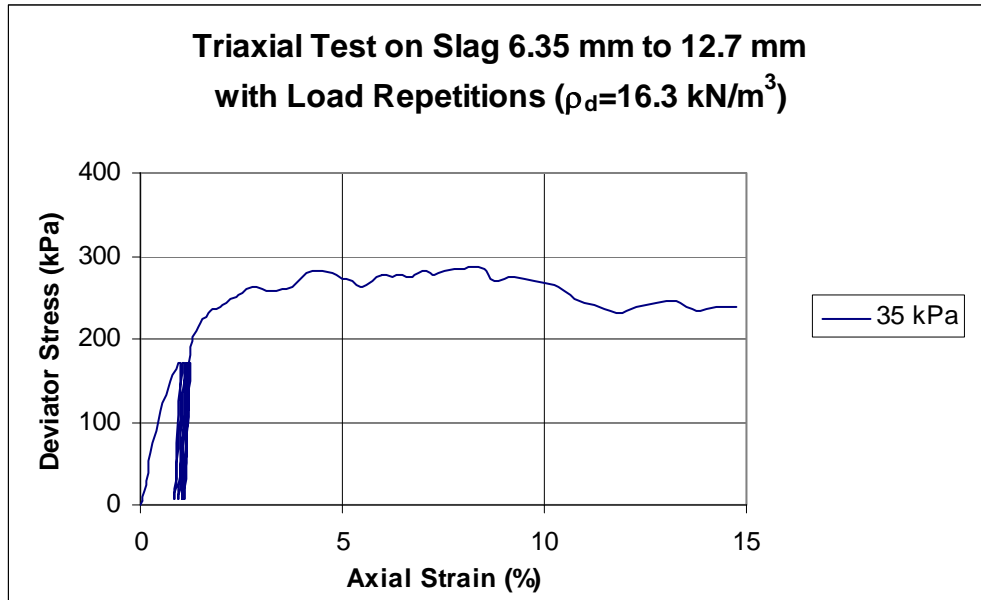


Figure C13

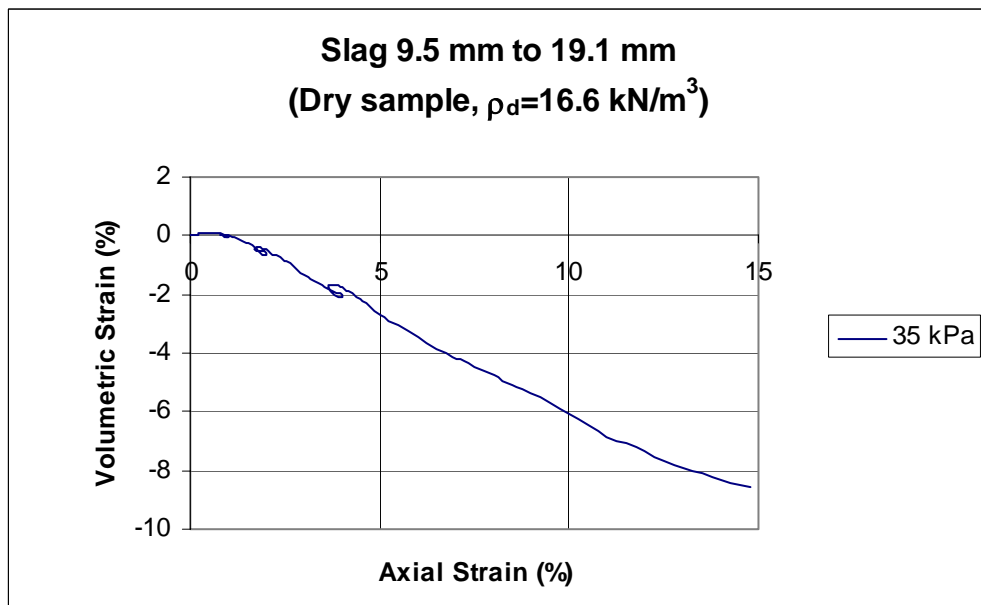
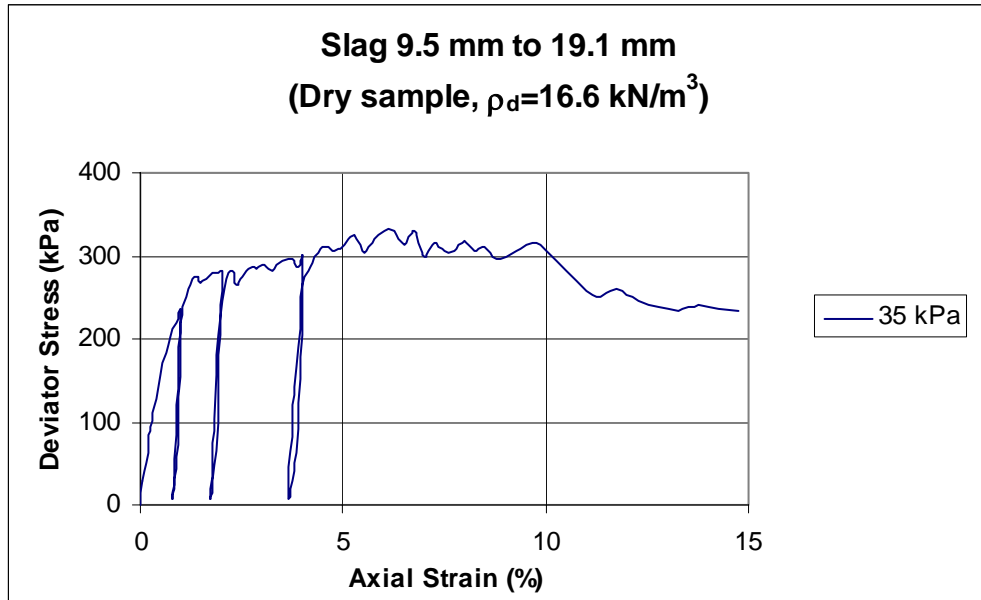


Figure C14

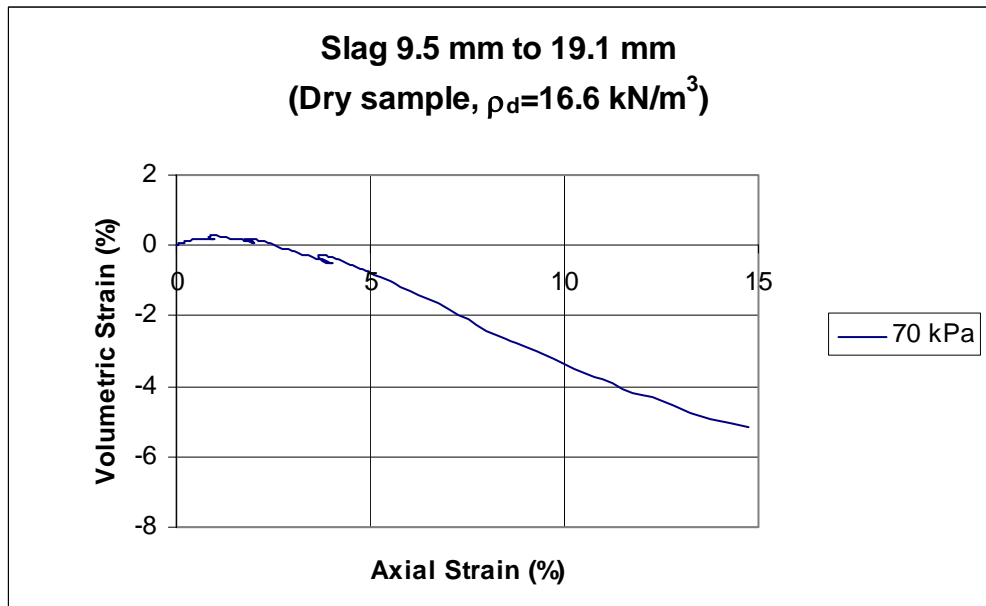
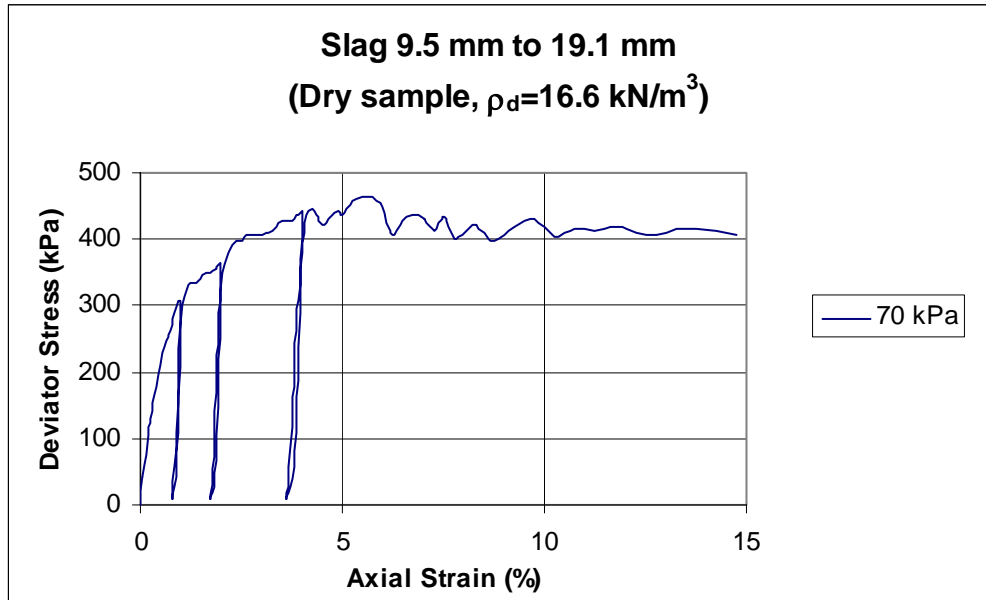


Figure C15

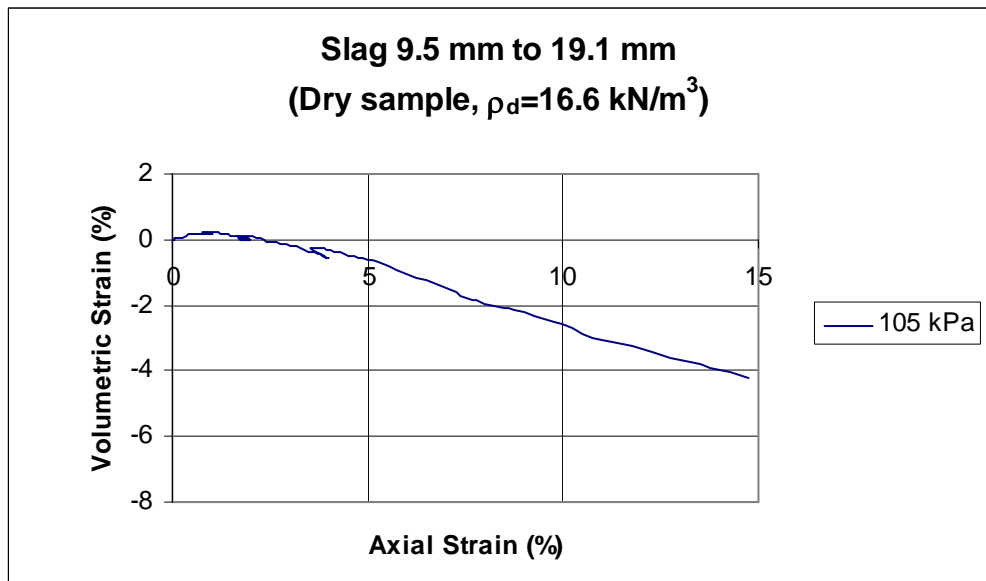
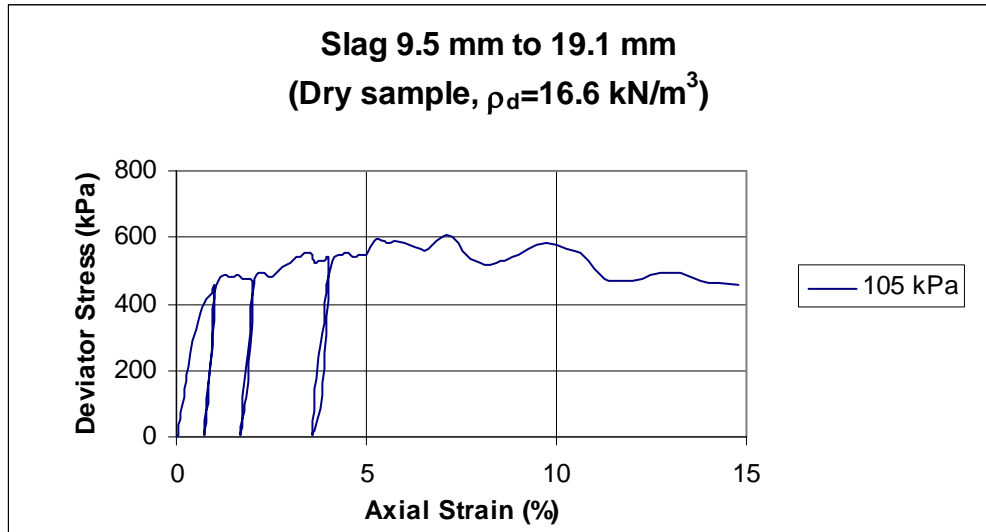


Figure C16

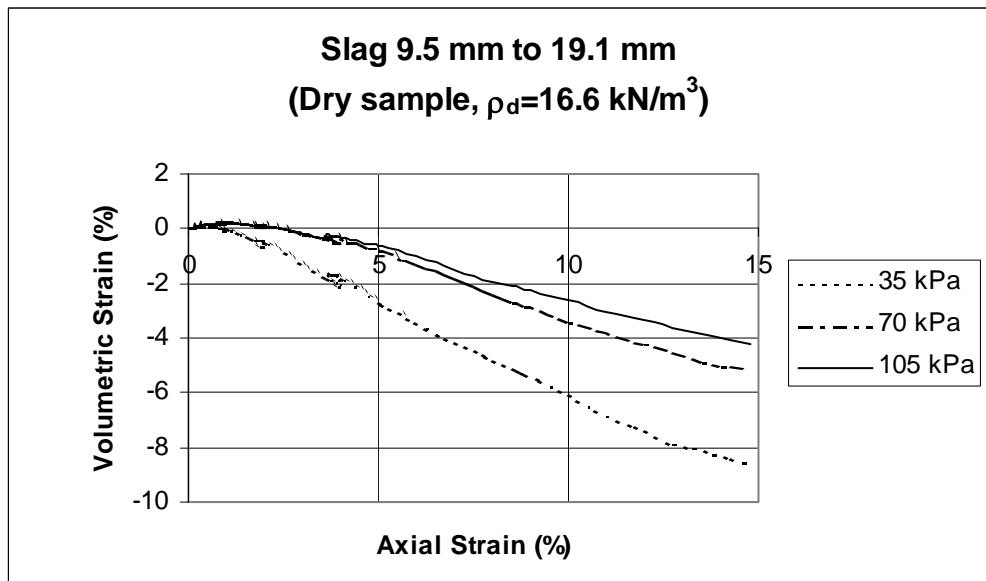
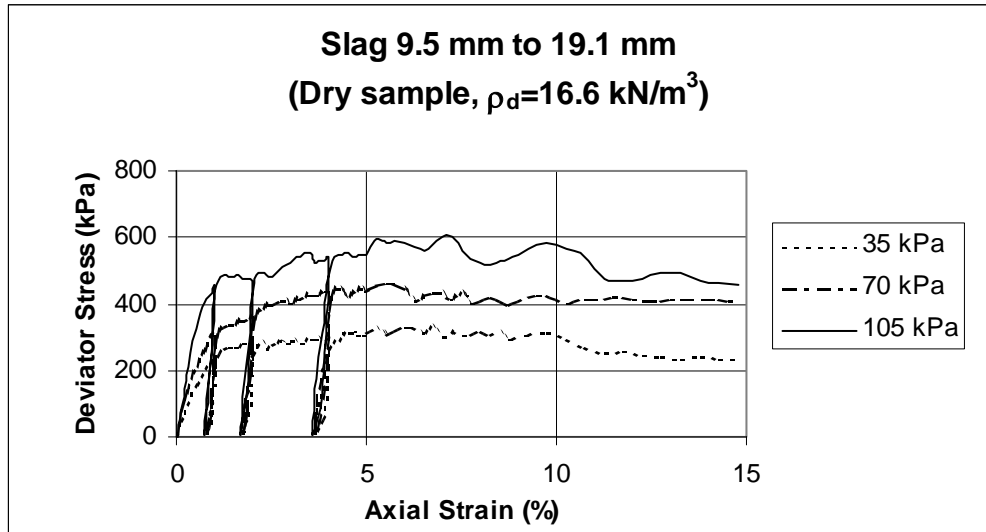


Figure C17

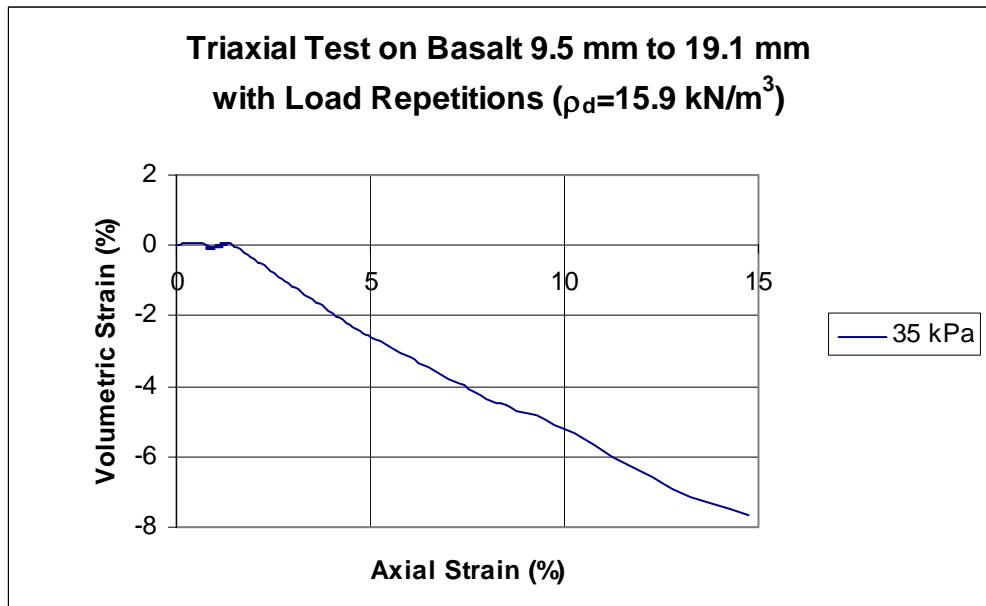
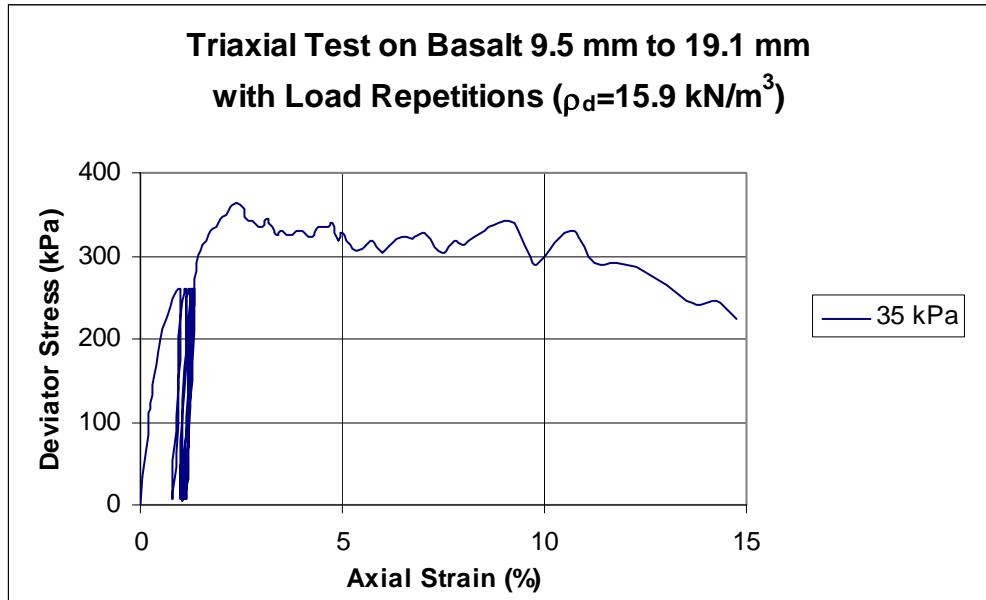


Figure C18

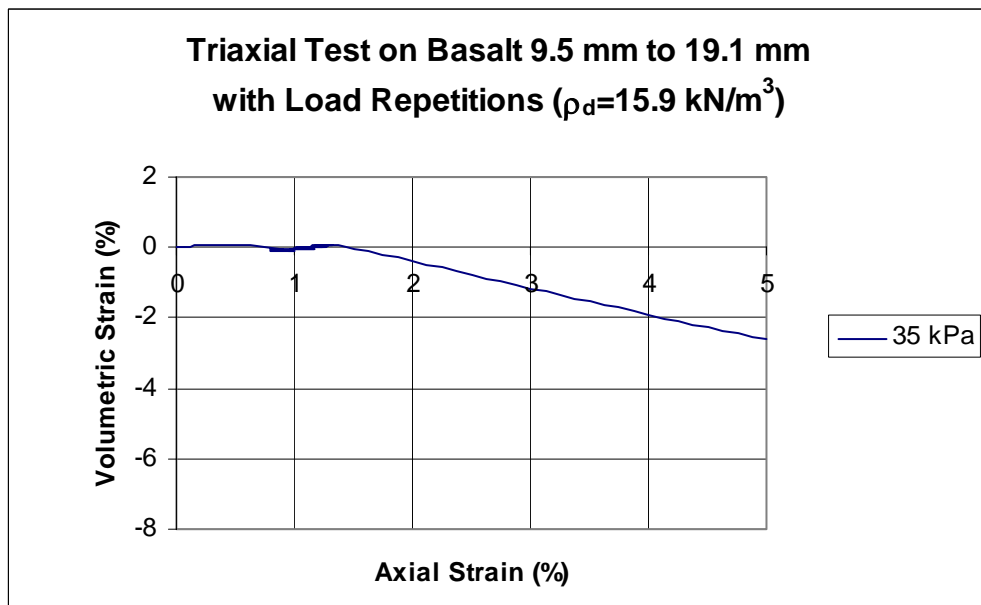
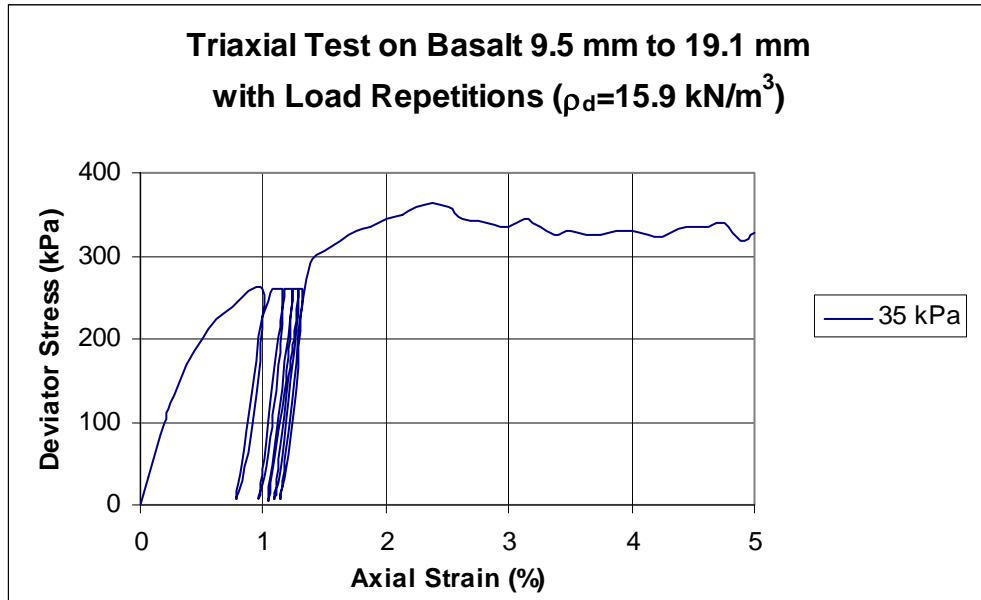


Figure C19

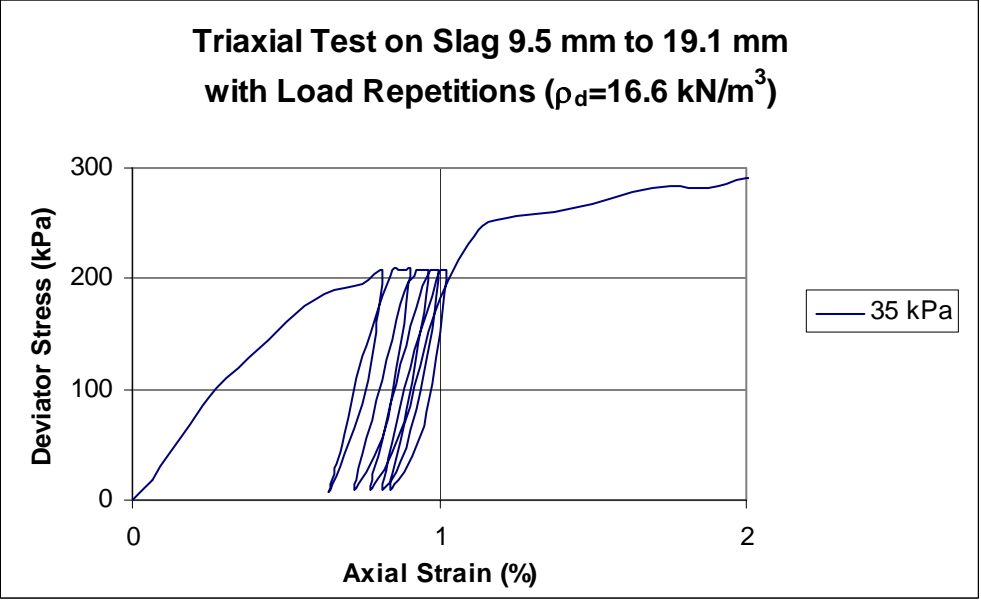
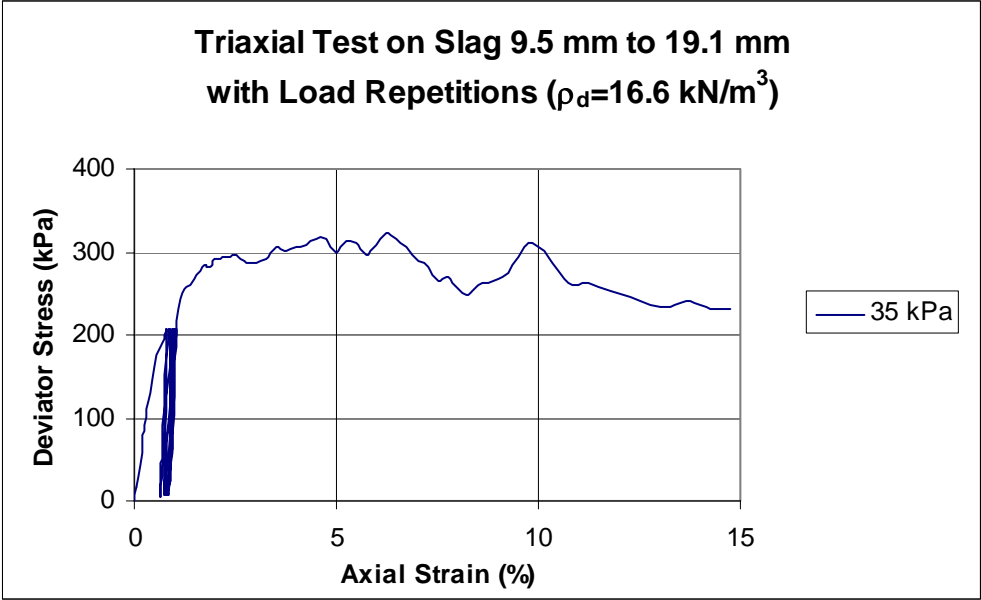


Figure C20

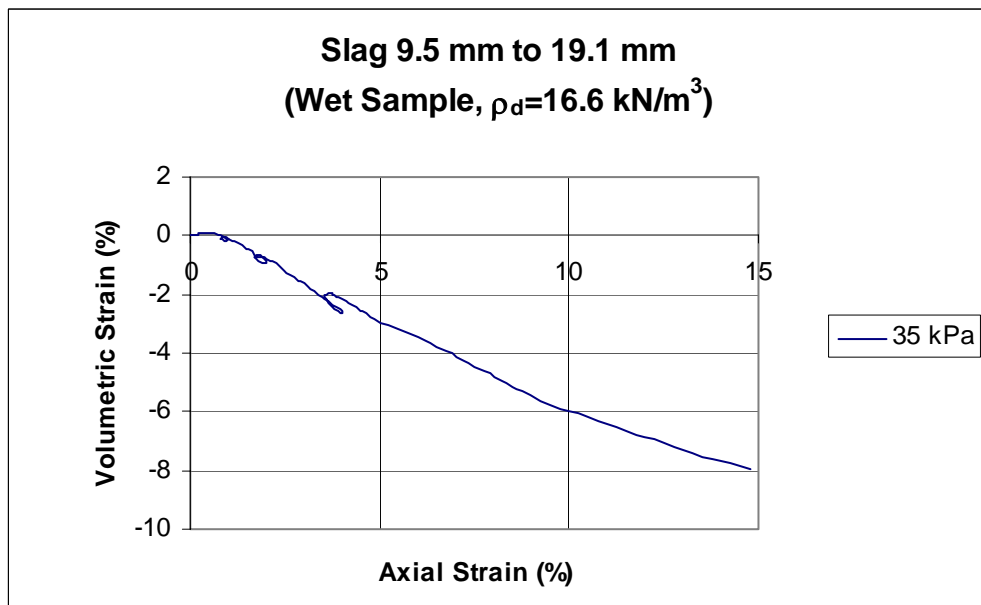
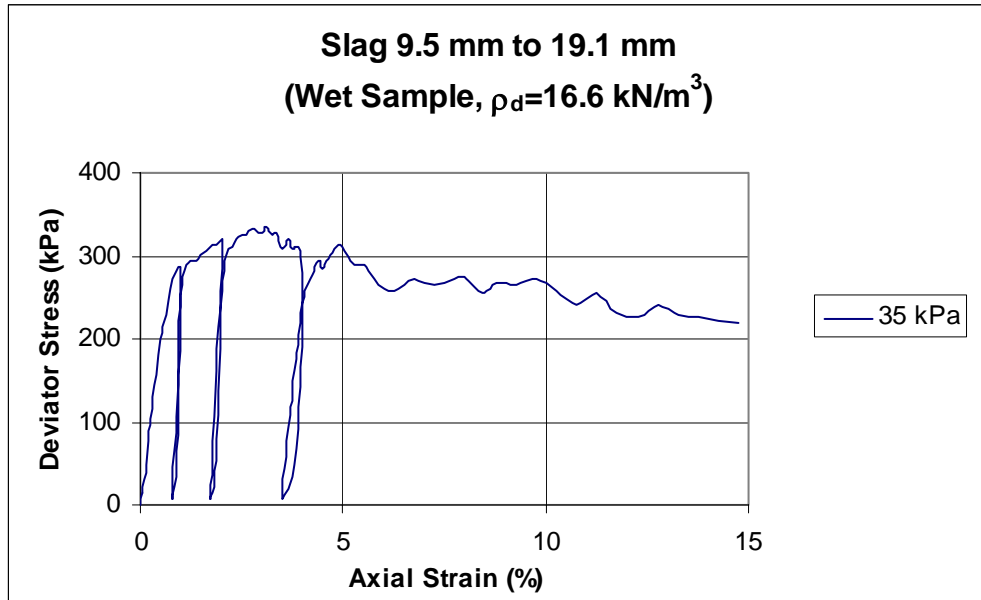


Figure C21

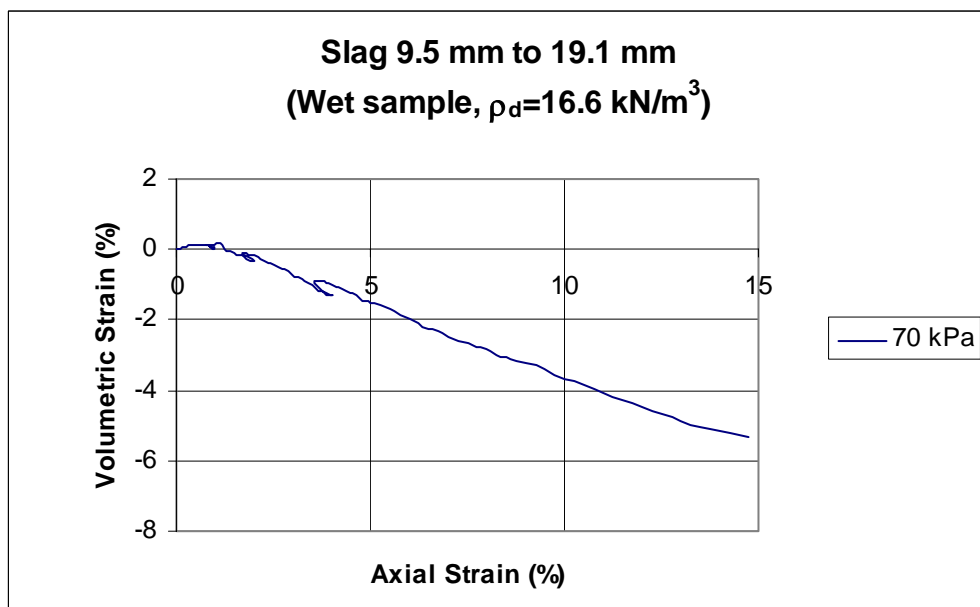
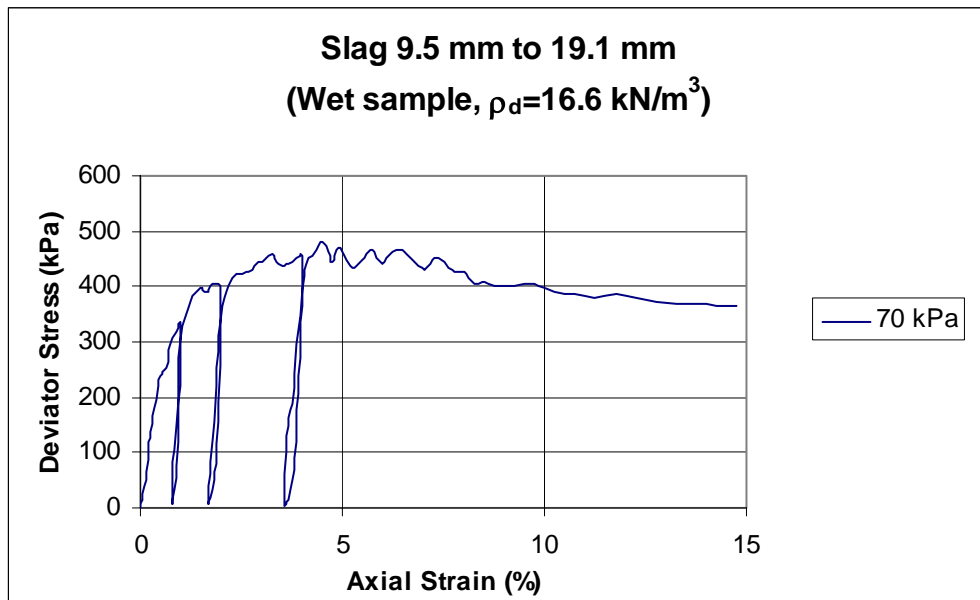


Figure C22

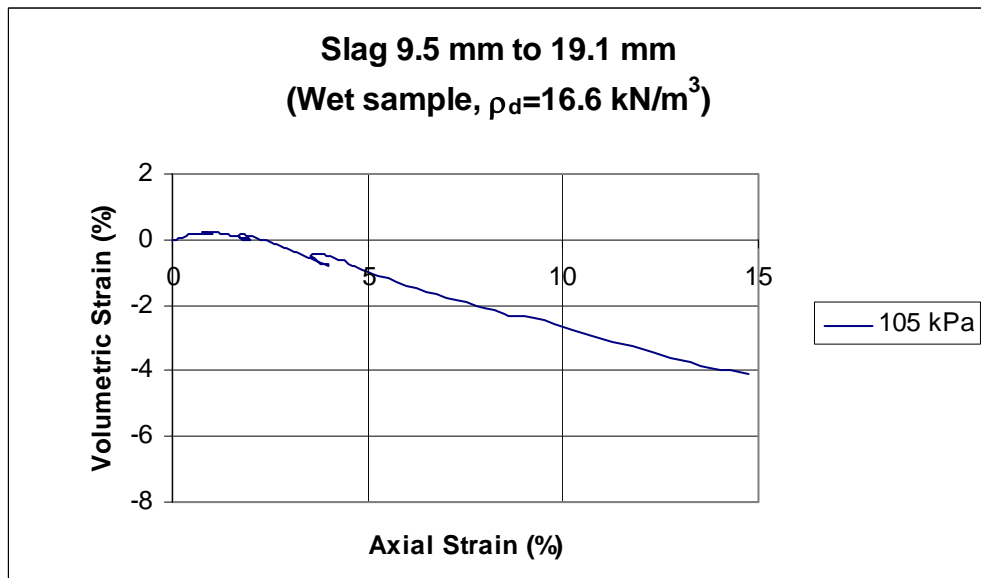
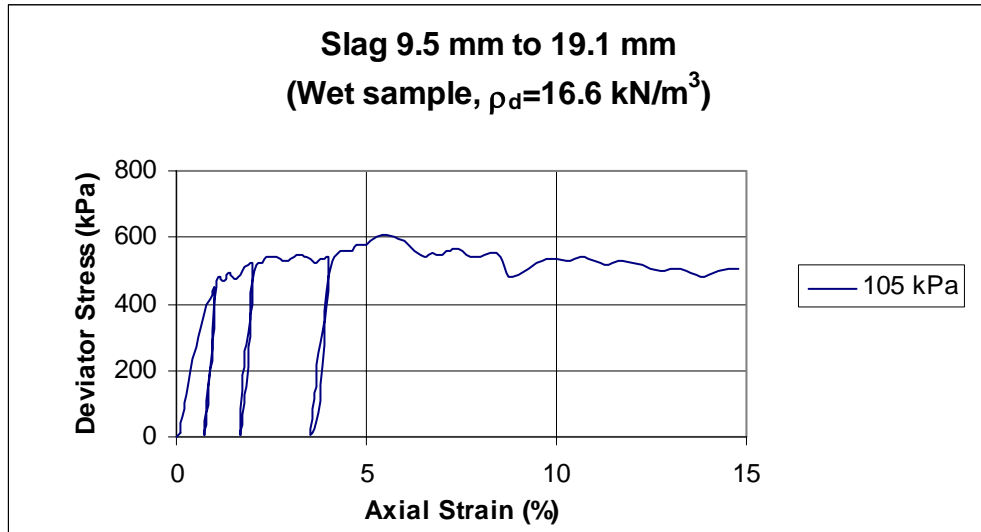


Figure C23

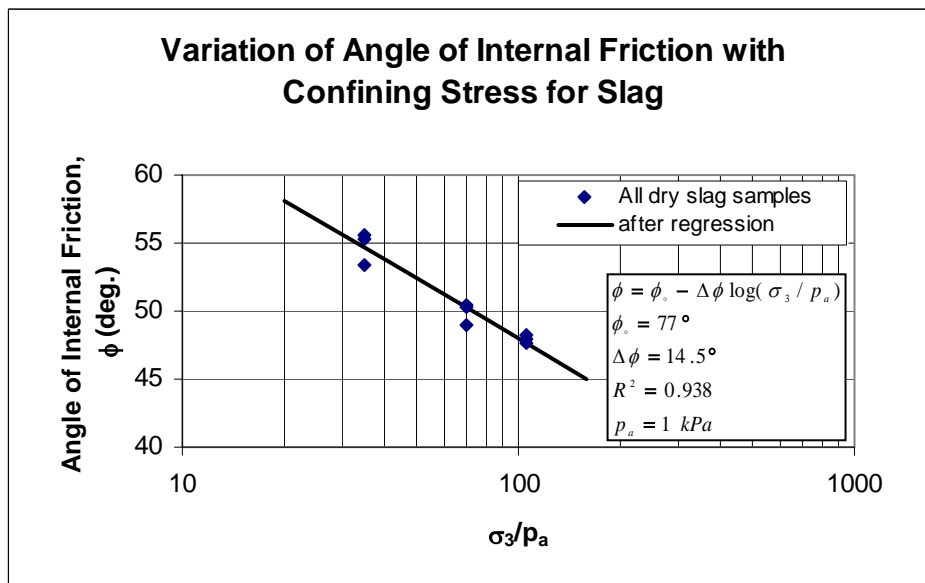
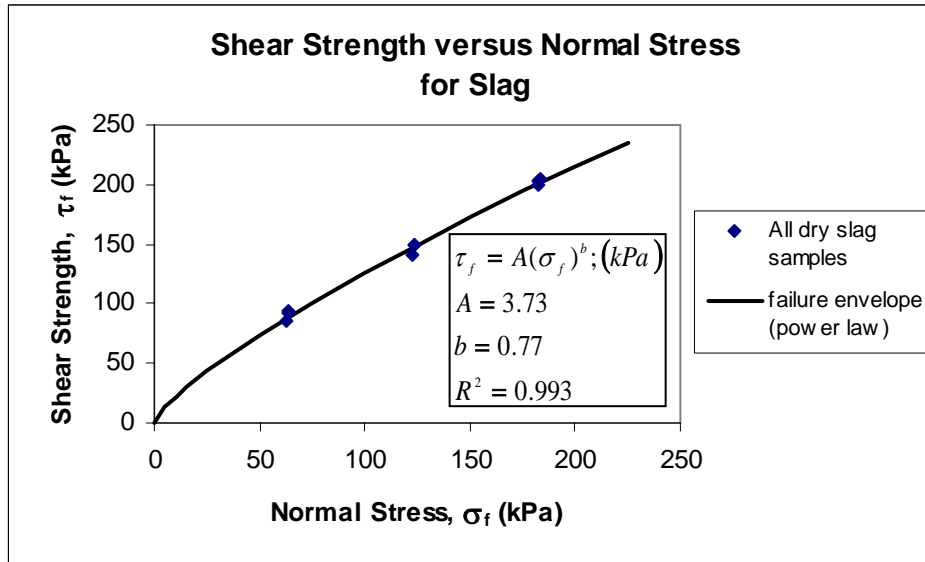


Figure C24

## VITA

Mustafa Kaya was born in Sivas, Turkey on January 11, 1967. He attended Middle East Technical University (METU), Ankara-Turkey and was graduated with a Bachelor of Science degree in 1989.

Upon graduation he worked as an Engineer for Turkish Railways until June 1993. Then he joined as a Research Assistant to Pamukkale University, Denizli-Turkey.

Sponsored by Pamukkale University, he entered the Graduate College of Illinois Institute of Technology, Chicago-Illinois in September 1993 and received his Master of Science degree in December 1994.

He attended the University of Colorado at Boulder for graduate studies. In September 1999, he resumed his Ph.D. at METU and has held appointment as a Research Assistant.